Universidade de Aveiro Departamento de Física,
2019

Carlos de Oliveira Amorim

Estudos Experimentais e Modelação de Heteroestruturas Multiferróicas Magnetoelétricas

Experimental and Modeling Studies of Magnetoelectric Multiferroic Heterostructured Materials

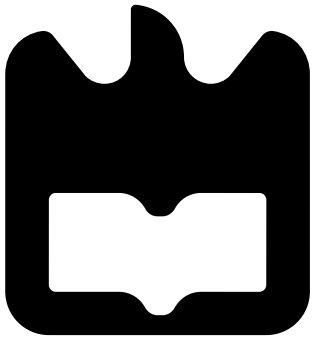

Universidade de Aveiro Departamento de Física,
2019

Carlos de Oliveira Amorim

Estudos Experimentais e Modelação de Heteroestruturas Multiferróicas Magnetoelétricas

Experimental and Modeling Studies of Magnetoelectric Multiferroic Heterostructured Materials

"I would rather have questions that can't be answered than answers that can't be questioned."

— Richard Feynman

Universidade de Aveiro Departamento de Física,
2019

Carlos de Oliveira Amorim

Estudos Experimentais e Modelação de Heteroestruturas Multiferróicas Magnetoelétricas

Experimental and Modeling Studies of Magnetoelectric Multiferroic Heterostructured Materials

Tese apresentada à Universidade de Aveiro para cumprimento dos requisitos necessários à obtenção do grau de Doutor em Física, realizada sob a orientação científica do Professor Doutor Vítor Brás de Sequeira Amaral, Professor Catedrático do Departamento de Física da Universidade de Aveiro e co-orientação do Doutor João Guilherme Correia, Investigador Principal do Instituto Superior Técnico da Universidade de Lisboa.

Tese realizada com apoio financeiro da FCT
através da bolsa SFRH/BD/93336/2013

o júri / the jury

presidente / president

Professor Doutor Vítor António Ferreira da Costa
Professor Catedrático da Universidade de Aveiro

vogais / examiners committee

Doutor Alessandro Stroppa
Investigador, Dipartimento di Fisica - Università degli Studi dell'Aquila

Professor Doutor Bernardo Gonçalves Almeida
Professor Auxiliar com Agregação da Universidade do Minho

Professor Doutor João Pedro Esteves de Araújo
Professor Associado da Universidade do Porto

Professora Doutora Maria do Rosário Pimenta Correia
Professora Auxiliar da Universidade de Aveiro

Professor Doutor Vítor Brás de Sequeira Amaral
Professor Catedrático da Universidade de Aveiro (Orientador)

agradecimentos / acknowledgements

A escrita de uma tese de doutoramento pode parecer apenas uma das etapas académicas para quem quer tentar a sua sorte no mundo da investigação científica. Porém, palavras como "apenas" e "sorte" no seio deste meio são claramente completamente desajustadas à realidade da situação. Ao longo minha tese de doutoramento verifiquei que há muitos obstáculos que vão aparecendo ao longo do percurso, fazendo com que haja uma esquizofrenia de sentimentos que vão desde o entusiasmo e satisfação de ver o nosso trabalho a dar frutos (sejam eles grandes ou pequenos), até ao desânimo e desespero quando surgem as "muralhas" que nos barram o caminho.
Não obstante, se há algo que se aprende rapidamente durante a jornada que é o doutoramento é que, assim como Sir Isaac Newton viu "mais longe por estar de pé sobre ombros de gigantes", também o estudante de doutoramento apenas consegue ver se tiver a fortuna de se poder "empoleirar nos ombros" dos seus colegas e amigos. Isto e uma pitada de audácia e destimidez, aliados a muita paixão pela ciência.
Desta forma, reservo esta parte da minha tese para agradecer a todos que me acompanharam durantes os últimos quatro anos.
Em primeiro lugar tenho de agradecer à FCT pela bolsa de doutoramento que me permitiu ter as capacidades financeiras necessárias à realização do trabalho feito durantes os quatro anos de doutoramento. Agradeço também ao departamento de Física da Universidade de Aveiro, assim como ao CICECO por terem fornecido as condições necessárias para o cumprimento do meu plano de trabalhos.
Agradeço à Professora Rosário Correia pela ajuda que me deu nas medidas de Raman, assim como na bibliografia que me indicou.
À Doutora Rosário Soares, por me ter ensinado a fazer as medidas de Difracção de raios-X, e por toda a simpatia que mostrou ao longo de todas as medidas feitas, mostrando-se sempre disponível quando tinha dúvidas no manuseamento do equipamento e/ou na utilização dos softwares de identificação de fases.
Ao Professor Armando Lourenço pela deposição das Heteroestruturas de titanato de bário e ferro usando o sputtering. Sem estas amostras a tese não seria certamente a mesma.
Ao Professor Marcus Dahlem e ao Karen, a quem devo as medidas de TEM e STEM/EDS, cruciais para a interpretação dos resultados dos filmes depositados por sputtering. Obrigado pela ajuda e por serem sempre tão prestáveis.
Um muito obrigado ao Professor Kristiaan Temst e ao Professor Lino Pereira por proporcionarem a minha estadia e acesso às instalações do IMBL em KU Leuven.

Agradeço também aos colegas de Leuven que me acompanharam e ajudaram no trabalho lá realizado, em particular ao Bas Opperdoes e ao Vincent Joly que me supervisionaram durante a deposição e caracterização dos filmes de ferro em MBE. Um obrigado especial ao Tiago Lima pela companhia e camaradagem durante os dois meses e meio que estive em Leuven, onde foi meu guia, em particular na degustação das cervejas locais, iguarias da cultura Belga (Ah, bela Westvleteren!).
Não posso deixar de agradecer aos colegas e amigos do meu grupo de trabalho: Abel, Ali, António, Amin, Daniel, Farzin, Maria João, João Nuno, João Horta, João Amaral, Pegah, Nuno Fortunato e Tiago.
Agradeço em particular ao Doutor João Nuno pela ajuda com os cálculos de DFT, assim como a ajuda na revisão dos textos da tese.
Ao Doutor João Amaral pela camaradagem e pelos conselhos relativos às opções de carreira científica que nem sempre consegui seguir por falta de perspicácia, mas que vão cada vez mais sendo assimilados. Obrigado também pela enorme ajuda na estruturação, escrita e revisão de artigos científicos.
Ao Abel pelas longas conversas que tivemos como amigos e alunos de doutoramento prestes a entregar a tese. Pelo trabalho conjunto e partilha de ideias. Pela enorme ajuda com os fits de PAC, assim como a hospitalidade aquando das minhas ias ao CERN. Pelo apoio mútuo nesta fase final da entrega da tese, onde o facto de estar numa situação idêntica fez com que as palavras de apoio viessem muitas vezes no momento certo.
Um agradecimento ao meu grupo de amigos: Anselmo e Pedro Correia (agora já doutores), Bruno Melo, Fábio Ferreira, João Costa, Pedro Prezas, Pedro Quinta e Rita, que me acompanharam durante toda a minha formação académica, e cujas amizades contribuíram para a sanidade mental necessária para escrita da tese.
Um particular destaque às tertúlias das "Conferências de Solvay", assim como ao meu parceiro de Boxe, Melo, ambos mecanismos de alívio de stress (no último caso o boxe/kickboxing e não o parceiro!).
Quero também agradecer ao meu coorientador, o Doutor João Guilherme Correia, pela disponibilidade na coorientação da minha tese, e por ser o pilar que sustenta a ponte entre Portugal e o ISOLDE, possibilitando assim as experiências baseadas em medidas de PAC.
É impossível acabar esta secção sem agradecer ao meu orientador, o Professor Vítor Amaral. Agradeço antes de mais por me ter acolhido no seio do seu grupo e me ter dado a oportunidade de trabalhar com ele desde o meu projecto de Licenciatura. Agradeço o gigante apoio científico, tendo sempre a capacidade de se debruçar sobre os resultados que fui obtendo com um olhar diferente, vendo sempre aquilo que não era óbvio, e retirando sempre alguma informação fascinante.

Agradeço as longas discussões de Física, que me espicaçaram ainda mais o gosto pela mesma, e onde aprendia sempre algo novo. Estas conversas tinham ainda o poder de me motivar mesmo quando julgava que o trabalho estava a correr mal. Obrigado também pela correção e competência científica, que me obrigou a evoluir não só como cientista, mas principalmente como pessoa. Por fim um muito obrigado pela sua compreensão, ajuda e principalmente pela sua amizade.

Finalmente quero agradecer às quatro pessoas mais importantes na minha vida.

Ao meu irmão, que sempre foi um verdadeiro irmão na acepção da palavra, e cuja amizade e irmandade me mostraram um lado mais maduro e adulto que desconhecia. Obrigado pela tua disponibilidade, partilha, apoio e altruísmo. Podes contar sempre comigo.

Aos meus pais tenho mesmo muito a agradecer! Tanto que se torna difícil pôr em palavras. É graças aos meus pais que tive a educação, formação e integridade que me definem atualmente como pessoa, e sem os quais não estaria neste momento a finalizar o doutoramento. Agradeço o apoio incondicional e a constante preocupação que têm comigo. Obrigado por acreditarem em mim e pelo investimento pessoal que fizeram na minha pessoa. Espero conseguir deixar-vos orgulhosos.

À Ana, minha namorada (agora noiva), minha companheira, minha confidente, meu amor. Obrigado pela paciência, cumplicidade, compreensão, e pelo apoio constante. Obrigado por seres o meu porto seguro, onde pude atracar sempre que me sentia perdido nesta difícil jornada que foi a tese. Obrigado gestos de carinho e por me teres proporcionado as condições para que eu me pudesse dedicar a 314.159% na escrita da tese.

Deixo também uma pequena menção às minhas duas gatas, Kiba e Tesla, que apesar de não serem pessoas, muita companhia me fizeram nas inúmeras noites que passei a escrever a teste.

Palavras-chave

$BaTiO_3$, Fe, Heteroestruturas, Filmes Finos, Teoria de Densidade Funcional, Materiais Magnéticos, Magnetismo, Ferromagnetismo, Paramagnetismo Antiferromagnetismo, Ferrimagnetismo, Óxidos Magnéticos, Ferroeletricidade, Polarização Elétrica, Propriedades Ferróicas, Materiais Multiferróicos, Acoplamento Magnetoelétrico, Estados de Spin, Transições de fase, Transições estruturais, Transições Ferroelétricas, Transições de Estado e Spin, Dispositivo Multiferróico, Estado de Spin Baixo, Estado de Spin alto, Estado de Spin Nulo, Densidade de Estados, Spins, Momento Magnético, Temperatura de Curie

Resumo

Materiais Multiferróicos são um tipo de materiais bastante exótico que apresentam simultaneamente dois ou mais tipos de propriedades ferróicas. Multiferróicos magnetoelétricos, em particular, são uma classe de materiais muito proeminente, principalmente devido às suas espantosas aplicações tecnológicas, tais como sensores magnéticos, dispositivos de conversão/colheita de energia, e memórias the alta eficiência.

Todavia, materiais magnetoelétricos intrínsecos são verdadeiramente raros e ainda não possuem propriedades adequadas ao uso do dia-a-dia. Uma das razões para que isto aconteça prende-se com o facto dos requisitos para existência de magnetismo e ferroeletricidade na matéria serem *a priori* contraditórios, uma vez que enquanto os primeiros necessitam de orbitais d^n semipreenchidas, os últimos tendem a favorecer orbitais d^0. Porém, Multiferróicos magnetoelétricos extrínsecos não sofrem desta limitação pois não partilham a mesma fase sendo portanto uma abordagem promissora para a construção de um bom Multiferróico magnetoelétrico.

Esta tese focar-se-á no estudo de sistemas contendo Fe e $BaTiO_3$ como meio de se alcançarem novos efeitos magnetoelétricos. Um auto-compósito de $BaTiO_3$:Fe é apresentado, que apesar da sua diminuta concentração de Fe (apenas 113 ppm atómicas), ainda assim apresenta um comportamento magnético ordenado. A magnetização do Fe apresenta duas variações bruscas no seu valor espontâneo, uma com $\Delta M/M \approx 32\%$ e outra com $\Delta M/M \approx 14\%$. Estas transições magnéticas estão correlacionadas com as transições de fase ferroelétricas do $BaTiO_3$ (ortorrômbica$\leftrightarrow$tetragonal e tetragonal$\leftrightarrow$cúbica).

Este auto-compósito magnetoelétrico foi a motivação par ao uso da Teoria de Densidade Funcional (DFT) como meio para descobrir os mecanismos microscópicos por trás deste acoplamento magnetoelétrico tão intenso. O estudo de uma mono-camada de Fe colocada sobre várias células unitárias de $BaTiO_3$ levaram à descoberta de várias interfaces com mudanças abruptas na sua magnetização espontânea, ora através do aumento ou diminuição dos momentos magnéticos do Fe, ora através da mudança entre a natureza antiferromagnética ou ferromagnética da camada de Fe.

Contudo, o destaque dos estudos de DFT reside na descoberta de um tipo particular de interfaces onde ocorre uma transição de estado High-Spin–Low-Spin que consegue colapsar completamente o momento magnético atómico dos átomos de Fe, dependendo do campo cristalino local sentido por esses mesmos átomos. Baseado neste efeito, um dispositivo Multiferróico magnetoelétrico foi proposto.

Sabendo a importância do campo cristalino para as transições de estado High-Spin–Low-Spin state, um estudo minucioso foi feito relativo ao gradiente de campo elétrico (EFG) nos sítios possíveis do $BaTiO_3$, usando um estudo combinado entre Correlações Angulares Perturbadas (PAC) e DFT. Neste estudo, concluiu-se que PAC não é uma técnica hiperfina adequada para o estudo quantitativo do tensor EFG de interfaces de $BaTiO_3$/Fe, dados os efeitos não desprezáveis das sondas radioativas na matriz de $BaTiO_3$.

Finalmente, foi feita a deposição de Heteroestruturas de BTO/Fe em substratos de $LaAlO_3$, MgO, Al_2O_3 e $SrTiO_3$ usando RF-Sputtering, assim como deposição de camadas de Fe em substratos de $BaTiO_3$ cortados nos planos (100), (110) e (111) planes, usando Molecular Beam Epitaxy (MBE), numa tentativa de recrear as interfaces com efeitos magnetoelétricos mais apelativos, previstos pela modelação DFT.

Os filmes finos depositados por sputtering mostraram o crescimento de múltiplos óxidos de Fe, Ba-Ti-O e Fe-Ti-O dependendo fortemente do substrato onde foram crescidos, assim como das condições de deposição e tratamentos térmicos. Porém, nenhum efeito magnetoelétrico foi observado nestes filmes.

Por outro lado, os filmes depositados nos substratos de $BaTiO_3$ mostraram grandes acoplamentos magnetoelétricos entre as fases ferroelétricas do BTO e a magnetização das camadas de Fe (à semelhança do que aconteceu no auto-compósito de $BaTiO_3$:Fe). A ordem de grandeza destes acoplamentos está fortemente correlacionada com a interface do BTO onde o Fe foi depositado, apresentando uma enorme variação na magnetização espontânea e na coercividade para o caso da transição romboédrica$\leftrightarrow$ortorrômbica, até $\Delta M/M \approx 148\%$ e $\Delta H_C/H_C \approx 183\%$ respetivamente para o caso da orientação (110).

Key-words

$BaTiO_3$, Fe, Heterostructures, Thin Films, Density Functional Theory, Magnetic Materials, Magnetism, Ferromagnetism, Paramagnetism Antiferromagnetism, Ferrimagnetism, Magnetic Oxides, Ferroelectricity, Electric Polarization, Ferroic Properties, Multiferroic Materials, Magnetoelectric Coupling, Spin State, Phase Transitions, Structural Transitions, Ferroelectric Transitions, Spin State Transitions, Multiferroic Device, Low Spin State, High Spin State, Null Spin State, Density of States, Spins, Magnetic Moment, Curie Temperature

Abstract

Multiferroic materials are a very exotic type of materials which present simultaneously two or more ferroic properties. Magnetoelectric multiferroics, in particular, are a very prominent class of materials, mainly due to their outstanding foreseen applications such as magnetic sensors, energy harvester/conversion devices, and high efficiency memories.

However, intrinsic magnetoelectric materials are quite rare and do not have, yet, the adequate properties to the everyday applications. One of the reasons for this to occur is due to the requirements for magnetism and ferroelectricity in matter being *a priori* contradictory, since the former needs unfilled d^n orbitals, while the latter favours d^0 orbitals. Nevertheless, extrinsic magnetoelectric multiferroics do not suffer from this problem because they do not share the same phase, hence being a very promising approach to engineer adequate magnetoelectric multiferroics.

This thesis focus on the study of Fe and $BaTiO_3$ systems as a means of achieving novel magnetoelectric effects. It is shown that a peculiar type of $BaTiO_3$:Fe auto-composite presents an ordered magnetic behaviour, despite the concentration of Fe being as low as 113 atomic ppm. The Fe magnetization displays two abrupt changes in its spontaneous value, one with $\Delta M/M \approx 32\%$ and the other with $\Delta M/M \approx 14\%$. These magnetic transitions are correlated the $BaTiO_3$ orthorhombic$\leftrightarrow$tetragonal and tetragonal$\leftrightarrow$cubic ferroelectric phase transitions.

This magnetoelectric auto-composite was the motivation to resort to Density Functional Theory (DFT) modeling as a means to discover the microscopic mechanism(s) behind such a strong magnetoelectric effect. The study of an iron monolayer placed upon several possible $BaTiO_3$ unit cells lead to the discovery of several interfaces with abrupt changes in their spontaneous magnetization, either through the enhancement and reduction of the Fe magnetic moments, or through the change between antiferromagnetic and ferromagnetic order of the Fe monolayer.

However, the highlight of these DFT studies lies in the discovery of a particular kind of interfaces, namely in the BTO221_2ndFe and BTO99_2ndFe supercells, where there is a High-Spin–Low-Spin state transition which can quench completely the atomic magnetic moment of each of Fe atom, depending on the local crystal field felt by the Fe atoms. Based on this specific effect, where it is possible to turn on and off the magnetic moments of the Fe atoms, a magnetoelectric multiferroic device was proposed.

Knowing the importance of the crystal field for the High-Spin–Low-Spin state transition, a thorough study regarding the Electric Field Gradient (EFG) of each possible $BaTiO_3$ site was performed, resorting to a combined study of DFT and Perturbed Angular Correlations (PAC) spectroscopy. In this study, it was concluded that the PAC spectroscopy is not the most adequate hyperfine technique to be used in a quantitative study of the $BaTiO_3$/Fe interfaces EFG tensor, due to the non-negligible effects of the radioactive probe on the $BaTiO_3$ matrix.

Finally, the deposition of BTO/Fe heterostructures on $LaAlO_3$, MgO, Al_2O_3 and $SrTiO_3$ substrates using RF-Sputtering, and the Molecular Beam Epitaxy (MBE) deposition of Fe layers on $BaTiO_3$ cut at the (100), (110) and (111) planes were performed as an attempt to recreate the interfaces with the most appealing magnetoelectric effects predicted in the DFT modeling. The thin films deposited using sputtering showed the growth of many Fe, Ba-Ti-O and Fe-Ti-O oxides depending strongly on their substrate, as well as in the deposition and annealing conditions. Still no magnetoelectric coupling was observed in such thin films.

On the other hand the Fe thin films deposited on $BaTiO_3$ substrates showed large magnetoelectric couplings between the $BaTiO_3$ ferroelectric phase transitions and the magnetization of the Fe layers (similarly to what happened in the $BaTiO_3$:Fe auto-composite). The magnitude of this magnetoelectric couplings is strongly correlated with the BTO interface where the Fe was deposited, showing a huge change in spontaneous magnetization and coercivity for the rhombohedral$\leftrightarrow$orthorhombic ferroelectric phase transition up to $\Delta M/M \approx 148\%$ and $\Delta H_C/H_C \approx 183\%$ respectively for the (110) case.

Contents

Contents i

List of Figures v

List of Tables xiii

1 Introduction 1

2 Theoretical Background 5
2.1 Classical Electromagnetism . . . 5
2.2 Magnetic Dipole Moment . . . 9
2.2.1 Quantum Magnetic Dipole Moment . . . 9
2.3 Magnetic Dipole Interactions . . . 12
2.4 The Exchange Integral . . . 12
2.4.1 Direct Exchange interaction . . . 14
2.4.2 Superexchange interaction . . . 14
2.4.3 RKKY interaction . . . 15
2.4.4 Double Exchange interaction . . . 16
2.4.5 Antisymmetric Exchange interaction . . . 17
2.4.6 Biquadratic Exchange interaction . . . 17
2.5 Crystal Field . . . 18
2.5.1 Orbital Quenching . . . 20
2.5.2 Jahn-Teller Effect . . . 21
2.5.3 High-Spin–Low-Spin transition . . . 22
2.6 Order Parameters and Symmetry Breaking . . . 23
2.6.1 Paramagnetism . . . 24
2.6.2 Ferromagnetism . . . 26
2.6.3 Antiferromagnetism . . . 29
2.6.4 Diamagnetism . . . 31
2.7 *Ab initio* calculations . . . 33
2.7.1 Born-Oppenheimer approximation . . . 33
2.7.2 The Hartree-Fock method . . . 34
2.7.3 Density Functional Theory . . . 35
2.7.4 The Exchange-Correlation Functional . . . 38
Local Density Approximation . . . 38
Generalized Gradient Approximation . . . 39
2.8 Hyperfine Interactions . . . 39

2.8.1 Hyperfine Magnetic Field . . . 40
2.8.2 Electric Field Gradient . . . 40

3 State of the Art 45
3.1 Multiferroic Materials . . . 45
3.2 The Magnetoelectric effect . . . 47
3.3 An historical retrospective of Magnetoelectric materials . . . 49
3.4 Multiferroics and Magnetoelectrics Popularity . . . 51
3.5 Magnetoelectric Multiferroic Materials . . . 53
3.5.1 Type I multiferroics . . . 54
Multiferroic Perovskites . . . 54
Lone Pairs based Ferroelectricity . . . 55
Improper Geometric Ferroelectricity . . . 55
Charge Ordering Ferroelectricity . . . 56
3.5.2 Type II multiferroics . . . 58
Magnetostrictive ferroelectricity . . . 58
Inverse Dzyaloshinskii-Moriya effect . . . 59
3.6 Magnetoelectric Multiferroic Applications . . . 60
3.6.1 Magnetic Sensors . . . 60
3.6.2 Energy Harvester and Conversion Devices . . . 61
3.6.3 Electrically Switchable Permanent Magnets . . . 61
3.6.4 Multiferroic Hard Disk . . . 61
3.6.5 MEMRAM . . . 62

4 Experimental Techniques 63
4.1 X-ray Diffraction . . . 63
4.1.1 Grazing Incidence X-ray Diffraction . . . 65
4.2 Rietveld refinement . . . 67
4.2.1 Quality Criteria . . . 68
4.3 Scanning Electron microscope . . . 69
4.3.1 Imaging Modes . . . 71
High-Resolution mode . . . 72
High-Current mode . . . 72
Low-Voltage mode . . . 73
Depth-of-Focus mode . . . 73
4.4 Scanning Transmission Electron Microscopy . . . 73
4.5 Characteristic X-ray Spectral lines . . . 75
4.6 *Bremsstrahlung* . . . 76
4.7 Energy-Dispersive X-ray Spectroscopy . . . 77
4.8 Particle Induced X-ray Emission Spectroscopy . . . 77
4.9 Raman Spectroscopy . . . 78
4.10 Superconducting Quantum Interference Device . . . 80
4.10.1 DC SQUID . . . 81
4.11 Perturbed Angular Correlations Spectroscopy . . . 82
4.12 Sputtering Deposition . . . 85
4.13 Molecular Beam Epitaxy . . . 87

5 A Peculiar Type of $BaTiO_3$:Fe **89**
5.1 The Ferroelectric Archetype . . . 89
5.1.1 $BaTiO_3$ magnetic properties . . . 90
5.1.2 $BaTiO_3$:Fe . . . 91
5.2 A Unique $BaTiO_3$:Fe . . . 92
5.2.1 X-ray Diffraction . . . 94
5.2.2 $BaTiO_3$:Fe_{113ppm} magnetic properties . . . 95
5.2.3 Raman Spectroscopy . . . 98
5.3 Searching Fe preferred coalescing sites . . . 100
5.3.1 SEM/EDS mapping and Fe statistical distribution . . . 101
5.3.2 Thermal annealing stability . . . 103
5.3.3 The role of $BaTiO_3$ grain boundaries . . . 104
5.4 Final considerations about $BaTiO_3$:Fe_{113ppm} . . . 105

6 DFT Modeling of $BaTiO_3$(001)/Fe interfaces **109**
6.1 BTO221_001/Fe and BTO99_001/Fe . . . 110
6.1.1 BTO/1stFe . . . 110
6.1.2 BTO/2ndFe . . . 128
6.1.3 High-spin–Null-spin phase transition . . . 143
Crystal Field effect in Hyperfine Interactions . . . 147
Nanoengineering towards a switchable spin state multiferroic . . . 150

7 DFT Modeling of other $BaTiO_3$/Fe interfaces **155**
7.1 BTO38 . . . 155
7.1.1 BTO38_1stFe . . . 158
7.1.2 BTO38_2ndFe . . . 163
7.1.3 BTO38_1stFe_O2 . . . 167
7.1.4 BTO38_2ndFe_O2 . . . 171
7.2 BTO160 . . . 175
7.2.1 BTO160_1stFe . . . 177
7.2.2 BTO160_2ndFe . . . 180
7.2.3 BTO160_3rdFe . . . 183
7.2.4 BTO160_Triangular . . . 186
7.3 Fe on top of BTO99 and BTO221 {110} and {111} lattice planes . . . 188
7.4 BTO221(99)_{110}/Fe . . . 193
7.4.1 Comparison between BTO38_1stFe and BTO_{110}/Fe . . . 193
7.4.2 Comparison between BTO38_2ndFe and BTO_{110} /Fe . . . 197
7.4.3 Comparison between BTO38/Fe_O2 and BTO_{110} /Fe_O2 . . . 200
7.5 BTO221(99)_110_2/Fe . . . 203
7.5.1 BTO221(99)_110_2_1stFe_BaO . . . 203
7.5.2 BTO221(99)_110_2_1stFe_BaO_Interstitial . . . 208
7.5.3 BTO221(99)_110_2_2ndFe_BaO . . . 212
7.5.4 BTO221(99)_110_2_1stFe_Ti2O4 . . . 215
7.5.5 BTO221(99)_110_2_2ndFe_Ti2O4 . . . 221
7.6 BTO221(99)_{111}/Fe . . . 223

8 $BaTiO_3$ EFG and PAC measurements **225**
8.1 DFT EFG predictions for pure Tetragonal $BaTiO_3$ . . . 225
8.2 DFT EFG predictions for $BaTiO_3$:Cd . . . 226
8.3 PAC spectroscopy of $BaTiO_3$ using ^{111m}Cd . . . 234
8.3.1 PAC and DFT crossover: final considerations . . . 236

9 RF-Sputtering of $BaTiO_3$/Fe/$BaTiO_3$ heterostructures **239**
9.1 RF-Sputtering of the BTO/Fe thin films . . . 239
9.2 Raman Spectroscopy results . . . 243
9.3 Grazing Incidence XRD results . . . 249
9.4 STEM/EDS analysis of the BTF thin films . . . 258
9.5 Magnetic Studies . . . 263
9.5.1 BTF4 Magnetic Results . . . 265
9.5.2 BTF6 Magnetic Results . . . 274
9.5.3 BTF5 Magnetic Results . . . 276

10 MBE deposition of Fe on $BaTiO_3$ substrates **283**
10.1 BTO/^{57}Fe/Fe/Au magnetic characterization . . . 284

11 Conclusions **293**

Bibliography **297**

Publications List **319**

List of Figures

2.1 Zeeman effect diagram. 11
2.2 Explicative scheme of the superexchange interaction. 15
2.3 Explicative diagram of the double exchange interaction. 16
2.4 Energy splitting of octahedral and tetrahedral environments. 19
2.5 Crystal field for the T_d, O_h and D_{4h} symmetry groups. 20
2.6 Energy diagrams of a Jahn-Teller distortion. 21
2.7 Diagram of the Low-spin and High-spin configurations. 23
2.8 Energy diagram of Fe^{2+} and Fe^{3+} Low-Spin and High-Spin states. 23
2.9 Types of magnetic ordering. 25
2.10 Susceptibility curves for an AFM material. 30
2.11 Scheme of two independent charge distributions. 41

3.1 Ferroic couplings and their respective mediator fields. 46
3.2 Relation between materials with electric and magnetic properties. 47
3.3 Number of annual publications about the topic *"Multiferroic"*. 52
3.4 Annual citations about the topic *"Multiferroic"*. 52
3.5 Number of annual publications about the topic *"Magnetoelectric"*. 52
3.6 Annual citations about the topic *"Magnetoelectric"*. 52
3.7 Number of "*Multiferroic*" based patents emitted through the years. 53
3.8 Schematic representation of a multiferroic perovskite. 54
3.9 Polarization due to lone pairs. 55
3.10 Representation the geometric mechanism behind $YMnO_3$ ferroelectricity. 56
3.11 Scheme of one dimension charge order systems. 57
3.12 Representation of a Bilayer of the FeO_2 triangular lattices in $LuFe_2O_4$. 58
3.13 Intrinsic magnetostrictive ferroelectricity. 59
3.14 Some spin arrangements and consequent polarization. 59
3.15 Schematic representation of a Magnetoelectric MRAM. 62

4.1 Representative scheme of Bragg's diffraction 63
4.2 Experimental configuration of a GIXRD setup. 66
4.3 GIXRD diffraction cones from the polycrystalline thin film. 66
4.4 Diagram of the SEM components. 70
4.5 Scheme of the electrons' interaction by-products. 71
4.6 Diagram describing the variables involved in the SEM electron probing beam . 72
4.7 Diagram of TEM operating modes. 74
4.8 STEM scheme. 75

4.9 Diagram of STEM operating mode. 75
4.10 Diagram of the interaction which originate the characteristic X-rays. 76
4.11 Transitions associated with the different types of radiaction scattering. 79
4.12 Typical Raman spectrum. 80
4.13 Scheme of the superconducting ring of a DC SQUID. 81
4.14 Figure 4.13 equivalent electric circuit. 81
4.15 ^{111m}Cd decay scheme. 83
4.16 Experimental configuration to measure the $\gamma_1 - \gamma_2$ angular correlation. 84
4.17 Sheme of a typical experimental configuration for DC sputtering. 86
4.18 Sheme of a typical experimental configuration for RF sputtering. 86
4.19 Sheme of a typical experimental configuration for MBE. 87

5.1 $BaTiO_3$ cubic unit cell. 89
5.2 $BaTiO_3$ phase transitions and respective spontaneous polarization directions. . 90
5.3 $BaTiO_3$ single crystal temperature dependent magnetization. 91
5.4 $BaTiO_3$ ZFC/FC curves. 92
5.5 $BaTiO_3$ RT XRD and its respective Rietveld refinement. 94
5.6 M(T) of $BaTiO_3$ with 113 ppm of Fe as two separate components. 95
5.7 $(M - M_S)^2$ vs T near the 325 K and 373 K magnetic anomalies. 96
5.8 M(H) of the pellet of $BaTiO_3$ with 113 ppm of Fe at 5 K. 97
5.9 M(H) curves and remanent magnetization dependence with temperature. 98
5.10 Temperature dependence of the Raman active modes. 99
5.11 Fe concentration distribution and its correspondent Poisson distribution. 101
5.12 M(T) of $BaTiO_3$:Fe for several annealing temperatures. 103
5.13 STEM micrograph and EDS results 104

6.1 BTO221_001_1stFe supercell 110
6.2 BTO99_001_1stFe supercell 110
6.3 Binding energy of the BTO221_001_1stFe supercell 112
6.4 Binding energy of the BTO99_001_1stFe supercell 112
6.5 Total magnetic moment of the BTO221_001_1stFe supercell. 112
6.6 Total magnetic moment of the BTO99_001_1stFe supercell. 112
6.7 Fe magnetic moments for the FM arrangement of BTO221(99)_001_1stFe . . . 113
6.8 Remaining moments for the FM arrangement of BTO221(99)_001_1stFe . . . 114
6.9 Fe magnetic moments for the AFM arrangement of BTO221(99)_001_1stFe . . 114
6.10 Remaining moments for the AFM arrangement of BTO221(99)_001_1stFe . . 115
6.11 Density of states of BTO221_001_1stFe_FM at $d = 7.8$ Å. 116
6.12 Density of states of BTO99_001_1stFe_FM at $d = 7.8$ Å. 116
6.13 Fe, Ti and O density of states of BTO221_001_1stFe_FM at $d = 7.8$ Å. 116
6.14 Fe, Ti and O density of states of BTO99_001_1stFe_FM at $d = 7.8$ Å. 116
6.15 Illustration of the A and B cross section planes of the charge density. 117
6.16 Spin and charge density of BTO221_001_1stFe_FM for $d = 7.8$ Å (A plane) . 118
6.17 Spin and charge density of BTO221_001_1stFe_FM for $d = 7.8$ Å (B plane) . 118
6.18 Density of states of BTO221_001_1stFe_AFM at $d = 7.5$ Å. 119
6.19 Density of states of BTO99_001_1stFe_AFM at $d = 7.5$ Å. 119
6.20 Fe, Ti and O density of states of BTO221_001_1stFe_AFM at $d = 7.5$ Å. . . . 120
6.21 Fe, Ti and O density of states of BTO99_001_1stFe_AFM at $d = 7.5$ Å. . . . 120

6.22 Spin and charge density of BTO221_001_1stFe_AFM for $d = 7.5$ Å(A plane) . 121
6.23 Spin and charge density of BTO221_001_1stFe_AFM for $d = 7.5$ Å(B plane) . 121
6.24 Density of states of BTO221_001_1stFe_AFM at $d = 6.0$ Å. 122
6.25 Density of states of BTO99_001_1stFe_AFM at $d = 6.0$ Å. 122
6.26 Fe, Ti and O density of states of BTO221_001_1stFe_AFM at $d = 6.0$ Å. . . . 122
6.27 Fe, Ti and O density of states of BTO99_001_1stFe_AFM at $d = 6.0$ Å. . . . 122
6.28 Top view of BTO221_001_1stFe_AFM supercell as a function of d. 123
6.29 Definition of A' and B' cross section planes 123
6.30 Spin and charge density of BTO221_001_1stFe_AFM for $d = 6.0$ Å (A' plane) 124
6.31 Spin and charge density of BTO221_001_1stFe_AFM for $d = 6.0$ Å (B' plane) 124
6.32 Density of states of BTO221_001_1stFe_FM at $d = 6.0$ Å. 125
6.33 Density of states of BTO99_001_1stFe_FM at $d = 6.0$ Å. 125
6.34 Fe, Ti and O density of states of BTO221_001_1stFe_FM at $d = 6.0$ Å. 126
6.35 Fe, Ti and O density of states of BTO99_001_1stFe_FM at $d = 6.0$ Å. 126
6.36 Spin and charge density of BTO99_001_1stFe_FM for $d = 6.0$ Å (A' plane) . . 127
6.37 Spin and charge density of BTO99_001_1stFe_FM for $d = 6.0$ Å (B' plane) . . 127
6.38 BTO221_001_2ndFe supercell 128
6.39 BTO99_001_2ndFe supercell 128
6.40 BTO221_001_2ndFe at $d = 7.5$ Å relaxed structure. 128
6.41 Binding energy of the BTO221_001_2ndFe supercell. 129
6.42 Binding energy of the BTO99_001_2ndFe supercell. 129
6.43 Total magnetic moment of the BTO221_001_2ndFe supercell. 129
6.44 Total magnetic moment of the BTO99_001_2ndFe supercell. 129
6.45 Fe magnetic moments for the FM arrangement of BTO221(99)_001_2ndFe. . . 130
6.46 Remaining moments for the FM arrangement of BTO221(99)_001_2ndFe. . . . 131
6.47 Fe magnetic moments for the AFM arrangement of BTO221(99)_001_2ndFe. . 131
6.48 Remaining moments for the AFM arrangement of BTO221(99)_001_2ndFe. . . 132
6.49 Density of states of BTO221_001_2ndFe_FM at $d = 7.5$ Å. 133
6.50 Density of states of BTO99_001_2ndFe_FM at $d = 7.5$ Å. 133
6.51 Fe, Ti and O density of states of BTO221_001_2ndFe_FM at $d = 7.5$ Å. . . . 133
6.52 Fe, Ti and O density of states of BTO99_001_2ndFe_FM at $d = 7.5$ Å. 133
6.53 Spin and charge density of BTO221_001_2ndFe_FM for $d = 7.5$ Å (A' plane) . 134
6.54 Spin and charge density of BTO221_001_2ndFe_FM for $d = 7.5$ Å (B' plane) . 135
6.55 Density of states of BTO221_001_2ndFe_AFM at $d = 8.2$ Å. 136
6.56 Density of states of BTO99_001_2ndFe_AFM at $d = 8.2$ Å. 136
6.57 Fe, Ti and O density of states of BTO221_001_2ndFe_AFM at $d = 8.2$ Å. . . 136
6.58 Fe, Ti and O density of states of BTO99_001_2ndFe_AFM at $d = 8.2$ Å. . . . 136
6.59 Spin and charge density of BTO221_001_2ndFe_AFM for $d = 8.1$ Å (A' plane) 137
6.60 Spin and charge density of BTO221_001_2ndFe_AFM for $d = 8.1$ Å (B' plane) 137
6.61 Density of states of BTO221_001_2ndFe_AFM at $d = 7.6$ Å. 138
6.62 Density of states of BTO99_001_2ndFe_AFM at $d = 7.6$ Å. 138
6.63 Fe, Ti and O density of states of BTO221_001_2ndFe_AFM at $d = 7.6$ Å. . . 138
6.64 Fe, Ti and O density of states of BTO99_001_2ndFe_AFM at $d = 7.6$ Å. . . . 138
6.65 Density of states of BTO221_001_2ndFe_AFM at $d = 6.9$ Å. 139
6.66 Density of states of BTO99_001_2ndFe_AFM at $d = 6.9$ Å. 139
6.67 Fe, Ti and O density of states of BTO221_001_2ndFe_AFM at $d = 6.9$ Å. . . 139
6.68 Fe, Ti and O density of states of BTO99_001_2ndFe_AFM at $d = 6.9$ Å. . . . 139

6.69 Spin and charge density of BTO221_001_2ndFe_AFM for $d = 7.5$Å(A' plane) 140
6.70 Spin and charge density of BTO221_001_2ndFe_AFM for $d = 7.5$Å(B' plane) 141
6.71 Spin and charge density of BTO221_001_2ndFe_AFM for $d = 7.1$Å(A' plane) 142
6.72 Spin and charge density of BTO221_001_2ndFe_AFM for $d = 7.1$Å(B' plane) 142
6.73 Energy diagram of the electron occupation for two crystal fields. 143
6.74 DOS of each d orbitals of Fe2 atom for BTO221_001_2ndFe 144
6.75 DOS of each d orbitals of Fe2 atom for BTO221_001_2ndFe 145
6.76 Distances between the atoms of the 2ndFe supercells. 146
6.77 Distances between the atoms of the 1stFe supercells. 147
6.78 EFG felt by each atom of the BTO221(99)_001_1stFe supercell. 148
6.79 EFG felt by each atom of the BTO221(99)_001_2ndFe supercell. 148
6.80 $E_{Binding}(d)$ and respective magnetic state for the BTO_001_2ndFe supercells. . 151
6.81 Heterostructure comprised of an Fe ML in a BTO matrix under an $\vec{E}$. 152
6.82 δ as a function of the $BaTiO_3$ lateral lattice parameter 153
6.83 Relative value of the BTO c-axis as a function of d 153

7.1 BTO38_1stFe supercell 156
7.2 BTO38_2ndFe supercell 156
7.3 BTO38_1stFe_O2 supercell 156
7.4 BTO38_2ndFe_O2 supercell 156
7.5 Illustration of the considered magnetic arrangements. 157
7.6 Binding energy of the BTO38_1stFe supercell. 158
7.7 Total magnetic moment of the BTO38_1stFe supercell. 158
7.8 The three types of structures present in the BTO38_1stFe supercell. 159
7.9 Fe magnetic moments of the BTO38_1stFe. 160
7.10 Remaining magnetic moments of BTO38/1stFe. 161
7.11 Binding energy of BTO38_2ndFe. 163
7.12 Total magnetic moment of BTO38_2ndFe. 163
7.14 Final relaxed structures for both BTO38_1stFe and BTO38_2ndFe. 163
7.13 Fe magnetic moments of BTO38_2ndFe. 164
7.15 Remaining magnetic moments of BTO38_2ndFe. 165
7.16 Binding energy of BTO38_1stFe_O2. 167
7.17 Total magnetic moment of BTO38_1stFe_O2. 167
7.18 Relaxed structures of the BTO38_1stFe_O2 supercell. 168
7.19 Side view of the ω, ζ and η structures at $d = 13$ Å. 168
7.20 Fe magnetic moments of the BTO38_1stFe_O_2. 169
7.21 Remaining magnetic moments of BTO38_1stFe_O2. 170
7.22 Binding energy of BTO38_2ndFe_O2. 171
7.23 Total magnetic moment of BTO38_2ndFe_O2. 171
7.24 Relaxed structures of the BTO38_2ndFe_O2 supercell. 172
7.25 Fe magnetic moments of BTO38_2ndFe_O2. 172
7.26 Remaining magnetic moments of BTO38_2ndFe_O2. 173
7.27 BTO160_1stFe supercell 175
7.28 BTO160_2ndFe supercell 175
7.29 BTO160_3rdFe supercell. 176
7.30 BTO160_Triangular supercell. 176
7.31 Binding energy of BTO160_1stFe supercell. 177

7.32 Total magnetic moment of BTO160_1stFe . . . 177
7.33 Relaxed structures of the BTO160_1stFe supercell. . . . 178
7.34 Fe magnetic moments of BTO160_1stFe. . . . 179
7.35 Remaining magnetic moments of BTO160_1stFe. . . . 179
7.36 Binding energy of BTO160_2ndFe. . . . 180
7.37 Total magnetic moment of BTO160_2ndFe . . . 180
7.38 Relaxed structures of the BTO160_2ndFe supercell. . . . 181
7.39 Fe magnetic moments of BTO160_2ndFe . . . 182
7.40 Binding energy of BTO160_3rdFe . . . 183
7.41 Total magnetic of BTO160_3rdFe . . . 183
7.42 Relaxed structures of the BTO160_3rdFe supercell. . . . 184
7.43 Fe magnetic moments of BTO160_3rdFe. . . . 184
7.44 Binding energy of the BTO160_Triangular supercell. . . . 186
7.45 Total magnetic moment of the BTO160_Triangular supercell. . . . 186
7.46 Relaxed structures of the BTO160_Triangular supercell. . . . 186
7.47 Individual magnetic moments of BTO160_Triangular. . . . 187
7.48 Construction of BTO221_110_1_1stFe supercell. . . . 188
7.49 Supercell families obtained from the (110) cut plane. . . . 188
7.50 All considered BTO221(99)_110_1/Fe supercells. . . . 189
7.51 All considered BTO221(99)_110_2/Fe supercells. . . . 189
7.52 Construction of BTO99_101_1stFe supercell . . . 190
7.53 All considered BTO221_101/Fe and BTO99_101/Fe supercells. . . . 190
7.54 Construction of BTO221_111_1stFe supercell . . . 191
7.55 All considered BTO221(99)_111/Fe supercells. . . . 192
7.56 Binding energy of BTO38_1stFe . . . 193
7.57 Binding energy of BTO99_101_1stFe . . . 193
7.58 Total magnetic moment of BTO38_1stFe . . . 193
7.59 Total magnetic moment of BTO99_101_1stFe . . . 193
7.60 Binding energy of BTO99_110_1_2ndFe . . . 195
7.61 Binding energy of BTO221_110_1_2ndFe . . . 195
7.62 Total magnetic moment of BTO99_110_1_2ndFe . . . 195
7.63 Total magnetic moment of BTO221_110_1_2ndFe . . . 195
7.64 Binding energy of BTO38_2ndFe . . . 197
7.65 Binding energy of BTO99_101_2ndFe . . . 197
7.66 Total magnetic moment of BTO38_2ndFe . . . 197
7.67 Total magnetic moment of BTO99_101_2ndFe . . . 197
7.68 Binding energy of BTO99_110_1_1stFe . . . 198
7.69 Binding energy of BTO221_110_1_1stFe . . . 198
7.70 Total magnetic moment of BTO99_110_1_1stFe . . . 198
7.71 Total magnetic moment of BTO221_110_1_1stFe . . . 198
7.72 Binding energy of BTO99_110_1_1stFe_O2 . . . 200
7.73 Binding energy of BTO221_110_1_1stFe_O2 . . . 200
7.74 Total magnetic moment of BTO99_110_1_1stFe_O2 . . . 200
7.75 Total magnetic moment of BTO221_110_1_1stFe_O2 . . . 200
7.76 Binding energy of BTO38_2ndFe_O2 . . . 201
7.77 Binding energy of BTO99_101_2ndFe_O2 . . . 201
7.78 Total magnetic moment of BTO38_2ndFe_O2 . . . 201

7.79 Total magnetic moment of BTO99_101_2ndFe_O2 . . . 201
7.80 Binding energy of BTO99_110_2_1stFe_BaO . . . 203
7.81 Binding energy of BTO221_110_2_1stFe_BaO . . . 203
7.82 Total magnetic moment of BTO99_110_2_1stFe_BaO . . . 203
7.83 Total magnetic moment of BTO221_110_2_1stFe_BaO . . . 203
7.84 Fe magnetic moments of the BTO(221)99_110_2_1stFe_BaO. . . . 204
7.85 DOS of BTO99_110_2_1stFe_BaO at $d = 6.3$ Å . . . 205
7.86 Spin and charge density of BTO99_110_2_1stFe_BaO_AFM1 . . . 206
7.87 Binding energy of BTO99_110_2_1stFe_BaO_Interstitial . . . 208
7.88 Binding energy of BTO221_110_2_1stFe_BaO_Interstitial . . . 208
7.89 Total magnetic moment of BTO99_110_2_1stFe_BaO_Interstitial . . . 208
7.90 Total magnetic moment of BTO221_110_2_1stFe_BaO_Interstitial . . . 208
7.91 Fe magnetic moments of the BTO(221)99_110_2_1stFe_BaO_Interstitial. . . 209
7.93 DOS of BTO221_110_2_1stFe_BaO_Interstitial at $d = 6.0$ Å . . . 210
7.94 Spin and charge density of BTO99_110_2_1stFe_BaO_Interstitial_FM . . . 211
7.95 Binding energy of BTO99_110_2_2ndFe_BaO . . . 212
7.96 Binding energy of BTO221_110_2_2ndFe_BaO . . . 212
7.97 Total magnetic moment of BTO99_110_2_2ndFe_BaO . . . 212
7.98 Total magnetic moment of BTO221_110_2_2ndFe_BaO . . . 212
7.99 Fe magnetic moments of the BTO(221)99_110_2_2ndFe_BaO. . . . 213
7.100 Binding energy of BTO99_110_2_1stFe_Ti2O4 . . . 215
7.101 Binding energy of BTO221_110_2_1stFe_Ti2O4 . . . 215
7.102 Total magnetic moment of BTO99_110_2_1stFe_Ti2O4 . . . 215
7.103 Total magnetic moment of BTO221_110_2_1stFe_Ti2O4 . . . 215
7.104 Fe magnetic moments of the BTO(221)99_110_2_1stFe_Ti2O4. . . . 216
7.105 DOS of BTO99_110_2_1stFe_Ti2O4_AFM1 at $d = 6.2$ Å . . . 218
7.106 Spin and charge density of BTO99_110_2_1stFe_Ti2O4_AFM1 . . . 219
7.107 Binding energy of BTO99_110_2_2ndFe_Ti2O4 . . . 221
7.108 Binding energy of BTO221_110_2_2ndFe_Ti2O4 . . . 221
7.109 Total magnetic moment of BTO99_110_2_2ndFe_Ti2O4 . . . 221
7.110 Total magnetic moment of BTO221_110_2_2ndFe_Ti2O4 . . . 221
7.111 Fe magnetic moments of the BTO(221)99_110_2_2ndFe_Ti2O4. . . . 222

8.1 BTO:Cd (Cd at the Ba site) structure after relaxation. . . . 227
8.2 $BaTiO_3$:Cd (Cd at the Ti site) structure after relaxation. . . . 227
8.3 $BaTiO_3$:Cd (Cd at the $O_{equatorial}$ site) structure after relaxation. . . . 228
8.4 $BaTiO_3$:Cd (Cd at the O_{apical} site) structure after relaxation. . . . 228
8.5 EFG magnitude of its neighbouring atoms at the Ba site . . . 228
8.6 Binding energy of the $BaTiO_3$:Cd at the Ba site . . . 228
8.7 EFG magnitude of its neighbouring atoms at the Ti site . . . 229
8.8 Binding energy of the $BaTiO_3$:Cd at the Ti site . . . 229
8.9 EFG magnitude of its neighbouring atoms at the $O_{equatorial}$ site . . . 230
8.10 EFG magnitude of its neighbouring atoms at the O_{apical} site . . . 230
8.11 Binding energy of the $BaTiO_3$:Cd at the $O_{equatorial}$ site . . . 231
8.12 Binding energy of the $BaTiO_3$:Cd at the O_{apical} site . . . 231
8.13 DFT predicted EFG of the $BaTiO_3$:Cd for the Ba site . . . 231
8.14 DFT predicted EFG of the $BaTiO_3$:Cd for the Ti site . . . 232

8.15 DFT predicted EFG of the $BaTiO_3$:Cd for the $O_{equatorial}$ site . . . 232
8.16 DFT predicted EFG of the $BaTiO_3$:Cd for the O_{apical} site . . . 233
8.17 PAC experimental spectra. . . . 235

9.1 Illustration of the seven layer heterostructure deposited by RF-Sputtering. . . . 241
9.2 Illustration of the trilayer heterostructure deposited by RF-Sputtering. . . . 241
9.3 Raman spectra for the thin films deposited on $LaAlO_3$. . . . 244
9.4 Raman spectra for the thin films deposited on MgO. . . . 244
9.5 Raman spectrum for the BTF_MgO_900C. . . . 245
9.6 Temperature-Oxygen's pressure phase diagram of the Fe–O system. . . . 246
9.7 Raman spectra for the thin films deposited on Al_2O_3. . . . 247
9.8 Raman spectra for the thin films deposited on STO. . . . 247
9.9 GIXRD of the thin films deposited on $LaAlO_3$ . . . 251
9.10 GIXRD of the thin films deposited on MgO . . . 252
9.11 GI XRD of the thin films deposited on Al_2O_3 . . . 254
9.12 GIXRD of the thin films deposited on STO . . . 255
9.13 BTF5.2_MgO_as_dep micrographs . . . 258
9.14 BTF5.2_MgO_as_dep STEM/EDS . . . 259
9.15 BTF4.2_MgO_as_dep micrographs . . . 260
9.16 BTF4.2_MgO_as_dep STEM/EDS . . . 261
9.17 BTF4.2_MgO_900C micrographs . . . 261
9.18 BTF4.2_MgO_900C STEM/EDS . . . 262
9.19 M(T) curves of the considered substrates. . . . 263
9.20 M(H) curves of the considered substrates. . . . 264
9.21 M(H) curve for the MgO substrate . . . 264
9.22 M(T) curves of BTF4.1_$LaAlO_3$ . . . 266
9.23 M(T) curves of the BTF4.2_MgO . . . 266
9.24 M(T) curves of the BTF4.3_Al_2O_3 . . . 266
9.25 M(T) curves of the BTF4.4_STO . . . 266
9.26 M(H) curves of BTF4.1_$LaAlO_3$ . . . 267
9.27 M(H) curves of BTF4.2_MgO . . . 268
9.28 M(H) curves of BTF4.3_Al_2O_3 . . . 270
9.29 M(H) curves of BTF4.4_STO . . . 270
9.30 Remanent magnetizations of BTF4.2_MgO_900C . . . 271
9.31 Curie temperatures and saturation of titanohematites . . . 272
9.32 M(T) curves of the BTF6.1_$LaAlO_3$ . . . 274
9.33 M(T) curves of the BTF6.2_Al_2O_3 . . . 274
9.34 M(T) curves of the BTF6.3_MgO . . . 275
9.35 M(T) curves of the BTF6.4_STO . . . 275
9.36 M(H) curves of BTF6.1_$LaAlO_3$ . . . 275
9.37 M(H) curves of BTF6.2_Al_2O_3 . . . 275
9.38 M(H) curves of BTF6.3_MgO . . . 276
9.39 M(H) curves of BTF6.4_STO . . . 276
9.40 M(T) curves of the BTF5.1_$LaAlO_3$ . . . 277
9.41 M(T) curves of the BTF5.2_MgO . . . 277
9.42 M(T) curves of the BTF5.3_Al_2O_3 . . . 277
9.43 M(T) curves of the BTF5.4_STO . . . 277

9.44 M(H) curves of BTF5.1_$LaAlO_3$ . . . 279
9.45 M(H) curves of BTF5.2_MgO . . . 280
9.46 M(H) curves of BTF5.3_Al_2O_3 . . . 281
9.47 M(H) curves of BTF5.4_STO . . . 281

10.1 Illustration of the heterostructure deposited by MBE . . . 284
10.2 M(H) and M(T) curves of the BTO substrate . . . 285
10.3 M(T) curves of BTO/Fe thin films . . . 286
10.4 M(T) curves of BTO(100)/Fe_RT . . . 287
10.5 M(T) curves of BTO(100)/Fe_350C . . . 288
10.6 M(T) curves of BTO(110)/Fe_RT . . . 289
10.7 M(T) curves of BTO(111)/Fe_RT . . . 290
10.8 M_r dependence with temperature. . . . 291
10.9 H_c dependence with temperature. . . . 291

List of Tables

5.1 PIXE results for the $BaTiO_3$ pellet. 93
5.2 Summary of the Rietveld analysis for the XRD data of the BTO pellet. 94

6.1 Hyperfine magnetic fields f the BTO221(99)_001_2ndFe supercells. 150

7.1 Relaxed strucures of BTO38_1stFe. 159
7.2 Relaxed strucures of BTO38_2ndFe. 164
7.3 Relaxed strucures in the BTO38_1stFe supercell. 167
7.4 Structures of the BTO38_2ndFe_O2 supercell. 171
7.5 Relaxed strucures of the BTO160_1stFe supercell. 178
7.6 Relaxed structures of the BTO160_2ndFe supercell. 180
7.7 Relaxed structures of the BTO160_3rdFe supercell. 183
7.8 DFT conditions of BTO221(99)_{110}/Fe and BTO221(99)_{111}/Fe 192

8.1 Pure tetragonal BTO DFT predicted EFG 226
8.2 $BaTiO_3$:Cd DFT predicted EFG 232
8.3 Experimental PAC results 234
8.4 Comparison between the EFG of BTO obtained through different aproaches. . . 236

9.1 Summary of the RF-Sputtering depositions 240
9.2 RF-Sputtering conditions for each deposition. 241
9.3 Thermal annealing details for each sample. 242
9.4 Active Raman modes for the main iron oxides. 244
9.5 Total M_s and correspondent maghemite:hematite proportion 269
9.6 Summary of the M_s for the BTF5 deposition thin films 278

10.1 BTO/Fe thin films MBE deposition conditions 285

Chapter 1

Introduction

Humanity's awe towards nature was constant through history. Thunders, lightnings and earthquakes gave birth to religions and cults regarding these mighty divine acts. Since the discovery of the magical stones which attracted each other, abundant in the city of Magnesia, magnetism took a great part in this fascination towards physical phenomena. The study of ferromagnetism gave insights about the understanding and control of magnetization/magnetic materials allowing the creation of many technological applications, in particular the possibility of high density data storing [1].

Magnetoelectric multiferroics are a rare type of materials which show ferroelectricity and magnetism simultaneously. Such a feature is very appealing, bringing forth diverse applications such as magnetic sensors, memory devices and energy harvesting/conversion.

This thesis will focus on the study of magnetoelectric materials, namely interfaces of $BaTiO_3$ and Fe, two archetypes of ferroelectrically and ferromagnetism respectively, as an attempt to unveil possible disruptive magnetoelectric effects/couplings.

Chapter 2 will cover the theoretical background used through the manuscript. This chapter is a good way for a non-specialist to gather most of the tools required to understand the topics and results presented in this thesis.

Chapter 3 contextualizes the importance of the study of magnetoelectric materials, explaining what is the magnetoelectric effect and its most well-known variants, as well as the most promising technological applications associated with these materials.

Chapter 4 makes a brief exposition of the principles behind the experimental techniques used through this thesis.

$BaTiO_3$ and Fe have been widely studied as possible candidates to the tailoring of a competitive extrinsic magnetoelectric multiferroic, still the magnetoelectric couplings associated with these multiferroics are still quite modest. Chapter 5 presents a very particular $BaTiO_3$:Fe compound where, through the analysis of its magnetic and vibrational (Raman) properties, was possible to identify the existence of a considerable magnetoelectric coupling between the magnetic properties of Fe and the ferroelectric properties of $BaTiO_3$. Chapter 5 also presents the usage of local techniques such as STEM/EDS, which was crucial to understand the specificity of the conditions necessary to the occurrence of such a peculiar magnetoelectric coupling. The work concerning this chapter was already published in [2] and [3].

Even though some of the conditions required for the magnetoelectric coupling presented in chapter 5 were already unveiled in that same chapter, the physical microscopic mechanism behind the effect was still unclear, thus, Density Functional Theory modeling was used in chapter 6 to try to understand the possible mechanisms associated with the $BaTiO_3$/Fe interfaces.

In chapter 6 the $BaTiO_3$/Fe heterostructure comprised of a cubic or tetragonal $BaTiO_3$ was chosen since it allows to study the influence of the $BaTiO_3$ tetragonal↔cubic ferroelectric phase transition on the Fe magnetic properties. In fact, this approach has also been used by other groups. Still, in chapter 6, other Fe placements are also considered, enabling other possible metastable interfaces which have completely different magnetoelectric couplings.

In chapter 7, motivated by potential effects of the $BaTiO_3$ rhombohedral↔orthorhombic and orthorhombic↔tetragonal ferroelectric phase transitions on $BaTiO_3$/Fe heterostructures, the simulation of $BaTiO_3$/Fe supercells containing the orthorhombic and rhombohedral ferroelectric phases of $BaTiO_3$ are performed using Density Functional Theory. The $BaTiO_3$ rhombohedral and orthorhombic ferroelectric phases are equivalent to its tetragonal or cubic unit cells when cut through the (111) and 110 planes respectively, thus to encompass the possible magnetoelectric couplings associated with the $BaTiO_3$ ferroelectric phase transitions, the exploration of these alternative cubic and tetragonal unit cells is also considered in chapter 7.

The studies presented in chapter 6 and chapter 7 show that the local chemical environment is very important to the magnetic properties of the Fe atoms/ions. Therefore, in chapter 8 the study of the electric field gradient of $BaTiO_3$ single crystals at different sites is presented,

using Density Functional Theory and Perturbed Angular Correlations.

The variety of interfaces and effects presented in chapters 6 and 7 shows the potential of $BaTiO_3$ heterostructures under very specific conditions. To seek the reproduction of such effects, the deposition of $BaTiO_3$ and Fe thin films was performed on different substrates – $LaAlO_3$, MgO, Al_2O_3 and $SrTiO_3$– using a RF-Sputtering. Chapter 9 presents the details and deposition conditions of these heterostructures, as well as the characterization of their magnetic and structural properties.

Additionally, to have more controlled and cleaner conditions, the deposition of Fe thin films was performed through Molecular Beam Epitaxy on $BaTiO_3$ substrates. The substrates were cut under the (100), (110) and (111) directions, thus enabling the controlled deposition of Fe in these three possible interfaces of $BaTiO_3$, similar to the cases simulated in chapter 7. The magnetic results of the thin films produced under these very controlled conditions are presented in chapter 10.

Chapter 2

Theoretical Background

2.1 Classical Electromagnetism

The understanding and control of electromagnetism is one of humanity's greatest achievements which enabled the beginning of a technological world. During the nineteenth century scientists such as Faraday and Maxwell were crucial to the development of this scientific area, being responsible for its theoretical framework which can be condensed in the well-known Maxwell equations (equations 2.1 and 2.2) [4, 5].

Differential equations (SI)

$$\vec{\nabla} \cdot \vec{E} = \frac{\rho}{\epsilon_0} \tag{2.1a}$$

$$\vec{\nabla} \cdot \vec{B} = 0 \tag{2.1b}$$

$$\vec{\nabla} \times \vec{E} = -\frac{\partial \vec{B}}{\partial t} \tag{2.1c}$$

$$\vec{\nabla} \times \vec{B} = \mu_0 \left(\vec{j} + \epsilon_0 \frac{\partial \vec{E}}{\partial t} \right) \tag{2.1d}$$

Integral equations (SI)

$$\oiint_{\partial V'} \vec{E} \cdot d\vec{S} = \iiint_{V'} \frac{\rho}{\epsilon_0} dV \tag{2.2a}$$

$$\oiint_{\partial V'} \vec{B} \cdot d\vec{S} = 0 \tag{2.2b}$$

$$\oint_{\Sigma} \vec{E} \cdot d\vec{\ell} = -\frac{d}{dt} \iint_{S'} \vec{B} \cdot d\vec{S} \tag{2.2c}$$

$$\oint_{\Sigma} \vec{B} \cdot d\vec{\ell} = \mu_0 \iint_{S'} \left(\vec{j} + \epsilon_0 \frac{\partial \vec{E}}{\partial t} \right) \cdot d\vec{S} \tag{2.2d}$$

Where $\vec{E}$ is the electric field, $\vec{B}$ is the magnetic flux density, ρ is the charge density, V' is the integration volume, ϵ_0 the electric vacuum permittivity, μ_0 is the magnetic vacuum permeability, S' is the surface which the magnetic flux passes through in (2.2c) case or which the electric current density passes through in (2.2d), and Σ is the closed path which encloses

S'.

Equations 2.1 and 2.2 are the same equations but in the differential and integral formulation respectively. Equations 2.1a and 2.2a refer to Gauss's law, equations 2.1b and 2.2b refer to Gauss law for magnetism, equations 2.1c and 2.2c refer to Faraday's law of induction (also known as Maxwell-Faraday equation), and finally equations 2.1d and 2.2d refer to Ampère's circuital law with Maxwell's correction.

These equations are the Rosetta stone to describe and understand all the electromagnetic phenomena involving discrete charges and currents in vacuum. However, these equations struggle at the description of macroscopic electromagnetism phenomena in matter.

To generalize the application of Maxwell equations to electromagnetic macroscopic behaviour in matter, concepts such as magnetization, $\vec{M}$, and polarization, $\vec{P}$, were introduced. Magnetization is an intensive quantity which describes the amount of magnetic moments, $\vec{\mathfrak{m}}$, per unit of volume of a given material, and is related to $\vec{B}$ by equation 2.3:

$$\vec{B} = \mu_0 \left(\vec{H} + \vec{M} \right) \ , \tag{2.3}$$

where $\vec{H}$ is the magnetic field strength. I should point out that both $\vec{B}$ and $\vec{H}$ can be called magnetic field, nevertheless in this manuscript I will always use magnetic flux density or magnetic induction when addressing the $\vec{B}$ field, and magnetic field, magnetic field strength or magnetizing force when I am referring to the $\vec{H}$ field.

Another important concept is the magnetic susceptibility ($\hat{\chi} = \hat{\chi}^m$), which defines how much a material magnetization is affected by a magnetizing field, as described by (2.4) for the particular case of a paramagnetic (PM) material [6–8].

$$\vec{M} = \hat{\boldsymbol{\chi}} \vec{H} \ . \tag{2.4}$$

Since the magnetization of a given material can be anisotropic an field dependent, the magnetic susceptibility must be a tensor, as defined by equation 2.5 [6–8]:

$$\chi_{ij} = \frac{\partial M_i}{\partial H_j} \ . \tag{2.5}$$

Putting together equations 2.3 and 2.4 we obtain equation 2.6:

$$\vec{B} = \mu_0 (1 + \chi) \vec{H} = \epsilon \vec{H} \ , \tag{2.6}$$

from which we can obtain the material effective magnetic permeability, described by (2.7) [6–10]:

$$\mu_0 (1 + \chi) = \mu = \mu_0 \mu_r \ , \tag{2.7}$$

where μ_r is the material relative magnetic permeability. Alternatively we can present the permeability in its differential formulation (2.8) [6–10]:

$$\mu_{ij} = \frac{\partial B_i}{\partial H_j} \ . \tag{2.8}$$

Analogously, for the electric counterpart, a susceptibility tensor can also be defined as the ability of an electric field to affect a material polarization, as shown in equation 2.9:

$$\chi^e_{ij} = \frac{\partial P_i}{\partial E_j} \ , \tag{2.9}$$

and in equation 2.10:

$$\vec{P} = \hat{\boldsymbol{\chi}}^e \vec{E} \ , \tag{2.10}$$

where $\vec{P}$ is an intensive quantity which describes the amount of electric dipoles, $\vec{\mathfrak{p}}$, per unit of volume of a given material. $\vec{\mathfrak{p}}$ is defined by equation 2.11:

$$\vec{\mathfrak{p}} = \iiint_{V'} \vec{r} \cdot \rho(r) dV \ . \tag{2.11}$$

Similarly to $\vec{B}$ there is an useful field which helps in the description of matter's electrical properties, the electric displacement field, $\vec{D}$, which is described by equation 2.12:

$$\vec{D} = \epsilon_0 \vec{E} + \vec{P} \ . \tag{2.12}$$

Substituting equation 2.10 in (2.12) we obtain equation 2.13:

$$\vec{D} = \epsilon_0 \left(1 + \frac{\chi^e}{\epsilon_0}\right) \vec{E} \ , \tag{2.13}$$

from which we obtain (2.14):

$$\epsilon_0 \left(1 + \frac{\chi^e}{\epsilon_0}\right) = \epsilon = \epsilon_0 \epsilon_r \ , \tag{2.14}$$

where ϵ is the effective electric permittivity of a given material, and ϵ_r is the relative permittivity, a dimensionless quantity also known as dielectric constant.

Using the new definitions of $\vec{B}$ (equation 2.6) and $\vec{D}$ (equation 2.13) in equations 2.1 and 2.2 results in the Maxwell equations in matter (equations 2.15 and 2.16) [4, 5]:

Differential equations (SI)		**Integral equations (SI)**	
$\vec{\nabla} \cdot \vec{D} = \rho_{\text{free}}$	(2.15a)	$\oiint_{\partial V'} \vec{D} \cdot d\vec{S} = \iiint_{V'} \rho_{\text{free}} \, dV$	(2.16a)
$\vec{\nabla} \cdot \vec{B} = 0$	(2.15b)	$\oiint_{\partial V'} \vec{B} \cdot d\vec{S} = 0$	(2.16b)
$\vec{\nabla} \times \vec{E} = -\dfrac{\partial \vec{B}}{\partial t}$	(2.15c)	$\oint_{\Sigma} \vec{E} \cdot d\vec{\ell} = -\dfrac{d}{dt} \iint_{S'} \vec{B} \cdot d\vec{S}$	(2.16c)
$\vec{\nabla} \times \vec{H} = \vec{j}_{\text{free}} + \dfrac{\partial \vec{D}}{\partial t}$	(2.15d)	$\oint_{\Sigma} \vec{H} \cdot d\vec{\ell} = \iint_{S'} \left(\vec{j}_{\text{free}} + \dfrac{\partial \vec{D}}{\partial t}\right) \cdot d\vec{S}$	(2.16d)

2.2 Magnetic Dipole Moment

While studying magnetic properties of matter, there is a concept which naturally arises, the magnetic dipole moment $\vec{\mathfrak{m}}$ (or $\vec{\mu}$), used to describe the magnetic force defined by equation 2.17:

$$\vec{F}_{Mag} = -\vec{\nabla}\left(\vec{\mathfrak{m}} \cdot \vec{B}\right) \ . \tag{2.17}$$

The classical magnetic dipole moment is defined by equation 2.18 [6,8]:

$$\vec{\mathfrak{m}} = \frac{1}{2}\iiint_{V'} \vec{r} \times \vec{j}(r) dV = \iint_{S'} I d\vec{S} \ , \tag{2.18}$$

where $\vec{r}$ is the position vector, $\vec{j}(r)$ is the electric current density, and S' is the surface enclosed by the electric current I.

Knowing that a $\vec{\mathfrak{m}}$ under the effect of a magnetic flux density produces a torque, $\vec{\Gamma}$, described by equation 2.19:

$$\vec{\Gamma} = \vec{\mathfrak{m}} \times \vec{B} \ , \tag{2.19}$$

and that the work done by this torque, between the angles θ_1 and θ_2, is described by equation 2.20:

$$W = \int_{\theta_1}^{\theta_2} \vec{\Gamma} \cdot \hat{n} \, d\theta \ , \tag{2.20}$$

we conclude that the energy associated with the interaction between a magnetic moment $\vec{\mathfrak{m}}$ and a magnetic flux density $\vec{B}$ is described by (2.21):

$$E_{mag} = \int_{\theta_1}^{\theta_2} \left(\vec{\mathfrak{m}} \times \vec{B}\right) \cdot \hat{n} \, d\theta = -\vec{\mathfrak{m}} \cdot \vec{B} \ . \tag{2.21}$$

2.2.1 Quantum Magnetic Dipole Moment

According to Bohr-van Leeuwen's theorem, classical statistical mechanics predicts that the average net magnetization of a given material should always be zero [6,8,9]. Nevertheless, we know for a fact that this cannot be true, otherwise there would not be magnets, wherefore,

magnetic properties of matter must be a direct consequence of the quantum character of nature.

For this reason, lets analyse the magnetic moment of an electron "orbiting" a nucleus, such as in the hydrogen case. Using a semi-quantum approach, it can be said that the electron motion around the nucleus is equivalent to the electric current of equation 2.22 [4, 9]:

$$I = \frac{dq}{dt} = \frac{q}{T} = f \cdot q = \frac{\omega}{2\pi} q = \frac{v}{2\pi r} q \ , \tag{2.22}$$

where q is the electron charge, T its period around the nucleus, f its corresponding frequency, ω the angular velocity, r the electron orbit radius, and v the electron velocity.

Since the magnetic moment can be described by the product of an electric current with the area enclosed by that current (equation 2.18), then multiplying the current of (2.22) with the electron orbit area $A = \pi r^2$, and taking into account that $\vec{L} = \vec{r} \times \vec{p}$ equation 2.23 is obtained [11, 12]:

$$\vec{\mathfrak{m}} = IA = \frac{\overbrace{rm_e v}^{\vec{L}}}{2m_e} q = \gamma \vec{L} \ , \tag{2.23}$$

where m_e is the electron mass and $\gamma = \frac{q}{2m}$ is the gyroscopic constant.

Since the quantum formulation states that for the ground state the angular momentum is $\vec{L} = \hbar\hat{n}$ [12, 13], it is possible to define the magnetic dipole moment of an electron "orbiting" a nucleus as equation 2.24 [1, 6]:

$$\mu_{\mathrm{B}} = \frac{e\hbar}{2m_e} \ , \tag{2.24}$$

where e is the electron charge. This quantity is also called Bohr magneton and is the building block of matter magnetic moments.

Till now we have only considered the orbital angular moment $\hat{\boldsymbol{L}}$, however in the quantum world the electron has its own intrinsic magnetic moment, its spin $\hat{\boldsymbol{S}}$. Therefore, we should consider the total angular momentum operator, $\hat{\boldsymbol{J}}$ as described in (2.25) [7, 8]:

$$\hat{\boldsymbol{J}} = \hat{\boldsymbol{L}} + \hat{\boldsymbol{S}} \tag{2.25}$$

to define the total magnetic moment of a given system, as described by equation 2.26:

$$\vec{\mathfrak{m}} = \gamma \vec{J} \ . \tag{2.26}$$

Looking again to equation 2.21 and considering the quantum approach, we obtain a new energy equation, the Zeeman equation (2.27) [7, 8]:

$$E_{mag} = -g_J \mu_B \left(\frac{\hat{\boldsymbol{J}}}{\hbar} \cdot \vec{B} \right) = -g_J \, \mu_B \, m_J B \ , \tag{2.27}$$

where m_J is the magnetic quantum number associated to the projection of the total angular momentum operator $\hat{\boldsymbol{J}}$ into an arbitrary axis, g_J is the Landé g-factor for a multi-electron atom and is described by equation 2.28 [7, 8] :

$$g_J = 1 + \frac{J(J+1) + S(S+1) - L(L+1)}{2J(J+1)} \ . \tag{2.28}$$

Inspecting equation 2.27 and figure 2.1 it is possible to see that the magnetic flux density $\vec{B}$ lifts the atom energy degeneracy into $2J+1$ different energy levels with an energy difference of $\Delta E = g_J \mu_B B$ [6, 7, 9, 13]. This energy splittings is called the Zeeman effect, or Zeeman splitting.

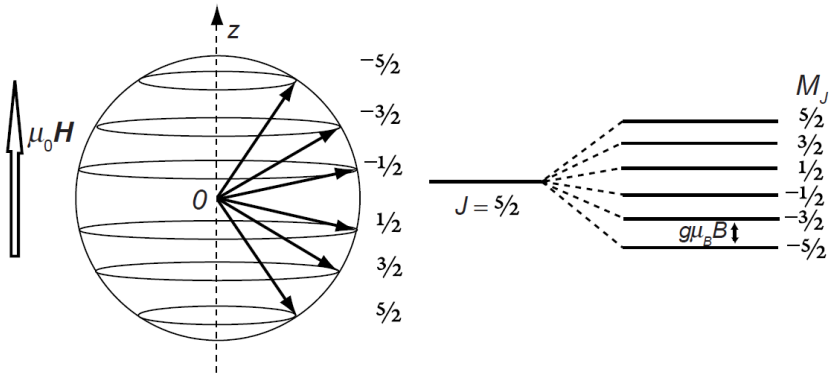

Figure 2.1: Diagram representing the m_J projection in an arbitrary axis z, and the Zeeman effect. From [6].

Lastly one can define an effective magnetic dipole moment using equation 2.29 [9]:

$$\mathfrak{m}_{eff} = \mu_{eff} = g_J \mu_B \sqrt{J(J+1)} \ , \tag{2.29}$$

which is the expression usually used to determine the total magnetic dipole moment of a multi-electron atom.

2.3 Magnetic Dipole Interactions

As considered in equation 2.3, a given material can have an intrinsic spontaneous magnetization even in the absence of a magnetizing field $\vec{H}$, thus there must be some kind of interaction responsible for such a spontaneous magnetic order. One of the immediate thoughts is that this ordering can come from the dipole interactions between the magnetic dipole moments present in the material. These dipole interactions are defined by equation 2.30:

$$E_{dip} = \frac{\mu_0}{4\pi r^3} \left[\vec{\mathfrak{m}}_1 \cdot \vec{\mathfrak{m}}_2 - 3 \left(\vec{\mathfrak{m}}_1 \cdot \hat{e}_r \right) \left(\vec{\mathfrak{m}}_2 \cdot \hat{e}_r \right) \right] \ , \tag{2.30}$$

where $\hat{e}_r$ is the unit vector with the direction that connects the magnetic dipole moment $\vec{\mathfrak{m}}_1$ and $\vec{\mathfrak{m}}_2$, and r the distance between them.

Analysing equation 2.30, assuming a separation of r =1 Å and $\vec{\mathfrak{m}}_1 = \vec{\mathfrak{m}}_2 = 1\mu_\mathrm{B}$ we obtain an energy equivalent to a temperature $T = {}^{E}/_{k_\mathrm{B}} \approx 1$ K. In other words, if these interactions were the source of spontaneous magnetization in matter, then we would only observe such a phenomenon at very low temperatures, and there would not be any permanent magnetization at room temperature. As a matter of fact, the source of spontaneous magnetization is directly related to a set of quantum interactions denominated exchange interactions, which are responsible for the long-range order of magnetic materials.

2.4 The Exchange Integral

Let's consider two electrons represented by the wave functions $\phi_a(r, s)$ and $\phi_b(r, s)$, as well as two positions r_1 and r_2, and two spins s_1 and s_2. It is possible to represent the wavefunction of a given electron as a product of its spatial and spin functions, $\phi_a(r_i, s_j) = \psi_a(r_i)\chi(s_j)$. Additionally, it is possible to represent two electrons as a single wave function which results from the product of both electrons' wavefunctions, $\Psi = \phi_a\phi_b$ [13].

Electrons are fermions, so their wavefunctions must be anti-symmetric, hence, for the wavefunction defining both electrons to be anti-symmetric we should have one of two possibilities.

Either we have the singlet wavefunction of equation 2.31 [7, 9, 13]:

$$\Psi_S = \frac{1}{\sqrt{2}} \left[\psi_a(r_1)\psi_b(r_2) + \psi_a(r_2)\psi_b(r_1)\right] \chi_S \ , \tag{2.31}$$

whose spatial part is symmetric and the spin part is a singlet $\chi_S \sim (\uparrow,\downarrow) \rightarrow S = 0$ (which is anti-symmetric); or we have the triplet wavefunction of equation 2.32 [7, 9, 13]:

$$\Psi_T = \frac{1}{\sqrt{2}} \left[\psi_a(r_1)\psi_b(r_2) - \psi_a(r_2)\psi_b(r_1)\right] \chi_T \ , \tag{2.32}$$

whose spatial part is anti-symmetric and the spin part is a triplet $\chi_T \sim (\uparrow,\uparrow) \rightarrow S = 1$ (which is symmetric) [7, 9, 13].

The energy for each state is given by equations 2.33 and 2.34 [7, 11]:

$$E_S = \iint \Psi_S^* \hat{\boldsymbol{\mathcal{H}}} \Psi_S \, dr_1 dr_2 = \mathsf{I} + \mathsf{J} \ , \tag{2.33}$$

$$E_T = \iint \Psi_T^* \hat{\boldsymbol{\mathcal{H}}} \Psi_T \, dr_1 dr_2 = \mathsf{I} - \mathsf{J} \ , \tag{2.34}$$

where I is the *Couloumb integral* described by equation 2.35 [9]

$$\boxed{\mathsf{I} = \iint |\psi_a(r_1)|^2 \hat{\boldsymbol{\mathcal{H}}} |\psi_b(r_2)|^2 \, dr_1 dr_2} \ , \tag{2.35}$$

and J is the *Exchange integral*. The exchange integral can be obtained calculating the energy difference between the singlet and triplet state, as shown in (2.36) [9]:

$$E_S - E_T = 2\mathsf{J} \Rightarrow \boxed{\mathsf{J} = \frac{E_S - E_T}{2} = \iint \psi_a^*(r_1)\psi_b^*(r_2) \hat{\boldsymbol{\mathcal{H}}} \psi_a(r_2)\psi_b(r_1) \, dr_1 dr_2} \ . \tag{2.36}$$

Analysing equation 2.36 it is perceptible that for $\mathsf{J} < 0$ the singlet state is the one with less energy, favouring anti-parallel magnetic moments (antiferromagnetic configuration). For $\mathsf{J} > 0$ the triplet state is the lowest energy state, favouring parallel magnetic moments (ferromagnetic configuration) [8].

This interpretation shows that the exchange integral correlated to the possible types of magnetic ordering. This magnetic ordering can be described using the Heisenberg Hamiltonian

of equation 2.37:

$$\hat{\mathcal{H}}_{spin} = -\sum_{ij}^{N} \mathsf{J}_{ij} \hat{\boldsymbol{S}}_{\boldsymbol{i}} \cdot \hat{\boldsymbol{S}}_{\boldsymbol{j}} \ , \tag{2.37}$$

where i and j are the indices referring to two different electrons and N the total number of electrons of the system in study [12].

There are several types of exchange interaction mechanisms which lead to different magnetic ordering and contributions to J_{ij}.

2.4.1 Direct Exchange interaction

The simplest exchange integration is the direct exchange interaction, where adjacent spins tend to align parallelly or anti-parallelly depending on the J_{ij} sign. As the name suggests, this exchange interaction does not need any mediator, therefore, since the electrostatic interactions lose substantially their strength as the distance between spins increases, this effect tends to be dominant between first neighbours [6].

This feature is clearly observed in rare earths, whose $4f$ orbitals are located closer to the nucleus than their $5s$ orbitals, resulting in weak interactions through this exchange mechanism, requiring other exchange interactions mechanisms and/or intermediate elements in order to present magnetic ordering at high temperatures.

2.4.2 Superexchange interaction

Once the direct exchange interaction is associated with quite small ranges, to designate longer interaction ranges the prefix "super" was adopted. The superexchange interaction is an indirect interaction, usually present in oxides, where the oxygen acts as a mediator bridge connecting the exchange interaction of two metals. This indirect interaction is characteristic of insulator ionic solids, where the electrons are relatively well localized [6, 9].

The superexchange interaction lies in the fact that the Oxygen's p orbitals overlap with the d or f orbitals of the magnetic ions, resulting in the hybridization of both orbitals. Figure 2.2 presents the superexchange mechanism between two transition metals (Mn) mediated by an oxygen atom. Configuration (a) is a ferromagnetic configuration and does not allow the mixing of its ground state with the exited states, where one or both oxygen electrons would transfer to

the Mn orbitals due to Pauli's exclusion principle. In the (b) antiferromagnetic configuration there can be a mixing between the ground and excited states, allowing the electrons to be delocalized between Mn's d orbitals and O's p orbitals, lowering their kinetic energy. Because of this, (b) configuration is more stable than configuration (a).

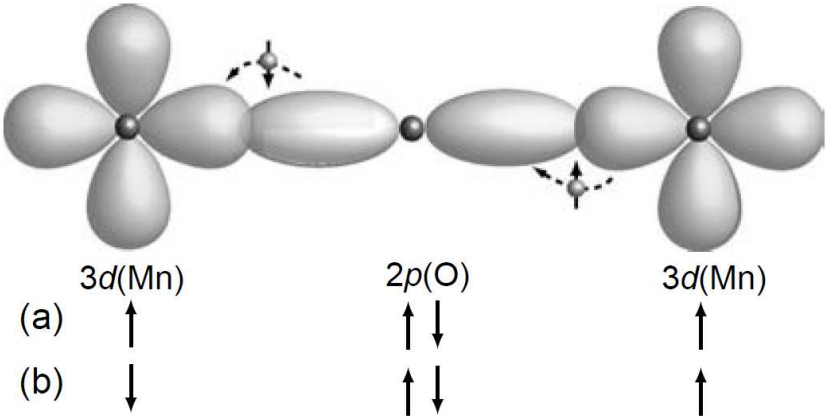

Figure 2.2: Explicative scheme of the superexchange interaction. From [6].

The superexchange interaction is of the order of $\mathsf{J} \sim -t^2/U$, where t is the $p-d$ hopping integral and U is the local Coulomb interaction. The hopping or transfer integral, t depends on the distance and angle between the metallic ions and the mediator anion. This way, it is possible to have a ferromagnetic arrangement for an angle $M-A-M$ of 90°, or the more common antiferromagnetic arrangement for an angle $M-A-M$ comprised between $120-180°$ [6].

2.4.3 RKKY interaction

Other indirect exchange interaction, but this time characteristic of metals, is the RKKY exchange interaction, whose acronym refers to the name of the scientists involved in its discovery (**R**uderman, **K**ittel, **K**asuya and **Y**osida) [11]. This exchange interaction arises from the spin polarization of conduction electrons by local magnetic ions. These polarized electrons serve as long range mediators to the exchange coupling of two local magnetic ions, which are frequently magnetic ion impurities of the host metal.

The RKKY interaction has a value which oscillates along the distance r as described in

equation 2.38:

$$J_{RKKY}(r) \propto \left(\frac{\sin(2k_F \cdot r)}{16(k_F \cdot r)^4} + \frac{\cos(2k_F \cdot r)}{8(k_F r)^3} \right) . \tag{2.38}$$

where k_F is the Fermi wave number. This exchange interaction is responsible for the phenomenon often designated as itinerant magnetism [6, 14, 15].

2.4.4 Double Exchange interaction

For some ions with mixed valence states such as Mn, which typically possess Mn^{3+} and Mn^{4+} valences, there can be a ferromagnetic exchange interaction named double exchange interaction. This coupling mechanism is very well known for the material $La_{1-x}Sr_xMnO_3$ which is a mixture between $LaMnO_3$ (La^{3+} and Mn^{3+} ions) and $SrMnO_3$ (with Sr^{2+} and Mn^{4+} ions). Both $LaMnO_3$ and $SrMnO_3$ are antiferromagnetic perovskites, thus $La_{1-x}Sr_xMnO_3$ is AFM for $x = 1$ and $x = 0$. Nevertheless, for a concentration of $x \approx 0.175$ this material becomes ferromagnetic! This is due to presence of double exchange interactions [9].

The double exchange mechanism is schematized in figure 2.3 where it is possible to observe that for a given ion Mn^{4+} the electron in the e_g energy levels can hop to the Mn^{3+} ion as long as both ions have their t_{2g} electrons aligned (figure 2.3a). If the t_{2g} electrons are not aligned (figure 2.3b) this mechanism becomes energetically unfavourable, thus there is a bias for the mixed valence ions to have their electrons in a ferromagnetic arrangement [6, 9].

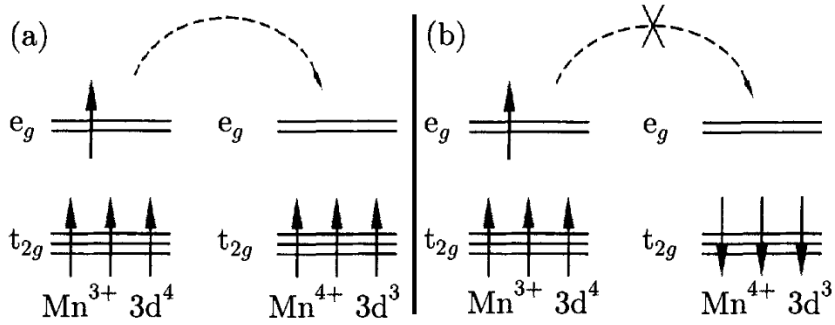

Figure 2.3: Explicative scheme of the mechanisms behind the double exchange interaction. Adapted from [9].

2.4.5 Antisymmetric Exchange interaction

Another very important exchange interaction is the Antisymmetric exchange interaction, which is described by the Hamiltonian of equation 2.39:

$$\hat{\boldsymbol{\mathcal{H}}}_{\boldsymbol{DM}} = \vec{D}_{ij} \cdot \left(\hat{\boldsymbol{S}}_{\boldsymbol{i}} \times \hat{\boldsymbol{S}}_{\boldsymbol{j}} \right) \ , \tag{2.39}$$

where $\vec{D}_{ij} \propto \vec{r}_i \times \vec{r}j$ is the Dzyaloshinsky-Moriya vector. The Antisymmetric exchange, also known as the Dzyaloshinsky-Moriya interaction, is a spin-orbit effect which favours the spin canting of antiferromagnetic spins and is the source the weak ferromagnetism behaviour, which for a long time was wrongly attributed to magnetic impurities in AFM materials [6, 9].

2.4.6 Biquadratic Exchange interaction

Beyond the above mentioned exchange interactions, there can be higher order exchange interactions such as the biquadratic exchange interaction, described by equation 2.40 [6]:

$$\hat{\boldsymbol{\mathcal{H}}} = -\mathfrak{B} \left(\hat{\boldsymbol{S}}_{\boldsymbol{i}} \cdot \hat{\boldsymbol{S}}_{\boldsymbol{j}} \right)^2 \ , \tag{2.40}$$

where $\mathfrak{B}$ is the second order exchange constant, analogous to the first order exchange constant of (2.37), J. Usually these higher order exchange interactions are quite weak, thus are usually neglected.

2.5 Crystal Field

When an atom/ion belongs to a given crystal lattice it will feel the effects of the surrounding atoms (the ligands). As a first approximation we can consider the influence of its neighbouring atoms as the point charge Coulomb interactions of equation 2.41 [6, 7, 9–11, 16–19]:

$$V_{\mathrm{cf}}(r) = \sum_{L=1}^{N} \frac{q_L}{4\pi\epsilon_0 \left|R_L - r\right|} \ , \tag{2.41}$$

or for a more accurate description, let's take into account the Coulomb interactions of the charge density surrounding the considered atom as in (2.42) [6, 7, 9, 11]:

$$V_{\mathrm{cf}}(r) = \int \frac{\rho(R')}{4\pi\epsilon_0 \left|R' - r\right|} d^3R' \ , \tag{2.42}$$

where r is the position of the centre atom, R_L and q_L and are the position and charge of the L index ligand, R' and $\rho(R')$ are the position and the charge density outside the charge density of the centre atom.

These considerations were originally referred as crystal field theory and took into consideration just the point charge model to calculate the interaction of the ligand atoms as described by (2.41). The crystal field theory was later developed so it also considered the effect of the overlap between the ligand electrons and the centre atom (also called ligand theory) adding to the latter's Hamiltonian the term of equation 2.43 [6, 7, 9, 11, 19]:

$$\hat{\boldsymbol{\mathcal{H}}}_{\mathrm{cf}} = \iint \frac{\rho_0(r)\rho(R')}{4\pi\epsilon_0 \left|R' - r\right|} d^3r d^3R' \ . \tag{2.43}$$

This term is added to the total Hamiltonian of an atom in an solid (equation 2.44) [6, 7, 9, 11, 19]:

$$\hat{\boldsymbol{\mathcal{H}}}_{\mathrm{total}} = \hat{\boldsymbol{\mathcal{H}}}_0 + \hat{\boldsymbol{\mathcal{H}}}_{\mathrm{cf}} + \hat{\boldsymbol{\mathcal{H}}}_{\mathrm{so}} + \hat{\boldsymbol{\mathcal{H}}}_{\mathrm{Z}} \ , \tag{2.44}$$

where $\hat{\boldsymbol{\mathcal{H}}}_0$ is the Hamiltonian term responsible for the Coulomb and exchange interactions, $\hat{\boldsymbol{\mathcal{H}}}_{\mathrm{so}}$ is the spin-orbit term, and $\hat{\boldsymbol{\mathcal{H}}}_{\mathrm{Z}}$ is the Zeeman term [6, 7, 9, 11, 19].

For $4d$ ions the magnitudes of the Hamiltonian terms have usually the following order: $\hat{\boldsymbol{\mathcal{H}}}_0 > \hat{\boldsymbol{\mathcal{H}}}_{\mathrm{so}} > \hat{\boldsymbol{\mathcal{H}}}_{\mathrm{cf}} > \hat{\boldsymbol{\mathcal{H}}}_{\mathrm{Z}}$ once the $4d$ valence electrons are shielded from V_{cf} by the $5s$ outer

orbitals, thus the contribution of $\hat{\mathcal{H}}_{\rm cf}$ is mostly neglected [6, 7, 9, 10].

In other hand, for $3d$ ions not only the $\hat{\mathcal{H}}_{\rm so}$ is lower than in $4d$ ions, due to their lower atomic mass, as there are no effective shielding of the $V_{\rm cf}$ potential. In this case the Hamiltonian terms are ordered as $\hat{\mathcal{H}}_0 \gtrsim \hat{\mathcal{H}}_{\rm cf} > \hat{\mathcal{H}}_{\rm so} > \hat{\mathcal{H}}_{\rm Z}$ [6, 7, 9, 19].

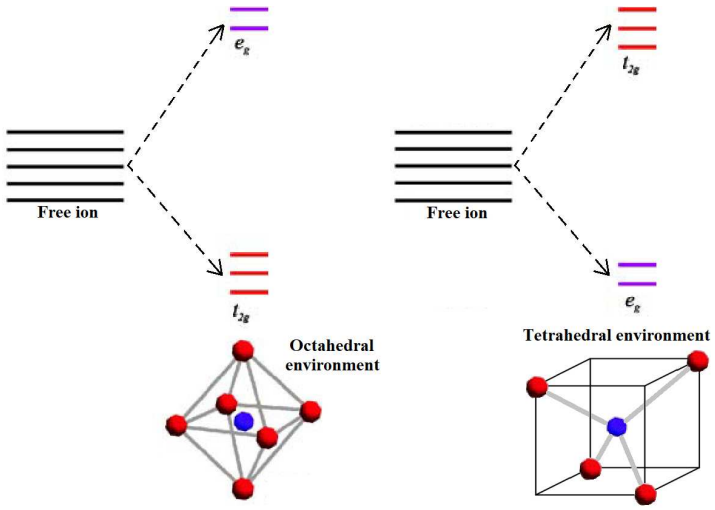

Figure 2.4: Each crystaline field promotes a diffeent energy splitting of the central magnetic ion. Adapted from [9].

For a free transition metal ion/atom there are five possible degenerate d orbitals whose wavefunctions can be described in cartesian coordinates by equations 2.45–2.49 [6,7,11,16,19]:

$$d_{xy} = R(r)xy \ , \tag{2.45}$$

$$d_{xz} = R(r)xz \ , \tag{2.46}$$

$$d_{yz} = R(r)yz \ , \tag{2.47}$$

$$d_{x^2-y^2} = R(r)(x^2 - y^2) \ , \tag{2.48}$$

$$d_{3z^2-r^2} = R(r)(2z^2 - x^2 - y^2) = R(r)(3z^2 - r^2) \ , \tag{2.49}$$

where $R(r)$ is the radial part of the d_i wavefunction.

The crystal field will lift the degeneracy of the five $3d$ orbitals depending in the symmetry and strength of (2.42). In fact, the symmetry of the crystal field is detrimental to the energy splitting. Group theory predicts that when a free $3d$ ion, which has spherical symmetry, is subjected to a cubic crystal field the original 5-dimensional degenerated d orbitals decompose to two irreducible representations: a 3-dimensional representation, T_2 (also known as t_{2g}),

which contains the d_{xy}, d_{xy} and d_{xy} degenerate orbitals, and a 2-dimensional representation, E (also known as e_g), which contains the $d_{3z^2-r^2}$ and $d_{x^2-y^2}$ orbitals [6,7,19]. Figure 2.4 shows two particular examples of energy splitting of two cubic symmetry chemical environments.

It is possible to see that the octahedral and tetrahedral chemical environments lift the energy degeneracy of the d orbitals in opposite ways.

Figure 2.5 shows the energy splitting for several symmetry groups. Δ is the energy splitting energy induced by the crystal field, or crystal field energy. It is possible to observe in figure

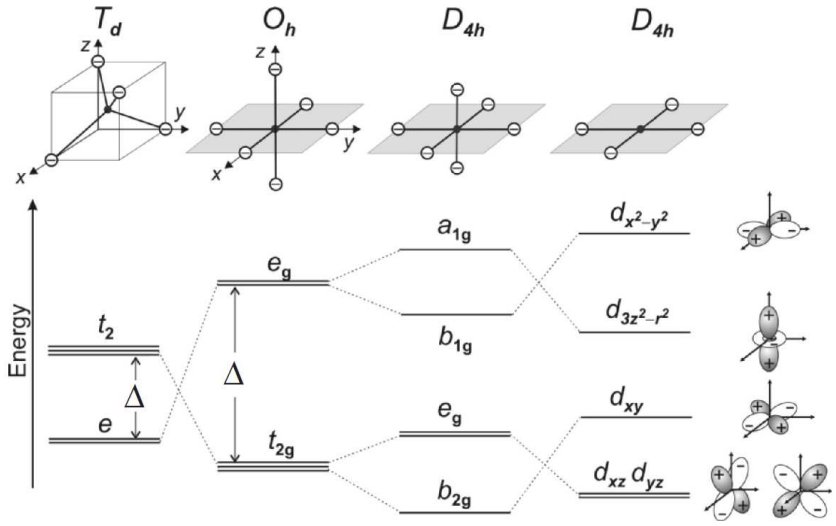

Figure 2.5: Crystal field induced energy splitting for the T_d, O_h, and two D_{4h} symmetry groups. Adapted from [7].

2.5 that the lower the symmetry the more energy splitting there are [7, 18, 19].

2.5.1 Orbital Quenching

The crystal field is in fact related to a well-known effect present in $3d$ magnetic ions of solids and in molecules, whose measured magnetic moments differ from the $\vec{\mathfrak{m}}$ expected from the total angular momentum predicted by Hund rules. The measured magnetic moments would only agree with the ones expected from Hund rules when $\hat{\boldsymbol{L}} = 0$ [6, 9]. In fact, the measured moments would agree quite well if we considered for all cases $\hat{\boldsymbol{L}} \approx 0 \Rightarrow \hat{\boldsymbol{J}} \approx \hat{\boldsymbol{S}}$. This effect is called "orbital quenching" and happens due to the crystal field interaction with the $3d$ orbitals [6, 9].

The crystal field Hamiltonians are always described by real functions[1], therefore their

[1]The octahedral crystal field for example is described by $V_{\text{cf}} \propto x^4 + y^2 + z^4 - \frac{3}{5}r^4 + O(r^6)$

eigenfunctions are all real [6, 7, 9, 16, 19]. Let's consider the specific case of a non-degenerate ground state $|0\rangle$. Since $\hat{\boldsymbol{L}}$ is Hermitian, its expected value $\langle 0|\,\hat{\boldsymbol{L}}\,|0\rangle$ must be real [6, 7, 9, 16, 19]. However $\hat{\boldsymbol{L}}$ is an imaginary operator, as equation 2.50 shows us:

$$\hat{\boldsymbol{L}} = -i\hat{\boldsymbol{r}} \times \nabla \ , \tag{2.50}$$

therefore, the only way to $\langle 0|\,\hat{\boldsymbol{L}}\,|0\rangle$ be real is when:

$$\langle 0|\,\hat{\boldsymbol{L}}\,|0\rangle = 0 \Longrightarrow \hat{\boldsymbol{L}} = 0 \ . \tag{2.51}$$

There are several ways to prove/interpret the source of the orbital quenching, however in the end, it all comes to the need of its quenching for the simultaneously real and imaginary nature of $\langle 0|\,\hat{\boldsymbol{L}}\,|0\rangle$ for $3d$ ions under a real non-zero crystal field [6, 7, 9, 16, 19].

2.5.2 Jahn-Teller Effect

Another fairly well known crystal field effect is the Jahn-Teller effect, where there is a distortion in the crystal lattice due to the energy lifting within the e_g and t_{2g} orbitals (figure 2.6) [6, 10, 16, 20]. In figure 2.6 it is possible to observe that for a tetragonal elongation

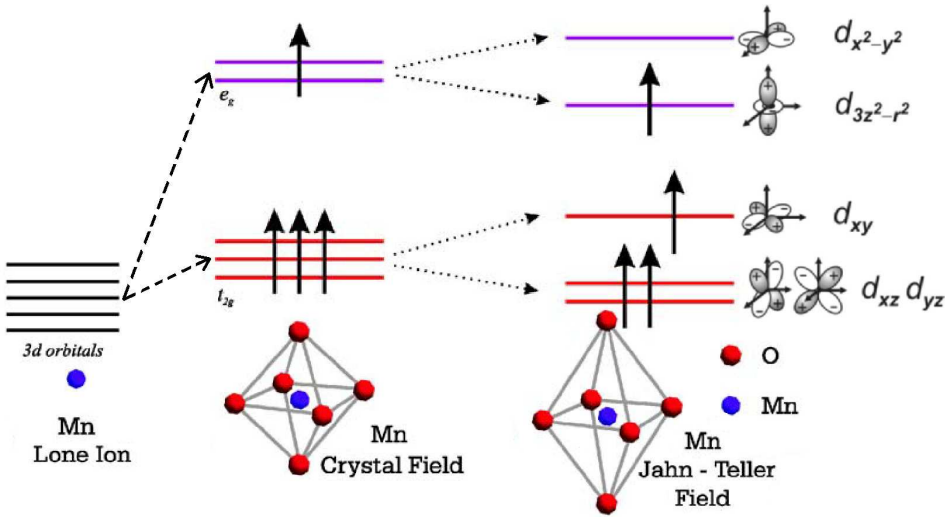

Figure 2.6: Energy diagrams of a Jahn-Teller distortion for the Mn^{3+} ion. Adapted from [20].

of the octahedral coordination the e_g and t_{2g} orbitals lift the degeneracy again (due to the further lowering of the crystal field symmetry) resulting in an overall lower energy electronic

occupation energy. This energy lowering is given by equation 2.52 [6, 16, 20]:

$$E_{\text{jt}} = -A\epsilon \ , \tag{2.52}$$

where A is a constant and ϵ is the tetragonal strain. It is also necessary to take into account the elastic energy resultant from the local elongation. This energy is described by equation [6, 7, 9, 16]:

$$E_{\text{elastic}} = +B\epsilon^2 \tag{2.53}$$

where B is a constant related to the elastic energy. To determine the equilibrium strain it is necessary to sum both (2.52) and (2.53) obtaining as a result equation 2.54

$$E_{\text{total}} = -A\epsilon + B\epsilon^2 \ . \tag{2.54}$$

Finally for a positive solution of equation 2.55 we find the equilibrium strain ϵ_0 [6, 7, 9, 16].

$$\frac{\partial E_{\text{total}}}{\partial \epsilon} = 0 \Longrightarrow \epsilon_0 = \frac{A}{2B} > 0 \tag{2.55}$$

2.5.3 High-Spin–Low-Spin transition

At last, I would like to discuss here the fascinating High-Spin–Low-Spin transitions. As discussed above, the crystalline field of ligand atoms will lift the degeneracy of the d orbitals by a crystal energy Δ. Notwithstanding, there is another quantity that should be considered to understand how the $3d$ orbitals will be filled in a multi-electron transition metal. This quantity is the pairing energy, U, and is related to the energy penalty resulting from the electrostatic repulsion between two electrons occupying the same orbital [6, 7, 17, 19].

Depending on relative magnitude of both Δ and U it is possible to have more than one way of filling the same ion $3d$ orbitals. Let's once again use the octahedral crystal field as an example. For $U \gg \Delta$ all the orbitals are firstly filled with just one electron per orbital, obeying the first Hund's rule. This scenario will result in the highest possible unpaired spins thus being a High-spin (HS) state (figure 2.7). Contrarily, for $U \ll \Delta$ the first Hund's rule is violated and all the t_{2g} orbitals are filled before filling the e_g orbitals. This scenario will result in the

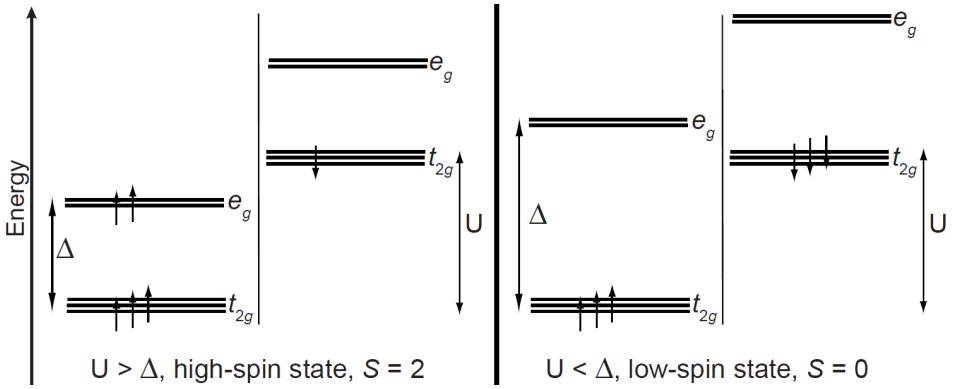

Figure 2.7: Explicative diagram of the mechanism behind the Low-spin and High-spin configurations. Adapted from [7].

lowest possible unpaired spins, being a Low-spin (LS) state (figure 2.7). Figure 2.8 shows the LS and HS configurations for two Fe ions under an octahedral crystal field [6, 7, 17, 19].

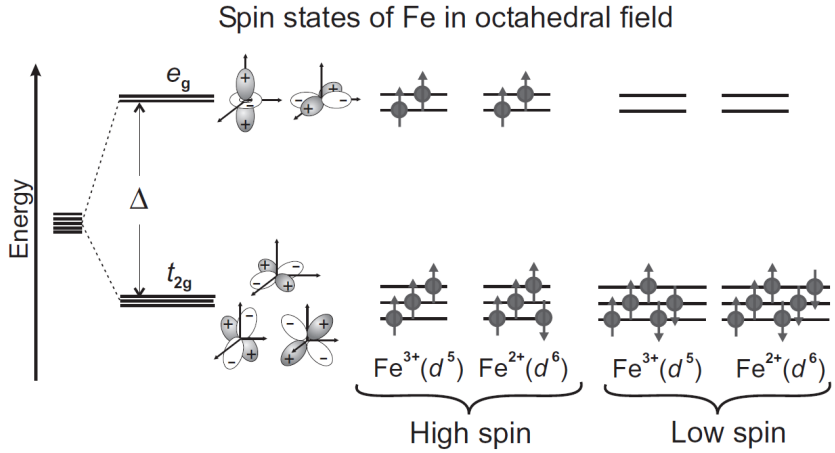

Figure 2.8: Energy diagram of Fe^{2+} and Fe^{3+} Low-Spin and High-Spin states. Adapted from [7].

Using external perturbations such as pressure and temperature it is possible to induce spin state transitions between the HS and LS configurations of specific ions, depending on their Δ, U and the magnitude of the external perturbation [17].

2.6 Order Parameters and Symmetry Breaking

The spontaneous order of a given physical quantity below a given temperature is a common but quite interesting phenomenon in nature. The emergence of spontaneous magnetization, spontaneous polarization, null resistivity are phenomena that happen below a critical temper-

ature T_C for the ferromagnetism, ferroelectricity and superconductivity respectively.

This symmetry breaking of a given system is quite similar to a phase transition, such as the transition from a liquid to a solid. Liquid water, for example, is in a high symmetry state, where all water molecules are randomly oriented, thus the system will seem to be in the same arrangement even after several symmetry operations. When the water freezes, its ordering constrains the possible symmetry operations which maintain the arrangement of the molecules apparently unchanged, so there was a symmetry break and, therefore, ice is a less symmetric state of the water molecules arrangement.

Lev Landau was probably the scientist which contributed the most to the thermodynamic study of phase transitions. In his theory a given system can be described around the vicinities of its critical point[2] by a thermodynamic potential, Φ, expanded in a power series with the order parameter η and an applied field Y, as described in (2.56) [21].

$$\Phi(x, y, \eta) = \Phi_0 + \Phi_1\eta + \Phi_2\eta^2 + \Phi_3\eta^3 \cdots - \eta Y \quad \text{where} \begin{cases} \eta = 0 & , \quad T > T_C \\ \eta \neq 0 & , \quad T < T_C \end{cases} \tag{2.56}$$

This approach turned out to be very useful and truly effective in most cases, being a very simple mean field approach which describes adequately many physical behaviours such as the magnetization of a given material [21, 22].

In a ferromagnetic system the order parameter is the magnetization, M, where $M = 0$ in the high temperature phase and $M \neq 0$ below the critical temperature, T_C, also known as Curie temperature.

2.6.1 Paramagnetism

Paramagnetism is the high symmetry phase of a magnetic system (such as Fe or Ni), where $M = 0$ in the absence of a magnetic field. In this phase the magnetic dipole moments (spins) are randomly oriented due to the overtake of the thermal energy over the exchange interactions, thus there is no overall well defined alignment of the material spins (figure 2.9). Nevertheless, if an external magnetic field is applied to the system its magnetic energy (2.27) increases, overcoming the thermal energy and so its net magnetization becomes non-zero.

[2] Point where there is a phase transition for which there is a drastic change between two types of behaviours. For a ferromagnetic material this critical point correspond to its Curie temperature

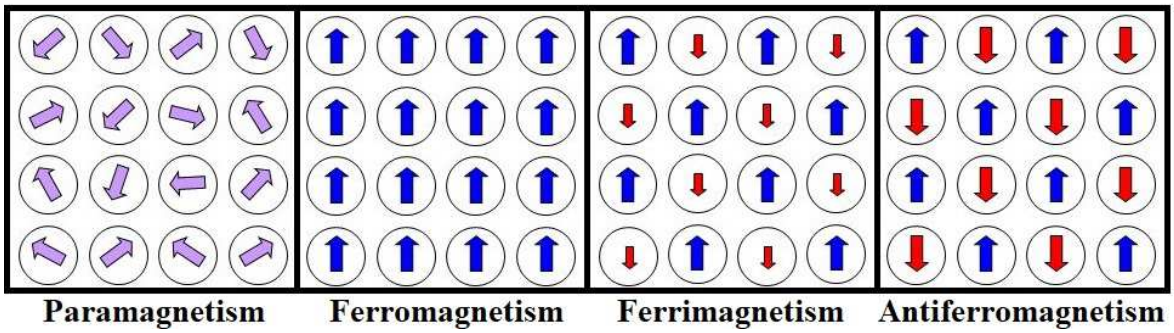

Figure 2.9: Types of magnetic ordering.

To describe PM with a simple case, let's consider a system where each atom contributes to the total magnetic moment with spin $J = S = 1/2$). There are two possible states for each spin, one for the up orientation $|\uparrow\rangle$ and other for the down orientation $|\downarrow\rangle$. Using equation 2.27 it is possible to determine the energy associated with both states, $E_{|\uparrow\rangle} = -\mu_B B$ and $E_{|\downarrow\rangle} = +\mu_B B$. To determine the magnetization as a function of the temperature and magnetic field for this system we can use the equation 2.57, the Maxwell-Boltzman distribution:

$$p(E) = Ae^{(-E/k_{\mathrm{B}}T)} \tag{2.57}$$

to determine the difference between the populations of $|\uparrow\rangle$ and $|\downarrow\rangle$. The population difference of these two states is proportional to the net magnetization as shown in equation 2.58:

$$M(B,T) \propto M(B,0)\frac{e^x - e^{-x}}{e^x + e^{-x}} = \tanh x \quad , \quad x = \frac{\mu_{\mathrm{B}} B}{k_{\mathrm{B}} T} \ , \tag{2.58}$$

where $M(B,0) = n\mu_{\mathrm{B}}$ for $n = {}^{N}/_{V}$ is the maximum possible magnetization (all spins are aligned in the same direction). Therefore, for this system the magnetization as a function of temperature and magnetic flux density is described by equation 2.59:

$$M(B,T) = n\mu_B \tanh(x) \tag{2.59}$$

Léon Brillouin generalized this idea for a system of atoms with many electrons, with a total angular momentum J by evaluating the total magnetic dipole thermodynamic average,

$\langle \mathfrak{m}_z \rangle$ for all possible $|m_J\rangle$ states, as shown in equation 2.60 :

$$\langle \mathfrak{m}_z \rangle = \frac{\sum_{i=-J}^{+J} g_J \cdot \mu_{\mathrm{B}} \cdot m_i \cdot e^{\left(-\frac{E}{k_{\mathrm{B}}T}\right)}}{\sum_{i=-J}^{+J} e^{\left(-\frac{E}{k_{\mathrm{B}}T}\right)}} \ . \tag{2.60}$$

After some algebra, the general magnetization equation is given by equation 2.61:

$$M(B,T) = M_s \mathcal{B}_J(y) \tag{2.61}$$

where $M_s = n g_J \mu_B J$ is the saturation magnetization, $y = xJ$, and $\mathcal{B}_J$ is the Brillouin function, defined as (2.62).

$$\mathcal{B}_J(y) = \frac{2J+1}{2J} \coth\left(\frac{2J+1}{2J} y\right) - \frac{1}{2J} \coth\left(\frac{y}{2J}\right) \tag{2.62}$$

Other particular case is the limit where $J \to \infty$ which results in the classical Langevin function, $\mathcal{B}_\infty(y) = \mathcal{L}(y)$, defined by equation 2.63.

$$\mathcal{L}(y) = \coth(y) - \frac{1}{y} \tag{2.63}$$

At high temperatures and magnetic fields not excessively large it is possible to approximate the description of a paramagnet material to the Curie law (2.64):

$$\chi = \frac{C}{T} = \frac{n\mu_0 \mu_B^2 g_J^2 J(J+1)}{3k_B} \cdot \frac{1}{T} \tag{2.64}$$

where χ is the magnetic susceptibility, and C is the Curie constant.

2.6.2 Ferromagnetism

Ferromagnetism (FM) is the paramagnetism counterpart, being the magnetic low symmetry ordered phase. In this ordered phase the exchange integral is $\mathsf{J} > 0$, thus having a spontaneous magnetization for a null external magnetic field. The ferromagnetic state of a given material only arises below a critical temperature, its Curie temperature, where there is the mentioned spontaneous magnetization. This happens since the Heisenberg term (2.37) of

the system's Hamiltonian overtakes the thermal energy, being responsible for the tendency of the magnetic moments to be aligned in the same direction (figure 2.9).

Before there was a quantum framework explaining the exchange interaction, Weiss developed a classical approach to interpret ferromagnetism. Weiss imagined a molecular field $\vec{B}_{\text{mf}} = \lambda\vec{M}$ which would be responsible for the alignment of the magnetic moments of the ferromagnet. The idea of a molecular field is just a mean field approximation and is conceptually inaccurate, as a matter of fact, a molecular field in the order of 10^3 T would be necessary to explain the existence of ferromagnetism in Fe.

Notwithstanding, using the effective magnetic field of equation 2.65:

$$\vec{B}_{\text{eff}} = \vec{B} + \vec{B_{\text{mf}}} = \vec{B} + \lambda\vec{M} \tag{2.65}$$

as the magnetic field considered in the Brillouin function (2.62) we obtain the transcendental equation 2.66:

$$M(B_{\text{eff}}, T) = M_s\mathcal{B}_J(y) \quad , \quad y = \frac{\mu_{\text{B}} J B_{\text{eff}}}{k_{\text{B}} T} = \frac{\mu_{\text{B}} J(B + \lambda M)}{k_{\text{B}} T} \ . \tag{2.66}$$

These kind of equations have the peculiarity that the magnetization depends on the material history, which translates in a hysteresis curve of magnetization with a coercive field H_{C} ($M(H_{\text{C}}) = 0$), and a spontaneous magnetization which for a very hard ferromagnet is the same as the saturation magnetization M_s.

In a ferromagnetic system, for $T \geq T_{\text{C}}$ it is possible to use the Curie-Weiss law to describe its paramagnetic susceptibility, as perceptible in equation 2.67:

$$\chi = \frac{C}{T - T_C} \tag{2.67}$$

It is also possible to correlate Weiss molecular field with the meaningful quantum exchange interactions, thus unveiling in (2.68) which are the physical quantities behind the molecular field constant λ:

$$\lambda = \frac{2z\mathsf{J}(g_J - 1)^2}{n g_J^2 \mu_B^2} \tag{2.68}$$

where z is the number of first neighbours.

Knowing that the Curie temperature is the product between the molecular field constant and the Curie constant, it is possible to define this critical temperature by equation 2.69:

$$T_C = \lambda C = \frac{2z\mathrm{J}(g_J - 1)^2}{3k_B} J(J+1) \tag{2.69}$$

Curie-Weiss law describes well the behaviour of a ferromagnetic material in its paramagnetic phase, however for $T \approx T_\mathrm{C}$ there is a singular behaviour (the Curie-Weiss law is only applicable for $T > T_\mathrm{C}$). To solve these problems, Landau theory (equation 2.56) can be used around the Curie temperature as another mean field approach. In this case, the order parameter η is clearly the magnetization M and the chosen thermodynamic potential is the Helmholtz free energy, F. To ensure that there is no energy distinction between two identical systems with net magnetization M and $-M$, only even terms are considered in the power expansion. Considering only the terms till the fourth power, equation 2.70 is obtained:

$$F(M,T) = F_0 + a(T)M^2 + bM^4 \tag{2.70}$$

where F_0, $b > 0$ and $a(T)$ are parameters characteristic from the system/material in study.

To find the minimum energies of the Helmholtz free energy equation 2.70 is differentiated, as shown in equation 2.71:

$$\frac{\partial F}{\partial M} = 2M\left[a_0(T - T_\mathrm{C}) + 2bM^2\right] = 0 \tag{2.71}$$

where it is assumed that $a(T) = a_0(T_\mathrm{C} - T)$ for a a_0 always positive. Solving equation 2.71 for M results in the two solutions[3] of equation 2.72:

$$M = 0 \quad \vee \quad M = \pm\left[\frac{a_0(T_\mathrm{C} - T)}{2b}\right]^{1/2}. \tag{2.72}$$

The second solution describes the spontaneous magnetization of a ferromagnet as a function of its temperature and only has real values for $T \leq T_\mathrm{C}$. For $T > T_\mathrm{C}$ the system is in its paramagnetic state and is described by the trivial solution of (2.72), $M = 0$.

When $b < 0$, the second solution of (2.72) has imaginary values even for $T < T_\mathrm{C}$. This

[3]The two possible signs of the second solution correspond to the two equivalent and degenerate opposite magnetizations

problem is characteristic of a first order phase transition and is solved considering the power series at least till the sixth power.

2.6.3 Antiferromagnetism

Antiferromagnetism is a type of collective magnetic ordering with an exchange integral $\mathsf{J} < 0$ leading to anti-parallelly aligned magnetic moments. Typical examples of antiferromagnets are metal oxides such as NiO, MnO, Fe_2O_3, etc.

If all magnetic moments possess the same magnitude, then the magnetic moments cancel out and the material net magnetization is zero, as represented in figure 2.9. However, if the anti-parallel moments have different magnitudes there will be an overall spontaneous magnetization and we are in the presence of a ferrimagnetic material (fM) (figure 2.9).

To describe a simple AFM material one can consider the superposition of two ferromagnetic crystal lattices, A and B, whose molecular fields have opposite orientations, as shown in equations 2.73 and 2.74:

$$\vec{B}^{\mathrm{A}}_{eff} = \lambda_{\mathrm{AA}}\vec{M}_{\mathrm{A}} + \lambda_{\mathrm{AB}}\vec{M}_{\mathrm{B}} + \vec{B} \ , \tag{2.73}$$

$$\vec{B}^{\mathrm{B}}_{eff} = \lambda_{\mathrm{BB}}\vec{M}_{\mathrm{B}} + \lambda_{\mathrm{BA}}\vec{M}_{\mathrm{A}} + \vec{B} \ . \tag{2.74}$$

In this physical model, suggested by Louis Néel, the magnetization is the sum of the two lattices as shown in equation 2.75:

$$M = M_{s_{\mathrm{A}}}\mathcal{B}_J\left(y_{\mathrm{A}}\right) + M_{s_{\mathrm{B}}}\mathcal{B}_J\left(y_{\mathrm{B}}\right) \ . \tag{2.75}$$

When $\lambda_{\mathrm{AA}} = \lambda_{\mathrm{BB}} = \lambda'$, $\lambda_{\mathrm{AB}} = \lambda_{\mathrm{BA}} = -\lambda$ and $M_{s_{\mathrm{A}}} = -M_{s_{\mathrm{B}}}$ we have an AFM ordering with $M = 0$.

The Curie-Weiss law can also be used to describe an AFM material. As a matter of fact, it is possible to formulate the general Curie-Weiss law of equation 2.76:

$$\chi = \frac{C}{T - \Theta_p} \tag{2.76}$$

where Θ_p is the Weiss temperature and is $\Theta_p = 0$ for a paramagnetic material, $\Theta_p = T_{\mathrm{C}}$ for a ferromagnetic material, and $\Theta_p = -T_N$ for an antiferromagnetic material, where T_N is the

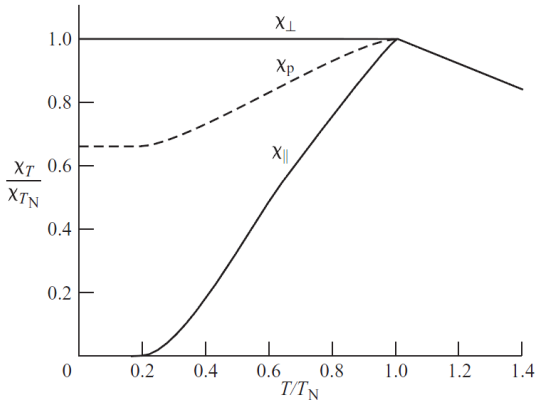

Figure 2.10: Susceptibility curves for an AFM material. χ_p is the magnetic susceptibility of a powder or a polycrystalline material where all crystallites are randomly dispersed.

Néel temperature and is described by equation 2.77:

$$T_N = \frac{C}{2\mu_0}\left(\lambda - \lambda'\right) \tag{2.77}$$

Like the FM case, the Curie-Weiss law just describes the AFM behaviour properly till its Néel temperature. For $T < T_N$ the magnetic susceptibility depends on the direction of the external magnetic field.

For a magnetic field parallel to the magnetic moments, the magnetic susceptibility $\chi_\parallel \to 0$ the closer $T \to 0$ K since for low magnetic the lowest the thermal energy the more antiparallel will the magnetic moments be, while its maximum value is reached at $T = T_N$. For a magnetic field perpendicular to the antiparallel magnetic moments there will be a small canting of the magnetic moments resulting in a magnetic susceptibility of (2.78):

$$\chi_\perp = -\frac{1}{\lambda_{\mathrm{AB}}}\ , \tag{2.78}$$

which is constant for all values of $T < T_N$ (figure 2.10). For the case of a powder, or a polycrystalline sample, all the moments are randomly distributed, thus its magnetization will be an average of the perpendicular and parallel susceptibilities (figure 2.10), as described by equation 2.79:

$$\chi_p = \frac{1}{3}\chi_\parallel + \frac{2}{3}\chi_\perp \tag{2.79}$$

2.6.4 Diamagnetism

Diamagnetism (DM) is a magnetic behaviour which in fact is not a type of ordering but is ubiquitous in all materials. The diamagnetism, as its name suggests, is the ability of a given material to counter/repel an external magnetic field. This phenomenon can be classically interpreted as a consequence of Faraday equation (2.15c) where there are orbital electron currents which counter the external magnetic fields through Lenz law.

Despite this helpful interpretation, remembering the theorem of Bohr van Leeuwen, it makes sense to be cautious and use a quantum approach to understand the source of such behaviour. Considering the canonical generalized momentum (2.80):

$$\vec{p} = m\vec{v} + q\vec{A} \tag{2.80}$$

$$\tag{2.81}$$

where $\vec{A}$ is the vector potential defined as $\nabla \times \vec{A} = \vec{B}$, it is possible to arrive to the Hamiltonian of equation 2.82:

$$\hat{\boldsymbol{\mathcal{H}}} = \hat{\boldsymbol{\mathcal{H}}}_{\mathbf{0}} + \mu_B g_J \hat{\boldsymbol{J}} \bullet \vec{B} + \frac{e^2}{8m_e} \sum_{i=1}^{Z} \left(\vec{B} \times \vec{r}_i \right)^2 \tag{2.82}$$

whose last term describes the diamagnetism of a given material [9].

Using first order perturbation theory, it is possible to determine that the energy shift of the perturbed state is given by equation 2.83:

$$\Delta E_0 = \frac{e^2 B}{12_e^m} \sum_{i=1}^{Z} \left\langle 0 \left| r_i^2 \right| 0 \right\rangle \ . \tag{2.83}$$

Given that the magnetization can be described as (2.84):

$$M = -\frac{\partial F}{\partial B} = -\frac{N}{V} \frac{\partial \Delta E_0}{\partial B} = -\frac{N e^2 B}{6 m_e V} \sum_{i=1}^{Z} \left\langle r_i^2 \right\rangle \tag{2.84}$$

$$\tag{2.85}$$

and that $\chi \approx \mu_0 \frac{M}{B}$, we can define the diamagnetic susceptibility as (2.86) [9]:

$$\chi = -\frac{N}{V}\frac{e^2\mu_0}{6m_e}\sum_{i=1}^{Z}\left\langle r_i^2\right\rangle \approx -\frac{N}{V}\frac{e^2\mu_0}{6m_e}Z_{eff}r^2 \tag{2.86}$$

where Z_{eff} is the number of last shell electrons of the diamagnetic atom, and r is the diamagnetic atom radius.

This property is always present in all materials, however, it is usually outshined by the paramagnetism and/or by magnetic ordered phases, being noticeable most of the times for materials with small (if any) magnetic moments. Inspecting (2.86) it is perceptible that the diamagnetic susceptibility is always negative and is temperature independent. Temperature changes can affect somehow its susceptibly, however these additional effects are usually negligible [6].

2.7 *Ab initio* calculations

To understand the microscopic mechanisms in atoms, molecules and crystals, a quantum mechanics description is required. The *ab initio* (first principles) approach is characterized by the Schrödinger equation [13, 23, 24]:

$$\hat{\boldsymbol{\mathcal{H}}} \left|\Psi(\vec{r},t)\right\rangle = i\hbar \frac{\partial}{\partial t} \left|\Psi(\vec{r},t)\right\rangle \ . \tag{2.87}$$

Here I will consider its simpler form, the time independent Schrödinger equation:

$$\hat{\boldsymbol{\mathcal{H}}} \left|\Psi(\vec{r})\right\rangle = E \left|\Psi(\vec{r})\right\rangle \ . \tag{2.88}$$

To describe a given system comprised of N atoms we will need the Hamiltonian which describes all the N nucleus and $N_e = \sum_i^N Z_i$ electrons of this system. In the absence of any external field, the exact Hamiltonian is given by equation 2.89 [13, 23, 24]:

$$\begin{aligned}\hat{\boldsymbol{\mathcal{H}}} = &-\frac{\hbar^2}{2}\sum_{i=1}^{N}\frac{\nabla^2}{M_i} - \frac{\hbar^2}{2}\sum_{i=1}^{N}\frac{\nabla^2}{m_i} + \frac{e^2}{8\pi\epsilon_0}\sum_{i\neq j}^{N}\frac{Z_i Z_j}{\left|\vec{R}_i - \vec{R}_j\right|} - \frac{e^2}{4\pi\epsilon_0}\sum_{i=1}^{N}\sum_{j=1}^{N_e}\frac{Z_i}{\left|\vec{R}_i - \vec{r}_j\right|} + \\ &+ \frac{e^2}{8\pi\epsilon_0}\sum_{i\neq j}^{N}\frac{1}{|\vec{r}_i - \vec{r}_j|} = \hat{T}_n + \hat{T}_e + \hat{V}_{n,n} + \hat{V}_{n,e} + \hat{V}_{e,e} \ ,\end{aligned} \tag{2.89}$$

where M_i is the mass of the i^{th} nucleus, m_i is the mass of the i^{th} electron, Z_i is the atomic number of the i^{th} nucleus, R_i is the position of the i^{th} nucleus and r_i is the position of the i^{th} electron. The first term $\hat{T}_n$ describes the kinetic energy of all nucleus, $\hat{T}_e$ the electrons kinetic energy, $\hat{V}_{n,n}$ the Coulomb interactions between nucleus, $\hat{V}_{n,e}$ the Coulomb interactions between nucleus and electrons, and $\hat{V}_{e,e}$ the Coulomb interactions between electrons [23, 24].

2.7.1 Born-Oppenheimer approximation

Apart from very specific cases, such as for the Hydrogen atom, there are no analytic solutions to the Schrödinger equation with the Hamiltonian (2.89), hence approximations are required [13].

Due to the much higher mass of any nucleus when compared to the mass of an electron, it is reasonable to consider that in the time scale of the electrons dynamics the nucleus remain

static. Doing this adiabatic approximation results in the vanishing of the $\hat{T}_n$ and in the simplification of the $\hat{V}_{n,n}$ term into a constant, while the $\hat{V}_{n,n}$ term can be approximated to an "external" electrostatic potential, $\hat{V}_{\text{ext}}$ (which in a crystal lattice is also periodic). This approximation is known as the Born-Oppenheimer approximation and greatly simplifies the (2.89) Hamiltonian into the Hamiltonian of equation 2.90 [6, 23–26]

$$\hat{\boldsymbol{\mathcal{H}}}_{\text{BO}} = \hat{T}_e + \hat{V}_{e,e} + \hat{V}_{\text{ext}} \ . \tag{2.90}$$

2.7.2 The Hartree-Fock method

It is possible to define the wavefunction of a N particle system as the product of the orthogonal particle wavefunctions $\Psi(r_1, r_2, \ldots, r_N) = \chi_1(r_1)\chi_2(r_2)\ldots\chi_N(r_N)$, also known as a Hartree product. However for fermions, such as electrons, the wavefunction must be antisymmetric (due to Pauli principle), which does not hold by itself for the previous product [6, 23–26].

Let's consider the simplest, two electrons, case. It is possible to define an antisymmetric wavefunction as a linear combination of the Hartree products of the individual electron wavefunctions (equation 2.91) [6, 23–26]:

$$\Psi(r_1, r_2) = \frac{1}{\sqrt{2}}\{\chi_1(r_1)\chi_2(r_2) - \chi_1(r_2)\chi_2(r_1)\} = \frac{1}{\sqrt{2}}\begin{vmatrix}\chi_1(r_1) & \chi_2(r_1)\\ \chi_1(r_2) & \chi_2(r_2)\end{vmatrix} \tag{2.91}$$

which can also be written as a determinant. If we put the two electrons in the same orbit $\chi_1 = \chi_2 \Rightarrow \Psi(r_1, r_2) = 0$ satisfying the Pauli principle.

The approach of equation 2.91 can be generalized to the N electrons case, writing its wavefunction via the Slater determinant (name given to this type of determinants) of equation 2.92 [6, 23–26]:

$$\Psi(r_1, r_2, \ldots, r_N) = \frac{1}{\sqrt{N}}\begin{vmatrix}\chi_1(r_1) & \chi_2(r_1) & \cdots & \chi_N(r_1)\\ \chi_1(r_2) & \chi_2(r_2) & \cdots & \chi_N(r_2)\\ \vdots & \vdots & \ddots & \vdots\\ \chi_1(r_N) & \chi_2(r_N) & \cdots & \chi_N(r_N)\end{vmatrix} \tag{2.92}$$

The Hartree-Fock (HF) method uses this approach to determine $\Psi(r_1, r_2, \ldots, r_N)$ multi-

electron wavefunction assuming that it can be approximated to a single Slater determinant. It considers the Born-Oppenheimer Hamiltonian (2.90), but neglects its electron correlation term, $\hat{V}_{e,e}$. Then using a variational method, it is possible to obtain the linear combinations of the set of functions ϕ_i (equation 2.93) [6, 23–27]:

$$\chi_i = \sum_{k=1}^{K} \alpha_{i,k}\phi_k \ , \tag{2.93}$$

which define each spin orbital, χ_i, and whose coefficients α_k minimize the energy eigenvalue.

Besides not considering the electrons correlations, the HF method also has other severe problem. For a 3-dimensional system of N atoms with N_e electrons each, which needs K functions to define each spin orbital χ_i, we will be before a $3 \times N \times N_e \times K$ dimensional wavefunction. For example, considering a cluster of 100 U atoms and a $K = 10$ we will have a 282000-dimensional wavefunction which is quite heavy from a numerical/computational point of view [25, 27].

2.7.3 Density Functional Theory

One way to solve this dimensionality problem would be to use the electron density of equation 2.94 [23, 25, 27]:

$$n(\vec{r}) = 2 \sum_{i=1}^{N_{total}} \psi_i^*(\vec{r}) \cdot \psi_i(\vec{r}) \ , \tag{2.94}$$

which only has 3 spatial coordinates, as a means of describing a N_{total} electron system, instead of using the full wavefunction with its $3N_{\text{total}}$ spatial coordinates[4]. The factor 2 in (2.94) arises due to the Pauli exclusion principle[5] [23, 25, 27].

As a matter of fact, $n(\vec{r})$ can be used to describe the above mentioned systems, as stated in Hohenberg-Kohn theorems [23, 25, 28].

Hohenberg-Kohn Theorem 1 *The ground-state energy from Schrödinger's equation is a*

[4]For the previous example we are talking about $3N_{\text{total}} = 3N_e \cdot N = 28200$ coordinates

[5]Here I use ψ_i to define the individual electron wavefunctions to differentiate from the individual electron wavefunctions χ_i of the HF method, despite $\psi_i \equiv \chi_i$.

unique functional of the electron density $n(\vec{r})$:

$$\Psi_0(\vec{r}_1, \vec{r}_2, \ldots, \vec{r}_N) = \Psi_0[n(\vec{r})]$$

The first theorem implies that for an observable $\hat{O}$, its expectation value is a functional of the exact ground state electron density [23, 25, 28]:

$$\langle \Psi | \hat{O} | \Psi \rangle = O[n(\vec{r})] \ . \tag{2.95}$$

If the observable of equation 2.95 is the Hamiltonian, then:

$$\langle \Psi | \hat{\boldsymbol{\mathcal{H}}} | \Psi \rangle = E[n(\vec{r})] \ . \tag{2.96}$$

Hohenberg-Kohn Theorem 2 *The electron density that minimizes the energy of the overall functional is the true electron density corresponding to the full solution of the Schrödinger equation.*

This theorem implies that if the functional mentioned in the first theorem is known, then it is possible to determine the correct electron density by finding the $n(\vec{r})$ which minimizes the ground state energy [23, 25, 28].

These theorems are the basis for the density functional theory (DFT), a popular *ab initio* approach to solve complex quantum mechanical systems. Nonetheless, despite the promising consequences of Hohenberg-Kohn theorems, they do not say how to determine the functional mentioned by them! Nonetheless it is possible to divide the ground state energy functional, $E[\Psi_0]$, in two different functionals [23, 25, 27]:

$$E[\Psi_0] = E_{\text{known}}[\Psi_0] + E_{\text{XC}}[\Psi_0] \ , \tag{2.97}$$

the known functional $E_{\text{known}}[\Psi_0]$ described by equation 2.98:

$$\begin{aligned} E_{\text{known}}[\Psi_0] =& \frac{\hbar}{m} \sum_{i=1}^{N_{total}} \int \psi_i^*(\vec{r}) \nabla^2 \psi_i(\vec{r}) d^3r + \\ &+ \int V(\vec{r}) n(\vec{r}) d^3r + \frac{e^2}{2} \iint \frac{n(\vec{r}) \cdot n(\vec{r}')}{|\vec{r} - \vec{r}'|} d^3r d^3r' + E_{\text{ion}} \end{aligned} \tag{2.98}$$

where the first term is the kinetic energy of the electrons, the second term the Coulomb interaction between the fixed nucleus and the electrons, the third term is the Coulomb interaction between the electrons and the last term is the a constant related to the Coulomb interactions between the nucleus. Any unknown part of the energy functional fits inside the exchange-correlation functional, $E_{\mathrm{XC}}[\Psi_0]$ [23, 25, 27].

Kohn and Sham proved that it was possible to find the correct energy density by solving a set of equations, the Kohn-Sham equations, one for each electron [23–26, 29, 30]. A single Kohn-Sham equation is given by:

$$\left[\frac{\hbar}{2m}\nabla^2 + V(\vec{r}) + V_H(\vec{r}) + V_{\mathrm{XC}}(\vec{r})\right]\psi_i(\vec{r}) = \varepsilon_i\psi_i(\vec{r}) \ , \tag{2.99}$$

where V_H is the Hartree potential given by:

$$V_H(\vec{r}) = e^2 \int \frac{n(\vec{r}')}{|r - r'|} d^3r' \tag{2.100}$$

and describes the Coulomb repulsion between the electron of ψ_i and the total electron density of (2.94). $V_{\mathrm{XC}}(\vec{r})$ defines the exchange and correlation contributions of the electrons, as well other possible corrections, and is described by [23–26, 29, 30]:

$$V_{\mathrm{XC}}(\vec{r}) = \frac{\delta E_{\mathrm{XC}}[\Psi_0]}{\delta n(\vec{r})} \ . \tag{2.101}$$

To solve this set of equations, they must be solved in an iterative self-consistent way, following the steps [23–26, 29, 30]:

1. Initially, an electron density $n(\vec{r})$ should be guessed.

2. Solve the Kohn-Sham equations to find each ψ_i wavefunction.

3. Calculate a new electron density, $n_{\mathrm{KS}}(\vec{r})$, using the wavefunctions ψ_i obtained in step 2 and substituting them in equation 2.94.

4. Compare the new $n_{\mathrm{KS}}(\vec{r})$ with the guessed $n(\vec{r})$.

    - If they are the same (within a pre-set tolerance value), then this electron density corresponds to the ground state of the system. End of the iteration cycle.

- If they are different the guessed electron density should be changed (using some kind of criteria) and then repeat this iteration cycle from step 2.

2.7.4 The Exchange-Correlation Functional

It is easy to understand that the success of DFT depends strongly on the adequacy of the used energy functional $E[\Psi_0]$. Equation 2.97 shows that part of this functional is well defined by (2.98), so in the end it all comes to the accurate description of the exchange-correlation functional $E_{\mathrm{XC}}[\Psi_0]$ [23, 25, 27, 29].

Here I will talk about the two most well known and widely used exchange-correlation functionals, the local density approximation (LDA) and the generalized gradient approximation (GGA).

Local Density Approximation

The LDA exchange-correlations functional is described by equation 2.102 [23, 25, 27, 29]:

$$E_{\mathrm{XC}}^{\mathrm{LDA}} = \int \epsilon(n(\vec{r})) \cdot n(\vec{r}) d^3\vec{r} \tag{2.102}$$

and assumes that the exchange-correlation energy, $\epsilon_{\mathrm{xc}}(n(\vec{r}))$ is a function of the $n(\vec{r})$ for a homogeneous electron gas. For convenience it is possible to separate the exchange and correlation parts from the exchange-correlation energy, $\epsilon_{\mathrm{xc}}(n(\vec{r})) = \epsilon_{\mathrm{x}}(n(\vec{r})) + \epsilon_{\mathrm{c}}(n(\vec{r}))$ [23, 25, 27, 29].

For spin polarized calculations the LDA functional turns into the local spin-density approximation (LSDA) and equation 2.102 is corrected to equation 2.103 [23, 25, 27, 29]:

$$E_{\mathrm{XC}}^{\mathrm{LSDA}} = \int \epsilon(n_\uparrow(\vec{r}), n_\downarrow(\vec{r})) \cdot (n_\uparrow(\vec{r}) + n_\downarrow(\vec{r})) d^3\vec{r} \tag{2.103}$$

where $n_\uparrow(\vec{r})$ and $n_\downarrow(\vec{r})$ are the up and down spin density respectively.

Despite its simplicity, the LDA functional describes successfully several atomic systems, as long as their electrons are not heavily correlated. In fact, LDA often gives ionizations energies with an accuracy of about $10 - 20\%$ and bond lengths with accuracies of $\sim 1\%$ [27].

Generalized Gradient Approximation

Another quite well known functional class is the generalized gradient approximation. The functionals based in this approximation try to improve the LSDA quality taking into account not only the local spin density but also the local gradients in electron/spin density. Equation 2.104 shows how this implementation is done [23, 25, 29]:

$$E_{\mathrm{XC}}^{\mathrm{GGA}} = \int \epsilon(n_{\uparrow}(\vec{r}), n_{\downarrow}(\vec{r}), \nabla_{\uparrow}(\vec{r}), \nabla_{\downarrow}(\vec{r})) \cdot (n_{\uparrow}(\vec{r}) + n_{\downarrow}(\vec{r}))d^3\vec{r} \tag{2.104}$$

Since there are several possible exchange-correlation energy functions for the conditions presented in equation 2.104, there are several GGA functional, such as the Perdew-Wang functional (PW91) and the Perdew-Burke-Ernzerhof functional (PBE) [31, 32].

2.8 Hyperfine Interactions

Till now, all the physical phenomena approached in this chapter involved mostly electric or magnetic interactions of a given external field with the electrons of an atom. In this framework we know that, for example, for electronic transitions we are dealing with energies in the order of the eV, while typical energy splitting of degenerate levels due to spin-orbit effects are in the order of meV. Transitions involving the latter have quite small energies when compared with typical electronic transitions and for this reason were historically called as the fine structure of atomic spectra.

Let's now consider effects involving the nucleus of an atom. While the nuclear transitions are of the order of keV or even MeV depending on the considered isotopes, the interactions between the degenerate nuclear levels are much smaller than the fine structure levels. In fact, transitions involving the nuclear quadrupole interactions with an electric field gradient (EFG) and/or the nuclear magnetic dipole interactions with a hyperfine magnetic field (HMF) are in the order of μeV, hence being called hyperfine interactions [33, 34].

2.8.1 Hyperfine Magnetic Field

Similarly to equation 2.26, the magnetic moment of a nucleus with a total angular momentum I can be given by equation 2.105 [33]:

$$\vec{\mathfrak{m}} = \vec{\mu} = \gamma \vec{I} = g_I \mu_N \vec{I} \,, \tag{2.105}$$

where $\mu_N = \frac{e\hbar}{2m_p}$ is the nuclear magneton and m_p is the proton mass.

It is possible to see that apart from some constants, we have an identical situation to the magnetic dipole moment of the overall angular moment of the electrons, J. For this reason, by simply replacing the adequate constants and operators in equation 2.27, we obtain equation 2.106 [33]:

$$E_{mag} = -g_I \mu_B \left(\frac{\hat{\boldsymbol{I}}}{\hbar} \cdot \vec{B} \right) = -g_I \, \mu_B \, m_I B \ . \tag{2.106}$$

This energy is actually quite useful for the local study of materials since the magnetic field of equation 2.106 can be induced by a hyperfine magnetic field, B_{hmf} which can result from the electrons magnetic moment and/or from the *in situ* magnetization. This approach allows for example to study the B_{hmf} of a given site of an AFM material which has an null net magnetization [33, 34].

2.8.2 Electric Field Gradient

For two independent arbitrary charge distributions (figure 2.11), the energy from their electrostatic potential interactions can be calculated as the interaction between the inner charge distribution (red charge distribution of figure 2.11) and the electrostatic potential created by the outer charge distribution (blue charge distribution of figure 2.11, as shown in equation 2.107 [35–37]:

$$E_{\text{elec}} = \int \rho(\vec{r}_{\text{in}}) \Phi(\vec{r}_{\text{out}}) d\vec{r}_{\text{in}} \ . \tag{2.107}$$

The electric potential, $\Phi(\vec{r}_{\text{out}})$, is described by :

$$\Phi(\vec{r}_{\text{out}}) = \frac{1}{4\pi\epsilon_0}\int \frac{\rho_{\text{out}}(\vec{r}_{\text{out}})}{|\vec{r}_{\text{out}} - \vec{r}_{\text{in}}|} d\vec{r}_{\text{out}} \ , \tag{2.108}$$

thus equation 2.107 can be explicitly described by equation 2.109:

$$E_{\text{elec}} = \frac{1}{4\pi\epsilon_0}\iint \rho_{in}(\vec{r}_{\text{in}})\frac{\rho_{\text{out}}(\vec{r}_{\text{out}})}{|\vec{r}_{\text{out}} - \vec{r}_{\text{in}}|} d\vec{r}_{\text{out}} d\vec{r}_{\text{in}} = \frac{1}{4\pi\epsilon_0}\iint \frac{\rho(\vec{r})\rho(\vec{R})}{|\vec{R} - \vec{r}|} d\vec{R} d\vec{r} \tag{2.109}$$

where $\vec{r}_{\text{in}} = r$ is the position vector of the inner charge distribution, $\rho_{in}(\vec{r}_{\text{in}}) = \rho(\vec{r})$ its charge density for a given point, $\vec{r}_{\text{out}} = R$ is the position vector of the outer charge distribution, and $\rho_{out}(\vec{r}_{\text{in}}) = \rho(\vec{R})$ its charge density for a given point.

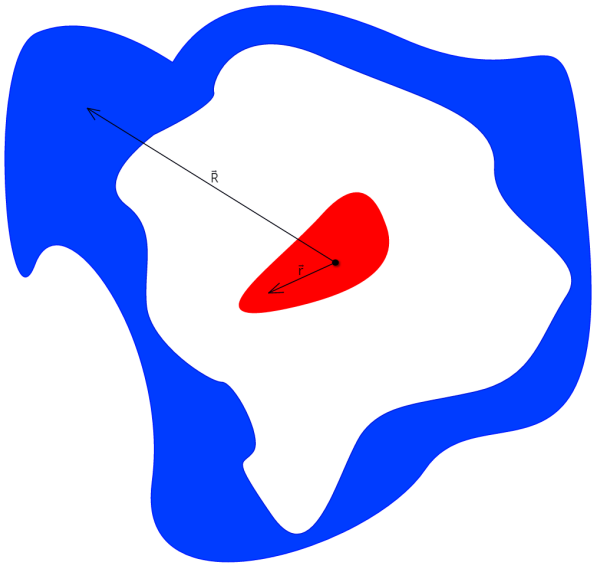

Figure 2.11: Scheme of two independent charge distributions. The inner red charge distribution can be though as the nucleus of an atom and outer blue charge distribution its electrons.

The $\frac{1}{|R-r|}$ term of equation 2.109 can be expanded by equation 2.110 [35–37]:

$$\frac{1}{|R-r|} = 4\pi\sum_{l,m}\frac{r^l}{R^{l+1}}\frac{1}{2l+1}Y_m^l(\theta_R,\phi_R)Y_m^l(\theta_r,\phi_r) \ . \tag{2.110}$$

where Y_m^l are the spherical harmonics. If r is always $< R$, then we can separate all terms which involve r from the terms which involve R, thus obtaining the multipole expansion of

equation 2.111 [35–37]:

$$E_{\text{elec}} = \sum_{l,m} Q_m^l V_m^l = E^{(0)} + E^{(1)} + E^{(2)} \dots \tag{2.111}$$

where Q_m^l and V_m^l are defined by equations 2.112 and 2.113 respectively.

$$Q_m^l = \sqrt{\frac{4\pi}{2l+1}} \int \rho(\vec{r}) r^l Y_m^l(\theta_r, \phi_r) d\vec{r} \tag{2.112}$$

$$V_m^l = -\frac{1}{4\pi\epsilon_0} \sqrt{\frac{4\pi}{2l+1}} \int \frac{\rho(\vec{R})}{r^{l+1}} Y_m^l(\theta_R, \phi_R) d\vec{R} \tag{2.113}$$

Let's consider that the two charge distributions are from an atom nucleus and its surrounding electrons. The terms of order zero ($E^{(0)}$) are the nucleus charge (2.114) and the monopole potential of the electrons charge (2.115), which are used in the Coulomb interactions of point charges [35–37].

$$Q_0^0 = q = \int \rho(\vec{r}) d^3r = Ze \tag{2.114}$$

$$V_0^0 = -\frac{1}{4\pi\epsilon_0} \int \frac{\rho(\vec{R})}{R} d^3\vec{R} \tag{2.115}$$

The electric dipole moment (2.116) and dipole potential (2.117) are vectors and correspond to the first-order terms of the multipole expansion ($E^{(1)}$).

$$Q_m^1 = p_i = \int x_i \rho(\vec{r}) d^3r \tag{2.116}$$

$$V_m^1 = -\frac{1}{4\pi\epsilon_0} \sqrt{\frac{4\pi}{3}} \int \frac{\rho(\vec{R})}{R^2} Y_m^1(\theta_R, \phi_R) d^3\vec{R} \tag{2.117}$$

Finally, the second-order terms (from $E^{(2)}$) are tensors corresponding to the electric quadrupole moment (2.118) and the electric field gradient of the electrons potential felt at the nucleus (2.119) [35–37].

$$Q_m^2 = Q_{ij} = \frac{1}{e} \int \rho(\vec{r})(3x_i x_j - r^2\delta_{ij}) d^3r \tag{2.118}$$

$$V_m^2 = V_{ij} = -\frac{1}{4\pi\epsilon_0} \sqrt{\frac{4\pi}{5}} \int \frac{\rho(\vec{R})}{R^3} Y_m^2(\theta_R, \phi_R) d^3\vec{R} = \frac{\partial\Phi}{\partial x_i x_j} \tag{2.119}$$

The energy terms related to the hyperfine interactions are the $E^{(0)}$ and $E^{(2)}$ terms. The

monopole terms result in isotope and/or isomer shifts present in nuclear techniques such as Mössbauer spectroscopy. The electric quadrupole moment characterizes the shape distribution of the nucleus charge density, while the EFG characterizes the electrons charge density. For a free ion/atom its EFG will be null, due to the spherical symmetry of its electrons. However, for an atom under an electrostatic field, such as in the case of an atom under a crystal field, the EFG might have non-zero values, therefore, this physical quantity is a good one to study the chemical environment of a given atom.

Assuming that there are no electrons in the nucleus, the EFG tensor is a symmetric tensor, thus diagonalizable, and traceless. For these reasons it can be completely described just by using one of its diagonal matrix components (V_{zz}) and an asymmetry parameter, η, defined by equation 2.120 [33]:

$$\eta = \frac{V_{xx} - V_{yy}}{V_{zz}} : |V_{zz}| \geq |V_{yy}| \geq |V_{xx}| \ . \tag{2.120}$$

Now, the quadrupole energy of an atom is usually defined by equation 2.121 [33]:

$$E_Q = \frac{e}{6} \sum_{i,j} Q_{ij}.V_{ij} \ , \tag{2.121}$$

which can also be written using the V_{zz} and η parameters, as shown in equation 2.122:

$$E_Q = \frac{eV_{zz}}{12} \cdot (3Q_{zz} + \eta(Q_{xx} - Q_{yy})) \ . \tag{2.122}$$

For a nucleus with a total angular momentum $\hat{\boldsymbol{I}}$, the quadrupole interaction Hamiltonian is given [33]:

$$\hat{\boldsymbol{\mathcal{H}}}_{\boldsymbol{Q}} = \omega_Q \hbar (3\hat{\boldsymbol{I}}_{\boldsymbol{z}}^{\boldsymbol{2}} - \hat{\boldsymbol{I}}_{\boldsymbol{z}}(\hat{\boldsymbol{I}}_{\boldsymbol{z}} + 1) + \eta(\hat{\boldsymbol{I}}_{\boldsymbol{x}}^{\boldsymbol{2}} - \hat{\boldsymbol{I}}_{\boldsymbol{y}}^{\boldsymbol{2}}) \ , \tag{2.123}$$

where ω_Q is the quadrupole frequency and is defined by equation 2.124 [33]:

$$\omega_Q = \frac{eQV_{zz}}{4I(2I-1)\hbar} \tag{2.124}$$

The Hamiltonian (2.123) cannot be solved analytically for the general case of quadrupole and magnetic interactions, being necessary a numerical approach to solve it. Nonetheless, for

$\eta = 0$ we arrive to the special case where the quadrupole energy is given by equation 2.125 [33]:

$$E_Q = \hbar\omega_Q(3m_I^2 - I(I+1)). \tag{2.125}$$

The energy of a transition between the state $|I, m_I\rangle$ and $|I, m_I'\rangle$ is given by [33]:

$$\Delta E_Q = 3\hbar\omega_Q({m_I}^2 - {m_I'}^2) \tag{2.126}$$

which results in a multiple of the fundamental transition frequency, ω_0 which can have the following values: $\omega_0 = 6\omega_Q$ for a half integer value of I and $\omega_0 = 3\omega_Q$ for a integer value of I.

Chapter 3

State of the Art

3.1 Multiferroic Materials

The prefix 'ferro' has its origin from the Latin word *ferrum* (iron), an archetype of ferromagnetism. Ferromagnetic materials are ordered magnetic phases with spontaneous magnetization (below its Curie Temperature) which possesses a hysteretic behaviour of the magnetization varying an applied magnetic field. All ferroic materials have a hysteresis loop and a critical temperature, T_C, which separates the ordered phase from the disordered one. Ferromagnetism hysteresis, as mentioned above, consists in the relation between the magnetization and a magnetic field [10]; for ferroelectricity the relation is between the polarization and an electric field; for ferroelasticity the relation is between the strain and a stress field [38]; and for ferrotoroidicity the relation between the toroidal moment and the spin arrangement [39].

A Multiferroic (MF) material, in the essence of the word, is a kind of material which possesses two or more ferroic properties which are coupled between them (figure 3.1). Let's imagine, for example, a material with a coupling between ferromagnetism and ferroelectricity, in this case it would be possible to control the polarization of this material using a magnetic field or its magnetization using an electric field. A material with such kind of coupling is called a magnetoelectric material (ME) – kind of coupling which will be the main subject of study of my PhD thesis. However, finding materials that bear at least two coupled ferroic properties is not an easy task. Therefore, the concept of multiferroic started to spread to a less demanding and more embracing group of materials (or composites) which have a coupling between magnetic, electric or elastic properties.

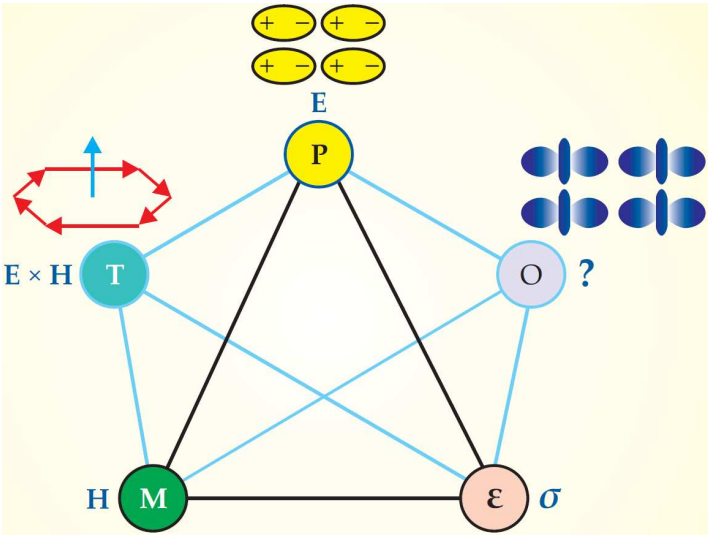

Figure 3.1: All the different ferroic coupling possibilities and their respective mediator fields. "O" represents other possible couplings. From [40].

We can divide multiferroic materials into two classes of multiferroics: intrinsic multiferroics and extrinsic multiferroics.

Intrinsic multiferroics have simultaneously two or more properties coupled in a single phase ($BiFeO_3$ and $YMnO_3$ are examples of intrinsic multiferroics which couple ferroelectric and ferromagnetic properties in the same phase).

On the other hand, extrinsic multiferroics consist of two or more phases, each one having their own properties, working together like a composite that somehow is able to couple their properties.

One common extrinsic mechanism is the change of an ordered property resorting to a lattice modifications, like in strain induced ferroelectricity. In this case, let's consider a heterostructure composed by a magnetostrictive and a piezoelectric material. The magnetostrictive material suffers a deformation when a magnetic field is applied, which can induce a strain in the piezoelectric material which will finally induce a polarization and vice versa. This is an example of an indirect multiferroic coupling (extrinsic coupling) through magnetostriction [1] and piezoelectricity [2] but can also have other types of couplings like piezomagnetism [3] and

[1] **Magnetostriction** – coupling between strain and a quadratic function of the applied magnetic field

[2] **Piezoelectricity** – coupling with linear relation between strain and electric field or a linear relation between polarization and applied stress

[3] **Piezomagnetism** – coupling with linear relation between strain and magnetic field or a linear relation between magnetization and applied stress

electrostriction [4] [41].

This thesis will focus mainly in magnetoelectric multiferroics which are by far the most studied multiferroics nowadays, mainly due to their very appealing applications.

3.2 The Magnetoelectric effect

The magnetoelectric effect describes the coupling between the electrical and magnetic properties of a given material. Figure 3.2 shows the possible material classification according to their magnetic and electric properties.

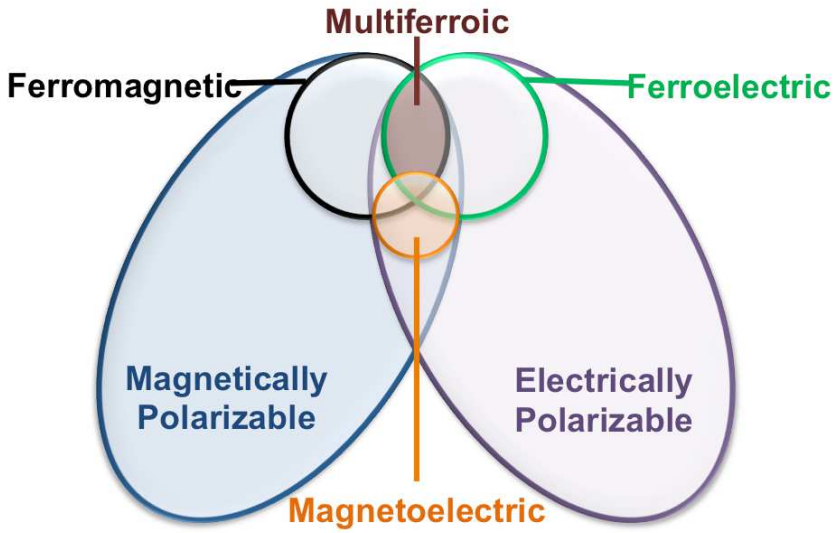

Figure 3.2: Materials classification according to their electric and magnetic properties. According to the purest concept of multiferroic, only a very small portion of materials would be considered multiferroic. From [42].

To describe the coupling in intrinsic magnetoelectric materials, it is possible to use the Helmholtz free energy as in equation 3.1 [43]:

$$dF = -SdT - \vec{P} \cdot d\vec{E}_0 - \vec{M} \cdot d\vec{B}_0 \ , \tag{3.1}$$

where F is the Helmholtz free energy thermodynamic function, S is the entropy, T is the temperature, $\vec{P}$ is the polarization, $\vec{M}$ is the magnetization, $\vec{E}_0$ is the applied electric field, and $\vec{B}_0$ is the magnetic flux density.

[4] **Electrostriction** – coupling between strain and a quadratic function of the applied electric field

Considering a constant temperature scenario, according to Landau [44] we can expand the free energy F as a power series [43]:

$$\begin{aligned} -F\left(\vec{E}_0,\vec{B}_0\right) &= \vec{P}_s \cdot \vec{E}_0 + \vec{M}_s \cdot \vec{B}_0 + \\ &+ \frac{\epsilon_0}{2}\sum_{i,j}\chi^e_{ij}E_{0i}E_{0j} + \frac{1}{2\mu_0}\sum_{i,j}\chi^m_{ij}B_{0i}B_{0j} + \frac{1}{\mu_0}\sum_{i,j}\alpha_{ij}E_{0i}B_{0j} + \cdots \end{aligned} \tag{3.2}$$

where $\vec{P}_s$ is the spontaneous polarization, $\vec{M}_s$ is the spontaneous magnetization, $\hat{\chi}^e$ and $\hat{\chi}^m$ are the electric and magnetic susceptibility tensors respectively, and $\hat{\alpha}$ is the linear magnetoelectric coupling tensor. Usually for the description of the ME effect we restrict the expansion the expansion till the coupling terms (second order terms).

Starting from (3.1) and (3.2) it is possible to determine the Polarization and Magnetization expressions [43]:

$$P_i = -\left(\frac{\partial F}{\partial E_{0i}}\right)_{B_0} = P_{si} + \epsilon_0\sum_j \chi^e_{ij}E_{0j} + \frac{1}{\mu_0}\sum_j \alpha_{ij}B_{0j} + \cdots \tag{3.3}$$

$$M_i = -\left(\frac{\partial F}{\partial B_{0i}}\right)_{E_0} = M_{si} + \frac{1}{\mu_0}\sum_j \chi^m_{ij}B_{0j} + \frac{1}{\mu_0}\sum_j \alpha_{ij}E_{0j} + \cdots \tag{3.4}$$

In both equations a cross coupling between electric and magnetic features appeares: the polarization is influenced by a magnetic field or the electric field affects the magnetization. Both cross terms are weighted by the magnetoelectric coupling tensor. So for a linear magnetoelectric coupling we have [43]:

$$\alpha_{ij} = \left(\frac{\partial P_i}{\partial B_{0j}}\right)_{E_0=B_0=0} = \mu_0\left(\frac{\partial M_i}{\partial E_{0j}}\right)_{B_0=E_0=0} . \tag{3.5}$$

Moreover, according to conventional theory, Brown *et al.* demonstrated that the following inequality must be satisfied [45]:

$$\alpha_{ij} \leq \sqrt{\epsilon_0\mu_0\chi^e_{ii}\chi^m_{jj}} . \tag{3.6}$$

The inspection of equation 3.6 suggests that a logical way to search for multiferroic materials with a high ME coupling consists in the search or tailoring of materials with the highest possible magnetic and electric susceptibilities.

On the other hand, extrinsic magnetoelectric materials were first proposed in 1972 by Van Suchtelen [46]. He suggested that the indirect ME_H effect ($P = \alpha H$) or the ME_E effect ($M = \alpha E$) of a two phase composite could be described by equations 3.7a and 3.7b respectively.

$$\mathrm{ME}_H \text{ effect} = \frac{\text{magnetic}}{\text{mechanical}} \times \frac{\text{mechanical}}{\text{electric}} \tag{3.7a}$$

$$\mathrm{ME}_E \text{ effect} = \frac{\text{electric}}{\text{mechanical}} \times \frac{\text{mechanical}}{\text{magnetic}} \tag{3.7b}$$

This coupling can be more accurately described taking into account equations 3.8 [47]:

$$\frac{\partial S}{\partial H} = \xi_m \tag{3.8a}$$

$$\frac{\partial P}{\partial S} = \xi_e \ , \tag{3.8b}$$

where S is the strain, H is the magnetic field, P is the polarization, and ξ_m and ξ_e are the piezomagnetic and piezoelectric coefficients respectively. Crossing equations 3.8a and 3.8b, and adding a coupling factor k_c ($0 \leq |k_c| \leq 1$), which determines the coupling between the two different phases of the composite, equation 3.9 is obtained:

$$\frac{\partial P}{\partial H} = k_c \xi_m \xi_e = \alpha \ . \tag{3.9}$$

Therefore, two different phases/materials, individually magnetic and ferroelectric, acquire a new property, magnetoelectricity, mediated by the magnetoelectric coupling coefficient α.

3.3 An historical retrospective of Magnetoelectric materials

The concept of a magnetoelectric material – a material whose magnetization could be induced by an electric field or/and whose polarization could be induced by a magnetic field – was first suggested in 1894, by Pierre Curie, using lattice symmetry arguments [48]. Curie suggested that similarly to the free space electromagnetism, magnetization and polarization could also be correlated/coupled in crystals [48]. As a matter of fact, Röntgen had already

discovered in 1888 that a moving dielectric would became magnetized when placed in an electric field [49]. Nevertheless, the term magnetoelectric coupling just emerged in 1926, in a paper from Debye [50].

In 1959, Dzyaloshinskii made the first theoretical prediction of a magnetoelectric effect, in the antiferromagnetic Cr_2O_3 [51], which was experimentally demonstrated in 1960 [52]. Additionally, in 1972, van Suchtelen proposed the existence of magnetoelectric heterostructures through the product property of a two-phase composite due to an elastic coupling (equations 3.7a–3.9) [46].

The magnetoelectric effect got plenty of attention from the scientific community, leading to the discovery of several magnetoelectric materials such as Ti_2O_3 [53], GaFeO3 [54], boracite and phosphate compounds [55,56], solid solutions like $PbFe_{0.5}Nb_{0.5}O_3$ [57], garnet films [58,59], etc.

However, after this initial enthusiasm about the magnetoelectric effect, the topic experienced a loss of interest from the scientific community. This was due to the rare and weak magnetoelectric couplings found at the time, and because there was still a lack of understanding on a microscopic level. In fact, it was believed that it would be extremely difficult to induce a magnetoelectric effect using an electric field in metals due to their short screening length [60, 61]. Moreover, the modern theory of polarization was not developed till the 90's [62, 63].

In 2000, the magnetic Curie temperature of the magnetic semiconductor (In,Mn)As was controlled electrically [64]. In the same year, Spaldin (Hill at the time) wrote a paper which exposed the reasons why the magnetic and electric properties were apparently incompatible [65], clarifying the challenges to overcome in the discovering/tailoring of magnetoelectric materials (or multiferroic materials, as referred by Schmid 1994 [66]).

Finally, in 2003, it was discovered that $BiFeO_3$ had a very large magnetoelectric coupling while having a large spontaneous polarization at room temperature [67]. The only problem resided in its weak ferromagnetism nature. Yet, this discovery was a milestone in magnetoelectric multiferroics research, giving birth to potential room temperature applications, hence reinvigorating the field.

Later, in the same year, a second disruptive material, $TbMnO_3$, was discovered. Despite its poor ferroelectricity (1/1000 of $BiFeO_3$ polarization), this material showed a completely

new magnetoelectric mechanism. In fact, $TbMnO_3$ polarization is induced by its magnetic behaviour, and has a strong magnetoelectric coupling, being able to completely flip its polarization when exposed to a magnetic field of a few Tesla [68].

Parallelly, magnetoelectric multiferroic heterostructures were also showing huge developments. In 2001, it was predicted that laminate composites of Terfenol-D/P(VDFTrFE) or Terfenol-D/PZT would exhibit giant magnetoelectric couplings. Such predictions were validated by experimental confirmation on the same year [69, 70].

In the following years, novel couplings were discovered. Nowadays, the magnetoelectric effect is referred not only to the change of polarization (magnetization) with a magnetic (electric) field, but also to changes in properties related to the magnetic and/or electric behaviours, namely: anisotropy, Curie Temperatures, exchange bias, and others [71–80].

While intrinsic ME materials are still widely searched for, the best proven results are coming from magnetoelectric heterostructures. These heterostructures show much higher magnetoelectric couplings and are more easily tuned than their intrinsic counterpart, which tend to present low operating temperatures and/or poor magnetization and/or polarization [71–73, 81, 82]. LSMO/BTO, Fe_3O_4/PMN-PT, CoFeB/PMN-PT, CFO-PZT FeRh/BTO are good examples of heterostructures which present good magnetic and electric properties along with high magnetoelectric couplings near room-temperature [83–87].

The composite approach also originates novel magnetoelectric couplings, due to interface effects, such as: chemical hybridization, charge and ion migration, changes in the local chemical environment and switching between antiferromagnetic and ferromagnetic states [73, 78, 80, 87].

The advent of the 2000's discoveries/approaches and the unpredictable emergence of further novel mechanisms make magnetoelectric multiferroics a very appealing field of research, being one of the hot topics of modern physics and materials science.

3.4 Multiferroics and Magnetoelectrics Popularity

Figures 3.3–3.6 are a good way to see the growing interest on multiferroic and magnetoelectric materials. The number of publications, as well as the number of citations of the "multiferroic" and "magnetolectric" topics show an exponential like curve.

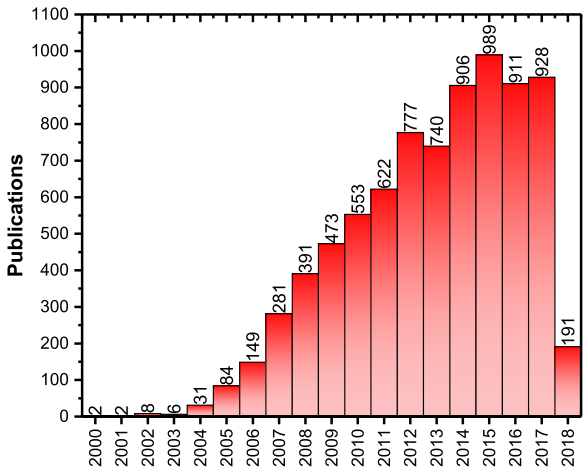

Figure 3.3: Number of annual publications about the topic *"Multiferroic"* obtained from *Web of Science* [88].

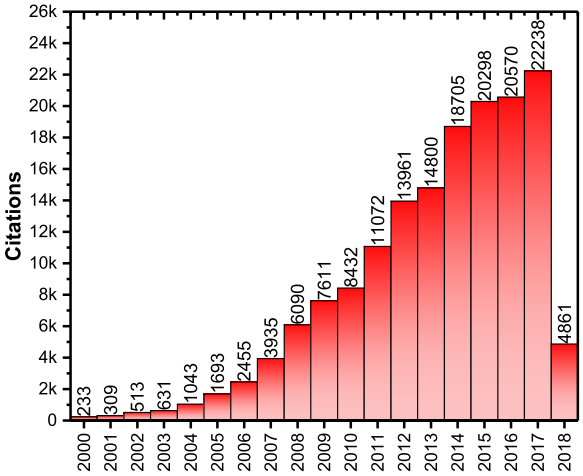

Figure 3.4: Annual citations about the topic *"Multiferroic"* obtained from *Web of Science* [88].

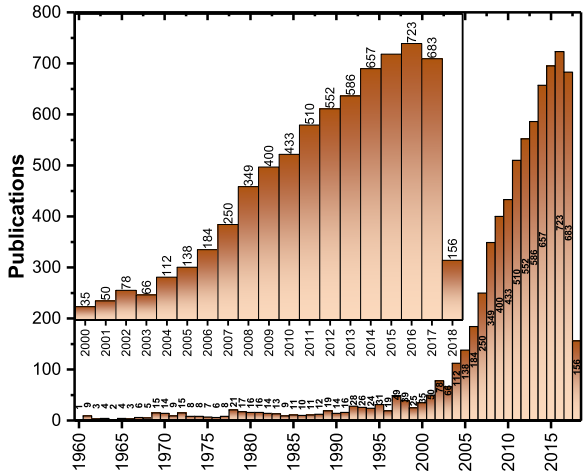

Figure 3.5: Number of annual publications about the topic *"Magnetoelectric"* obtained from *Web of Science* [88]. The inset shows the results for the last 18 years

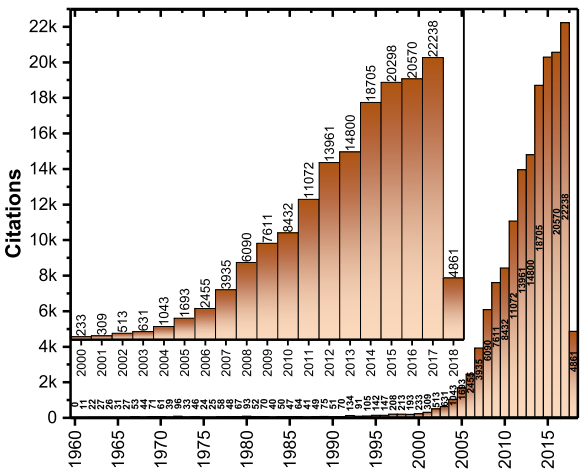

Figure 3.6: Annual citations about the topic *"Magnetoelectric"* obtained from *Web of Science* [88]. The inset shows the results for the last 18 years

Such an intense investigation incites the industry interest in this kind of materials. In fact, after a worldwide search for patents with the keyword "multiferroic" we can obtain 181 patents already registered[5], whose time distribution is given by figure 3.7.

[5] A search using word "magnetoelectric" was also made, having thousands of results. However, after a careful investigation, it was possible to see that this word was used in many magnetic and electric devices, even if they were not coupled.

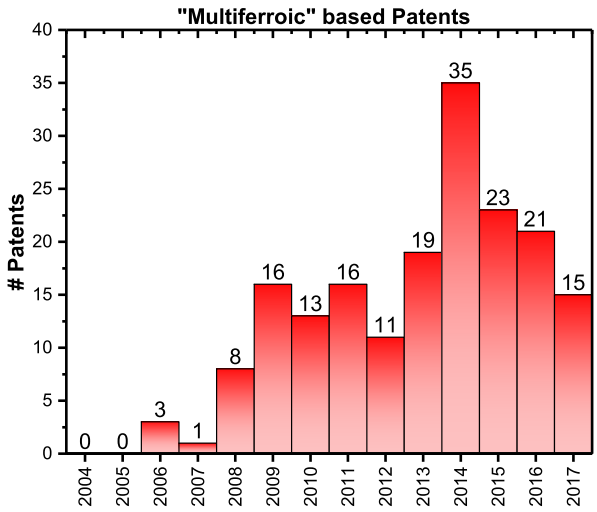

Figure 3.7: Number of "*Multiferroic*" based patents emitted through the years. Searched at Espacenet [89].

3.5 Magnetoelectric Multiferroic Materials

Magnetoelectric multiferroic materials are materials with both spontaneous polarization (ferroelectric) and spontaneous magnetization (either by ferromagnetism, ferrimagnetism or weak ferromagnetism). This requirement is *a priori* very demanding, since from a symmetry point of view, from the 122 Shubnikov-Heesch point groups, among the 31 that show spontaneous magnetization and the 31 that show spontaneous polarization, only 13 groups present both properties [90].

According to the mechanism behind the magnetoelectric coupling we can categorize the multiferroic magnetoelectric materials into two major types: **type I multiferroics** and **type II multiferroics**.

Type I multiferroics, the more abundant and the first type to be discovered/studied, are multiferroics with different sources for the magnetic and electric order. They are usually very good ferroelectric materials and are the more conventional multiferroics. Some of these type of materials have both magnetic and ferroelectric Curie temperatures above room temperature, but, unfortunately tend to have a weak magnetoelectric couplings. Type II are materials whose polarization has its origin through magnetic related mechanisms, which leads usually to stronger magnetoelectric couplings.

3.5.1 Type I multiferroics

In the text below, some type I multiferroics are reviewed according to their ferroelectricity origin.

Multiferroic Perovskites

Perovskites – $A^{2+}B^{4+}X_3^{2-}$ – are some of the most well-known ferroelectrics like $BaTiO_3$ and $Pb(ZrTi)O_3$, thus being good candidates to tailor magnetoelectric materials. However, whereas magnetic materials need semi-filled d^n (or f^n) orbitals, ferroelectric perovskites need that the transition metal has empty d^0 orbitals [65]. Proper ferroelectrics usually need these empty d^0 orbitals because they will be used to establish strong covalency with the surrounding anions.

For instance, in the case of $BaTiO_3$ the empty d^0 Ti orbitals tend to bond strongly with 3 oxygens of the O_6 octahedra due to a hopping between the O p orbitals. This bonding shifts the centre of the O_6 octahedra towards 1 (or 3) oxygen(s) weakening the bonds with the other 3 oxygens, and culminating in the creation of a dipole moment. This dipole moment will promote the same mechanism in neighbouring unit cells, thus propagating the creation of other electric dipoles in a preferential direction and resulting in a net polarization [65, 91–93].

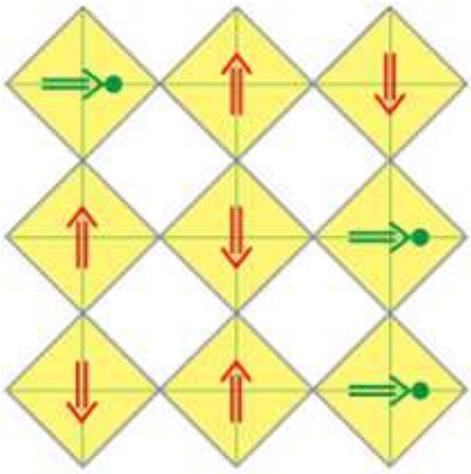

Figure 3.8: Schematic representation of a multiferroic perovskite. Green circles represent the d^0 ions, yellow diamonds represent O_6 octahedra, whereas the green and red arrows represent the electric and magnetic dipole moments respectively. From [91].

Since the semi-filled d^n tend to destroy the off-centre responsible for the creation of the electric dipole moment, a way to have a multiferroic perovskite is to have a heterogeneous

mixture of ferroelectric and magnetic unit cells, with d^0 valence B cations and d^n valence B' cations respectively, such as in $PbFe^{3+}_{1/2}Nb^{5+}_{1/2}O_3$ and $PbFe^{3+}_{2/3}W^{6+}_{1/3}O_3$(figure 3.8). This approach would guarantee a macroscopic magnetoelectricity with possibly strong magnetic and ferroelectric nature, nevertheless such arrangement's coupling is expected to be tenuous [91–93].

Lone Pairs based Ferroelectricity

Notwithstanding, there are some materials which apparently violate the d^0 requirement to ferroelectricity like $BiMnO_3$ and $BiFeO_3$. These materials are intrinsic type I magnetoelectric multiferroics but possess magnetic transition metal ions – Mn^{3+} (d^4) and Fe^{3+} (d^5) – in the perovskite B site [91, 92, 94].

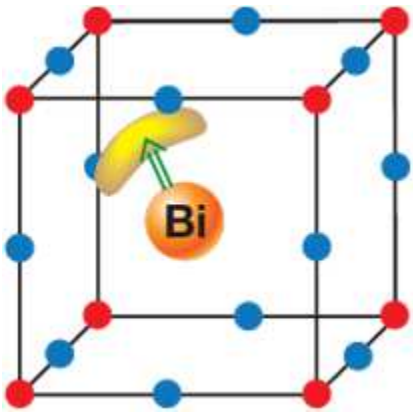

Figure 3.9: Polarization due to lone pairs (represented by the yellow lobe). The green arrow represents the electric dipole moment. From [91].

Yet, these perovskites are not exception for the necessary but not sufficient "d^0 orbitals rule". Their ferroelectric character's origin is related not with the B site cations but with the A site cations, Bi^{3+} and Pb^{2+}, which have lone pairs electrons.

These lone pairs do not engage in any bonds and so they are highly polarizable and end up creating local electric dipoles, which will order ferroelectrically as we can observe in figure 3.9 [91–93].

Improper Geometric Ferroelectricity

Another exception of the d^0 rule is the ferroelectricity behind the hexagonal manganites $RMnO_3$ (R= small rare earths like Y). Despite the ABO_3 formula, the Mn^{3+} are not located

in a O_6 octahedra, but in the centre of a O_5 trigonal biprism [91–93].

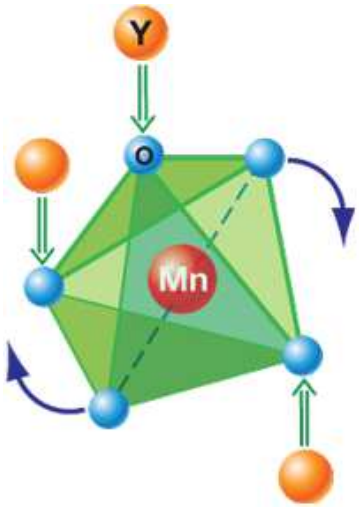

Figure 3.10: Representation of the geometric mechanism behind the ferroelectricity of $YMnO_3$. From [92].

The polarization does not come from the off-centre of the Mn^{3+} (its shift is too small to provide the ferroelectricity). For the $YMnO_3$ specific case, the MnO_5 block tilts to provide a closer packing of the unit cell, moving the oxygen anions close to the Y ions. Once there are two "up" electric dipole per "down" dipole, a macroscopic polarization can be measured (figure 3.10) [91–94].

This way we can say we are before an improper ferroelectric since the first order parameter is not the polarization but the rotation of the $YMnO_3$ (geometric cause), and the polarization only appears as a collateral effect [95].

Charge Ordering Ferroelectricity

Other source of ferroelectricity has to do with the charge ordering of a given material. To have a better understanding about the general charge ordering mechanism let's look at figure 3.11.

In figure 3.11a it is possible to observe a neutral chain which has inversion symmetry wherever we put mirror planes [96].

In figure 3.11b we have site centred charge order, however this charge order only exists locally, if we use a mirror plane – either using a negative site (red plane) or a positive site (blue plane) – it is possible to see that both sides of the plane are equivalent, meaning that

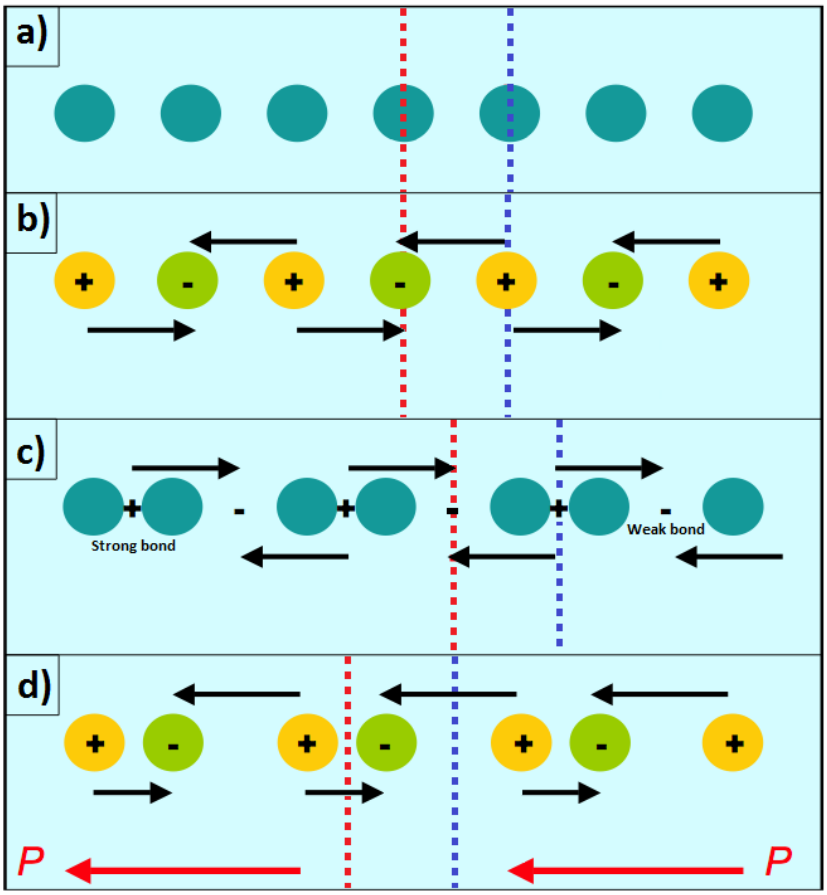

Figure 3.11: Scheme of one dimension charge order systems. a) Neutral chain. b) Site centred ordering. c) Bond centred ordering. d) Combination of site and bond centred ordering. Red and blue dash lines represent mirror planes crossing two different positions of the chain, dividing the system in two different regions. Adapted from [96].

this arrangement preserves the inversion symmetry and, therefore, lacks a net polarization.

Figure 3.11c shows another type of charge ordering, the bond centred charge order, where a stronger or a weaker bond present different charge densities. Once again, for this type of charge order, there is not a net polarization, since if we put a mirror plane in the centre of any kind of bond we can see that the inversion symmetry remains unbroken [91–94, 96].

Finally in figure 3.11d it is possible to see a combination of site and bond centred ordering. Here the inversion symmetry is broken, as perceptible by inspection of the regions divided by the mirror planes of 3.11d, thus having a net polarization.

The charge order ferroelectricity itself can manifest in many ways and understanding the charge order pattern is not always simple. For example, the well-known magnetite (Fe_3O_4) is ferroelectric below its Verwey temperature, $T_V = 120K$, due to the appearance of charge

order. However its pattern is still unknown in the present day [91, 92, 96].

Taking this in consideration, we can say that Fe_3O_4, besides being the first discovered magnetic material was also the first magnetoelectric multiferroic [1].

$LuFe_2O_4$ is also a multiferroic whose ferroelectricity originates from a charge order effect. This material has a triangular disposition of Fe^{2+} and Fe^{3+} ions, and due to charge frustration, the first layer has a ratio of Fe^{2+}/Fe^{3+} of 1:2 and the second layer a ratio of 2:1. This different ratios of Fe^{2+} and Fe^{3+} ions between adjacent layers leads to a net polarization as we can see in figure 3.12 [91–94, 96].

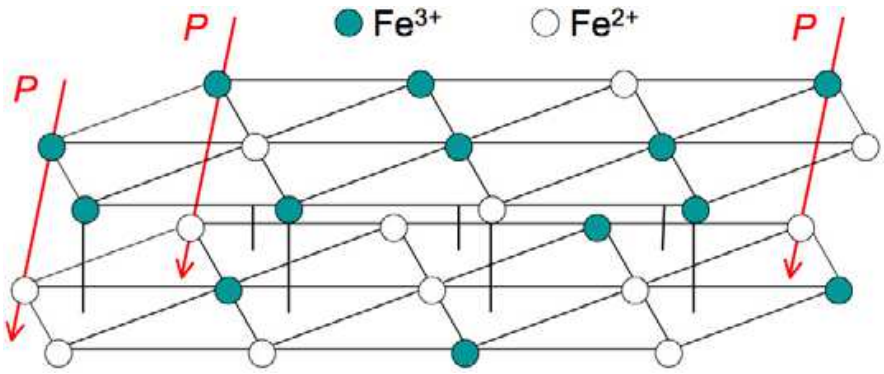

Figure 3.12: Representation of a Bilayer of the FeO_2 triangular lattices in $LuFe_2O_4$. From [96].

3.5.2 Type II multiferroics

Magnetostrictive ferroelectricity

A type II multiferroic is illustrated in figure 3.13, where there is a magnetostrictive source of ferroelectricity. In this case, a material which possesses two magnetic ions with inequivalent charges can bond due to their exchange interaction, shortening the distance between both ions and breaking the inversion symmetry (figure 3.13b). This mechamism results on a situation equivalent to the charge ordering present in figure 3.11d [96, 97].

One good example of this magnetostrictive ferroelectricity is Ca_3CoMnO_6, where the Co^{2+} and the Mn^{4+} alternate as shown in figure 3.13a, and below $T_N = 16K$ they order magnetically between them, similarly to what we can see in 3.13b, creating a macroscopic polarization [96, 97].

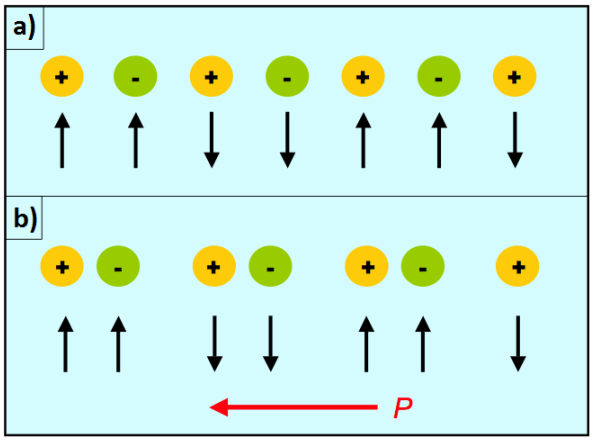

Figure 3.13: Intrinsic magnetostrictive ferroelectricity. a) chain of electrically inequivalent magnetic ions is equally separated. b) at a magnetic ordering temperature magnetic ions tend to bond due to their exchange interaction. Adapted from [96].

Inverse Dzyaloshinskii-Moriya effect

Nevertheless, the most prominent type II multiferroics are the ones associated with an inverse Dzyaloshinskii-Moriya effect [97–99].

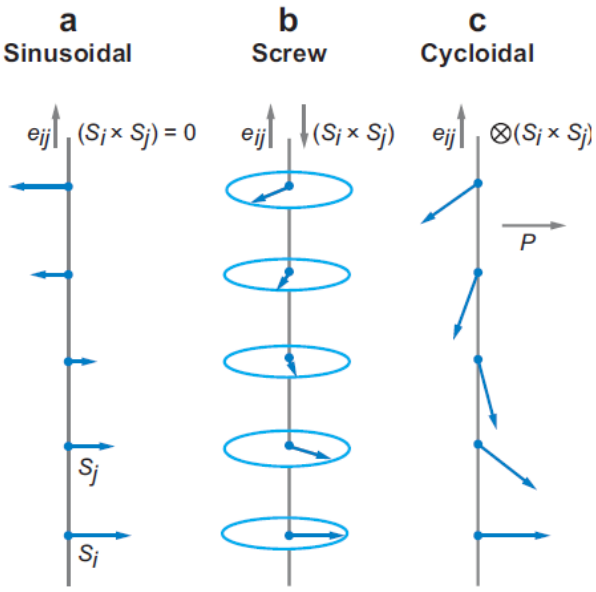

Figure 3.14: Some spin arrangements and consequent polarization. Only the cycloidal spin canting results in a non-zero polarization. Adapted from [99].

This kind of multiferroic is based in the fact that a polarization can induce certain spin arrangements as it can be verified through inspection of equation 3.10 [99]:

$$\vec{P} \propto \gamma\, \vec{e}_{ij} \times \left(\vec{S}_i \times \vec{S}_j\right) \tag{3.10}$$

where γ is a constant proportional to the spin-orbit and superexchange coupling interaction, and $\vec{e}_{ij}$ is the vector which connects the $\vec{S}_i$ and $\vec{S}_j$ spins [99].

As we can see in figure 3.14a and 3.14b the materials do not show any net polarization since for 3.14a the spin rotation vector is null and for 3.14b, despite having a non-zero rotation vector, it is parallel to the spin propagation vector. Whereas for 3.14c both spin propagation and rotation vectors are finite, resulting in a net polarization.

This kind of multiferroicity had a huge potential since the magnetoelectric effect occurs as a direct consequence of a magnetic arrangement, thus having a high magnetoelectric. However it usually has a flaw that has to do with the nominal magnetization and/or polarization, that is not obligatorily high, and not with the coupling itself [91, 93, 97–99]. Examples of inverse Dzyaloshinskii-Moriya effect induced polarization type II multiferroics are $TbMnO_3$, $Ni_3V_2O_8$ and $MnWO_4$ [96, 99].

3.6 Magnetoelectric Multiferroic Applications

The research on materials gets a boost whenever an application is proposed. Multiferroic magnetoelectric materials, in particular, have very appealing potential applications, such as: energy harvesting [100], tunable inductors [101], gyrators and transformers [102, 103], electric and magnetic field tunable micro(milli)meter wave devices [104,105], miniature antennas [106], magnetic-field sensors [107–109], and multiferroic memories [110–113].

Here I will briefly mention some of the applications that are proposed.

3.6.1 Magnetic Sensors

Magnetic multiferroic sensors are one of the most captivating applications regarding the magnetoelectric effect. Its explanation is quite forward, the possibility to know a magnetic field by measuring the polarization of the multiferroic material [93, 114, 115].

So, for a material with a gigantic magnetoelectric coupling, we could develop a fairly simple and sensitive magnetic sensor. Such simple mechanism would be much more practical and

cheaper than a SQUID [107–109, 114], and could serve purposes like magnetoencephalography and magnetocardiography [114].

This kind of sensors have also the potential of being miniaturized by photolithography processing, enabling their use as a local probe magnetic microscopy to directly sense the magnetic field of a given place by measuring an induced voltage instead of using the force induced in a magnetic tip [114, 116].

3.6.2 Energy Harvester and Conversion Devices

Ubiquitous power sources like heat, vibrations, human related motion, acoustic noise and the electromagnetic wireless communications energy can be harvested by many kinds of materials.

Typically, we can think about thermoelectric and piezoelectric materials as good harvester candidates. Magnetoelectric materials can be proposed as energy harvesters as well, which could for instance collect the mechanical power sources by magnetostriction, which would then be converted into electric power using its magnetoelectric character [100, 115].

3.6.3 Electrically Switchable Permanent Magnets

The inverse mechanism applied in the magnetoelectric sensors could also be used to switch the magnetization of a permanent magnet. Once again, if the magnetoelectric coupling is high enough it would be possible to invert the magnetization of a very hard multiferroic magnetic without the need of applying huge magnetic fields [114].

This ability could itself have many applications, like the possibility of manufacturing smaller, more energy efficient magnetic tips to perform magnetic data recording [114].

3.6.4 Multiferroic Hard Disk

Magnetic data record density has reached critical limits, since smaller magnetic bits begin to enter in the superparamagnetic regime. This limitation could be overcome by using bits made of magnetic materials with very high coercive fields. However, this would imply higher currents in the inductive heads (therefore very energy inefficient writing process) and the size of the inductive head would be itself a limitation for these devices (due to the difficulty of applying very localized magnetic fields) [114].

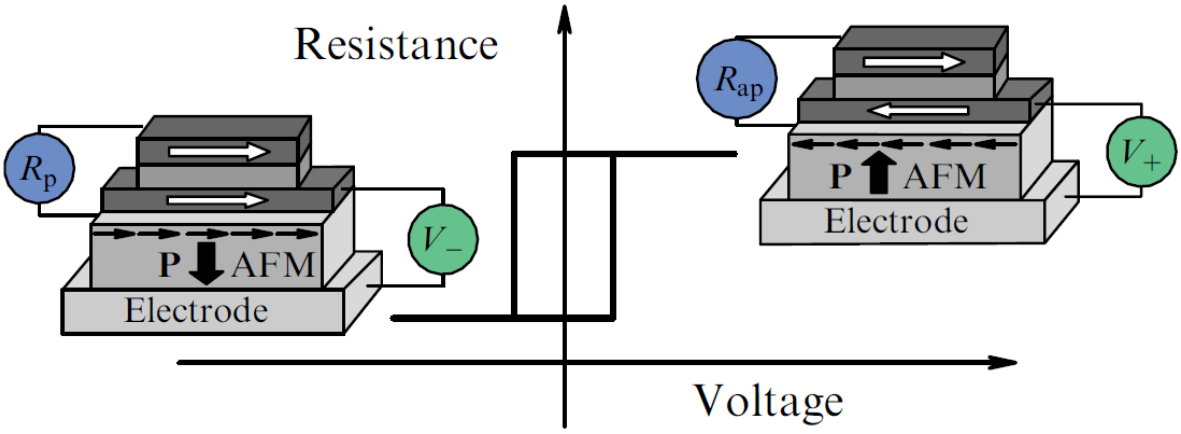

Figure 3.15: Schematic representation of a Magnetoelectric MRAM, showing the high and low resistance states of the device operating solely by electrical means. Extracted from [114].

To address these issues, one could replace the inductive heads by smaller high magnetization multiferroic heads (already mentioned above). We could also use high coupling magnetoelectric materials as high coercive field bits, which would easily change their magnetization state using electric fields [114, 117].

Still, one of the most disruptive approaches is the creation of 4 state devices. Nowadays the data storage comprises of 2 state bits that can result from a charged $(+)$ or uncharged $(-)$ capacitor, or using magnetic media instead, result from a upward $(\uparrow)$ or downward $(\downarrow)$ magnetization. Using materials that are both ferroelectric and magnetic we can have 4 different state bits: $(\uparrow,+)$, $(\uparrow,-)$, $(\downarrow,+)$ and $(\downarrow,-)$, hence increasing the data recording density [118, 119].

3.6.5 MEMRAM

MRAM are already considered the new generation of RAM's which has both the advantage of being a non-volatile memory and has high operations speeds. Its sole flaw has to do with its magnetic writing, which is still the bottleneck of MRAM's, compromising their energy efficiency and miniaturization potentiality.

The magnetoelectric MRAM (MEMRAM) could solve these limitations. As we can see in figure 3.15 the introduction of a Multiferroic layer would allow to change the magnetization states using an electric tension, allowing therefore a fully electrical operation [110–113, 120].

Chapter 4

Experimental Techniques

4.1 X-ray Diffraction

X-ray diffraction (XRD) is a characterization technique vastly used in materials research due to its non-destructive nature and its ability to give information about the crystalline structure of the studied sample, allowing to identify its symmetry and even chemical nature [121, 122].

Bragg suggested the diffraction would occur due to reflections of the atomic planes as described by figure 4.1 [121, 123–125]. Due to the crystal lattice periodicity, the number of variables required to describe such phenomenon was greatly reduced. The condition for constructive interference arises when the path difference of two incident beams, represented in red at figure 4.1, is an integer multiply of the wavelength, as described by Bragg's law [124]:

$$\lambda = 2d_{hkl} \sin\theta \ . \tag{4.1}$$

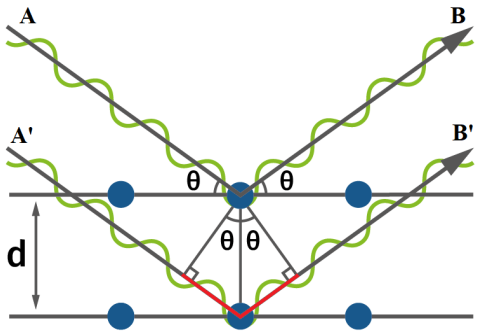

Figure 4.1: Representative scheme of Bragg's diffraction. From [126].

The electromagnetic radiation involved in the diffraction process comes from the scattering of photons by the electrons surrounding the atoms of the material which we want to analyse. This scattering is a feature of the atomic scattering factor, f, which is correlated with the electrons local density, ϱ, and the atom's vibration amplitude, u, as can be seen in equations 4.2-4.4 [121, 122, 124, 127]:

$$f = f_0 \cdot e^{\left(-\frac{B\sin^2\theta}{\lambda^2}\right)} \ , \tag{4.2}$$

$$f_0 = \int_0^\infty \varrho(r)\frac{\sin(kr)}{kr}dr \ , \tag{4.3}$$

$$B = 8\pi^2 u^2 \quad , \quad \varrho(r) = 4\pi r^2|\Psi|^2 \quad , \quad k = 4\pi\frac{\sin\theta}{\lambda} \ . \tag{4.4}$$

Using Bragg's law it is possible to determine the distance between the atomic planes of a given crystalline lattice by inspecting its diffractogram and seeing for which angles there are constructive interference, as well as by the observation of their relative intensity [122,123,125]. The determination of the expected intensity for each diffracted crystal plane, defined by the *hkl* Miller indexes, is related to their structure factor by equation 4.5 [122, 124, 127]:

$$I_{hkl} \propto F_{hkl}^2 \ . \tag{4.5}$$

Lastly the structure factor is related to the atomic scattering factor of the diffracted atoms and the symmetry of the crystal primitive cell by equation 4.6:

$$F_{hkl} = \sum_{j=1}^{N} f_j \cdot e^{[2\pi i(hx_j + ky_j + lz_j)]} \ , \tag{4.6}$$

$$\tag{4.7}$$

where N is the number of atoms within the primitive cell, f_j is the atomic scattering factor of the atom which is in position j, and x_j, y_j and z_j are the components of the position vector of atom j.

XRD diffraction can also be used to estimate the average crystallite size of a powder sample

or a polycrystalline material. This can be done using Scherrer equation 4.8 [122, 128, 129]:

$$\tau = \frac{K\lambda}{\beta \cos\theta} \ , \tag{4.8}$$

where τ is the average crystallite diameter, λ is the diffracted wavelength, θ is the Bragg angle, β is the full width at half height (FWHM) of the diffraction peak (usually the peak with highest intensity), and K is a dimensionless shape factor which depends on the crystallite geometry (0.9 for spherical crystallites) [122, 128, 129].

4.1.1 Grazing Incidence X-ray Diffraction

X-rays are a type of electromagnetic radiation with a considerable penetration depth, thus XRD is not a surface sensitive technique *per se*. This feature is quite inconvenient if one desires to study crystalline properties of a thin film deposited on a given substrate. In fact, considering, for example, a 100 nm thin film deposited in a graphite substrate we can conclude that for a typical $\theta - 2\theta$ configurations two problems contribute to a poor analysis of the thin film XRD [130, 131].

First the small volume of interaction, inherent to the low thickness of the considered film, results in very feeble diffraction peaks. Second, there will be a huge contribution from the substrate which will act as background radiation, outshining the film peaks. For the graphite substrate example there would be a penetration depth of about 500 μm, therefore, comparing with the 100 nm film, we would have a ratio between the film/substrate contribution of about $1/5000 = 2 \times 10^{-4}$ [130].

To overcome these limitations it is possible to use a configuration such as the one of figure 4.2 where the incident X-ray beam has a very low incident angle, resulting in Grazing Incidence X-ray Diffraction (GIXRD) if the thin film is polycrystalline. This grazing incidence will increase the path made by the beam in the thin film, thus increasing its interaction volume [130, 131]. It will also partially or completely eliminate the beam interaction with substrate and for these reasons the thin film peak intensities will increase while the substrate contribution will decrease substantially.

It should be noted that for a given film thickness there is always an incident angle, α, which will completely eliminate the substrate contribution, however, if this angle is much

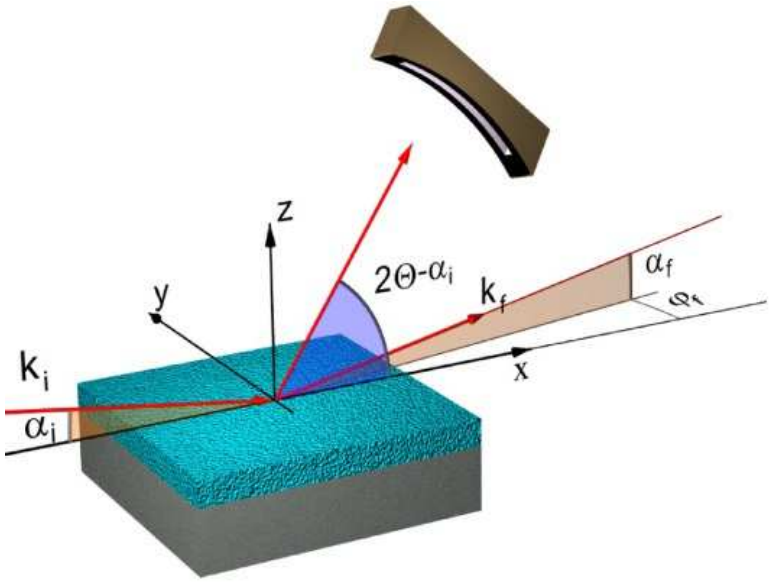

Figure 4.2: Experimental configuration of a GIXRD setup. From [132].

less than the critical angle, α_c, the beam will be completely reflected and there will not be any diffraction. For this reason a compromise must be found and the substrate might still contribute to the spectrum [130, 131].

In the GIXRD configuration the low angle incident beam remains fixed and it is the detector that will move around the 2θ angle (figure 4.2). For polycrystalline thin films the diffraction will happen in cones such as the ones of figure 4.3, thus moving the detector will allow to find for which angles the diffraction occurs, similarly to a powder diffraction spectrum.

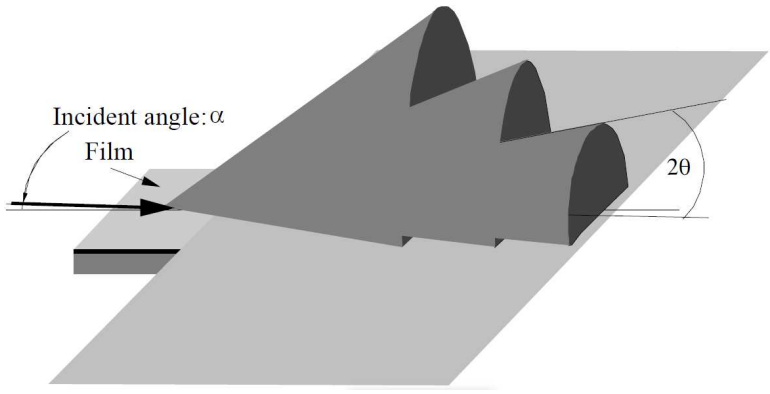

Figure 4.3: Diffraction cones originating from the randomly oriented grains of a polycrystalline thin film for GIXRD. From [131].

For strong enough diffraction peaks, this might enable a quantitative identification of the

crystalline phases using methods such as Rietveld refinements. Nonetheless, in polycrystalline thin films a quantitative analysis is rarely possible and the GIXRD is more often used to qualitatively identify the possible phases present in the material [130, 131].

On the other hand, if the thin film is epitaxial or if it has very well defined orientations the diffraction conditions will not be generally met (the diffraction would occur if the incident beam caught a specific diffraction plane) [130, 131].

4.2 Rietveld refinement

The Rietveld refinement method, developed mainly by Hugo Rietveld, tries to fit the experimental diffractogram to the theorectical diffraction peaks taking into account their intensity for each Bragg angle [129, 133, 134]. This method is based on fits using a least squares analysis with the objective to iteratively minimize the quantity χ^2 [129, 133, 135]:

$$\chi^2 = \sum_{i=1}^{N} w_i (y_{io} - y_{ic})^2 \ , \tag{4.9}$$

where N is the number of points observed in the diffractogram, y_{io} is the height (intensity) of the ith point of the diffractogram, y_{ic} is the theoretical intensity for the same ith point, and $w_i = {}^{1}\!/\!_{\sigma^2} = {}^{n}\!/\!_{y_{ic}} \approx {}^{n}\!/\!_{y_{io}}$ is the weight of each point (where n is the number of detectors used to measure the ith point) [129, 133, 134].

To minimize χ^2 one should find the solution of equation 4.10 [129, 133, 135]:

$$\sum_{j}^{P} \frac{\partial \chi^2}{\partial p_j} = 0 \ , \tag{4.10}$$

where P is the number of parameters used in the fit and p_j is the jth parameter of equation 4.10 sum.

The theoretical parameter is defined as [133]:

$$y_{ic} = y_{ib} + s \sum_{K} L_K \left| F_K \right|^2 \phi \left(2\theta_i - 2\theta_K \right) A \, P_K \ , \tag{4.11}$$

where y_{ib} is the background contribution for the ith point, s is a scale factor, K represents the Miller indices (hkl) of a given Bragg angle, L_K contains the polarization, Lorentz and

multiplicity factors, F_K is the structure factor, A is the absorption coefficient, P_K is the preferential orientation function, and $\phi\,(2\theta_i - 2\theta_K)$ is the reflection profile function. The latter takes into account experimental effects, such as the setup geometry, sample misalignment and absorption effects. The reflection profile function can have several curve types, but the most usual are Gauss, Lorentz, Voigt or Pseudo-Voigt functions.

4.2.1 Quality Criteria

Using numerical minimization methods, we can adjust the fit parameters, hence we should have a set of criteria which allow to determine the quality and confidence of the obtained fit. Therefore, Rietveld users developed the R-factors as a means of evaluating the quality of the Rietveld analysis. Some of these factors are presented below [133, 134, 136, 137]:

$$R_{wp} = \sqrt{\frac{\sum_{i=1}^{N} w_i (y_{io} - y_{ic})^2}{\sum_{i=1}^{N} w_i\, {y_{io}}^2}} \times 100\% = \sqrt{\frac{\chi^2}{\sum_{i=1}^{N} w_i\, {y_{io}}^2}} \times 100\% \tag{4.12a}$$

$$R_p = \frac{\sum_{i=1}^{N} |y_{io} - y_{ic}|}{\sum_{i=1}^{N} y_{io}} \times 100\% \tag{4.12b}$$

$$R_B = \frac{\sum_{i=1}^{N} |I_{Ko} - I_{Kc}|}{\sum_{i=1}^{N} I_{Ko}} \times 100\% \tag{4.12c}$$

$$R_F = \frac{\sum_{i=1}^{N} \left|\sqrt{I_{Ko}} - \sqrt{I_{Kc}}\right|}{\sum_{i=1}^{N} \sqrt{I_{Ko}}} \times 100\% \tag{4.12d}$$

$$R_{exp} = \sqrt{\frac{N - P + C}{\sum_{i=1}^{N} w_i\, {y_{io}}^2}} \times 100\% \tag{4.12e}$$

$$S = \frac{R_{wp}}{R_{exp}} = \sqrt{\frac{\chi^2}{(N - P + C)}} \tag{4.12f}$$

$$d = \sqrt{\frac{\sum_{i=2}^{N} (\Delta y_i - \Delta y_{i-1})^2}{\sum_{i=1}^{N} {\Delta y_i}^2}} \tag{4.12g}$$

From a pure mathematical point of view, the most relevant R-factor is the R_{wp} once it is a weighted factor and therefore the most relevant points (the ones with less variance) are responsible for most of the R_{wp} value. Another widely used factor is R_p which consists in the sum of all relative differences between the observed and calculated points. The Bragg R-factor, R_B, and the structure R-factor, R_F, are similar to the R_p and R_{wp} respectively, however, instead of using the intensity of each point, they use the integrated area I_K for a given combination of Miller indices (hkl).

The R_{exp} factor is a quality indicator of the experimentally obtained diffractogram, since it takes into account the total measured points, N, the number of parameters used on the fit, P, and the imposed constrains, C. R_{exp} is directly related with the S value, given by equation 4.12f, which is closer to 1 the better the Rietveld refinement is. S must not be less than 1 regardless of the quality of the other R-factors.

Determining and subtracting the background is crucial to the Rietveld refinement since it can erroneously influence the R_{exp} value. The background itself is the ubiquitous electromagnetic radiation originated from the X-rays interactions with the sample and from the X-rays coming from the source, such as K_α and K_β spectral lines.

Equation 4.12g shows the Durbin-Watson factor, where $Dy_i = y_{io} - y_{ic}$. This factor is an additional quality indicator whose ideal value is 2 [129, 133].

In summary the Rietveld method allows the quantification of crystallographic properties of the studied material, however such an approach should only be done after proper identification of its crystallographic phase(s).

4.3 Scanning Electron microscope

The Scanning Electron microscope (SEM) is a widely used technique to study the morphology of materials surfaces. It is able to take high magnification images of about $10 - 10^5 \times$ and has a high spatial resolution. SEM is also well known by its high depth of field which grants some three-dimensionality to its images [138–141].

Figure 4.4 shows SEM's three main components: the electron gun, the electromagnetic lenses and their aperture controlling system, and the particle and photon sensors. The electron gun has an electron source which is typically a W filament heated by an electric current resulting in the thermionic emission of electrons. These electrons are accelerated by an electric potential of about $0.1 - 50$ keV making this way the electron beam used in the SEM.

The electron beam is controlled by electromagnetic lenses whose magnetic and electric fields bend the electron beam path as described by Lorentz equation [4]:

$$\vec{F} = q\left[\vec{E} + \left(\vec{v} \times \vec{B}\right)\right] \ . \tag{4.13}$$

This way, and using different slits, it is possible to manipulate the electron beam to do the

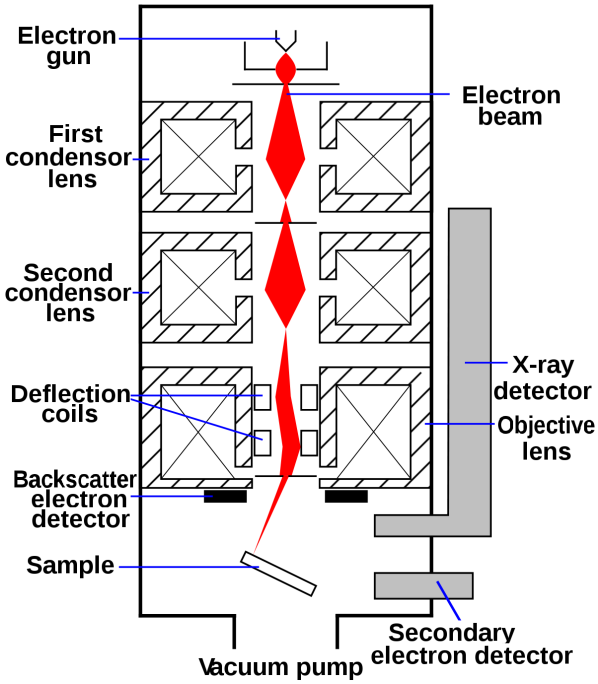

Figure 4.4: Diagram of the SEM components. From [142].

scanning at the desired sites and speed.

The electromagnetic lenses are a crucial factor to the spatial resolution of this microscope, being usually the bottleneck of the SEM final resolution [138, 139].

Unlike an optical microscope or a TEM, the SEM supplies an image originated from the electron beam scanning site by site, giving an image contrast produced from the signal difference obtained in each scanned pixel. Due to the high kinetic energy of the beam electrons, they interact with the sample giving birth to several types of by-product radiation (figure 4.5).

The backscattering electrons are high energy electrons which have suffered elastic scattering. These electrons are more scattered the higher is the atomic number, Z, hence being used in contrast images of substances with distinct values of Z [138, 141].

The secondary electrons originate from the inelastic scattering between high energy electrons and the electrons of the material in study. The lost energy induces the ejection of an electron from the target atom outer shells, with a kinetic energy of $E < 50$ eV. Secondary electrons are used in most SEM images, since they are highly sensitive to sudden changes in the sample topography due to their low energy. This feature enables the creation of images with high texture contrast, high amplification, and high spatial resolution.

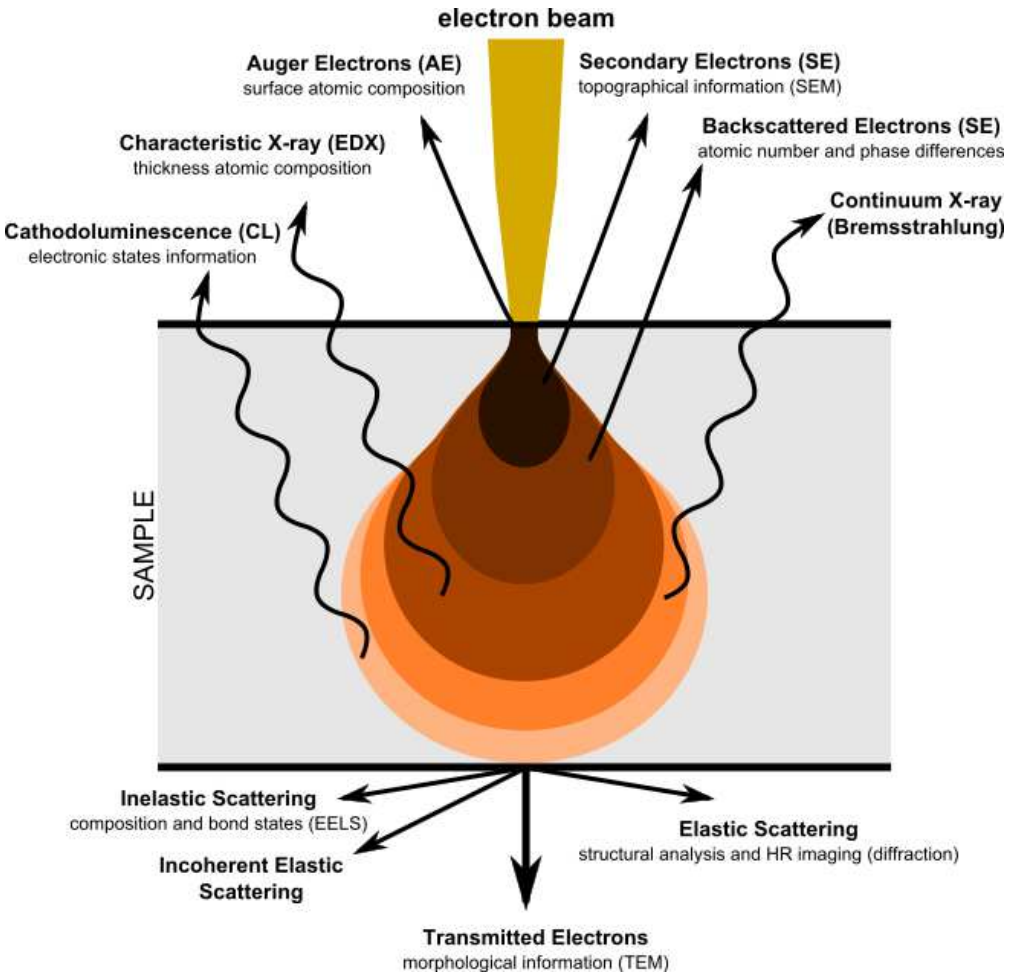

Figure 4.5: Scheme of the by-products resulting from the interaction of the electron beam with the sample. It should be stressed out that each depth has its own characteristic radiation by-product. From [143].

4.3.1 Imaging Modes

As mentioned, the way one can build an image using a SEM depends in which interaction by-product we choose to use as our signal. So, it is only natural that for different interaction by-products we have different imaging capabilities/modes. The most important beam parameters are directly related to the electrons which probe the sample and are represented in figure 4.6. $\mathbf{V_0}$ is the voltage applied to the electrons and is proportional to their energy ($V_0 = {}^{E_0}/_{e}$), $\boldsymbol{\alpha}$ is the electron probe convergence, $\mathbf{i_p}$ is the electron probe current, and $\mathbf{d}$ is the electron probe diameter.

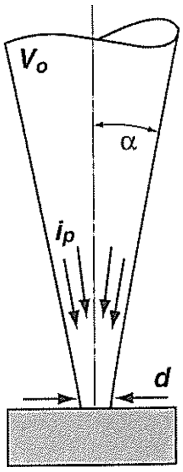

Figure 4.6: Diagram describing the variables involved in the SEM's electron probing beam. From [139].

High-Resolution mode

The high-resolution mode consists in reducing the electron probe diameter to the limits of the experimental apparatus using equation 4.14 parameters [139]:

$$d = \left(C_s^{1/4}\lambda^{3/4}\right)\left[1 + \frac{i_p}{\beta\lambda^2}\right]^{3/8} , \tag{4.14}$$

where C_s is the spherical aberration due to the electromagnetic lenses, λ is the electron beam wavelength, and β is the brightness of the electron source.

Since the electron source is strongly correlated to the electron probe diameter (informally called spot diameter), one can use other electron sources apart from the common W filament. Another alternative is the LaB_6 filament which has a brightness about 10× higher, or field effect sources which have a brightness about 1000× higher.

High-Current mode

Using high electron probe currents, we are able to obtain the best possible image visibility and quality at the cost of spatial resolution. For this reason, to improve the global image quality, a compromise between the High-Current mode and the High-Resolution mode needs to be found.

Low-Voltage mode

In the Low-Voltage mode, electron energies < 5 keV are used. These electrons interact with the sample surface, giving superficial information which can be masked if higher voltages are used [138].

Depth-of-Focus mode

The Depth-of-Focus mode uses very low convergence angles and profits from one of the most remarkable features of the SEM, the Depth of Field. As it was already mentioned, this feature allows to obtain information/images with three-dimensionality, something impossible for other microscopy techniques such as optical microscopy or atomic force microscopes [138].

Lastly, one should mention that the sample and measurements preparation are quite simple which eases the SEM usage as an everyday technique in materials characterization [138–141].

4.4 Scanning Transmission Electron Microscopy

For very small particles the spatial resolution of SEM will decrease, mainly due to all the scattering that will arise from the lower layers of the sample. In fact, for small size powders the electron probe beam might even be transmitted till the sample holder inserting another source of noise, increasing the required current intensity thus decreasing the spatial resolution of the SEM.

To avoid these problems, the samples are made thinner and thinner till the region which will be probed by the electron beam has tenths of nanometres. This sample preparation changes the analysis paradigm from the scattered electron microscopy to a Transmission Electron Microscopy (TEM). Apart from the electron source, the electromagnetic lenses, and apertures which control the electron beam till its interaction with the sample, a TEM will also have a system of lenses and aperture controllers after the sample position (figure 4.7). In a conventional TEM the electron beam probe will cross a given region of the sample and the diffracted transmitted electrons will then be detected by a given sensor (it used to be a fluorescent screen, but nowadays is a CCD) and, depending on the converged plane, it will display a micrograph or a reciprocal space image of the sample (figure 4.7).

The Scanning Transmission Electron Microscopy (STEM) uses the strengths of both SEM

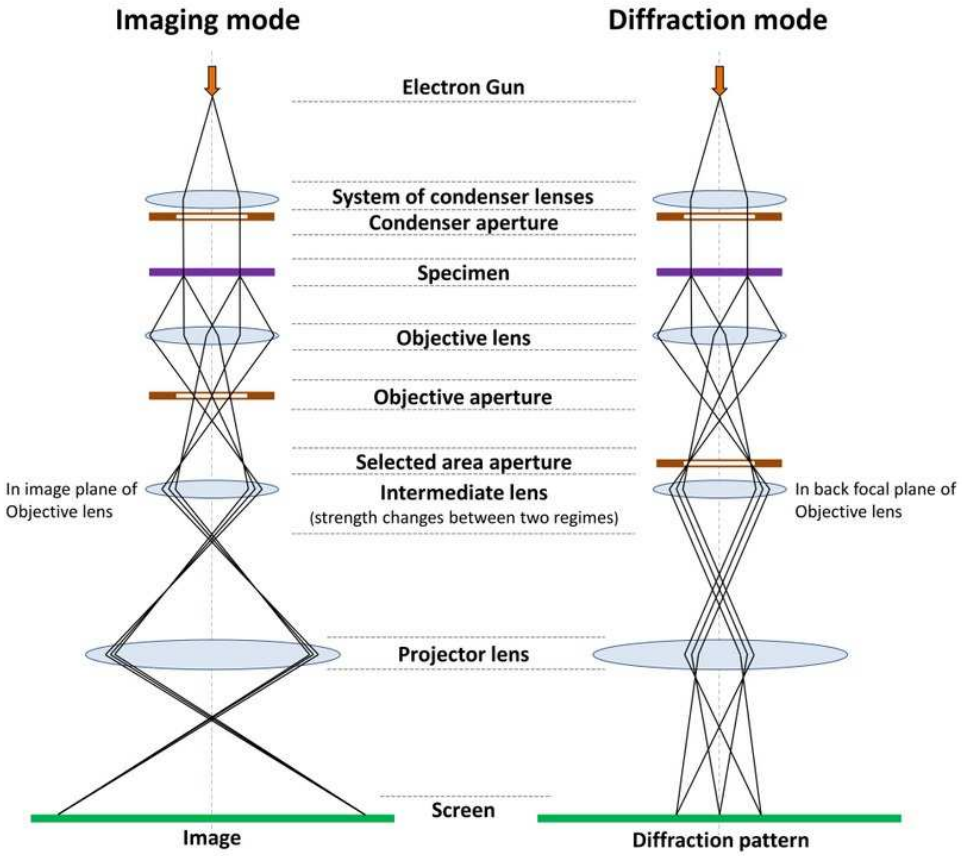

Figure 4.7: Diagram of TEM operating modes. From [144].

and TEM. A STEM will resort to an electron beam probe which is completely converged at a given point/region of the sample, with a spot size which might have sub-nanometre sizes [138, 140]. This small probe size will be transmitted through the sample and will contribute to a pixel of the micrograph. After doing a scan on the sample the desired micrograph is obtained, contrarily to the conventional TEM where the micrograph is obtained from the probe interaction with the whole region of interest at once. The experimental apparatus of both STEM and TEM are identical, being usually possible to use the same microscope to operate in both ways just by altering the configurations and parameters of its components (figure 4.8 and 4.9) [138–140].

The STEM can operate in the Bright-Field (BF) mode which results from quantification of the electrons that reach the detector after the their transmission through a specific region of the sample and its spatial resolution will be higher for higher α angles (given that the

electron beam converges in the probe) (figure 4.8). Besides the low β_1 angle transmitted electrons (figure 4.8), some electrons are scattered from the sample at high angles (mainly in elements with a high Z). The latter will be used to produce Dark-Field (DF) images, or High-Angle Annular Dark-Field (HAADF)imaging which can complement the information previously given by the BF imaging [138].

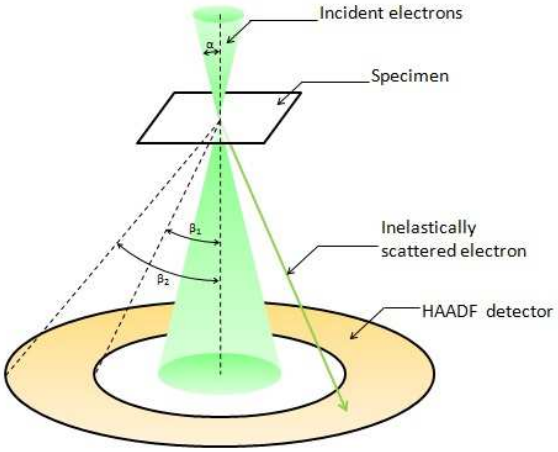

Figure 4.8: Scheme of STEM. It is possible to observe that the central detector is used to measure in the Bright-Field mode while the outer detector is used to measure the Dark-Field mode. Adapted from [145].

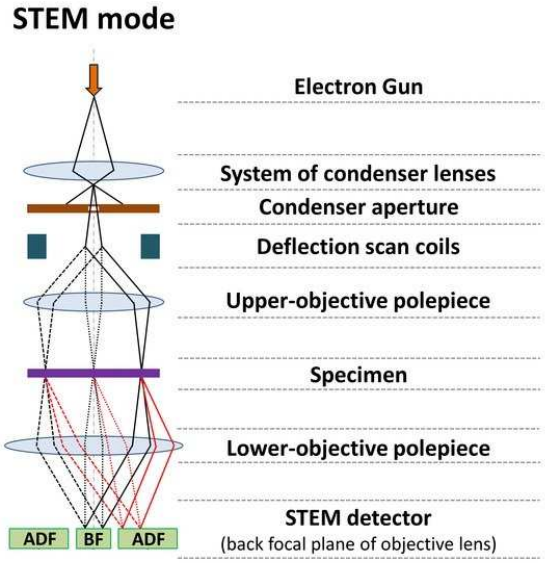

Figure 4.9: Diagram of STEM operating mode. Adapted from [146].

The STEM can produce high resolution imaging (at the atomic level), higher than the SEM, and suffers much less from sample drift problems than the TEM (despite the fact that the STEM needs a longer time to make a micrograph when compared with the conventional TEM) [138–140].

4.5 Characteristic X-ray Spectral lines

When high energy electrons interact with the sample's inner shell electrons, the latter are ejected as schematized in figure 4.10. The remaining electrons redistribute themselves after about 10^{-15} s, occupying the inner shells with the electrons that were previously in outer shells [34]. However, to complete this process, the outer electron must release some energy in order to occupy the vacant lower energy level. This energy difference can be released by emitting a characteristic X-ray photon, or by ejection of an Auger electron due to its energy transfer to other valence electrons.

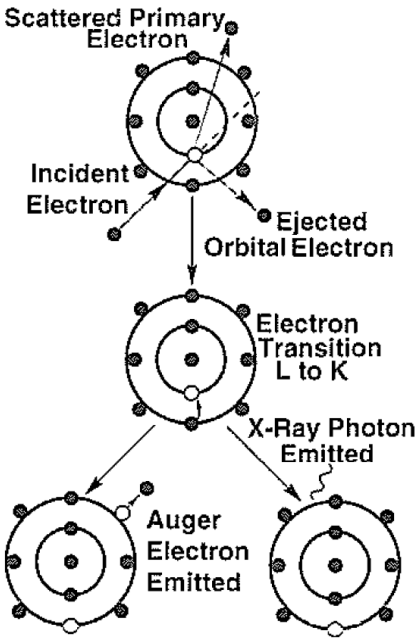

Figure 4.10: Diagram of the interaction which originate the characteristic X-rays. Adapted from [138].

Since quantum mechanics states that the energy levels of an electron in a specific shell of a given atom are well defined by Schrödinger equation, it is possible to identify to which element an emitted spectral line belongs to [34, 138, 139].

4.6 *Bremsstrahlung*

From electrodynamics its known that a charged particle emits electromagnetic radiation when accelerated, as described by equations 4.15 and 4.16:

$$P = \frac{q^2\gamma^6}{6\pi\epsilon_0 c}\left[\dot{\beta}^2 - \left(\vec{\beta}\times\dot{\vec{\beta}}\right)^2\right] = \begin{cases} P_{\vec{a}\perp\vec{v}} = \dfrac{q^2a^2\gamma^4}{6\pi\epsilon_0 c^3} \\ \\ P_{\vec{a}\parallel\vec{v}} = \dfrac{q^2a^2\gamma^6}{6\pi\epsilon_0 c^3} \end{cases} \xrightarrow[\text{approximation } v\ll c]{\text{In the classical non-relativistic}} \tag{4.15}$$

$$\Rightarrow P = \frac{q^2a^2}{6\pi\epsilon_0 c^3}\ . \tag{4.16}$$

where P is the irradiated power, q is the charge of the accelerated particle, c is the speed of light, ϵ_0 is the electric permittivity in vacuum, $\beta = v/c$, v is the charge velocity, a is the charge acceleration, and $\gamma = \frac{1}{\sqrt{1 - v^2/c^2}}$ is the Lorentz factor [35–37]. *Bremsstrahlung* is a German word which means "braking radiation" and is the name given in physics to the radiation emitted by a decelerating charge. The X-ray continuum resulting from the interaction between SEM's electron beam and a given material, as shown in figure 4.5, is nothing more than the *Bremsstrahlung*. This radiation is ubiquitous for interactions of charged particles with matter and effects greatly the signal background and therefore the overall spectral resolution of chemical characterization such as Energy-Dispersive X-ray Spectroscopy.

4.7 Energy-Dispersive X-ray Spectroscopy

As it can be seen in figure 4.5, in addition to the backscattered and secondary electrons, there are other radiation types originated from the electron beam interaction with the sample atoms. For this reason, it is possible to take advantage of all these radiations to give further information about the sample just by adding the adequate sensors in the experimental setup.

Energy-**D**ispersive X-ray **S**pectroscopy, EDS or EDXS takes advantage of the element specific characteristic X-rays to make the chemical characterization of a given material. EDS uses accelerated electrons to produce the characteristic X-rays, therefore it is quite common to implement an adequate spectrometer in SEM or STEM experimental setup to combine both microscopy and chemical analysis. This technique is quite versatile and has a lower limit of detection which can reach values as low as 0.1% of atomic concentration.

4.8 Particle Induced X-ray Emission Spectroscopy

The Particle Induced X-ray Emission, or PIXE is a spectroscopic technique based on the same main physical principles of EDS, however in the former the K electron is ejected using a high energy ion instead of an electron. In PIXE spectroscopy the ions typically used are protons or He nucleus which are accelerated to energies of the order of MeV [34, 147].

Thanks to the above-mentioned difference, PIXE spectroscopy suffers a huge boost in its sensitivity to identify characteristic X-rays. This can be explained due to the significant mass difference between the particles used in PIXE and EDS (a proton for example is about 1836

times more massive than an electron [147]). This difference in mass results in less lost kinetic energy, increasing the penetration depth and focus ability.

Additionally, due to PIXE's particles having higher masses, there is much less deceleration than in the electron case, hence having a much lower *Bremsstrahlung*, whose contribution in PIXE is predominantly from the secondary electrons formed by the ions interaction with the sample [147, 148]. This aspect of PIXE eases the detection of characteristic X-ray spectral lines allowing a much higher spectral resolution [147, 148].

In addition to protons, PIXE uses heavier ions (like He ions), however as the ion get bigger/heavier the sample damage also increases and for this reason it is not usual to use high mass ions in PIXE spectroscopy [147, 148].

PIXE is a characterization technique which presents a sensitivity in the order of ppm of atomic concentration for $Z \geq 12$, hence being quite useful in the detection of trace elements [147, 148].

4.9 Raman Spectroscopy

The study of the vibration modes of a given system can give information about its structural and chemical characteristics. Knowing that, an electromagnetic wave can be defined as the electric field sinusoidal function of equation 4.17 [4]:

$$E = E_0 cos\left(2\pi\nu_0 t\right) \ , \tag{4.17}$$

and the polarization of a given material is described by the product of the polarizability tensor and the applied electric field:

$$\vec{\mathfrak{p}} = \hat{\boldsymbol{\alpha}}\vec{E} \ , \tag{4.18}$$

if we consider the expansion of the polarizability in the power series of the normal coordinate of vibration, q, presented in equation 4.19 till the first order term:

$$\alpha = \alpha_0 + \left(\frac{\partial \alpha}{\partial q}\right)_0 q + \frac{1}{2}\left(\frac{\partial^2 \alpha}{\partial q^2}\right)_0 q^2 + \cdots \tag{4.19}$$

$$\left(\frac{\partial \alpha}{\partial q}\right)_0 \neq 0 \tag{4.20}$$

putting together equations 4.18 and 4.17, and considering $q = q_0 \cos[2\pi\nu_m t]$, we obtain equation 4.21:

$$\mathfrak{p} = \underbrace{\alpha_0 E_0 cos\left(2\pi\nu_0 t\right)}_{\text{Rayleigh}} + \frac{1}{2}\left(\frac{\partial \alpha}{\partial q}\right)_0 q_0 E_0 \left[\underbrace{cos\left[2\pi\left(\nu_0 + \nu_m\right)t\right]}_{\text{Anti–Stokes}} + \underbrace{cos\left[2\pi\left(\nu_0 - \nu_m\right)t\right]}_{\text{Stokes}}\right] . \tag{4.21}$$

Equation 4.21 has three main parts. The first term describes the Rayleigh scattering which is the pure elastic scattering of electromagnetic radiation, being for this reason the most intense component. The two remaining terms describe the Anti–Stokes and Stokes scattering respectively and consist in inelastic scattering of the electromagnetic radiation. The inelastic scattering shifts the Anti–Stokes and Stokes scattering frequencies by ν_m with relation to the Rayleigh scattering frequency (Raman shifts with an energy quanta of $E = h\nu_m$) [149, 150].

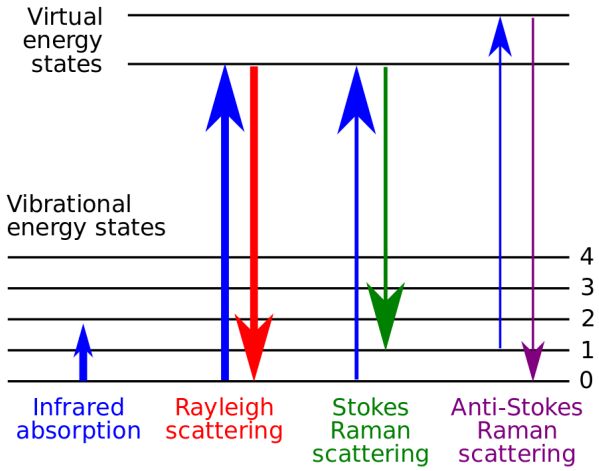

Figure 4.11: Diagram with the transitions associated with the different types of radiaction scattering. From [151].

Raman Spectroscopy studies the Stokes scattering spectrum by checking where the intensity peaks and their respective Raman shifts are . For temperatures low enough (such as room temperature), the vibrational ground state is much more populated than the first excited

vibrational state. For this reason, the Stokes spectrum is chosen instead of the Anti–Stokes since the former's transitions originate from the vibrational ground state, hence having more intense peaks than the latter, whose transitions originate from the less populated first excited vibrational state, as shown in figures 4.11 and 4.12. It should be stressed out that even for the more intense Stokes spectrum, its peak intensities are about 10^3 (for solids) to 10^6 (for gases) times less intense than the peak due to Rayleigh scattering [149, 150, 152].

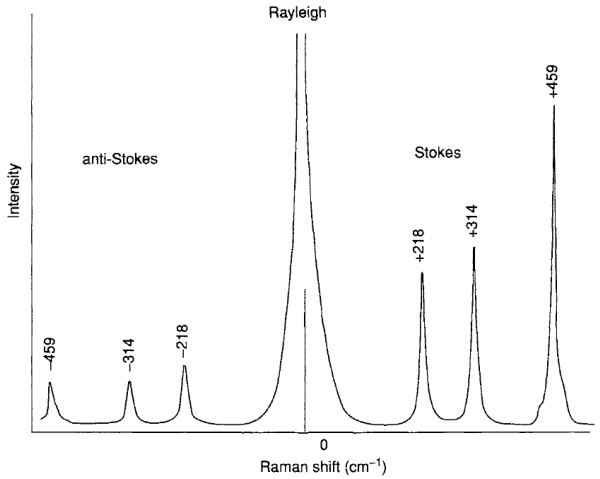

Figure 4.12: Typical Raman spectrum. From [152].

Raman spectroscopy is a very versatile non-destructive characterization technique which does not require complex sample preparation and, besides the chemical and structural information of the material in study, it can also enable the study of electrical properties, since as it can be observed in equation 4.20, the Raman active vibrational transitions are directly correlated with its electric polarizability tensor [149, 150].

4.10 Superconducting Quantum Interference Device

It is known that in a superconducting ring with a circulating current J, if a portion of the ring is insulator or has a critical current smaller than J, as long as that portion is smaller than the coherence distance ξ, then the Cooper pairs can tunnel through that material portion without any voltage drop or energy dissipation. That insulator part is called a Josephson junction and it just induces a phase difference, δ, between the macroscopic wavefunction of the two extremities of the Josephson junction [153]. It is also known that it is only possible to enclose an internal magnetic flux in a superconducting ring as long as it is a multiple of

the flux quanta described by equation 4.22 [153–157]:

$$\Phi_0 = \frac{h}{2e} \ . \tag{4.22}$$

A **S**uperconducting **QU**antum **I**nterference **D**evice (SQUID) is a magnetometer which is known for its high sensitivity and is often used to measure very small magnetic moments. This device is based on the Josephson effect and can operate in the direct current (DC) regime or in the alternating current (AC) regime [153–157]. The AC regime is also known as RF SQUID (radio frequency SQUID) since the alternating current is induced by radio frequency in the superconducting ring containing the Josephson junction.

4.10.1 DC SQUID

In the DC SQUID two identical Josephson junctions are placed in a superconducting ring with a bias DC current I which is divided into two currents, I_1 and I_2, as shown in figures 4.13 and 4.13. Besides the bias current there is also the current J due to the enclosed magnetic flux $\Phi_{in} = \mathscr{L}J$. It should be noted that the critical current I_C results from the sum of the critical currents of both Josephson junctions $I_{C,1}$ and $I_{C,2}$.

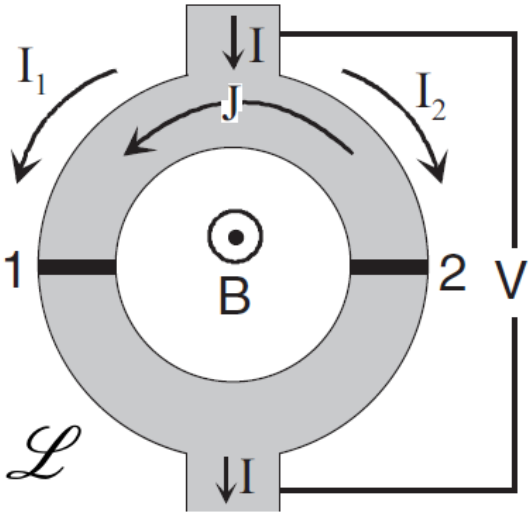

Figure 4.13: Scheme of the superconducting ring of a DC SQUID. From [154].

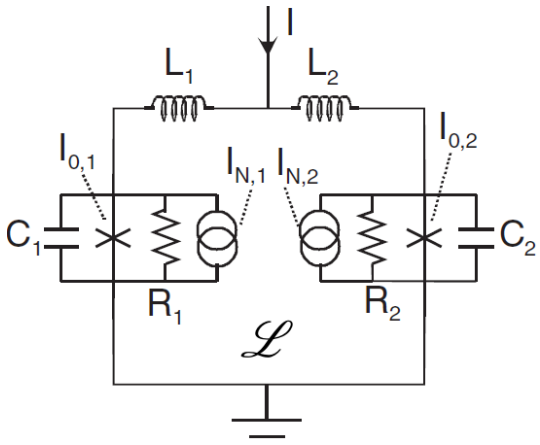

Figure 4.14: Figure 4.13 equivalent electric circuit. From [154].

The DC SQUID has two operating modes: in the first one the magnetic flux enclosed in the superconducting ring modulates I_C with a period Φ_0. This modulation is caused by the wave functions interference coming from the two branches of the superconducting ring and

which have a phase difference $\Delta\delta$. This way it is possible to measure I_C increasing the bias current I to the point there is a voltage between the Josephson junctions.

In the second operating mode a bias current slightly higher than the critical current of the superconducting ring is supplied. This way, for $I \gtrsim I_C$ is possible to directly measure the voltage V as a function of the applied magnetic flux, Φ_a. When I_C reaches its maximum value, V reaches its minimum value and *vice versa* [153].

The most impressive feature of the DC SQUID is its huge sensitivity and measurement resolution. This magnetic sensor can measure magnetic fields of the order of $fT - pT$ with typical resolution of about 5 fT [156, 157]. However, there are some noise sources such as white noise and thermal fluctuations. To lower the possible noise sources, one should reduce the best we can the capacitance and inductance of the Josephson junction, as well as the SQUID temperature, as it can be seen through inspection of the noise energy of equation 4.23 [153, 157]:

$$E_N = 16 k_B T \sqrt{\mathscr{L} C} \ . \tag{4.23}$$

4.11 Perturbed Angular Correlations Spectroscopy

Perturbed Angular Correlations (PAC) spectroscopy is a nuclear technique which allows the measurement of the EFG or/and the HMF felt by a given radioisotope probe nucleus. This characterization technique is based on the angular correlation of a two consecutive γ photon cascade, for the $\gamma - \gamma$ case (figure 4.15) or a cascade of a conversion electron and a γ photon for the $e^- - \gamma$ case [33, 158, 159].

For a nucleus excited state with total angular momentum I, such as the one shown in figure 4.15, it is is possible to determine the probability of emission of a γ_2 photon with a propagation vector $\vec{k}_2$ after the emission of a first γ_1 photon with a vector $\vec{k}_1$ [33, 160]. For randomly oriented nucleus and taking as reference the vector $\vec{k}_1$ (figure 4.16), the probability $W(\theta)$ of consecutive γ-ray emission is expressed by equation 4.24 [33, 158, 160]:

$$W(\theta) = \sum_{k=0}^{k_{\max}} A_k(\gamma_1) A_k(\gamma_2) P_k(cos(\theta)) \ , \tag{4.24}$$

where only even values of k will be used in the sum due to parity conservation of the elec-

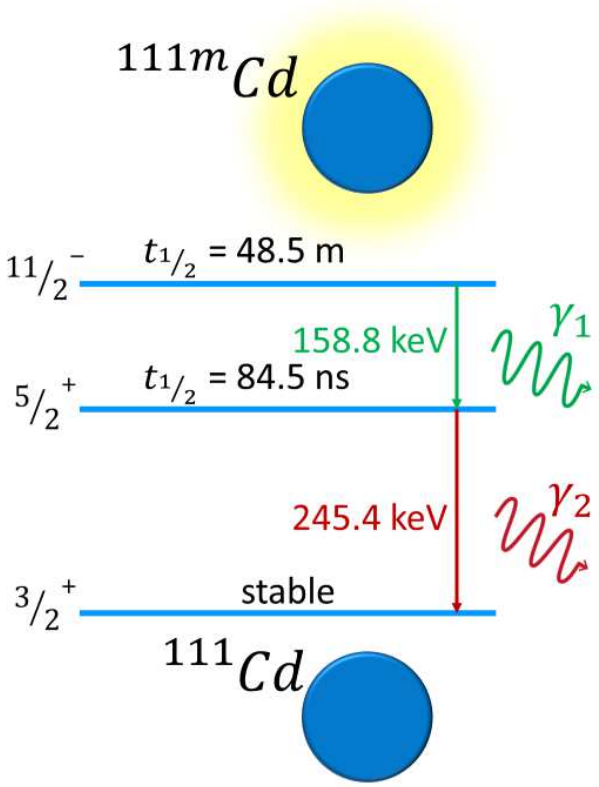

Figure 4.15: ^{111}Cd decay scheme of the $\gamma_1 - \gamma_2$ cascade from the exited ^{111m}Cd to its stable state.

tromagnetic interaction. $k_{\max}$ is defined as the $min\{2I; (l_2 + l_2'); (l_1 + l_1')\}$, where l_i and l_i' are allowed angular momentum values carried by each γ-ray between two consecutive nuclear states. $P_k(cos(\theta))$ are the Legendre polynomials and $A_k(\gamma_1)$ and $A_k(\gamma_2)$ are the anisotropy terms which describe the coincidence probability deviations from the isotopic case where $W(\theta) = 1$ [33, 158, 160].

The expression of equation 4.24 holds for an ensemble of free radioisotopes due to the $2I + 1$ degenerate states being equally populated. However, if the radioisotope is within a crystal lattice then there might be an energy split of the degenerate states. In fact, as long as the chemical environment of the radioactive probe is not cubic, the intermediate state (second energy level of figure 4.15) will be perturbed and there will be an energy splitting which will alter the populations of each m_I state, thus affecting the angular probability distribution, $W(\theta)$ [161–163].

The new coincidence probability $W(\theta)$ will become a time dependent perturbation func-

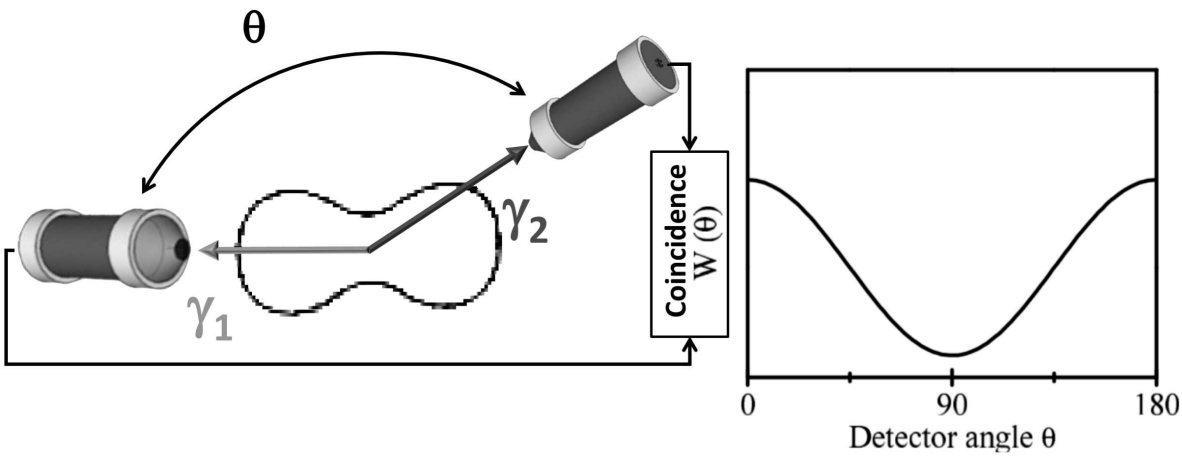

Figure 4.16: **(Left)** Experimental configuration to measure the $\gamma_1 - \gamma_2$ angular correlation. **(Right)** Plot of the coincidence probability as a function of the angle θ. Adapted from [159].

tion, $G_{k_1,k_2}^{N_1,N_2}(t)$, as shown in equation 4.25 [33, 160]:

$$W(\theta,t) = \sum_{k_1,k_2,N_1,N_2}^{k_{\max}} A_k(\gamma_1)A_k(\gamma_2)\frac{Y_{k_1}^{N_1}(\theta_1,\phi_1)Y_{k_2}^{N_2}(\theta_2,\phi_2)}{\sqrt{(2k_1+1)(2k_2+1)}}G_{k_1,k_2}^{N_1,N_2}(t) \ , \tag{4.25}$$

where $Y_{k_i}^{N_i}(\theta_i,\phi_i)$ are the spherical harmonics, and $|N_i| \leq k_i$. The perturbation function, $G_{k_1,k_2}^{N_1,N_2}(t)$, contains all the information related to the hyperfine fields (EFG and/or HMF) which will interact with the intermediate state [33, 160].

For a polycrystalline host lattice, and if the interaction Hamiltonian is static, equation 4.25 is simplified and equation 4.26 is obtained [33, 160]:

$$W(\theta,t) = \sum_{k=0}^{k_{\max}} A_k(\gamma_1)A_k(\gamma_2)P_k(cos(\theta))G_{kk}(t) \ . \tag{4.26}$$

To measure the hyperfine fields felt at the probe site, the perturbation function, $G_{kk}(t)$, must be experimentally determined. To do so the coincidence count rate as a function of time, $N(\theta,t)$, for the two γ photons of the $\gamma_1 - \gamma_2$ cascade should be measured. This is achieved with an even number of detectors (usually 4 or 6 detectors are used) that are oriented in pairs of antiparallel (180°) and perpendicular (90°) configurations [33, 158–160, 164].

For the 6 detectors configuration there are 30 detector pair combinations with 180° (6) and 90° (24) between them providing coincidence spectra. The spectra are combined and the term of the intermediate nuclear state half-life is eliminated through the anisotropy ratio function

presented in equation 4.27 [160, 164]:

$$R(t) = 2\frac{\sqrt[6]{\prod_j^6 N_j(180°,t)} - \sqrt[24]{\prod_i^{24} N_i(90°,t)}}{\sqrt[6]{\prod_j^6 N_j(180°,t)} + 2\sqrt[24]{\prod_i^{24} N_i(90°,t)}} \ . \tag{4.27}$$

For a 4 detectors configuration there are 12 detector pair combinations with 180° (4) and 90° (8) between and its ratio function is presented in equation 4.28 [160, 164]:

$$R(t) = 2\frac{\sqrt[4]{\prod_j^4 N_j(180°,t)} - \sqrt[8]{\prod_i^8 N_i(90°,t)}}{\sqrt[4]{\prod_j^4 N_j(180°,t)} + 2\sqrt[8]{\prod_i^8 N_i(90°,t)}} \ . \tag{4.28}$$

The fitting function is calculated by numerically diagonalizing the quadrupole interaction Hamiltonian to produce the equivalent observable perturbation function to $R(t)$ [160, 164]. The theoretical perturbation function is described by equation 4.29:

$$R(t) = \sum A_{kk} G_{kk}(t) \ , \tag{4.29}$$

where A_{kk} are the effective anisotropy coefficients of the nuclear decay cascade and $G_{kk}(t)$ is the perturbation factor containing the hyperfine interaction frequencies, ω_n, through equation 4.30 [158, 160, 164]:

$$G_{kk} = \sum_i f_i \sum_n^3 S_{kn}^i \cos(\omega_n^i t) \exp(-\omega_n^i \delta^i t) \ . \tag{4.30}$$

where f_i represents the fraction of the probes that interact with different environments, $\sum_i f_i = 1$, with interaction frequencies ω_n, amplitudes S_{kn}, and attenuation δ. In this thesis, to extract the electric field gradients from quadrupole hyperfine interaction we use the quadrupole moment of the ^{111m}Cd's $5/2^+$ intermediate state (figure 4.15), $Q = 0.683(77)$b [165].

4.12 Sputtering Deposition

Sputtering is one of the most widely used physical vapour deposition (PVD) techniques. It allows the deposition of several materials without the need of heating the source materials

(the target) [166–168]. Figures 4.17 and 4.18 show typical experimental setups for sputtering deposition, for which a target and a substrate are placed inside a vacuum chamber, where an inert gas, such as Ar, is injected. Then an electric potential is applied between the target (used as cathode) and the substrate (used as anode), which will strip some electrons from the Ar atoms, ionising them. The charged particles (electrons and Ar^+) will be accelerated by the electric potential, colliding with the neutral Ar atoms, further enhancing their ionization, thus creating a plasma inside the chamber between the target and the substrate [166–168].

The positively charged Ar ions are attracted by the cathode, colliding with the target which results in the ejection of the atoms from the target source material and their deposition on the substrate. The substrate can be heated to improve not only the adhesion of the sputtered material during the condensation phase, but also as a means of improving the crystallinity of the deposited phase [166–168].

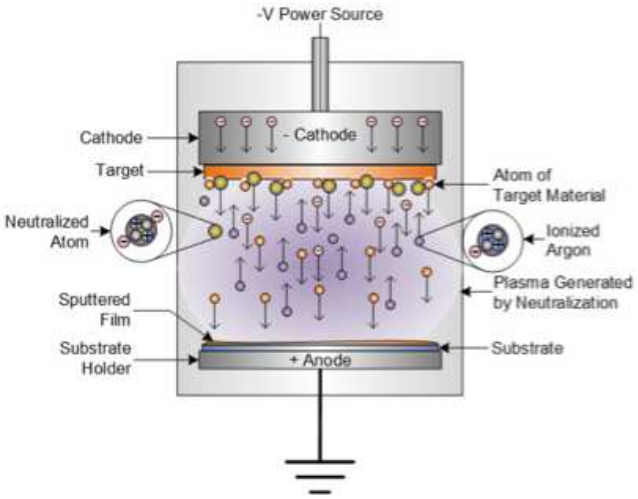

Figure 4.17: Sheme of a typical experimental configuration for DC sputtering. From [169].

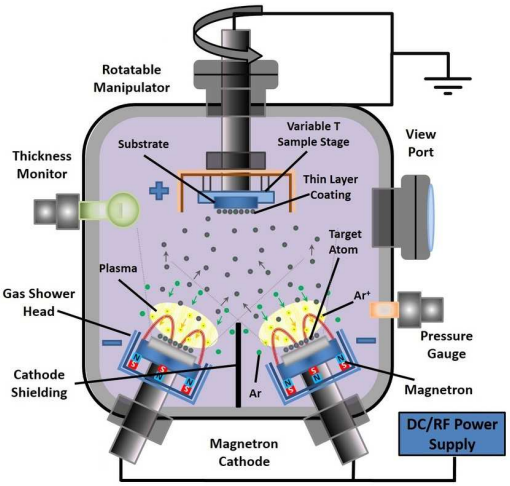

Figure 4.18: Sheme of a typical experimental configuration for RF sputtering. From [170].

Using a DC sputtering configuration (figure 4.17), the Ar ions that eject the atoms from the target will remain in the cathode, resulting in a positive charge accumulation for an isolating target source material. This charge accumulation will produce a screening field which will gradually lower the sputtering efficiency [166–168]. To solve this problem, a RF configuration can be used, where the DC power supply is replaced by an AC power supply instead.

In this last configuration it is usual to incorporate magnetrons which allow the confinement of the plasma in a smaller region. This approach presents several advantages since it will enhance the ionization of the Ar atoms while using much less gas pressure (pressures in the

order of 10^{-5} mbar can be used instead of the typical 10^{-2}–10^{-3} mbar), thus having cleaner deposition conditions [166–168].

This deposition technique is relatively easy to implement and allows the deposition of high sublimation temperature materials, reasons which make the sputtering deposition such a widely used deposition technique.

4.13 Molecular Beam Epitaxy

Molecular Beam Epitaxy (MBE) is known as a very thorough PVD method which allows the epitaxial growth of very thin films under very clean conditions. Figure 4.19 shows the experimental apparatus usually associated with MBE deposition. It is composed of an ultra-high vacuum chamber (UHV), Knudsen-cells, a rotative substrate holder (and respective heater), and some *in situ* characterization techniques (such as Reflection High-Energy Electron Diffraction, RHEED, and Low Energy Electron Diffraction, LEED) [166, 167, 171, 172].

Before the film deposition, the substrate and its holder should be completely cleaned and baked at a temperature higher than the temperature at which the deposition will take place. This procedure is usually done inside a UHV chamber to release possible adsorbed and absorbed organic substances from the substrate warranting good vacuum conditions during the deposition process [171, 172].

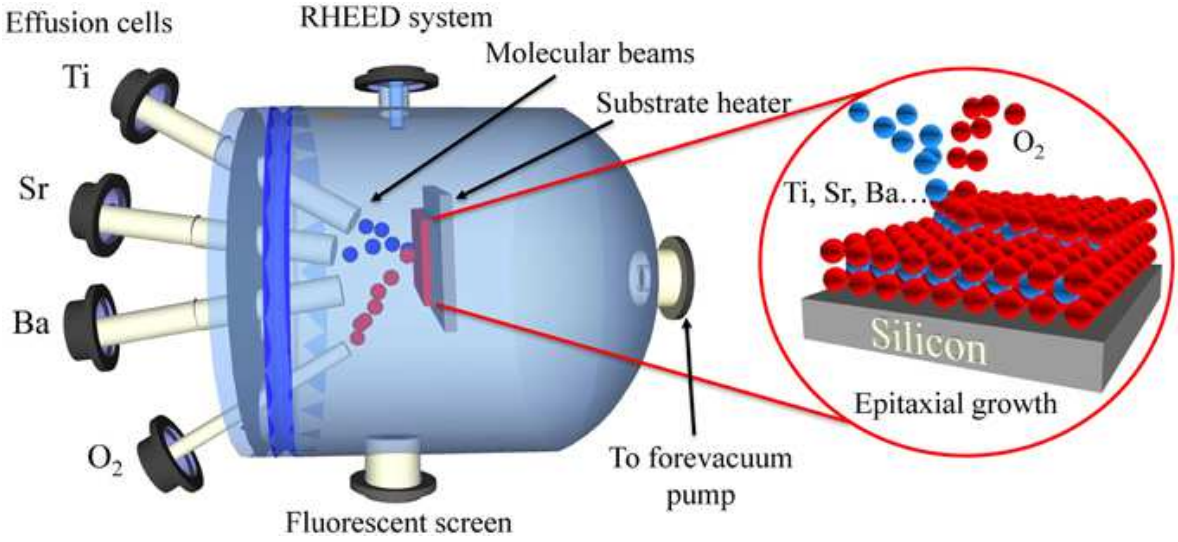

Figure 4.19: Sheme of a typical experimental configuration for MBE. From [173].

After the cleaning and baking procedure, the substrate is maintained at the desired de-

position temperature and then the Knudsen (or effusion cells) are heated to the temperature correspondent of a given deposition rate, which was previously calibrated. To enhance the homogeneity of the film deposition, the substrate is rotated during the deposition process. Each Knudsen-cell is responsible for a individual atomic/molecular beam thus it is possible to deposit a composite and control the desired stoichiometry by adjusting each beam deposition rate, after taking into account the adhesion of each element [166, 167, 171, 172].

MBE deposition enables very high purity thin film deposition due to the UHV conditions, typically $\leq 10^{-10}$ mbar, and epitaxial films thanks to the low deposition rates of this deposition technique [166, 167, 171, 172].

As mentioned above, the MBE experimental apparatus often possesses complementary characterization techniques, such as RHEED and LEED, which allow the *in situ* control of the thin film deposition. These capabilities allow the correction of the effusions cells or/and the opening or closing of their shutters during the growth of heterostructures/composites [171,172].

Despite the high accuracy, homogeneity, good film adhesion and the slow epitaxial growth allowed by the MBE, its expensive and complex apparatus makes this deposition technique restricted to just a few laboratories and, therefore, it is not as accessible as other PVD techniques [166, 167, 171, 172].

Chapter 5

A Peculiar Type of $BaTiO_3$:Fe

5.1 The Ferroelectric Archetype

$BaTiO_3$ (BTO) is a ferroelectric perovskite with high dielectric constant[1], which possesses an ABO_3 structure with A=Ba and B=Ti, as shown in figure 5.1.

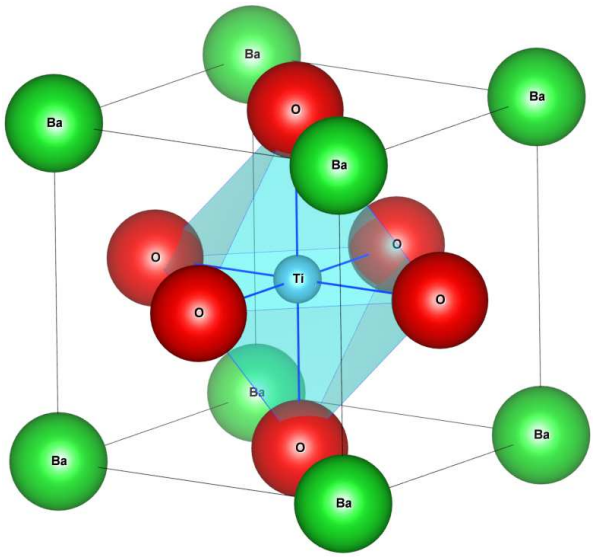

Figure 5.1: $BaTiO_3$ cubic unit cell.

According to Goldschimdt the perovskite stability is given by equation 5.1:

$$t = \frac{r_A + r_O}{\sqrt{2}\,(r_B + r_O)}\ , \tag{5.1}$$

[1] $\epsilon_r \approx 4600$ for a single crystal at room temperature (RT) [174]

where r_A, r_B and r_O are the ionic radii for the A, B and O ions respectively, and $t \approx 1$ defines a perfect perovskite. When $t > 1$ a small distortion at the O_6 octahedra is created, which for the $BaTiO_3$ case results in a net polarization [175].

Barium titanate has three ferroelectric phases below its Curie temperature, as shown in figure 5.2. Its cubic paraelectric phase has a $Pm\bar{3}m$ structure that, at $T_C = 393\,K$, changes to its $P4mm$ tetragonal ferroelectric phase. This phase has a spontaneous polarization $P_s = 27\,\mu C.cm^{-2}$ in the [001] direction. At $T \approx 273\,K$ there is a transition to an orthorhombic phase ($Amm2$) with a spontaneous polarization $P_s = 36\,\mu C.cm^{-2}$ along the [011] direction, and finally at $T \approx 190\,K$ it changes to its rhombohedral phase ($R3m$) with a spontaneous polarization of $P_s = 33\,\mu C.cm^{-2}$ along the [111] direction [176, 177]. $BaTiO_3$ also has a hexagonal phase at $T \approx 1853\,K$ [178], right before its melting point temperature at $T \approx 1898\,K$ [179].

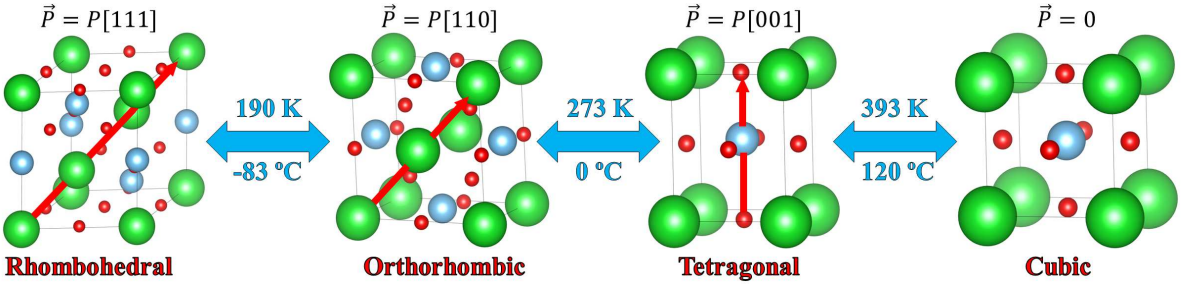

Figure 5.2: $BaTiO_3$ phase transitions and respective spontaneous polarization directions.

This ferroelectric archetype is well known for its uses in technological applications, being a proper ferroelectric with appealing ferroelectric properties and which can be produced using environment friendly and common non-critical raw materials.

5.1.1 $BaTiO_3$ magnetic properties

Barium Titanate is a perovskite without very interesting magnetic properties. It is a diamagnetic material with a typical magnetic susceptibility of $\chi_{dmag} \approx -10^{-7}$ emu/g [180], therefore having a negative, almost temperature independent magnetization, as we can see in figure 5.3.

The presence of extrinsic magnetic effects in nanocrystalline $BaTiO_3$, apart from its characteristic intrinsic diamagnetism, has already been reported by R Pazik [180] and RVK Mangalam [181], where a hysteretic ferromagnetic like curve is reported in an apparently pure

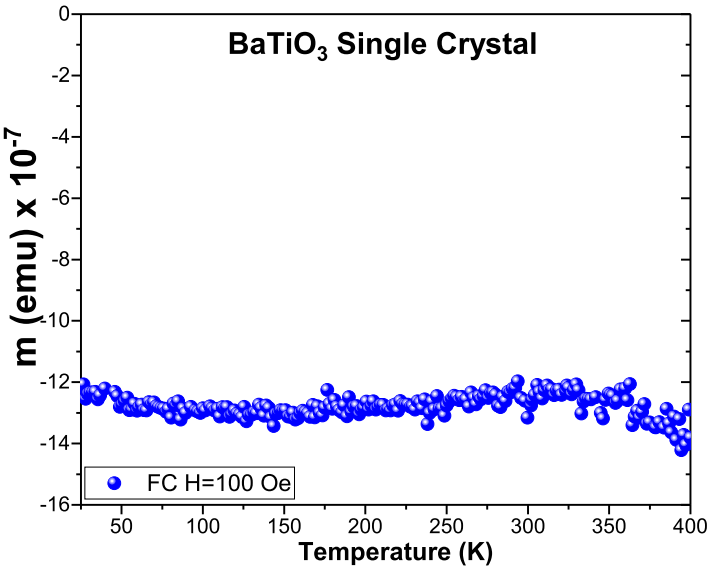

Figure 5.3: $BaTiO_3$ single crystal temperature dependent magnetization curve.

BTO. One of the presented arguments is that these magnetic effects would be due to the existence of Ti^{3+} cations on the surface of barium titanate grains [180], however after estimating the number of Ti^{3+} cations required to reproduce the magnetization values reported, we can verify that such a proposition is not reasonable for the grain size reported by R Pazik and RVK Mangalam (by a factor of 200) [182].

Another reason to justify a supposed ferromagnetism behaviour, pointed by RVK Mangalam [181] and Z Zhang [183], would be due to the presence of oxygen vacancies in perovskites. Yet, since their claims are based in very low magnetization signals, other scenarios as contamination by magnetic ions should also be considered [184].

5.1.2 $BaTiO_3$:Fe

Many studies were done where $BaTiO_3$ was doped with transition metals. These studies were done due to BTO's very appealing ferroelectric properties, hence being a suitable candidate to be a multiferroic perovskite [185]. The addition of Fe, in particular, is a very popular approach and there are many studies regarding the incorporation of this transition metal, using different concentrations, in a $BaTiO_3$ ferroelectric system.

All these studies show that even for high Fe concentrations, the Fe atoms tend to occupy substitutional positions in the $BaTiO_3$ matrix either in the Ti sites (B site) or in the Ba sites (A site), depending on the synthesis procedure [186]. The X-ray diffractograms of the

studies above do not show segregation of any secondary phase containing Fe [185–190]; there is however a distortion in the crystalline structure to the $BaTiO_3$ hexagonal allotrope above a certain threshold concentration because of the tensions caused by the Fe ions [187, 188]. This results in the degradation of BTO electric properties while not producing significant magnetoelectric couplings.

5.2 A Unique $BaTiO_3$:Fe

To have a deeper understanding of the possible magnetic effects present in $BaTiO_3$, the study of a nanocrystalline powder was performed. The preparation of the $BaTiO_3$ compound was done by the solid-state sintering method from TiO_2 and $BaCO_3$ 99.9% grade reagents from Merck. The heterogeneously mixed reagents had two stages of calcinations (one at 700°C and the other at 900°C) and the resultant power was sintered at 1100°C and 900°C for about 40 and 20 hours respectively. Finally, the powder was pressed into a series of pellets to ease their characterization. The following results/studies were already published in [2] and [2].

The pressed pellets were magnetically characterized using Quantum Design MPMS-5S SQUID and MPMS3 SQUID-VSM instruments from 5 to 400 K.

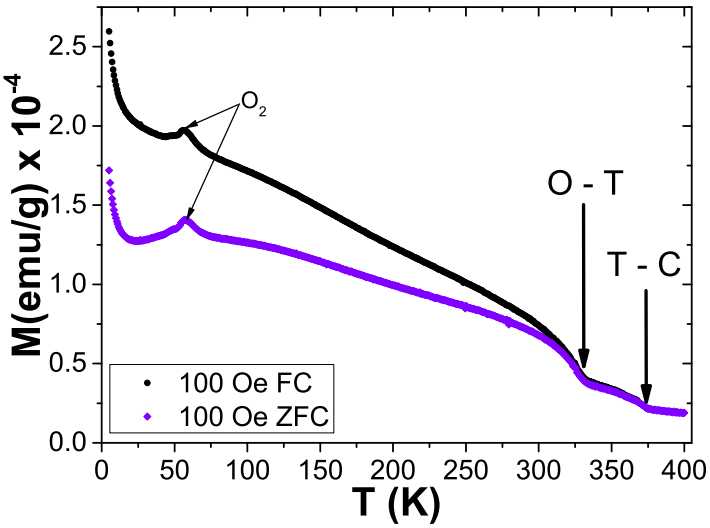

Figure 5.4: $BaTiO_3$ magnetization as a function of the temperature under ZFC/FC conditions. From [2].

Figure 5.4 shows the temperature dependence of the magnetization plot of a $BaTiO_3$ pellet. Surprisingly, instead of the expected pure diamagnetic behaviour, the magnetization

has always a positive value. It is also possible to observe two magnetic anomalies at high temperatures, and paramagnetic like behaviour at low temperatures.

Both anomalies occur above room temperature and suggest two transitions of magnetic ordered phases. The "strongest" transition occurs at 325 K, also coinciding with the temperature where the ZFC [2] and FC [3] curves converge, while the smallest one occurs around 373 K. It should be noted that these two magnetic transitions are startlingly close to the temperatures where two ferroelectric phase transitions of $BaTiO_3$ are known to occur (figure 5.2). Additionally there is a faint anomaly near 190 K, at the same temperature where the BTO rhombohedral↔orthorhombic phase transition.

There is also a magnetic local maximum around 55 K associated with the paramagnetic ↔ antiferromagnetic transition of O_2, which can arise due to an air leak in the SQUID sample chamber (as reported by the manufacturer [193]).

Element	**μg/g**	**ppm (atomic)**
Si	6800	11235
P	560	839
Cl	490	641
K	180	214
Ca	770	892
Fe	136	113

Table 5.1: PIXE results for the $BaTiO_3$ pellet. Data obtained at CTN-IST [194].

As referred before, there should not be any plausible reason for a pure BTO sample to have magnetic ordering, therefore, in order to look for the presence of magnetic trace elements, a chemical analysis was performed resorting to PIXE spectroscopy. The results of this analysis, presented in table 5.1, showed 113 ppm of Fe content. In fact, the Fe presence is justified by a possible 60ppm Fe concentration in the reagents (Merck 101714 and 100808 Specs) [195,196], as indicated in the specifications, and is a good candidate be the source of the atypical magnetic

[2] **Zero Field Cooling** – measurement procedure where we cool the sample without applying any external magnetic field. At the lowest temperature, a constant external magnetic field is applied to the sample and then measure the M-T curve while rising the temperature [191, 192].

[3] **Field Cooling** – measurement procedure where we cool the sample while applying the external magnetic field that will be used during the data acquisition stage. Then we measure the M-T curve while rising the temperature with the same external magnetic field [191, 192].

curve shown in figure 5.4.

These results triggered a more thorough experimental characterization of this particular BTO compound, which will be presented in the following sections.

5.2.1 X-ray Diffraction

First, to check the quality of growth and phase purity of the BTO pellets, XRD was performed using a *Panalytical X'Pert Pro* equipped with *X'Celerator* detector and secondary monochromator for $\lambda(\text{Cu } K_{\alpha 1}) = 1.5405(98)$Å at room temperature.

The results obtained are shown in figure 5.5. Additionally, after identifying the crystalline phases present in the BTO pellet, Rietveld refinements of the XRD data were done using the software *Powder Cell 2.4* to quantify the phases present. The results are summarized in table 5.2.

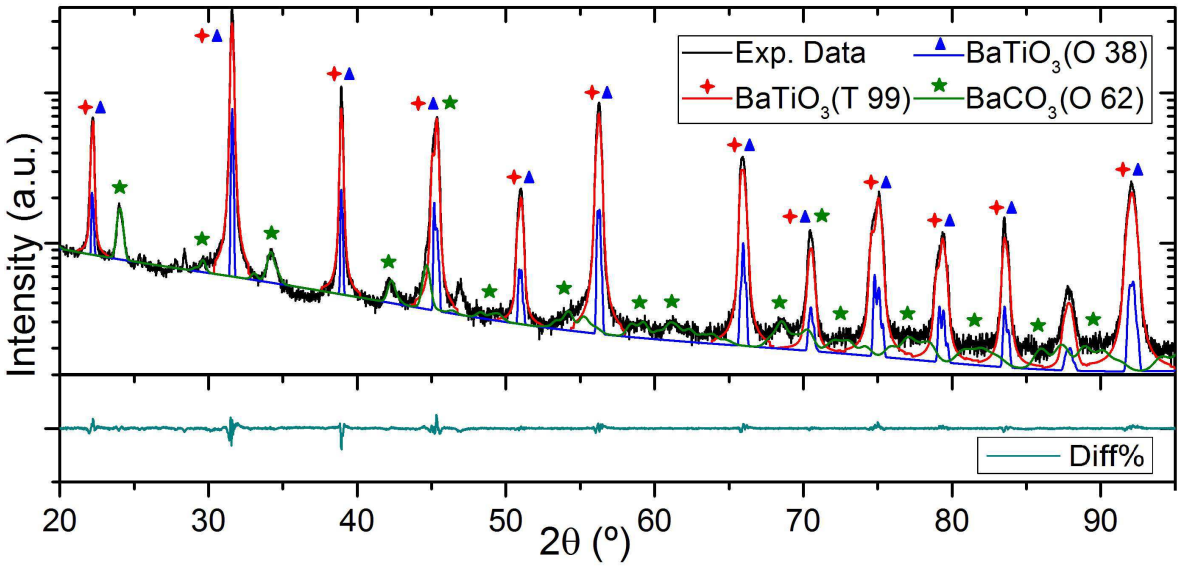

Figure 5.5: Barium Titanate room temperature diffractogram and its Rietveld refinement. From [2].

Two different phases of Barium Titanate, 83% of tetragonal $BaTiO_3$ and a 10% of or-

Phase	Crystal system	Symmetry	Lattice parameter (Å)			fraction (%)	Crystallite (nm)	R-factor		
			a	*b*	*c*			R_p	R_{wp}	R_{exp}
$BaTiO_3$	tetragonal	99	3.9993	3.9993	4.0241	83	108	4.97	6.87	3.68
	orthorhombic	38	3.9947	5.6768	5.6722	10	234	4.97	6.87	3.68
$BaCO_3$	orthorhombic	62	6.5340	5.2458	8.9371	7	37	4.97	6.87	3.68

Table 5.2: Summary of the Rietveld analysis for the XRD data of the BTO pellet.

thorhombic $BaTiO_3$ were detected, both with a crystallite size of $\gtrapprox 100\,\text{nm}$. This phase mixing comes from the shifting in temperature of the phase transitions in certain grains [197–200]. All impurities peaks belong to $BaCO_3$ in a 7% fraction, whose diminutive presence does not interfere with $BaTiO_3$ ferroelectric properties. As expected, the small concentration of Fe is undetectable in the diffractogram, which means that the global macroscopic structural properties are governed by the BTO lattice.

5.2.2 $BaTiO_3$:Fe_{113ppm} magnetic properties

Looking closely to the lower temperature regime of the magnetic curve of figure 5.4. It is possible to separate the observed paramagnetic behaviour, evident at $T < 50\,\text{K}$, in the Field Cooled curve, by fitting a Curie curve according to equation 5.2 in the interval $T \in [5, 300]\,\text{K}$.

$$M = \frac{C}{T} + AT^{3/2} + B\ . \tag{5.2}$$

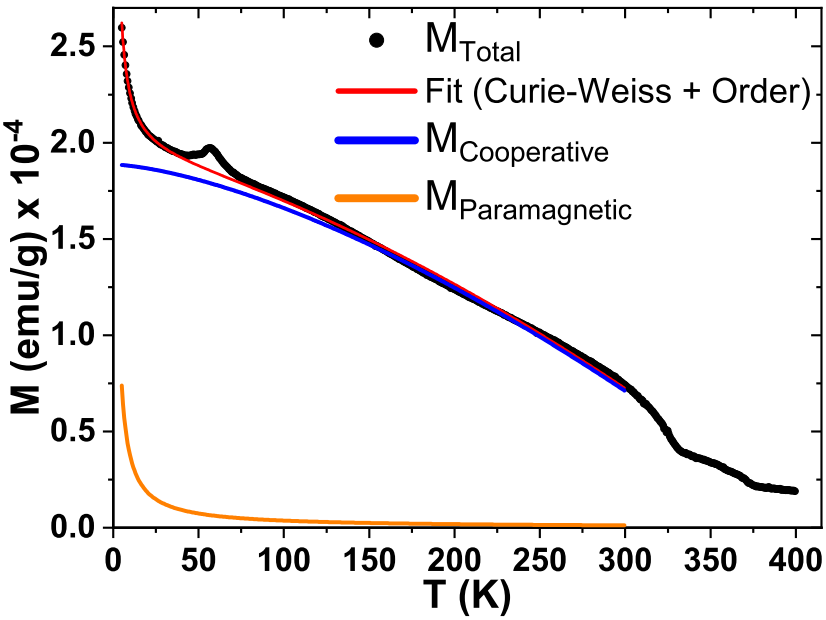

Figure 5.6: M(T) of $BaTiO_3$ with 113 ppm of Fe showing the ordered and paramagnetic behaviours as two separate components. Adapted from [2].

The second term of (5.2) is assigned to the total ordered behaviour, in the same temperature interval, considering the spin waves magnetization as a function of temperature. The points at the O_2 peak ($T \approx 55\,\text{K}$), as well as their neighbouring points, were not considered

in the fit to enhance the quality of the Curie law fit. Figure 5.6 shows the paramagnetic contribution to the magnetization, obtained using (5.2) and the remaining contribution due to cooperative phenomena.

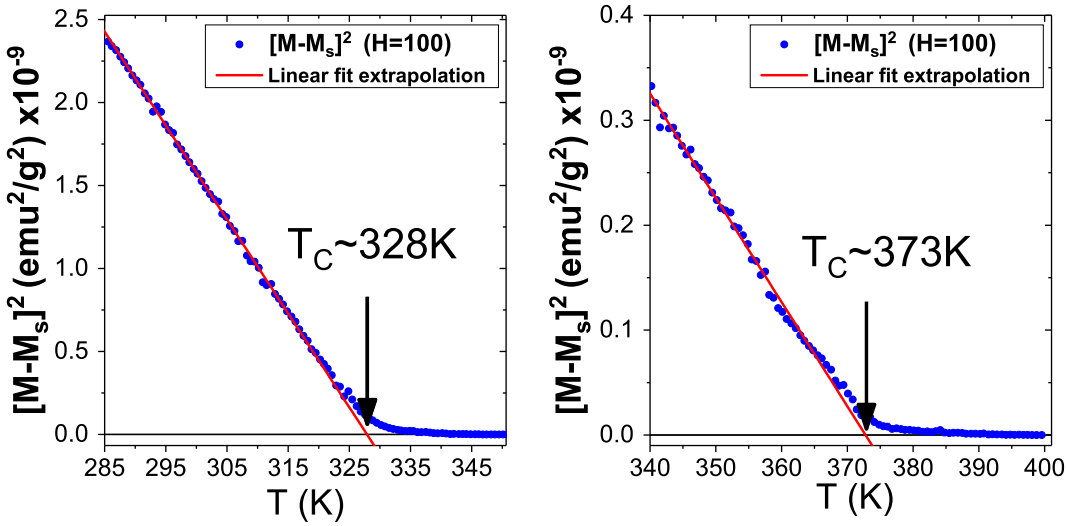

Figure 5.7: $[M - M_S]^2$ vs T around the 325 K and 373 K magnetic anomalies. Adapted from [2].

From the Curie constant (equation 2.64) the product $NJ(J+1)$ is obtained. Considering that the magnetic ordered behaviours are due to Fe, a transition metal, it is reasonable to assume the orbital quenching of Fe atoms and this product can be written as $NS(S+1)$. Now, considering the Fe^{3+} valence ($J = S = 5/2$) a concentration of 39 ppm of diluted paramagnetic atoms is obtained, while for Fe^{2+} valence ($S = 2$) a concentration of 56 ppm of dilute paramagnetic atoms. This reasoning leaves about 74 ppm or 57 ppm respectively in an ordered magnetic phase(s) associated with Fe.

Using a spontaneous magnetization Landau model based on equation 2.72, and representing the magnetization of figure 5.6 as $[M - M_S]^2$ vs T, it is possible to determine the T_C's of the ordered magnetic phases. For the lower temperature transition, using a spontaneous magnetization $M_{S_1} \approx M(350\,\mathrm{K})$ and fitting the linear part of figure 5.7 left plot, a $T_C \approx 328\,\mathrm{K}$ is obtained. Analogously using a $M_{S_2} \approx M(400\,\mathrm{K})$ a $T_C \approx 373\,\mathrm{K}$ is obtained for the higher temperature transition, when the linear part of figure 5.7 right plot is fitted.

Figure 5.8 shows the magnetization of the BTO:Fe pellet as a function of the magnetic field after removing the diamagnetic component. To infer the diamagnetic contribution, the slope of the high field data points of the 400 K M-H was determined, and it was assumed that this

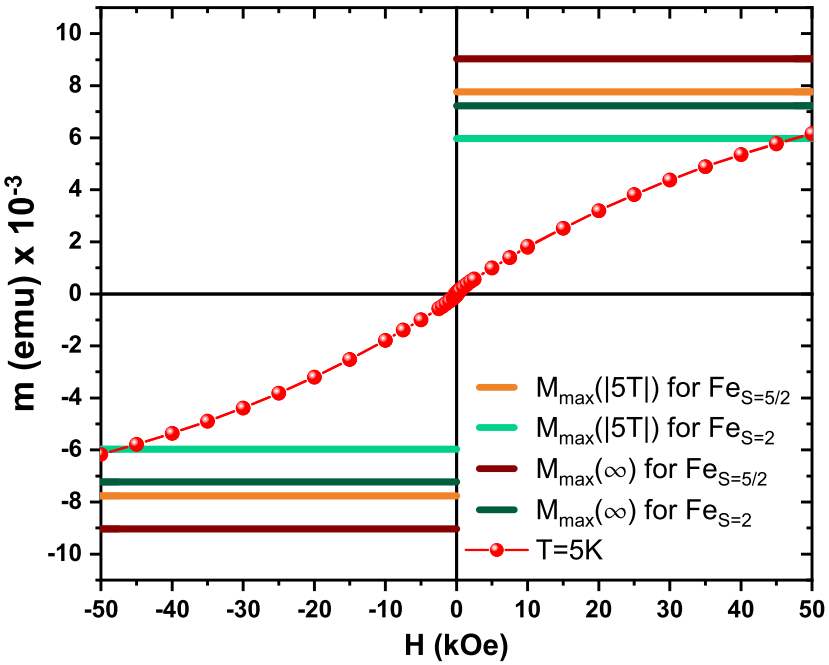

Figure 5.8: M(H) of the pellet of $BaTiO_3$ with 113 ppm of Fe at 5 K. The horizontal coloured lines represent the maximum possible magnetization values for several scenarios considering the 113 ppm of Fe ions.

component would remain constant through all temperatures. Figure 5.8 also shows the maximum possible magnetization values considering that all 113 ppm of iron are completely aligned with the magnetic field[4], $M = M_{sat}$, for the $S = 5/2$ or $S = 2$ cases. The expected magnetization values considering a Brillouin function, $M = M_{sat}\mathcal{B}_{5/2}(5\,T)$ and $M = M_{sat}\mathcal{B}_2(5\,T)$, are also represented in figure 5.8.

As expected, the value of magnetization for 5T, which is close to saturation, is in the same order of magnitude as the maximum possible values considering the amount of iron obtained by PIXE spectroscopy.

Figure 5.9 presents the low field detail of the magnetic field dependence measured at temperatures from 10-400 K, between ±70 kOe (7 T) (only in the decreasing field branch). The values are normalized to the Fe weight after subtracting the diamagnetic component of its host matrix.

Figure 5.9 shows that there are temperature dependent remanent magnetization and coercive field (that can reach about 170 Oe at 10 K). The dependence of the remanent magnetization with the temperature is displayed in the inset of figure 5.9. This inset proves that

[4]This corresponds to the saturation magnetization and is defined as $M_{sat} = |M(H = \pm\infty)|$

the transitions seen in figure 5.6 are indeed related to spontaneous/remanent magnetization changes instead of mere susceptibility changes. The spontaneous magnetization changes are quite significant, reaching $^{\Delta M}/_{M} \approx 14\%$ for the high temperature transition and $^{\Delta M}/_{M} \approx 32\%$ for the lower temperature transition.

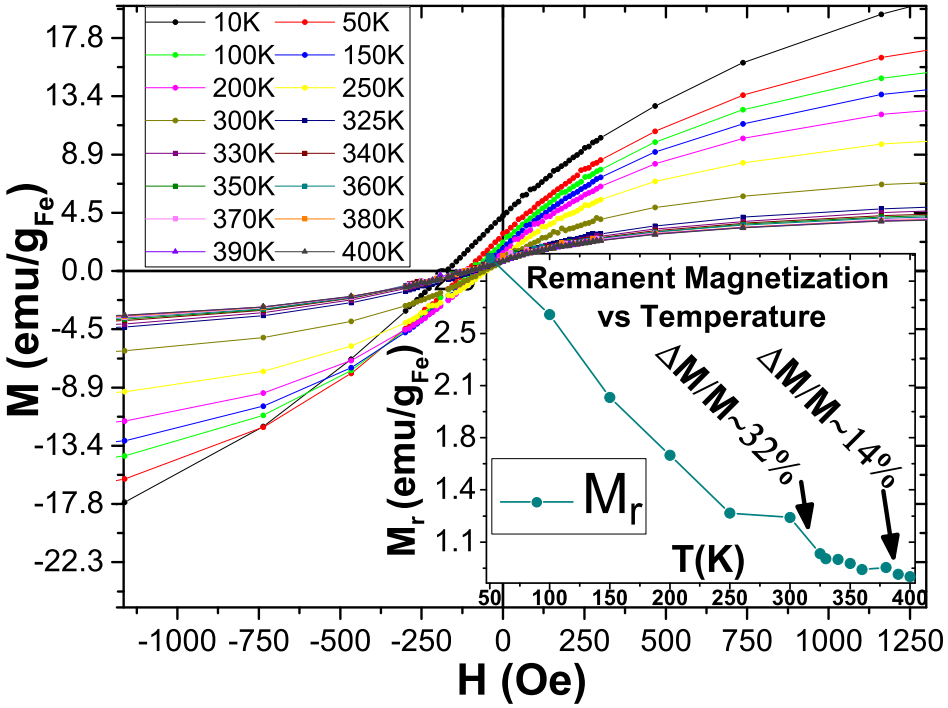

Figure 5.9: Magnetic field dependence of the $BaTiO_3$:Fe magnetization for several temperatures (the diamagnetism of $BaTiO_3$ was subtracted). Inset shows the remanent magnetization dependence with temperature. From [2].

5.2.3 Raman Spectroscopy

As previously stated, the two magnetic anomalies detected around 325 K and 373 K are suspiciously near the $BaTiO_3$ Ferroelectric phase transitions (273 K and 393 K for a $BaTiO_3$ single crystal) [174]. Given Raman spectroscopy's sensitivity to the polarizability tensor, to analyse the correlation of the magnetization anomalies with $BaTiO_3$ ferroelectric properties, Raman spectroscopy measurements were performed in the range 250-760 cm^{-1}, using a Jobin Yvon 64000 Raman spectrometer and a 532 nm laser as incident radiation from 77 to 465 K.

Figure 5.10 shows the temperature dependence of two Raman active vibrational modes, the 520 cm^{-1} $[E(TO) + A_1(TO)]$ and 487 cm^{-1} $[E(LO) + A_1(TO) + E(TO)]$. These are the most adequate vibrational modes to identify the ferroelectric phase transitions of $BaTiO_3$. In

particular, the 487 cm^{-1} mode is known to vanish in the orthorhombic → tetragonal transition [201–204]. This was confirmed by the observation of a reference sample, a $BaTiO_3$ single crystal purchased from *MaTeck* and whose 487 cm^{-1} mode disappears around the typical orthorhombic → tetragonal transition temperature (figure 5.10) [174].

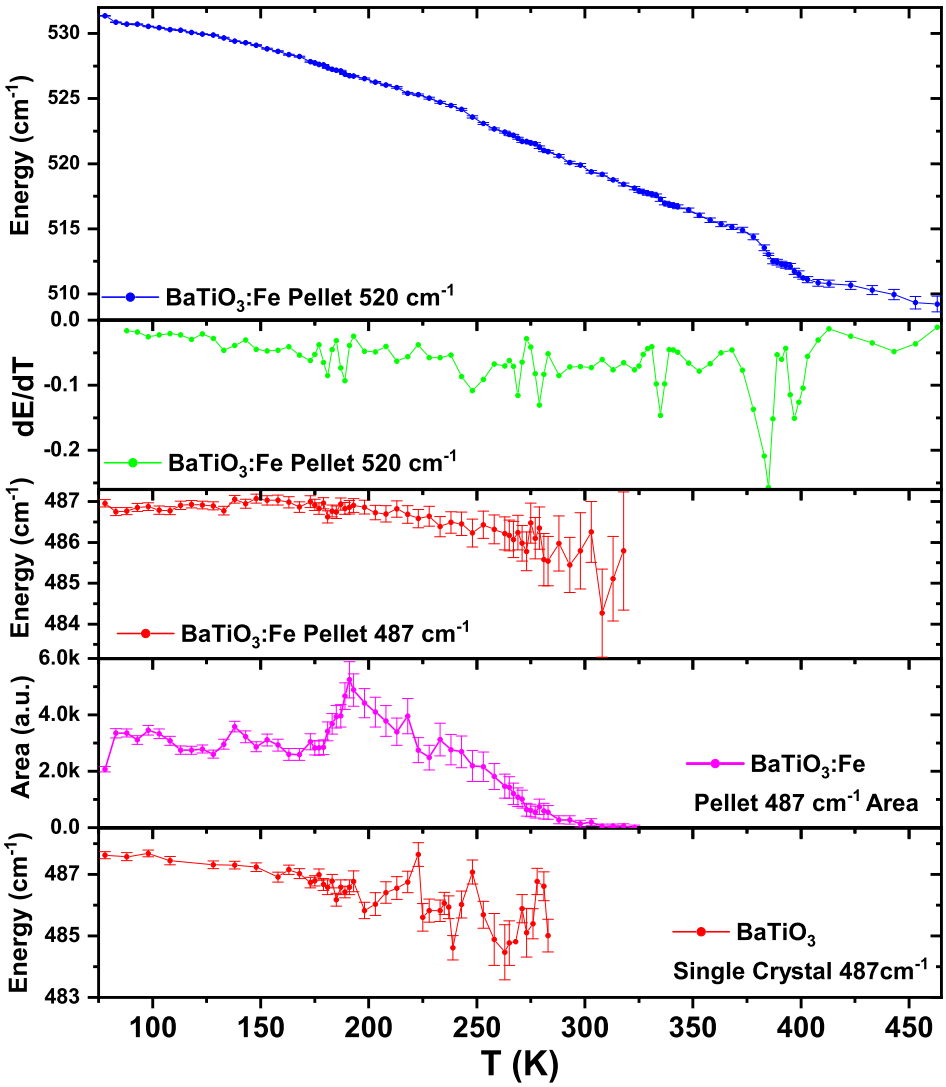

Figure 5.10: Temperature dependence of the Raman active modes near 520 cm^{-1} and 487 cm^{-1} of polycrystalline $BaTiO_3$ and a $BaTiO_3$ single crystal reference. From [2].

Analysing the 487 cm^{-1} mode of the pellet sample, which is seen to vanish around 320 K, it is possible to determine when the $BaTiO_3$ is exclusively in its tetragonal phase. For this reason we confirm the assigning the magnetic anomaly seen around 325 K (figure 5.4) with the $BaTiO_3$ orthorhombic ↔ tetragonal transition.

It is also perceptible that around the temperature where this mode disappears in the single crystal ($T =\approx 280\,\mathrm{K}$, there is an accentuated decrease in the intensity of the mode's intensity in the polycrystalline sample. This suggests that a portion of the sample has already changed its phase to the tetragonal structure, in good agreement with the pellet XRD that shows a coexistence of both $BaTiO_3$ phases (common in nanocrystalline BTO [197–199]).

Analysing now the $520\,\mathrm{cm}^{-1}$ mode, it is perceptible that its energy decreases gradually as the temperature increases, with abrupt changes at specific temperatures. To have a better perception of these changes, the $^{\partial E}/_{\partial T}$ plot is also presented in figure 5.10. The most evident is indubitably the one around 380 K which is associated to the magnetic anomaly seen around 373 K and is attributed to the tetragonal $\leftrightarrow$ Cubic transition.

The Raman spectra also gives information about BTO's lowest ferroelectric phase transition temperature. The intensity of the $487\,\mathrm{cm}^{-1}$ vibrational mode (area plot of figure 5.10) shows that around 192 K the intensity starts to decrease which is a characteristic of the rhombohedral $\leftrightarrow$ orthorhombic transition, and matches with anomalies in the $520\mathrm{cm}^{-1}$ mode around the same temperature). The faint (and broad) anomaly in the magnetization M(T) curve near 190 K may be related to this.

Combining the Raman spectroscopy and the magnetometry results, it is therefore possible to correlate the two magnetic anomalies around 373 K and 325 K with the $BaTiO_3$ tetragonal $\leftrightarrow$ cubic and orthorhombic $\leftrightarrow$ tetragonal ferroelectric phase transitions, respectively. Therefore, we can conclude that we are before an above room temperature magnetoelectric multiferroic compound. Using the same methodology as Duan *et al.* [205], relating the magnetization change with the electrical coercive field, to estimate the magnetoelectric coupling $\alpha \approx \mu_0 \Delta M/E_C$ we arrive to a value $\alpha \approx 5 \times 10^{-3}\,\mathrm{G.cm/V}$.

5.3 Searching Fe preferred coalescing sites

The amount of iron present in the BTO pellets corresponds to such a tiny concentration, 113 ppm, that one would expect the homogeneous dilution of the Fe atoms through the barium titanate matrix. In fact *Sugata Ray et al.* report in their *ab initio* calculations, for concentrations of about 1% (100 times higher than in our case), that Fe ions were homogeneously diluted across the host matrix [206].

Since we observe a magnetic ordered behaviour induced by the ferroelectric phase transi-

tions we can suppose that the existent Fe atoms "prefer" to be at least partially segregated in regions that favour cooperative magnetic interactions, instead of remaining loosely dispersed in the $BaTiO_3$ matrix.

5.3.1 SEM/EDS mapping and Fe statistical distribution

To infer this conjecture, a detailed SEM/EDS mapping was performed. The SEM/EDS map was done by a HR-SEM-SE/EDS with a *Hitachi SU-70* as the SEM part and a *Bruker QUANTAX 400* as the EDS part. Due to the lower limit of detection of the EDS technique being well above the 113 ppm obtained in the PIXE, one would expect to detect the iron using EDS only if it was concentrated in particular limited sites, with increased Fe local microscopic concentration.

103 regions were measured, each with an area of about 1150 μm^2 with an average value of Fe concentration of $\bar{x} \approx 0.068\%$ and $\bar{\sigma} \approx 0.022\%$. The 20 areas represented by pink dots in figure 5.11 signal the regions where Fe was detected with a 3σ confidence, and show where these ions have congregated.

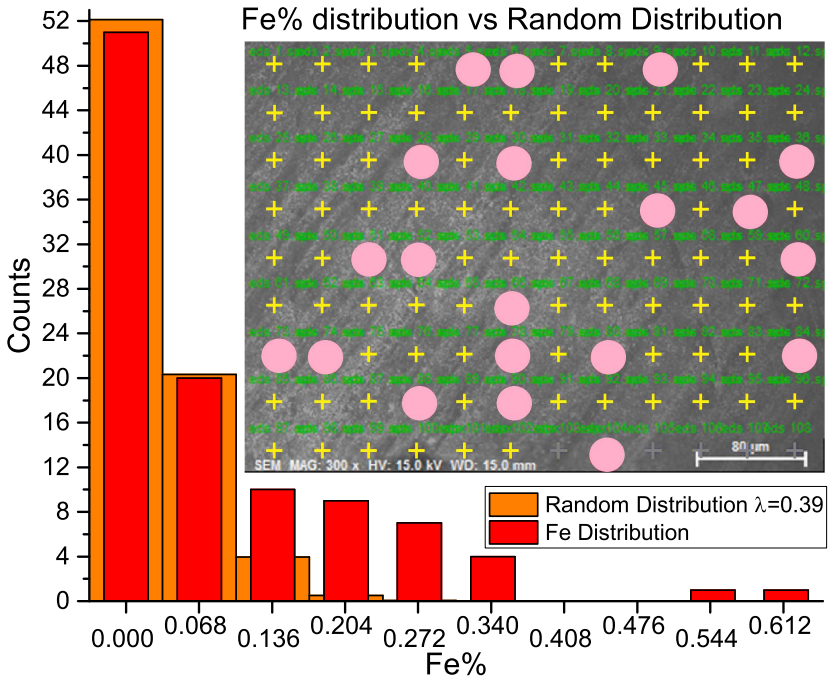

Figure 5.11: Comparison between the observed Fe concentration distribution and its correspondent Poisson random distribution (binning = $\bar{x}$). The inset shows the areas where EDS was performed (+ symbol). Pink dots indicate the regions where Fe was detected with a 3σ confidence. From [2].

Figure 5.11 also presents the observed Fe concentration distribution. Comparing the statistical display of the results obtained in the EDS map with an analogous random distribution, it is confirmed that the Fe ions aren't distributed randomly, favouring certain locations to coalesce in higher concentrations.

The statistical distribution of Fe concentration obtained experimentally suggests a superposition of two distributions: one leading to Poisson distribution with $\lambda = 0.39\bar{x}$, associated with the homogeneous paramagnetic ions and the random nature of the statistical measurement, and an inhomogeneous distribution of Fe. It should be stressed that the probability of finding both $8\bar{x}$ and $9\bar{x}$ concentrations in such a random distribution is 1 in 3×10^{17}. To have a more concrete idea of the meaning of this probability, its value represents an event about 20 times more unlikely than winning the first prize of the "EuroMillions" lottery twice in a row.

A quantitative analysis of the excess values of the real Fe distribution, when compared with the Poisson distribution, shows that about 82% of Fe belongs to the inhomogeneous cooperative distribution and 18% belongs to the random paramagnetic arrangement. This result corroborates the estimate made from the Paramagnetic behaviour of higher Fe concentration in the ordered phase, closer to the $S = 5/2$ scenario.

Nevertheless, the mere segregation of Fe atoms does not justify the correlation between magnetic and ferroelectric phase transitions. Actually, this is quite bizarre since in studies using Fe doped $BaTiO_3$, even for concentrations as high as 1% (concentration 100× higher than in our case) [206], 3.5% (350×) [185], 5% (500×) [190, 206], 7%, 15%, 30%, 70% (700×, 1500×, 3000×, 7000×) [186] and even for 75% (7500×) [207] their M-T curve is insensitive to the $BaTiO_3$ ferroelectric transitions. This means that more than the ammount of Fe segregated, where and how it segregates takes a preponderant role in the magnetoelectric coupling here reported [2].

There are several studies demonstrating the tendency for the Fe ions to diffuse into specific places. F. Figueiredo *et al.* showed that in $CaTiO_3$ – a perovskite similar to $BaTiO_3$ – Fe ions tend to diffuse to the grain boundaries, resulting in core-shell structured grains where the core is constituted of practically pure $CaTiO_3$ while the shell is an Fe rich phase of $CaTi_{1-x}O_3Fe_x$ [208].

5.3.2 Thermal annealing stability

These kind of specific segregations are also observed in $La_{0.95}Sr_{0.05}Ga_{0.90}Mg_{0.10}O_{3-\delta}$ (LSGM) ceramics, where once again, we can perceive that Fe ions tend to accumulate in the grain boundaries ($\lessapprox 1\%$) whereas the interior of the grains maintain an approximately Fe free LSGM composition [209]. Such an effect behaves differently depending on parameters such as the grain size and thermal treatments; it is perceptible that for a high enough thermal treatment the Fe dilutes homogeneously all over the sample [209, 210]. To check the stability of the magnetic phases with the temperature, we have also made thermal treatments to our polycrystalline $BaTiO_3$:Fe, as it is presented in figure 5.12.

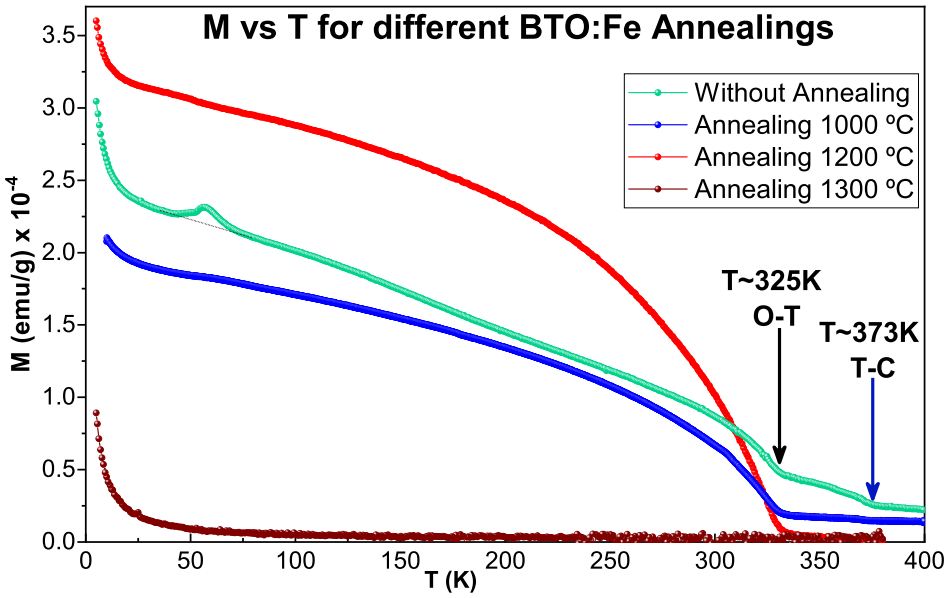

Figure 5.12: M(T) of $BaTiO_3$:Fe for several annealing temperatures. Adapted from [3].

The thermal annealings were done in a cumulative way, which means that the higher thermal treatments were done after the lower temperature thermal treatments. It is possible to see that, as we increase the annealing temperature, there is a decrease in the higher temperature magnetic ordered phase (the one from the $T_C \approx 373\,K$, as well as a decrease of the intrinsic spontaneous magnetization which had existed even at M(400 K). On the other hand, there is an increase in the quantity and the slope of the magnetic transition induced by the orthorhombic $\leftrightarrow$ tetragonal ferroelectric phase transition. However, when the annealing reaches 1300°C the iron is irreversibly diluted all over the sample, as in Ref [209, 210], resulting in a pure paramagnetic behaviour of the Fe ions [3].

5.3.3 The role of $BaTiO_3$ grain boundaries

To ascertain the importance of the grain boundaries in the Magnetoelectric effect that here reported, ion implantation of 1% of Fe was made using a 100 keV ^{57}Fe beam in a region of 1.5×10^{-3} mm^3 (5 mm × 3 mm × 100 nm estimated by the TRIM program) on a $BaTiO_3$ single crystal. Despite the higher concentration of Fe ions, the M-T curve was paramagnetic like, and did not show any sensibility to the Barium Titanate phase transitions. On the other hand, R.P. Borges *et al.* [211] have implanted 4% Fe concentration in $BaTiO_3$ (in a region identical to the one implanted by us) but even so no substantial magnetoelectric coupling was reported, apart from a small thermal hysteresis perceptible around the Ferroelectric phase transitions ($\Delta M/M \leq 2.8\%$).

Such results suggest a preponderant role of grain boundaries, not only for the Fe segregation, but also for the mechanism behind the magnetoelectric coupling. To validate the conjecture that special sites in the grain boundaries should play a meaningful role in the reported magnetoelectric coupling, a thorough STEM/EDS study was performed to analyse the element distribution in more confined scales. The STEM/EDS study was carried out by a HR-TEM200-SE/EDS: HR-(EF)TEM JEOL, 2200FS and Oxford INCA Energy TEM 250.

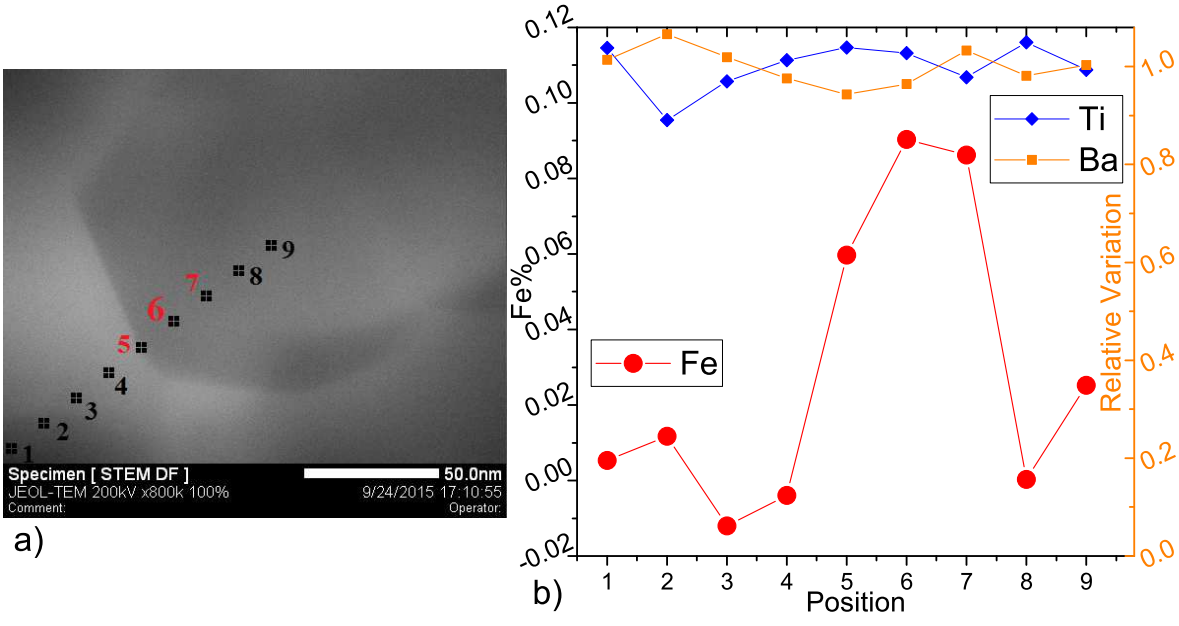

Figure 5.13: **a)** Image obtained by STEM. The numbered points show the specific location where a EDS analysis was made. **b)**Fe nominal concentration and Ti and Ba relative concentrations obtained from STEM/EDS analysis of the points indicated in a). The standard deviation is $\sigma \approx 0.037\%$. From [2].

Figure 5.13a shows an STEM image of a $BaTiO_3$ grain and its grain boundaries. An EDS analysis was performed along a line of points across the grain boundary, labelled from 1-9, each one separated of about 13 nm.

In Figure 5.13b the EDS results for Fe, Ba and Ti are presented. One can clearly observe a sudden variation of Fe concentration from about 0% to about 0.09%. This increase happens exactly in the grains interface, as can be seen in points 5-7 of figure 5.13a.

Fluctuations in the concentration are observed, resulting from a $\sigma \approx 0.037\%$ of each individual analysis' fit. The increase of Fe concentration at the interface is clearly well beyond statistical uncertainties. On the other hand, the relative variation of Ti and Ba concentrations fluctuate around the average, hence indicating that the $BaTiO_3$ itself is homogeneous.

We are therefore led to infer that Fe is not homogeneously distributed, but partially present in aggregates at the interfaces between grains. These are large enough to support cooperative magnetic behaviour, in close contact with the $BaTiO_3$ matrix, supporting the observed magnetoelectric coupling.

5.4 Final considerations about $BaTiO_3$:Fe_{113ppm}

Our results show that we are before a quite peculiar type of $BaTiO_3$:Fe with a close entanglement between magnetic and ferroelectric properties. However, the observed mechanism behind the magnetoelectric coupling is still unclear.

Since Fe is strongly correlated with the $BaTiO_3$ matrix, it is quite improbable that this ferromagnetic element is in its metallic form, being instead in an oxidized $Fe_xO_yTi_zBa_w$ configuration.

As a matter of fact, many experimental and *ab initio* evidences demonstrate that an electric displacement, $\vec{D}$, creates a buffer oxide between a Fe/$BaTiO_3$ interface [212–215]. The creation of such an oxide can be non-homogeneous, where different $\vec{D}$ can lead to different oxide configurations (either magnetic, non-magnetic or a mixture of both).

Experimental results show that the fraction of magnetic oxides tends to disappear for high values of $\vec{D}$, an effect that is reversible if $\vec{D}$ is not too high, resulting in the variation of the coercive magnetic field (H_c) with $\vec{D}$ [212, 213]. Such effects can occur due to the inherent polarization, $\vec{P}$, of the $BaTiO_3$ ferroelectric domains and therefore different oxides configurations would be present for the different ferroelectric phase transitions [213, 215].

Considering the hypothesis where the Fe ions are concentrated in/between grain boundaries, we could interpret this arrangement as a composite of an Fe rich phase interface with the $BaTiO_3$ matrix. Such composites configurations have been widely studied since CG Duan *et al.* made DFT calculations of $Fe/BaTiO_3$ multilayers where the authors show a Magnetoelectric coupling due to the different character of the chemical bonds between the interface atoms for each possible polarization of the tetragonal $BaTiO_3$ ($\vec{P}_\downarrow$ and $\vec{P}_\uparrow$) [205].

These multilayer DFT studies, as well as experimental ones, were also carried by other groups which not only studied the $Fe/BaTiO_3$ layout [205, 216–218] but also iron oxides interfaces like the $Fe_3O_4/BaTiO_3$ composite. This composite also exhibits a magnetoelectric coupling [219–221], supporting the conjecture of a $BaTiO_3/Fe_xO_yTi_zBa_w/BaTiO_3$ interface as the responsible for our results.

In these composites the polarization of the different ferroelectric phases of Barium Titanate induces different charge/electron densities near the interface which leads to distinct kinds of hybridization between the Fe ions and the $BaTiO_3$. For magnetite, an insulator iron oxide, the polarization effects do not suffer from screening effects, being able to enhance its influence in the local bonds of this composite [219]. This diversity of results suggests that a $BaTiO_3/Fe_xO_yTi_zBa_w/BaTiO_3$ interface may present a rich variety of relations between magnetic and ferroelectric properties.

The hybridization between the interface atoms usually plays a crucial role in the magnetoelectric effect and although a change in polarization might not modify the magnetic moments of the Fe ions themselves [205, 215, 217, 218, 222], the moments of the Ti and O atoms can change considerably, either by direct or indirect hybridization with the Fe atoms. For Fe_3O_4, in particular, the occurrence of Oxygen vacancies favours the magnitude of the magnetoelectric coupling given the resulting valences and wave functions distributions that arise from these vacancies [219].

R. Radaelli *et al.* demonstrated that the chemical bonds between BTO and the iron oxide, namely the Fe–O–Fe angle, will dictate the nature of the magnetic cooperative behaviour in this interface [213]. When the polarization is pointing towards the iron oxide ($\vec{P}_\uparrow$) there will be a ferromagnetic behaviour, while for $\vec{P}_\downarrow$ the ordered phase is antiferromagnetic; which leads to one of the largest magnetoelectric couplings reported in the literature ($\alpha = 2\times10^{-9}\,\mathrm{G\,cm^2/V}$). Supposing that we have a similar effect in our results, this could mean that for $T \leq 325\,\mathrm{K}$

we could have a summation of two components $M_{\text{total}} = M_{\text{oxide1(FM)}} + M_{\text{oxide2(FM)}}$ and for $T > 325\,\text{K}$ we would have $M_{\text{total}} = M_{\text{oxide1(AFM)}} + M_{\text{oxide2(FM)}}$ which could justify the higher change in magnetization reported in our work.

In addition to what we discuss above, we cannot exclude the contribution from strain effects that arise from the magnetostriction caused by the piezoelectric effect native of the $BaTiO_3$ matrix inherent of the ferroelectric phase transitions or solely due to the structural changes themselves [223]. These effects are reported experimentally in both the Fe/$BaTiO_3$ interface [224] and the Fe_3O_4/$BaTiO_3$ interface [220, 221] and can be seen in the M-T curves of interfaces, where abrupt changes in the magnetization around the ferroelectric phase transitions occur. These interfaces have different mismatches and distortions in the interface atoms and consequently different magnetic anisotropies [220–222, 224].

The different polarizations vectors can change the length of the chemical bonds and therefore the magneto-crystalline anisotropy is affected [205, 217, 218]. Ultimately these alterations in the anisotropy energy between the different $BaTiO_3$ ferroelectric phases culminates in changes of the coercive fields and remanent magnetizations [220, 222, 224].

According to these strains effects one should expect a higher magnetoelectric effect from the R↔O transition [220, 225] ($^{\Delta M}/_{M} \approx 25\%$ for the Fe/$BaTiO_3$ interface and $^{\Delta M}/_{M} \approx 2.2\%$ for the Fe_3O_4/$BaTiO_3$ interface [221, 224]), which we do not observe. However in the Fe_3O_4/$BaTiO_3$ interface C. Vaz *et al.* (S Sahoo *et al.* for the Fe/$BaTiO_3$ interface) reports that for different magnetic fields the variation of magnetization can either be positive or negative. This means that, for the particular situation where these interfaces would appear to be non-arbitrarily oriented, the summation could result in an insignificant change of the magnetization for the R↔O transition whereas in the O↔T transition the result could be sizeable [220, 221]. H Tian *et al.* also justify this concealing of the R↔O transition from the different disposition of the $BaTiO_3$ ferroelectric domains [220]. These observations may explain why the change in magnetization at the R↔O transition is mild.

Chapter 6

DFT Modeling of $BaTiO_3(001)$/Fe interfaces

As stated in chapter 5, the magnetoelectric mechanism behind the clear correlation between the ferroelectric phase transitions of $BaTiO_3$ and the Fe magnetic transitions is still unclear. In the same chapter it was shown that the grain boundaries must play a preponderant role in this mysterious magnetoelectric coupling, thus it is natural to attribute such coupling to interface effects.

Following this line of thought, a general study based on DFT calculations was done considering unit cells containing interfaces of BTO and Fe. This study was based in the Duan and Tsymbal's work [205], where supercells composed of unit cells of body centred Fe in contact with cubic and tetragonal unit cells of BTO were considered.

In this thesis, due to time and computational constrains, only the effects at the interfaces of supercells composed of a single unit cell of $BaTiO_3$ and a monolayer of Fe atoms were considered. The density functional theory calculations were performed using the Vienna *ab-initio* simulation package, VASP [226] (version 5.4.1) , which implements the projector augmented wave method [227]. The exchange correlation functional is the generalized gradient approximation (GGA) with the Perdew-Burke-Ernzerhof (PBE) parametrization [32].

The study was done considering several physical quantities as a function of a specific distance, d, defined as the total length of the considered supercell along the z axis. All calculations were made allowing full atomic relaxation for all fractional coordinates, minimizing the Hellmann-Feynman forces below a tolerance value of $0.02\,\mathrm{eV/Å}$.

6.1 BTO221_001/Fe and BTO99_001/Fe

6.1.1 BTO/1stFe

Firstly, we considered both a cubic and tetragonal BTO unit cells, here defined as BTO221 and BTO99 respectively[1]. Figure 6.1 describes a supercell composed by a Fe monolayer obtained by aligning its bcc [110] axis with the [001] axis of a cubic BTO unit cell, while figure 6.2 shows the same Fe monolayer on top of a tetragonal BTO unit cell.

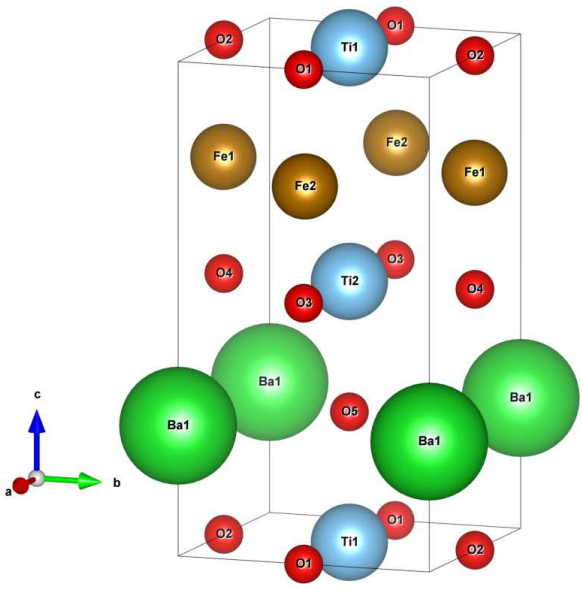

Figure 6.1: BTO221_001_1stFe supercell

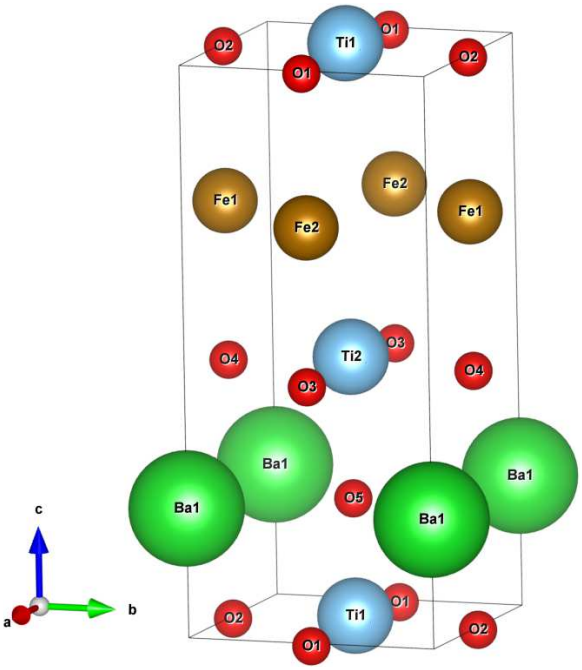

Figure 6.2: BTO99_001_1stFe supercell

The lattice constants $a = b$ were considered to be fixed to the experimental lattice constants of BTO, $a = a_C = 4.0286$ Å for the cubic unit cell and $a = a_T = 3.9925$ Å for the tetragonal unit cell [174].

Each supercell has the two Fe atoms directly on top of the equatorial Oxygens of the Ti2 atom (and directly below Ti1's Oxygens). This Fe monolayer disposition will be designated as the 1stFe monolayer system, hence the supercells composed of the Fe monolayer and the cubic or tetragonal BTO unit cells will be designated as BTO221_001_1stFe and BTO99_001_1stFe respectively. The TiO_2 layer was chosen as Barium Titanate's termina-

[1]The 221 and 99 refer to the space group number of the BTO unit cell. Future BTO unit cells will also have the number correspondent to its space group.

tion layer since it has been shown that it the most probable termination in $BaTiO_3$–Fe/Fe_xO_y heterostructures [205, 213].

The electronic self-consistent cycles were considered converged when the energy differences between two iterations were less than 10^{-8} eV. A $8 \times 8 \times 4$ k-points grid was considered for the calculations in reciprocal space, and the cut-off energy for the plane waves was set as 500 eV. Before relaxation of the whole supercell, the initial BTO Ti1-Ti2 distance, as well as all the fractional coordinates of the BTO unit cell were considered to be the same as the corresponding bulk values.

To encompass different magnetic arrangements of Fe, for each BTO initial structure the cases of Fe ferromagnetic and antiferromagnetic input arrangements were considered[2].

Figure 6.3 shows the binding energy of BTO221_001_1stFe as a function of the supercell size along the z component, d, and which is defined by equation 6.1:

$$E_{\text{Binding}} = E_{\text{BTO221\_001\_1stFe}} - (2E_{\text{Fe}} + E_{\text{Ba}} + 2E_{\text{Ti}} + 5E_{\text{O}}) \ , \tag{6.1}$$

where $E_{\text{BTO221\_001\_1stFe}}$ is the energy of the BTO221_001_1stFe supercell, and E_{Fe}, E_{Ba}, E_{Ti} and E_{O} are the energies of the individual Fe, Ba, Ti and O atoms respectively. The energy of each individual atoms was determined by separately calculating the isolated atom in a $1\,\text{nm}^3$ vacuum box. The observation of the binding energy of both ferromagnetic and antiferromagnetic input arrangements of the BTO221_001_1stFe interface demonstrates that for $d \in [6.1, 9]$ Å the FM input arrangement is energetically more favourable, while for $d = 6$ Å the AFM arrangement is the most favourable one.

This binding energy behaviour is actually quite similar to the BTO99_001_1stFe heterostructure behaviour, where the ferromagnetic arrangement is the most favourable for all the considered d values, as it is possible to see in figure 6.4.

Analogously, for this structure the binding energy is defined by equation 6.2:

$$E_{\text{Binding}} = E_{\text{BTO99\_001\_1stFe}} - (2E_{\text{Fe}} + E_{\text{Ba}} + 2E_{\text{Ti}} + 5E_{\text{O}}) \ , \tag{6.2}$$

[2]In this thesis I will be calling FM and AFM input arrangements, or just FM and AFM input, mostly to the initial input of the magnetic configurations. When I want to refer to the actual result of the calculation, which sometimes can differ from the initial input configurations, I will favour the usage of FM or AFM states terminology. This approach will also hold for other possible magnetic configurations defined in the future.

where $E_{\text{BTO99\_001\_1stFe}}$ is the energy of the BTO99_001_1stFe supercell.

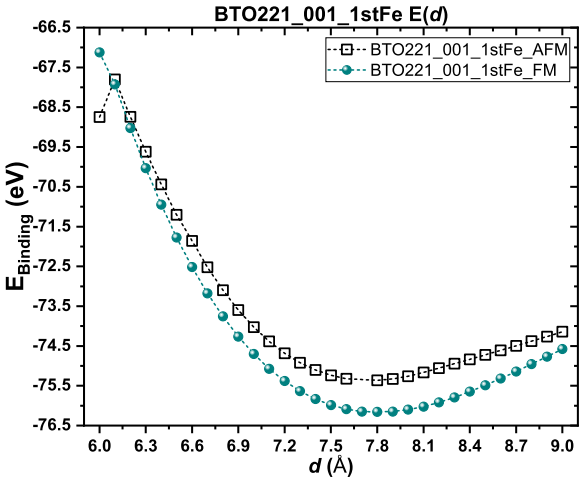

Figure 6.3: Binding energy for all the considered magnetic arrangements of the BTO221_001_1stFe supercell (cubic lattice parameters).

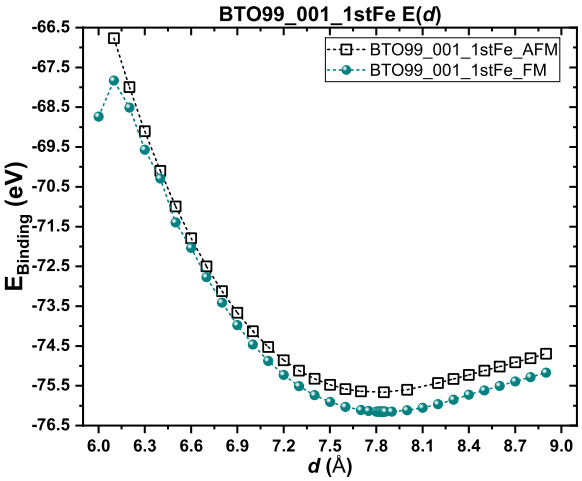

Figure 6.4: Binding energy for all the considered magnetic arrangements of the BTO99_001_1stFe supercell (tetragonal lattice parameters).

Looking now at figures 6.5 and 6.6, it is possible to see that the total magnetic moments of the BTO221_001_1stFe and BTO99_001_1stFe supercells are very similar. In fact, such a conclusion is not that surprising since as one changes the value of d, the BTO221_001_1stFe supercell will not contain a cubic BTO unit cell but a "pseudo-cubic" unit cell. This pseudo-cubic BTO unit cell is actually a tetragonal unit cell with the cubic $a = b$ lattice parameters and whose calculations were done using the initial cubic fractional coordinates.

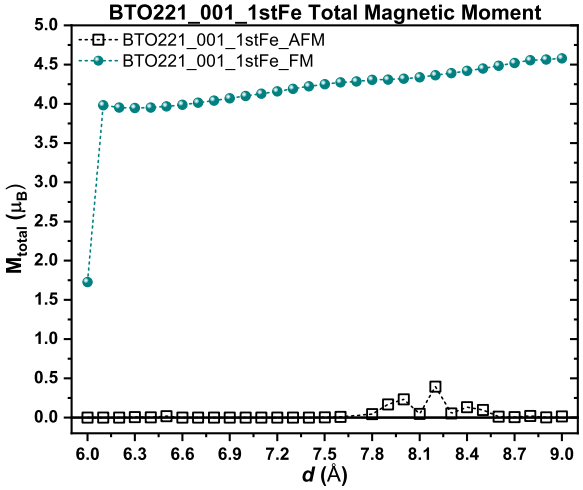

Figure 6.5: Total magnetic moment for all the considered magnetic arrangements of the BTO221_001_1stFe supercell.

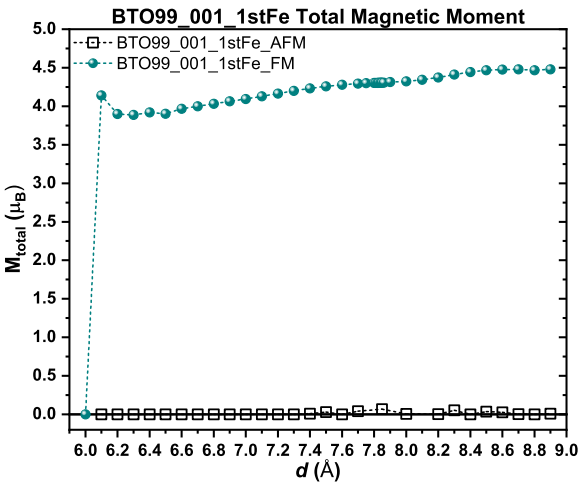

Figure 6.6: Total magnetic moment for all the considered magnetic arrangements of the BTO99_001_1stFe supercell.

The ferromagnetic input arrangement of both tetragonal and pseudo-cubic supercells shows a total magnetic moment around (4.2±0.4) μ_B for all its d values, except for $d = 6.0$ Å, where there is an abrupt decrease of the total magnetic moment. Figures 6.7 and 6.8 show the detailed information about the magnetic moment for each individual atom. The Fe magnetic moments can be different from the typical m=2.2 μ_B of the metallic Fe, depending on the value of d (figure 6.7). The enhancement of the Fe magnetic moment was reported by Duan *et al.* [205], which simulated the same exact BTO/Fe interfaces[3] as the ones present in the BTO221_001_1stFe and BTO99_001_1stFe supercells.

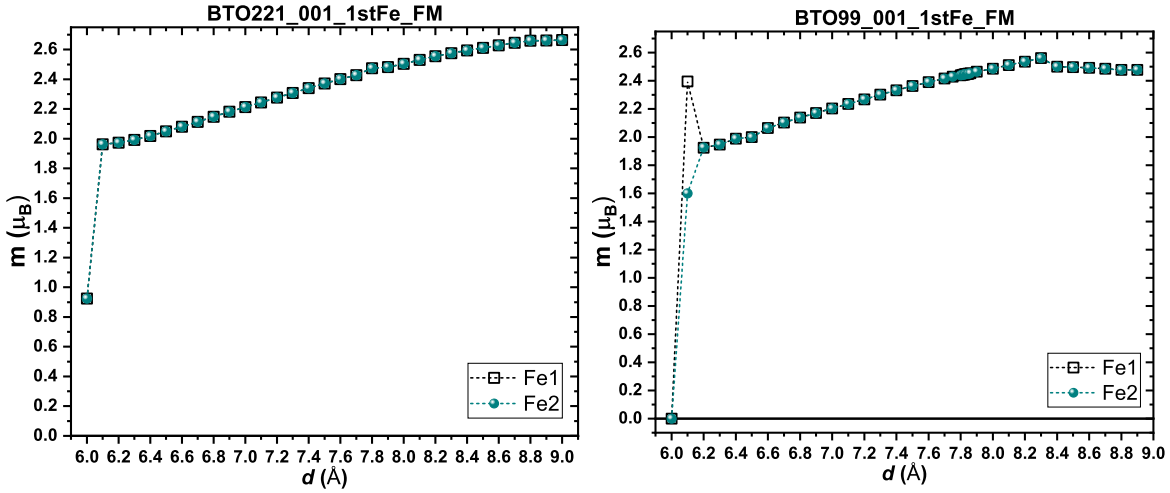

Figure 6.7: Fe magnetic moments for the ferromagnetic input arrangement of BTO221_001_1stFe (left) and BTO99_001_1stFe (right) supercells.

Duan considered the contact of Fe with both ends of a stack of tetragonal BTO unit cells to emulate the switch of an electric field originating from the up and down polarizations of the tetragonal BTO. He reported an enhancement of the interface Fe magnetic moment (even for $\vec{P} = 0$), which would be different for the up and down polarization.

This enhancement of the magnetic moments is also present here, in figure 6.7, hence the reported change in the Fe magnetic moments is due to different interatomic distances of the considered supercell, which would be equivalent to different values of d in the ferromagnetic plots of figure 6.7. Additionally, figure 6.8 shows the induced magnetic moments in the O

[3]When I say interface, I am referring to the contact of the BTO TiO_2 layer with the Fe layer. The supercell used by Duan and the one here considered are actually different.

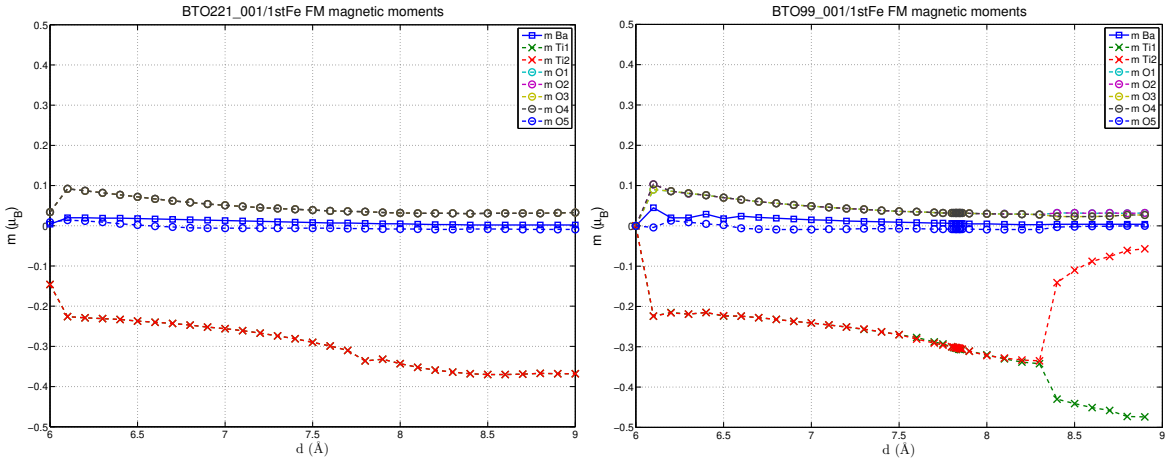

Figure 6.8: Magnetic moments of all atoms, apart from Fe, for the ferromagnetic input arrangement of BTO221_001_1stFe (left) and BTO99_001_1stFe (right) supercells.

(ferromagnetic to Fe) and Ti (antiferromagnetic to Fe) atoms, also reported by Duan *et al.*, resulting in a more smooth change in the total magnetic moment as a function of d. For these reasons, one could say that the ferromagnetic arrangement of both the BTO221_001_1stFe and BTO99_001_1stFe supercells reproduce fairly well the main results from the work of Duan *et al.*.

Nevertheless, let's consider the AFM initial arrangement of the BTO221_001_1stFe and BTO99_001_1stFe supercells (figures 6.9 and 6.10).

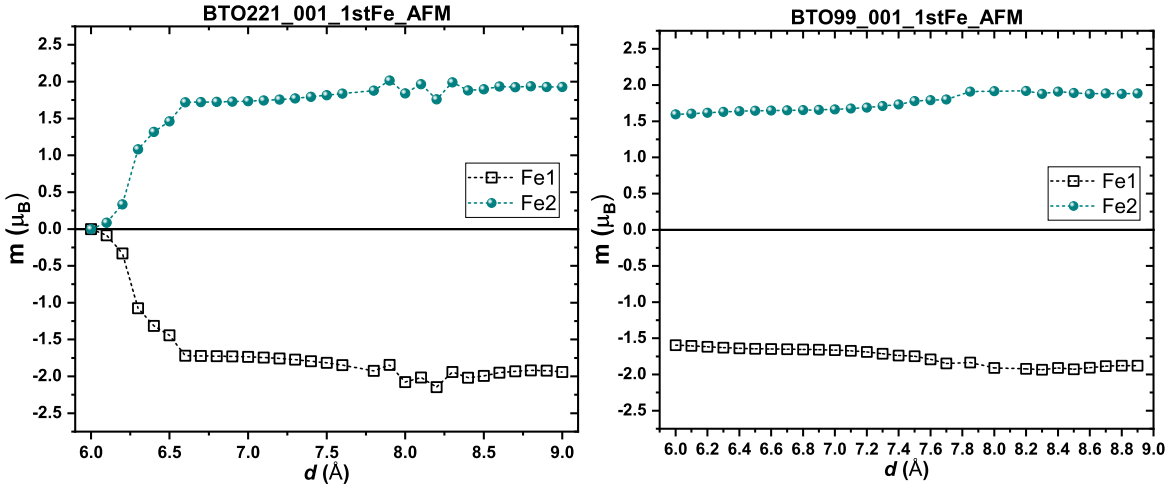

Figure 6.9: Fe magnetic moments for the antiferromagnetic input arrangement of BTO221_001_1stFe (left) and BTO99_001_1stFe (right) supercells.

For $d \geq 6.5$ Å the Fe atoms are in a perfect (or at least close to perfect) antiferromagnetic

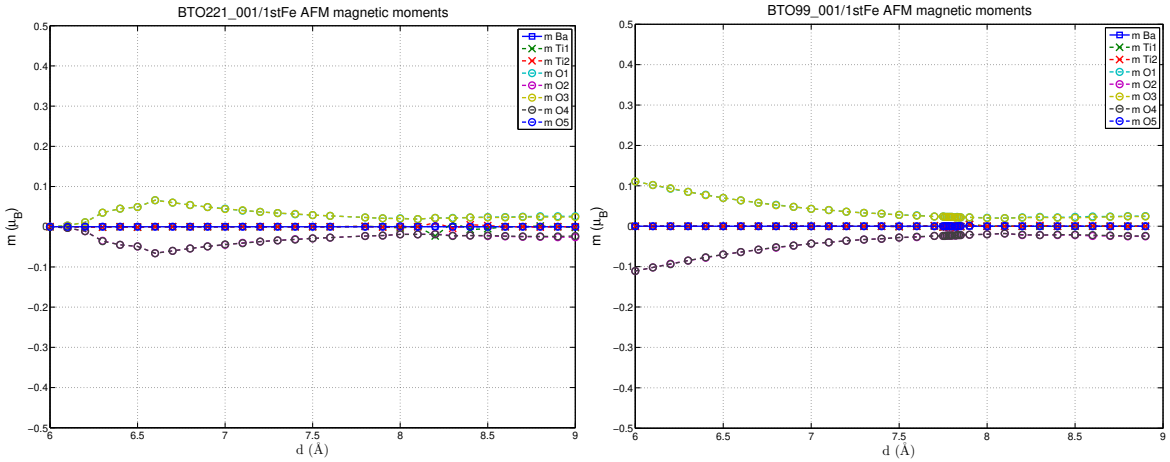

Figure 6.10: Magnetic moments of all atoms, apart from Fe, for the antiferromagnetic input arrangement of BTO221_001_1stFe (left) and BTO99_001_1stFe (right) supercells.

state[4] with $m \approx |2.0|\,\mu_B$, and whose absolute values have a slightly positive slope. Similarly to the FM case, the equatorial Oxygens have an induced magnetic moment, below $|0.1|\,\mu_B$, which are ferromagnetically aligned to its closest Fe atom. Their magnetic moment value decreases with the increase of d.

For $d \leq 6.5\,\text{Å}$ there is a clear distinction in the behaviour of the BTO221_001_1stFe and BTO99_001_1stFe supercells. While for the BTO99_001_1stFe the magnetic moments follow the trend seen at $d \geq 6.5\,\text{Å}$, in BTO221_001_1stFe there is a sharp decrease of the Fe absolute magnetic moment and of its corresponding induced Oxygen's moments, till their complete quench at $d = 6.0\,\text{Å}$. Note that $d = 6.0\,\text{Å}$ is the special point where the AFM arrangement is energetically more favourable than the FM arrangement in the BTO221_001_1stFe supercell. In fact, after a careful observation, one can infer that the BTO99_001_1stFe_AFM magnetic properties correspond to the BTO221_001_1stFe_AFM curves shifted to the left (lower d), hence, it could be expected that the quench of the Fe magnetic moment would appear for a value of d low enough. Conversely the BTO99_001_1stFe_FM magnetic properties correspond to the BTO221_001_1stFe_FM curves shifted to the right (higher d). Note that the binding energy of BTO99_001_1stFe_FM is quite close to the binding energy of BTO221_001_1stFe_AFM at $d = 6.0\,\text{Å}$, point where both have the quench of the magnetic moments.

[4]In this manuscript the expression perfect antiferromagnetic state will be used several times when referring to a AFM state whose opposing magnetic moments have the same magnitude, thus having $M_{total} = 0$.

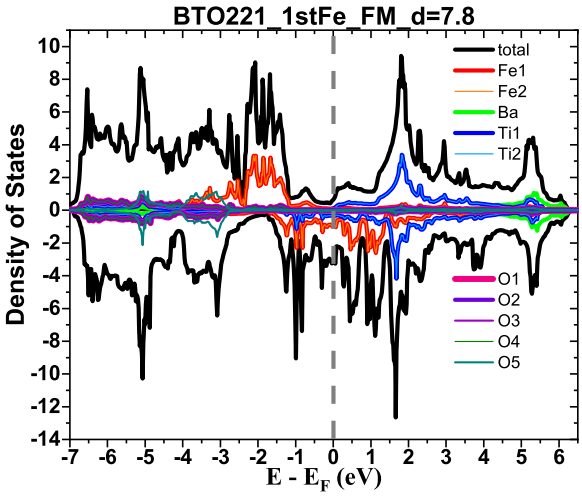

Figure 6.11: Density of states of BTO221_001_1stFe_FM at $d = 7.8$ Å.

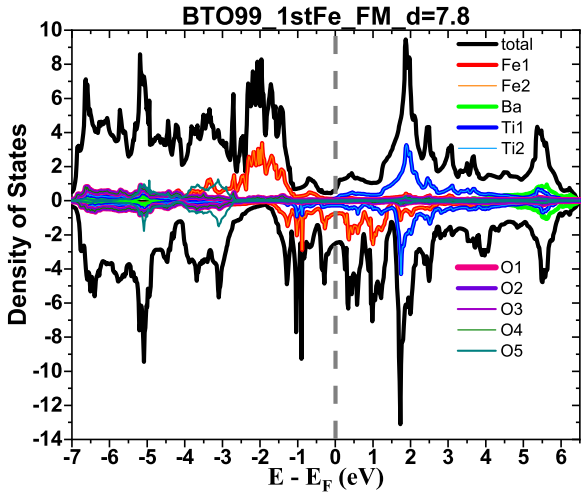

Figure 6.12: Density of states of BTO99_001_1stFe_FM at $d = 7.8$ Å.

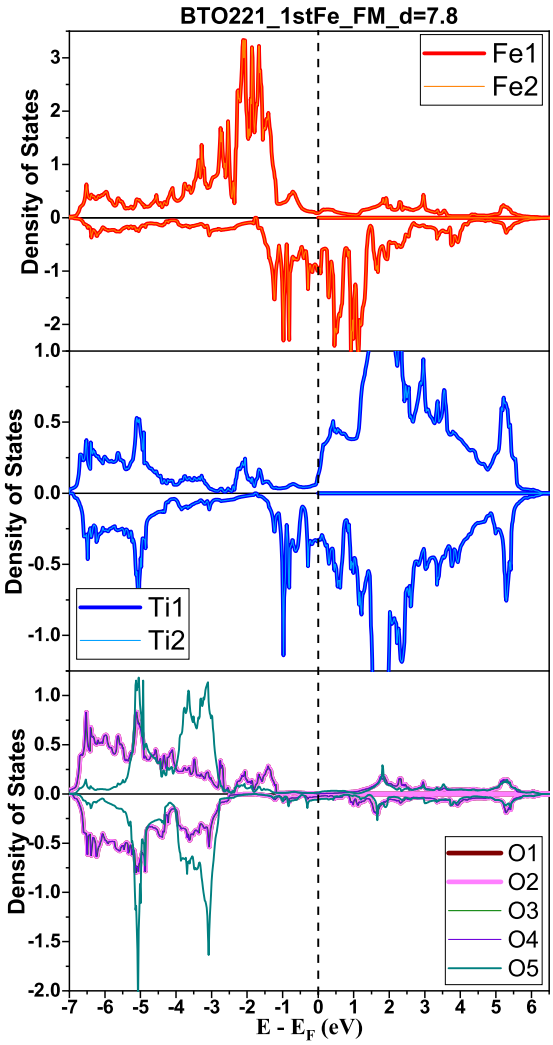

Figure 6.13: Fe, Ti and O density of states of BTO221_001_1stFe_FM at $d = 7.8$ Å.

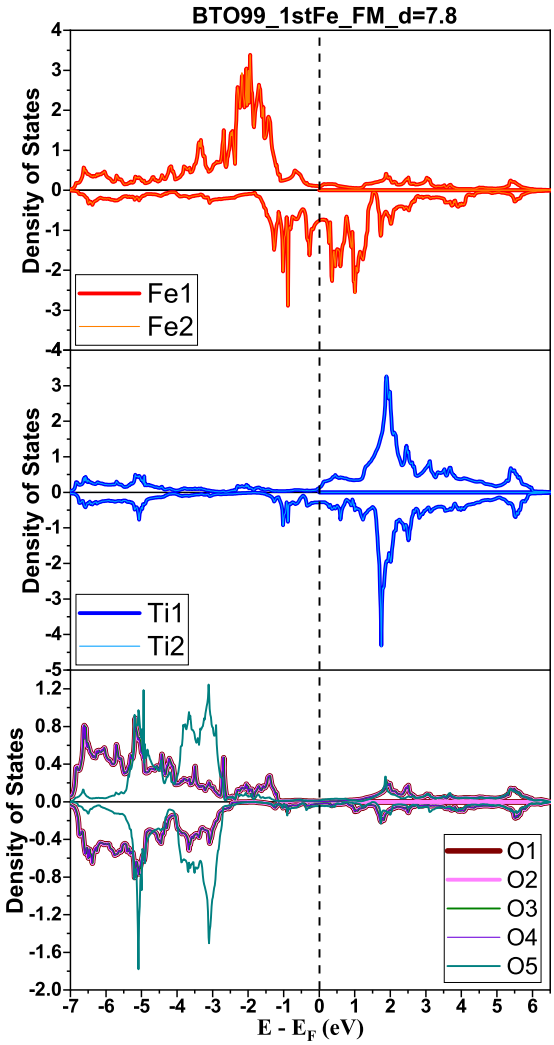

Figure 6.14: Fe, Ti and O density of states of BTO99_001_1stFe_FM at $d = 7.8$ Å.

From the previous results, it is possible to identify three families of magnetic behaviours in BTO221_001_1stFe and BTO99_001_1stFe supercells: a FM state with Fe magnetic moments with the same magnitude and close to the metal value, a AFM state which cancels the total magnetic moment of the supercell, and a state where all magnetic moments are null. Figures 6.11 and 6.12 show the density of states (DOS) of the FM arrangement of both supercells at $d = 7.8\,\text{Å}$. These figures show that immediately below the Fermi level, E_F[5], the total density of states is clearly dominated by Fe's DOS. For a more detailed presentation of this physical quantity, the DOS of Fe, Ti and O are represented separately in figures 6.13 and 6.14. For this energy range Ba DOS are barely present, thus they are not represented here with greater detail.

Figures 6.13 and 6.14 confirm the FM state at $d = 7.8\,\text{Å}$, and show that both Fe1 and Fe2 have the same DOS distribution, with the majority of states being occupied by a preferencial spin direction (up). Note that for both supercells the DOS are qualitatively the same.

Around -1 eV the down spins of Fe1 and Fe2 hybridise with the down spins of Ti1 and Ti2 atoms, explaining the induced magnetic moments of Ti atoms (antiferromagnetic to the Fe majority spins) seen in figure 6.8.

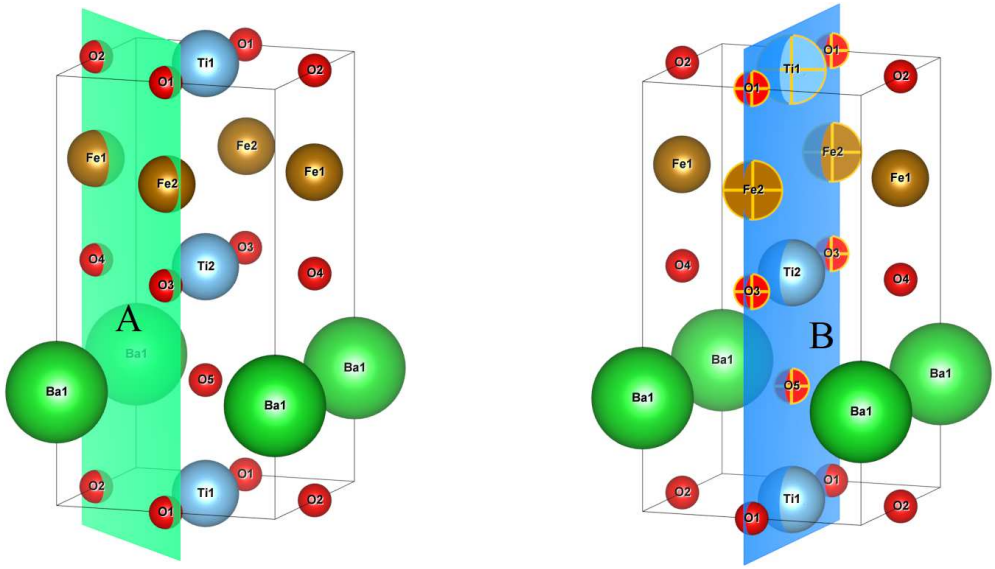

Figure 6.15: A and B cross section planes considered in the charge density representation. The A (green) plane is defined by the intersection of the Fe1, Fe2, O1, O2, O3 and O4. The B (blue) plane is defined by the intersection of the Fe1, Fe2, Ti1, Ti2, O2, O4 and O5.

[5]Since DFT calculations are done assuming T=0 K the Fermi energy and the Fermi level have the same value.

To have an intuitive visual representation of bondings and hybridizations, the charge density (ρ_{Total}) and spin polarized (SP) charge density difference ($\rho_\uparrow - \rho_\downarrow$) will be presented across the A and B cross section planes defined in figure 6.15.

The BTO221_001_1stFe charge density and SP charge density difference for E-E_F $\in [-3, 0]$ eV at $d = 7.8$ Å are presented in figure 6.16 (plane A) and 6.17 (plane B).

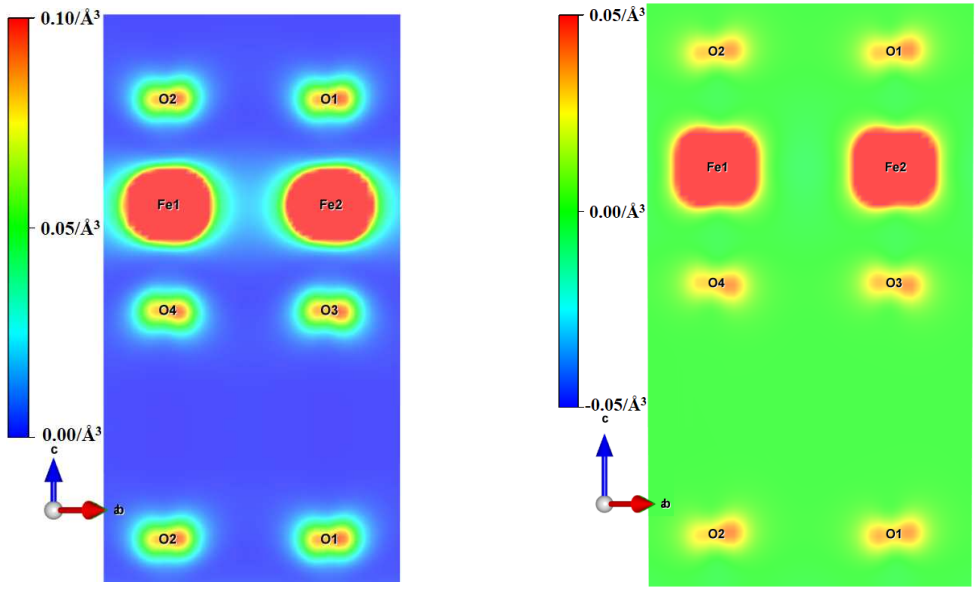

Figure 6.16: Charge density (left) and SP charge density difference (right) of the BTO221_001_1stFe_FM for $d = 7.8$ Å across plane A, calculated for E-E_F $\in [-3, 0]$ eV.

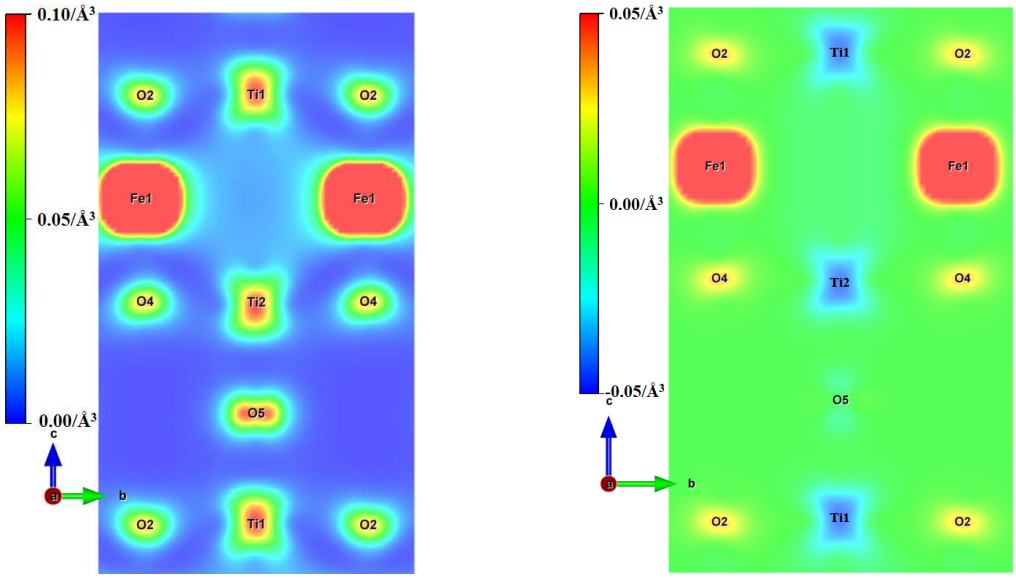

Figure 6.17: Charge density (left) and spin polarized charge density difference (right) of the BTO221_001_1stFe_FM at $d = 7.8$ Å across plane B, calculated for E-E_F $\in [-3, 0]$ eV.

In the plane A (figure 6.16) it is possible to see that the electron density of Fe atoms do not have any significant superposition with the O electron density, in spite of the superposition of DOS peaks around -2 eV. The difference of the spin polarized electron density confirms the ferromagnetic nature of the Fe and O atoms.

The charge density of plane B shows a clear hybridization between the Fe and Ti orbitals (figure 6.17) as well as between the Ti and O atoms. In fact, in figure 6.13 there is the hybridization of the Ti and O electrons around -2 eV . These hybridizations explain the induced moments in Ti and O atoms seen in figure 6.8, as well as the enhancement of the Fe magnetic moments. The B plane SP charge difference confirms Ti's induced magneti moments, antiparallel to the Fe moment.

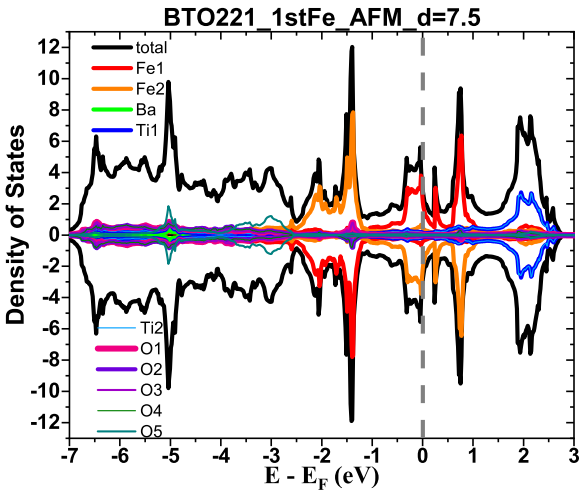

Figure 6.18: Density of states of BTO221_001_1stFe_AFM at $d = 7.5$ Å.

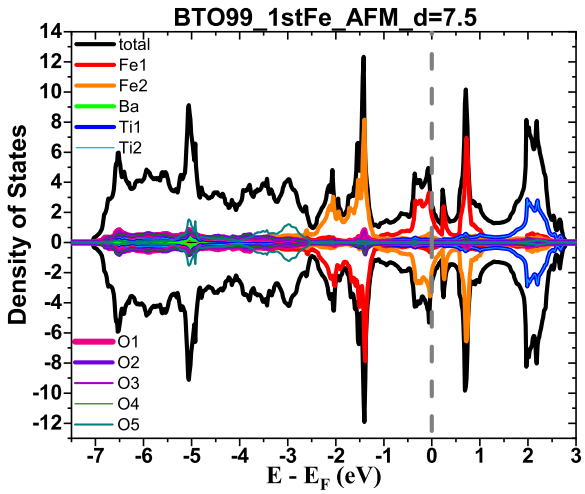

Figure 6.19: Density of states of BTO99_001_1stFe_AFM at $d = 7.5$ Å.

Figures 6.18 and 6.19 show the density of states of the AFM arrangement of both supercells for $d = 7.5$ Å. Once again, the DOS around the Fermi level are dominated by the Fe DOS, and the Ba DOS are negligible for the presented energy range. Figures 6.20 and 6.21 show a more detailed presentation of Fe, Ti and O DOS.

At $d = 7.5$ Å the DOS of BTO221_001_1stFe_AFM and BTO99_001_1stFe_AFM are also identical, thus the following observations hold for both cases. Figure 6.20 shows that there is a hybridization for Fe, Ti and O atoms near the Fermi level and around -0.5 eV and -1.5 eV. However, in this case, while the Ti atoms have about the same up and down electron DOS, each Fe atom has symmetric spin DOS with relation to each other, justifying their AFM

nature (figure 6.9). Similarly figure 6.20 shows that O1 and O3 DOS are symmetric to to O2 and O4 DOS resulting in their AFM alignment (figure 6.10).

The absolute charge density shown in the A and B planes of figures 6.22 and 6.23 are actually quite similar to the ones of BTO221_001_1stFe_FM at $d = 7.8$ Å (figures 6.16 and 6.17), hence it is only possible to infer the magnetic nature of BTO221_001_1stFe_AFM's individual atoms at $d = 7.5$ Å after looking at the SP charge density difference of figures 6.22 and 6.23.

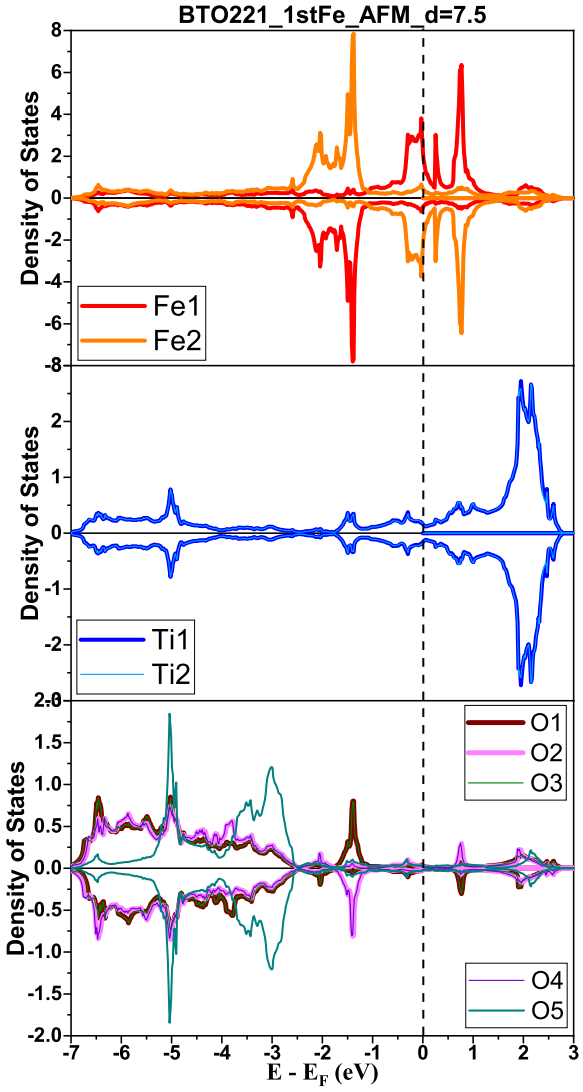

Figure 6.20: Fe, Ti and O density of states of BTO221_001_1stFe_AFM at $d = 7.5$ Å.

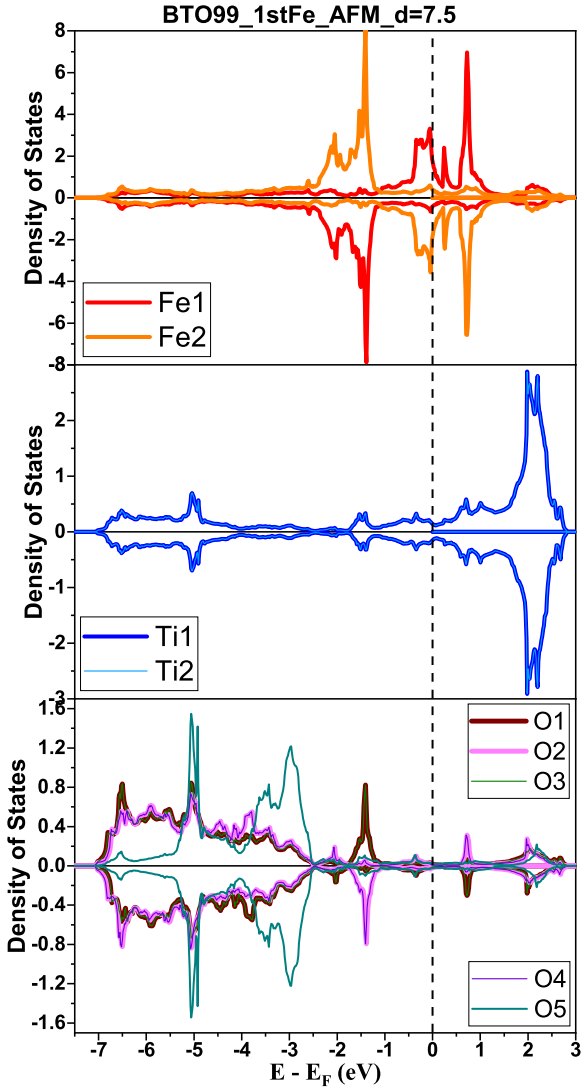

Figure 6.21: Fe, Ti and O density of states of BTO99_001_1stFe_AFM at $d = 7.5$ Å.

The SP charge density difference of figure 6.22 clearly shows the opposite magnetic moments of Fe1 and Fe2. In the same plane it is also possible to observe that the O atoms have

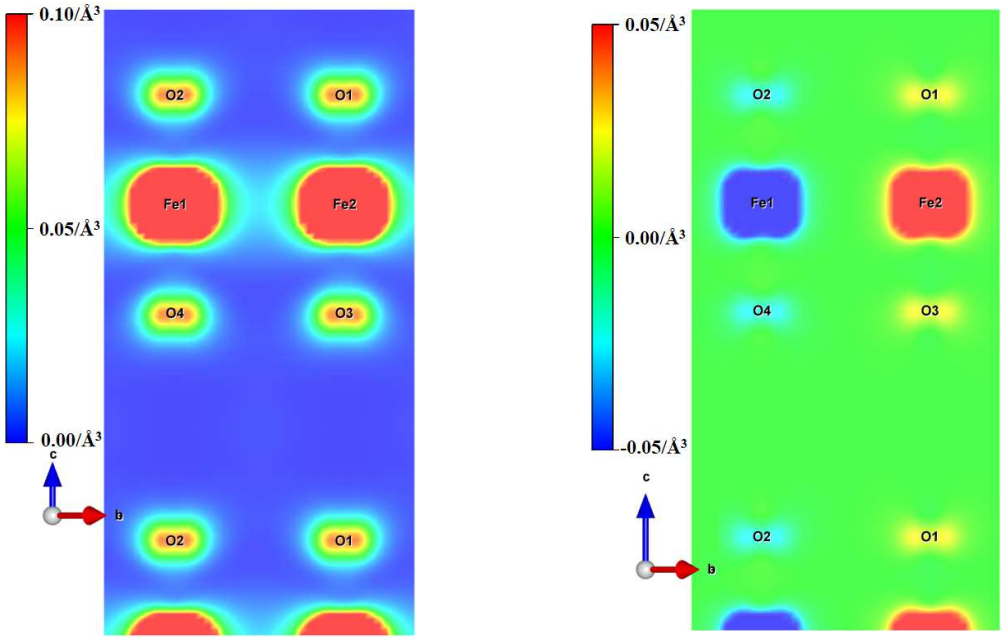

Figure 6.22: Charge density (left) and SP charge density difference (right) of the BTO221_001_1stFe_AFM for $d = 7.5\,\text{Å}$ across plane A, calculated for E-E$_\text{F}$ $\in [-3, 0]\,\text{eV}$.

an induced magnetic moment aligned with the Fe atom to whom they are adjacent.

On the other hand, the SP charge density difference of the B plane, shown in 6.23, confirms the close to null total magnetic moment of the Ti atoms[6].

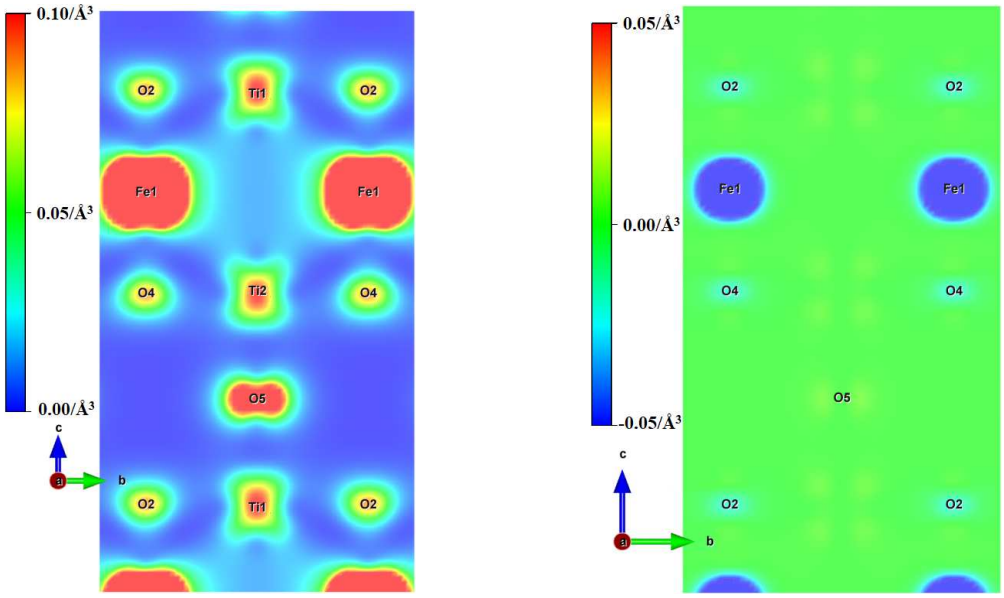

Figure 6.23: Charge density (left) and SP charge density difference (right) of the BTO221_001_1stFe_AFM for $d = 7.5\,\text{Å}$ across plane B, calculated for E-E$_\text{F}$ $\in [-3, 0]\,\text{eV}$.

[6]The slightly positive SP charge density difference can be due to small unbalances of the DOS values characteristic from the calculation method precision.

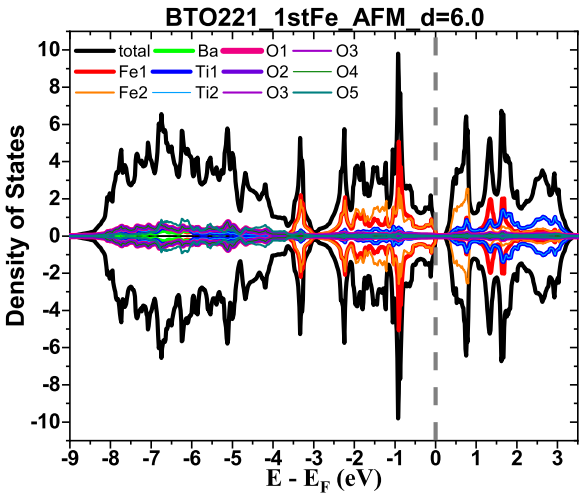

Figure 6.24: Density of states of BTO221_001_1stFe_AFM at $d = 6.0$ Å.

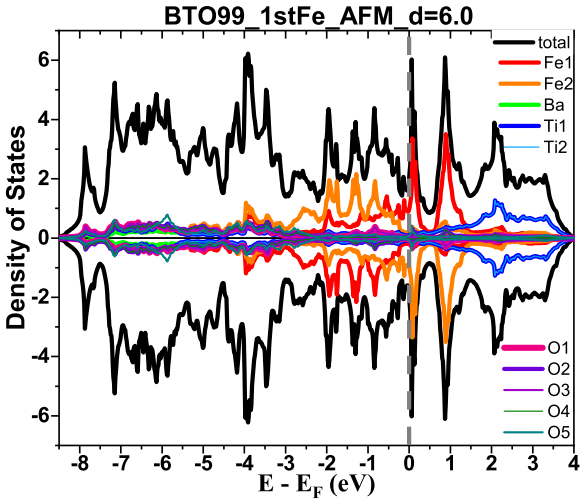

Figure 6.25: Density of states of BTO99_001_1stFe_AFM at $d = 6.0$ Å.

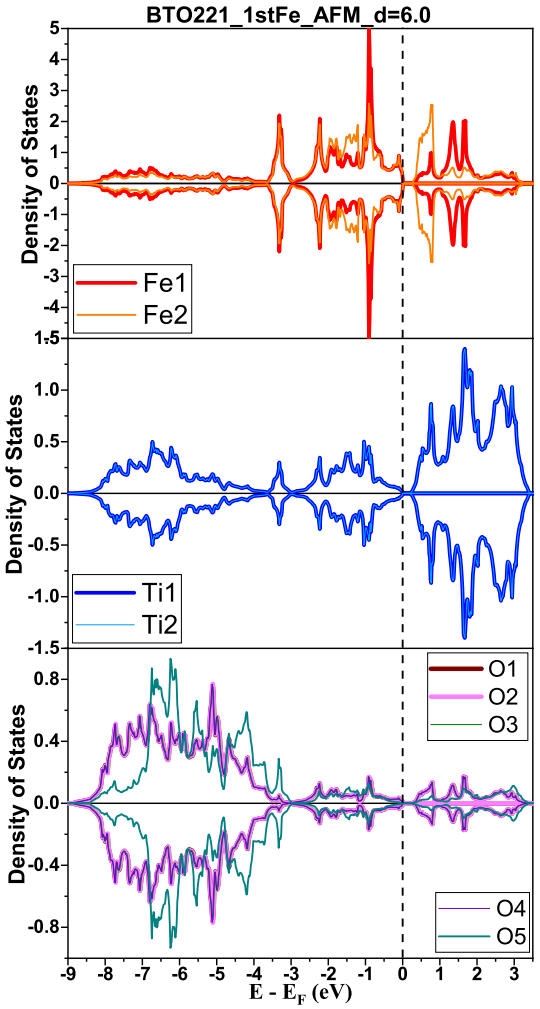

Figure 6.26: Fe, Ti and O density of states of BTO221_001_1stFe_AFM at $d = 6.0$ Å.

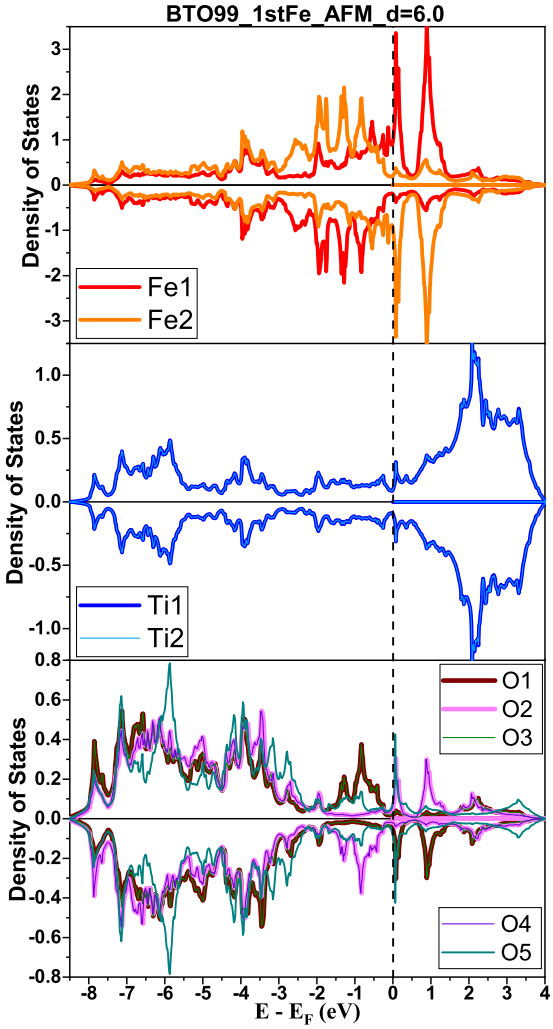

Figure 6.27: Fe, Ti and O density of states of BTO99_001_1stFe_AFM at $d = 6.0$ Å.

Let's now look at BTO221_001_1stFe_AFM and BTO99_001_1stFe_AFM at $d = 6.0$ Å. It is expected that for BTO99_001_1stFe_AFM there is an AFM state such as the one observed for $d = 7.5$ Å. This fact is confirmed by the DOS of figures 6.25 and 6.27, which apart from some quantitative differences, have the same qualitative features, namely the symmetric DOS of the Fe atoms, the symmetric DOS of the O atoms, and the balanced up and down DOS in each Ti atom.

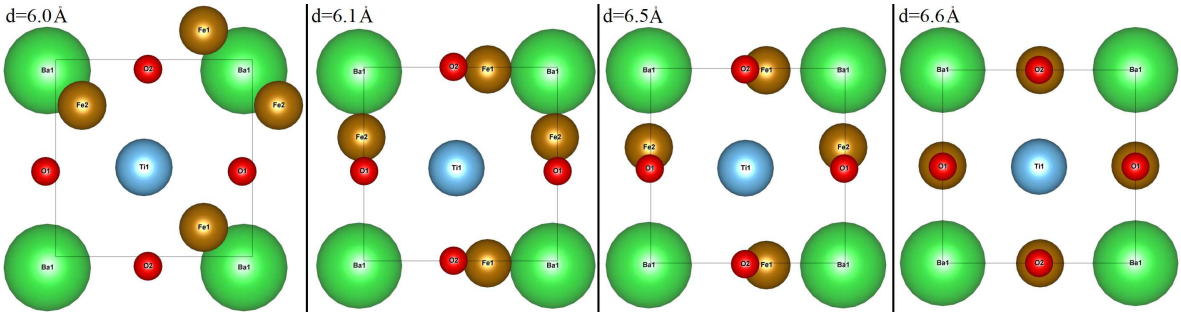

Figure 6.28: Top view of the evolution of the BTO221_001_1stFe_AFM supercell as a function of d.

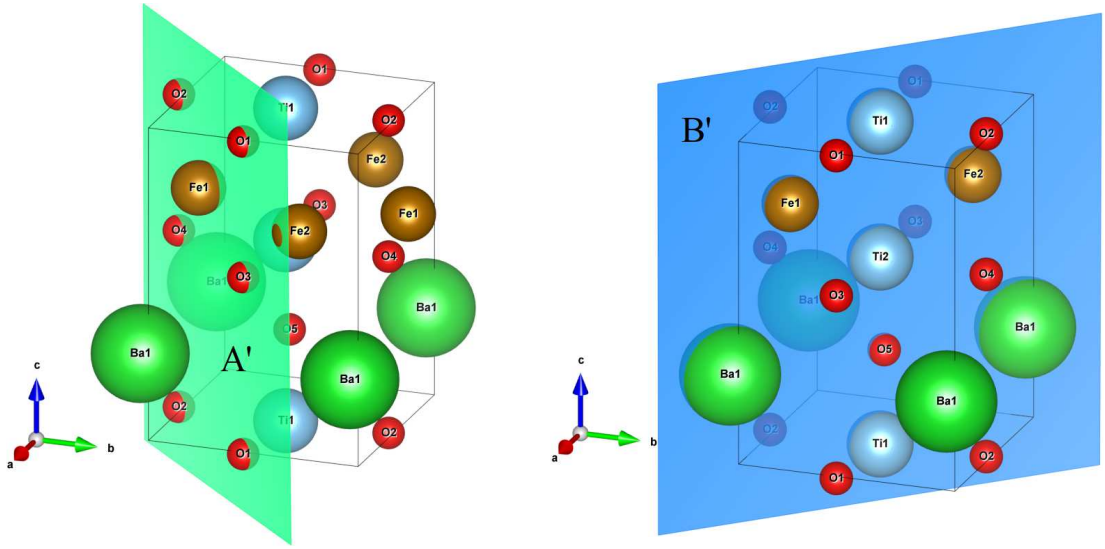

Figure 6.29: A' and B' cross section planes considered in the charge density representation. The A' (green) plane is defined by the interception of the Fe1, O1, O2, O3 and O4. The B' (blue) plane is defined by the intersection of the Fe1, Fe2, Ti1, Ti2, O2, O4 and O5.

From the observation of the individual magnetic moments of BTO221_001_1stFe_AFM's atoms (figures 6.9 and 6.10), a quench of each atom's magnetic moment is expected. Figures 6.24 and 6.26 confirm this expectation, since the DOS of each atom have exactly the same

number of up and down spin electrons. Moreover the DOS presented in figures 6.24 and 6.26 also show the opening of an energy gap of about 200 meV degenerating the previously metallic (or semimetallic) character of the supercell into a p-type semiconductor.

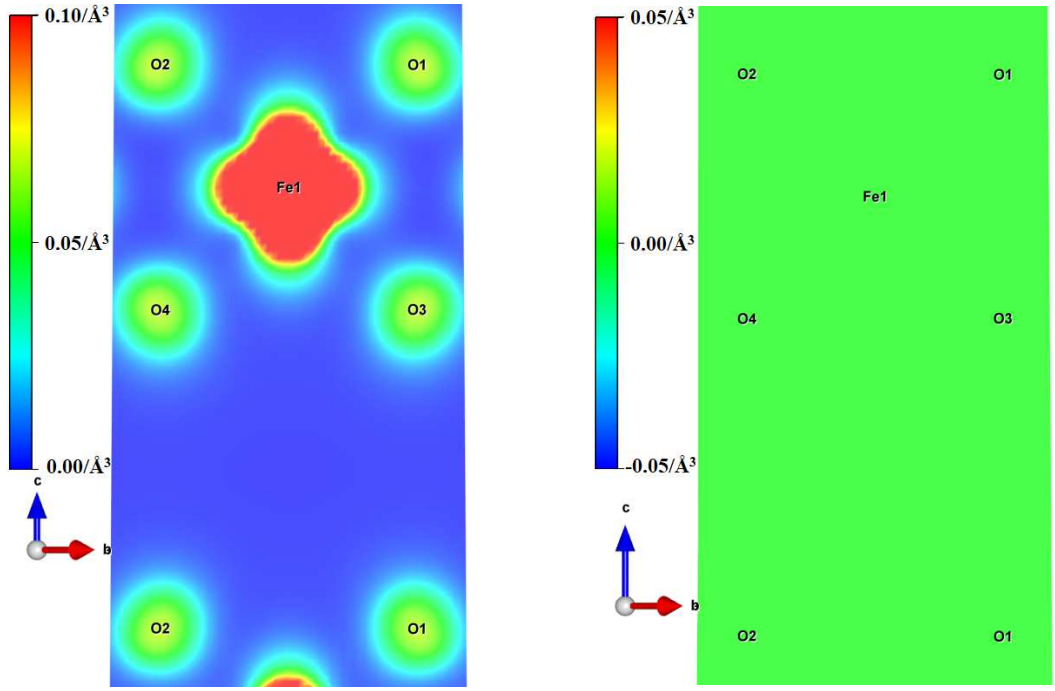

Figure 6.30: Charge density (left) and SP charge density difference (right) of the BTO221_001_1stFe_AFM for $d = 6.0$ Å across plane A', calculated for E-$E_F \in [-3, 0]$ eV.

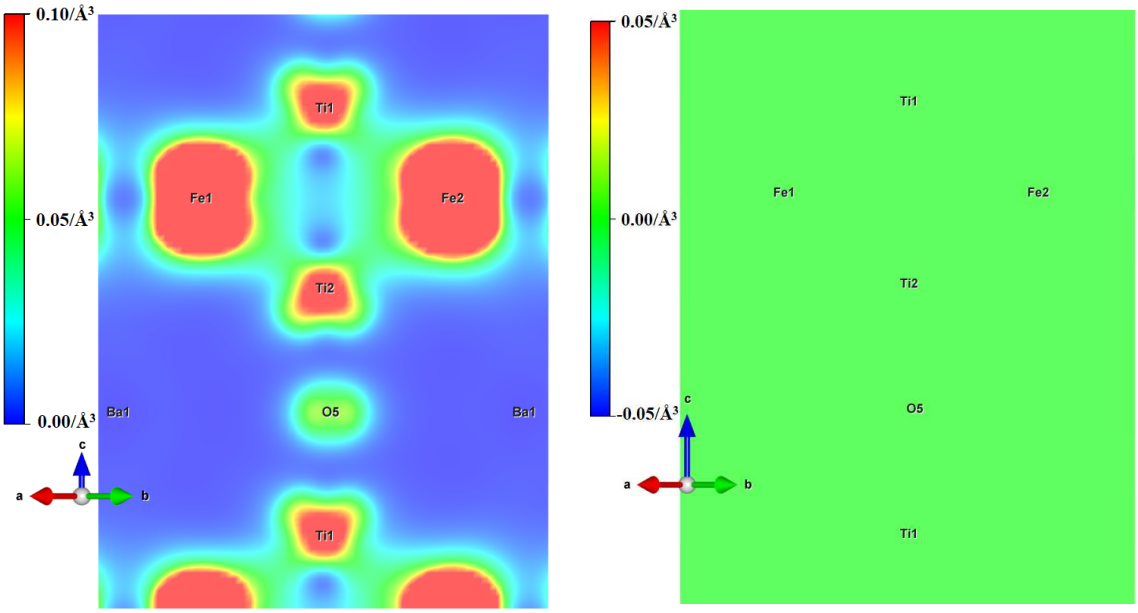

Figure 6.31: Charge density (left) and SP charge density difference (right) of the BTO221_001_1stFe_AFM at $d = 6.0$ Å across plane B', calculated for E-$E_F \in [-3, 0]$ eV.

Figure 6.28 shows the top view of the BTO221_001_1stFe_AFM supercell for different values of d. While for $d \geq 6.6\,\text{Å}$ the fractional coordinates remain approximately equal to the initial structure (figure 6.1), at $d = 6.5\,\text{Å}$ a distortion of the Fe atoms begins to take place. Note that $d = 6.5\,\text{Å}$ is the first point of the abrupt decrease of Fe individual magnetic moments (figure 6.9). For even lower values of d it is possible to see larger distortions of the Fe atoms till the point of a complete change of symmetry at $d = 6.0\,\text{Å}$ point where it is observed the complete quench of all magnetic moments (figures 6.9 and 6.10).

Later, it will be verified that this new emplacement of the Fe atoms is the same as the yet undefined 2ndFe monolayer system. Therefore, to analyse the charge density of the new atomic coordinates seen at $d = 6.0\,\text{Å}$, the A' and B' planes, defined in figure 6.29, are used.

Figure 6.30 presents the A' plane and shows that the Fe electrons tend to be as far as possible from the O's electrons, whereas the SP charge density difference shows the complete annihilation of any magnetic moment. This extinction of all the magnetic moments is also perceptible by observation of the SP charge density difference at the B' plane of figure 6.31. The charge density seen in the B' plane shows a considerable superposition of the Fe and Ti electrons.

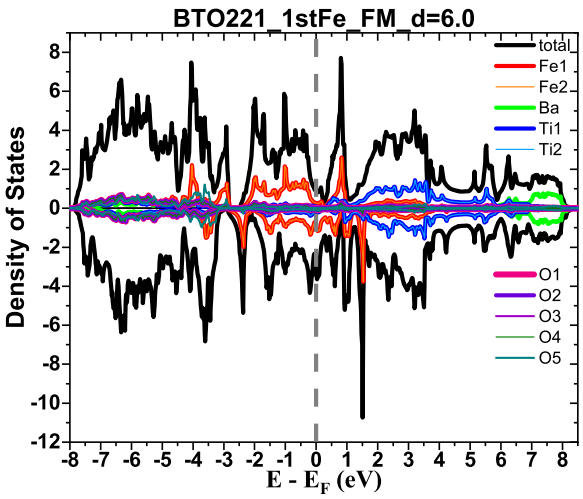

Figure 6.32: Density of states of BTO221_001_1stFe_FM at $d = 6.0\,\text{Å}$.

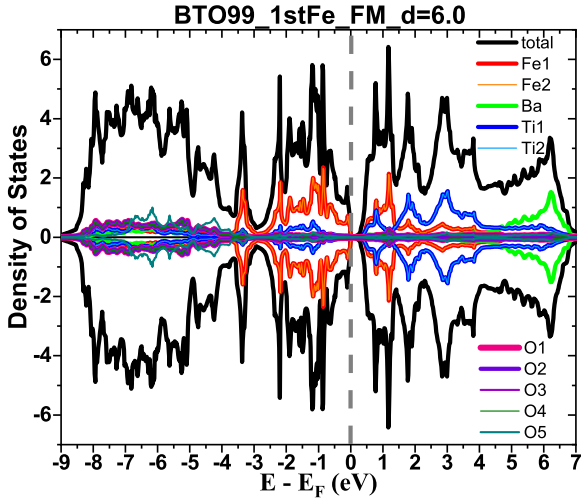

Figure 6.33: Density of states of BTO99_001_1stFe_FM at $d = 6.0\,\text{Å}$.

Finally, the DOS of BTO221_001_1stFe_FM and BTO99_001_1stFe_FM at $d = 6.0\,\text{Å}$ are shown in figures 6.32 and 6.33. At this value of d, the DOS of figure 6.32 differ qualitatively from the DOS of figure 6.33, since the former presents unbalanced up and down electrons, whereas the latter perfectly balances up and down electrons. As a matter of fact, the BTO221_001_1stFe_FM at $d = 6.0\,\text{Å}$ (figures 6.32 and 6.34) is in a intermediate state

between the ferromagnetic state of BTO221_001_1stFe_FM at $d \geq 6.1$ Å and the null-spin state present in BTO99_001_1stFe_FM at $d = 6.0$ Å

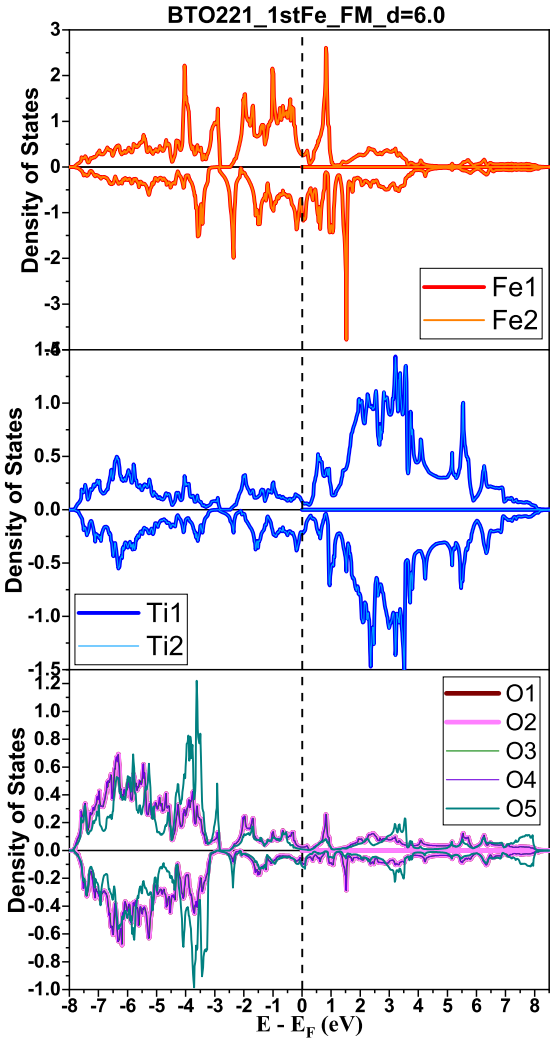

Figure 6.34: Fe, Ti and O density of states of BTO221_001_1stFe_FM at $d = 6.0$ Å.

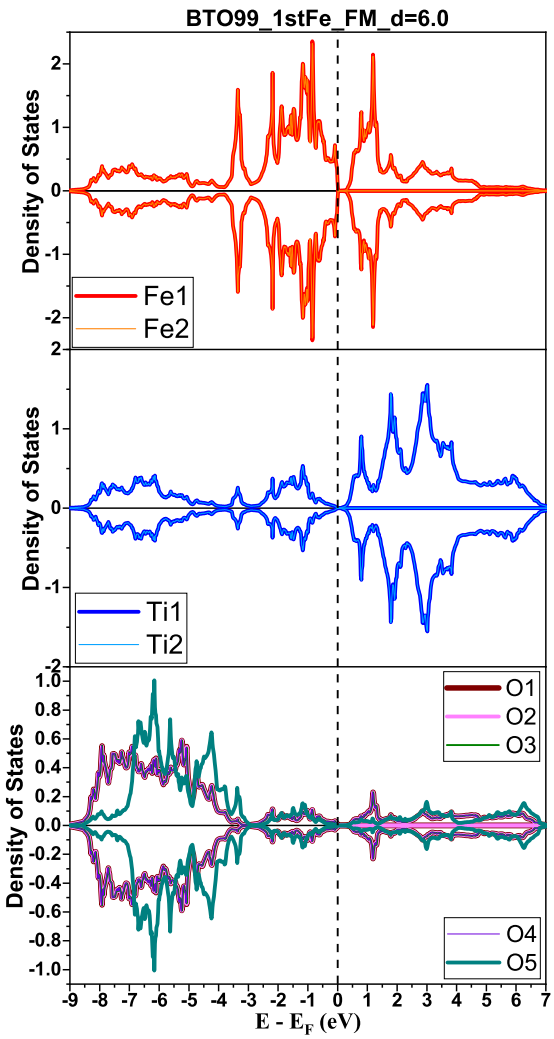

Figure 6.35: Fe, Ti and O density of states of BTO99_001_1stFe_FM at $d = 6.0$ Å.

Figures 6.33 and 6.35 show that the DOS of BTO99_001_1stFe_FM at $d = 6.0$ Å are identical to BTO221_001_1stFe_AFM for $d = 6.0$ Å. In fact, in the former case the supercell suffers the same structure changes as in the latter. Because of this feature, BTO99_001_1stFe-_FM at $d = 6.0$ Å has basically the same charge density and SP charge density difference as BTO221_001_1stFe_AFM for $d = 6.0$ Å, as it is possible conclude by the comparison of figures 6.36 and 6.37 with 6.30 and 6.31.

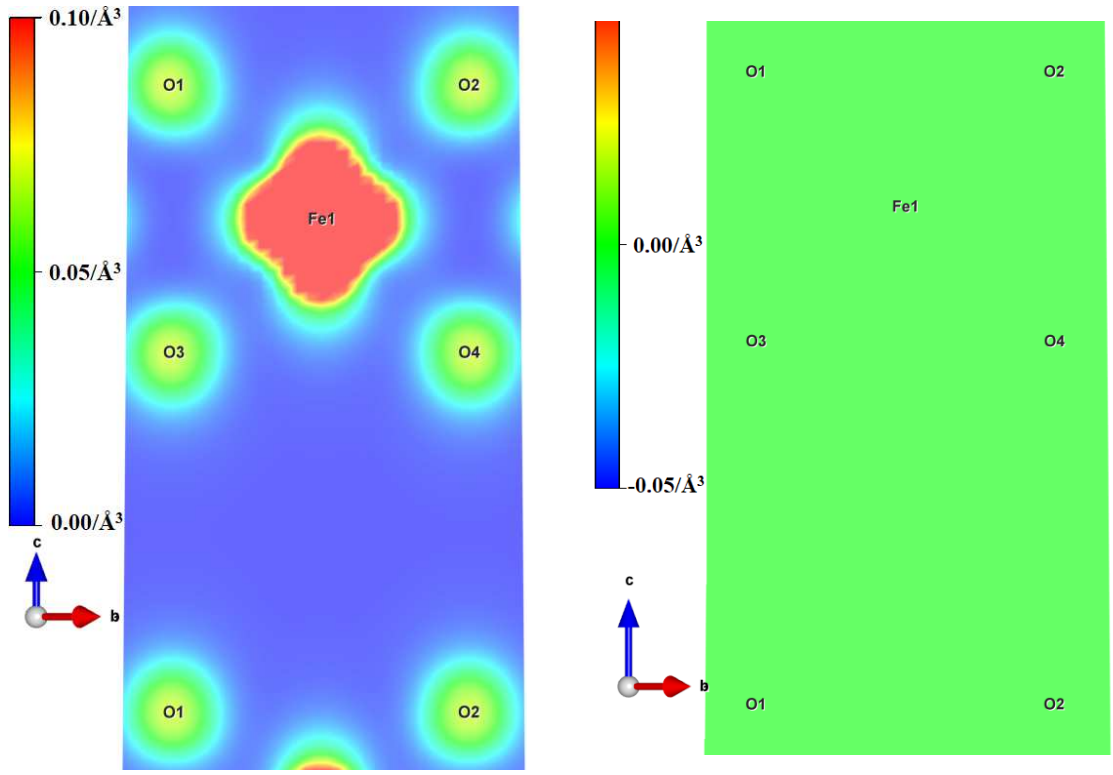

Figure 6.36: Charge density (left) and SP charge density difference (right) of the BTO99_001_1stFe_FM for $d = 6.0\,\text{Å}$ across plane A', calculated for E-E$_\text{F}$ $\in [-3, 0]\,\text{eV}$.

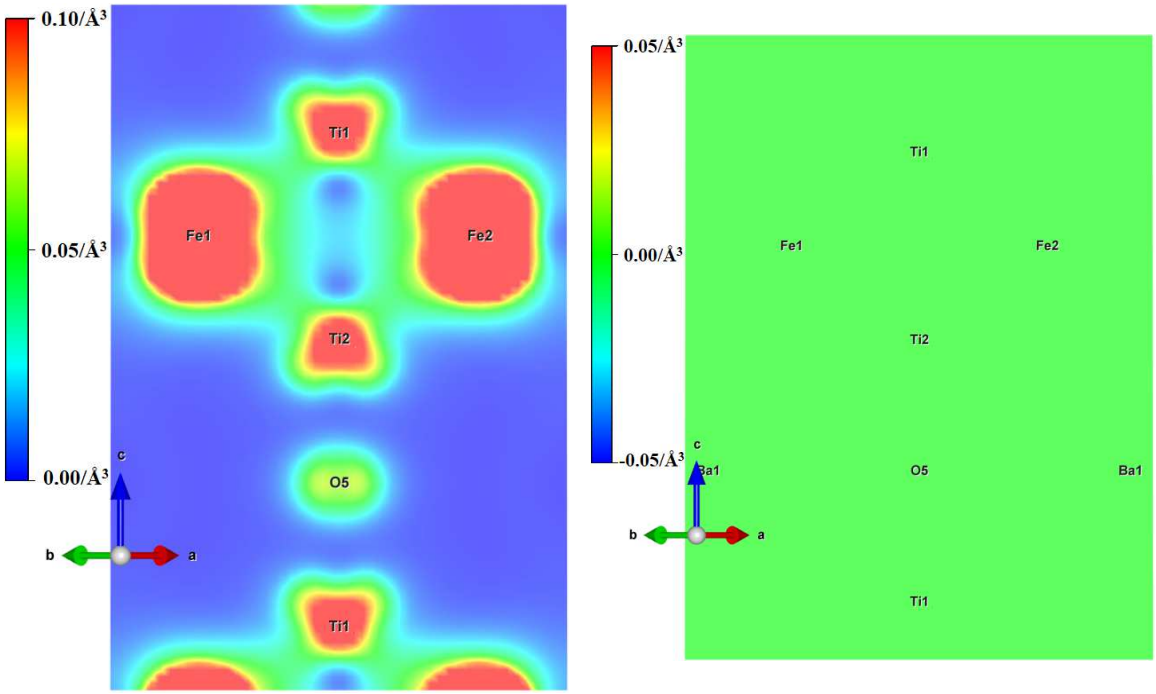

Figure 6.37: Charge density (left) and SP charge density difference (right) of the BTO99_001_1stFe_FM for $d = 6.0\,\text{Å}$ across plane B', calculated for E-E$_\text{F}$ $\in [-3, 0]\,\text{eV}$.

6.1.2 BTO/2ndFe

Another possible way of placing the Fe atoms on top of BTO unit cells is presented in figures 6.38 and 6.39. In this case the supercells are defined as BTO221_001_2ndFe (figure 6.38) and BTO99_001_2ndFe (figure 6.39) and each one has two Fe atoms on the corner and centre positions of the supercell.

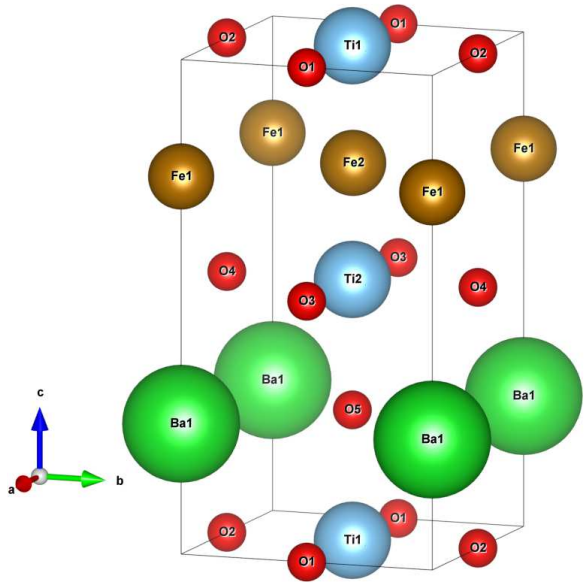

Figure 6.38: BTO221_001_2ndFe supercell

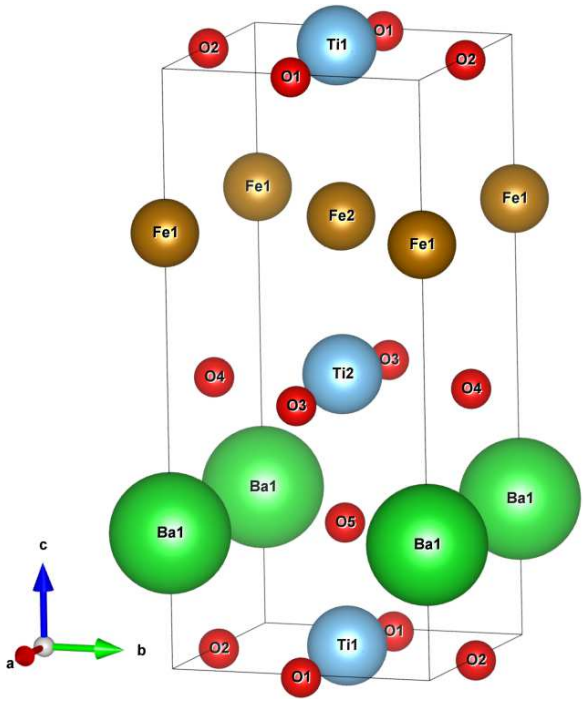

Figure 6.39: BTO99_001_2ndFe supercell

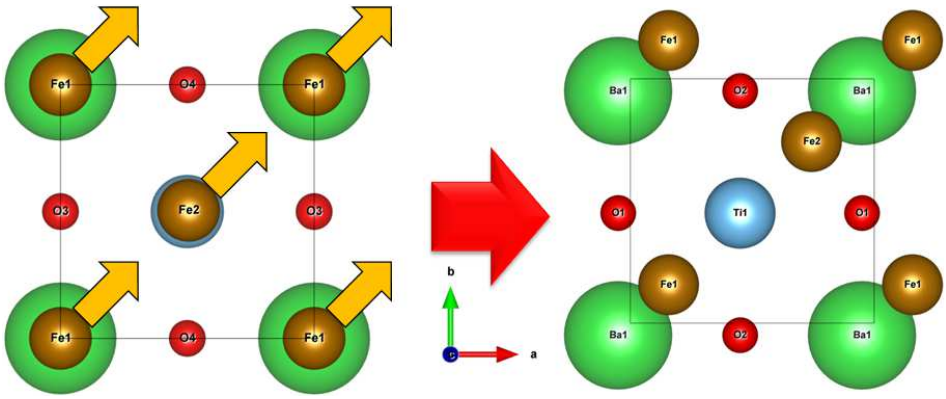

Figure 6.40: Top view of the structural change from the initial BTO221_001_2ndFe at $d = 7.5\,\text{Å}$ to its atomic relaxed structure. The last TiO_2 layer of the left figure is not shown to ease the comprehension of the structural displacements.

The study made in the 1stFe monolayer system was also done for the 2ndFe monolayer system case using the same calculation methods and parameters. The only difference between the

BTO221(99)_1stFe and the BTO221(99)_2ndFe supercells is solely the Fe initial positions.

In all considered values of d, for BTO221_001_2ndFe and BTO99_001_2ndFe, after letting the supercell relax its Hellmann-Feynman forces below the tolerance value, the initial fractional coordinates of Fe atoms suffer a displacement along one of the face diagonals of the supercell, as illustrated in figure 6.40. As it is perceptible, the resultant structure is identical to the BTO221_001_1stFe_AFM and BTO99_001_1stFe_FM at $d = 6.0\,\text{Å}$ (where there was a quench of all the magnetic moments).

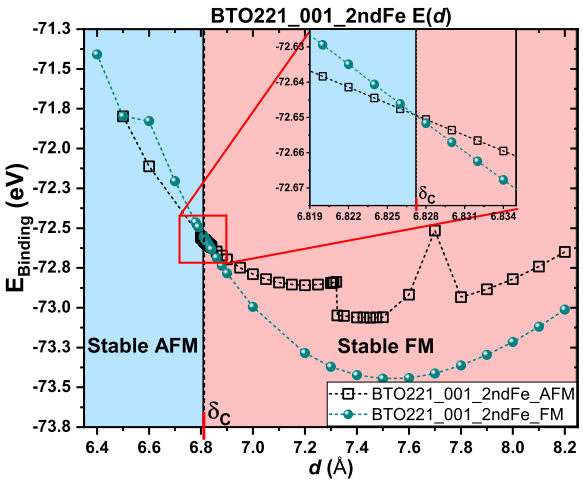

Figure 6.41: Binding energy for all the considered magnetic arrangements of the BTO221_001_2ndFe supercell (cubic lattice parameters).

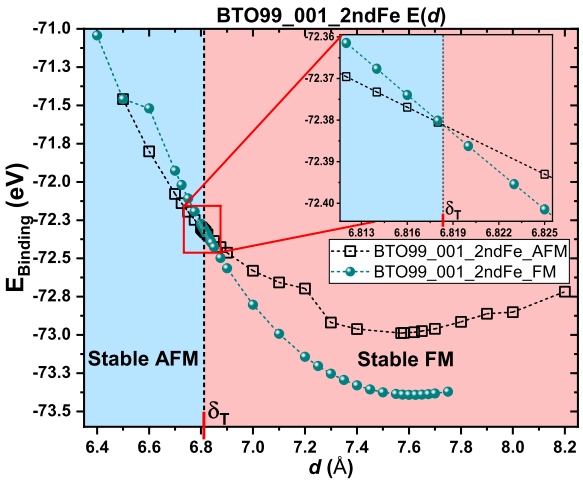

Figure 6.42: Binding energy for all the considered magnetic arrangements of the BTO99_001_2ndFe supercell (tetragonal lattice parameters).

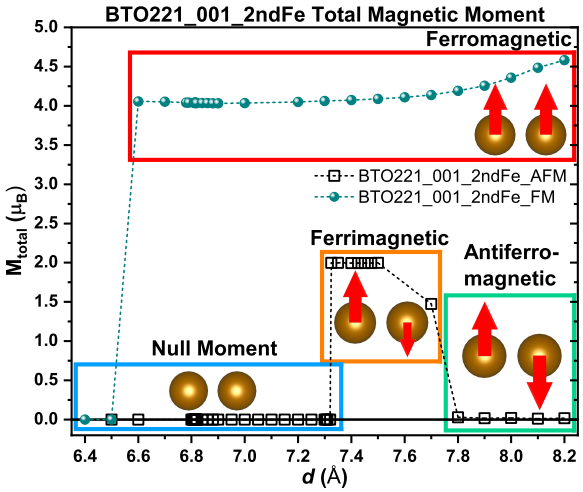

Figure 6.43: Total magnetic moment for all the considered magnetic arrangements of the BTO221_001_2ndFe supercell.

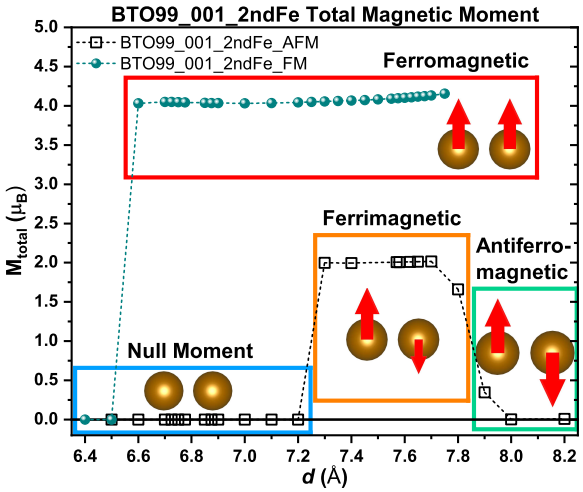

Figure 6.44: Total magnetic moment for all the considered magnetic arrangements of the BTO99_001_2ndFe supercell.

The binding energies of the BTO221_001_1stFe and BTO99_001_1sFe for both FM and AFM initial input arrangements are shown in figure 6.41 and 6.42 respectively. Contrary to the 1stFe monolayer system, in the 2ndFe monolayer system there is a distance d which separates the range region where the FM arrangement is energetically more favourable from the region where the AFM is more favourable. This point occurs at $d = \delta_T = 6.818\,\text{Å}$ for BTO99_001_1sFe and $d = \delta_C = 6.827\,\text{Å}$ for BTO221_001_1sFe. Moreover, in both figures 6.41 and 6.44 it is perceptible, just by the observation of the energy curves, that there are several different behaviours in the AFM arrangement of the 2ndFe monolayer system.

Figures 6.43 and 6.44 show the total magnetic moment of the BTO221_001_2ndFe and BTO99_001_2ndFe supercells for both FM and AFM input arrangements. The FM arrangement of both "pseudo cubic" and tetragonal supercell presents a ferromagnetic state with an overall magnetic moment of $M_{total} \in [4, 4.5]\,\mu_B$ for $d \geq 6.6\,\text{Å}$, whereas for $d < 6.6\,\text{Å}$ the total magnetic moment vanishes.

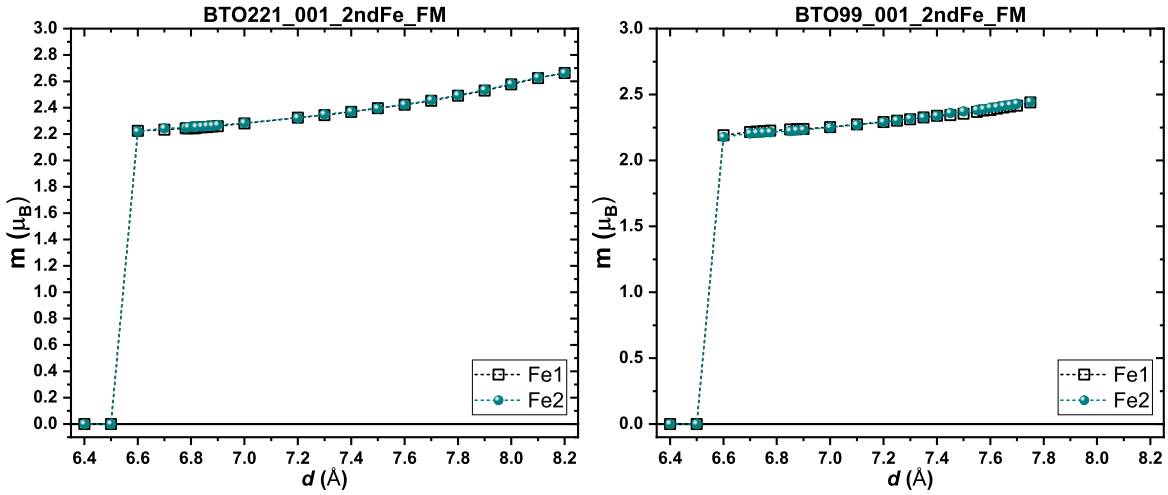

Figure 6.45: Fe magnetic moments for the ferromagnetic input arrangement of BTO221_001_2ndFe (left) and BTO99_001_2ndFe (right) supercells.

The observation of figures 6.45 and 6.46 allows to infer that the FM state for $d \geq 6.6\,\text{Å}$ is mainly due to the ferromagnetic Fe atoms, whose individual magnetic moments are enhanced as d increases. The enhancement can reach magnetic moments as high as $m \approx 2.7\,\mu_B/Fe_{atom}$ (figure 6.45), which nevertheless results in a $M_{total} \neq 5.4\,\mu_B$ due to the magnetic moments induced in the Ti atoms being antiparallel to the Fe magnetic moments (figure 6.46). The

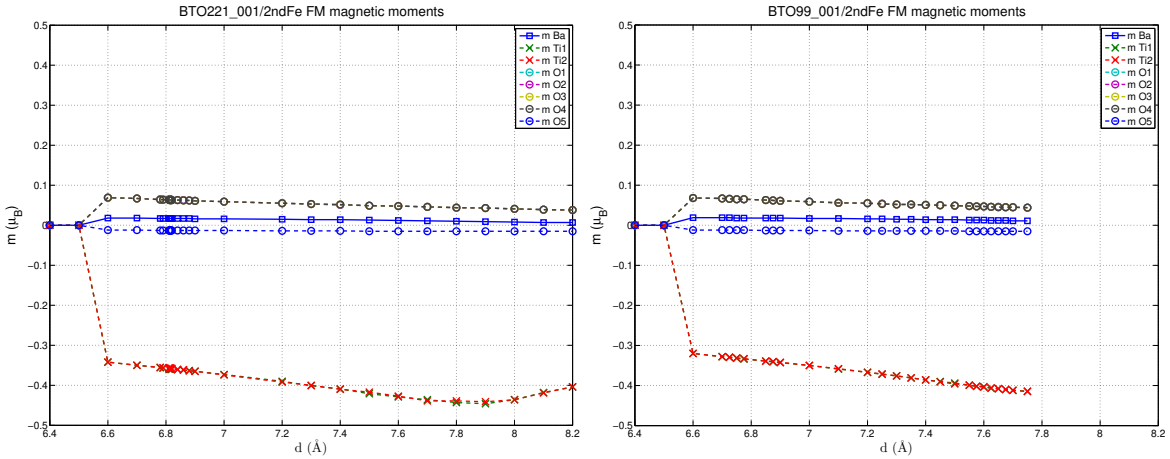

Figure 6.46: Magnetic moments of all atoms, apart from Fe, for the ferromagnetic input arrangement of BTO221_001_2ndFe (left) and BTO99_001_2ndFe (right) supercells.

induced moments in Ti can reach values as high as $m \approx 0.4\,\mu_B/\mathrm{Ti_{atom}}$, similar to the BTO221(99)_1stFe case. The O atoms from the TiO_2 layers also have an induced magnetic moment, parallel to the Fe atoms, which can be as high as $m \approx 0.1\,\mu_B/\mathrm{O_{atom}}$ but contrarily to Fe, its magnitude decreases as d increases.

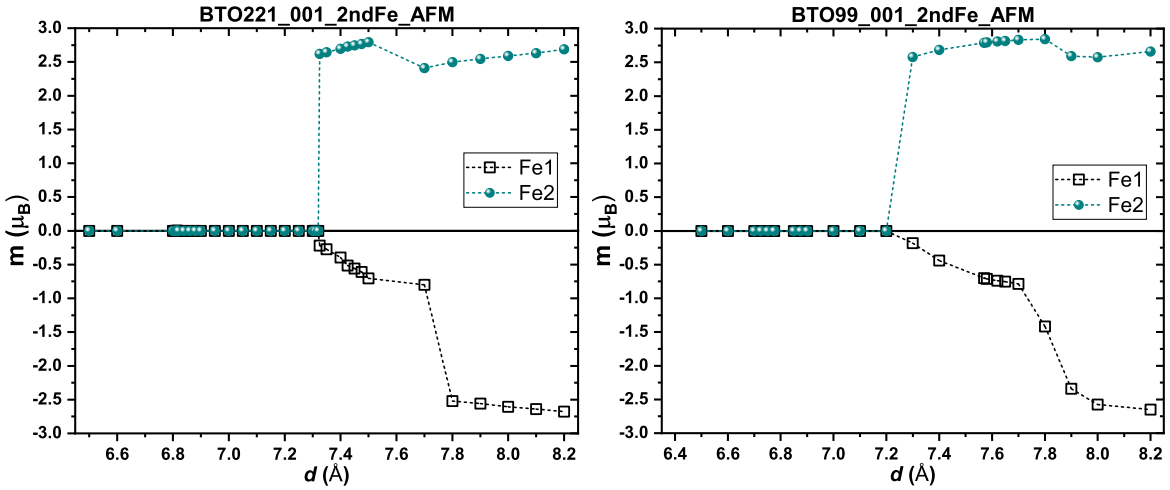

Figure 6.47: Fe magnetic moments for the antiferromagnetic input arrangement of BTO221_001_2ndFe (left) and BTO99_001_2ndFe (right) supercells.

In figures 6.43 and 6.44, it is possible to see that the AFM input arrangement has three families of magnetic behaviours. For $d \geq 7.8\,\text{Å}$ in the BTO221_001_2ndFe case or $d \geq 8.0\,\text{Å}$ in the BTO99_001_2ndFe there is a null total magnetic moment. This magnetic moment arises from the antiferromagnetic interaction of the Fe atoms which have exactly the same opposing magnitude.

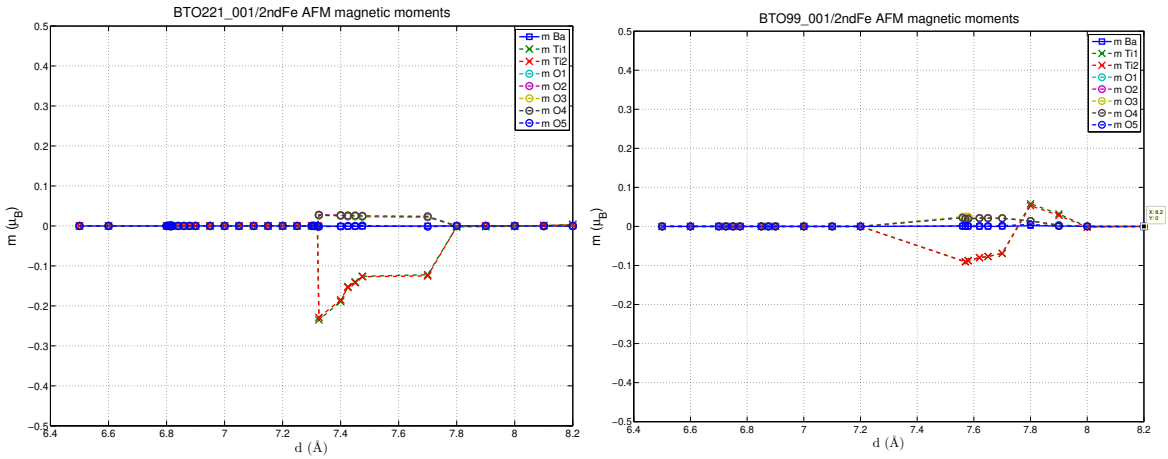

Figure 6.48: Magnetic moments of all atoms, apart from Fe, for the antiferromagnetic input arrangement of BTO221_001_2ndFe (left) and BTO99_001_2ndFe (right) supercells.

For $7.325 \leq d < 7.8\,\text{Å}$ in the pseudo-cubic case and $7.2 \leq d < 8.0\,\text{Å}$ in the tetragonal case the Fe1 atom suffers a decrease in the magnitude of its magnetic moment and for this reason the previously balanced antiferromagnetic state turns into an unbalanced ferrimagnetic state with a total magnetic moment which can be as high as $M_{total} \approx 2\,\mu_B$. This FiM state has the most negative binding energy from all the possible AFM states, thus being the most energetically stable state assuming $p = 0\,\text{Pa}$. In this range there is also the inducement of magnetic moments of the TiO_2 layer's atoms, where the Ti atoms are ferromagnetic to the Fe1 atom and the O atoms ferromagnetic to the Fe2 atom.

The last family of magnetic behaviour occurs at $d < 7.325\,\text{Å}$ and $d < 7.2\,\text{Å}$ for the pseudo-cubic and tetragonal supercells respectively. This particular state has all its atoms with null magnetic moments, being therefore analogous to the quenched state previously seen in the 1stFe monolayer system for low d values. It is also verifiable that such a magnetic moment quenching is also present for $d \leq 6.5\,\text{Å}$ in the BTO221(99)_001_2ndFe_FM case. In fact, after looking to the latter's binding energy (figures 6.41 and 6.42), one can realize that in this region the BTO221(99)_001_2ndFe_FM collapses to the BTO221(99)_001_2ndFe_AFM structure, thus having the exact same energy.

Figures 6.49 and 6.50 show the DOS of BTO221(99)_001_2ndFe_FM supercells at $d = 7.5\,\text{Å}$. Since the Ba DOS are negligible near the Fermi level, I will focus in figures 6.51 and 6.52 which show the Fe, Ti and O DOS with more detail.

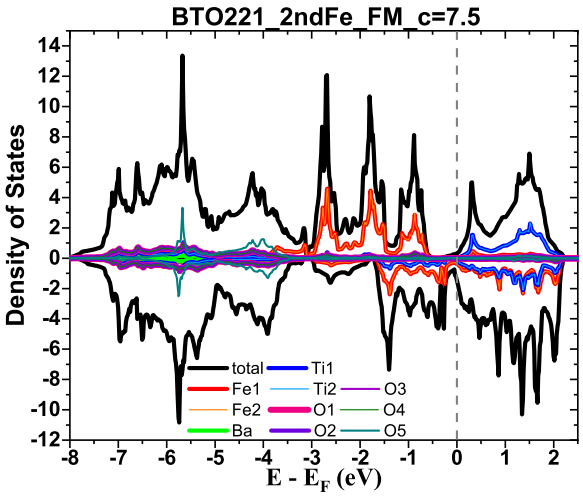

Figure 6.49: Density of states of BTO221_001_2ndFe_FM at $d = 7.5$ Å.

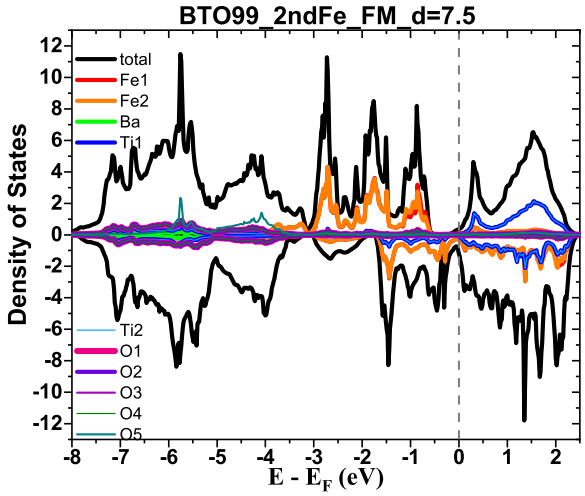

Figure 6.50: Density of states of BTO99_001_2ndFe_FM at $d = 7.5$ Å.

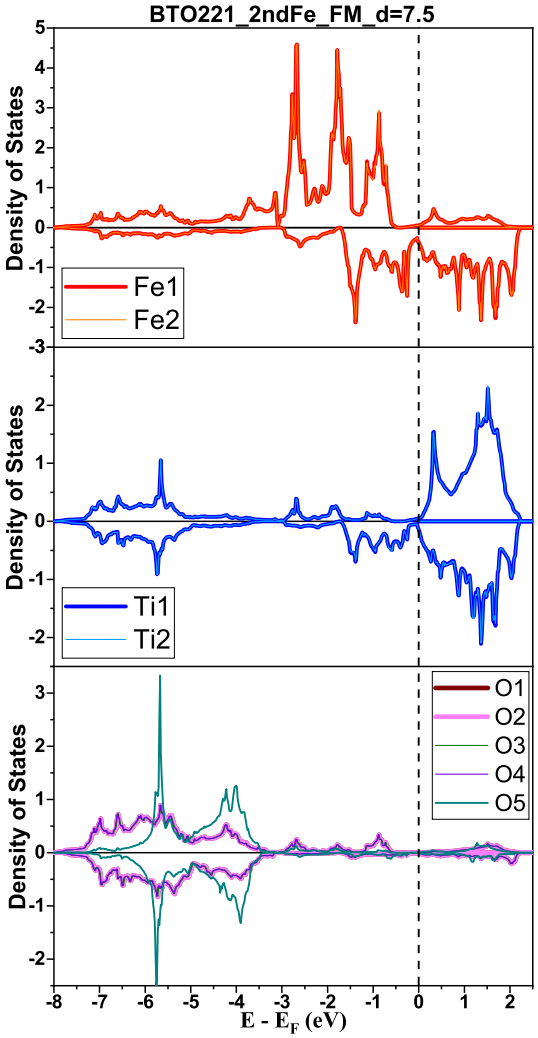

Figure 6.51: Fe, Ti and O density of states of BTO221_001_2ndFe_FM at $d = 7.5$ Å.

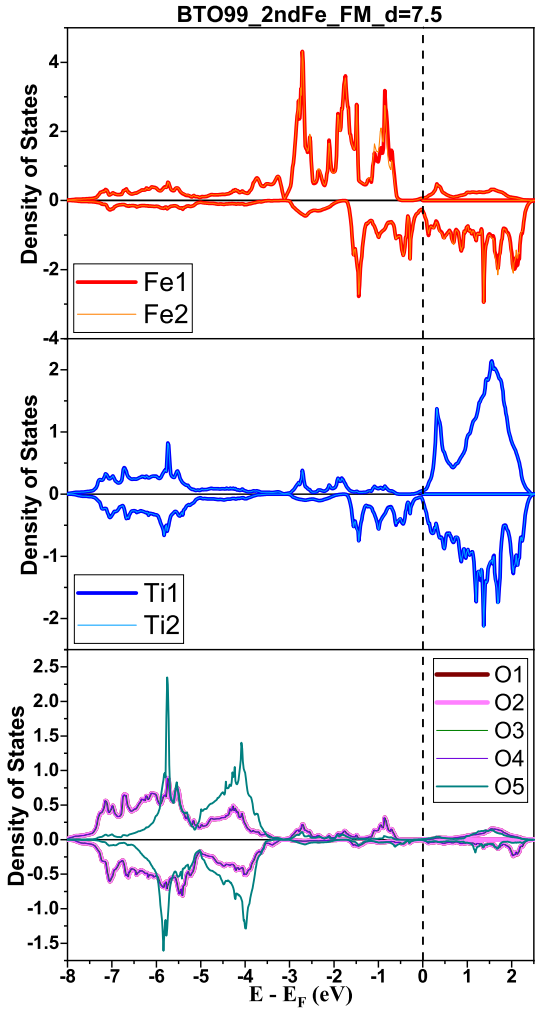

Figure 6.52: Fe, Ti and O density of states of BTO99_001_2ndFe_FM at $d = 7.5$ Å.

The total DOS confirms the ferromagnetic nature of the BTO221(99)_001_2ndFe_FM supercell (seen in figures 6.45 and 6.46), with both Fe atoms having the same DOS, thus having the same magnetic moment magnitude. The Fe minority electrons (spin down electrons) hybridize with the Ti down electrons around -1.75–0 eV, justifying the induced magnetic moments seen in figure 6.46. The O atoms of the TiO_2 layer, on the other hand, have local maxima in the same energies as the Fe and Ti atoms, around 2.75 eV, which is also associated to the induced magnetic moments of these O atoms.

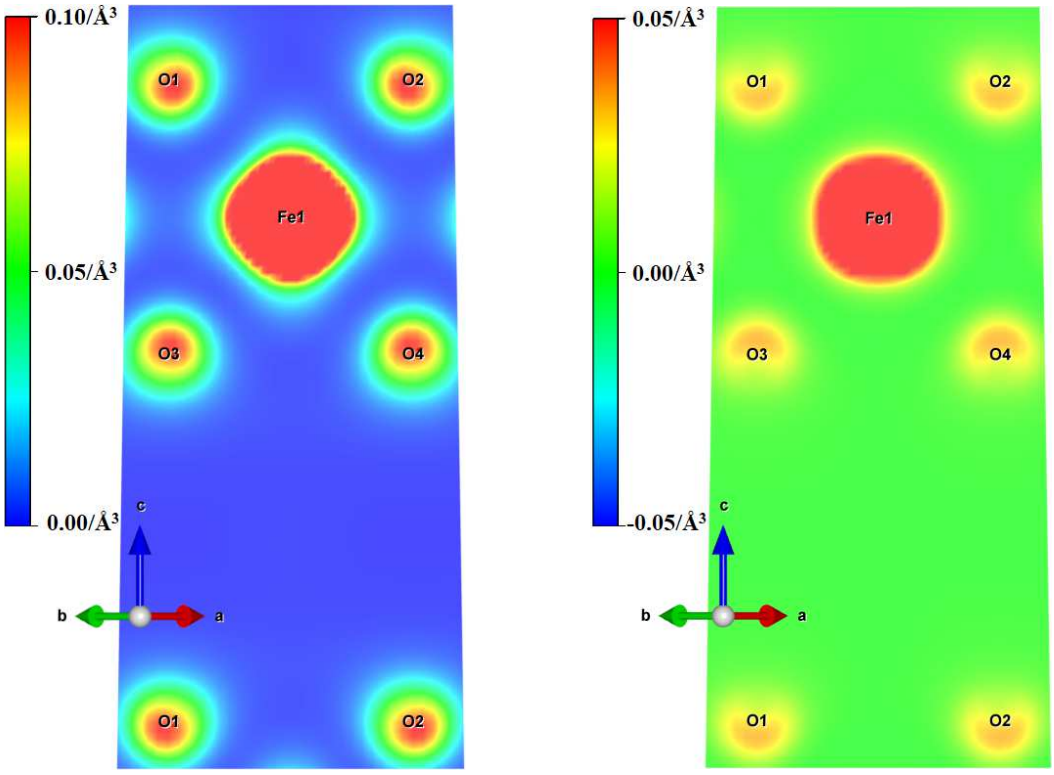

Figure 6.53: Charge density (left) and SP charge density difference (right) of the BTO221_001_2ndFe_FM for $d = 7.5$ Å across plane A', calculated for E-$E_F \in [-3.75, 0]$ eV.

Since the qualitative behaviour of each family of magnetic states is identical, as confirmed recurrently by the observation of the DOS, the charge density of each magnetic behaviour will be represented by a single value of d of the pseudo-cubic supercell in that behaviour's region.

The charge density represented in the A' and B' planes (figures 6.53 and 6.54) shows that while there is no overlap between the O and Fe orbitals, there is a considerable superposition of Fe and Ti electrons. The SP charge density difference of A' and B' planes make explicit the ferromagnetic nature of Fe ions as well as the induced magnetic moments in the TiO_2

Oxygens (parallel to Fe magnetic moment) and in the Ti atoms (antiparallel to Fe moments).

Figures 6.55 and 6.56 show the DOS of the AFM arrangement at $d = 8.2\,\text{Å}$. In this state there are the same number of DOS in the up and down spin electrons due the cancellation of Fe1 DOS with the symmetric Fe2 DOS, and to the intrinsic balanced spins in the remaining individual atoms (figures 6.57 and 6.58).

Once again, the charge density figures are an intuitive way to illustrate the results previously presented regarding the BTO221(99)_2ndFe_AFM in the perfectly antiferromagnetic regime (figure 6.59 and 6.60). It is quite interesting to see in the SP charge density difference across the A' plane that while the overall moment of the Fe atom has a well-defined spin polarization, the O atoms have a spatial sensitive spin polarization, despite their overall zero magnetic moment. The same can be seen in the B' plane but for the Ti case. The B' plane also confirms the antiferromagnetic nature of Fe atoms, seen in its perfectly symmetric spin difference.

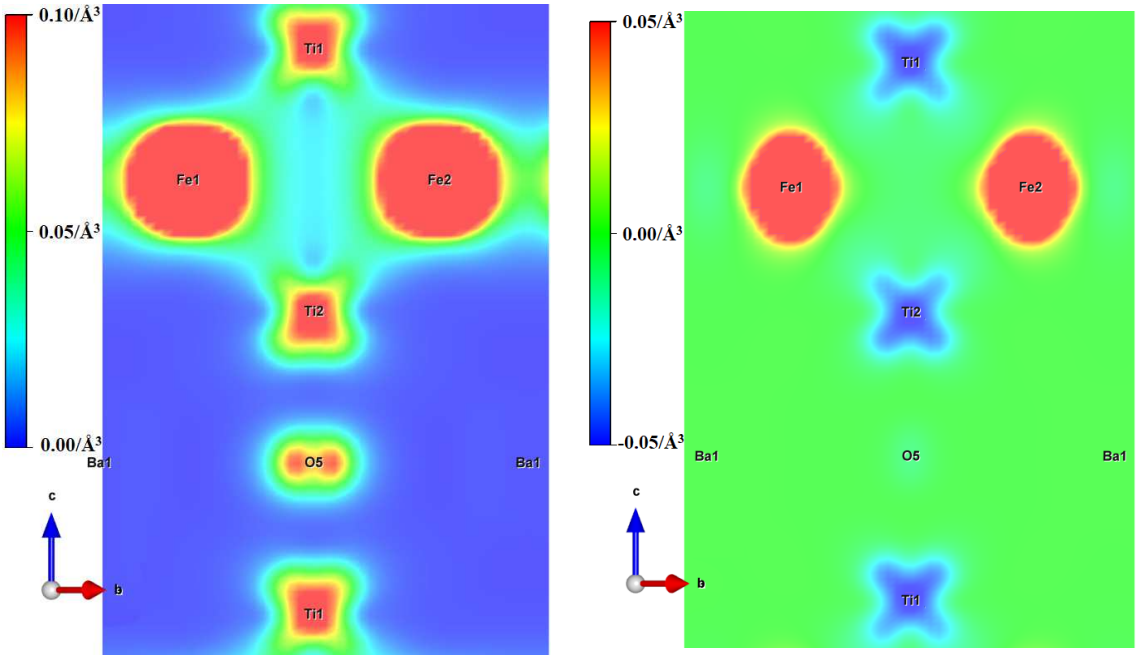

Figure 6.54: Charge density (left) and SP charge density difference (right) of the BTO221_001_2ndFe_FM for $d = 7.5\,\text{Å}$ across plane B', calculated for E-E$_\text{F}$ $\in [-3.75, 0]$ eV.

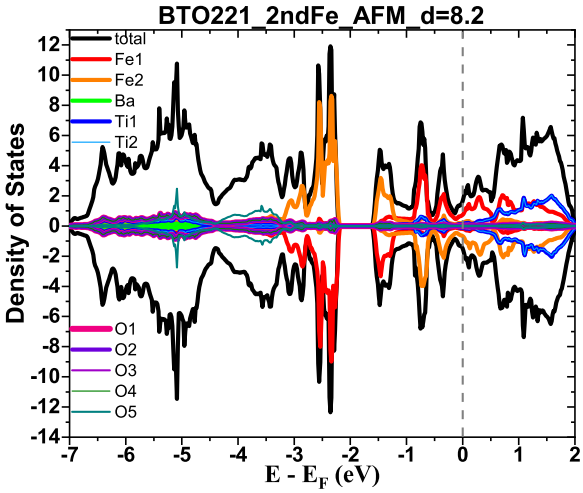

Figure 6.55: Density of states of BTO221_001_2ndFe_AFM at $d = 8.2$ Å.

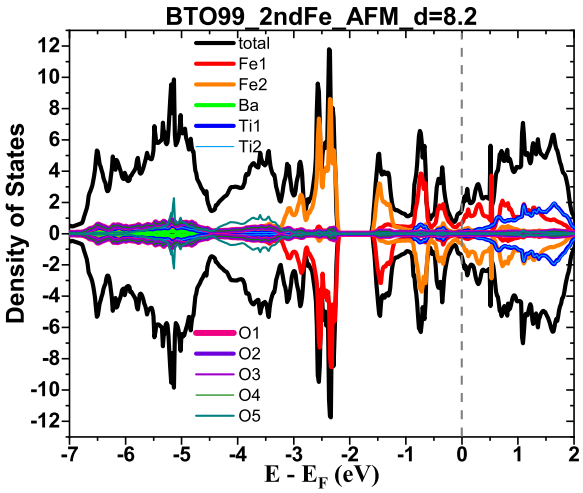

Figure 6.56: Density of states of BTO99_001_2ndFe_AFM at $d = 8.2$ Å.

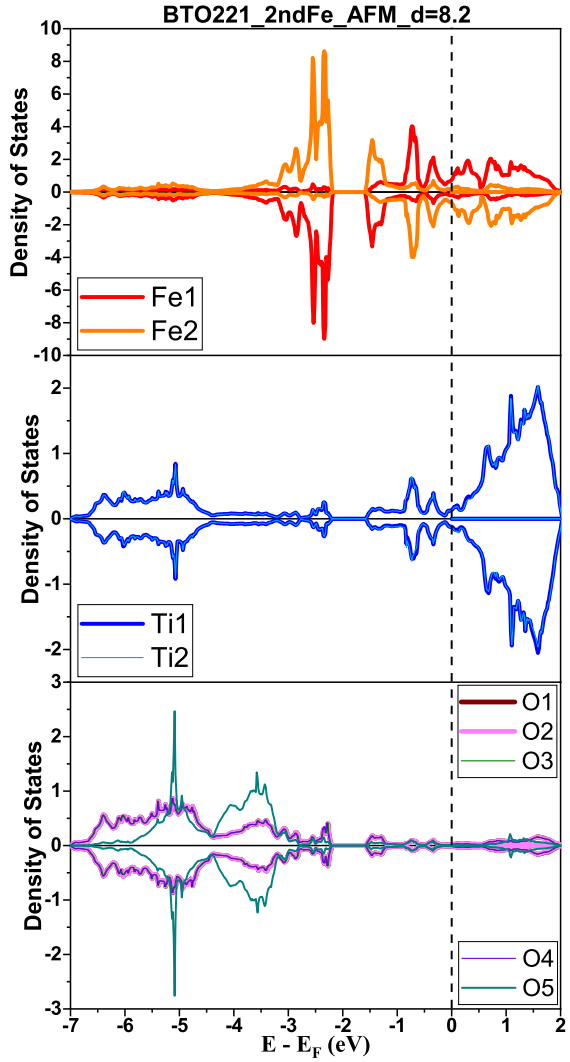

Figure 6.57: Fe, Ti and O density of states of BTO221_001_2ndFe_AFM at $d = 8.2$ Å.

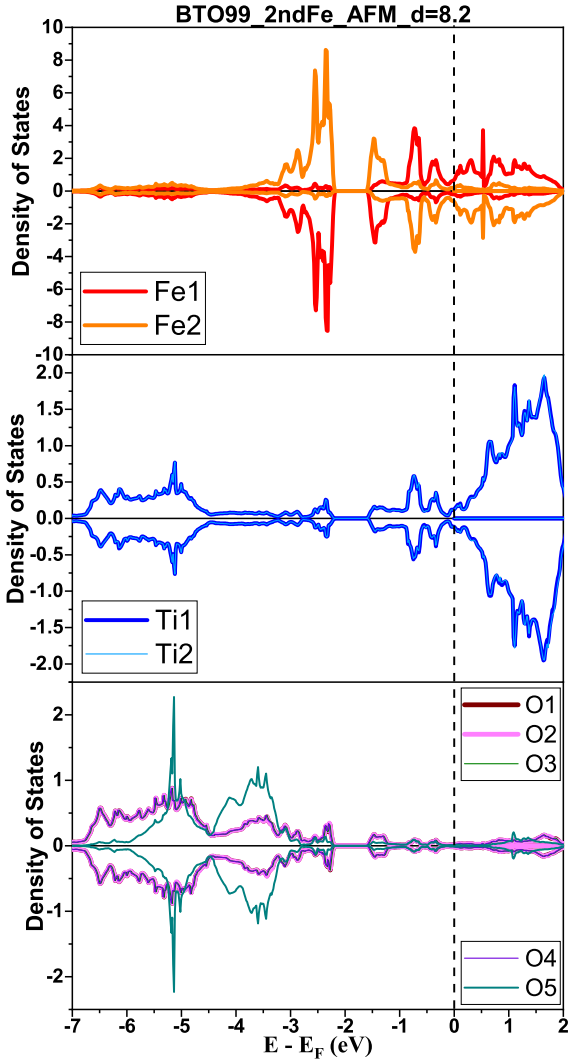

Figure 6.58: Fe, Ti and O density of states of BTO99_001_2ndFe_AFM at $d = 8.2$ Å.

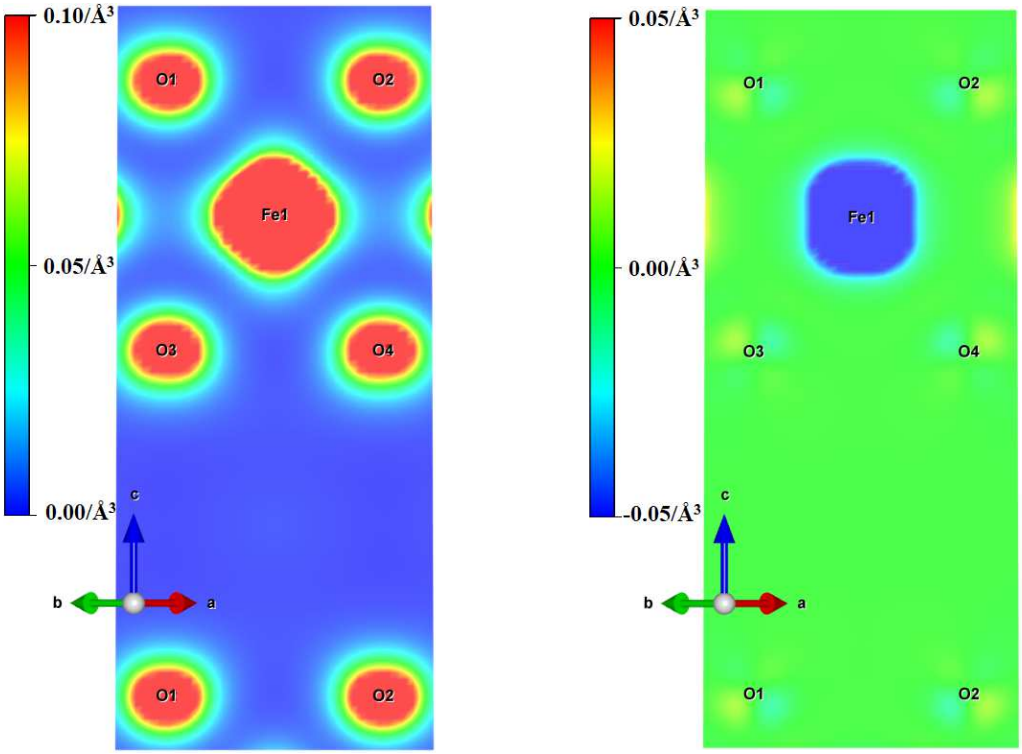

Figure 6.59: Charge density (left) and SP charge density difference (right) of the BTO221_001_2ndFe_AFM for $d = 8.1$ Å across plane A', calculated for E-E$_F$ $\in [-3.75, 0]$ eV.

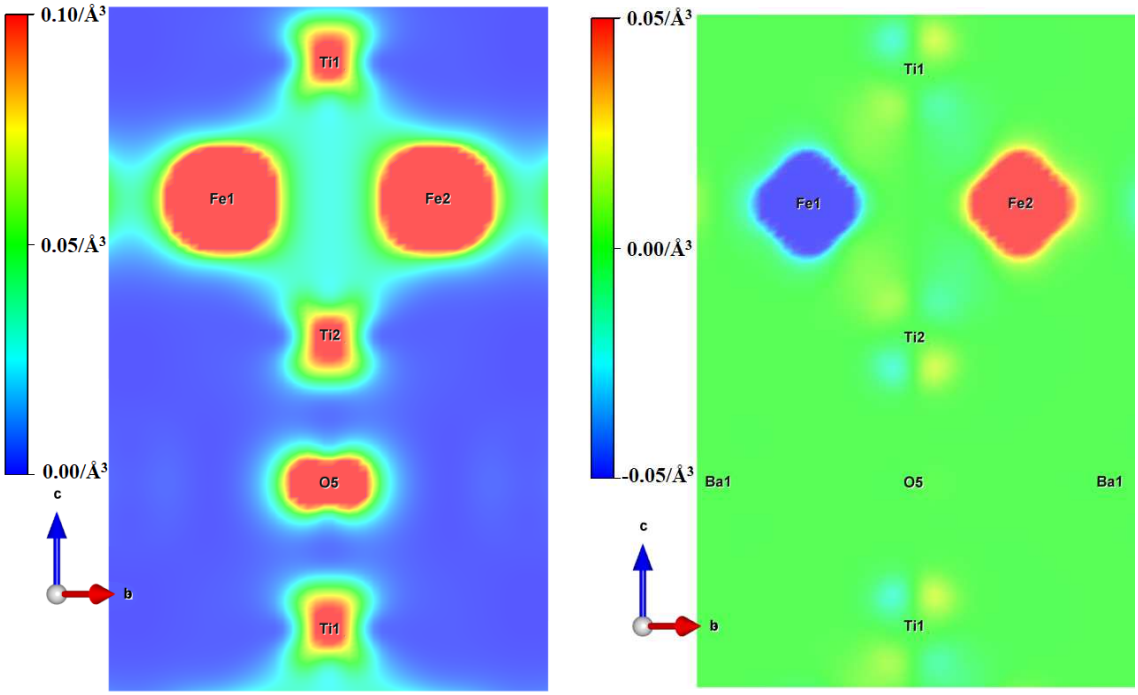

Figure 6.60: Charge density (left) and SP charge density difference (right) of the BTO221_001_2ndFe_AFM for $d = 8.1$ Å across plane B', calculated for E-E$_F$ $\in [-3.75, 0]$ eV.

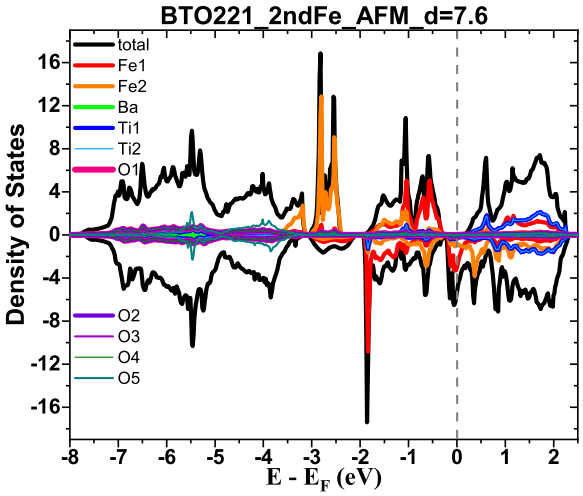

Figure 6.61: Density of states of BTO221_001_2ndFe_AFM at $d = 7.6$ Å.

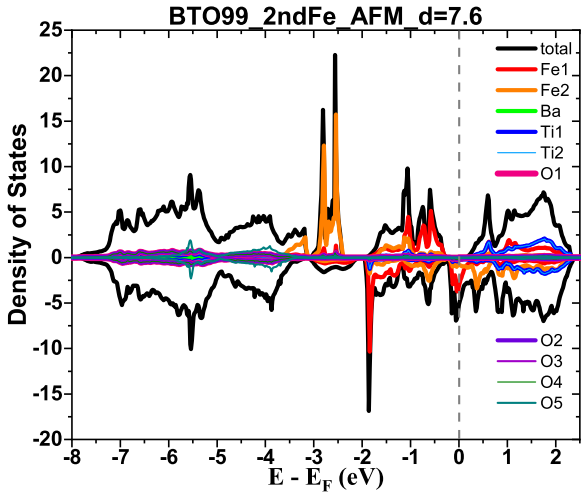

Figure 6.62: Density of states of BTO99_001_2ndFe_AFM at $d = 7.6$ Å.

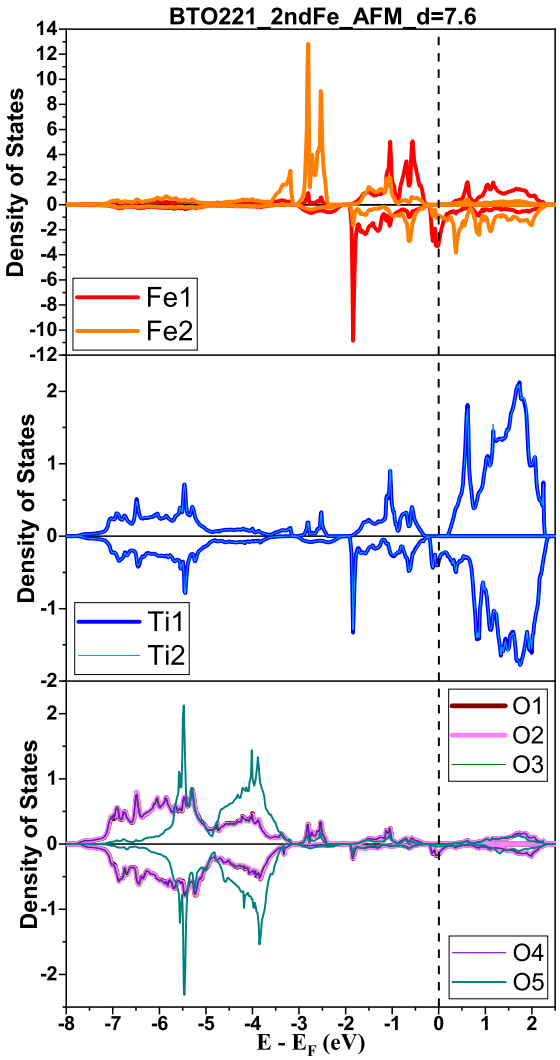

Figure 6.63: Fe, Ti and O density of states of BTO221_001_2ndFe_AFM at $d = 7.6$ Å.

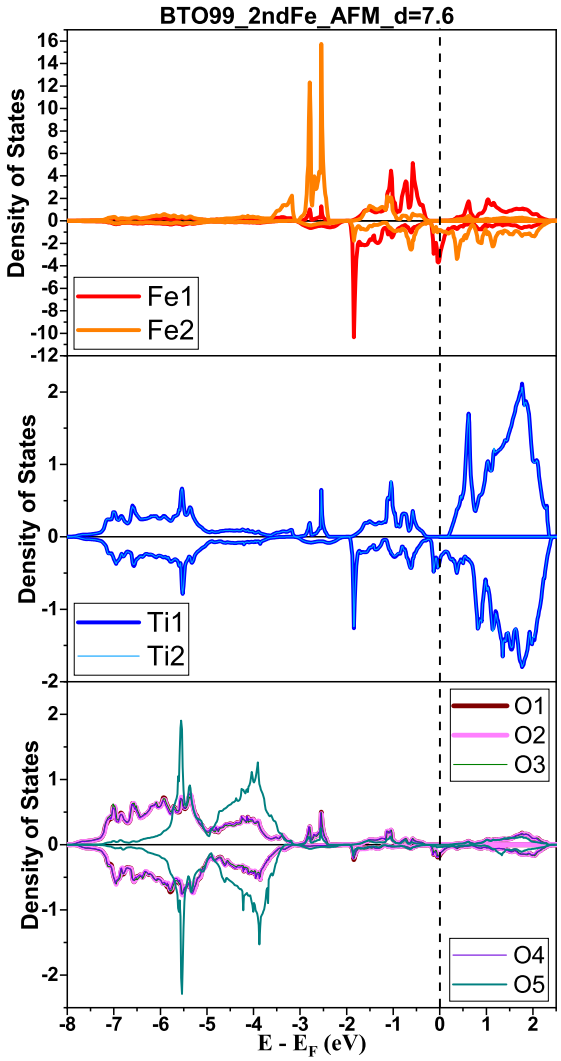

Figure 6.64: Fe, Ti and O density of states of BTO99_001_2ndFe_AFM at $d = 7.6$ Å.

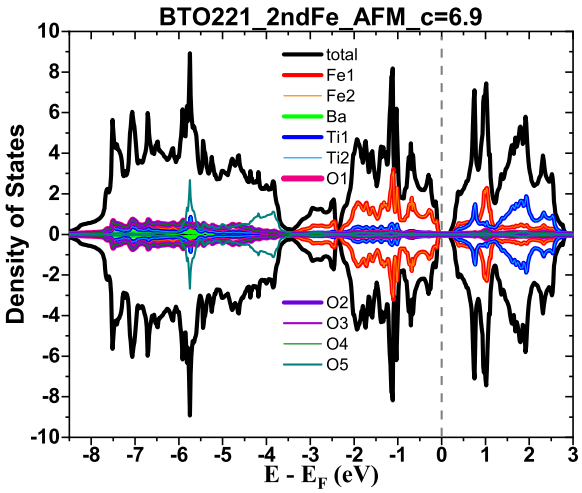

Figure 6.65: Density of states of BTO221_001_2ndFe_AFM at $d = 6.9$ Å.

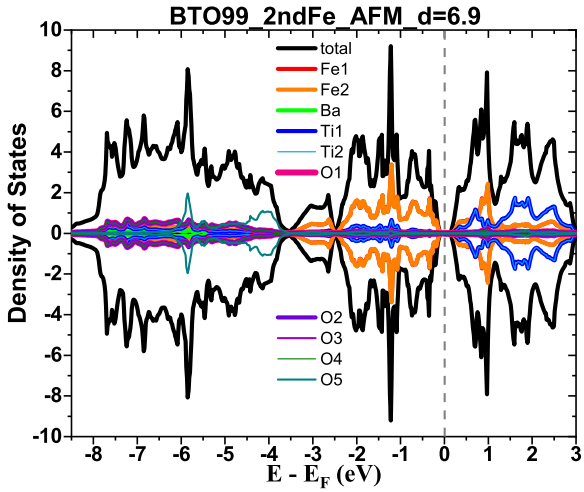

Figure 6.66: Density of states of BTO99_001_2ndFe_AFM at $d = 6.9$ Å.

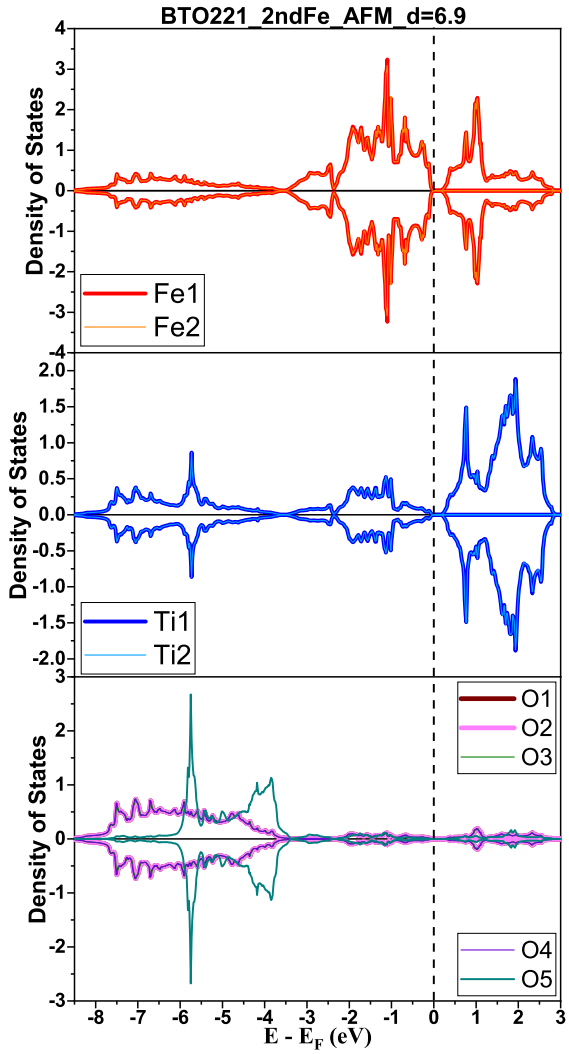

Figure 6.67: Fe, Ti and O density of states of BTO221_001_2ndFe_AFM at $d = 6.9$ Å.

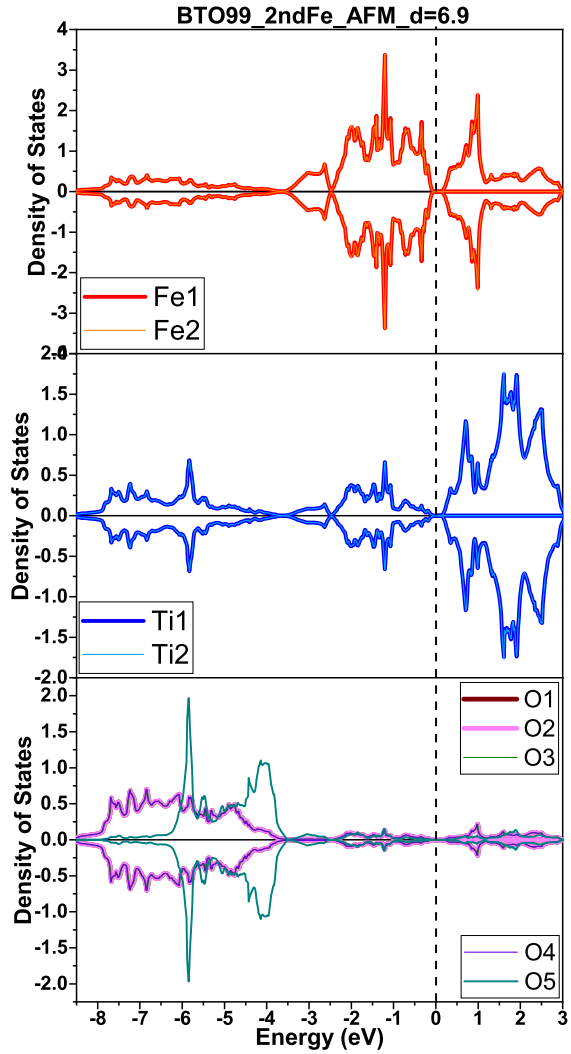

Figure 6.68: Fe, Ti and O density of states of BTO99_001_2ndFe_AFM at $d = 6.9$ Å.

The ferrimagnetic state region is represented by the DOS of figures 6.61–6.64. While the Fe1 have its up and down spin electrons almost balanced, the Fe2 atom clearly has its majority DOS in the up spin electrons, corroborating the FiM state.

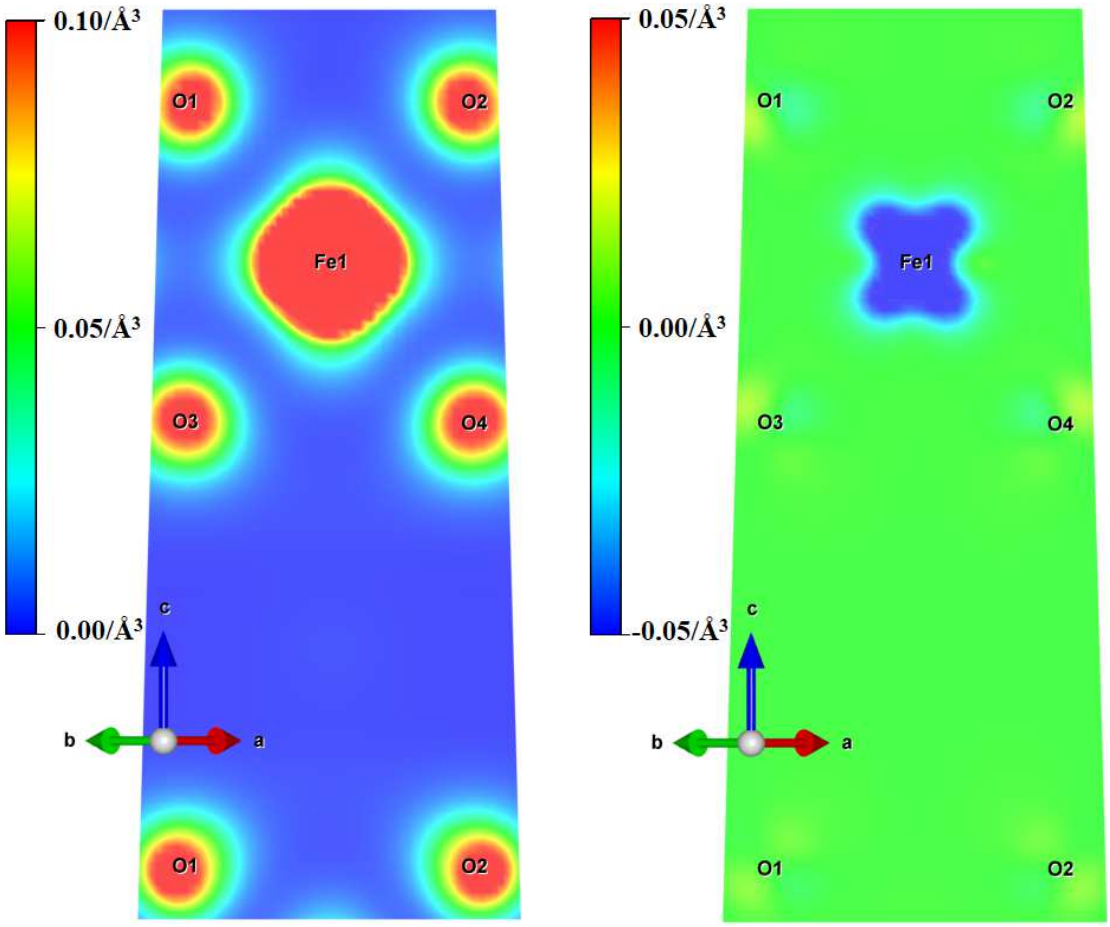

Figure 6.69: Charge density (left) and SP charge density difference (right) of the BTO221_001_2ndFe_AFM for $d = 7.5$ Å across plane A', calculated for E-$E_F \in [-3.75, 0]$ eV.

The charge density presented in figures 6.69 and 6.70 shows an asymmetric orbital hybridization between the Fe and Ti atoms across the B' plane. This is also seen in the DOS of figure 6.63 and suggests that the Ti atoms have a preponderant role in the magnetic properties of the Fe atoms.

The SP charge density difference (figures 6.69 and 6.70) shows that across the A' plane there is a superposition between the partially filled $d_{3z^2-r^2}$ and the d_{zi} orbitals[7] (where i can be either x or y). Such statement is reinforced by the vanishing of the d_{zi} orbitals when the

[7]From an atomic point of view the x and y directions are arbitrary since a=b. The "chosen" x and y directions will be defined by the neighbouring atoms.

cross section changes to the B' plane, where only the $d_{3z^2-r^2}$ is visible.

Figure 6.70 clearly shows the expected asymmetric magnitude of the opposite Fe moments, as well as a local asymmetry in the Ti atoms spin density.

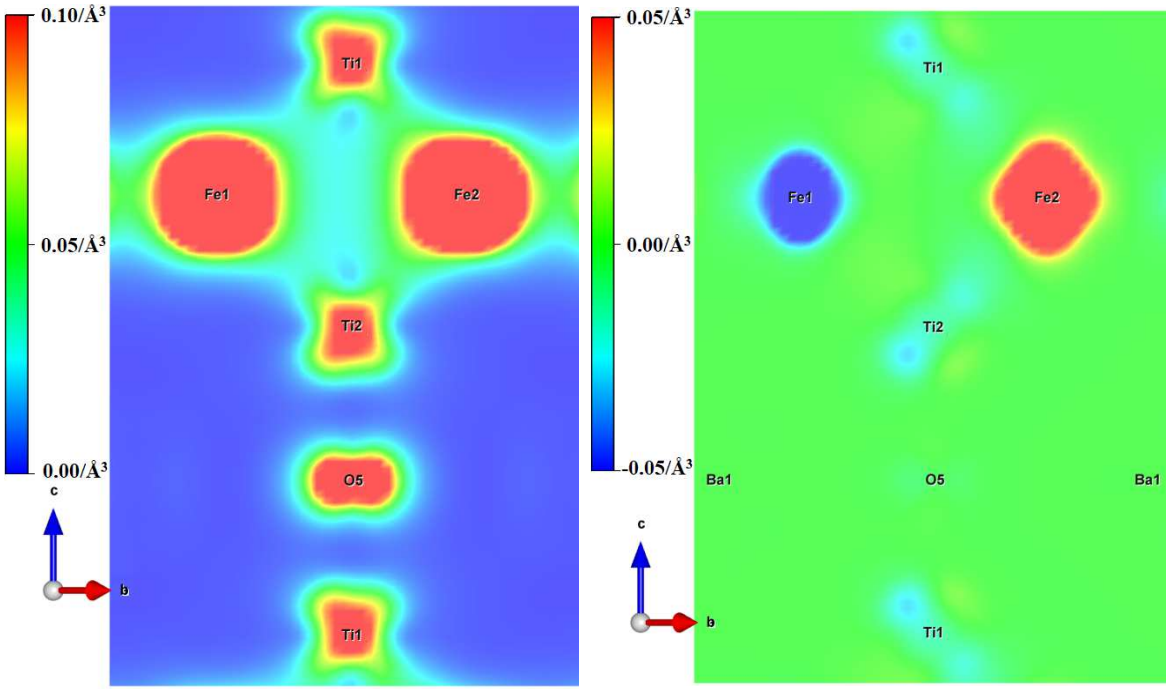

Figure 6.70: Charge density (left) and SP charge density difference (right) of the BTO221_001_2ndFe_AFM for $d = 7.5\,\text{Å}$ across plane B', calculated for E-E$_\text{F}$ $\in [-3.75, 0]\,\text{eV}$.

Finally, figures 6.65-6.68 present the DOS of the null spin state region. As it was already seen in the DOS of the BTO221_001_1stFe_AFM and BTO99_001_1stFe_FM at $d = 6.0\,\text{Å}$ (figures 6.26 and 6.35), the DOS of the BTO221(99)_001_2ndFe_AFM supercell's individual atoms at $d = 6.9\,\text{Å}$ have completely symmetric up and down spin electrons. This results in the quench of all the magnetic moments, thus the quenching of the supercell total magnetic moment. In fact, not only the DOS of this null spin state are identical when comparing the pseudo-cubic and tetragonal supercell, as they are also identical to the 1sFe monolayer when in this same magnetic state.

In the 2ndFe monolayer system, as in the 1stFe monolayer system, only the null spin state possesses a band gap (of about 200 meV), whereas the remaining magnetic states have a metallic or semimetallic nature. The charge density of figure 6.72 shows a considerable hybridization of the Ti and Fe atoms (plane B'), consonant to the DOS of figure 6.67, whereas the O electrons do not show any superposition with either the Fe or Ti electrons (figure 6.71).

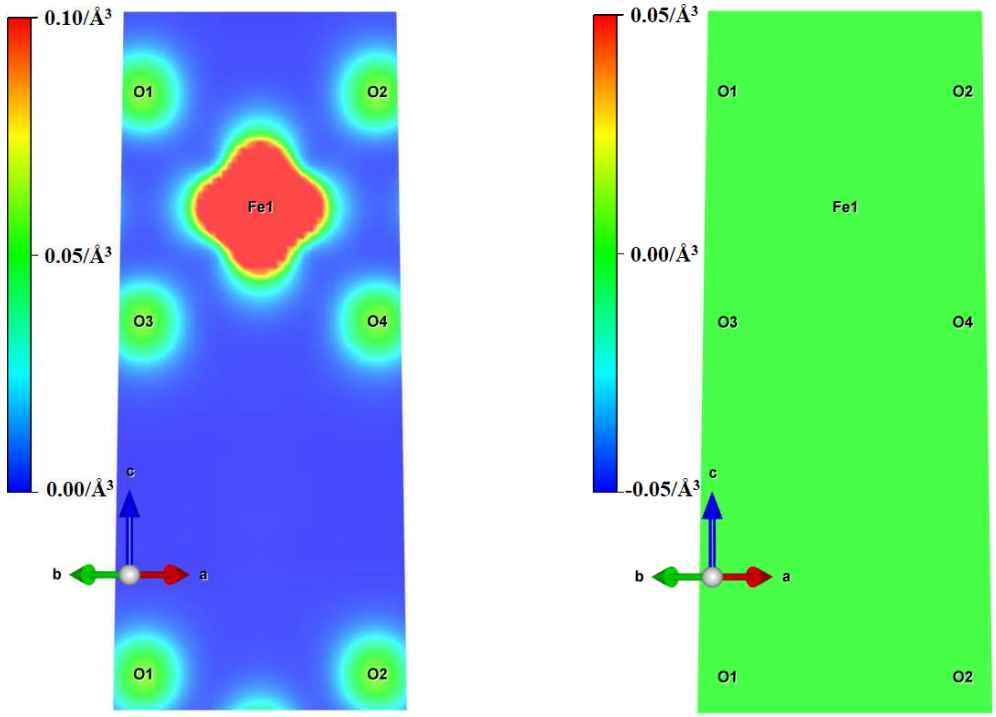

Figure 6.71: Charge density (left) and SP charge density difference (right) of the BTO221_001_2ndFe_AFM for $d = 7.1$ Å across plane A', calculated for E-$E_F \in [-3.75, 0]$ eV.

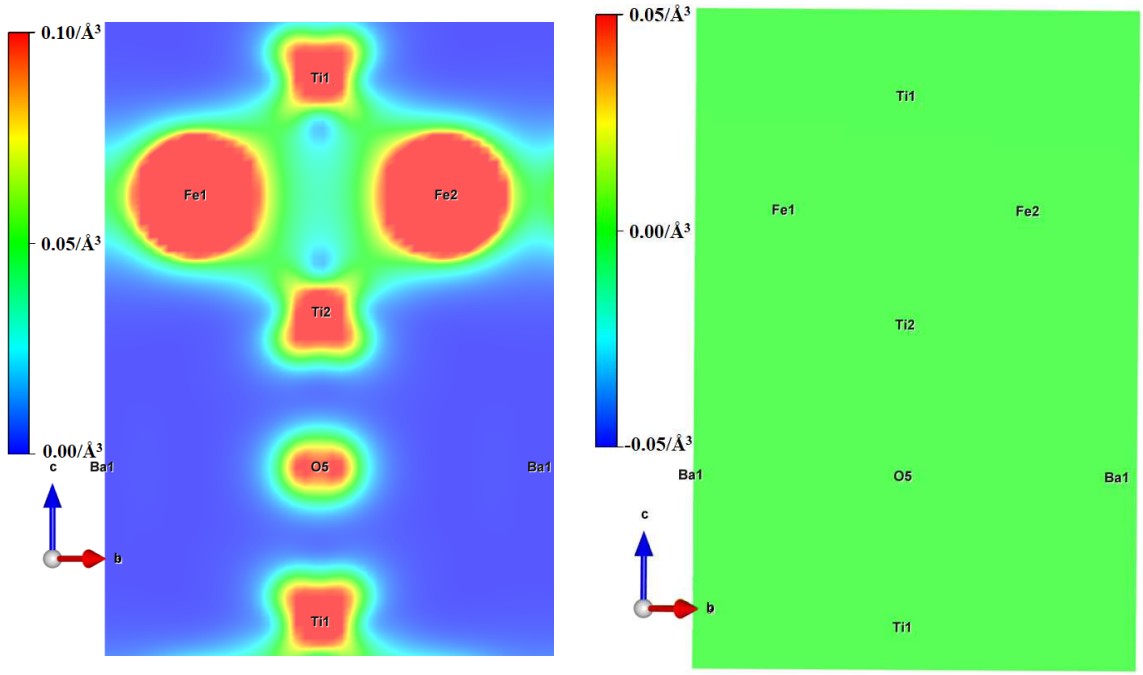

Figure 6.72: Charge density (left) and SP charge density difference (right) of the BTO221_001_2ndFe_AFM for $d = 7.1$ Å across plane B', calculated for E-$E_F \in [-3.75, 0]$ eV.

Besides the null SP charge density difference through all the unit cell, there is an interesting detail in this magnetic state. This detail has to do with the shape of the Fe electron cloud across the A' plane of figure 6.71, which as if tries to be the farthest away from O electron cloud. This also occurs in the other magnetic states, but it is not as evident as in this particular case. This gives some hints about the strength of the O electrons' electric field felt by the Fe atom.

6.1.3 High-spin–Null-spin phase transition

As it was described in the text above, the interface of BTO and Fe can give rise to several different magnetic behaviours, yet, it is the magnetic moment quenching of the individual atoms that is the most astonishing one. This kind of spin state transition is similar to a molecular High-spin–Low-spin state transition mentioned in section 2.5.3, but here present in a solid state system.

The source of this High-spin–Low-spin state transition can be explained partially using the crystal field theory, since as shown in figure 6.71, the O electrons' electric field is strong enough to constrain the Fe orbitals, affecting their shape. Moreover, the clear hybridization between the Fe and Ti atoms (figure 6.72), ubiquitous through all calculations involving the BTO221(99)_001_2ndFe supercells, must play a crucial role in this High-spin–Low-spin state transition, since they completely change the symmetry of the crystal field felt by the Fe atoms.

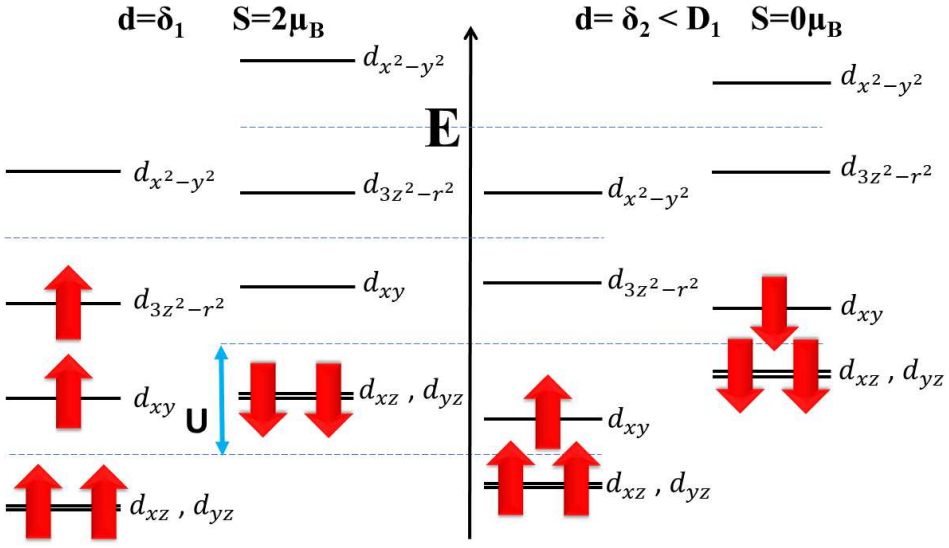

Figure 6.73: Energy diagram of the electron occupation in the d orbitals of a Fe^{2+} atom considering two different crystal fields.

Figure 6.73 shows a High-spin–Low-spin state transition which could possibly represent the one reported in this manuscript. To ensure the complete cancellation of the Fe spins, an even number of valence electrons is required, thus an even valency Fe must be involved (Fe, Fe^{2+} and Fe^{4+}). In figure 6.73 a Fe^{2+} was considered. The left part of the diagram shows a possible configuration with a crystal field which could justify the Fe magnetic moment of the FM, AFM and FiM[8] states for a given value $d = \delta_1$. Decreasing the distance d would increase the energy of the d orbitals involving the z component, while lowering the remaining d orbitals to conserve the energy centre, till the system reaches a point such as δ_2. For $d = \delta_2$ the before lower energy $d_{3z^2-r^2}$ is now in a higher energy state, hence its electron completes the occupation of d_{xy} orbital.

This explanation, despite being apparently plausible in a single atom/ion picture, is based on several naive assumptions. Firstly, although a crystal field interpretation is a good intuitive approach, there is also the possibility of sharing and exchanging electrons between atoms (with Ti for example). Moreover, the fact that we are before a solid-state system, and due to the impossibility of two electrons having the same quantum state, there will be a band like occupation of the d orbitals instead of the discrete energy diagram presented in figure 6.73.

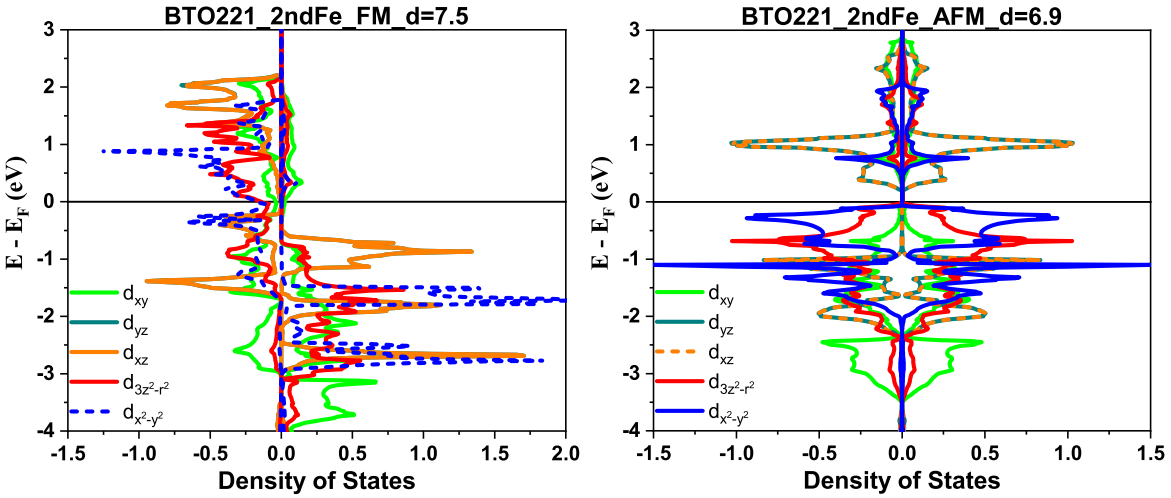

Figure 6.74: Density of states of each d orbitals of Fe2 atom for the BTO221_001_2ndFe supercell in the high-spin state (left) and in the null-spin state (right).

Figure 6.74 shows the actual d orbital occupation for the Fe2 atom (which is the same as in Fe1 for these two particular cases). It is possible to see that for the null spin case there is indeed degeneracy in the t_{2g} orbitals involving the z axis, whereas for the high spin

[8]In this case I am considering the Fe with higher magnetic moment

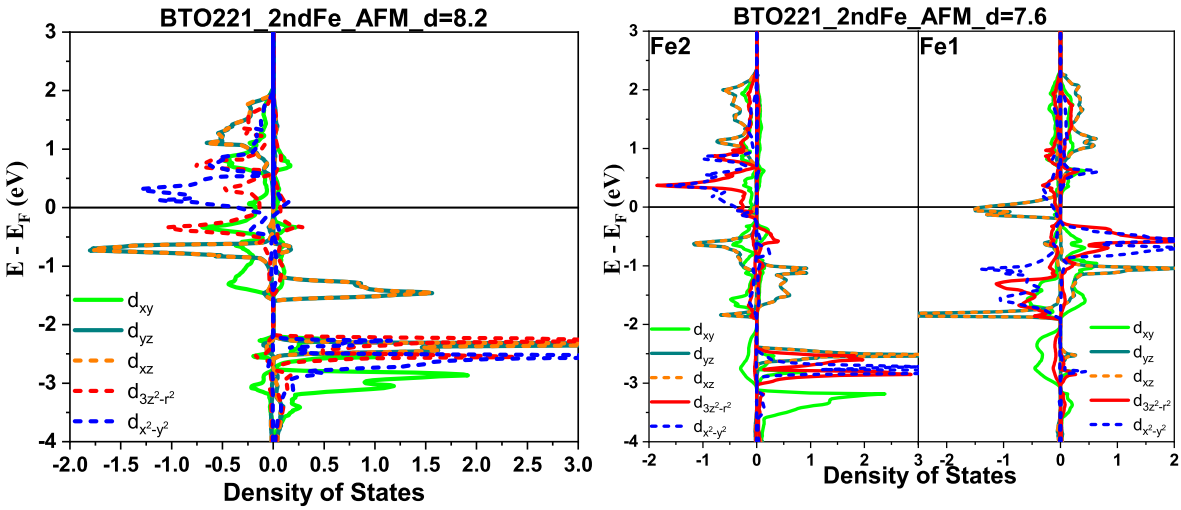

Figure 6.75: Density of states of each d orbitals of Fe2 atom for the BTO221_001_2ndFe supercell in the high-spin antiferromagnetic state (left) and in the ferrimagnetic state (right). For the FiM state the Fe1 DOS are also presented.

state there is no orbital degeneracy. The remaining magnetic states from the remaining AFM branch family have their d orbital DOS represented in figure 6.75 and also show the energy degeneracy of the t_{2g} orbitals involving the z axis.

The observation of the DOS of figures 6.74 and 6.75 also exposes other weakness in the reasoning associated with the single ion crystal field picture of figure 6.73, since the in latter is assumed that a gradual decrease in the distance d would gradually raise the orbitals involving the z axis while lowering the others, yet the lower energy t_{2g} orbitals of Fe2 in the AFM state actually lower their energy in the FiM state. The Fe1 atom, in other hand, has its t_{2g} orbitals raised, obtaining an overall DOS shape which reminds a primordial DOS on the verge of collapsing in the null-spin state.

Another assumption which is too simple is the unchanging pairing energy, U, which as it can be seen can change drastically from a band point of view, due to the d orbitals shape constrains which arise from the electrons of the neighbouring atoms, and mainly due to the new vacant occupations from the ensemble of adjacent d orbitals.

In sum, description of the magnetic moment quenching is evidently too complex to use only the single atom crystal field approach, however this description is a good mental image which in fact is close to the real physical mechanism in qualitative terms.

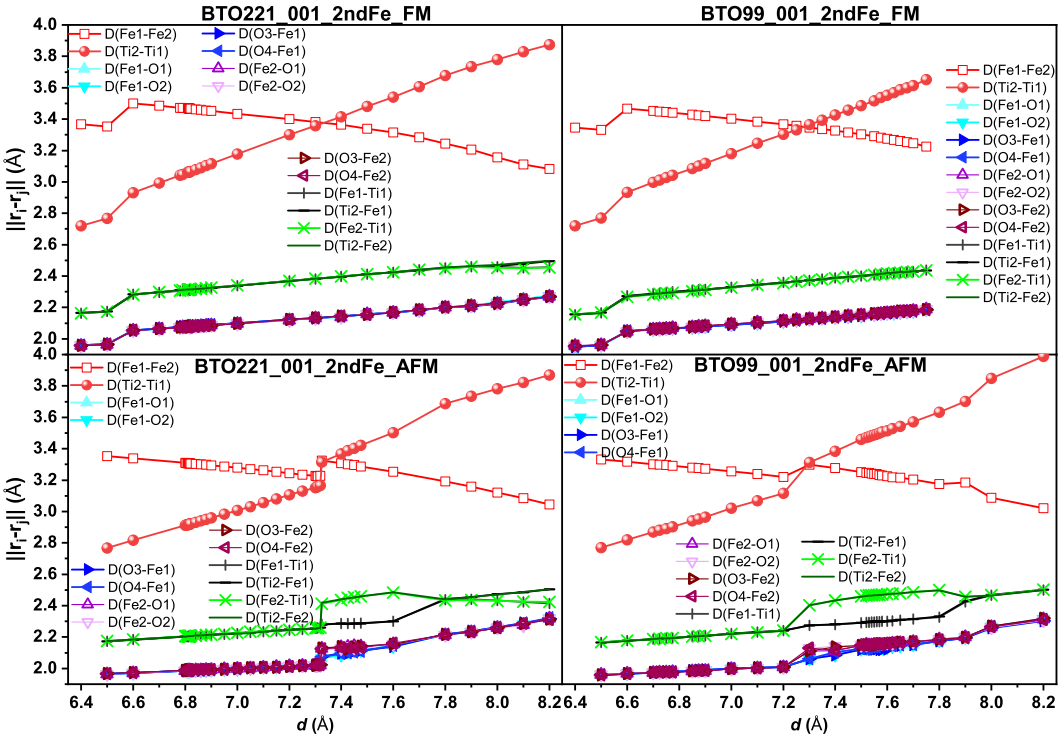

Figure 6.76: Distances between the atoms of the TiO_2 layers and the Fe atoms of each of the BTO221(99)_001_2ndFe supercells.

Once it is now evident that the Fe neighbouring atoms are crucial to understand this new paradigm, the distances between the atoms of the TiO_2 layers and the Fe atoms of the 2ndFe termination are presented in figure 6.76.

It is clear that for the Ferromagnetic input arrangements, the distances have smooth monotonous curves, however when the FM state quenches, there is an abrupt change in the distances here presented.

Note that the distance D(Ti2-Ti1) can be seen as the height of the Fe monolayer, c_{Fe}, and d-D(Ti2-Ti1) the height of the of the BTO unit cell for the correspondent distance d, c_{BTO}. This reinforces the idea that Fe orbitals are filled in a completely unique way where there is the magnetic quench, in such a way that the spatial size of the Fe monolayer suffers an abrupt change.

In the AFM input arrangements the distance curves presented in figure 6.76 have always a perturbation in its slope wherever there is a change in magnetic state, yet when the magnetic moments reach the null spin state this change is more perceptible. Furthermore, the Ti–Fe distances have a bifurcation in the beginning of the FiM state, in line with the asymmetric

hybridization shown in figure 6.54.

Additionally, as a means of comparison, the distances between the atoms of the TiO_2 layers and the Fe atoms of the 1stFe monolayer system are presented in figure 6.77.

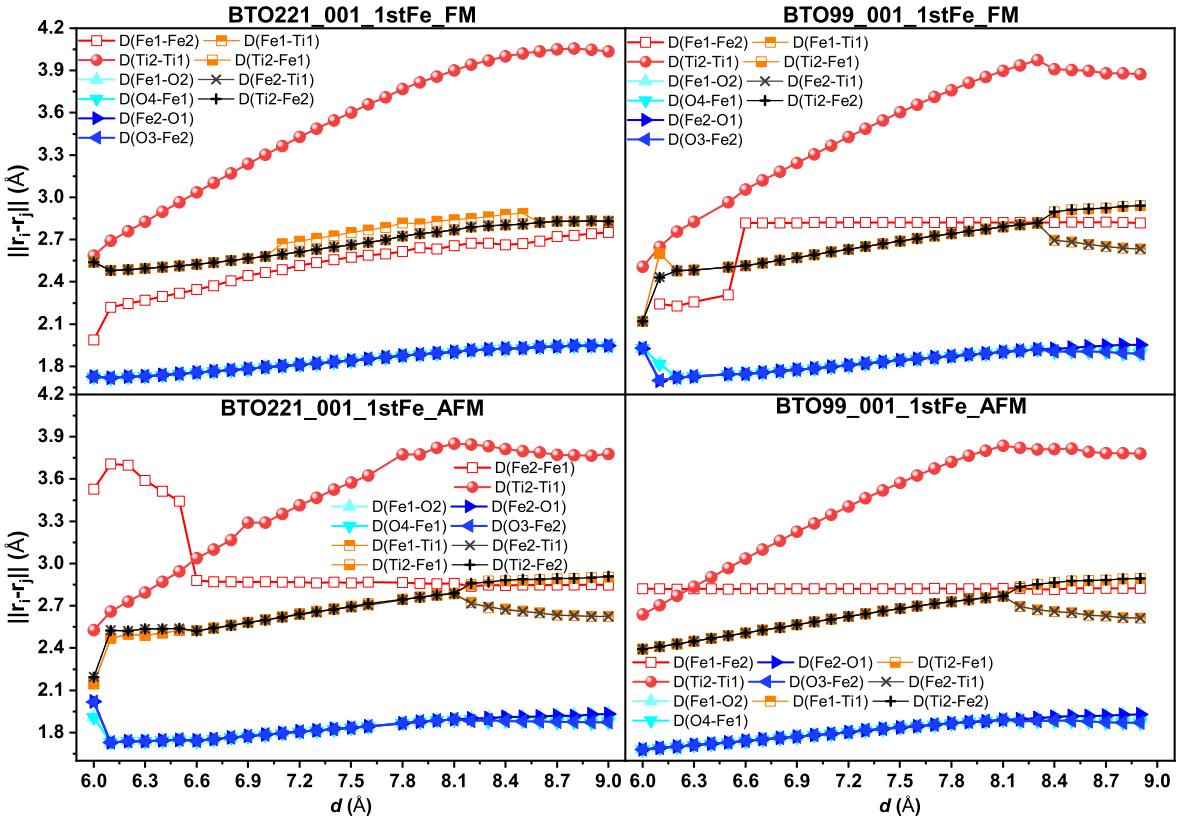

Figure 6.77: Distances between the atoms of the TiO_2 layers and the Fe atoms of each of the BTO221(99)_001_1stFe supercells.

The distance curves are also monotonous, except in the transition between the 1stFe and the 2ndFe monolayer systems, where the distances between the Fe atoms change drastically. The value of c_{Fe} changes quite smoothly here, which is explained by the different fractional coordinates of the Fe neighbours. This results in different occupied d orbitals in the 1stFe monolayer system, closer to the orbitals occupied in the null-spin state, thus a smoother change in its size along the z axis.

Crystal Field effect in Hyperfine Interactions

Given the here discussed crystal field theory philosophy, it is only natural to study the effect of the different magnetic states in the electric field gradient and hyperfine magnetic

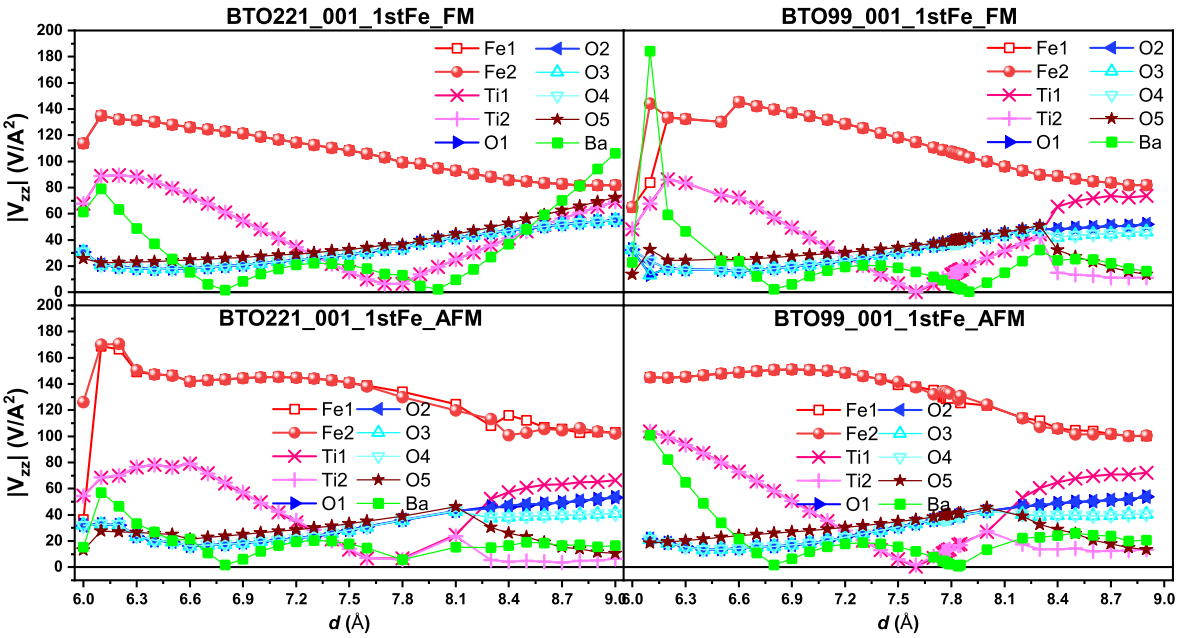

Figure 6.78: V_{zz} component of the EFG felt by each atom of the BTO221(99)_001_1stFe supercell.

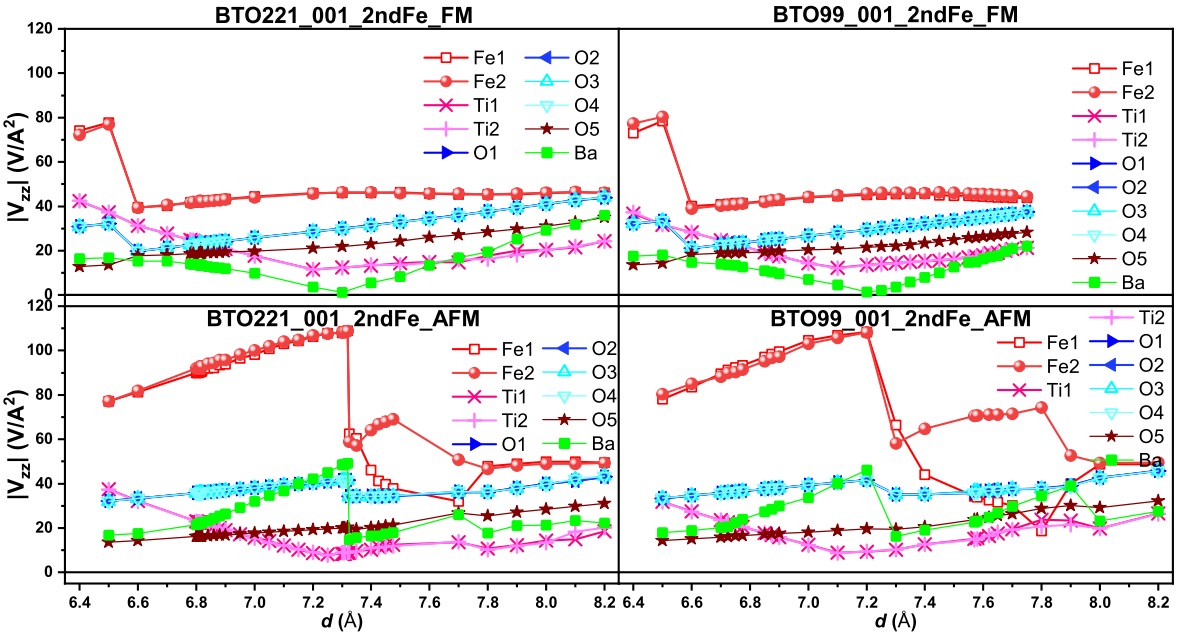

Figure 6.79: V_{zz} component of the EFG felt by each atom of the BTO221(99)_001_2ndFe supercell.

field felt by the different atoms of the considered supercells. Figures 6.78 and 6.79 show the V_{zz} component of the EFG felt by each atom, which is a measurable quantity using hyperfine

techniques such as PAC spectroscopy[9].

The EFG values for the 1stFe monolayer system (figure 6.78) show that for the same magnetic states, the V_{zz} values, like in the distances case, change quite smoothly. Actually these values present some of the quirkiness's also seen in the distances plots (figure 6.77). Nevertheless, the substantial changes in the values of the EFG are clearly seen when there is the magnetic moment quench (mainly for the Fe atoms case).

Figure 6.79 shows the EFG values for the 2ndFe monolayer system. Here it is possible to see that Fe V_{zz} is quite sensitive to the magnetic state of the Fe atoms, being possible to spot where the AFM-FiM transitions occur, as well as where there is the magnetic moment quench (the latter resulting in an increase to twice the Fe atoms V_{zz} value when decreasing d). This conclusion points to the fact that hyperfine studies may be a quite valid approach to study and explore the magnetic moments quenching in alike heterostructures.

Hyperfine magnetic field calculations of the BTO221(99)_001_2ndFe supercells for each magnetic state were also carried out using particular values of d. To perform the hyperfine magnetic field calculations, the L/AWP+lo [(Linearized) augmented plane wave method plus local orbitals] method was used as implemented in WIEN2K code, version 17 [228]. The calculations used the GGA-PBE exchange-correlation approximation, the reciprocal space integrations used at least 200 k-points in the full Brillouin zone, and the basis set size was set by the parameter $R_{mt}K_{max} = 7$, where R_{mt} is the muffin-tin radius of the smallest sphere and K_{max} is the maximum wave number. The following magnetic hyperfine field contributions were calculated: Fermi contact term (spin electron density at the nucleus), and the on-site orbital and spin dipole moment interactions [229]. Spin-orbit was included in the calculations, calculated from the scalar-relativistic result with a second-variational procedure, with the magnetization along [001].

The hyperfine magnetic fields in each atom site are summarized in table 6.1. As expected, the hyperfine magnetic field of the Null-spin state is zero.

For the FM state, in both the pseudo-cubic and tetragonal supercells, the hyperfine magnetic field felt by each Fe atom is the largest of all predicted magnetic states, and as expected $B_{hmf}(\text{Fe1}) \approx B_{hmf}(\text{Fe2})$. Its value is somewhere between the B_{hmf} of metallic Fe (33 T at 293K [230, 231]) and the B_{hmf} of Fe_3O_4 (45 and 49 T for each Fe valency at 300K [230, 232]),

[9]The reason why its shown $|V_{zz}|$ is due to the fact that this is what is measured in PAC spectroscopy, which cannot distinguish between the positive and negative values of V_{zz}.

		Hyperfine Magnetic Field (T)										
Supercell	**d (A)**	**Fe1**	**Fe2**	**Ba**	**Ti1**	**Ti2**	**O1**	**O2**	**O3**	**O4**	**O5**	**State**
BTO221_001_2ndFe_AFM	6.9	0.0	0.0	0.0	0.0	0.0	0.0	0.0	0.0	0.0	0.0	**NS**
	7.6	6.0	-24.8	0.2	0.3	0.4	0.1	0.4	0.1	0.0	0.3	**FiM**
	8.2	15.6	-17.1	-0.1	0.1	-0.1	0.0	0.0	0.0	0.0	0.0	**AFM**
BTO221_001_2ndFe_FM	7.5	-27.8	-27.7	5.1	-2.1	-2.0	4.5	4.5	4.5	4.5	-1.0	**FM**
BTO99_001_2ndFe_AFM	6.9	0.0	0.0	0.0	0.0	0.0	0.0	0.0	0.0	0.0	0.0	**NS**
	7.6	4.4	-25.2	0.3	0.5	0.5	-0.2	0.2	0.3	-0.1	0.3	**FiM**
	8.2	15.6	-15.8	0.1	0.0	-0.1	0.0	0.0	0.0	0.0	0.0	**AFM**
BTO99_001_ndFe_FM	7.5	-36.7	-37.0	1.7	-3.1	-3.1	3.0	2.9	3.0	2.9	-1.3	**FM**

Table 6.1: Hyperfine magnetic fields at representative points of each magnetic state of the BTO221(99)_001_2ndFe supercells.

closer to the metallic Fe.

The FiM and AFM states have hyperfine magnetic fields lower than the B_{hmf} of metallic Fe. In the perfect AFM state $B_{\mathrm{hmf}}(\mathrm{Fe1}) \approx -B_{\mathrm{hmf}}(\mathrm{Fe2})$, while in the FiM state $B_{\mathrm{hmf}}(\mathrm{Fe1}) < B_{\mathrm{hmf}}(\mathrm{Fe2})$.

Similarly to the EFG, the hyperfine magnetic field is a physical quantity which can be used to explore the behaviour of BTO/Fe heterostrucures, namely using Mössbauer spectroscopy, since Fe hyperfine magnetic fields of each predicted states are quite different.

Nanoengineering towards a switchable spin state multiferroic

The above mentioned High-spin–Null-spin phase transition is a very appealing phenomenon from a technological point of view. Furthermore, this effect occurs in $BaTiO_3$/Fe heterostructure, which has been mentioned as an excellent candidate to be a magnetoelectric multiferroic. As a matter of a fact, the motivation for the DFT modelling made in this chapter was to explain the magnetoelectric coupling of chapter 5.

That said, let's focus again in the energy dependence of figures 6.41 and 6.42. For the "cubic" and tetragonal supercells there is a tipping point, δ_{C} and δ_{T} respectively, which separates the region where the FM arrangement is more energetically favourable from the part where the AFM is more favourable. Taking this into consideration, we can obtain an energy curve showing only the most favourable arrangement, as shown in figure 6.80.

Figure 6.80 also shows a drastic change in the magnetization state depending on d. As it can be seen in figure's 6.80 inset, for the tetragonal supercell, the heterostructure is in the Low (Null) Spin State ($\mathrm{M} = 0\,\mu_{\mathrm{B}}$/s.c) for $d < \delta_{\mathrm{T}} = 6.818\,$Å and is in a High Spin State ($\mathrm{M} \approx 4\,\mu_{\mathrm{B}}$/s.c.) for $d > \delta_T$, whereas for the cubic BTO the tipping point occurs at

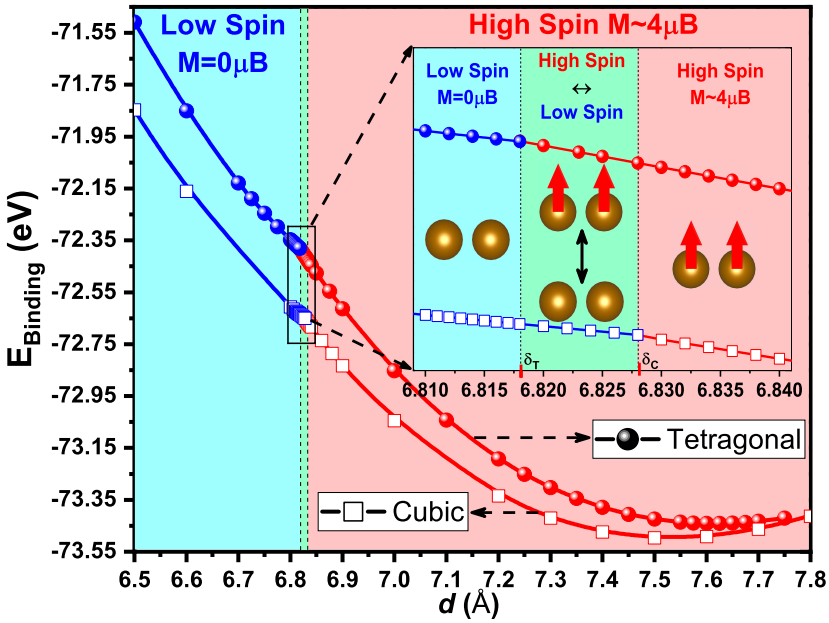

Figure 6.80: $E_{Binding}(d)$ curves and respective magnetic state for the cubic ($a = a_C$) and tetragonal ($a = a_T$) BTO_001_2ndFe supercells. Inset shows a detailed graph around the High-spin–Null-spin transition.

$d = \delta_C = 6.827\,\text{Å} \neq \delta_T$.

To tame this High-spin–Null-spin phase transition, a magnetoelectric device such as the one presented in figure 6.81 is suggested. This device consists in a heterostructure composed by an Fe monolayer deposited between two bulk crystals of $BaTiO_3$, in such a way that the Fe is deposited as in the BTO99_001_2ndFe supercell. If this heterostructure is close enough to the switching point δ_T, using external perturbations such as an electrical field, it is possible to willingly switch between the ferromagnetic high-spin state and the null-spin state.

Additionally, one can take advantage of the ferroelectric phase transitions of BTO to promote the above mentioned non-linear giant magnetoelectric effect (GME). Let's consider that the bulk part of the BTO is in its cubic paraelectric phase. It is known that the application of an electric field can induce a first order phase transition to the BTO tetragonal phase, therefore the hysteretic nature of the polarization will also induce a hysteresis in the magnetization curve. Such magnetization response to the polarization is shown illustrated in figure 6.81 and defines the extrinsic magnetoelectric coupling of the suggested device. Hence, for an electric field $E < E_1$ the bulk BTO will always be in its cubic phase therefore Fe ions will be in a null spin state. For $E > E_2$ the first order phase transition to the tetragonal ferroelectric

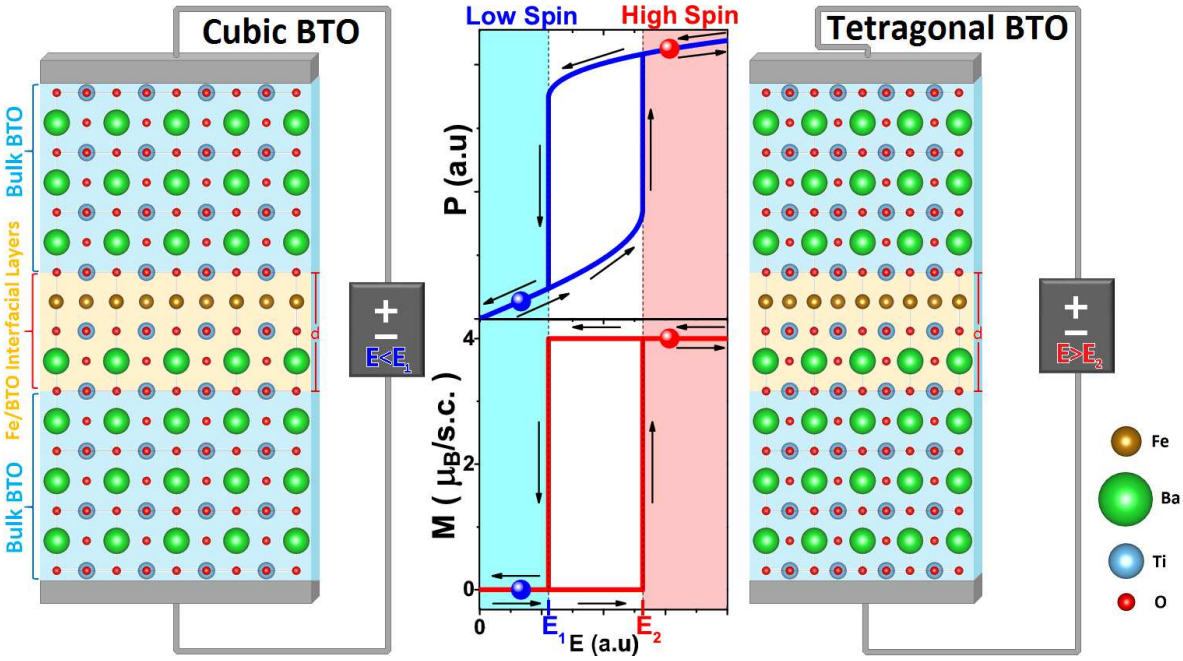

Figure 6.81: Heterostructure comprised of an Fe monolayer in a BTO matrix under an electric field E. Below the critical value E_1, the BTO structure is cubic and has a calculated Fe spin moment of zero (Left). For $E > E_2$ BTO becomes Tetragonal and the calculated Fe spin moment is $4\,\mu_B$/s.c. (Right). **(Center)** Electric field-driven magnetization response of the proposed multiferroic device.

phase of bulk BTO drives the change to the high spin state. It should should be pointed out that the polarization here shown corresponds to the bulk substrate polarization and not to the interfacial $BaTiO_3$ layers. Moreover, besides its colossal magnetization change, this extrinsic magnetoelectric multiferroic can operate well above room temperature (near BTO ferroelectric T_C).

Yet, there are some nuances to this approach involving the required initial d value, d_i. There are three possible scenarios:

In the first scenario d increases by an amount $\Delta d = |d_f - d_i|$ when BTO changes from its cubic phase to its tetragonal phase, *i.e.* $d_f > d_i$. In this situation the heterostructure must have a d_i which satisfies the condition $d_i + \Delta d > \delta_T \ \wedge \ d_i < \delta_C$, warranting a spin state transition from the null spin state to the high spin state.

In the second scenario d decreases by an amount $\Delta d > \Delta\delta = \delta_C - \delta_T$ when BTO changes from its cubic phase to its tetragonal phase, *i.e.* $d_f < d_i \ \wedge \ \Delta d > \Delta\delta$. In this situation the heterostructure must have a d_i which satisfies the condition $d_i - \Delta d < \delta_T \ \wedge \ d_i > \delta_C$,

warranting a spin state transition from the high spin state to the null spin state.

In the third and last scenario d decreases by an amount $\Delta d < \Delta\delta$ when BTO changes from its cubic phase to its tetragonal phase, *i.e.* $d_f < d_i \ \wedge \ \Delta d < \Delta\delta$. In this situation the heterostructure must have a d_i which satisfies the condition $d_i - \Delta d > \delta_{\mathrm{T}} \ \wedge \ \delta_{\mathrm{T}} < d_i < \delta_{\mathrm{C}}$, warranting a spin state transition from the high spin state to the null spin state. There is a special case of this scenario where d remains constant, *i.e.* $d_i = d_f$, thus resulting in the conditions $\delta_{\mathrm{T}} < d_i < \delta_{\mathrm{C}}$. The size of this window of values depends on the value of the lateral lattice parameters of the BTO unit cell in both cubic and tetragonal phases, as it can be inferred by observation of figure 6.82.

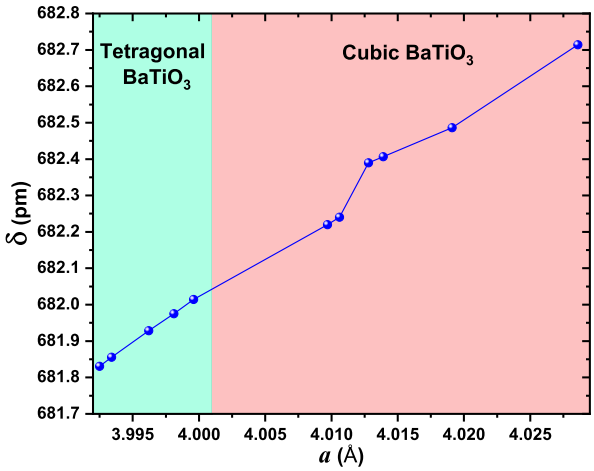

Figure 6.82: Switching distance δ as a function of the $BaTiO_3$ lateral lattice parameter, $a = b$.

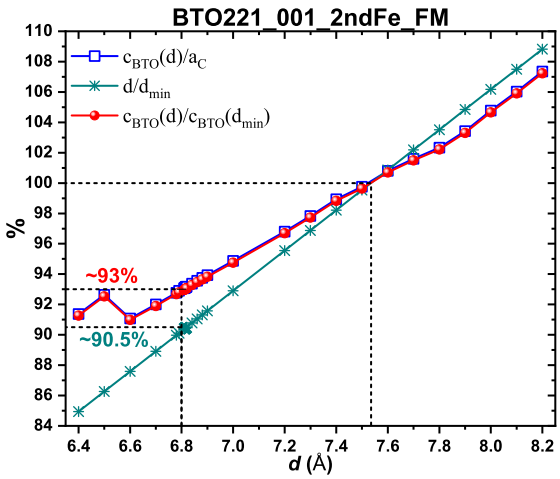

Figure 6.83: Percentages of the BTO c-axis as a function of d considering different approaches.

Another possible concern of this proposed device is how to build an heterostructure with the adequate d, close to $d = 6.8\,\text{Å}$, knowing that this value is deviated from the predicted global minimum, d_{min}. Firstly, one can follow the value of the corresponding BTO c-axis, $c_{\mathrm{BTO}} = d - c_{\mathrm{Fe}} = d - \mathrm{D(Ti2\text{-}Ti1)}$ instead of the ratio d/d_{min}. Figure 6.83 shows the percentage of c_{BTO} when comparing its experimental value to its value at d_{min} for the BTO221_001_2ndFe_FM supercell. These two values are practically the same, as it would be expected once at $d = d_{\mathrm{min}}$ the BTO unit cell should be literally cubic, having a nonlinear curve. At $d = 6.8\,\text{Å}$ the percentage of the c_{BTO} is about 93%, instead of the d/d_{min} percentage which is about 90.5%. This means that it would be necessary to compress the c_{BTO} by 7% of the thermodynamically stable c_{BTO} instead of the 9.5%.

Nevertheless, the energy curves of figure 6.80 is done assuming $\mathrm{T} = 0\,\mathrm{K}$, and does not

consider other external fields such as pressure, which can be used to help lowering the d value as well as to tune the standard BTO FE $T_C \approx 393\,K$ to a suitable working T_C. Additionally, the bulk material can be a chemical variant of the standard BTO such as $Ba_xSr_{1-x}TiO_3$ [174], since as seen in the present chapter, only the atoms of the TiO_2 layers influence the Fe magnetic moment. As a matter of fact, there is no real need to have the bulk material of BTO or any of its variants, as long as in the interface of the Fe monolayer there are the TiO_2 with the same distances and symmetries as the ones in BTO221_001_2ndFe supercell at its null-spin state. Notwithstanding, these chemical variants, as well as the addition of other dopants, can be used to create a "chemical pressure" helping to attain the desired distance d.

Finally, taking into account this ferroelectric phase induced High-spin–Low-spin switching paradigm, let's go back to the magnetoelectric coupling mentioned in chapter 5. Needless to say that both phenomena are alike, which raises the possibility of the here presented GME being be the mechanism behind the magneto electric coupling present in the BTO:Fe_{113ppm}.

In this hypothesis the grain boundaries would act as the place where the Fe would segregate forming an auto-composite which would locally look like as the BTO221_001_2ndFe supercell. Due to the possible variance in the lattice parameters, mainly in the grain boundaries, where there are several displacements and strains of the bulk unit cell, there would be some specific locations which could have the adequate conditions to replicate the interface shown in figure 6.81. For $T > T_C$ the analogous d distance would respect the first of the three possible scenarios regarding the d value, meaning that all its Fe atoms would have no magnetic moment at all. After the BTO changes to its tetragonal phase these particular atoms would switch on their moment, resulting in the abrupt change in magnetization seen in figures 5.6 and 5.9 higher temperature magnetic transition.

Chapter 7

DFT Modeling of other $BaTiO_3$/Fe interfaces

7.1 BTO38

The discovery of such interesting properties in a BTO/Fe heterostructure depending on where the Fe atoms are placed, as well as on the distances between them and the interface atoms raises questions about what will happen in interfaces involving Fe atoms and the other ferroelectric phases of $BaTiO_3$. In this line of though, using a similar approach to the BTO221(99)_001 supercells, several possible supercells were considered in an exploratory way, as a means of searching for other novel magnetic effects.

Let's begin by considering supercells comprised of an orthorhombic unit cell of $BaTiO_3$ and a monolayer of Fe. There are two possible BTO layer terminations: the BaTiO layer and an O_2 layer. The same Fe monolayers used in the tetragonal and the pseudocubic supercells were used but repeated twice – thus each supercell has four Fe atoms – due to the bigger size of the a and b lattice parameters of the orthorhombic BTO unit cell.

The 1stFe monolayer is the one where the corner Fe atoms are placed on top of the Ba atoms for the BaTiO termination (figure 7.1) and where some of its atoms are placed on top of the O atoms for the O_2 termination (7.3). On the other hand, the 2ndFe monolayer consists in a translation of 25% of the b lattice along this same axis, placing one of its atoms on top of the Ti atom for the BaTiO termination (figure 7.2) while avoid being placed on top of the O atoms for the O_2 termination (7.4).

The a and b parameters of the supercell are made fixed to the experimental values $a = 3.9874\,\text{Å}$ and $b = 5.6751\,\text{Å}$ [233]. The calculations were carried out using the same parameters used on the BTO221(99)_001 supercells calculations, but here the electronic self-consistent cycles were considered converged when the energy differences between two iterations were less than $10^{-5}\,\text{eV}$. A $5 \times 4 \times 2$ k-points grid was considered for the calculations in reciprocal space.

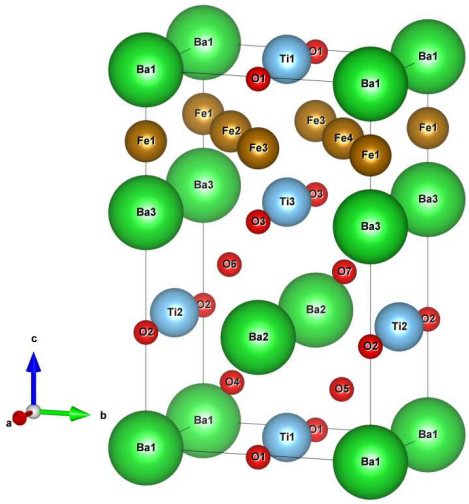

Figure 7.1: BTO38_1stFe supercell

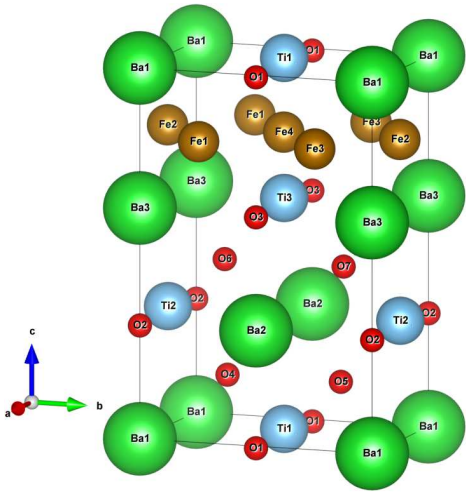

Figure 7.2: BTO38_2ndFe supercell

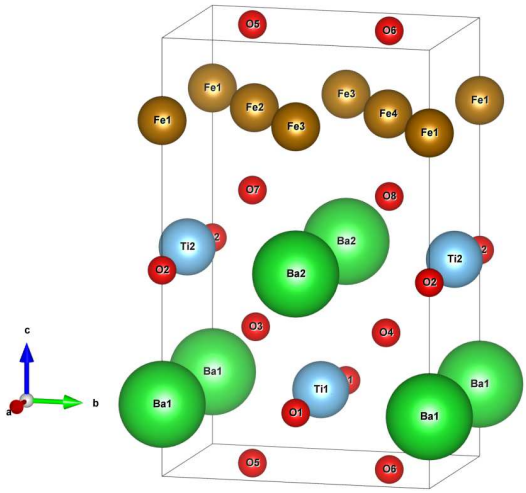

Figure 7.3: BTO38_1stFe_O2 supercell

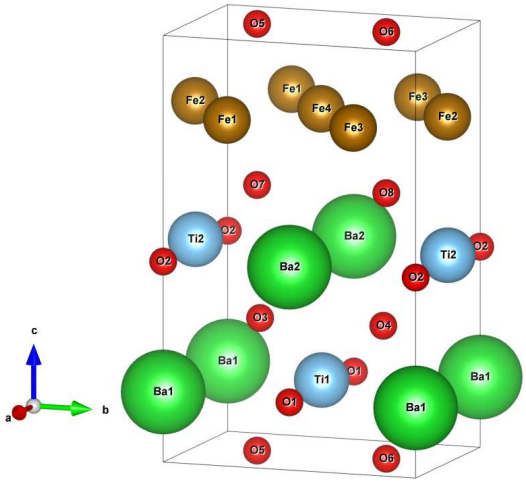

Figure 7.4: BTO38_2ndFe_O2 supercell

Ferromagnetic and antiferromagnetic initial arrangements were considered for each supercell. Since there are four Fe atoms in the supercell there are more than one possible antiferromagnetic inputs as illustrated in Figure 7.5. The AFM input arrangements here considered have the same number of up and down spins and are characterized by the sign of the

exchange interactions J_i, for i=1,2,3, where $|J_1| > |J_2|$ and $|J_3| > |J_4|$. The AFM1 arrangement considers $J_1 > 0$, $J_2 < 0$, $J_3 < 0$ and $J_4 < 0$. The AFM2 arrangement considers $J_1 < 0$, $J_2 > 0$, $J_3 < 0$ and $J_4 < 0$. The AFM3 arrangement considers $J_1 < 0$, $J_2 < 0$, $J_3 > 0$ and $J_4 > 0$. Finally, the FM arrangement considers $J_1 > 0$, $J_2 > 0$, $J_3 > 0$ and $J_4 > 0$.

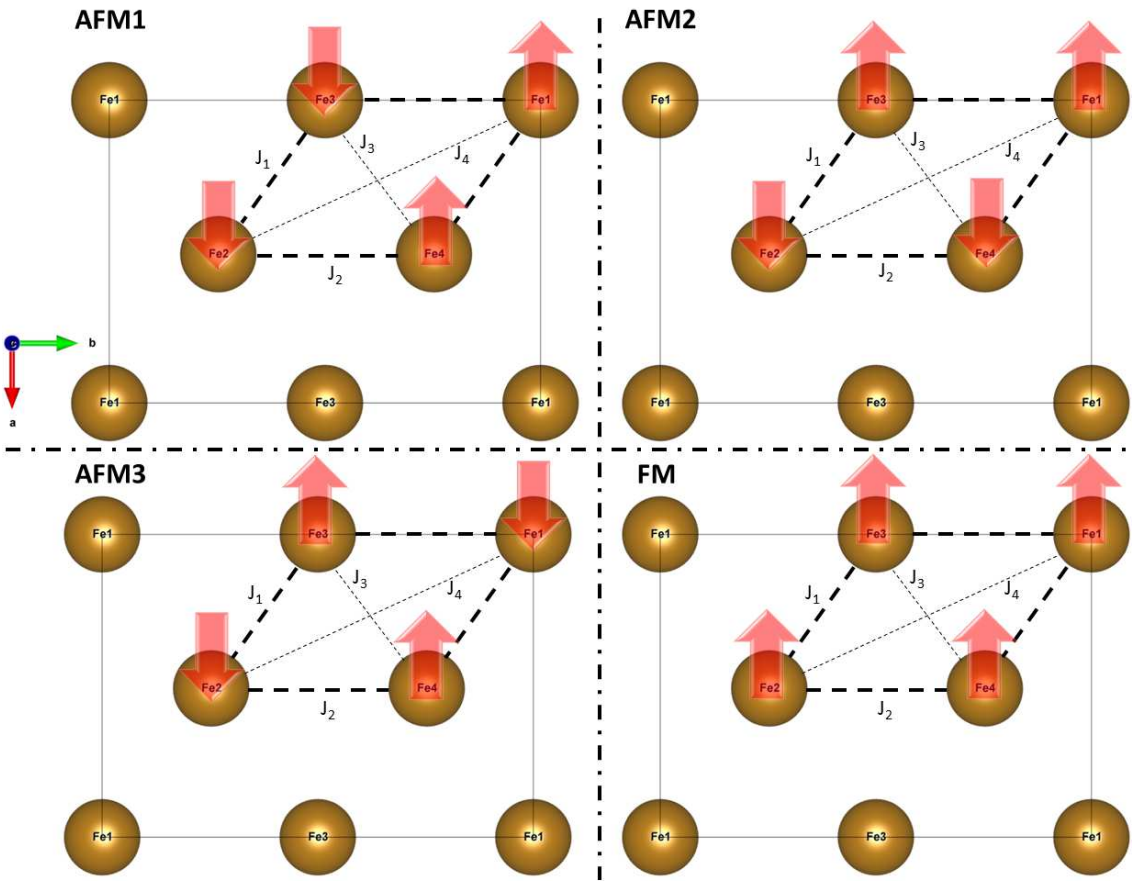

Figure 7.5: Illustration of the considered magnetic arrangements for the BTO38_1stFe supercell.

7.1.1 BTO38_1stFe

The binding energy and total magnetic moment for the BTO38_1stFe supercell (figure 7.1) are shown in figures 7.6 and 7.7.

The binding energy is defined by equation 7.1:

$$E_{\text{Binding}} = E_{\text{BTO38\_1stFe}} - (4E_{\text{Fe}} + 3E_{\text{Ba}} + 3E_{\text{Ti}} + 7E_{\text{O}}) \ , \tag{7.1}$$

where $E_{\text{BTO38\_1stFe}}$ is the energy of the BTO38_1stFe supercell.

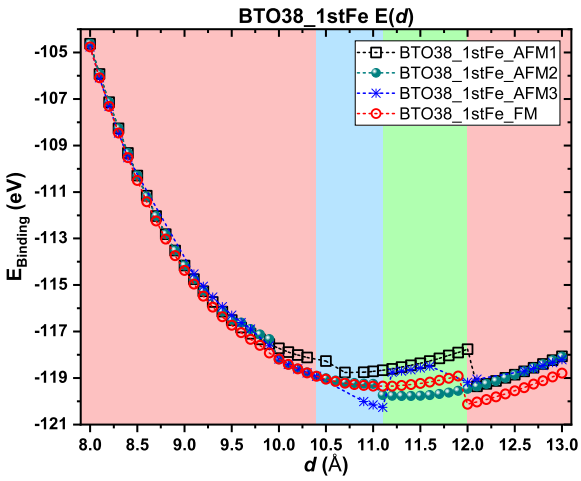

Figure 7.6: Binding energy for all the considered magnetic arrangements of the BTO38_1stFe supercell. The coloured regions indicate the most energetically favourable magnetic arrangement.

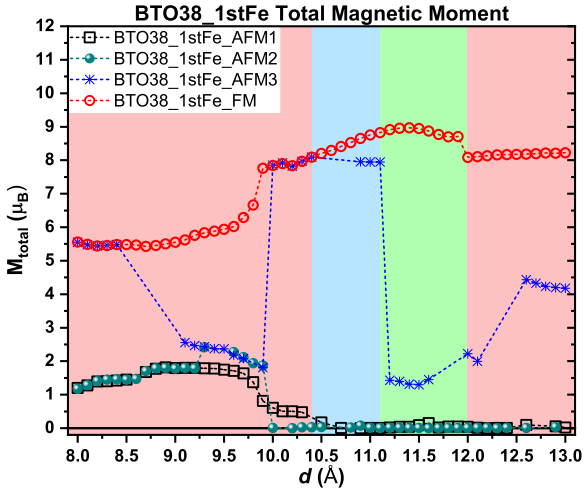

Figure 7.7: Total magnetic moment for all the considered magnetic arrangements of the BTO38_1stFe supercell. The coloured regions indicate the most energetically favourable magnetic arrangement.

The coloured regions indicate which of the magnetic arrangements is the most energetically favourable for a given value of d, this way a light gray region indicates a more stable AFM1 arrangement, a green region indicates a more stable AFM2 arrangement, a blue region indicates a more stable AFM3 arrangement, and a red region indicates a more stable FM arrangement.

Figure 7.7 shows that there are several magnetic behaviours within each magnetic arrangement curve. While the AFM1 and AFM2 arrangements remain mostly in a balanced AFM state, the AFM3 has always a non-zero total magnetic moment. The ferromagnetic arrangement has three distinct behaviours and a total magnetic moment $\text{M}_{\text{total}} \in [5.5; 9]\,\mu_{\text{B}}$. In fact these three regions are explained by the three structural changes – α, β and γ – as it can be

seen in figure 7.8[1] and table 7.1.

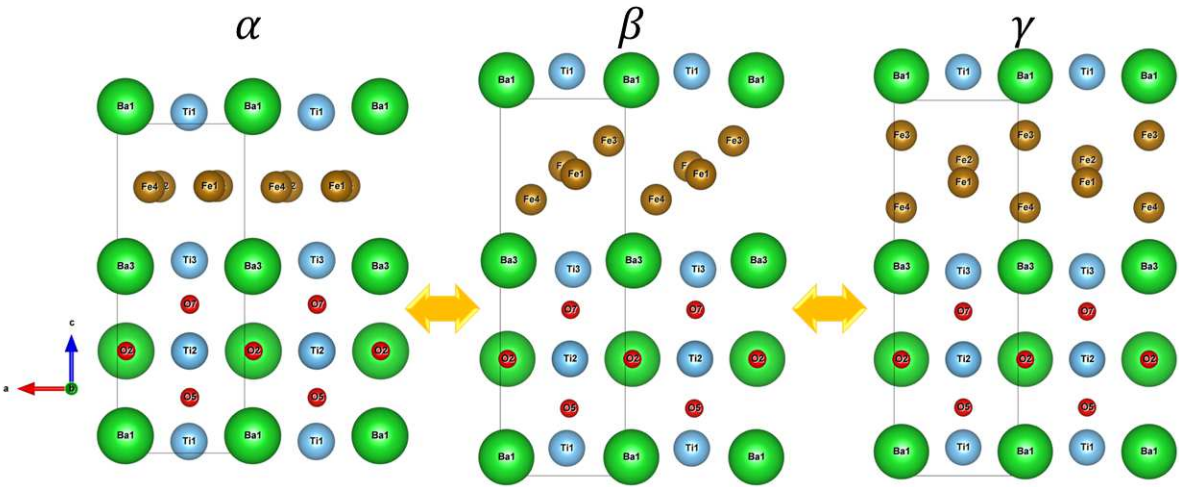

Figure 7.8: The three types of structures present in the BTO38_1stFe supercell. To illustrate these structures the relaxed structure of the BTO38_1stFe_AFM1 supercell is used for different values of d. The α structure corresponds to $d = 10.3\,\text{Å}$, the β structure to $d = 12\,\text{Å}$ and the γ structure to $d = 12.1\,\text{Å}$.

Supercell	α	β	γ
BTO38_1stFe_AFM1	$d \in [8; 10.3]$ Å	$d \in [10.4; 12]$ Å	$d \in [12.1; 13]$ Å
BTO38_1stFe_AFM2	$d \in [8; 9.9]$ Å	$d \in [10; 11.1]$ Å	$d \in [11.1; 13]$ Å
BTO38_1stFe_AFM3	$d \in [8; 9.9]$ Å	$d \in [10; 11.6]$ Å	$d \in [11.7; 13]$ Å
BTO38_1stFe_FM	$d \in [8; 9.8]$ Å	$d \in [9.9; 11.9]$ Å	$d \in [12; 13]$ Å

Table 7.1: Interval of d values for the α, β and γ structures in the BTO38_1stFe supercell.

To have a deeper understanding about the magnetic phenomena, it is useful to inspect the value of each atom magnetic moment presented in figures 7.9 and 7.10. Here it's possible to see that for $d > 10.3\,\text{Å}$ the BTO38_1stFe_AFM1 supercell's up and down magnetic moments always cancel out, whereas for $d \leq 10.3\,\text{Å}$ there is a slight unbalance in the up and down moments giving birth to a total magnetic moment which can be as high as $M_{\text{total}} \approx 2\,\mu_B$. The full range of the α, as well as the ranges of the β and γ structures are presented in table 7.1. These structures clearly influence the different behaviours of the BTO38_1stFe_AFM1, since it's in the α structure that occurs the unbalance between the up and down moments. Even though the β and γ have balanced up and down moments, their individual atom magnetic moment curves are quite different as it is possible to see in figures 7.9 and 7.10 within the

[1]The structures presented in figure 7.8 are defined qualitatively, having small differences for different values of d and for different magnetic arrangements. Apart from these small differences, each structure has approximately the same structural characteristics.

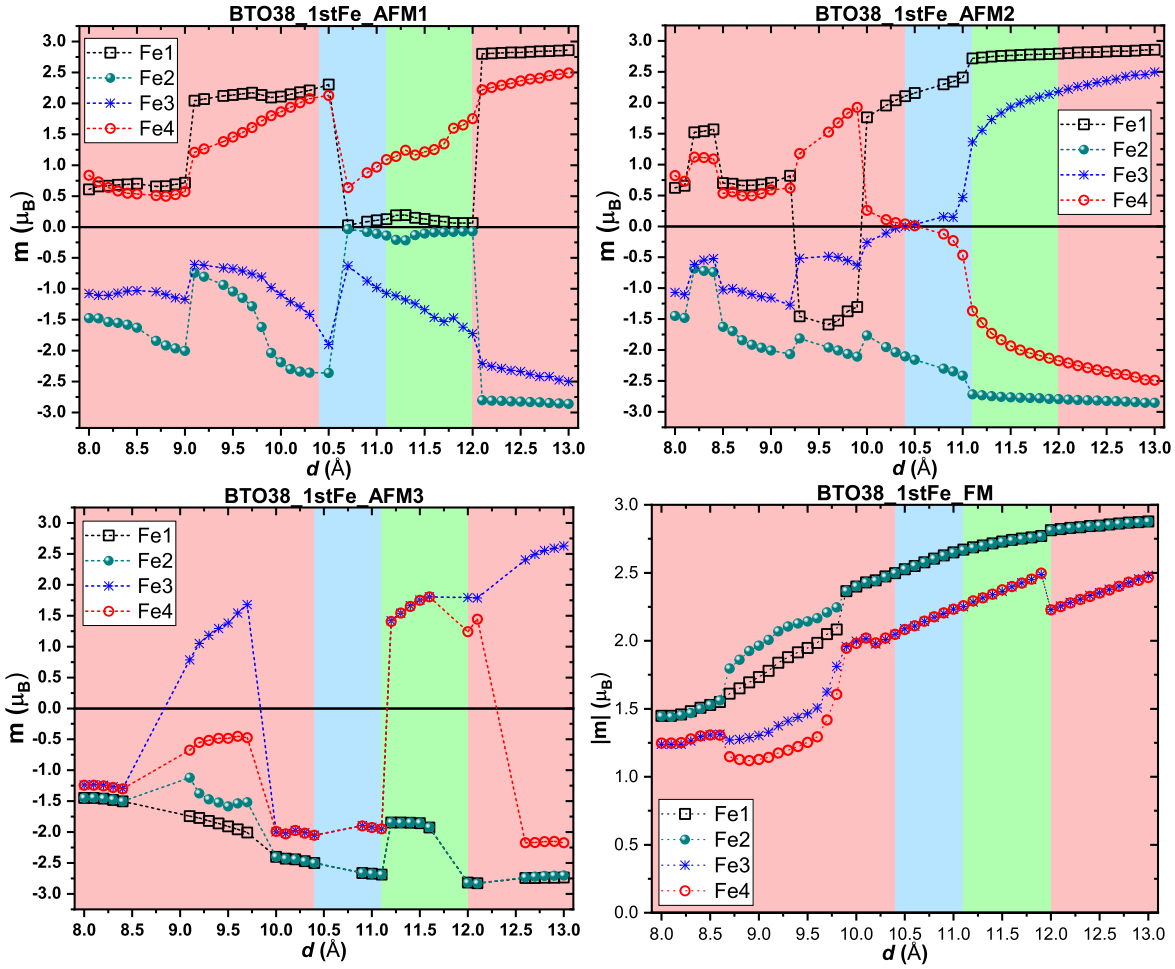

Figure 7.9: Fe magnetic moments for different magnetic arrangements of the BTO38_1stFe supercell.

mentioned d intervals.

The BTO38_1stFe_AFM1 and BTO38_1stFe_AFM2 supercells have about the same binding energy and magnetic moment behaviours at their β and γ structures, in spite of the regions where both occur not being exactly the same. Something similar occurs for the α structure for $d \leq 9.2$ Å, however for $9.2 < d < 10$ Å the BTO38_1stFe_AFM2 is in state where three of its Fe atoms are aligned ferromagnetically, while the last one is antiferromagnetic to the first three (figure 7.9). This magnetic state will be address as AFM4 in the rest of this thesis.

The BTO38_1stFe_AFM3 is the most exotic antiferromagnetic arrangement since, as shown in figures 7.9 and 7.10, it has several AFM states independently of the structure it has. Moreover, it also assumes several times a completely ferromagnetic state, overlapping its

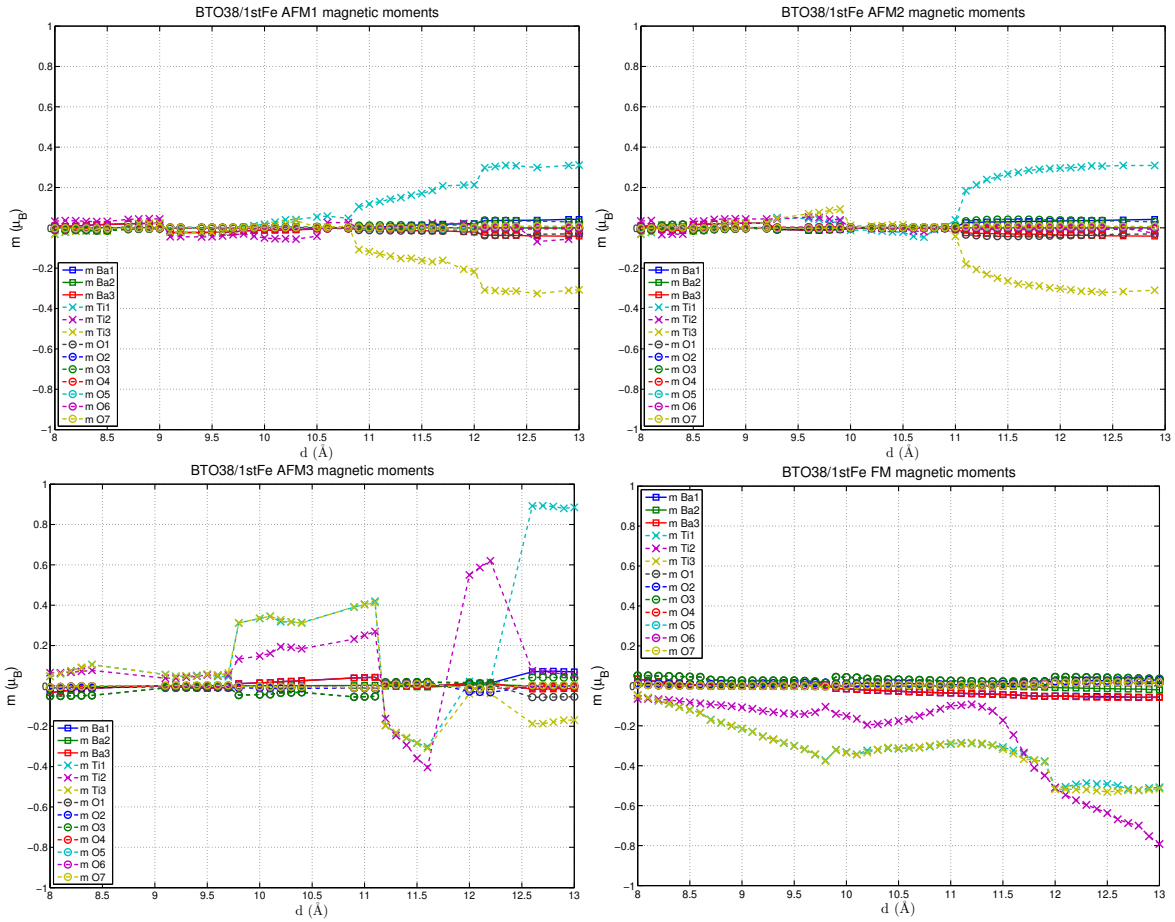

Figure 7.10: Magnetic moments of all atoms except Fe for different magnetic arrangements of the BTO38/1stFe supercell.

binding energy and total magnetic moments curves with the ones from BTO38_1stFe_FM for some given values of d.

Finally, as already mentioned, the BTO38_1stFe_FM has three distinct FM regions. It is clear from observation of figures 7.9 and 7.10 that two of the Fe magnetic moments can have magnetic moments as high as $3\,\mu_B$, however this magnetic moment enhancement[2] does not result in an equivalent increase of the total magnetic moment due to the opposite Ti's magnetic moments which can have values has high as -0.8 μ_B.

The BTO38_1stFe supercell has a very interesting region at $d_0 = d \approx 11.36\,\text{Å}$, where there is a local energy minimum. This minimum, belonging to the BTO38_1stFe_AFM2 supercell, is quite close to other two local minima: one at $d_l = d \approx 11.1\,\text{Å}$, belonging to BTO38_1stFe_AFM3, and the other at $d_r = d \approx 11.1\,\text{Å}$, belonging to BTO38_1stFe_FM.

[2]When compared with the 2.2 μ_B of the metallic Fe

This is very promising from the experimental point of view, since the supercell has a null total magnetic moment at d_0 but $\approx 8\,\mu_B$ for d_l and d_r, hence it might be possible to alternate between two (or even three) of these states using some external field to control the value of d.

7.1.2 BTO38_2ndFe

The binding energy and total magnetic moment for the BTO38_2ndFe supercell (figure 7.2) are shown in figures 7.11 and 7.12.

The binding energy is defined by equation 7.2:

$$E_{\text{Binding}} = E_{\text{BTO38\_2ndFe}} - (4E_{\text{Fe}} + 3E_{\text{Ba}} + 3E_{\text{Ti}} + 7E_{\text{O}}) \ , \tag{7.2}$$

where $E_{\text{BTO38\_2ndFe}}$ is the energy of the BTO38_2ndFe supercell. The coloured regions indicate the most energetically favourable magnetic arrangement.

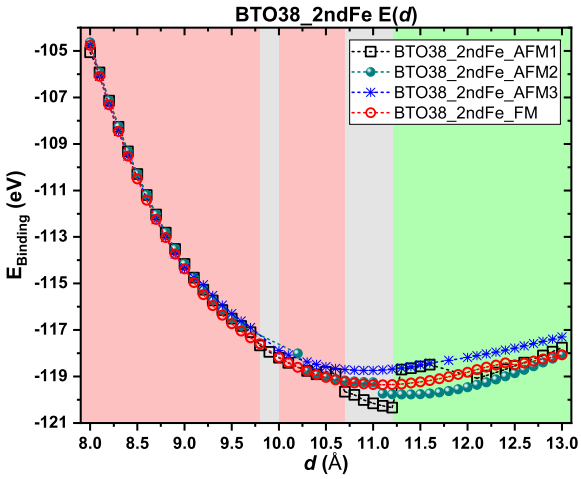

Figure 7.11: Binding energy for all the considered magnetic arrangements of the BTO38_2ndFe supercell.

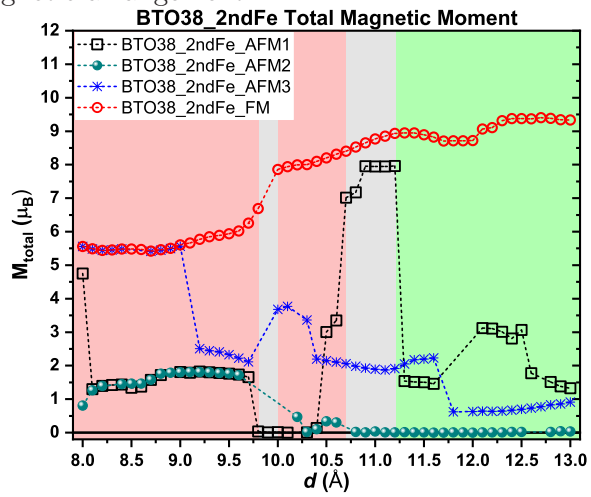

Figure 7.12: Total magnetic moment for all the considered magnetic arrangements of the BTO38_2ndFe supercell.

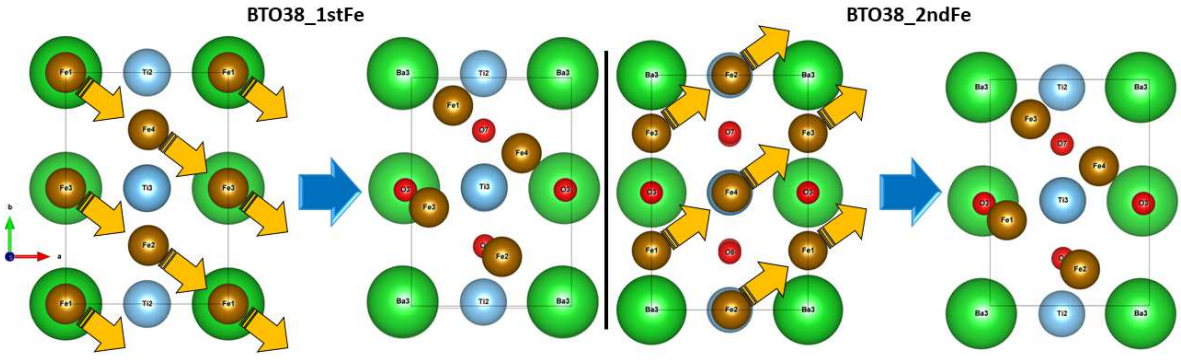

Figure 7.14: Illustration of the structural distortions of the final relaxed structures with relation to the starting fractional coordinates for both the BTO38_1stFe and BTO38_2ndFe supercells.

Similarly to the BTO38_1stFe supercell, the BTO38_2ndFe supercell also suffers the

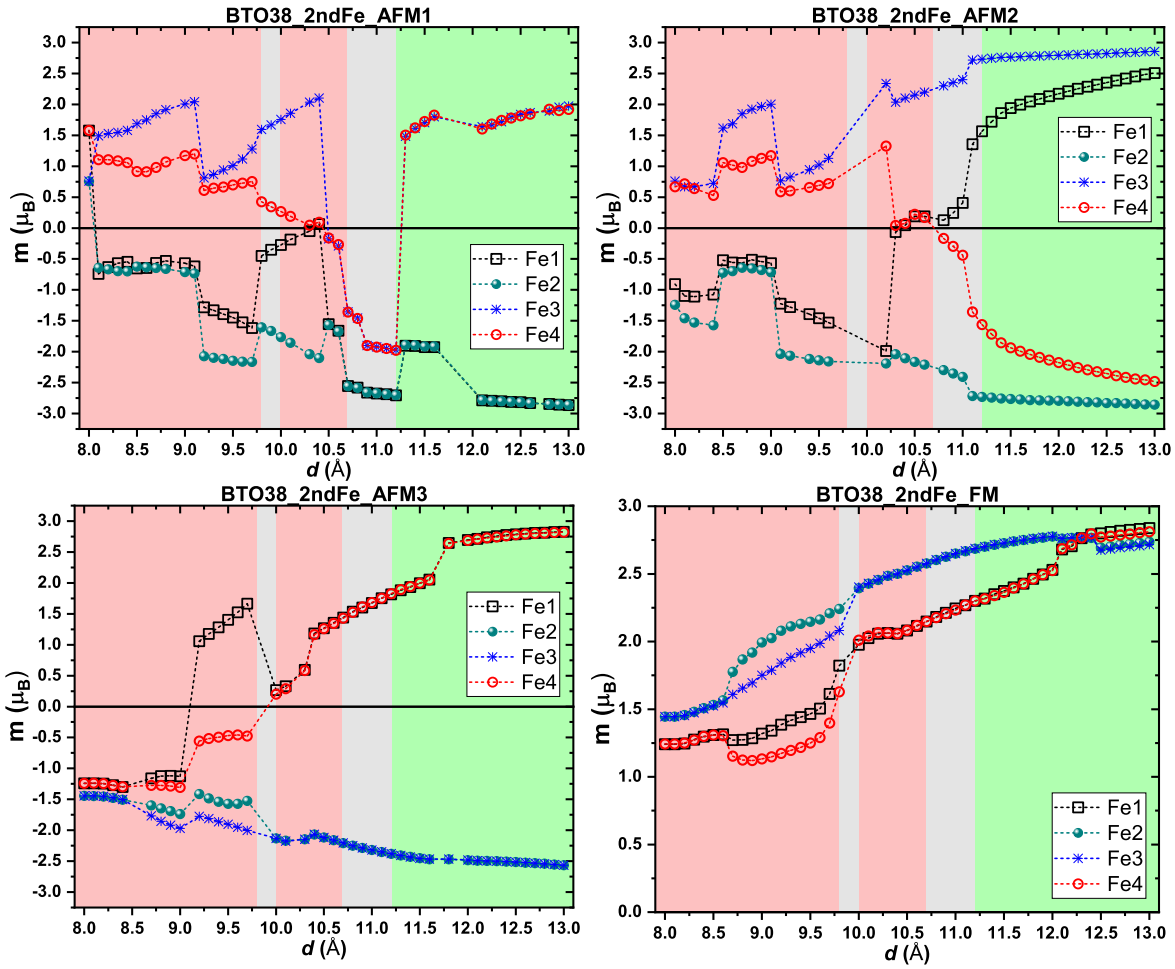

Figure 7.13: Fe magnetic moments for different magnetic arrangements of the BTO38_2ndFe supercell.

Supercell	α	β	γ
BTO38_2ndFe_AFM1	$d \in [8.1; 9.7]$ Å	$d \in [9.8; 10.6]$ Å	$d \in [10.7; 13]$ Å
BTO38_2ndFe_AFM2	$d \in [8; 9.8]$ Å	$d \in [9.8; 11.7]$ Å	$d \in [11.8; 13]$ Å
BTO38_2ndFe_AFM3	$d \in [8; 9.7]$ Å	$d \in [9.7; 13]$ Å	×
BTO38_2ndFe_FM	$d \in [8; 9.9] \cup [12.5; 13]$ Å	$d \in [10; 12.4]$ Å	×

Table 7.2: Interval of d values for the α, β and γ strucures in the BTO38_2ndFe supercell.

structural changes previously seen in figure 7.8 and the range of values where they occur can be seen in table 7.2. Moreover, the lateral fractional coordinates also suffer distortions as illustrated in figure 7.14. A similar phenomenon occurs in the BTO38_1stFe supercell, thus in the end, the final structures are actually quite similar in both BTO38_1stFe and BTO38_2ndFe supercells, in spite of the calculation starting points being completely different. This justifies the similarities in the binding energy (figure 7.11) and in the magnetic moment

curves of each atom (figures 7.13 and 7.15).

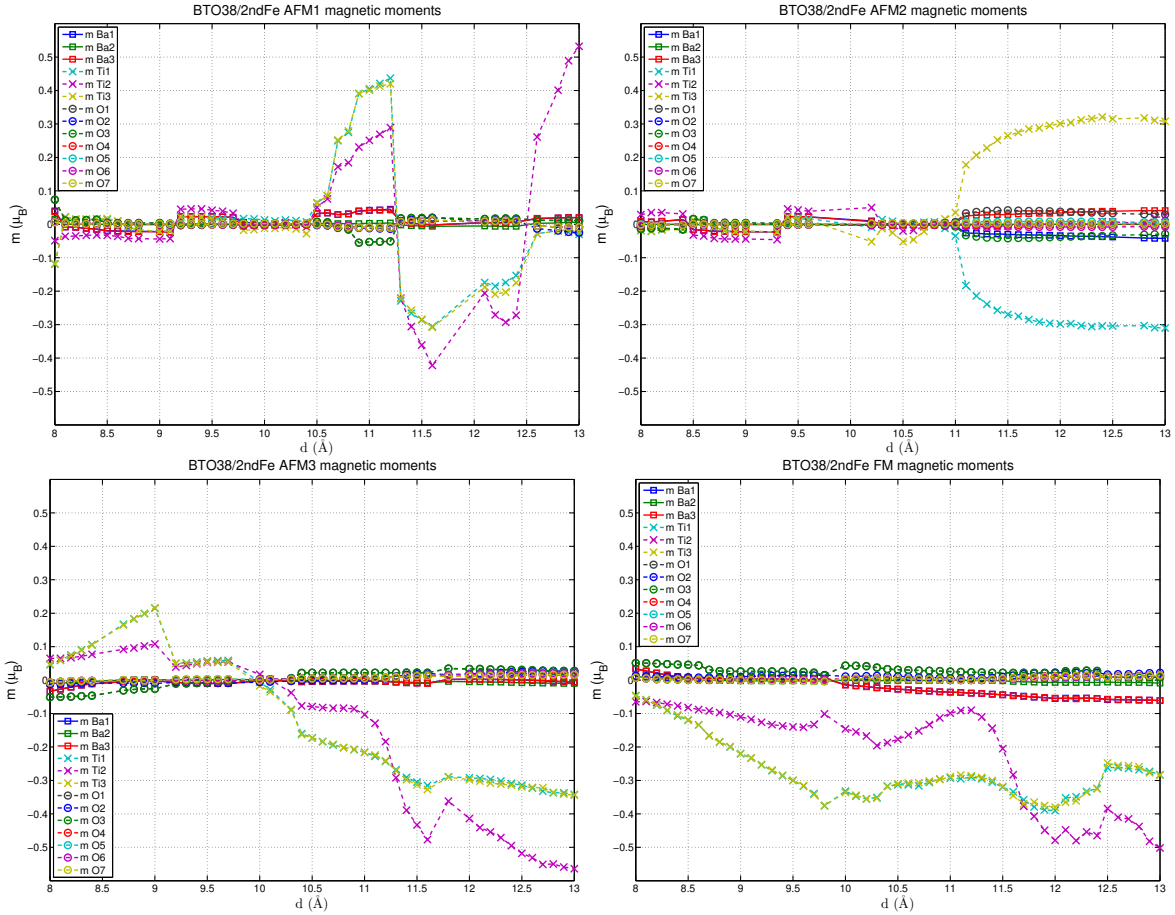

Figure 7.15: Magnetic moments of all atoms except Fe for different magnetic arrangements of the BTO38_2ndFe supercell.

While the BTO38_2ndFe_AFM2 supercell has approximately the same M_{total} curve as in its 1stFe counterpart (figure 7.12), in the BTO38_2ndFe_AFM1 case this just occurs in its α and β structures. For BTO38_2ndFe_AFM1 γ structure, instead of the perfectly AFM state, the supercell is in a FM state for $10.5 < d < 11.3\,\text{Å}$ and in a FiM for $d \geq 11.3\,\text{Å}$, being closer to the 1stFe AFM3 arrangement (figures 7.12 and 7.13).

The BTO38_2ndFe_AFM3 supercell, on the other hand, did not relax into a γ structure, having a FiM state in its β state, whereas its α structure has a FM state ($d < 9\,\text{Å}$) and a AFM4 state (figure 7.13).

The BTO38_2ndFe_FM supercell has basically the same properties as its 1stFe counterpart, apart from the $d > 12.4\,\text{Å}$ region which did not relax into a γ structure, having an α structure instead, thus having a higher total magnetic moment (figures 7.12, 7.13 and 7.15).

The observation of both figures 7.11 and 7.12 shows that the BTO38_2ndFe supercell also has a high technological potential. This supercell has two local minima close together, each one with very distinct M_{total}: the first one at $d = 11.2\,\text{Å}$, belonging to BTO38_2ndFe_AFM1 with $M_{total} \approx 8\,\mu_B$ and the other at $d = 11.36\,\text{Å}$, belonging to BTO38_2ndFe_AFM2 with $M_{total} \approx 0\,\mu_B$ enabling the alternation between the two.

7.1.3 BTO38_1stFe_O2

The binding energy and total magnetic moment for the BTO38_1stFe_O2 supercell are shown in figures 7.16 and 7.17.

The binding energy is defined by equation 7.3:

$$E_{\text{Binding}} = E_{\text{BTO38\_1stFe\_O2}} - (4E_{\text{Fe}} + 2E_{\text{Ba}} + 2E_{\text{Ti}} + 8E_{\text{O}}) \ , \tag{7.3}$$

where $E_{\text{BTO38\_1stFe\_O2}}$ is the energy of the BTO38_1stFe_O2 supercell.

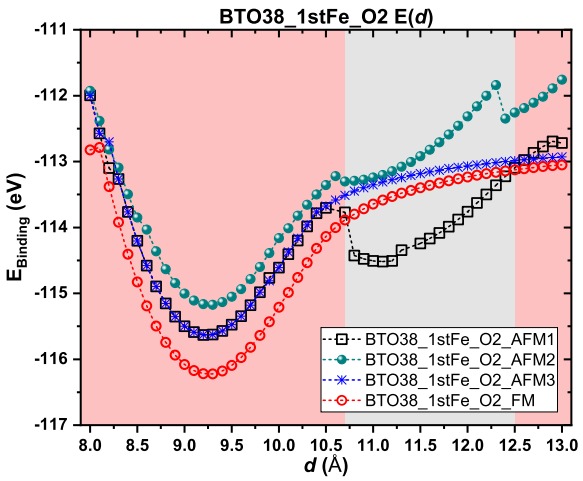

Figure 7.16: Binding energy for all the considered magnetic arrangements of the BTO38_1stFe_O2 supercell.

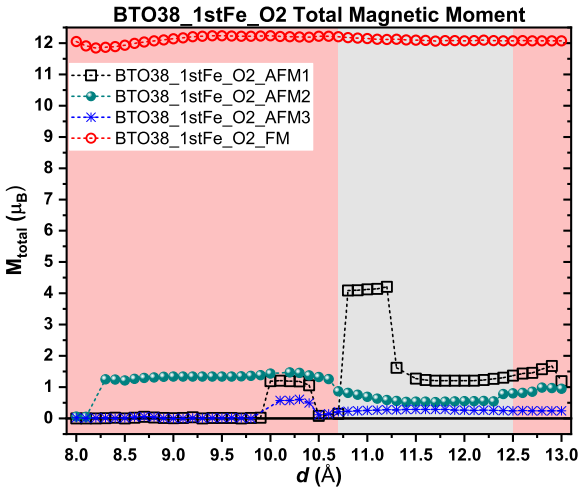

Figure 7.17: Total magnetic moment for all the considered magnetic arrangements of the BTO38_1stFe_O2 supercell.

The BTO38_1stFe_O2 supercell can have many structural distortions after letting the system relax its Hellmann-Feynman forces below the tolerance value. Figure 7.18 illustrates the possible structure types, which are designated as ω, ζ, η and α'. The range for which each magnetic arrangement relaxes into these structures is presented in table 7.3, showing that the α' structure (the only single layered one) just occurs for the BTO38_1stFe_O2_FM supercell at its lowest considered value of d .

Supercell	α'	ω	ζ	η
BTO38_1stFe_O2_AFM1	×	$d \in [8; 10.5]$ Å	$d \in [10.6; 13]$ Å	×
BTO38_1stFe_O2_AFM2	×	$d \in [8; 10.5]$ Å	×	$d \in [10.6; 13]$ Å
BTO38_1stFe_O2_AFM3	×	$d \in [8; 13]$ Å	×	×
BTO38_1stFe_O2_FM	$d = 8$ Å	$d \in [8.1; 13]$ Å	×	×

Table 7.3: Interval of d values for the α', ω, ζ and η structures in the BTO38_1stFe supercell.

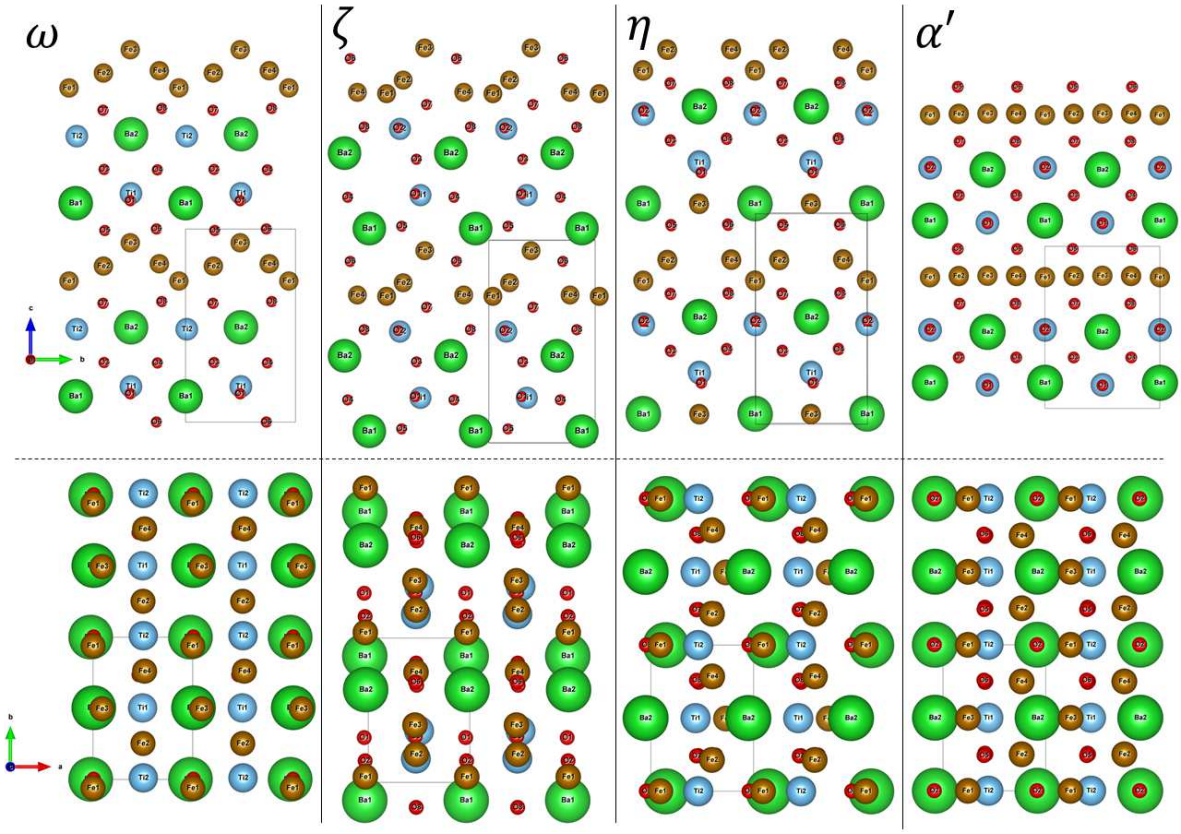

Figure 7.18: Side (top figures) and top (bottom figures) views of the ω, ζ, η and α' relaxed structures of the BTO38_1stFe_O2 supercell.

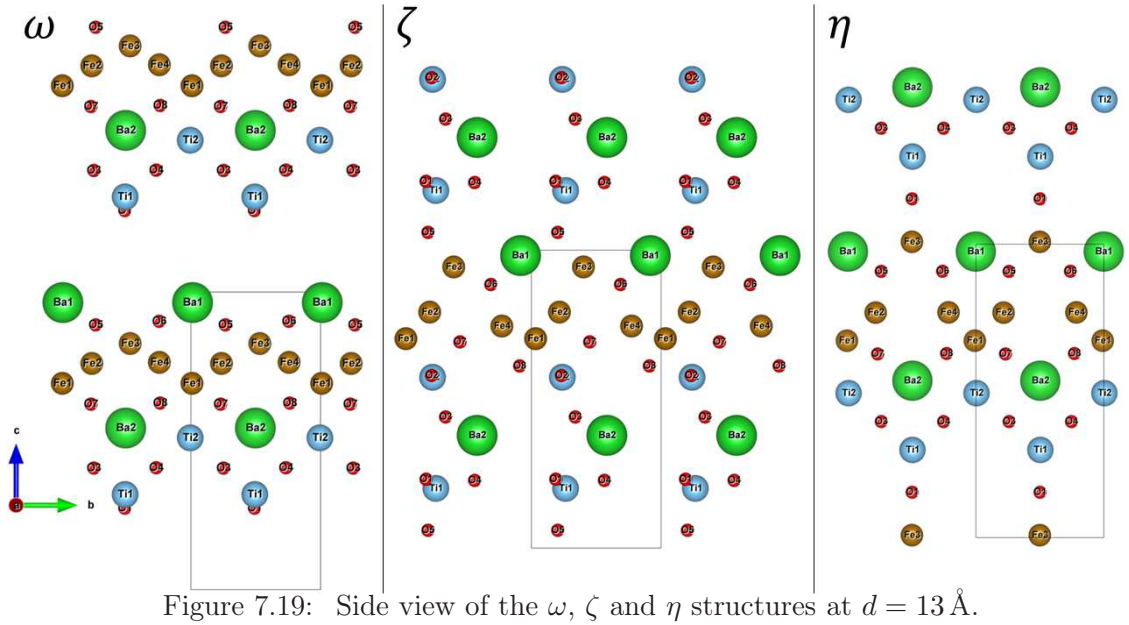

Figure 7.19: Side view of the ω, ζ and η structures at $d = 13\,\text{Å}$.

Figures 7.20 and 7.21 show the magnetic moment curves of all individual atoms. By observation of these curves and the M_{total} (figure 7.17) it is possible to see that both the

AFM1 and AFM3 arrangements have a perfectly balanced AFM state in their ω structure, apart from the interval $10 < d \leq 10.5\,\text{Å}$ where the Ti2 induced magnetic moment contributes to a non-zero M_{total}. Then, for $d > 10.5\,\text{Å}$ the BTO38_1stFe_O2_AFM3 supercell remains with an ω structure, having a close to zero M_{total}, whereas the BTO38_1stFe_O2_AFM3 supercell has a ζ structure which results in a AFM4 state with $M_{total} \approx 4\,\mu_B$ for $d \in [10.; 11.2]$ and a FiM state with $M_{total} \approx 1.3\,\mu_B$ for the remaining values of d.

The BTO38_1stFe_O2_AFM2 supercell also has a ω structure for $d < 10.5\,\text{Å}$, yet it results in a FiM state with $M_{total} \approx 1.3\,\mu_B$ mainly due the asymmetric value of the Fe atoms (figure 7.20). For $d < 10.5\,\text{Å}$ BTO38_1stFe_O2_AFM2 shifts to a η structure lowering even more the M_{total} due to the Ti atoms induced magnetic moments (figure 7.21).

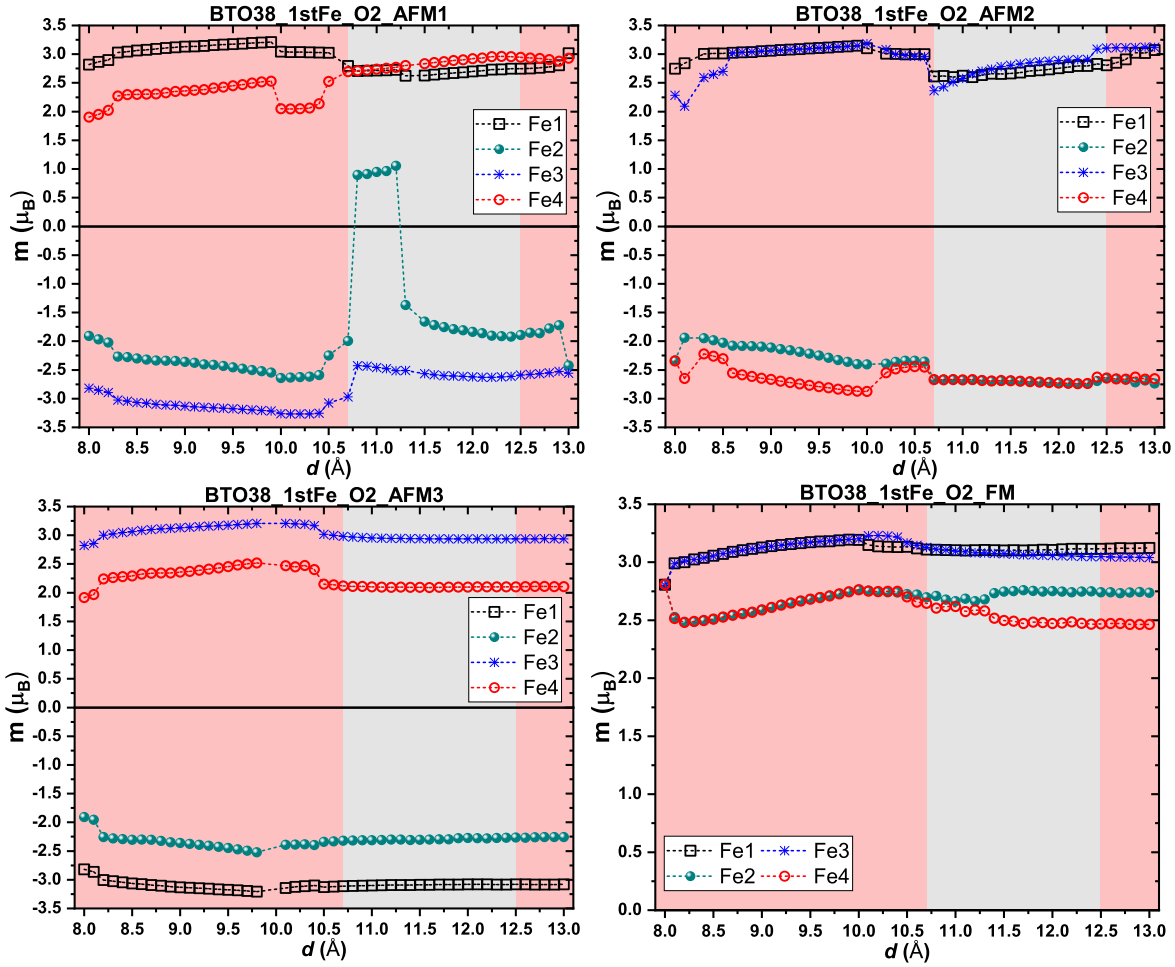

Figure 7.20: Fe magnetic moments for different magnetic arrangements of the BTO38_1stFe_O_2 supercell.

The BTO38_1stFe_O2_FM supercell has a $M_{total} \approx 12\,\mu_B$ ($\approx 4\,\mu_B/Fe_{atom}$) indepen-

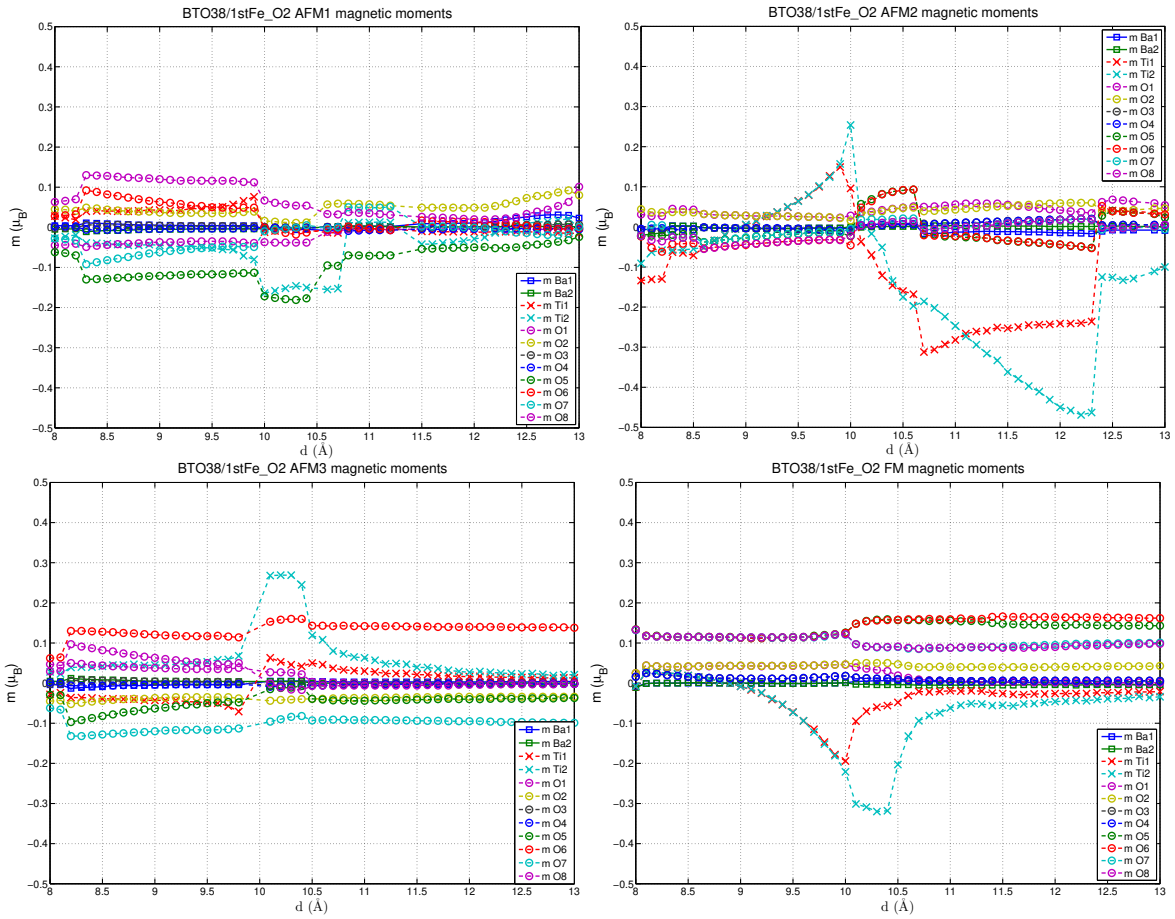

Figure 7.21: Magnetic moments of all atoms except Fe for different magnetic arrangements of the BTO38_1stFe_O2 supercell.

dently of its structure (α' or ω), in spite of the induced magnetic moments of the Ti atoms being opposite to the Fe atoms.

It is relevant to point out that at $d \gtrapprox 11.5\,\text{Å}$ for the ω and ζ structures, or at $d \gtrapprox 12\,\text{Å}$ for the η structure, their correspondent BTO38_1stFe_O2 supercell (independently of its magnetic arrangement) stops being a compact supercell. To better understand this statement, figure 7.19 is presented. It is clear that in the ω structure, the supercell has two smaller unit cells separated by a vacuum gap whose size increases with d. In the ζ and η structures a similar phenomenon occurs, but instead of an actual vacuum gap separation, both smaller unit cells are connected by a single O atom in the η case, or a at least there is a considerable amount of a pseudo porosity for the ζ case. Therefore, in this range d values, the supercell would be impractical to build since its layers would just slide off, thus being mostly likely too brittle, whatever its binding energy.

7.1.4 BTO38_2ndFe_O2

Figures 7.22 and 7.23 show the binding energy and total magnetic moment for the BTO38_2ndFe_O2 supercell.

The binding energy is defined by equation 7.4:

$$E_{\text{Binding}} = E_{\text{BTO38\_2ndFe\_O2}} - (4E_{\text{Fe}} + 2E_{\text{Ba}} + 2E_{\text{Ti}} + 8E_{\text{O}}) \ , \tag{7.4}$$

where $E_{\text{BTO38\_2ndFe\_O2}}$ is the energy of the BTO38_2ndFe_O2 supercell.

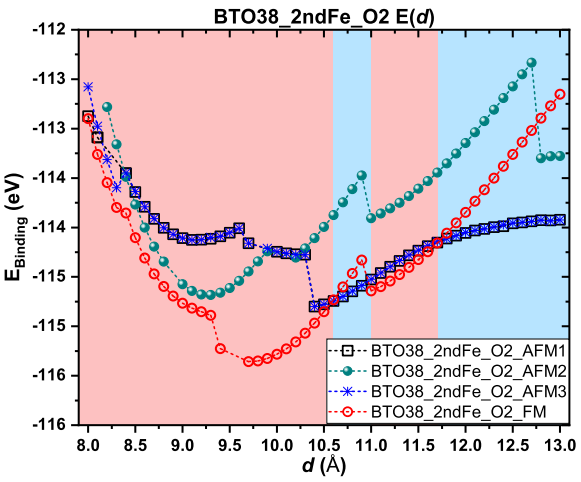

Figure 7.22: Binding energy for all the considered magnetic arrangements of the BTO38_2ndFe_O2 supercell.

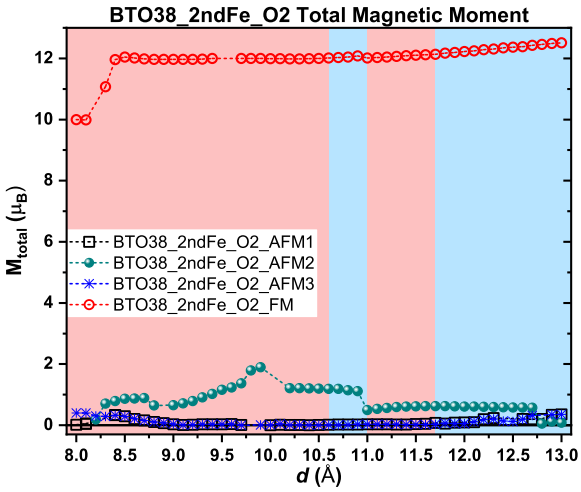

Figure 7.23: Total magnetic moment for all the considered magnetic arrangements of the BTO38_2ndFe_O2 supercell.

Due to the different initial Fe placement there is a change in the binding energy curves, yet the M_{total} curves of figure 7.23 do not differ greatly from the ones of figure 7.17 for most of the considered d values. These differences in the binding energy curves are assigned to the new relaxed structures which are illustrated in figure 7.24 and which occur in the regions presented in table 7.4.

Supercell	ε	θ	ζ'	ν	ν'	ν''
BTO38_2ndFe_O2_AFM1	$d \in [8; 9.6]$ Å	$d \in [9.7; 13]$ Å	×	×	×	×
BTO38_2ndFe_O2_AFM2	×	×	$d \in [8; 10]$ Å	$d \in [10.1; 10.9] \cup [12.8 - 13]$ Å	×	$d \in [11; 12.7]$ Å
BTO38_2ndFe_O2_AFM3	$d \in [8; 9.6]$ Å	$d \in [9.7; 13]$ Å	×	×	×	×
BTO38_2ndFe_O2_FM	$d \in [8; 8.3]$ Å	×	×	×	$d \in [8.4; 9.3]$ Å	$d \in [9.4; 13]$ Å

Table 7.4: Range of d values for the ε, θ, ν, ν' and ν'' structures in the BTO38_2ndFe_O2 supercell.

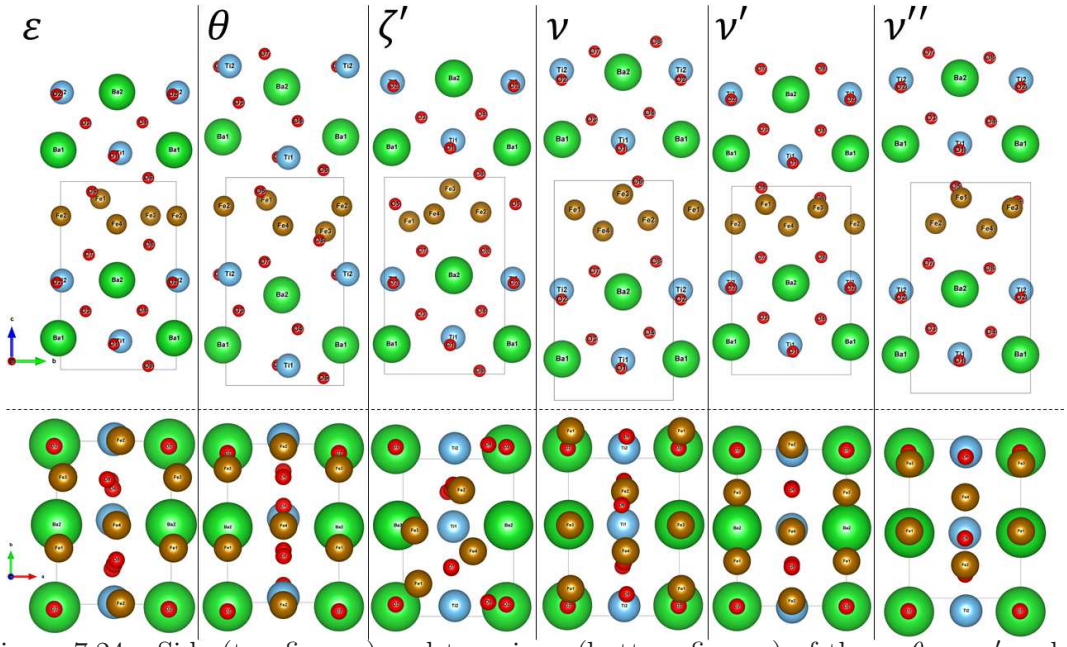

Figure 7.24: Side (top figures) and top views (bottom figures) of the ε, θ, ν, ν' and ν'' relaxed structures of the BTO38_2ndFe_O2 supercell.

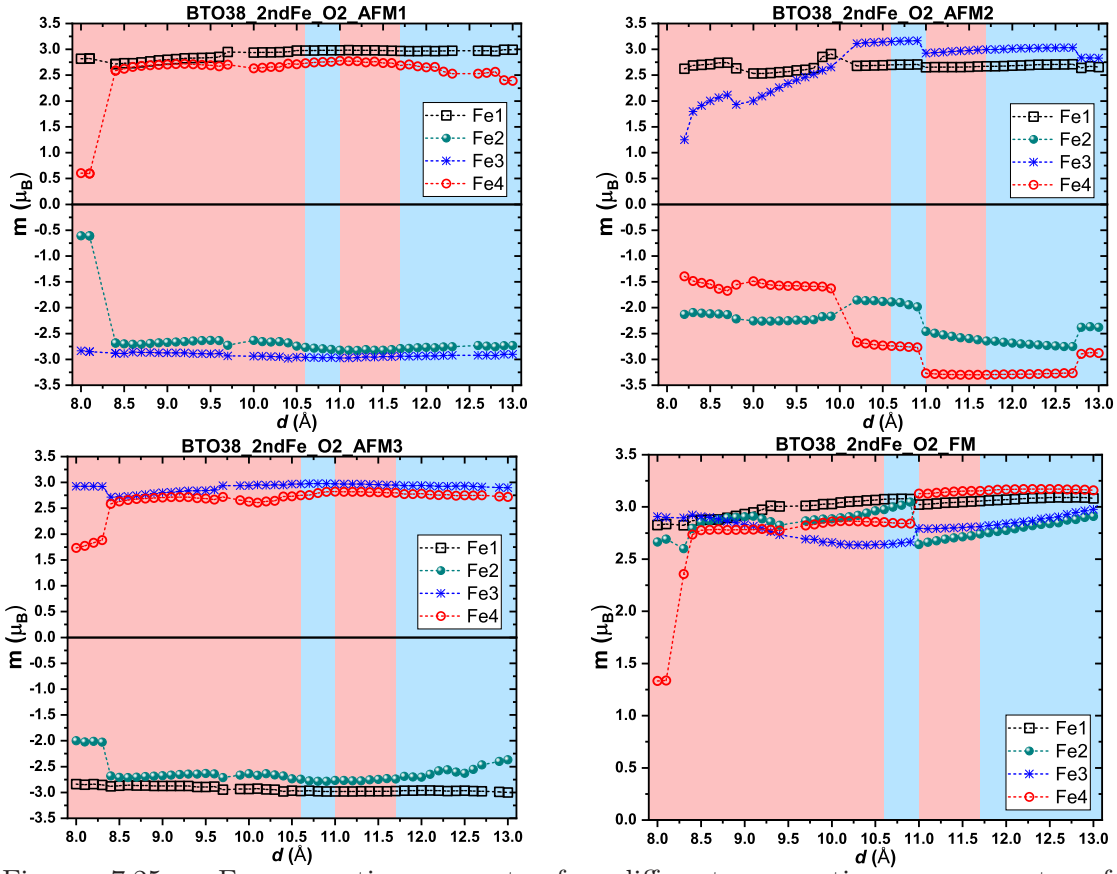

Figure 7.25: Fe magnetic moments for different magnetic arrangements of the BTO38_2ndFe_O2 supercell.

The BTO38_2ndFe_O2_AFM1 and BTO38_2ndFe_O2_AFM3 supercells have overlapping energy and M_{total} curves. This corroborates the fact that each of these supercells relax their initial fractional positions into the same final structures, ε and θ, as presented in table 7.4. It is curious to see that even though the individual magnetic moments of BTO38_2ndFe_O2_AFM1 and BTO38_2ndFe_O2_AFM3 are not exactly the same (figures 7.25 and 7.26), their sum results in the same M_{total}, and their energy curves are indistinguishable.

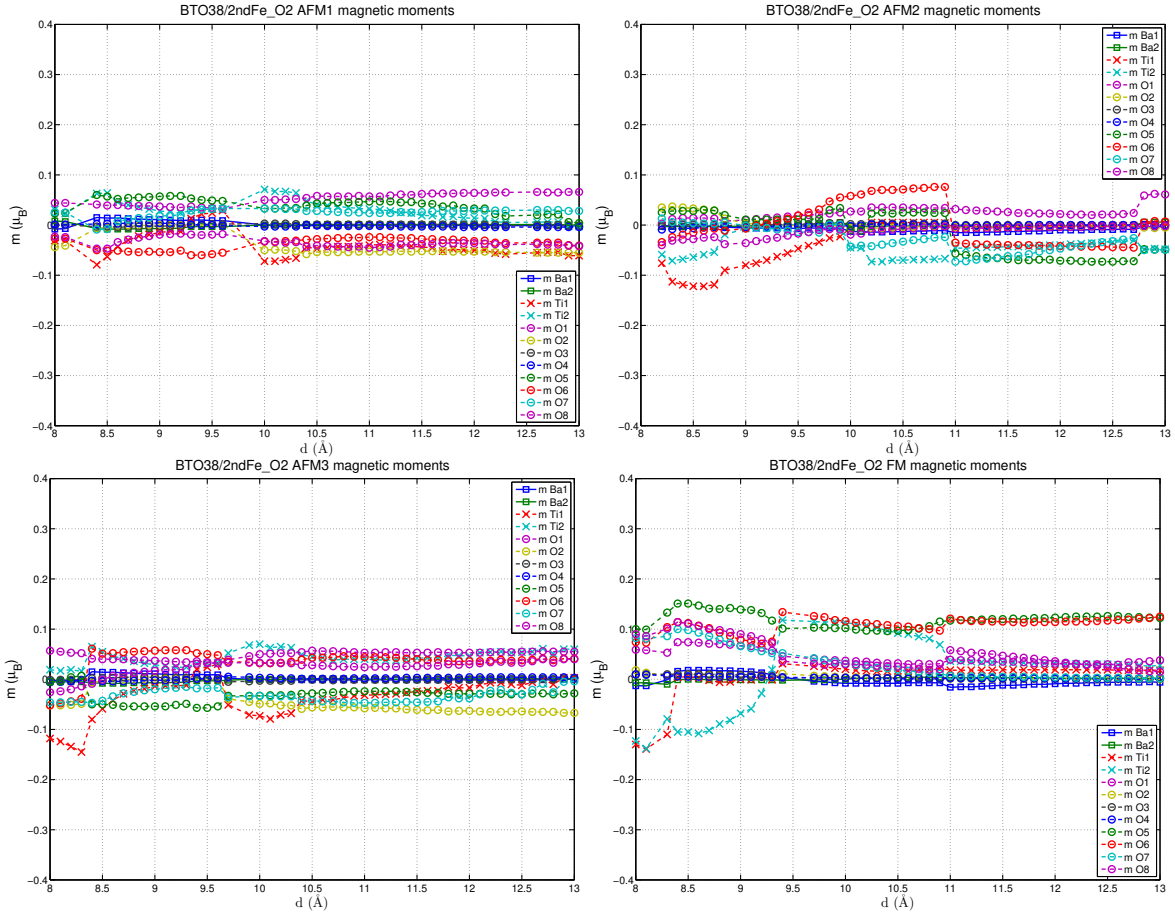

Figure 7.26: Magnetic moments of all atoms except Fe for different magnetic arrangements of the BTO38_2ndFe_O2 supercell.

As in BTO38_1stFe_O2_AFM2, the BTO38_2ndFe_O2_AFM2 supercell is the one which presents the most atypical behaviour within all the input AFM arrangements. Figures 7.25 and 7.26 show the asymmetry in the up and down magnetic moments of BTO38_2ndFe_-O2_AFM2 which gives the FiM character to this supercell. The differences in the magnitude of the individual magnetic moments are directly correlated to its ζ', ν and ν'' relaxed structures.

The BTO38_2ndFe_O2_FM supercell also has a FM state with $M_{total} \approx 12\,\mu_B$ for $d \geq 8.4\,\text{Å}$, as in its 1stFe counterpart, despite having different relaxed structures (ν' and ν'') and different individual magnetic moments curves (figure 7.25 and 7.26). For $d < 8.4\,\text{Å}$ this supercell relaxes into the ε structure which induces a decrease in the M_{total} of $\approx 2\,\mu_B$.

7.2 BTO160

Now let's consider the last ferroelectric phase of BTO, its low temperature rhombohedral phase, to build a supercell comprised of this unit cell and a Fe monolayer on top of it. Figures 7.27-7.29 show the three considered placements of the Fe monolayer with four atoms per unit cell. The BaO_3 layer is chosen as the termination layer once the Ti and remaining O atoms are mostly interstitial atoms in the BTO rhombohedral phase, hence one cannot consider them as being actual layers.

The BTO160_1stFe has its Fe atoms on top of the atoms from the BaO_3 layer (Ba4, O10, O11 and O12), whereas in the BTO160_2ndFe and BTO160_3rdFe supercells the Fe atoms are placed in the same lateral coordinates as the remaining BaO_3 layers.

Taking the BTO160_1stFe supercell and removing the Fe atom which is upon the Ba atom, the supercell of figure 7.30 is created. This supercell is designated as BTO160_Triangular.

For all the calculations the a and b parameters of the supercell are made fixed to the experimental values $a = b = 5.654\,\text{Å}$ [233]. The calculations were carried out using the same parameters used on the BTO38/Fe supercells calculations, but a $5 \times 5 \times 2$ k-points grid was considered for the calculations in reciprocal space.

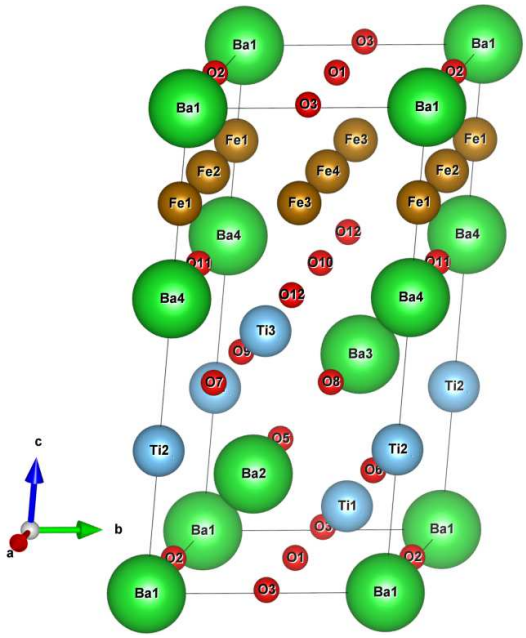

Figure 7.27: BTO160_1stFe supercell

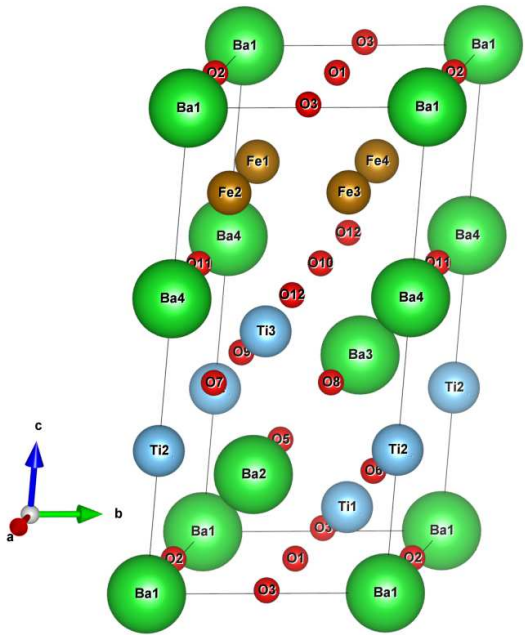

Figure 7.28: BTO160_2ndFe supercell

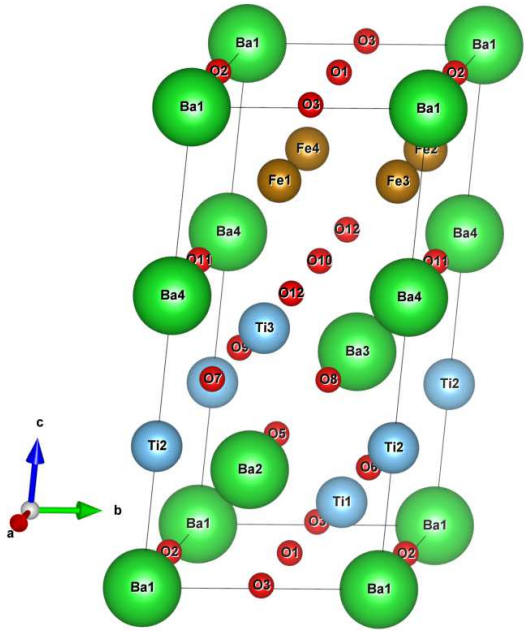

Figure 7.29: BTO160_3rdFe supercell

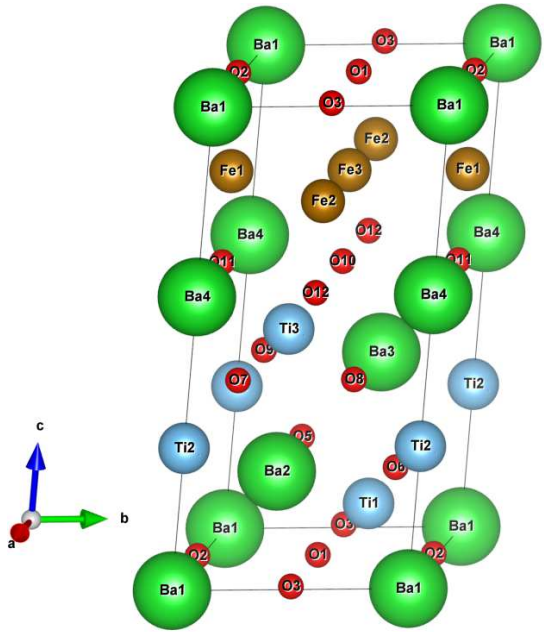

Figure 7.30: BTO160_Triangular supercell

Ferromagnetic and antiferromagnetic initial arrangements were considered for each supercell. The AFM considered arrangements can be understood in the same way as illustrated in figure 7.5 since the number of Fe atoms is the same. However in this particular case $J_1 = J_2$, hence only two AFM arrangements are considered: the AFM1 arrangement which considers $J_1 > 0$, $J_2 < 0$, $J_3 < 0$ and $J_4 < 0$, and the AFM2 arrangement which considers $J_1 < 0$, $J_2 < 0$, $J_3 > 0$ and $J_4 > 0$. Finally the FM arrangement considers $J_1 > 0$, $J_2 > 0$, $J_3 > 0$ and $J_4 > 0$[3].

[3]It is possible to see that the AFM2 magnetic arrangement of a BTO160/Fe system is actually equivalent to the AFM3 of a BTO38/Fe system

7.2.1 BTO160_1stFe

Figures 7.31 and 7.32 show the binding energy and total magnetic moment for the BTO160_1stFe supercell.

Its binding energy is defined by equation 7.5:

$$E_{\text{Binding}} = E_{\text{BTO160\_1stFe}} - (4E_{\text{Fe}} + 4E_{\text{Ba}} + 3E_{\text{Ti}} + 12E_{\text{O}}) \ , \tag{7.5}$$

where $E_{\text{BTO160\_1stFe}}$ is the energy of the BTO160_1stFe supercell.

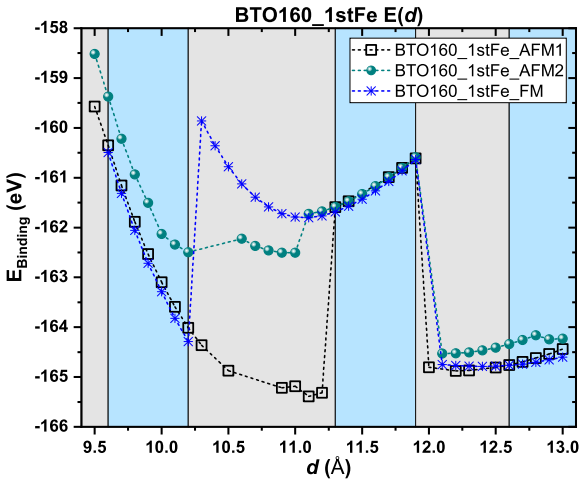

Figure 7.31: Binding energy for all the considered magnetic arrangements of the BTO160_1stFe supercell.

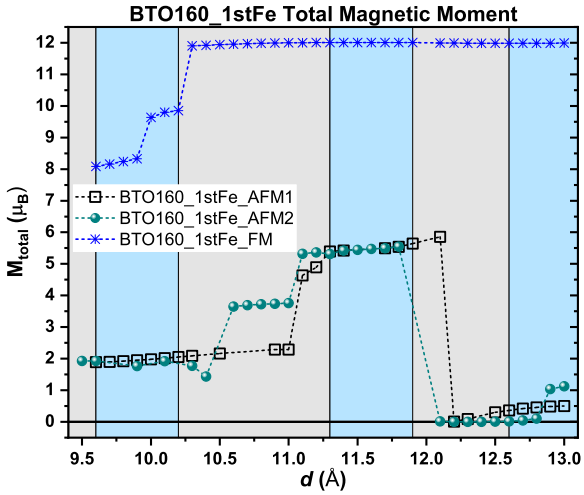

Figure 7.32: Total magnetic moment for all the considered magnetic arrangements of the BTO160_1stFe supercell.

The coloured regions indicate which of the magnetic arrangements is the most energetically favourable. The light gray region indicates a more stable AFM1 arrangement, a green region indicates a more stable AFM2 arrangement, and a blue region indicates a more stable FM arrangement.

All the possible magnetic arrangements can have different final relaxed structures, which are illustrated in figure 7.33. The intervals of d where each of these structures are presented in table 7.5.

For BTO160_1stFe_AFM1 σ structure the Fe1 atom goes down to the adjacent BaO_3 layer, right next to the O12 atom (figure 7.33). This greatly decreases its magnetic moment when comparing with its parallel Fe2 magnetic moment (figure 7.34) which results in the FiM state with $M_{\text{total}} \approx 2\,\mu_B$ shown in figure 7.32. When BTO160_1stFe_AFM1 supercell relaxes into the φ structure, the Fe1 atom inverts its moment and a AFM4 sate occurs, increasing

the M_{total} to values which increase with d till $\approx 6\,\mu_B$. Then, BTO160_1stFe_AFM1 relaxes into the χ structure which results in another inversion of the Fe1 atom magnetic moment and confers a nearly perfectly balanced AFM sate to the supercell.

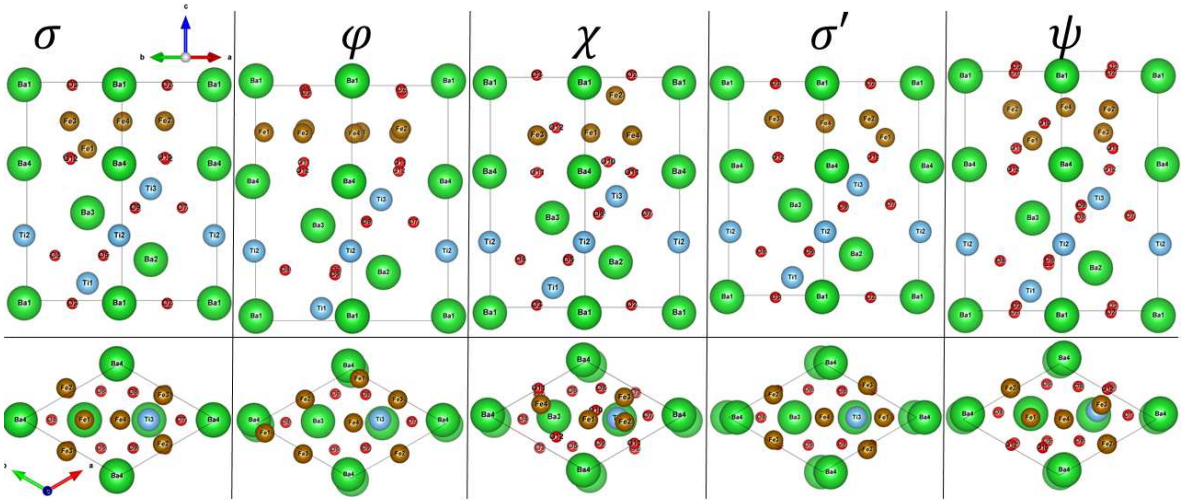

Figure 7.33: Side (top figures) and top views (bottom figures) of the σ, φ, χ, σ' and ψ relaxed structures of the BTO160_1stFe supercell.

Supercell	σ	φ	χ	σ'	ψ
BTO160_1stFe_AFM1	$d \in [9.5; 11.2]$ Å	$d \in [11.3; 11.9]$ Å	$d \in [12; 13]$ Å	×	×
BTO160_1stFe_AFM2	×	$d \in [11; 11.9]$ Å	×	$d \in [9.5; 10.9]$ Å	$d \in [12; 13]$ Å
BTO160_1stFe_FM	×	$d \in [10.3; 11.9]$ Å	$d \in [9.5; 10.2]$ Å	×	$d \in [12; 13]$ Å

Table 7.5: Range of d values for the σ, φ, χ, σ' and ψ strucures in the BTO160_1stFe supercell.

The structure σ', adopted by BTO160_1stFe_AFM2 at its lower values of d, is actually quite similar to the σ structure, hence the physical lowering of the Fe1 atom (figure 7.33) and respective decrease in it magnetic moment (figure 7.34), justifying the identical M_{total} curve in figure 7.32. Figure 7.33 shows that here the φ also promotes a AFM4 sate, but for $d \geq 12$ Å, this supercell relaxes into the ψ structure which has a perfect AFM state for most of its values of d as seen in figure 7.34.

As it is possible to see in table 7.5, BTO160_1stFe_FM relaxes into three possible structures: φ, χ and ψ. The different energy curves of each curve are clearly seen in figure 7.31. In the M_{total} curves, the χ and ψ structures have both $M_{total} \approx 12\,\mu_B$ as it is possible to seen in figure 7.32, despite having two completely different binding energies. To tell the differences in magnetic properties it is necessary a further inspection, looking at the individual atoms magnetic moments of figures 7.34 and 7.35, where it is possible to assign the changes of binding energy curves to changes of the individual Fe atoms magnetic moment.

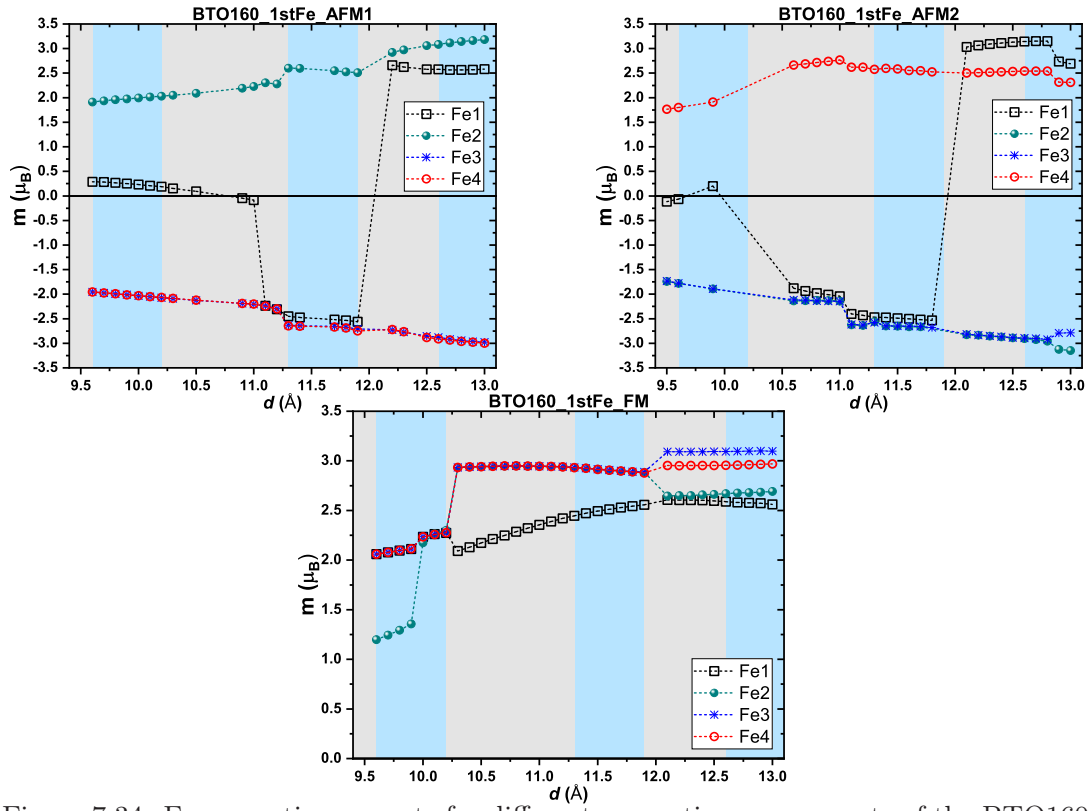

Figure 7.34: Fe magnetic moments for different magnetic arrangements of the BTO160_1stFe supercell.

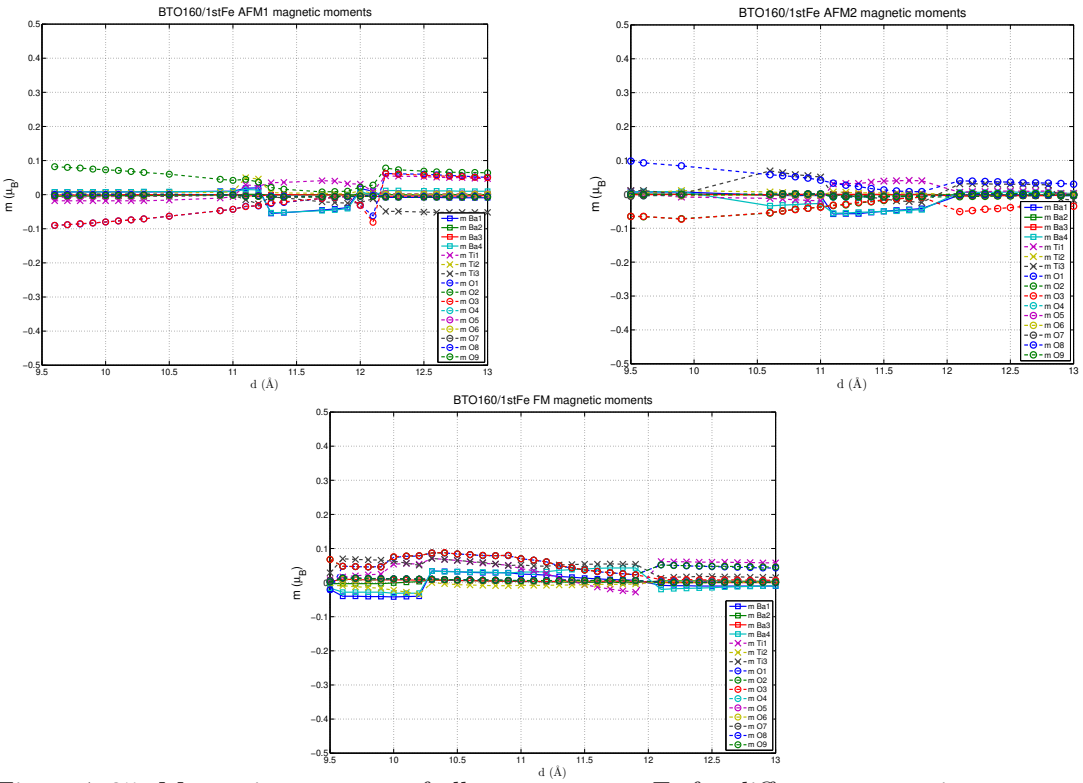

Figure 7.35: Magnetic moments of all atoms except Fe for different magnetic arrangements of the BTO160_1stFe supercell.

7.2.2 BTO160_2ndFe

Figures 7.36 and 7.37 show the binding energy and total magnetic moment for the BTO160_2ndFe supercell.

Its binding energy is defined by by equation 7.6:

$$E_{\text{Binding}} = E_{\text{BTO160\_2ndFe}} - (4E_{\text{Fe}} + 4E_{\text{Ba}} + 3E_{\text{Ti}} + 12E_{\text{O}}) \ , \tag{7.6}$$

where $E_{\text{BTO160\_2ndFe}}$ is the energy of the BTO160_2ndFe supercell.

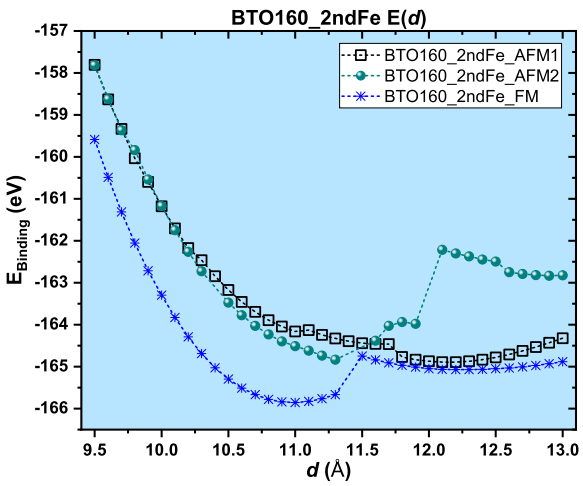

Figure 7.36: Binding energy for all the considered magnetic arrangements of the BTO160_2ndFe supercell.

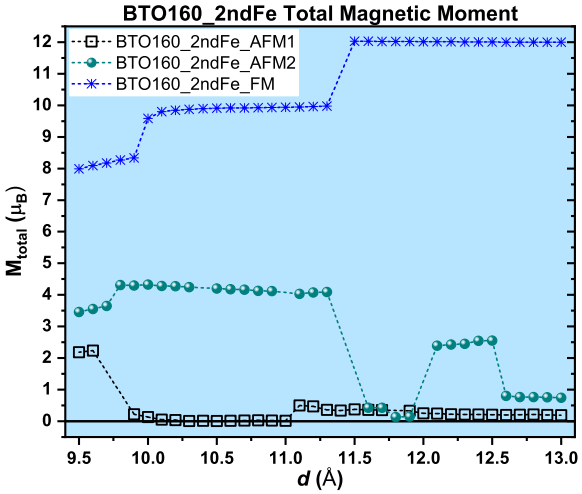

Figure 7.37: Total magnetic moment for all the considered magnetic arrangements of the BTO160_2ndFe supercell.

The BTO160_2ndFe supercell can relax into different structures depending on its initial magnetic arrangement. These structures are the χ, σ', ξ, λ and ψ' structures, thus relaxing to some of the BTO160_1stFe supercell and some newer ones as illustrated in figure 7.38. In table 7.6 all the BTO160_2ndFe relaxed structures are presented and assigned to their respective magnetic arrangements.

Supercell	χ	σ'	ξ	λ	ψ'
BTO160_2ndFe_AFM1	$d \in [9.5; 13]$ Å	×	×	×	×
BTO160_2ndFe_AFM2	×	$d \in [11.4; 11.9]$ Å	$d \in [9.5; 11.3]$ Å	$d \in [12; 13]$ Å	×
BTO160_2ndFe_FM	×	×	×	$d \in [9.5; 11.3]$ Å	$d \in [11.4; 13]$ Å

Table 7.6: Range of d values for the χ, σ', ξ, λ and ψ' structures in the BTO160_2ndFe supercell.

The BTO160_2ndFe_AFM1 supercell relaxes into the χ structure for all the considered values of d. Figure 7.39 shows that for this structure the BTO160_2ndFe_AFM1 has an AFM

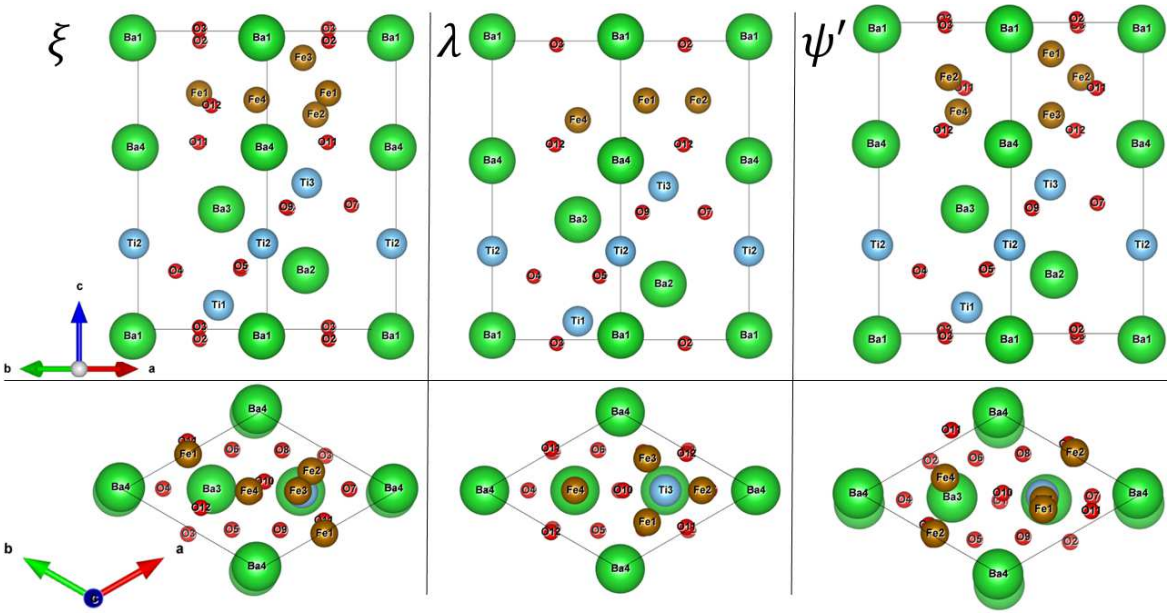

Figure 7.38: Side (top figures) and top views (bottom figures) of the ξ, λ and ψ' relaxed structures of the BTO160_2ndFe supercell.

state with a M_{total} close to zero (figure 7.37), apart from the two lowest values of d where this supercell has an AFM4 state resulting in a $M_{total} \approx 2\,\mu_B$.

The BTO160_2ndFe_AFM2 supercell, in other hand, has an AFM4 state through its ξ structure (figure 7.39) which is the structure which BTO160_2ndFe_AFM2 adopts in the majority of the considered d. This peculiar magnetic state has a $M_{total} \approx 4.5\,\mu_B$ and arises due to the separation of the Fe1 atom from the remaining three Fe atoms which have a ferromagnetic alignment to avoid magnetic frustration. Just before its relaxation into the σ' structure the Fe4 atom is the one which has an opposite moment to the remaining Fe atoms (figure 7.39). For the σ' structure the Fe1 (or Fe4) is not "isolated" from the others anymore, resulting in a AFM state with a $M_{total} \approx 0\,\mu_B$ (figure 7.37). For $d \geq 12$ Å the BTO160_2ndFe_AFM2 is in the λ structure which has a ferrimagnetic state with $M_{total} \approx 2.5\,\mu_B$ or $M_{total} \approx 0.8\,\mu_B$ depending on the value of d.

In the BTO160_2ndFe_FM case there are two possible relaxed structures: the λ and the ψ' which are clearly seen in the two different binding energy curves of figure 7.36. Despite having two possible structures, the BTO160_2ndFe_FM supercell has three possible values of M_{total}, one assigned to the ψ' structure, $M_{total} \approx 12\,\mu_B$, and two assigned to the λ structure, $M_{total} \approx 10\,\mu_B$ and $M_{total} \approx 8\,\mu_B$ respectively.

It is noteworthy that, apart from the Fe atoms, the up and down magnetic moments of the

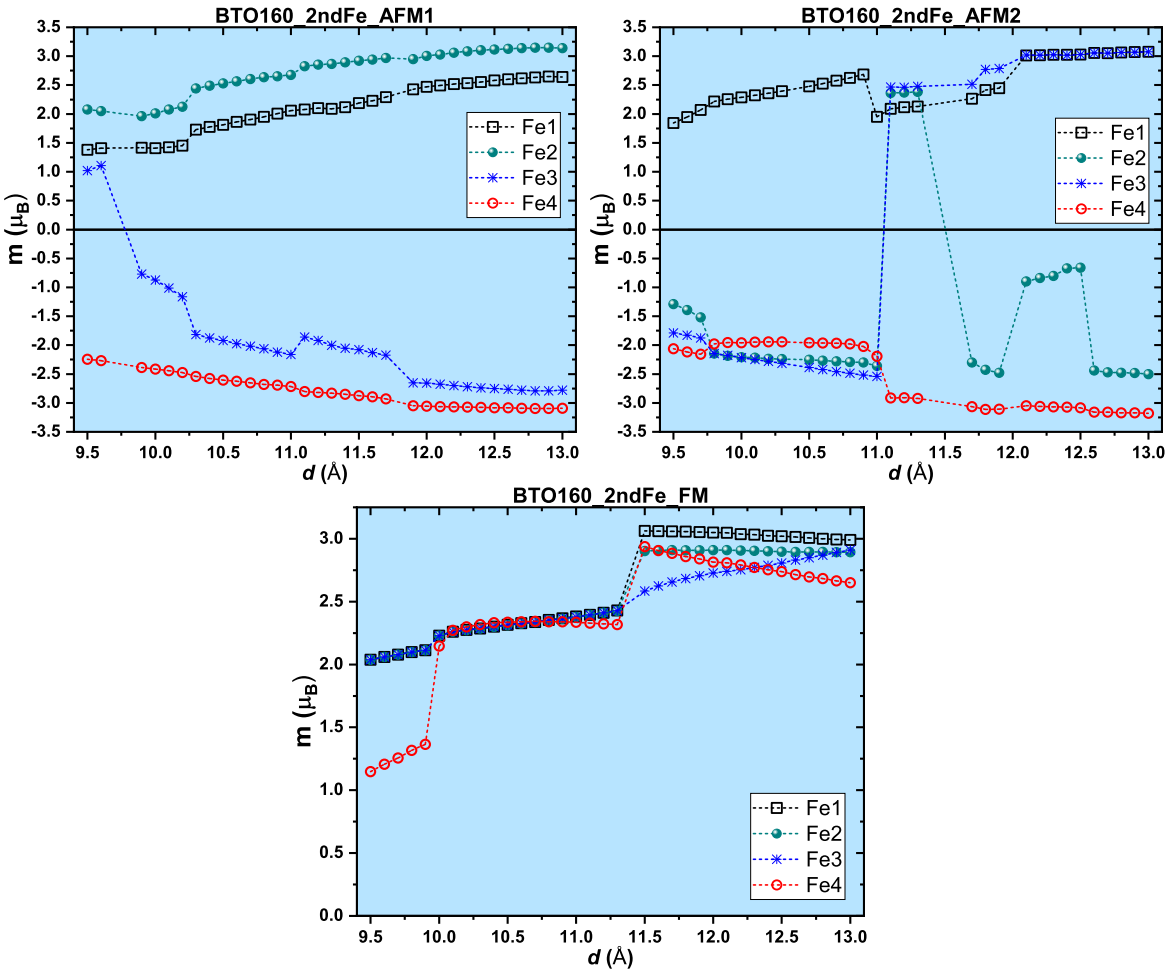

Figure 7.39: Fe magnetic moments for different magnetic arrangements of the BTO160_2ndFe supercell.

individual atoms seem to cancel out relatively well in this supercell, similarly to what happens in figure 7.35, hence the remaining atoms magnetic moments are not explicitly shown.

7.2.3 BTO160_3rdFe

Figures 7.40 and 7.41 show the binding energy and total magnetic moment for the BTO160_3rdFe supercell.

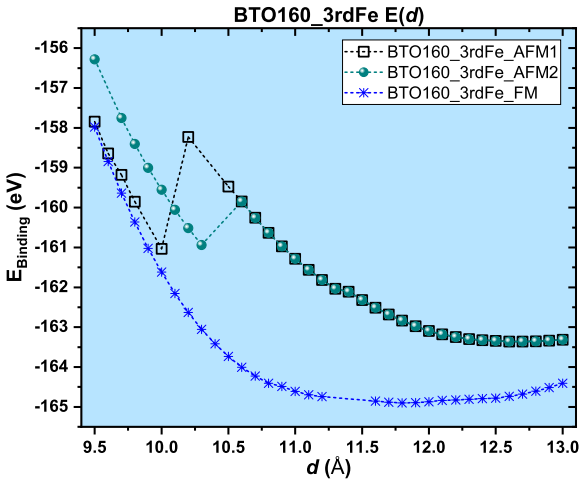

Figure 7.40: Binding energy for all the considered magnetic arrangements of the BTO160_3rdFe supercell.

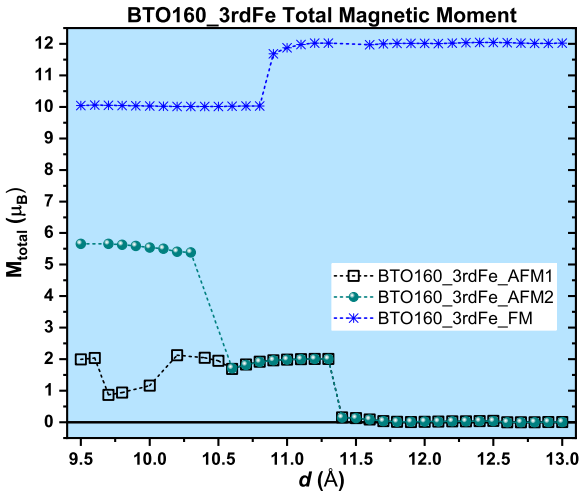

Figure 7.41: Total magnetic moment for all the considered magnetic arrangements of the BTO160_3rdFe supercell.

Its binding energy is defined by equation 7.7:

$$E_{\text{Binding}} = E_{\text{BTO160\_3rdFe}} - (4E_{\text{Fe}} + 4E_{\text{Ba}} + 3E_{\text{Ti}} + 12E_{\text{O}}) \ , \tag{7.7}$$

where $E_{\text{BTO160\_3rdFe}}$ is the energy of the BTO160_3rdFe supercell.

Besides the already mentioned relaxed structures, the new different relaxed structures obtained in the study of the BTO160_3rdFe supercell, ψ'', ξ' and ξ'', are represented in figure 7.42. The assignment of each structure to the possible d values for all the initial magnetic arrangements is presented in table 7.7.

Supercell	λ	χ	ψ	ψ''	ξ'	ξ''
BTO160_3rdFe_AFM1	×	$d \in [9.5; 10]$ Å	×	×	$d \in [10.1; 13]$ Å	×
BTO160_3rdFe_AFM2	×	×	×	$d \in [9.5; 10.5]$ Å	×	$d \in [10.6; 13]$ Å
BTO160_3rdFe_FM	$d \in [9.5; 11.3]$ Å	×	$d \in [11.4; 13]$ Å	×	×	×

Table 7.7: Range of d values for the χ, ψ, ψ'', ξ', and ξ'' structures in the BTO160_3rdFe supercell.

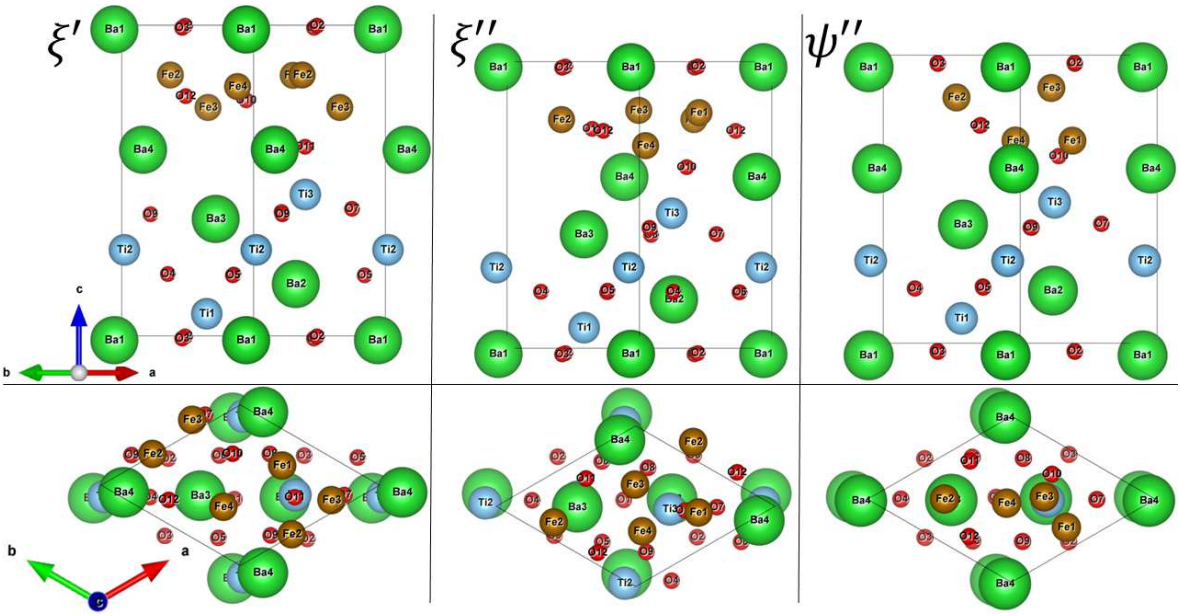

Figure 7.42: Side (top figures) and top views (bottom figures) of the ξ', ξ'' and ψ'' relaxed structures of the BTO160_3rdFe supercell.

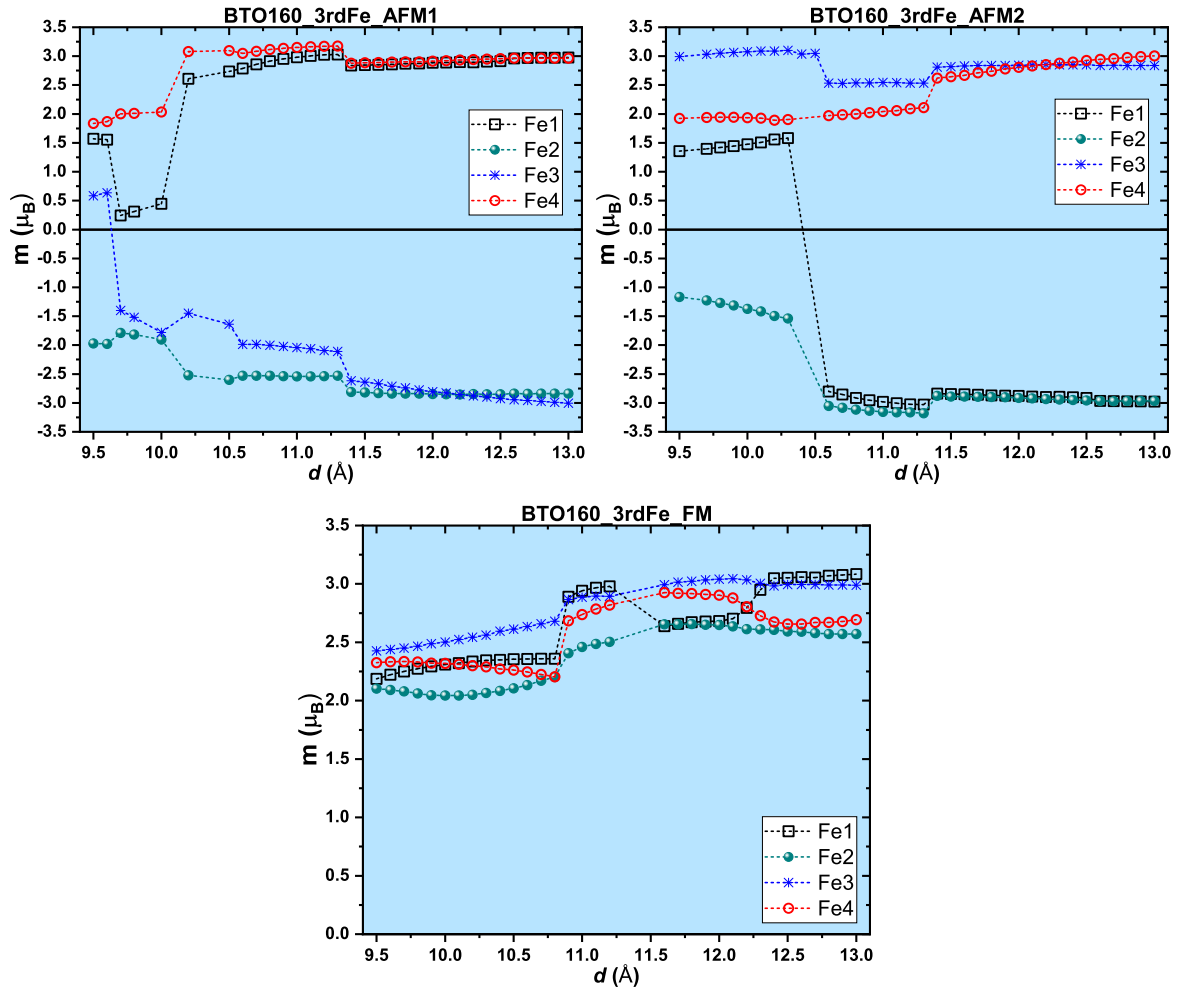

Figure 7.43: Fe magnetic moments for different magnetic arrangements of the BTO160_3rdFe supercell.

The binding energy curve of figure 7.40 allows to clearly distinguish the regions where the BTO160_3rdFe_AFM1 relaxes to its χ and ξ', and the two regions where the ψ'' and the ξ'' structures of the BTO160_3rdFe_AFM2 occur. The marginal differences between the ξ' and ξ'' structures result in the same magnetic states on both magnetic arrangements (figure 7.43), thus their energy curves and M_{total} curves overlap for $d \geq 10.6\,\text{Å}$.

Figure 7.43 shows that for $d < 10.6\,\text{Å}$ BTO160_3rdFe_AFM1 can be in a AFM4 state with $M_{total} \approx 2\,\mu_B$ or in ferrimagnetic sate with $M_{total} \approx 1 - 2\,\mu_B$. On the other hand, the BTO160_3rdFe_AFM2 supercell has always a AFM4 state with $M_{total} \approx 5.5\,\mu_B$ when in its ψ'' structure.

Finally the BTO160_3rdFe_FM can relax either into a λ like structure with $M_{total} \approx 10\,\mu_B$ or into the ψ structure with $M_{total} \approx 12\,\mu_B$.

After analysing all the magnetic arrangements for the 1stFe, 2nFe and 3rdFe terminations of the BTO160/Fe supercells it is possible to reach several conclusions. Firstly, there is a myriad of possible final relaxed structures which can be achieved in an heterostructure comprised of a rhombohedral BTO unit cell and a monolayer with four Fe atoms in between BTO unit cells. Nevertheless, this multitude of possible structures results in just a few possible magnetic states. Figures 7.32, 7.37 and 7.41 show that for the ferromagnetic state there are three possible M_{total} with $\approx 8, 10$ and $12\,\mu_B$. For the AFM arrangements there is a perfectly AFM state $M_{total} = 0\,\mu_B$, and then there are several FiM states with $M_{total} \approx 1, 2, 4$ and $5.5\,\mu_B$, depending on the relaxed structures.

7.2.4 BTO160_Triangular

Figures 7.44 and 7.45 show the binding energy and total magnetic moment for the BTO160_Triangular supercell.

Its binding energy is defined by equation 7.8:

$$E_{\text{Binding}} = E_{\text{BTO160\_Triangular}} - (3E_{\text{Fe}} + 4E_{\text{Ba}} + 3E_{\text{Ti}} + 12E_{\text{O}}) \ , \tag{7.8}$$

where $E_{\text{BTO160\_Triangular}}$ is the energy of the BTO160_Triangular supercell.

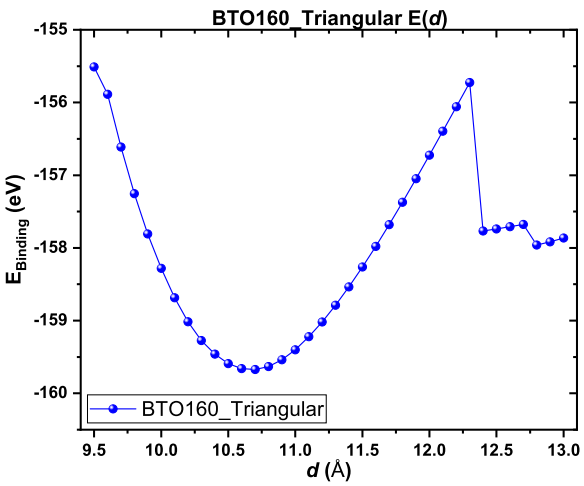

Figure 7.44: Binding energy of the BTO160_Triangular supercell.

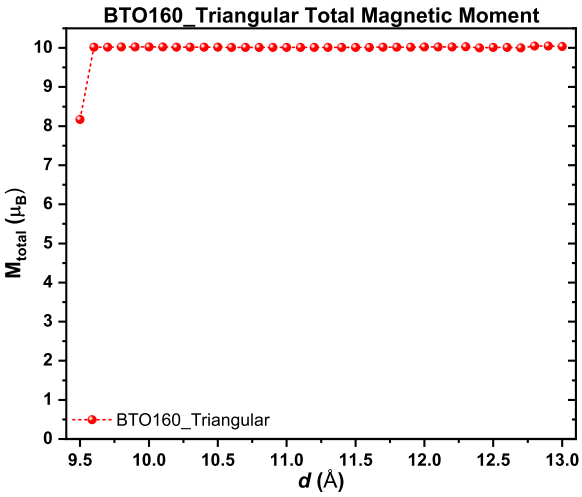

Figure 7.45: Total magnetic moment of the BTO160_Triangular supercell.

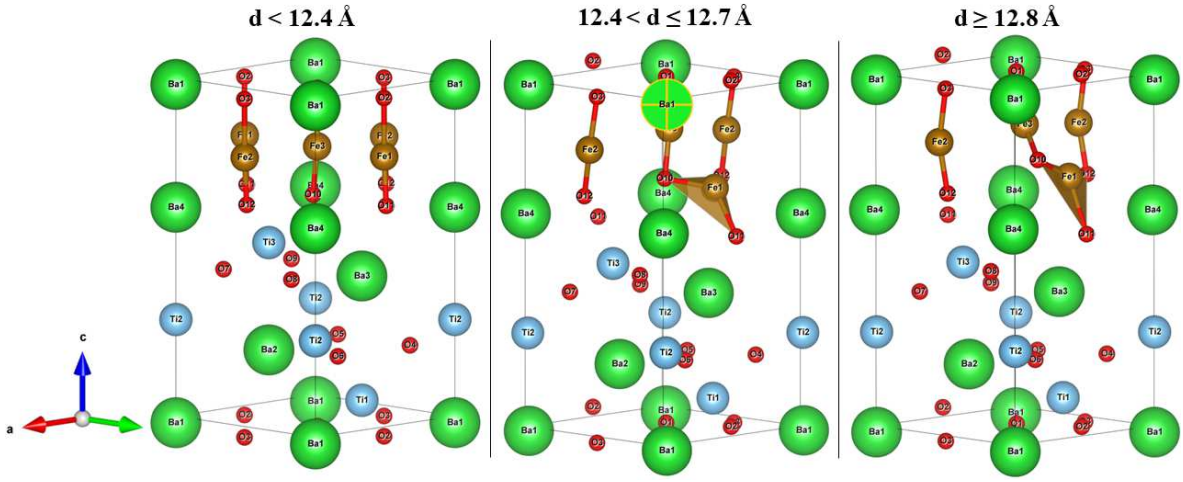

Figure 7.46: Relaxed structures of the BTO160_Triangular supercell.

The creation of the BTO160_Triangular supercell had as motivation the study of the

magnetic effects of a more compact Fe monolayer. This was achieved by removing the Fe atom from the top (bottom) of the big Ba4 (Ba1) atom(s). Indeed, as seen in figure 7.46, in this supercell the Fe monolayer manages to remain bidimensional for most of the considered values of d. The Fe atoms just start to have vertical shifts when the d distance is so large that its binding energy gets too large to sustain the bidimensional configuration and it is energetically more favourable to occupy the created vertical space with the Fe atoms (figure 7.44).

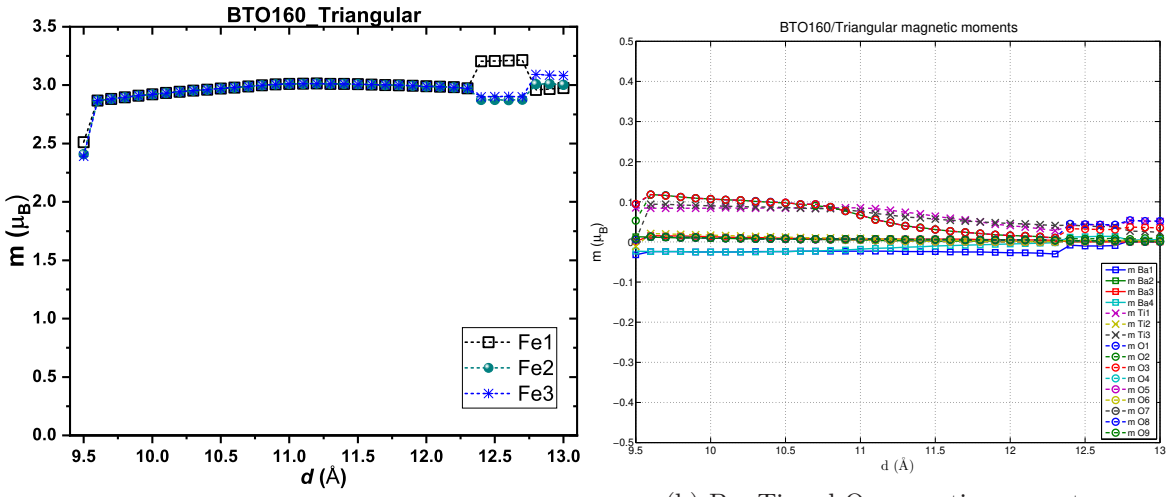

(a) Fe magnetic moments

(b) Ba, Ti and O magnetic moments

Figure 7.47: Magnetic moments for each individual atom of the BTO160_Triangular supercell.

To avoid magnetic frustration between the triangular like Fe disposition, only the ferromagnetic arrangement was considered. Figure 7.45 shows a $M_{total} \approx 10\,\mu_B$ through most of the considered interval of d. This should give about $3.3\,\mu_B$ per Fe atom, yet the observation of figure 7.47a shows that the individual Fe atoms barely reach $3.0\,\mu_B$ for most of the considered d interval. The observation of figure 7.47b solves this puzzle since it shows that the O atoms which surround the Fe atoms have an induced magnetic moment. These also induce a magnetic moment in their closest Ti atoms, hence there is an overall moment enhancement due to the *a priori* non magnetic atoms of the BTO160_Triangular supercell.

7.3 Fe on top of BTO99 and BTO221 {110} and {111} lattice planes

Another conjecture considers that the Fe is in contact with different planes of BTO. This is quite probably happening in some of the auto-composite interfaces of the BTO:Fe_{113ppm} mentioned in chapter 5. Therefore, to emulate this conjecture the following methodology was adopted: Firstly let's take the BTO99_001 and BTO221_001 unit cells and "cut" them through a chosen plane. Then the smallest unit cell built from the selected plane is found, and finally a Fe monolayer is placed on top of it.

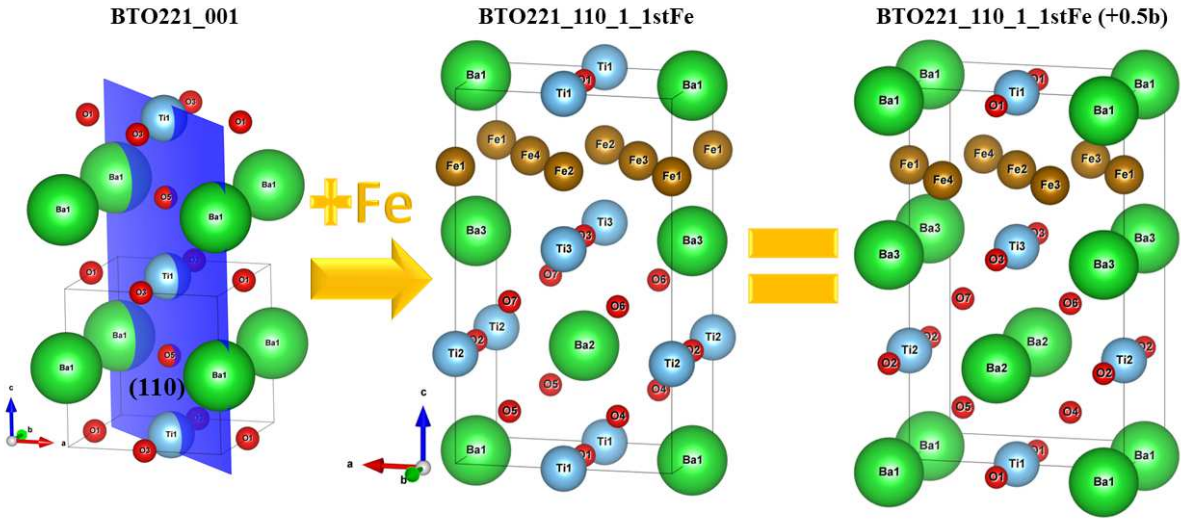

Figure 7.48: Construction of BTO221_110_1_1stFe supercell from the (110) plane of a BTO221_001 unit cell and a 1stFe monolayer.

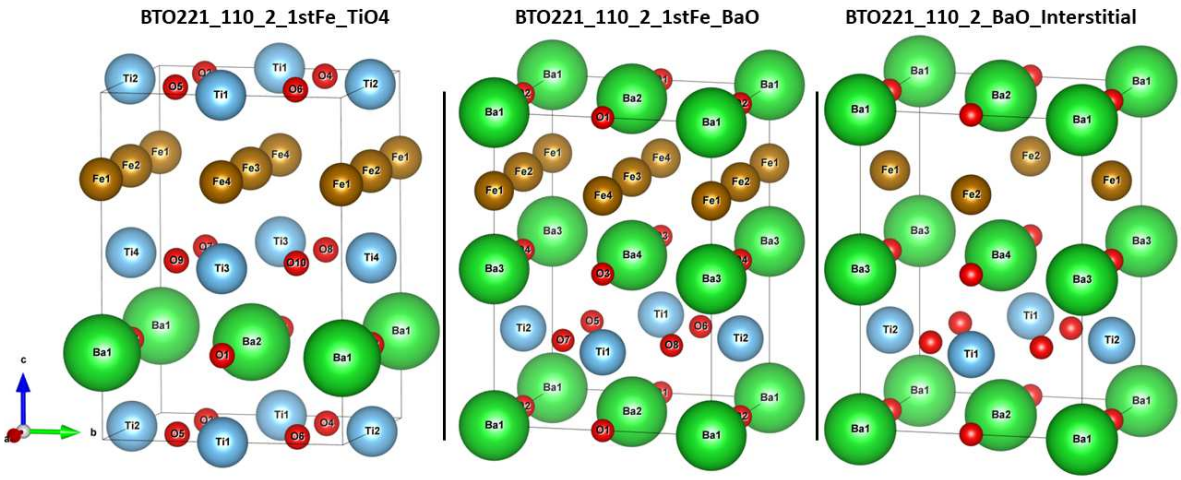

Figure 7.49: The three possible supercell families obtained from the (110) cut plane of a BTO221_001 unit cell.

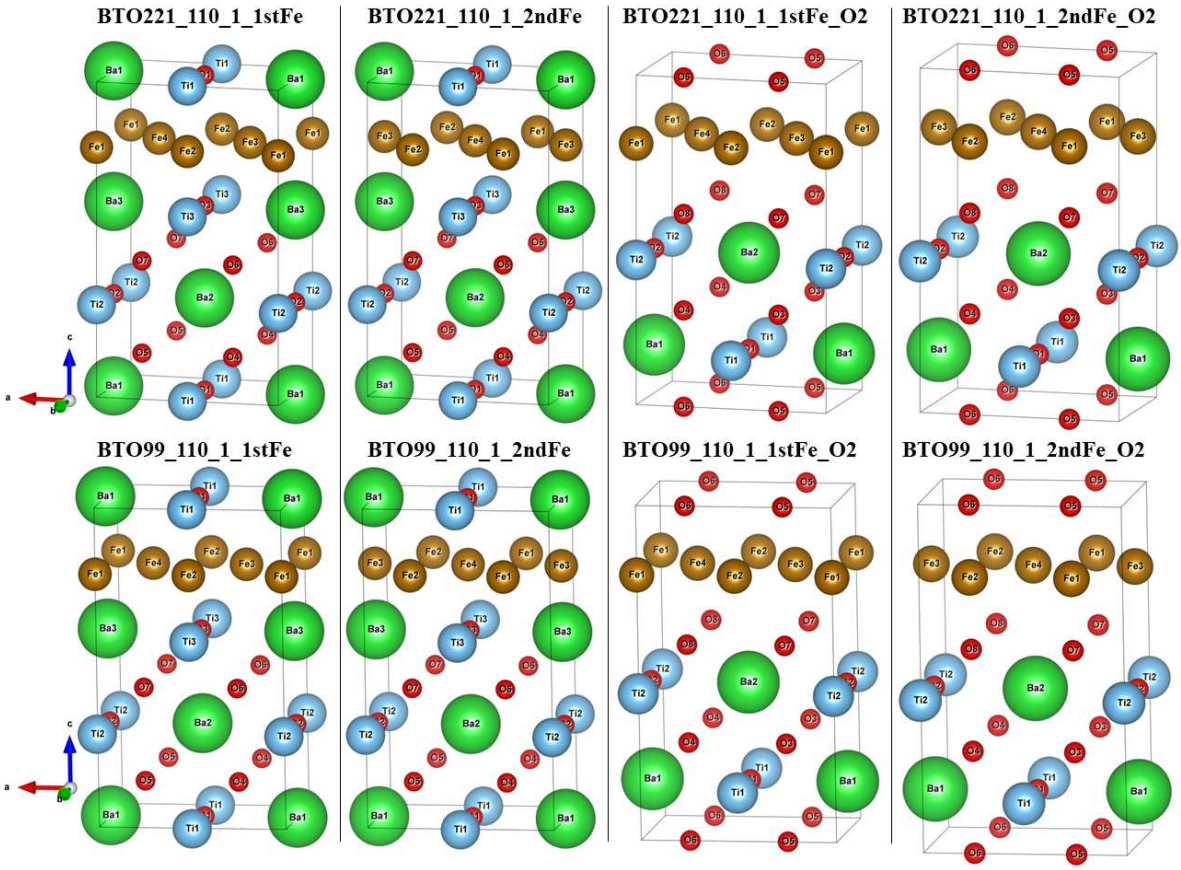

Figure 7.50: All considered BTO221_110_1/Fe and BTO99_110_1/Fe supercells.

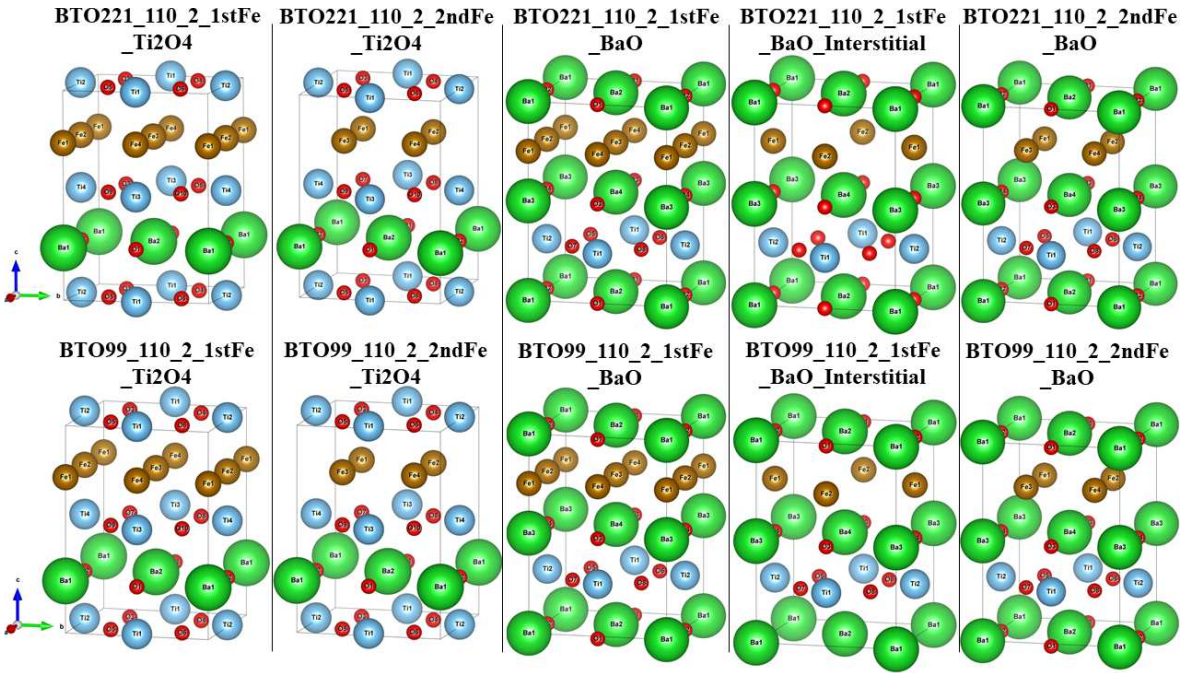

Figure 7.51: All considered BTO221_110_2/Fe and BTO99_110_2/Fe supercells.

Figure 7.48 shows the construction of the BTO221_110_1_1stFe supercell using the (110) plane of a BTO221_001 unit cell and a Fe monolayer in the 1stFe placement. This same methodology was used to build the BTO99_110_1_1stFe supercell when the BTO99_001 unit cell is used instead. It is possible to see that after a translation of $[0, 0.5b, 0]$, the BTO221(99)_110_1_1stFe supercells are quite similar to the BTO38_2ndFe supercell. This way, the only differences between the BTO221_110_1_1stFe, BTO99_110_1_1stFe and BTO38_2ndFe supercell are the values of each lattice parameters and some small deviations from the atomic coordinates of each atom.

As in the BTO38/Fe supercells, besides the BaTiO layer, the O_2 layer of the BTO_110_1 unit cells was considered as a BTO termination, as well as their respective 1stFe and 2ndFe monolayers. All the considered BTO221(99)_110_1/Fe supercells are presented in figure 7.50.

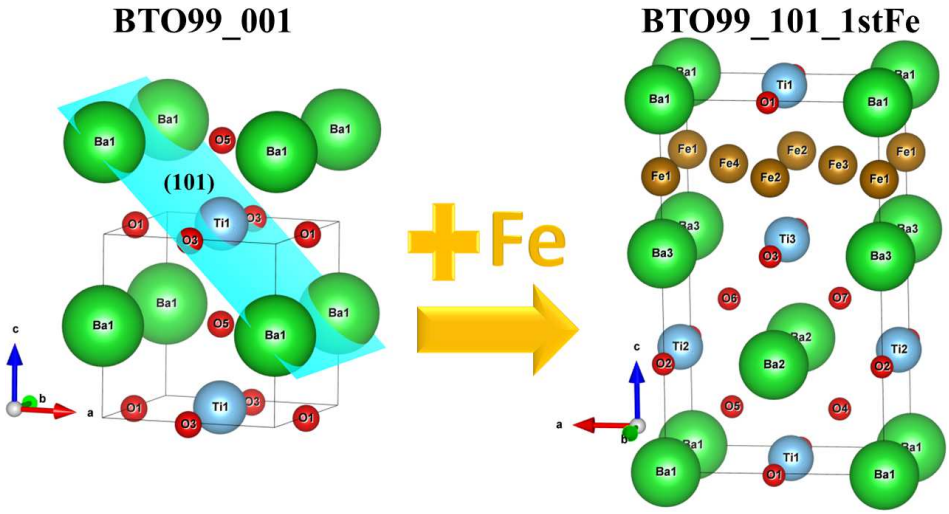

Figure 7.52: Construction of BTO99_101_1stFe supercell from the (101) plane of a BTO99_001 unit cell and a 1stFe monolayer.

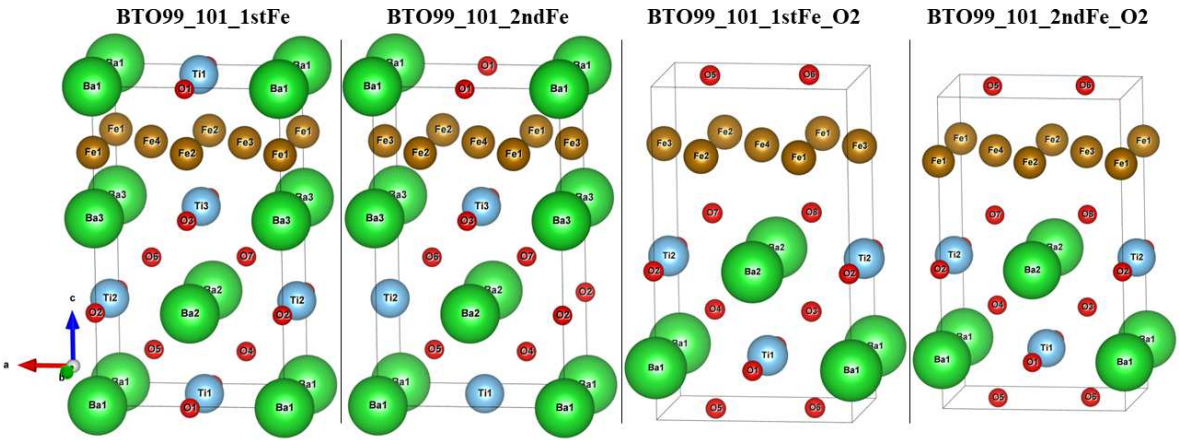

Figure 7.53: All considered BTO99_101/Fe supercells.

If in the methodology illustrated in figure 7.48, before placing the Fe atoms on top of the BTO221(99)_110 unit cell, a rotation of 90° is done using the a lattice parameter as the rotation axis, then the BTO221(99)_110_2_1stFe_Ti2O4 supercell is obtained (figure 7.49). Figure 7.49 also presents the BTO221(99)_110_2_1stFe_BaO supercell, built by placing the Fe atoms upon the BaO layer. Based on this structure, by removing the Fe atoms that were on top of the Ba atoms, the BTO221(99)_110_2_BaO_Interstitial was also built (figure 7.49). All the BTO221_110_2/Fe and BTO99_110_2/Fe supercells considered in this thesis are presented in 7.51.

In the case of the BTO99 unit cell, contrarily to the BTO221 case, the c lattice parameter is different from the $a = b$ lattice parameters. For this reason cutting the unit cell trough the plane (101) is not exactly the same as cutting through the (110) plane. Hence, as presented in figure 7.52, for the tetragonal case of BTO, the construction of the BTO99_101_1stFe was also done and considered in the calculations. This supercell is identical to the orthorhombic BTO38_1stFe, apart from the lattice parameters and some deviations of the atoms coordinates (as in BTO221(99)_110_1_2ndFe). All the BTO99_101/Fe supercells here considered are presented in 7.53.

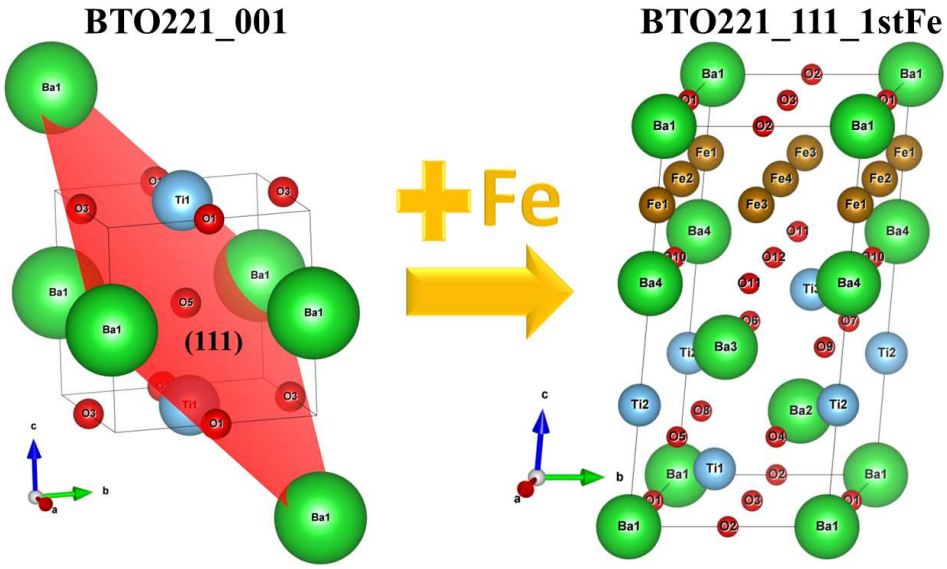

Figure 7.54: Construction of BTO221_111_1stFe supercell from the (111) plane of a BTO221_001 unit cell and a 1stFe termination.

Finally, by cutting the BTO221 unit cell through the (111) plane, as shown in figure 7.54, BTO221_111_1stFe is obtained. This supercell is clearly similar to the rhombohedral BTO160_1stFe unit cell, thus all the BTO160/Fe variants were also considered in the

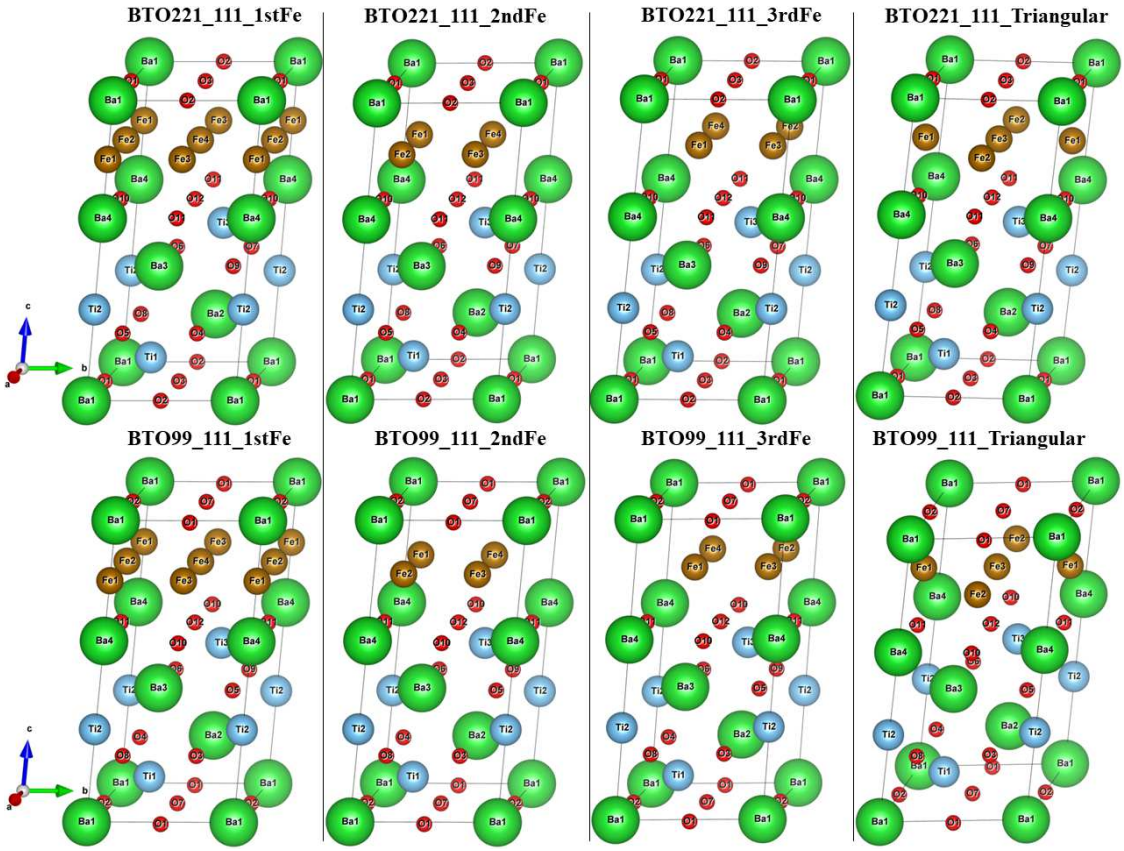

Figure 7.55: All considered BTO221_111/Fe and BTO99_111/Fe supercells.

BTO221_111/Fe case. A similar methodology was also implemented using a BTO99 unit cell. All the considered BTO221_111/Fe and BTO99_111/Fe supercells considered in the calculations are presented in figure 7.55.

The DFT calculations conditions of BTO221(99)_{110}/Fe and BTO221(99)_{111}/Fe supercells are presented in table 7.8. The considered input magnetic arrangements are in the same conditions as the ones defined in previous sections.

					Lattice parameters (Å)	
Supercells	**E_{diff} (eV)**	**HF Forces (eV/Å)**	**E_{cut} (eV)**	**k-points**	a	b
BTO221_110/Fe	10^{-5}	0.02	500	5 4 2	5.6839	4.0191
BTO99_110_1/Fe	10^{-5}	0.02	500	4 5 2	5.6475	4.0348
BTO99_101/Fe	10^{-5}	0.02	500	5 4 2	5.6769	3.9934
BTO221_110_2/Fe	10^{-5}	0.02	500	5 4 2	5.6769	5.6769
BTO99_110_2/Fe	10^{-5}	0.02	500	5 5 3	5.6475	5.6475
BTO221_111/Fe	10^{-5}	0.02	500	5 5 2	5.68387	5.68387
BTO99_111/Fe	10^{-5}	0.02	500	5 5 2	5.6769	5.6769

Table 7.8: DFT calculations conditions of the BTO221(99)_{110}/Fe and BTO221(99)_{111}/Fe supercells.

7.4 BTO221(99)_{110}/Fe

7.4.1 Comparison between BTO38_1stFe and BTO_{110}/Fe

As mentioned previously, the BTO221(99)_{110}/Fe supercell family has a direct correspondence with the BTO38/Fe supercells. Here we compare the BTO38_1stFe supercells with the equivalent BTO99_101_1stFe and BTO221(99)_110_1_2ndFe supercells. Figures 7.56–7.63 present the binding energies and total magnetic moments for all the considered magnetic arrangements of these supercells.

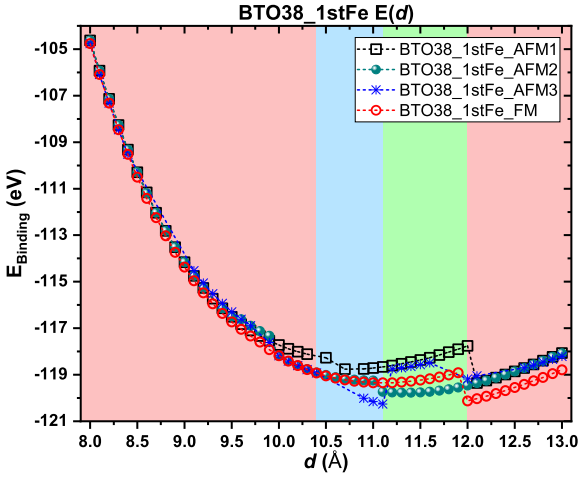

Figure 7.56: Binding energy for all the considered magnetic arrangements of the BTO38_1stFe supercell.

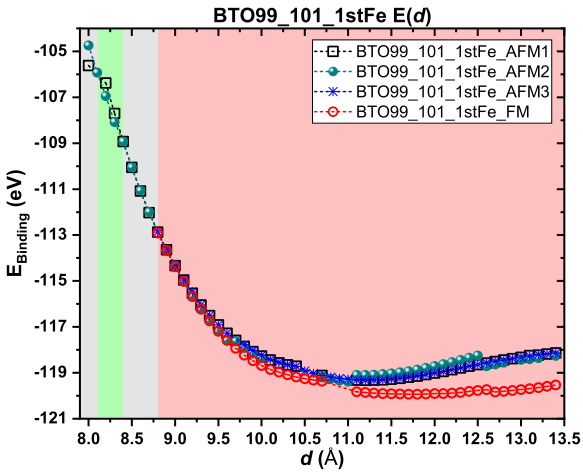

Figure 7.57: Binding energy for all the considered magnetic arrangements of the BTO99_101_1stFe supercell.

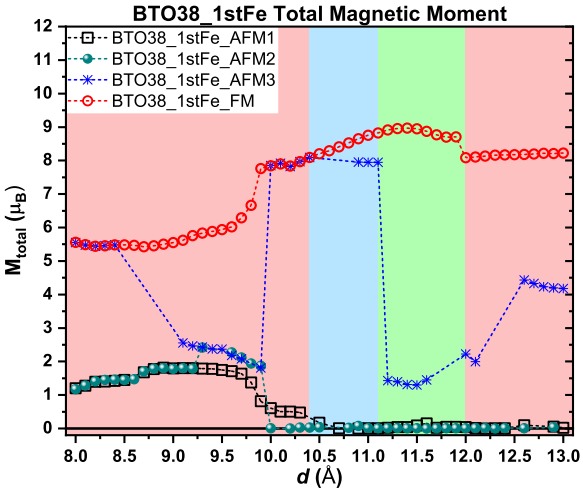

Figure 7.58: Total magnetic moment for all the considered magnetic arrangements of the BTO38_1stFe supercell.

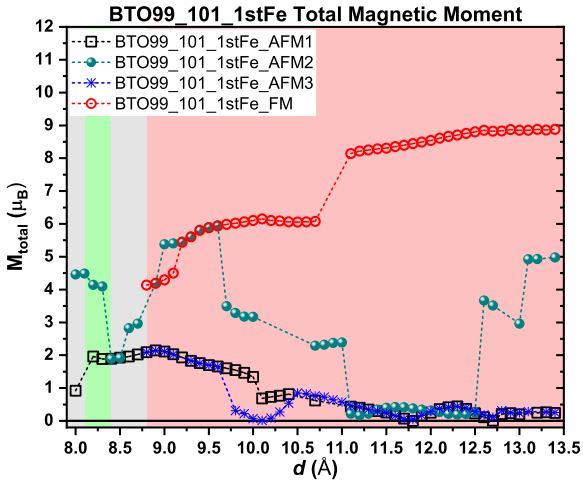

Figure 7.59: Total magnetic moment for all the considered magnetic arrangements of the BTO99_101_1stFe supercell.

The binding energies and M_{total} curves have qualitatively the same kind of behaviours, yet the regions where they occur have some differences due to the different lattice parameters and initial atomic coordinates. These differences result in distinct volumes and equilibrium atomic positions for each supercell, leading to the relaxation of structures similar to the ones discussed in section 7.1.1. Therefore, it will be assumed that the individual magnetic moment curves are akin, thus the final resultant M_{total} will be immediately discussed.

It is possible to see in figures 7.57 and 7.59 that for the BTO99_101_1stFe supercell its ferromagnetic state is the most stable magnetic behaviour. This occurs for almost all the considered d values (for $d \geq 8.9\,\text{Å}$), namely around the global minimum (at $d \approx 11.7\,\text{Å}$). A similar behaviour is also displayed by the BTO221_110_1_2ndFe supercell, which is ferromagnetic for $d \geq 8.9\,\text{Å}$ and has its global minimum at $d \approx 11.2\,\text{Å}$), as seen in figures 7.61 and 7.63.

These two supercells contrast with BTO38_1stFe (figures 7.56 and 7.58) and BTO99_-110_1_2ndFe supercells (figures 7.60 and 7.62), which have at least two different magnetic behaviours near their local minima. This feature can be exploited in several scenarios.

First, let's consider that we have a BTO99_101_1stFe supercell near its predicted global minimum (figure 7.57). If a structural phase transition is induced on this supercell, changing it to the BTO38_1stFe supercell, and its d value remains within the $11.1 \leq d \leq 12\,\text{Å}$ range, there will be a magnetic order change from the BTO99_110_1_2ndFe FM state with $M_{total} \approx 8.5\,\mu_B$ (figure 7.59) to BTO38_1stFe's AFM state with $M_{total} \approx 0\,\mu_B$ (figure 7.58). Such an abrupt magnetization switching is truly interesting from a technological point of view, thus being a very appealing configuration.

Other possible scenario involves the tetragonal BTO99_110_1_2ndFe supercell around its $d \approx 11.3\,\text{Å}$ minimum (figure 7.60). At this point, the tetragonal supercell is in a AFM state with $M_{total} \approx 0\,\mu_B$ (figure 7.62), yet if there is a transition to its cubic counterpart, without a substantial change of d, then it will change to a FM BTO221_110_1_2ndFe supercell with $M_{total} \approx 8.5\,\mu_B$ (figure 7.63).

Another possibility involving BTO99_110_1_2ndFe, consists in a phase transition associated with a decrease of d from its tetragonal local minimum at $d \approx 11.3\,\text{Å}$ to any value $d \leq 11.1\,\text{Å}$ of its orthorhombic supercell. In this scenario there is a magnetic phase transition from the AFM state of BTO99_110_1_2ndFe with $M_{total} \approx 0\,\mu_B$ to the FM state of BTO38_1stFe with $M_{total} \approx 8.5\,\mu_B$.

It should be pointed out that in this last scenario the magnetic phase transition of the Fe monolayer is coupled with the "ferroelectric" phase transitions of the BTO[4]. The reason why this last statement might sound familiar is due to the occurrence of an identical behaviour in chapter 5, where there was a huge change in magnetization when the tetragonal $BaTiO_3$:Fe_{113ppm} changed to its orthorhombic ferroelectric phase.

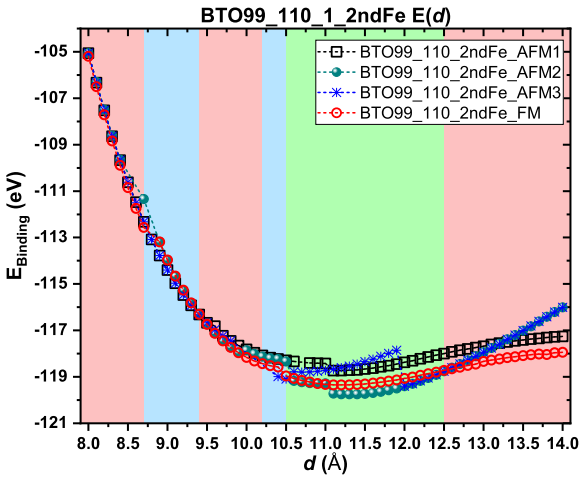

Figure 7.60: Total magnetic moment for all the considered magnetic arrangements of the BTO99_110_1_2ndFe supercell.

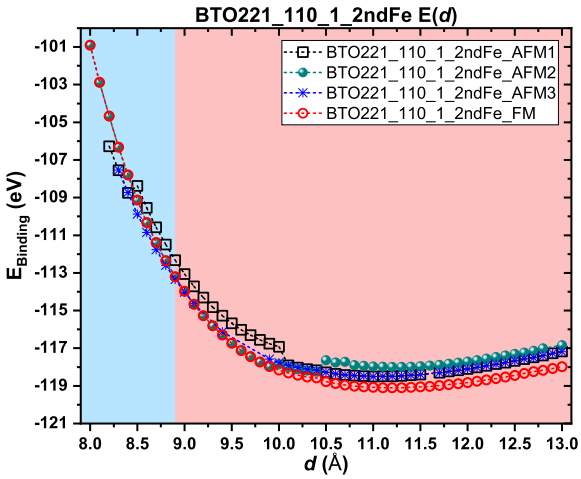

Figure 7.61: Total magnetic moment for all the considered magnetic arrangements of the BTO221_110_1_2ndFe supercell.

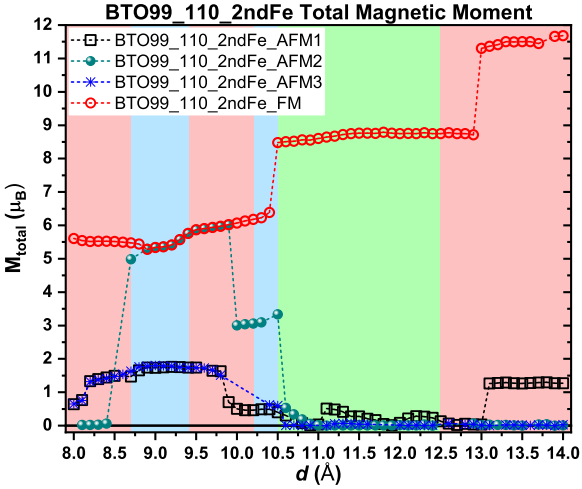

Figure 7.62: Total magnetic moment for all the considered magnetic arrangements of the BTO99_110_1_2ndFe supercell.

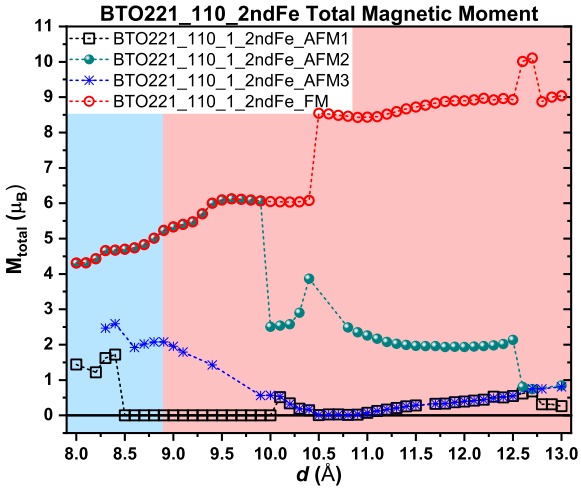

Figure 7.63: Total magnetic moment for all the considered magnetic arrangements of the BTO221_110_1_2ndFe supercell.

[4]Similarly to the approach made in section 6.1.3, when it is said that there is BTO phase transition it is assumed that it is possible to control the lateral lattice parameters by attaching a substrate-like BTO to the heterostructures of each studied supercell. This bulk BTO substrate will impose the lateral lattice parameters of the supercell according to its structural phase.

In fact, this effect could justify the O↔T magnetoelectric transition of chapter 5, assuming that some of the special sites where the Fe segregates, have an interface identical to the one presented in the BTO99_110_1_2ndFe supercell. However, its T→C transition would actually have an increase in its magnetization, contrarily to what is observed in chapter 5. Still, this could be explained by a competition of more than one effect in the T→C transition, such as the magnetic moment quench of section 6.1.3, whose sum would result in an overall decrease of magnetization at the T→C transition.

7.4.2 Comparison between BTO38_2ndFe and BTO_{110} /Fe

Now let's compare the BTO38_2ndFe supercells with the equivalent BTO99_101_2ndFe and BTO221(99)_110_1_1stFe supercells. Figures 7.64–7.71 present the binding energies and total magnetic moments for all the considered magnetic arrangements of these supercells.

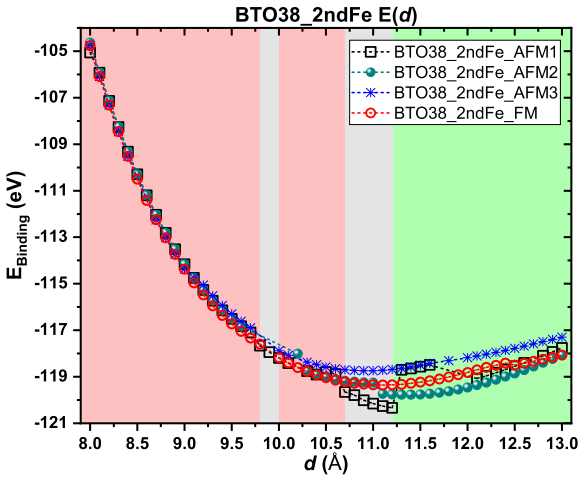

Figure 7.64: Binding energy for all the considered magnetic arrangements of the BTO38_2ndFe supercell.

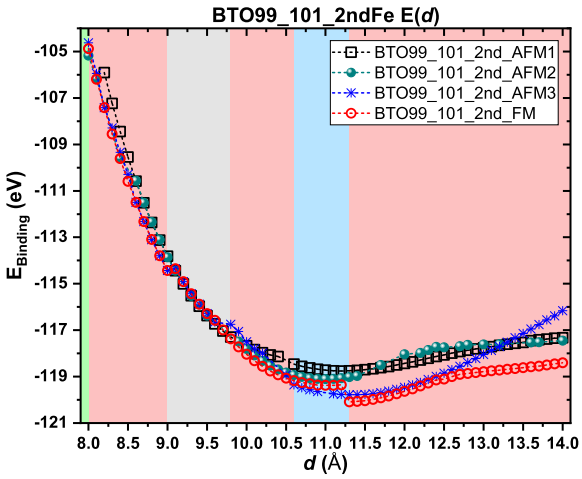

Figure 7.65: Binding energy for all the considered magnetic arrangements of the BTO99_101_2ndFe supercell.

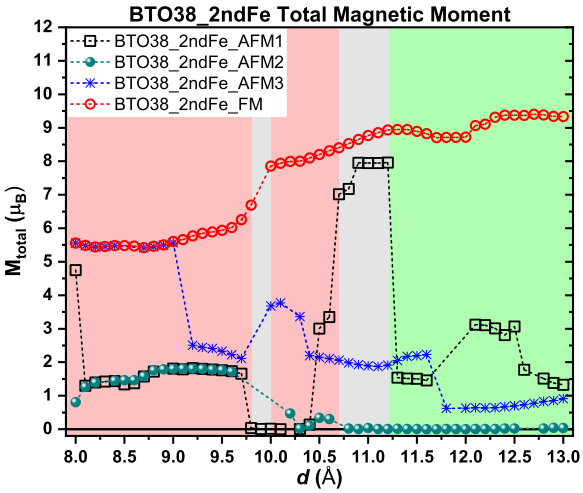

Figure 7.66: Total magnetic moment for all the considered magnetic arrangements of the BTO38_2ndFe supercell.

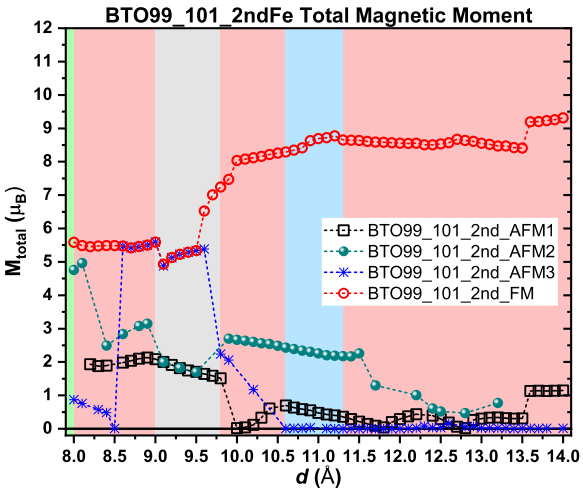

Figure 7.67: Total magnetic moment for all the considered magnetic arrangements of the BTO99_101_2ndFe supercell.

Once again, it is possible to see that the BTO_{110}/Fe is equivalent to the BTO38_2ndFe supercells have mostly the same magnetic behaviours and identical binding energy curves (figures 7.64, 7.65, 7.68 and 7.69). Additionally, the BTO38_2ndFe supercells are also quite

similar to the BTO38_1stFe supercells, hence the possible interesting magnetic phenomena are identical to the ones described in last section (figures 7.66, 7.67, 7.70 and 7.71).

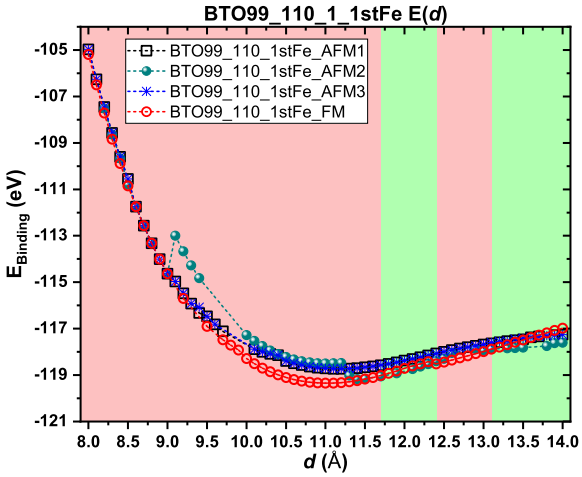

Figure 7.68: Binding energy for all the considered magnetic arrangements of the BTO99_110_1_1stFe supercell.

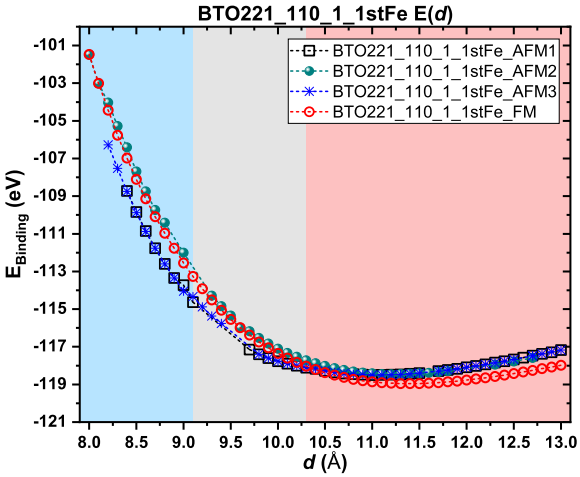

Figure 7.69: Binding energy for all the considered magnetic arrangements of the BTO221_110_1_1stFe supercell.

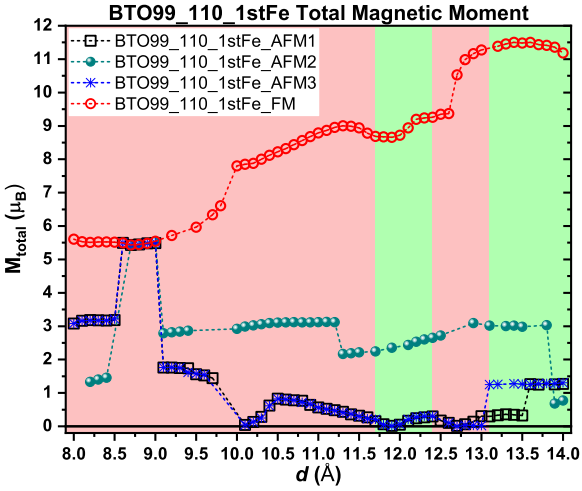

Figure 7.70: Total magnetic moment for all the considered magnetic arrangements of the BTO99_110_1_1stFe supercell.

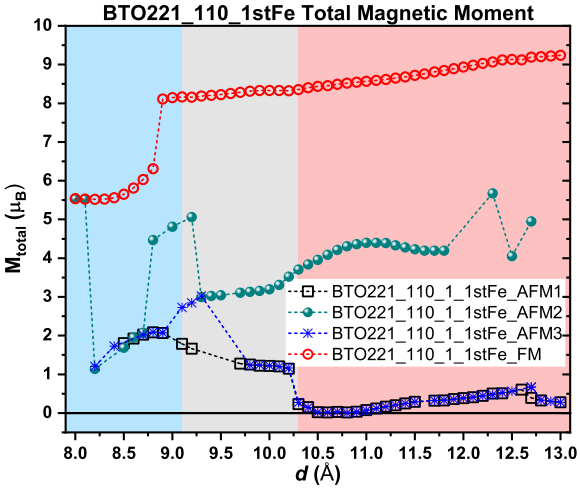

Figure 7.71: Total magnetic moment for all the considered magnetic arrangements of the BTO221_110_1_1stFe supercell.

Here, BTO99_101_2ndFe is the most noteworthy supercell, since apart from the BTO38_2ndFe supercell, it is the only one which has more than one magnetic state around its global minimum at $d \approx 11.3\,\text{Å}$ (figure 7.65). At $d \approx 11.3\,\text{Å}$ this supercell can be either in a FM state with $M_{total} \approx 8.5\,\mu_B$ or in a AFM state with $M_{total} \approx 0\,\mu_B$, once its minimum is in the vicinity of these two magnetic states (figure 7.67). This means that this supercell may be by

itself a good magnetoelectric interface with the capability of switching between the AFM and FM states with the help, for example, of an electric field.

Nonetheless, this supercell has also the ability to couple its magnetic state/order to the BTO ferroelectric states. As long as its starting d value is within $10.6 \leq d \leq 11.3$, this tetragonal supercell will be in the previously mentioned AFM state and can be switched to one of the FM states of the orthorhombic BTO38_2ndFe supercell (figure 7.66), depending on the change of d induced by the structural phase transition.

Using the same starting range of d, it is also possible to induce a AFM to FM magnetic phase transition correlated with the BTO's tetragonal to cubic phase transition (figure 7.71).

7.4.3 Comparison between BTO38/Fe_O2 and BTO_{110} /Fe_O2

The BTO_{110} /Fe supercells with an O_2 termination were also studied. Since most of these supercells have similar binding energy and total magnetic moment curves, privileging a FM state through the here considered range of d, most of these supercells will not be further mentioned in this thesis. Still, there are three – the BTO99_110_1_1stFe_O2, BTO221_110_1_1stFe_O2 and BTO99_101_2ndFe_O2 supercells – which have promising magnetic properties.

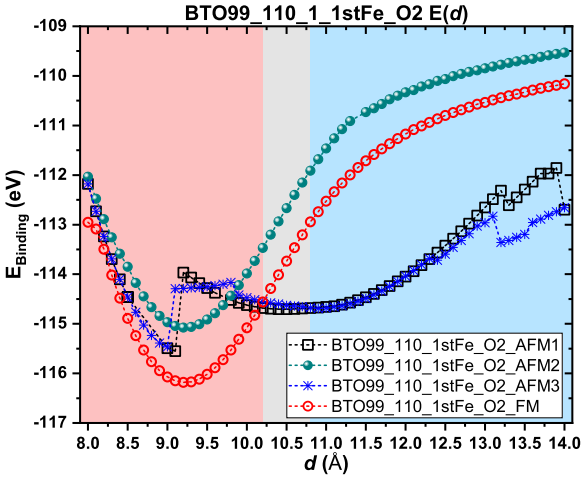

Figure 7.72: Binding energy for all the considered magnetic arrangements of the BTO99_110_1_1stFe_O2 supercell.

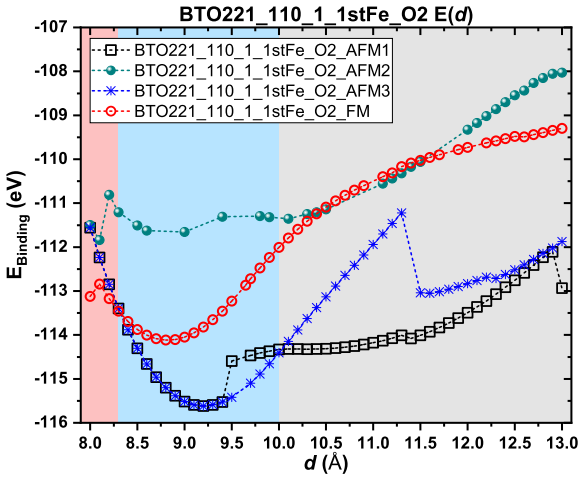

Figure 7.73: Binding energy for all the considered magnetic arrangements of the BTO221_110_1_1stFe_O2 supercell.

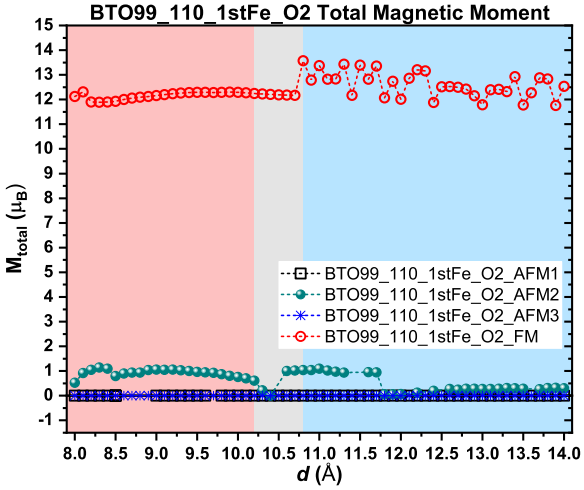

Figure 7.74: Total magnetic moment for all the considered magnetic arrangements of the BTO99_110_1_1stFe_O2 supercell.

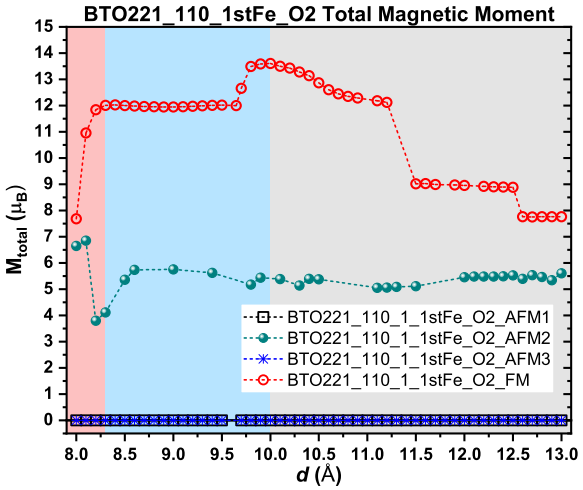

Figure 7.75: Total magnetic moment for all the considered magnetic arrangements of the BTO221_110_1_1stFe_O2 supercell.

Looking at the binding energies of the BTO99_110_1_1stFe_O2 and BTO221_110_1_-1stFe_O2 supercells (figures 7.72 and 7.73), it is possible o see that the pseudo-cubic supercell has a perfect AFM state for most of the considered values of d, namely near its global minimum at $d \approx 9.2\,\text{Å}$ (figure 7.73). This contrasts with the $M_{total} \approx 12.2\,\mu_B$ FM state of the BTO99_110_1_1stFe_O2 supercell around its global minimum, also at $d \approx 9.2\,\text{Å}$ (figure 7.72). If a bulk-like BTO attached to these interfaces suffers a phase transition, then there would be a magnetic phase transition between the $M_{total} = 0\,\mu_B$ AFM state and the $M_{total} \approx 12.2\,\mu_B$ FM state, hence these supercells would also be good candidates to explain the T↔C magnetoelectric phase transitions seen in chapter 5.

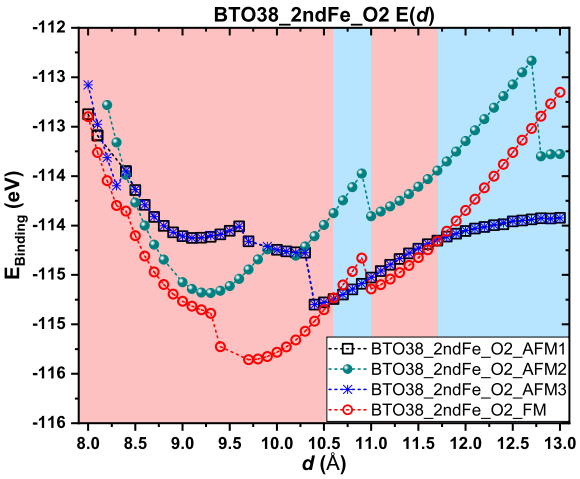

Figure 7.76: Binding energy for all the considered magnetic arrangements of the BTO38_2ndFe_O2 supercell.

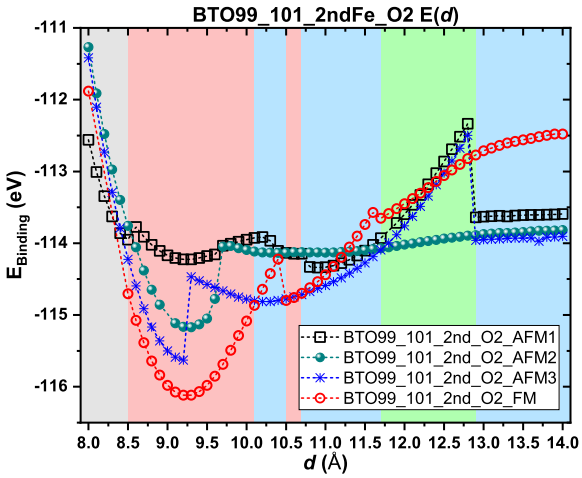

Figure 7.77: Binding energy for all the considered magnetic arrangements of the BTO99_101_2ndFe_O2 supercell.

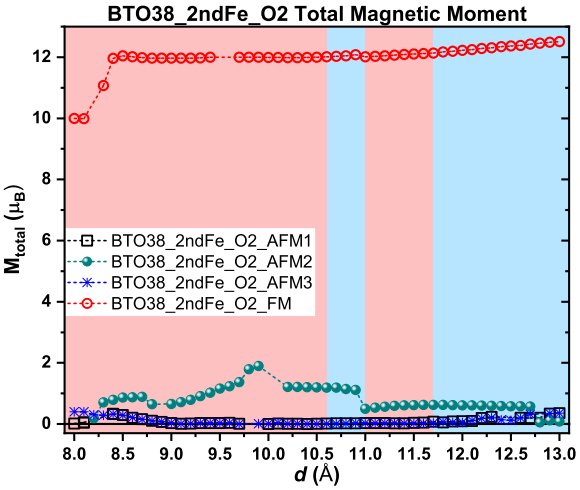

Figure 7.78: Total magnetic moment for all the considered magnetic arrangements of the BTO38_2ndFe_O2 supercell.

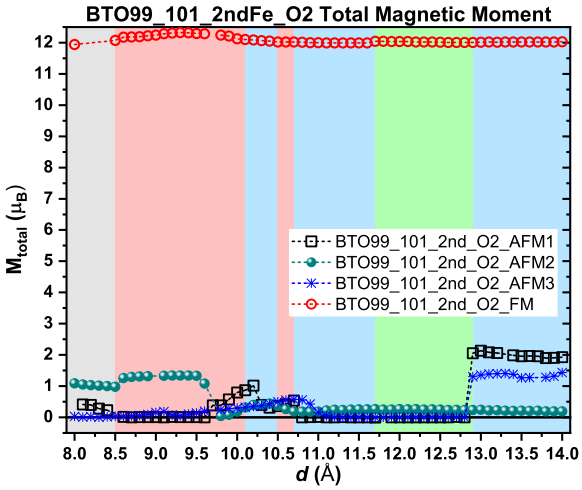

Figure 7.79: Total magnetic moment for all the considered magnetic arrangements of the BTO99_101_2ndFe_O2 supercell.

On the other hand, figure 7.77 shows a metastable minimum at $d \approx 10.2\,\text{Å}$ for the BTO99_101_2ndFe_O2 supercell. This metastable state is associated with a close to perfect AFM state, as shown in figure 7.79. Still, at $d \approx 10.2\,\text{Å}$ there is a metastable FM state with $M_{total} \approx 12\,\mu_B$, which could be accessed by decreasing the value of d by about 3% of its AFM equilibrium value, with the resort of some sort of external perturbation.

Moreover, since this supercell is equivalent to the BTO38_2ndFe_O2 supercell, it makes sense to see what would happen if the O↔T phase transition occurred. Figures 7.76 and 7.78 show that the BTO38_2ndFe_O2 supercell has its global minimum around $d \approx 9.7\,\text{Å}$, thus a phase transition from the tetragonal to the orthorhombic phase would induce a magnetization increase due to the change of the $M_{total} \approx 0\,\mu_B$ AFM state to the $M_{total} \approx 12\,\mu_B$ FM state. However, figure 7.77 shows that the BTO99_101_2ndFe_O2 supercell has its global minimum at $d \approx 9.3\,\text{Å}$, hence this magnetic transition, if thermally activated, would be irreversible.

7.5 BTO221(99)_110_2/Fe

7.5.1 BTO221(99)_110_2_1stFe_BaO

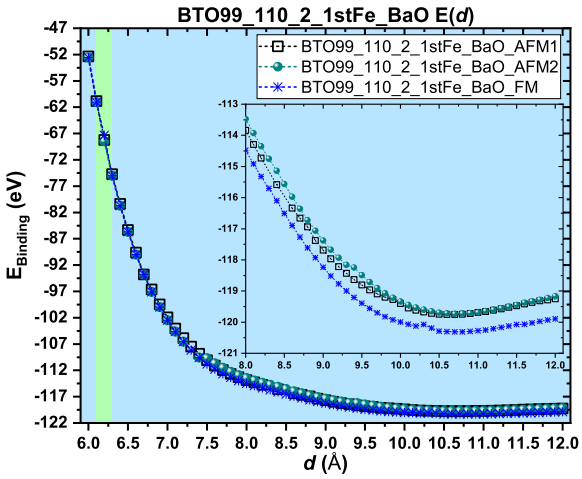

Figure 7.80: Binding energy for all the considered magnetic arrangements of the BTO99_110_2_1stFe_BaO supercell.

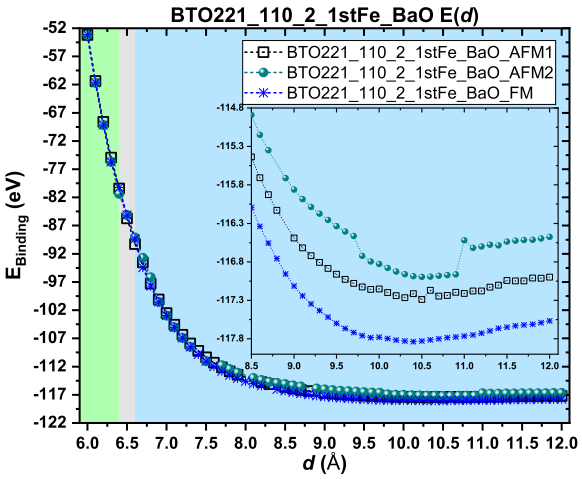

Figure 7.81: Binding energy for all the considered magnetic arrangements of the BTO221_110_2_1stFe_BaO supercell.

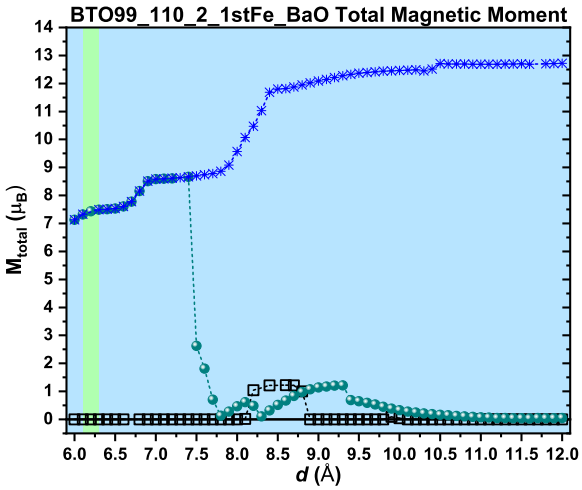

Figure 7.82: Total magnetic moment for all the considered magnetic arrangements of the BTO99_110_2_1stFe_BaO supercell.

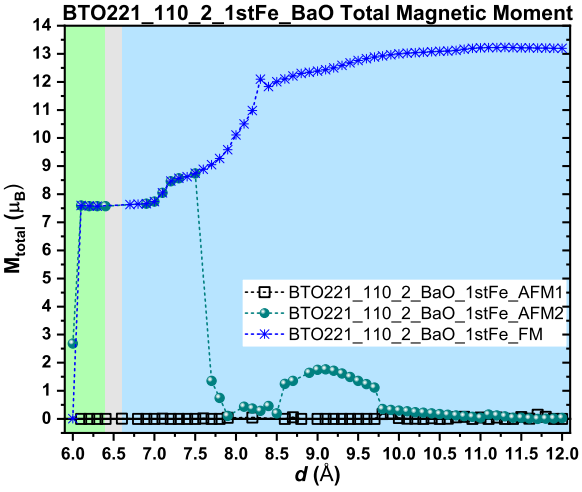

Figure 7.83: Total magnetic moment for all the considered magnetic arrangements of the BTO221_110_2_1stFe_BaO supercell.

The binding energy and total magnetic moment for the BTO221(99)_110_2_1stFe_BaO supercells (figure 7.51) are shown in figures 7.80–7.83.

The binding energy is defined by equation 7.9:

$$E_{\text{Binding}} = E_{\text{BTO221(99)\_110\_2\_1stFe\_BaO}} - (4E_{\text{Fe}} + 4E_{\text{Ba}} + 2E_{\text{Ti}} + 8E_{\text{O}}) \ , \qquad (7.9)$$

where $E_{\text{BTO221(99)\_110\_2\_1stFe\_BaO}}$ is the energy of the BTO221(99)_110_2_1stFe_BaO supercells.

The observation of both the binding energies and total magnetic moment curves shows that they are identical for both the BTO221(99)_110_2_1stFe_BaO supercells. For this reason, to avoid unnecessary plot repetition, only BTO99_110_2_1stFe_BaO individual Fe moments for the different magnetic arrangements are presented (figure 7.84). This approach will also be used later in BTO221(99)_110_2/Fe supercells.

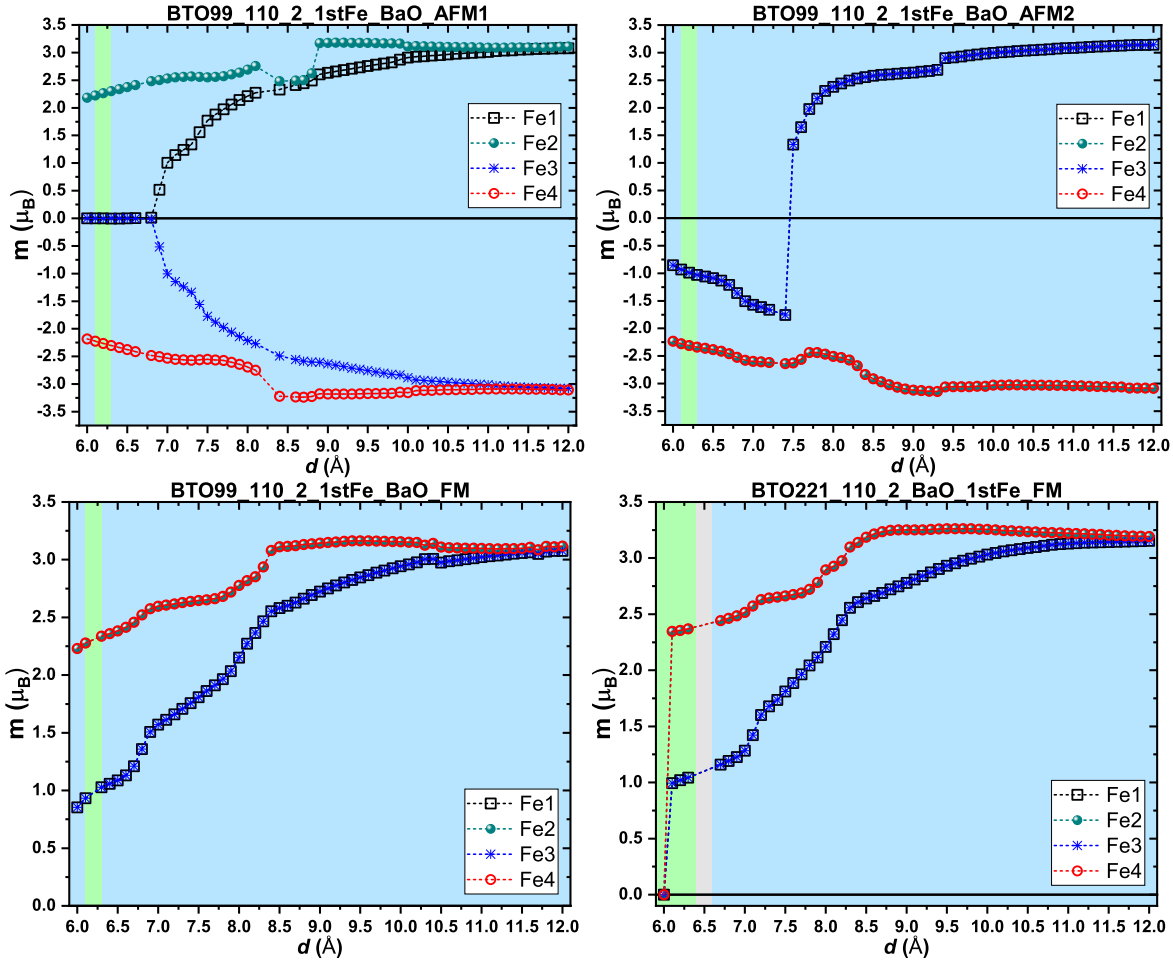

Figure 7.84: Fe magnetic moments for different magnetic arrangements of the BTO(221)99_110_2_1stFe_BaO supercells.

All the considered magnetic arrangements relax into one of two final structures. The first has a Fe monolayer, as in its initial placement, while in the second structure the Fe1 and Fe3 atoms go upward, conserving their lateral positions, resulting in a Fe bilayer. Figure 7.84 shows that the BTO99_110_2_1stFe_BaO_AFM1 supercell has a completely balanced AFM state

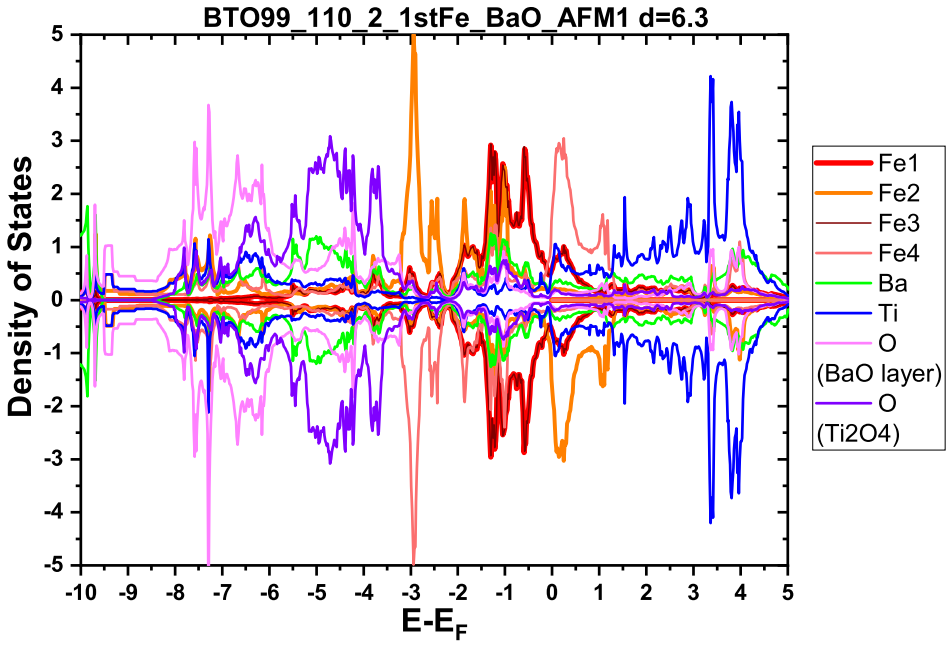

Figure 7.85: Density of states of the BTO99_110_2_1stFe_BaO supercell at $d = 6.3\,\text{Å}$.

through most of the considered d range. This supercell has an Fe monolayer structure for $d \leq 8\,\text{Å}$ and the bilayered structure for $d > 8\,\text{Å}$. Still, curiously, this structural change does not seem to affect considerably its magnetic properties[5]. However, there is a quite interesting effect seen in BTO99_110_2_1stFe_BaO_AFM1 at $d \leq 6.8\,\text{Å}$, where the Fe1 and Fe3 atoms, which are between the Ba atoms, have their magnetic moments quenched. To understand this particular phenomenon, let's look at the DOS of BTO99_110_2_1stFe_BaO_AFM1 at $d = 6.3\,\text{Å}$, shown in figure 7.85, and the charge and SP charge density difference of figure 7.86.

It is visible that the Fe1 and Fe3 atoms have exactly the same DOS, which consist of equally occupied up and down spin electrons. These DOS are in line with their magnetic moments, $m = 0\,\mu_\text{B}$. On the other hand, the DOS of the Fe2 and Fe4 atoms are symmetric to each other, and have up and down spin majority electrons respectively, which together with the other's null moments result in a $\text{M}_\text{total} = 0\,\mu_\text{B}$. Additionally, it is important to point out that for the presented energy range there are quite few Ba DOS (which partially overlap with the Fe1 and Fe3 atoms), and that the majority of O's DOS does not overlap with Fe DOS.

These features are clearly perceptible in the charge density of figure 7.86, which was calculated for $\text{E-E}_\text{F} \in [-3, 0]\,\text{eV}$. The Ba atoms do not show an expressive charge density, and

[5]The same monolayered and bilayered structures occur in the remaining magnetic arrangements for the tetragonal supercells around the same range, still their magnetic curves also seem unaffected by the dire structural change.

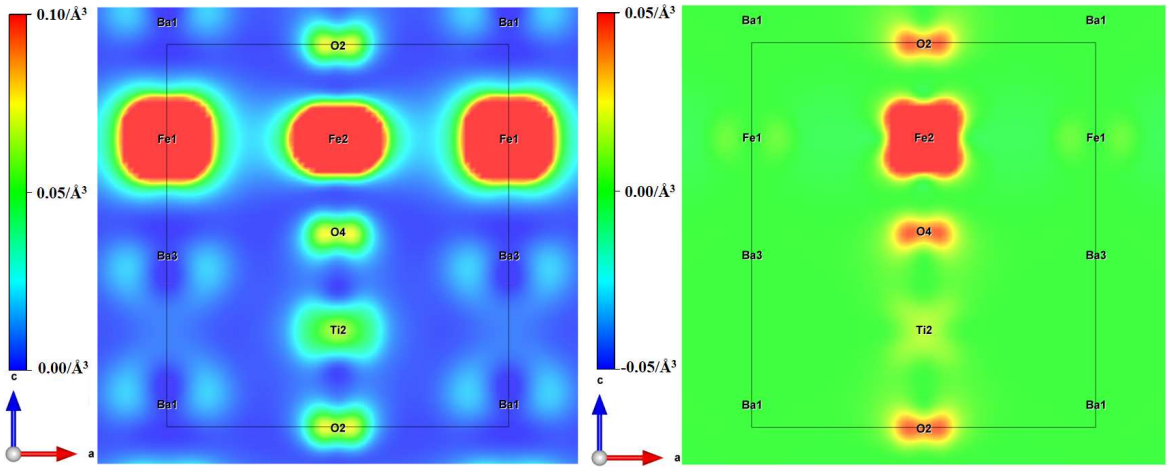

Figure 7.86: Charge density (left) and SP charge density difference (right) of the BTO99_110_2_1stFe_BaO_AFM1 for $d = 6.3\,\text{Å}$ across one of the supercell faces, calculated for E-$E_F \in [-3, 0]\,\text{eV}$.

the one that is perceptible does not overlap at all with Fe charge density. The O atoms, as in section 6.1.2, have part of their electrons overlapping with Ti's electrons but not with Fe's electrons, distorting the latter's shape as if they were tying to be the farthest away possible from the O's electrons. Still, as it is perceptible in the SP charge density charge of figure 7.86 it is possible to see that the Fe atoms which have their moments quenched are the ones between the Ba atoms. This happens due to the huge pressure exerted on the Fe atoms by the Ba atoms ($p \approx 152\,\text{GPa}$ along the z direction), which makes their magnetic moment to collapse, similar to what happens in iron-rich materials when subjected to high enough pressures [234–236]. Moreover, looking at the binding energies of BTO99_110_2_1stFe_BaO_AFM1 at its global minimum, around $d = 10.65\,\text{Å}$ ($E_{\text{Binding}} \approx -119.5\,\text{eV} \rightarrow p = 0\,\text{Pa}$), and at the value where the magnetic moment first collapses, $d = 6.8\,\text{Å}$ ($E_{\text{Binding}} \approx -96.9\,\text{eV} \rightarrow p \approx 152\,\text{GPa}$), it is possible to see that there is a difference of about 22 eV between these two points. This is completely different from what happens in the BTO221(99)_001_2ndFe cases, once figures 6.41 and 6.42 show that there is a local minimum for the null-spin state, thus the magnetic moment quench can occur even at $p = 0\,\text{Pa}$. This implies, once again, that the role of the Ti atom is in fact crucial to the spin state of Fe.

Figure 7.84 shows that BTO99_110_2_1stFe_BaO_AFM2 supercell can have two states, a perfect or nearly perfect AFM state for $d > 7.5\,\text{Å}$ and a ferromagnetic state for $d \leq 7.5\,\text{Å}$. The latter's is actually the same state which can be seen in BTO221(99)_110_2_1stFe_BaO_FM supercells.

Finally, the most stable magnetic arrangement for most of the considered d is the one considered in BTO221(99)_110_2_1stFe_BaO_FM supercells. These supercells have always a FM state whose M_{total} decreases along with d. However, at $d = 6$ Å the magnetic moments of BTO221_110_2_1stFe_BaO_FM collapse. Even though the magnetic collapse is not seen for the BTO99_110_2_1stFe_BaO_FM supercell, it should also occur if d is further decreased, since, as seen in section 6.1.2, the different lateral lattice parameters often induce a shift at the energy and magnetic properties curves.

7.5.2 BTO221(99)_110_2_1stFe_BaO_Interstitial

The binding energy and total magnetic moment of the BTO221(99)_110_2_1stFe_BaO-_Interstitial supercells (figure 7.51) are shown in figures 7.87–7.90.

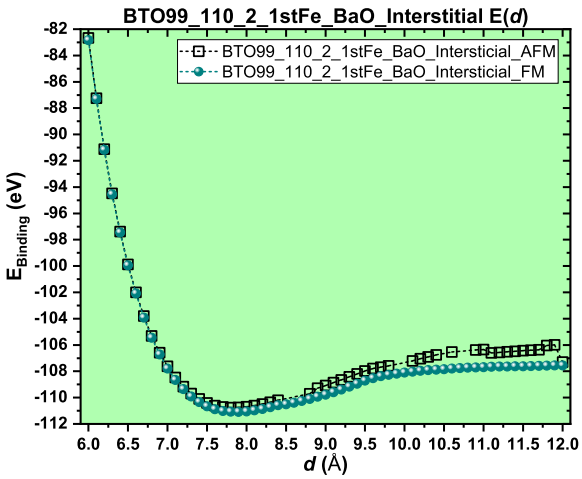

Figure 7.87: Binding energy for all the considered magnetic arrangements of the BTO99_110_2_1stFe_BaO_Interstitial supercell.

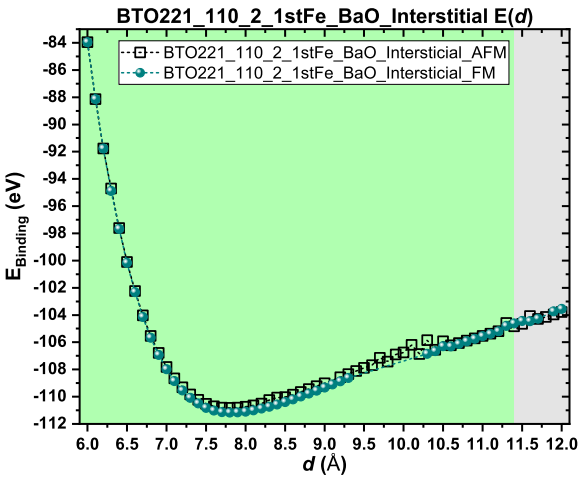

Figure 7.88: Binding energy for all the considered magnetic arrangements of the BTO221_110_2_1stFe_BaO_Interstitial supercell.

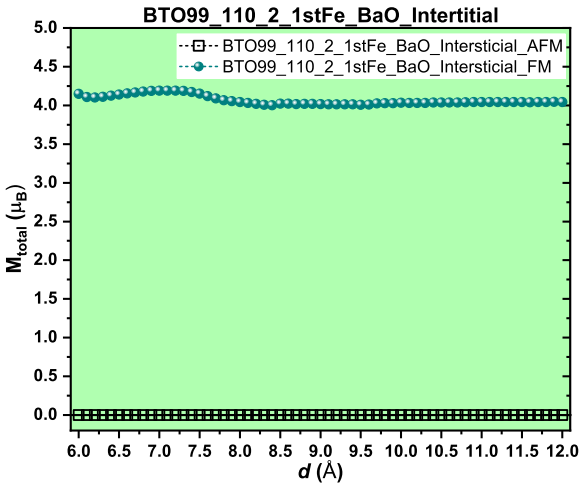

Figure 7.89: Total magnetic moment for all the considered magnetic arrangements of the BTO99_110_2_1stFe_BaO_Interstitial supercell.

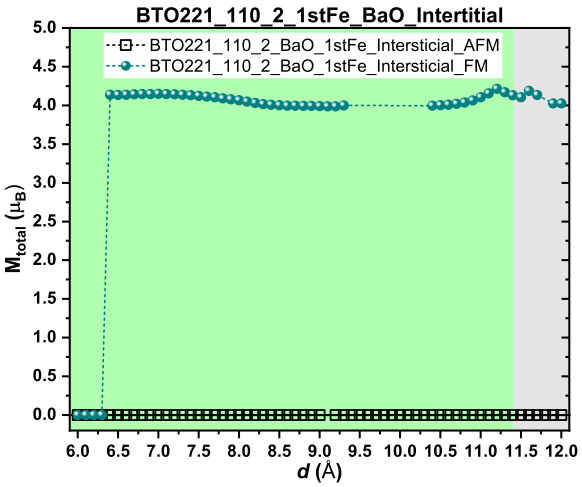

Figure 7.90: Total magnetic moment for all the considered magnetic arrangements of the BTO221_110_2_1stFe_BaO_Interstitial supercell.

Their binding energy is defined by equation 7.10:

$$E_{\text{Binding}} = E_{\text{BTO221(99)\_110\_2\_1stFe\_BaO\_Interstitial}} - (2E_{\text{Fe}} + 4E_{\text{Ba}} + 2E_{\text{Ti}} + 8E_{\text{O}}) \ , \quad (7.10)$$

where $E_{\text{BTO221(99)\_110\_2\_1stFe\_BaO}}$ is the energy of the BTO221(99)_110_2_1stFe_BaO-_Interstitial supercells.

It is perceptible from the observation of figures 7.87–7.90 that, also here, the binding energies and M_{total} of both the tetragonal and cubic supercells are identical. Actually, comparing the individual Fe moments curves of figure 7.91 with the ones from figure 7.84, one can conclude that the BTO221(99)_110_2_1stFe_BaO_Interstitial supercells have the same magnetic moment curves as the Fe2 and Fe4 magnetic moment curves from the BTO221(99)_110_2_1stFe-_BaO supercells. This happens since the design of the BTO221(99)_110_2_1stFe_BaO-_Interstitial supercells consists on the removal of the Fe1 and Fe3 atoms from the BTO221(99)_110_2_1stFe_BaO supercells, yet it is somehow surprising that no substantial changes occur when relaxing this new supercells.

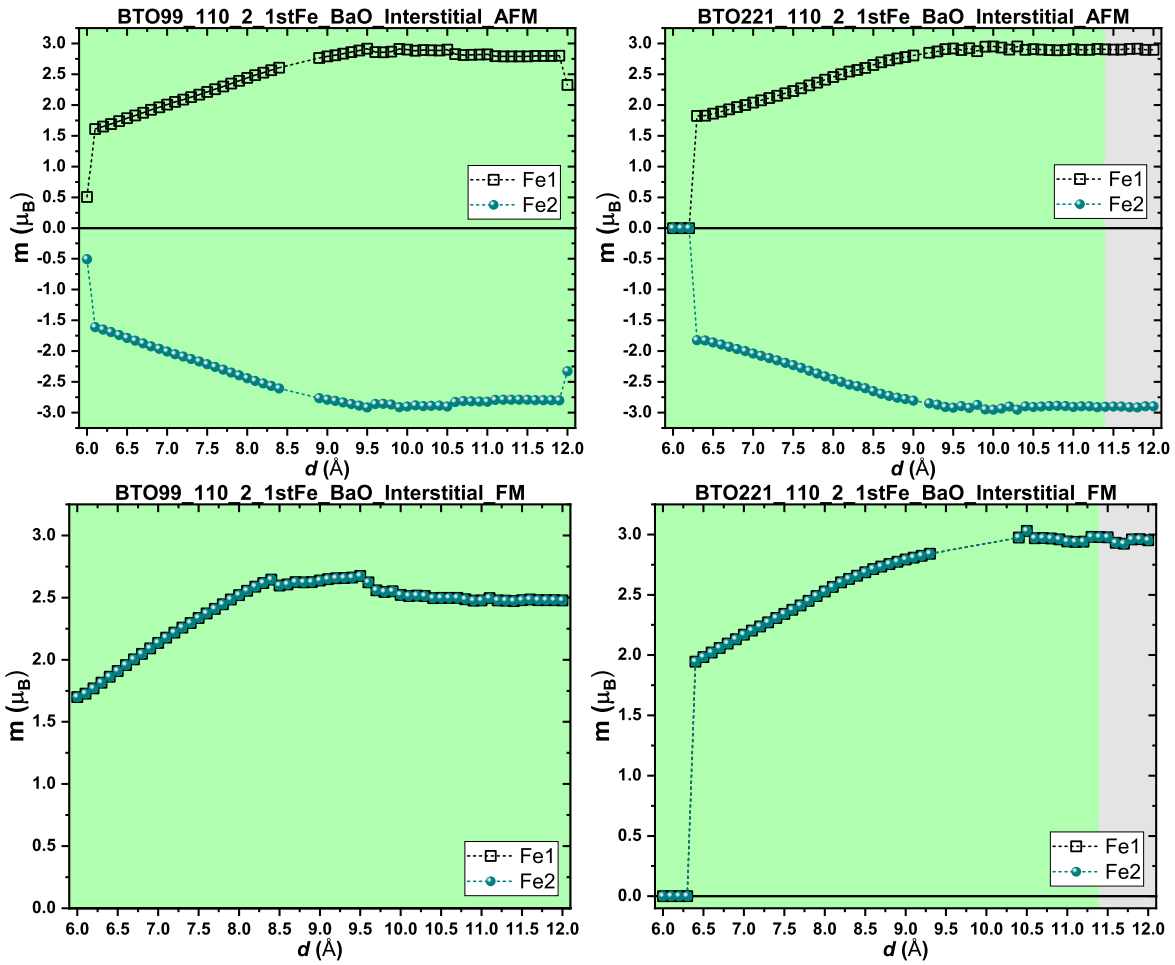

Figure 7.91: Fe magnetic moments for different magnetic arrangements of the and BTO(221)99_110_2_1stFe_BaO_Interstitial supercells.

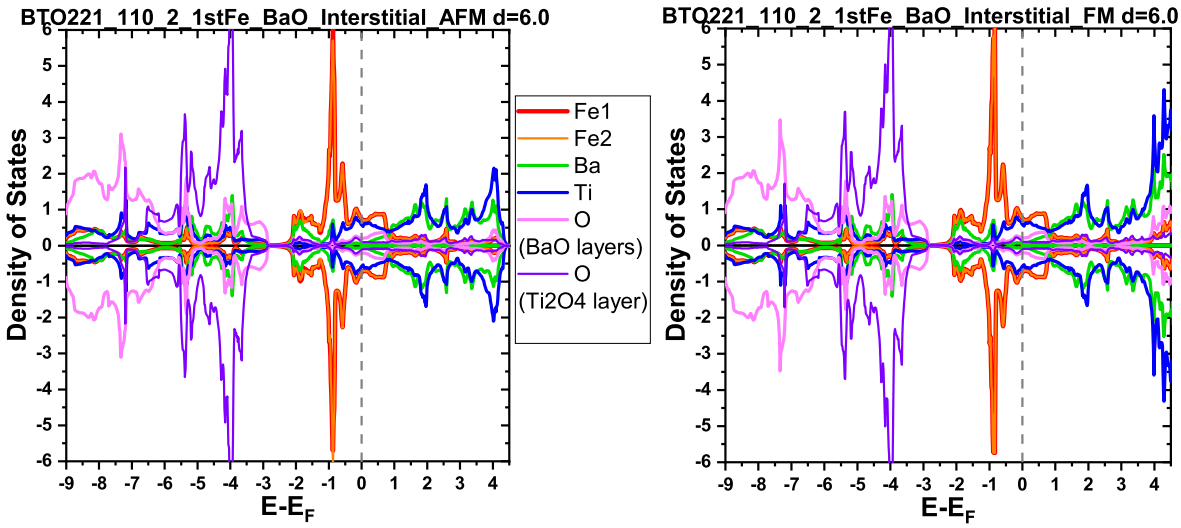

Figure 7.93: Density of states of the BTO221_110_2_1stFe_BaO_Interstitial_AFM and BTO221_110_2_1stFe_BaO_Interstitial_FM supercells at $d = 6.0$ Å.

Notwithstanding, even though the BTO221(99)_110_2_1stFe_BaO_Interstitial supercells do not possess the Fe placed between the Ba atoms, there is still the quench of the remaining Fe atoms for the BTO221_110_2_1stFe_BaO_Interstitial supercells at $d \lessapprox 6.4$ Å, as seen in the figure 7.91. To further understand this phenomenon, let's look at figure 7.93 which shows the DOS of both BTO221_110_2_1stFe_BaO_Interstitial_AFM and BTO221_110_2_1stFe_BaO_Interstitial_FM supercells at $d = 6.0$ Å. First of all, it is clear that below the Fermi level both supercells have exactly the same DOS, which means that both the AFM and FM arrangement are in the same state at $d = 6.0$ Å.

Secondly, it is also possible to see that the characteristics of the Fe DOS of figure 7.93 are similar to the Fe1 and Fe3 DOS from the BTO99_110_2_1stFe_BaO at $d = 6.3$ Å (figure 7.85), namely their metallic nature which contrasts with the semi-conductive nature of the BTO221(99)_001_2ndFe supercels at their null-spin state. The favouring of the metallic nature of the BTO99_110_2_1stFe_BaO and BTO99_110_2_1stFe_BaO_Interstitial null-spin state supercells agrees with the work of Pasternak *et al.*, where Fe_3O_4 also favours a metallic nature when its magnetic moments collapse [236]. This is clearly different from the BTO221(99)_001_2ndFe supercells which tend to be more insulators when in their null-spin state than in their high-spin state.

Moreover, figure 7.94 shows that in the BTO221_110_2_1stFe_BaO_Interstitial_FM supercell, although there is a clear flattening of the Fe charge density due to the O electric

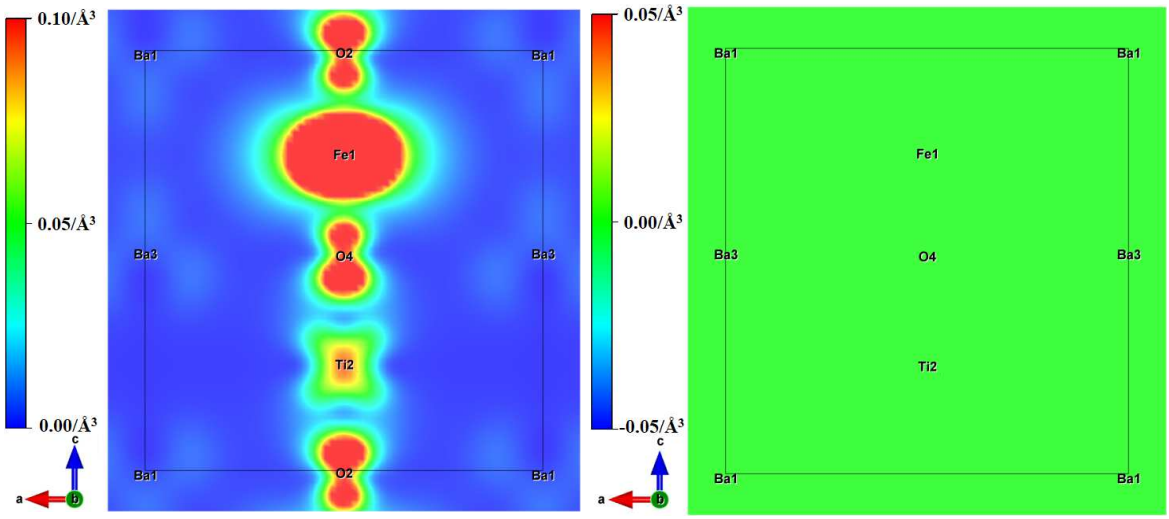

Figure 7.94: Charge density (left) and SP charge density difference (right) of the BTO99_110_2_1stFe_BaO_Interstitial_FM for $d = 6.0\,\text{Å}$ across one of the supercell faces, calculated for E-$E_F \in [-3, 0]\,\text{eV}$.

field, this time the latter's electrons clearly overlap with Fe electron cloud. It should be noticed that the Fe atom of figure 7.94 is not as flattened as its equivalent Fe atom from BTO99_110_2_1stFe_BaO at $d = 6.3\,\text{Å}$ (figure 7.85). This might have to do with latter's ability to overlap its Fe electron cloud with its neighbouring Fe atoms, while in the former case such is not possible once there aren't any neighbour Fe atoms available. Therefore, since there are no Fe between the Ba atoms, the pressure effects of O ($p \approx 135\,\text{GPa}$ for $d = 6.4\,\text{Å}$) are enough to induce the collapse of the Fe magnetic moments.

7.5.3 BTO221(99)_110_2_2ndFe_BaO

The BTO221(99)_110_2_2ndFe_BaO (figure 7.51) supercells families are a very special kind of supercells. Let's look at their binding energy and total magnetic moment which are shown in figures 7.95–7.98.

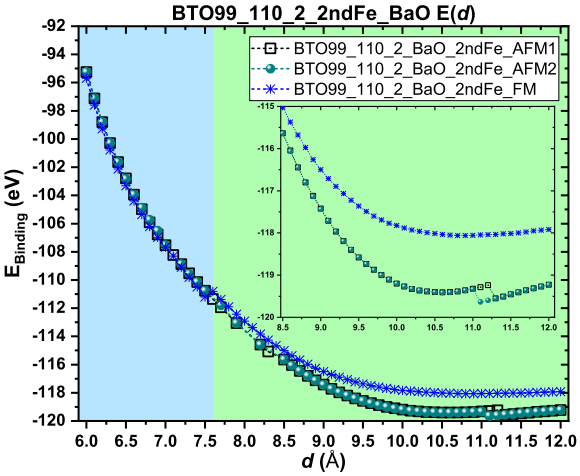

Figure 7.95: Binding energy for all the considered magnetic arrangements of the BTO99_110_2_2ndFe_BaO supercell.

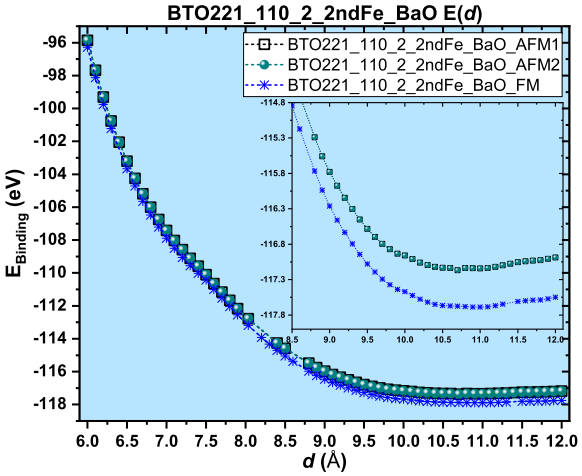

Figure 7.96: Binding energy for all the considered magnetic arrangements of the BTO221_110_2_2ndFe_BaO supercell.

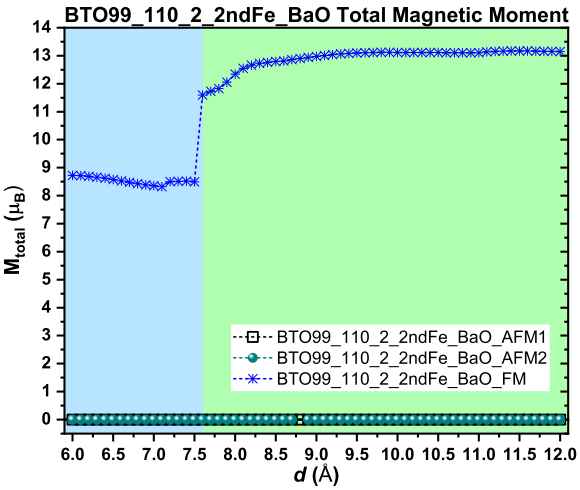

Figure 7.97: Total magnetic moment for all the considered magnetic arrangements of the BTO99_110_2_2ndFe_BaO supercell.

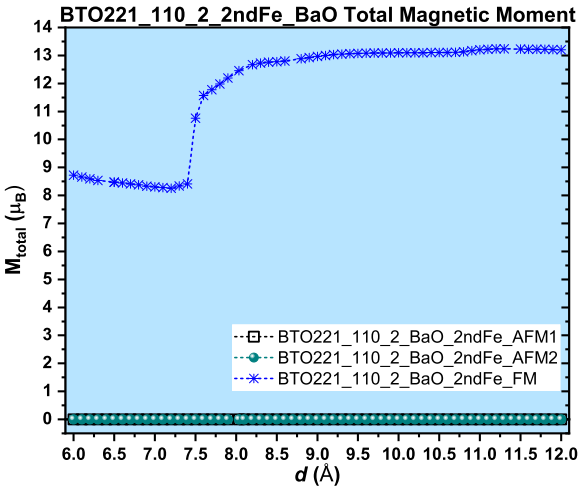

Figure 7.98: Total magnetic moment for all the considered magnetic arrangements of the BTO221_110_2_2ndFe_BaO supercell.

Here their binding energy is defined by equation 7.11:

$$E_{\text{Binding}} = E_{\text{BTO221(99)\_110\_2\_2ndFe\_BaO}} - (4E_{\text{Fe}} + 4E_{\text{Ba}} + 2E_{\text{Ti}} + 8E_{\text{O}}) \ , \qquad (7.11)$$

where $E_{\text{BTO221(99)\_110\_2\_2ndFe\_BaO}}$ is the energy of the BTO221(99)_110_2_2ndFe_BaO supercells.

It is perceptible that around their global minimum they have completely different magnetic states. While the BTO99_110_2_2ndFe_BaO supercell has a more stable AFM state, the BTO221_110_2_2ndFe_BaO supercell clearly favours a FM state.

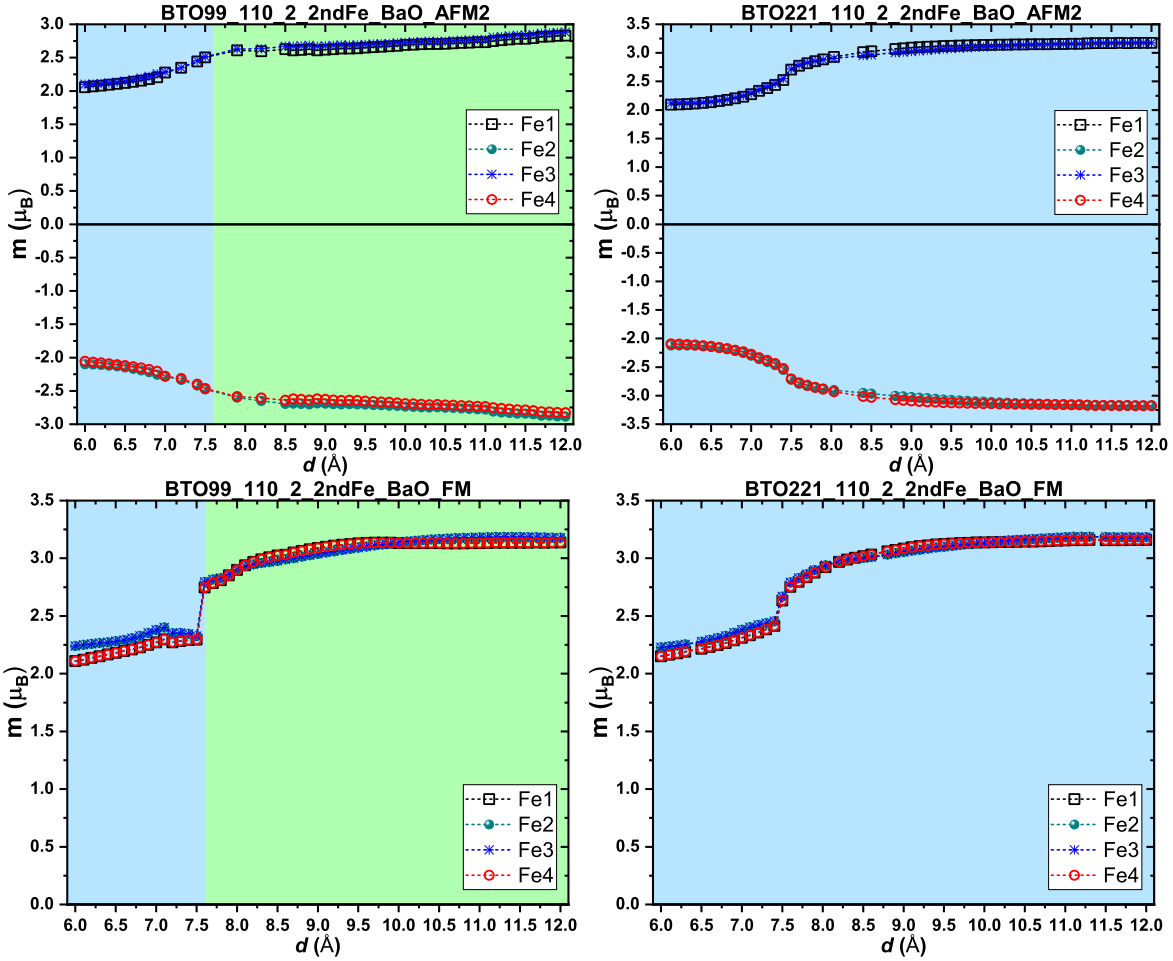

Figure 7.99: Fe magnetic moments for different magnetic arrangements of the and BTO(221)99_110_2_2ndFe_BaO supercells.

This is quite surprising for several reasons. First, both supercells have very similar structures, with its Fe monolayer remaining placed at the same lateral position as the initial input. Secondly, after a careful observation of both the M_{total} and their individual Fe magnetic moments curves for all the BTO221(99)_110_2_2ndFe_BaO supercells, it is possible to see that they are actually identical. Nevertheless, the BTO99_110_2_2ndFe_BaO_AFM[6]

[6]In the BTO99_110_2_2ndFe_BaO supercells the AFM1 and AFM2 result exactly in the same magnetic

curves are almost 2 eV more stable than its FM counterpart, while in the cubic supercells the BTO221_110_2_2ndFe_BaO_FM is the more stable one.

This has a huge technological potential since one can exploit such a feature to deposit a Fe monolayer between a BTO221_110_2 bulk-like BTO and use an electric field to induce its tetragonal phase (similar to what was suggested in section 6.1.2), which will result in a magnetoelectric coupling between the AFM state for the BTO tetragonal phase and the FM state for the cubic phase. Another promising characteristic is the fact that this happens at the predicted global minimum, making it easier to reproduce from an experimental point of view.

and binding energy curves , thus only one is presented. The same happens in the BTO221_110_2_2ndFe_BaO AFM1 and AFM2 supercells.

7.5.4 BTO221(99)_110_2_1stFe_Ti2O4

Figures 7.100–7.103 present the binding energy and total magnetic moment of the BTO221-(99)_110_2_1stFe_Ti2O4 supercells (figure 7.51).

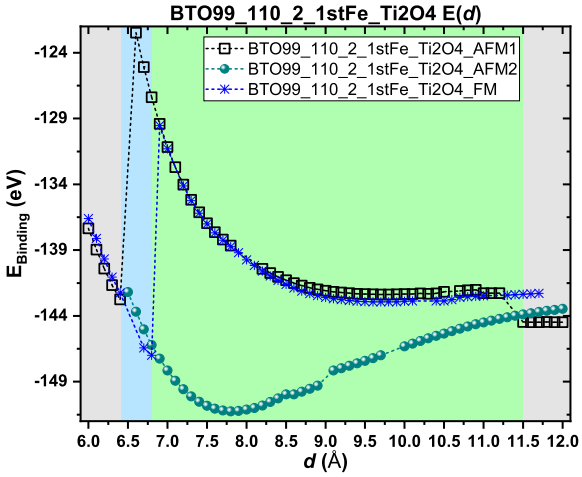

Figure 7.100: Binding energy for all the considered magnetic arrangements of the BTO99_110_2_1stFe_Ti2O4 supercell.

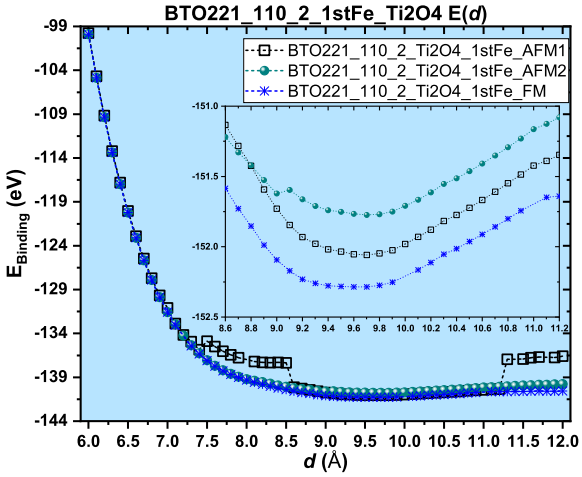

Figure 7.101: Binding energy for all the considered magnetic arrangements of the BTO221_110_2_1stFe_Ti2O4 supercell.

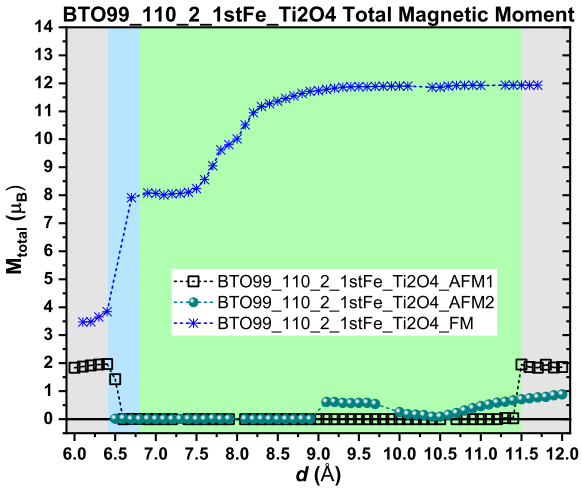

Figure 7.102: Total magnetic moment for all the considered magnetic arrangements of the BTO99_110_2_1stFe_Ti2O4 supercell.

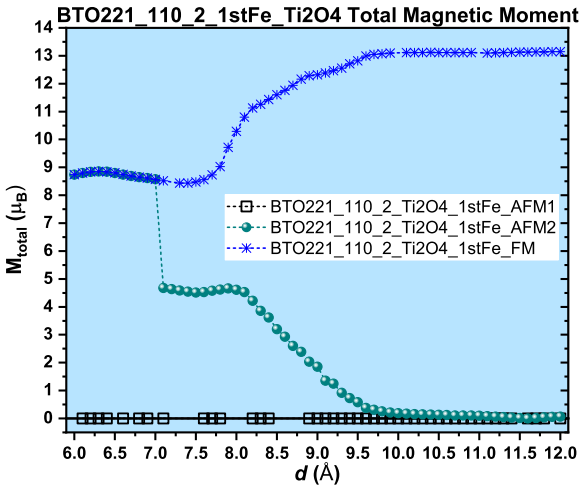

Figure 7.103: Total magnetic moment for all the considered magnetic arrangements of the BTO221_110_2_1stFe_Ti2O4 supercell.

The binding energy is defined by equation 7.12:

$$E_{\text{Binding}} = E_{\text{BTO221(99)\_110\_2\_1stFe\_Ti2O4}} - (4E_{\text{Fe}} + 2E_{\text{Ba}} + 4E_{\text{Ti}} + 10E_{\text{O}}) \ , \qquad (7.12)$$

where $E_{\text{BTO221(99)\_110\_2\_1stFe\_Ti2O4}}$ is the energy of the BTO221(99)_110_2_1stFe_Ti2O4 supercells.

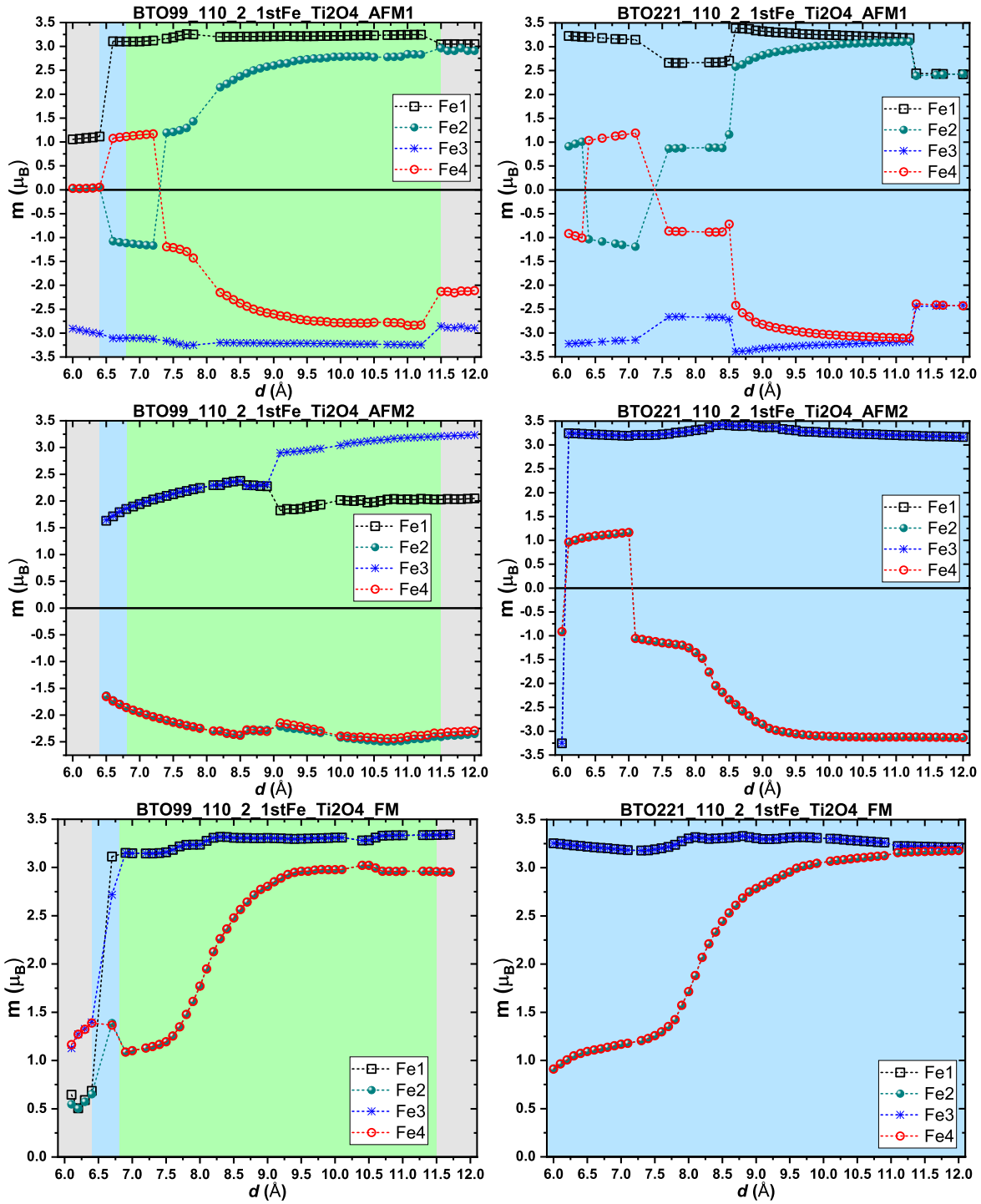

Figure 7.104: Fe magnetic moments for different magnetic arrangements of the and BTO(221)99_110_2_1stFe_Ti2O4 supercells.

The binding energy curves show that there is a substantial difference on the favoured magnetic states between the BTO221(99)_110_2_1stFe_Ti2O4 supercells (figures 7.100 and

7.101). While BTO221_110_2_1stFe_Ti2O4 has a more stable FM state among all its considered magnetic arrangements at all the considered d, BTO99_110_2_1stFe_Ti2O4 has many regions with different stable magnetic states (figure 7.100). As a matter of fact, for $6.9 \leq d \leq 11.3$, in both the BTO221(99)_110_2_1stFe_Ti2O4 supercells the AFM1 and FM initial arrangements have, for the most part, the same binding energies in the tetragonal and cubic cases. However, the AFM2 curves are completely different for the tetragonal and cubic supercells, where in the former's case it is the most stable arrangement at the above mentioned range.

These differences in their binding energies are also reflected on their total and individual magnetic moments (figures 7.102, 7.103 and 7.104). The BTO99_110_2_1stFe_Ti2O4-_AFM2 supercell has a perfect AFM state for $d < 9\,\text{Å}$, and a close to perfect AFM sate for the remaining values, with $M_{total} < 1\,\mu_B$. The BTO221_110_2_1stFe_Ti2O4_AFM2 supercell, on the other hand, has a ferromagnetic state for $d < 7\,\text{Å}$, which overlaps with the cubic's FM arrangement curve in the same range of d. For $d > 7\,\text{Å}$ it has a ferrimagnetic state with $M_{total} < 4.5\,\mu_B$ which decreases gradually as d increases till the complete cancellation of M_{total} through the compensation of the Fe magnetic moments (figure 7.104).

Figure 7.104 shows the FM arrangement of both BTO221(99)_110_2_1stFe_Ti2O4 supercells which have identical magnetic curves, showing a gradual decrease of the Fe2 and Fe4 magnetic moments.

Finally, let's discuss the AFM1 arrangement. In the cubic supercell, its magnetic moments always cancel out, independently of the considered d, whereas for the tetragonal case this just occurs between $6.5 < d < 11.3\,\text{Å}$, while for the remaining values of d this supercell has a FiM state with $M_{total} \approx 2\,\mu_B$. Nonetheless the peculiarity of the BTO99_110_2_1stFe_Ti2O4-_AFM1 supercell lies in the individual magnetic moments of its Fe2 and Fe4 atoms at $d \leq 6.5\,\text{Å}$, which have a null value. At first glance, one could say that this phenomenon is analogous to the one reported for the BTO99_110_2_1stFe_BaO_AFM1, where only two of its four Fe atoms have their magnetic moment quenched as well, as seen in figure 7.104. Still, looking at the binding energies of figure 7.100 , one can see that the energy actually decreases substantially for the magnetic quench, unlike to the swiftly increase reported in the BTO99_110_2_1stFe_BaO_AFM1 (figure 7.80).

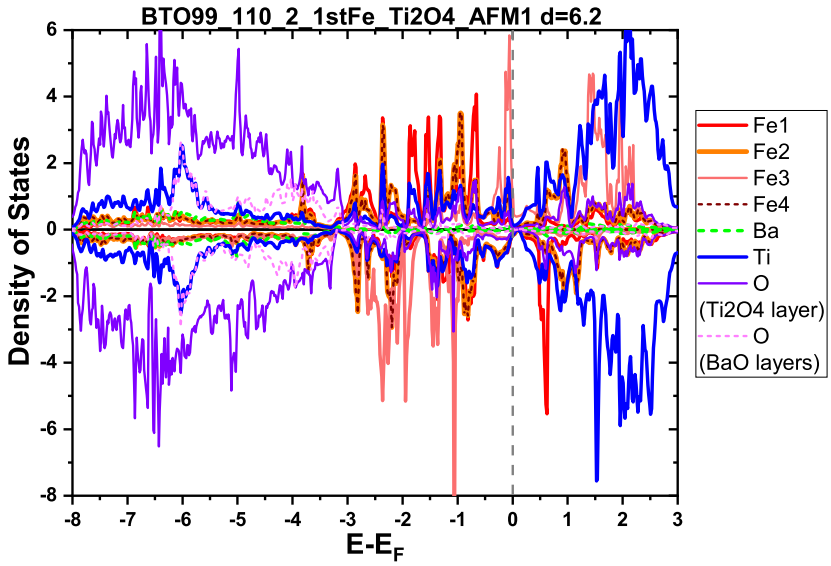

Figure 7.105: Density of states of the BTO99_110_2_1stFe_Ti2O4_AFM1 supercell at $d = 6.2$ Å.

To further understand the mechanism behind this effect, the DOS of the BTO99_110_2-_1stFe_Ti2O4_AFM1 at $d = 6.2$ Å are presented in figure 7.105. The observation of the Fe1 and Fe3 DOS justifies their unbalanced magnetic moments once it is perceptible that the Fe3 possesses more spin down electrons (its majority electrons) than the Fe1 up spin majority electrons. The Fe2 and Fe4 atoms, on the other hand have overlapping DOS curves which possess the same number of up and down electrons, hence having a null individual magnetic moment, despite the up and down DOS not being completely symmetric. In this supercell, for the presented range of energies, there are almost no Ba DOS. Figure 7.105 also shows that a good portion of the Ti atoms hybridize with the Fe1, Fe2 and Fe4 atoms, while the remaining DOS tend to overlap with the O DOS, which in their way, do not show any substantial overlapping with Fe DOS. Finally it is noteworthy that this supercell would also be a p-type semiconductor (as in the BTO221(99)_001_2ndFe null-spin state) if it wasn't for the Fe3 DOS, having instead a half-metallic nature.

Until now, everything points to the fact that the mechanism which induces the magnetic quench of the BTO99_110_2_1stFe_Ti2O4_AFM1 is different from the magnetism collapse of the BTO99_110_2_1stFe_BaO_AFM1 supercell. To confirm the previous statement, the charge and SP charge densities were calculated and are presented in figure 7.106. Since this supercell relaxed coordinates are quite different from the initial atoms placement, it is impracticable to show the charge densities through cross section planes. Nevertheless, figure

7.106 shows an appropriately chosen isosurface of the charge density (or SP charge density difference), enabling a clear exposition of the present phenomena.

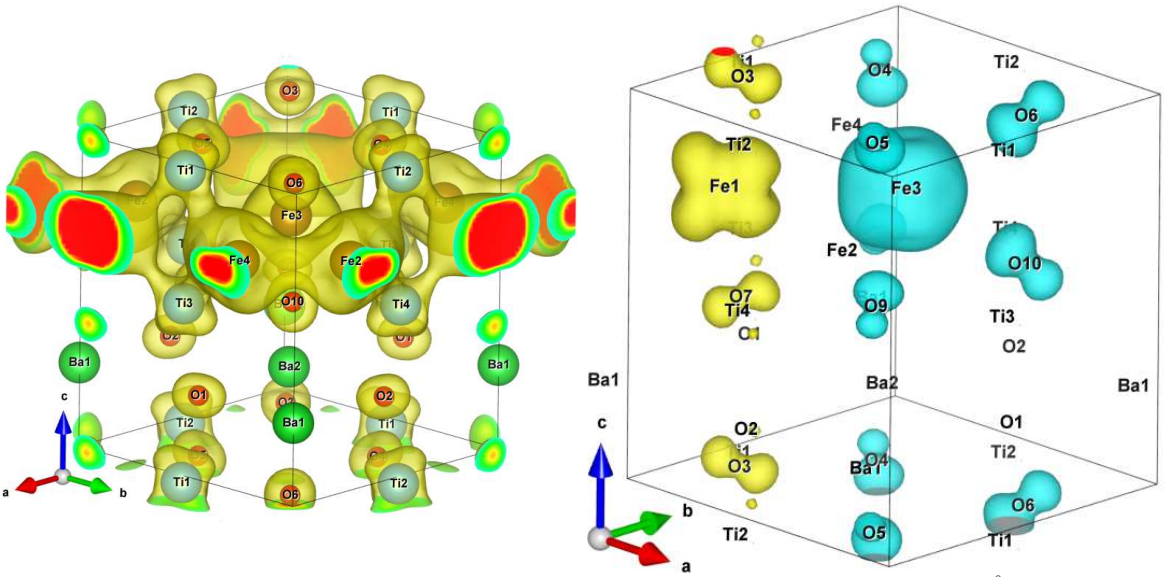

Figure 7.106: Isosurfaces of the charge density (0.03 electrons/Å^3), at the left, and SP charge density difference (0.01 electrons/Å^3), at the right, for the BTO99_110_2_1stFe_Ti2O4_AFM1 at $d = 6.2$ Å, calculated for E-E$_F$ $\in [-3, 0]$ eV.

It should be pointed out that the Fe2 and Fe4 atoms have a hybridization of their electrons, and that each one has its orbitals hybridized with two Ti atoms. The neighbouring O atoms also deform the Fe2 and Fe4 orbitals, without having any hybridization. The now described scenario is actually quite similar to the one reported for the BTO221(99)_001_2ndFe supercells, implying that the magnetic quench occurs due to an equivalent mechanism. This reinforces the hypothesis that the Ti hybridization, together with the O electric field, are crucial to the appropriate crystal field to induce the Fe magnetic moment quench[7]. On the oher hand, the Fe1 and Fe3 are not in the same conditions as Fe2 and Fe4.

The Fe3, in the center of the supercell, is surrounded by 8 O atoms, which in spite of shaping Fe3's charge density, do not affect its magnetic moment.

The Fe1 atom is placed between two O atoms, leading to the flattening of its electron cloud, and hybridizes with four distinct Ti atoms. This atomic configuration results in a depletion of its magnetic moment to $m \approx 1 \neq 0$. Therefore, although the Fe1 has a crystal field caused by Ti and O atoms, there is not a complete quench of its magnetic moment, most likely due

[7]In the BTO221(99)_001_2ndFe supercells there was also a clear hybridization of the Fe atoms, which means that, probably this factor is also important to the magnetic moment quench.

to the inadequate symmetry of the neighbouring atoms, or due to the lack of an aditional Fe neighbour and the excess of Ti atoms.

Finally, the observation of figure 7.106 SP charge density difference confirms the null magnetic moment of the Fe2 and Fe4 atoms, and the FiM nature of the Fe1 and Fe3 atoms (the yellow and blue isosurfaces represent the positive and negative difference of SP electrons respectively).

7.5.5 BTO221(99)_110_2_2ndFe_Ti2O4

The binding energy and total magnetic moment for the BTO221(99)_110_2_2ndFe-_Ti2O4 supercells (figure 7.51) are shown in figures 7.107–7.110.

The binding energy is defined by equation 7.13:

$$E_{\text{Binding}} = E_{\text{BTO221(99)\_110\_2\_2ndFe\_Ti2O4}} - (4E_{\text{Fe}} + 2E_{\text{Ba}} + 4E_{\text{Ti}} + 10E_{\text{O}}) \ , \qquad (7.13)$$

where $E_{\text{BTO221(99)\_110\_2\_2ndFe\_Ti2O4}}$ is the energy of the BTO221(99)_110_2_2ndFe_Ti2O4 supercells.

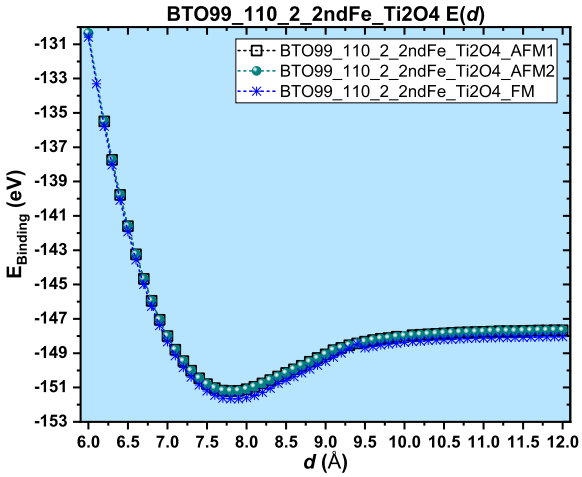

Figure 7.107: Binding energy for all the considered magnetic arrangements of the BTO99_110_2_2ndFe_Ti2O4 supercell.

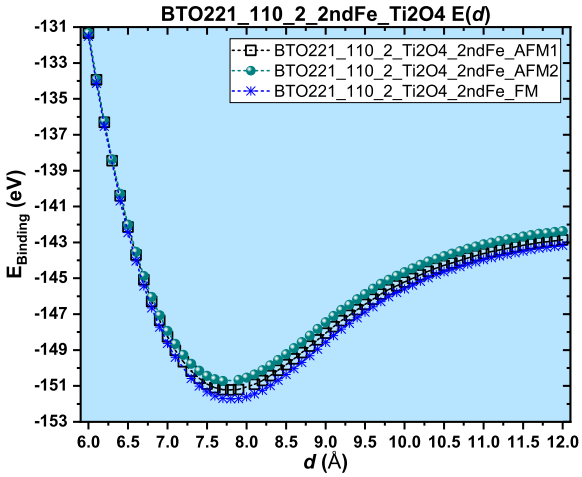

Figure 7.108: Binding energy for all the considered magnetic arrangements of the BTO221_110_2_2ndFe_Ti2O4 supercell.

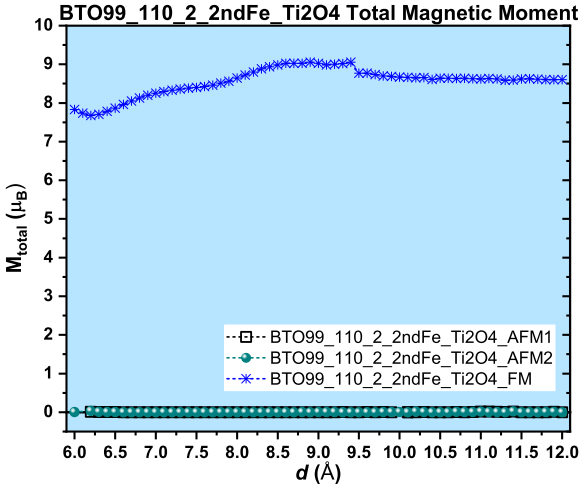

Figure 7.109: Total magnetic moment for all the considered magnetic arrangements of BTO99_110_2_2ndFe_Ti2O4.

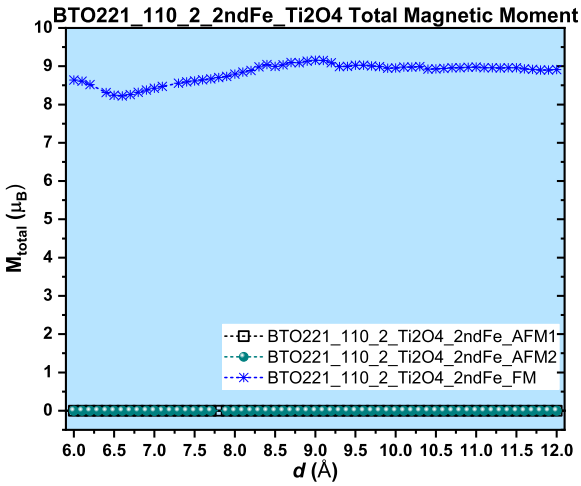

Figure 7.110: Total magnetic moment for all the considered magnetic arrangements of BTO221_110_2_2ndFe_Ti2O4.

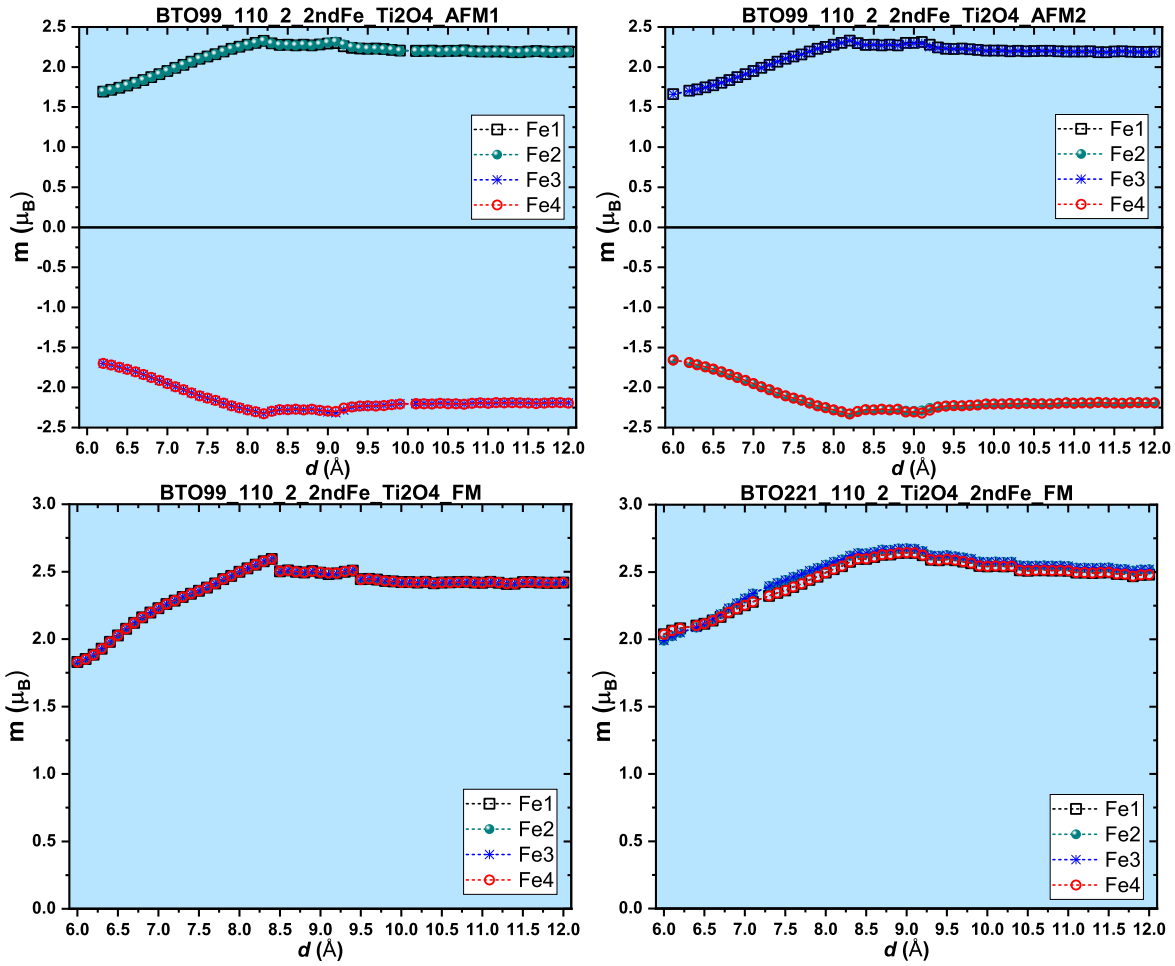

Figure 7.111: Fe magnetic moments for different magnetic arrangements of the BTO(221)99_110_2_2ndFe_Ti2O4 supercells.

The binding energies show that in the cubic and tetragonal supercells the ferromagnetic state is the more stable one. The remaining magnetic curves are associated with balanced AFM order for in both the BTO221(99)_110_2_2ndFe_Ti2O4, as it is perceptible by the observation of figure 7.111.

The constancy in magnetic behaviours trough all the considered range of d and the close similarities between the cubic and tetragonal supercells, result in a lack of magnetoelectric coupling in these particular interfaces, thus these supercells have a low technological potential for magnetoelectric applications.

7.6 BTO221(99)_{111}/Fe

In section 7.2 it was seen that the BTO160/Fe supercells for the 2ndFe,3rdFe and Triangular monolayers were ferromagnetic for all the considered range of d. Similarly, the BTO221(99)_{111}/Fe supercells also present a more stable ferromagnetic state. For this reason they will not be individually presented in this thesis, due to the lack of substantial new information.

Chapter 8

$BaTiO_3$ EFG and PAC measurements

In chapter 6 it was seen that the crystal field and other local effects at the atomic scale can be determinant to the magnetic moment of the Fe atoms. For this reason, and as seen in the same chapter, hyperfine properties are very good candidates to study the different local effects/environments of the BTO/Fe heterostructures. In order to infer the potential and validity of such studies, namely the usage of techniques such as PAC spectroscopy, a DFT and experimental study of the $BaTiO_3$ EFG at the different possible sites, will be presented in this chapter.

As discussed in chapter 4, to use PAC spectroscopy a radioactive probe which has a $\gamma - \gamma$ cascade is required. Here the ^{111m}Cd isotope will be considered as the probe candidate, since it is an isotope widely used by our group at ISOLDE, CERN.

To perform the density functional theory calculations I used the Vienna *ab-initio* simulation package, VASP [226] (version 5.4.1) , which implements the projector augmented wave method [227]. The exchange correlation functional is the generalized gradient approximation (GGA) with the Perdew-Burke-Ernzerhof (PBE) parametrization [32].

8.1 DFT EFG predictions for pure Tetragonal $BaTiO_3$

Firstly, the calculation of the EFG for the case of a pure BTO supercell was done. In this stage of the study, a BTO supercell containing $3 \times 3 \times 3$ tetragonal BTO unit cells was considered, with the experimental lattice parameters $a = b = 3.9925\,\text{Å}$ and $c = 4.0365\,\text{Å}$ [174], resulting in an overall supercell parameters of $a_{\text{super}} = b_{\text{super}} = 11.9775\,\text{Å}$ and $c_{\text{super}} = 12.1095\,\text{Å}$.

The calculations were made allowing full atomic relaxation for all fractional coordinates, minimizing the Hellmann-Feynman forces below a tolerance value of 0.01 eV/Å. The electronic self-consistent cycles were considered converged when the energy differences between two iterations were less than 10^{-6} eV. A $3 \times 3 \times 3$ k-points grid was considered for the calculations in reciprocal space, and the cut-off energy for the plane waves was set as 500 eV.

Table 8.1 shows the summary of the EFG results for each non-equivalent site of the tetragonal BTO supercell. Each of the 135 atoms of the considered BTO supercell has an EFG value equal to its correspondent site, with a possible deviation from the table value only in the 3rd decimal case. The Ba and Ti V_{zz} values are in good agreement with the NMR experimental values measured for BTO [237], mainly when taking into account that for EFG values close to zero there might be a bigger relative "uncertainty" [238].

	DFT EFG BTO			
Site	$\mathbf{V}_{xx}$ **(V/Å^2)**	$\mathbf{V}_{yy}$ **(V/Å^2)**	$\mathbf{V}_{zz}$ **(V/Å^2)**	η
Ba	2.72	2.72	-5.44	0.00
Ti	-1.17	-1.17	2.34	0.00
$\mathbf{O_{equatorial}}$	-14.63	-11.11	25.74	0.14
$\mathbf{O_{apical}}$	-8.19	-8.19	16.40	0.00

Table 8.1: Pure BTO DFT predicted EFG at the different possible sites.

The values of table 8.1 will be considered as the reference values to compare with the results obtained in the $BaTiO_3$:Cd case. Additionally the binding energy of equation 8.1:

$$E_{\text{Binding}} = E_{\text{BTO}} - (27E_{\text{Ba}} + 27E_{\text{Ti}} + 81E_{\text{O}}) \approx -1027.2\,\text{eV} \ , \tag{8.1}$$

was also determined, where E_{BTO} is the energy of the $3 \times 3 \times 3$ pure BTO supercell, and E_{Ba}, E_{Ti} and E_{O} are the energy of the each individual atom.

8.2 DFT EFG predictions for $BaTiO_3$:Cd

To study the effects of the Cd atom in the BTO matrix, several calculations were performed where an atom of the previously considered BTO supercell was replaced by a Cd atom. To

do such a study, all the possible non-equivalent sites were considered, thus individual sets of calculations for each of the Ba, Ti, $O_{equatorial}$ and O_{apical} sites were performed using the same calculation methodology and parameters used in the pure BTO supercell.

The 1/135 dilution of the Cd in the $3 \times 3 \times 3$ supercell was necessary to mimic the diluted implantation typically used in PAC spectroscopy, reducing the effects of the "next" Cd atom from the periodic boundaries conditions, while remaining in a feasible and practical computational regime[1].

To determined the binding energy of each supercell containing Cd, equations 8.2–8.5 were defined:

$$E_{\text{Binding(Ba)}} = E_{\text{BTO:Cd(Ba)}} - (E_{\text{Cd}} + 26E_{\text{Ba}} + 27E_{\text{Ti}} + 81E_{\text{O}}) \,, \quad (8.2)$$

$$E_{\text{Binding(Ti)}} = E_{\text{BTO:Cd(Ti)}} - (E_{\text{Cd}} + 27E_{\text{Ba}} + 26E_{\text{Ti}} + 81E_{\text{O}}) \,, \quad (8.3)$$

$$E_{\text{Binding}(O_{\text{equatorial}})} = E_{\text{BTO:Cd}(O_{\text{equatorial}})} - (E_{\text{Cd}} + 27E_{\text{Ba}} + 27E_{\text{Ti}} + 80E_{\text{O}}) \,, \quad (8.4)$$

$$E_{\text{Binding}(O_{\text{apical}})} = E_{\text{BTO:Cd}(O_{\text{apical}})} - (E_{\text{Cd}} + 27E_{\text{Ba}} + 27E_{\text{Ti}} + 80E_{\text{O}}) \,, \quad (8.5)$$

where $E_{\text{BTO:Cd(Ba)}}$, $E_{\text{BTO:Cd(Ti)}}$, $E_{\text{BTO:Cd}(O_{\text{equatorial}})}$ and $E_{\text{BTO:Cd}(O_{\text{apical}})}$ are the energy of the $BaTiO_3$:Cd supercell for the Cd subtitution on the Ba, Ti, $O_{equatorial}$ and O_{apical} sites respectively, and E_{Cd}, E_{Ba}, E_{Ti} and E_{O} are the energy of the each individual atom.

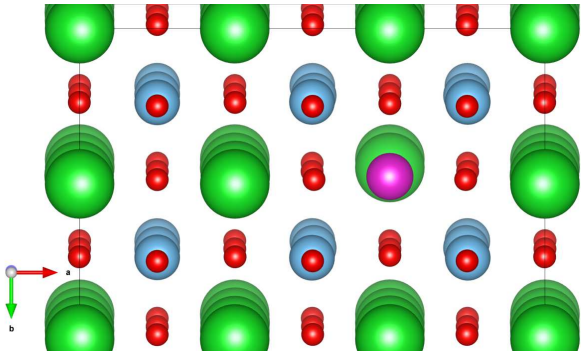

Figure 8.1: BTO:Cd (Cd at the Ba site) structure after relaxation.

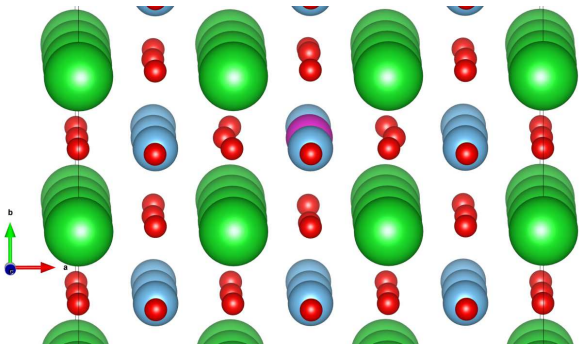

Figure 8.2: $BaTiO_3$:Cd (Cd at the Ti site) structure after relaxation.

[1] A $4 \times 4 \times 4$ supercell would result in calculations involving 320 atoms, which would be quite a challenge from the computational point of view since the calculation time increases approximately with the cube of the number of valence electrons.

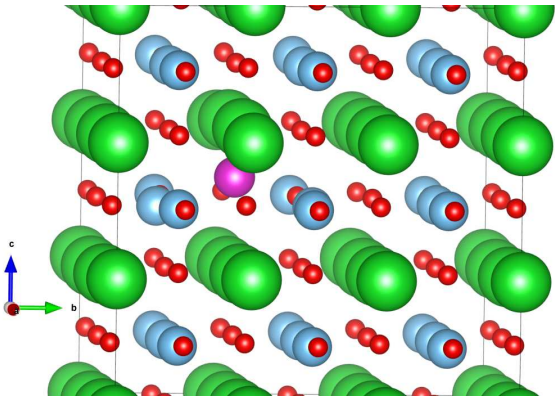

Figure 8.3: $BaTiO_3$:Cd (Cd at the $O_{equatorial}$ site) structure after relaxation.

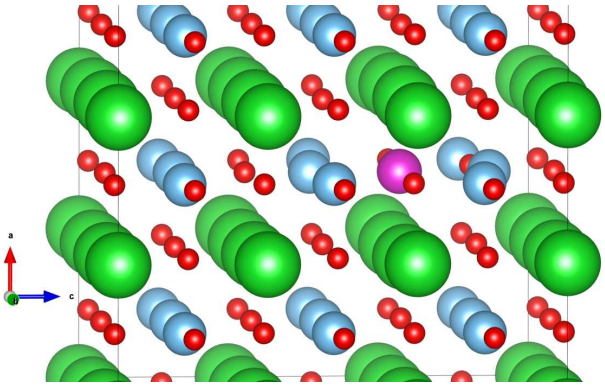

Figure 8.4: $BaTiO_3$:Cd (Cd at the O_{apical} site) structure after relaxation.

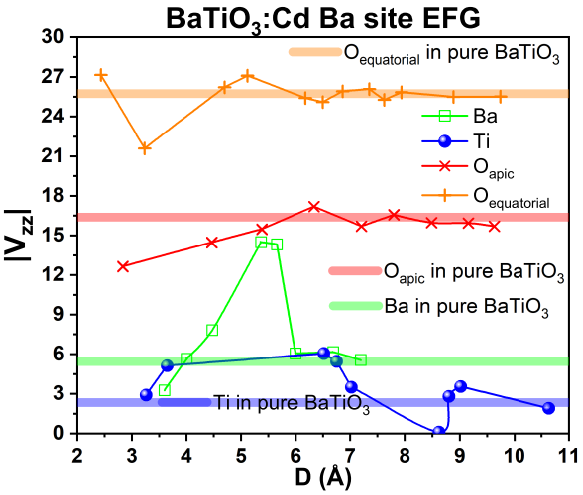

Figure 8.5: Cd effects on the EFG magnitude of its neighbouring atoms. The Cd atom is at the Ba site

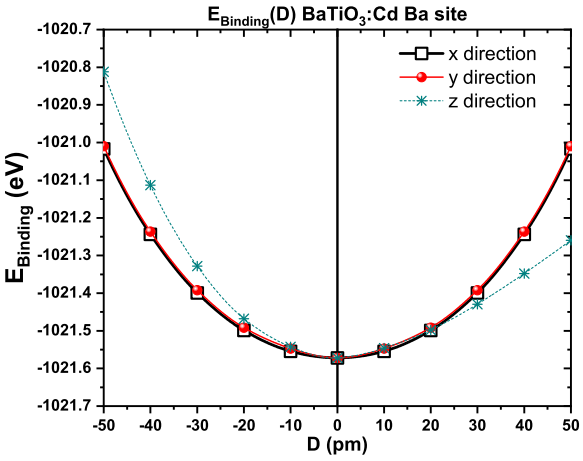

Figure 8.6: Binding energy of the $BaTiO_3$:Cd at the Ba site for different positions of the Cd atom with relation to its equilibrium position.

Figures 8.1-8.4 show the distortions of the BTO:Cd supercell, caused by Cd atom to its surrounding atoms, after the atomic relaxation below the tolerance value for each possible Cd substituting site. At the Ba site (figure 8.1) there is a small repulsion of the Cd first neighbours (O atoms) and a even smaller attraction of its second neighbours (Ti atoms), suggesting that the Cd would have a less positive (or more negative) charge than the Ba atom, typically in Ba^{2+} valency, from whom the site had belonged. Figure 8.5 shows the EFG magnitude for the different atoms surrounding the Cd atom. This figure shows that there is a clear deviation from the EFG calculated in the pure BTO supercell, mainly for the atoms closer to the Cd atom. This deviations get attenuated for larger distances, fact more evident for the O atoms, which "converge" to their reference BTO EFG when they are around 6 Å away from the Cd.

The equilibrium binding energy for the $BaTiO_3$:Cd at the Ba site is about -1021.6 eV, being slightly less stable than the binding energy of the pure $BaTiO_3$ (figure 8.6). The equilibrium binding energy corresponds to the energy of the BTO:Cd supercell after the atomic relaxation of its Hellmann-Feynman forces below the tolerance value, and the D variable is a translation of the Cd around its equilibrium point along the indicated x, y or z axis.

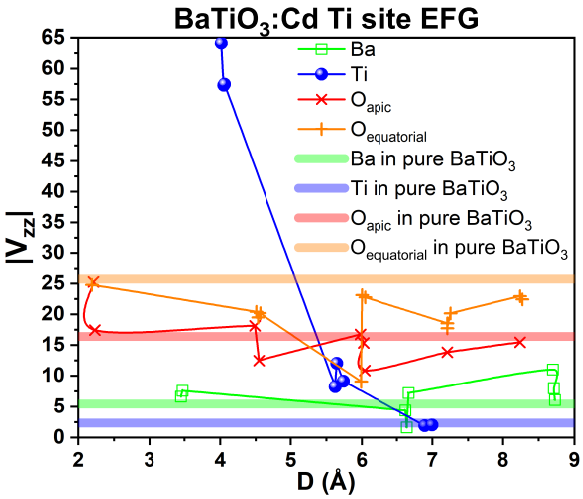

Figure 8.7: Cd effects on the EFG magnitude of its neighbouring atoms. The Cd atom is at the Ti site

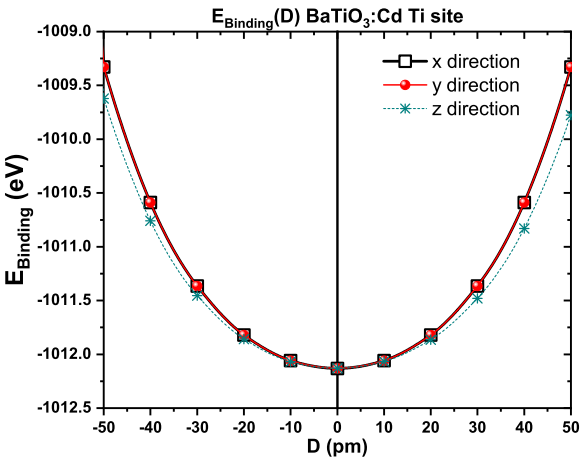

Figure 8.8: Binding energy of the $BaTiO_3$:Cd at the Ti site for different positions of the Cd atom with relation to its equilibrium position.

Figure 8.2 shows the local distortions induced by the Ti substitution by the Cd atom after the atomic relaxation of the whole supercell. It is possible to see a considerable amount of repulsion of the closest O atoms which is perceptible even for the Cd second O neighbours, being clearly a more substantial effect than the one seen in the Ba site case, probably due to the bigger difference of the valency between the Ba^{2+} and the Ti^{4+} ions. Figure 8.7 presents, in a quantitative way, the effects of these distortions, showing a clear shift of the O EFG when compared with the pure BTO supercell. Nevertheless, it is at the Ti neighbour atoms where it is seen the biggest effect of the distortion on the EFG, which can reach values as high as $65\,V/Å^2$. Still the structural effects seem to vanish for the atoms which are around $\geq 7\,Å$ away, as their EFG values approach the ones from the pure BTO supercell. The equilibrium binding energy for the $BaTiO_3$:Cd at the Ti site is about -1012.1 eV (figure 8.8), less stable than the binding energy of the $BaTiO_3$:Cd at the Ba site and consequently much less stable than the pure $BaTiO_3$.

Even though the distortion effects of the Ti substitution by a Cd atom are already consid-

erable, the greatest effects on the BTO lattice occur for the substitution of the O sites by the Cd atom, independently if the substitution is made at the $O_{equatorial}$ or at the O_{apical} sites. Figures 8.3 and 8.4 show a huge repulsion of the Ti and Ba atoms (mainly for the Ti atoms) which surround the Cd atom, confirmed by the EFG of the Cd neighboring atoms presented in figures 8.9 and 8.10. In both the $O_{equatorial}$ and O_{apical} substitution, the closest Ba atoms have EFG's quite different (up to 20 times) from the pure BTO case, reaching $V_{zz} \approx 112\,V/Å^2$ and $\approx 75\,V/Å^2$ respectively, and only the Ba neighbours at $D \geq 7.5\,Å$ reach approximately their pure BTO reference value. The remaining atoms tend to stabilize their EFG magnitude to values close to their correspondent pure BTO sites for $D \gtrapprox 4.5\,Å$.

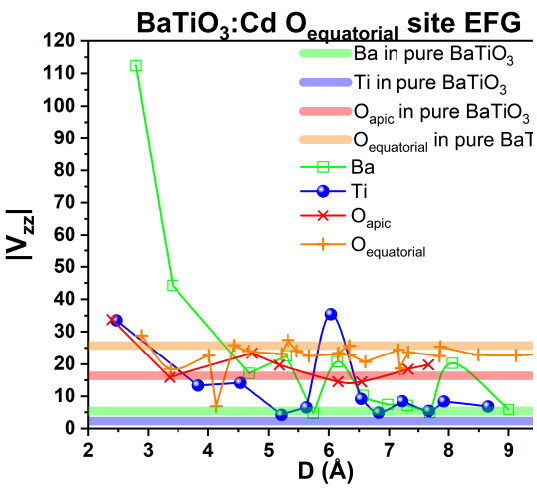

Figure 8.9: Cd effects on the EFG magnitude of its neighbouring atoms. The Cd atom is at the $O_{equatorial}$ site

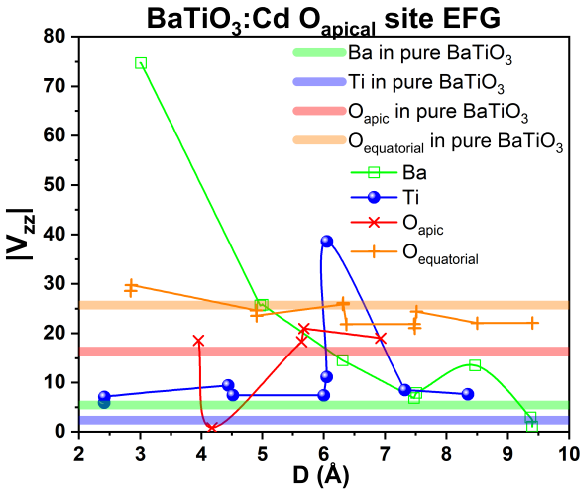

Figure 8.10: Cd effects on the EFG magnitude of its neighbouring atoms. The Cd atom is at the O_{apical} site

The binding energies for the BTO:Cd at the $O_{equatorial}$ and O_{apical} sites are presented in figures 8.11 and 8.12, showing an equilibrium binding energy of about -1013.5 eV and -1013.3 eV respectively. This means that, from the predicted binding energies, if the supercells stabilities were to be ordered from the most favourable to the least one, the order would be the following: pure BTO, BTO:Cd(Ba site), BTO:Cd($O_{equatorial}$ site), BTO:Cd(O_{apical} site) and finally BTO:Cd(Ti site).

Let's now analyse the EFG felt by the Cd atom for the studied BTO:Cd supercell. Table 8.2 shows the EFG felt by the Cd atom for each of the non equivalent positions of the BTO lattice. It is clear from the comparison of both table 8.2 and table 8.1 that the EFG completely changes due to the Cd presence, not only because of its effect on the local charge density, but

also because of its effect on the local structure of the lattice. The latter effect was already discussed above, being visible to the naked eye in figures 8.1-8.4 and quantitatively estimated through the V_{zz} values for each neighbouring atom in figures 8.5, 8.7, 8.9 and 8.10.

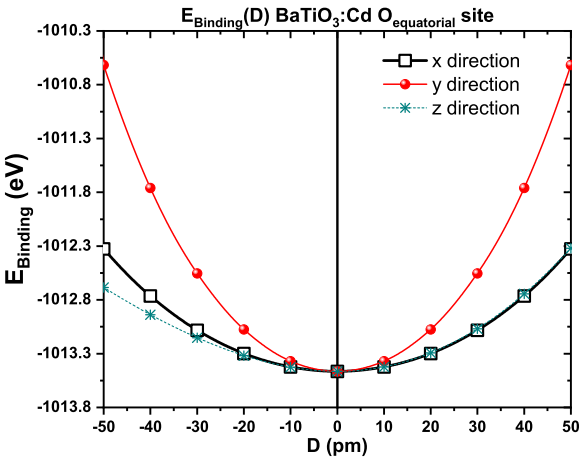

Figure 8.11: Binding energy of the $BaTiO_3$:Cd at the $O_{equatorial}$ site for different positions of the Cd atom with relation to its equilibrium position.

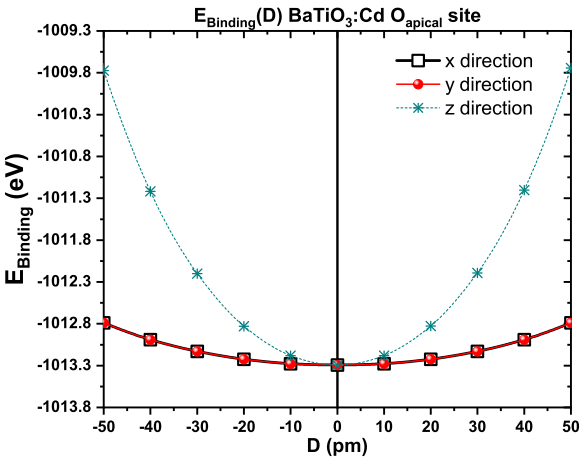

Figure 8.12: Binding energy of the $BaTiO_3$:Cd at the O_{apical} site for different positions of the Cd atom with relation to its equilibrium position.

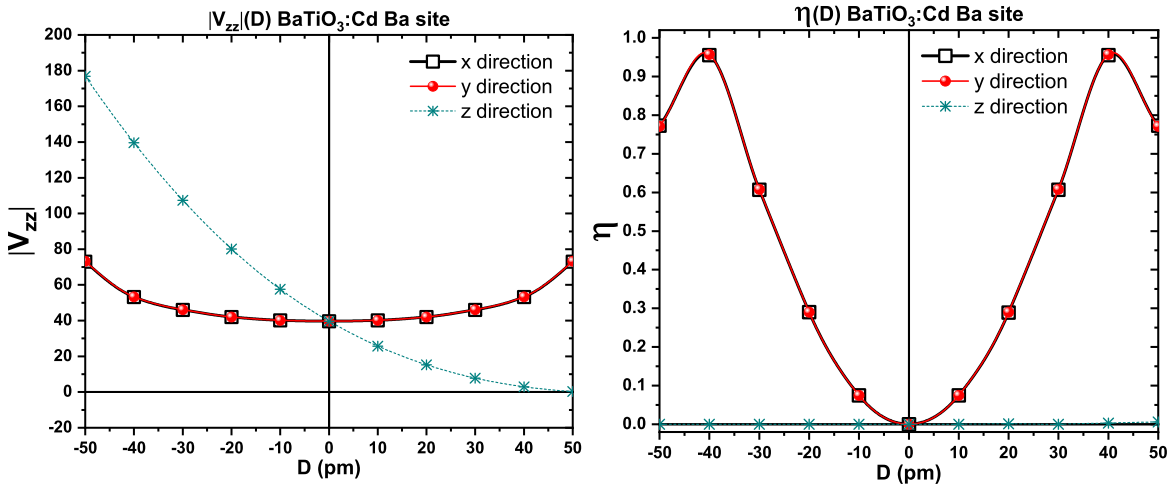

Figure 8.13: DFT predicted EFG of the $BaTiO_3$:Cd for the Ba site

Figures 8.13-8.16 show the EFG of the BTO:Cd for each non-equivalent BTO site, as a function of the distance D from Cd equilibrium position. Each calculation was done just by moving the Cd by the amount D along one of the x, y or z axis, and serves as a way of gauging a pseudo-error bar for the DFT predicted EFG values presented in table 8.2. These EFG vs D curves also serve as a way to infer the sensitivity of the EFG for deviations and/or distortions of the Cd in the BTO lattice.

	DFT EFG $BaTiO_3$:Cd				BTO with Sternheimer
Site	V_{xx} (V/Å^2)	V_{yy} (V/Å^2)	V_{zz} (V/Å^2)	η	V_{zz} (V/Å^2)
Ba	-19.81	-19.81	39.62	0.00	-1.73
Ti	-8.42	-8.42	16.84	0.00	7.07
$O_{equatorial}$	-53.47	-44.566	98.03	0.09	52.70
O_{apical}	21.95	21.95	-43.90	0.00	33.55

Table 8.2: $BaTiO_3$:Cd DFT predicted EFG at the different substitutional sites considered. The last column contains the V_{zz} values of the pure BTO supercell after making Sternheimer anti-shielding corrections for Cd^{2+}.

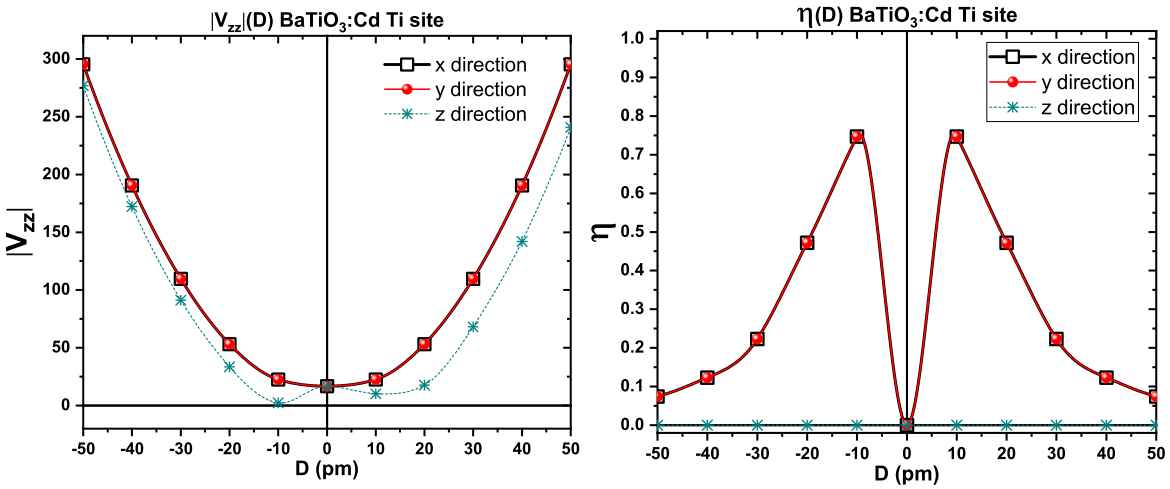

Figure 8.14: DFT predicted EFG of the $BaTiO_3$:Cd for the Ti site

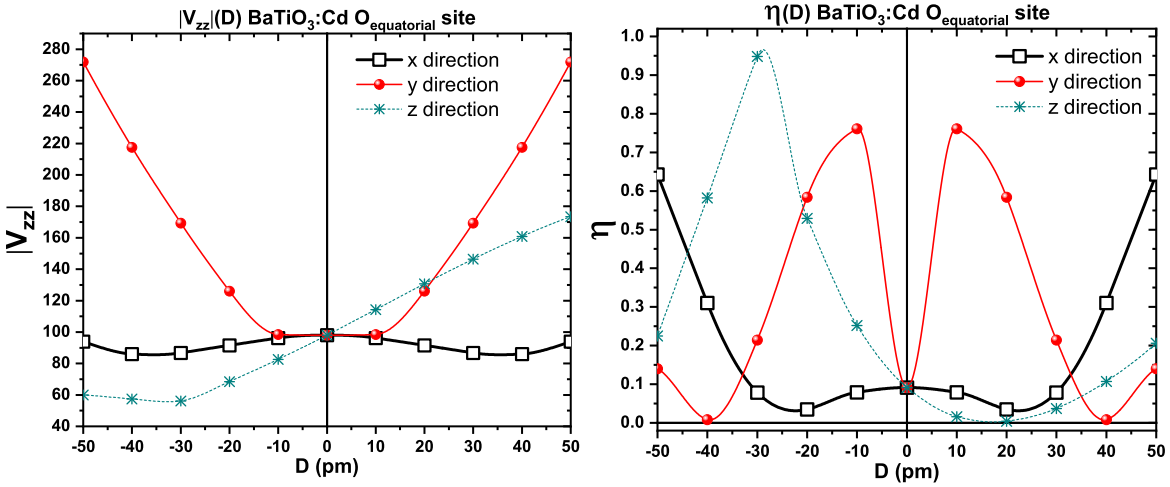

Figure 8.15: DFT predicted EFG of the $BaTiO_3$:Cd for the $O_{equatorial}$ site

For all the considered sites, the V_{zz}(D) along the x and y axis presents symmetrical curves, however the same is not true along the z axis. There are two possible sources for this feature, the asymmetry of the equilibrium position along the z axis with relation to the neighbouring

atoms and the fact that the tetragonal BTO supercell possesses a spontaneous polarization which breaks the vertical symmetry of the studied systems and which is known to be directly correlated to the BTO EFG [239].

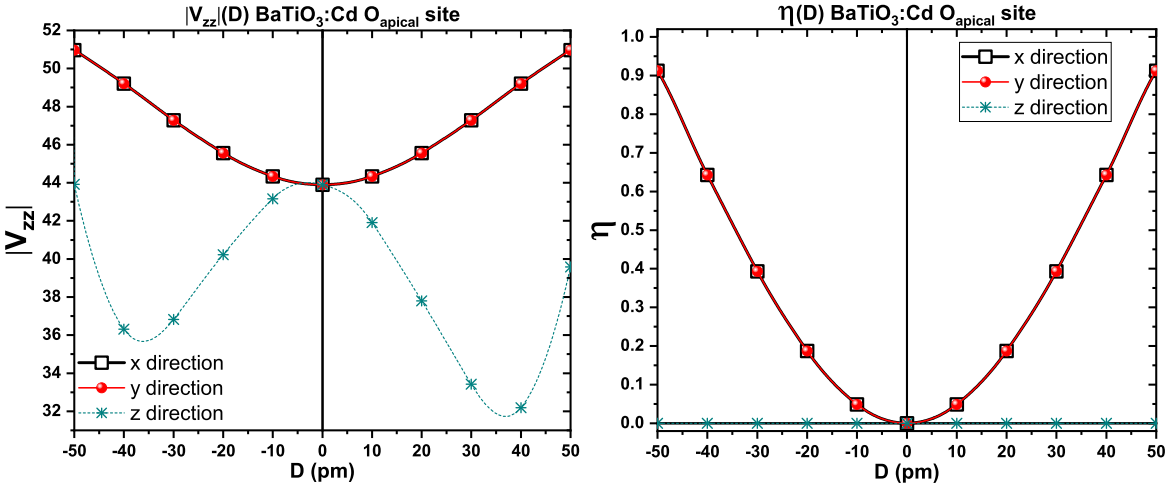

Figure 8.16: DFT predicted EFG of the $BaTiO_3$:Cd for the O_{apical} site

8.3 PAC spectroscopy of $BaTiO_3$ using ^{111m}Cd

To validate the EFG results obtained through DFT calculations, several $BaTiO_3$ single crystal pieces (of about $3 \times 3 \times 1$ mm) acquired from MaTeck [240] were studied using PAC spectroscopy. The PAC study was done using the ^{111m}Cd radioactive isotope, produced online at ISOLDE (CERN) [241, 242] by bombardment of a lead target with the 1.4 GeV proton beam from the CERN Proton Synchrotron Booster. The Cd beam with 30 keV energy was then redirected to the GLM beam line where the BTO single crystal pieces were mounted inside a dedicated vacuum chamber. The ion implantation was done till a dose of about 10^{11}atoms/cm^2 of ^{111m}Cd was implanted in each BTO single crystal piece.

After the ^{111m}Cd implantation, the BTO single crystals were subjected to a thermal annealing, during 20 minutes in an air atmosphere, to repair implantation damage and to promote the proper accommodation of the Cd atoms in the $BaTiO_3$ lattice. As reported by M. Dietrich *et al.* [243], the Cd tend to diffuse out of the BTO single crystals at high temperatures, hence, in order to reduce this effect, a "sandwich" comprised of 2 pieces of BTO single crystals was made (with the faces which were implanted in contact with each other). The PAC study was done for several annealing temperatures, ranging from 1000-1300°C.

The PAC spectroscopy measurements were also performed at ISOLDE on a 6 BaF_2 detector spectrometer [164], which measured the $\gamma - \gamma$ cascade of the ^{111m}Cd whose decay scheme was presented in figure 4.15. The PAC spectra and corresponding fits for each of the different thermal annealing are presented in figure 8.17. The fits results are summarized in table 8.3, where it was considered a ^{111}Cd quadrupole moment value of Q($5/2^+$)=0.683b [244].

	PAC EFG $BaTiO_3$:Cd						
Sample	f_1 (%)	δ_1	f_2 (%)	ω_0 (**Mrad/s**)	$\mathbf{V}_{zz}$ (**V/Å^2**)	η	δ_2
BTOSC_1000C	81±1	1±0	19±1	135±2	92±4	0.01±0.01	1.6±0.1
BTOSC_1100C	82±4	1±0	18±2	134±2	92±4	0.01±0.01	1.6±0.2
BTOSC_1200C	53±4	36±1	47±2	57±1	39±2	0.00±0.01	11.8±0.3
BTOSC_1300C	54±1	35±3	46±4	58±1	39±1	0.00±0.01	6.7±0.2

Table 8.3: BTO:^{111m}Cd experimental PAC results for different annealing temperatures.

Two fractions of probe nuclei surrounded by different local environments were considered through the fit of all the considered samples: one fraction, f_1, corresponding to delocalized probes or/and a close to cubic frequency (EFG ≈ 0)[2], and a well defined frequency which is

[2]The existence of such a phase has to do with the implantation damage of the BTO single crystal, which tends to get amorphous around the path taken by the implanted ions, thus the need of the thermal annealing.

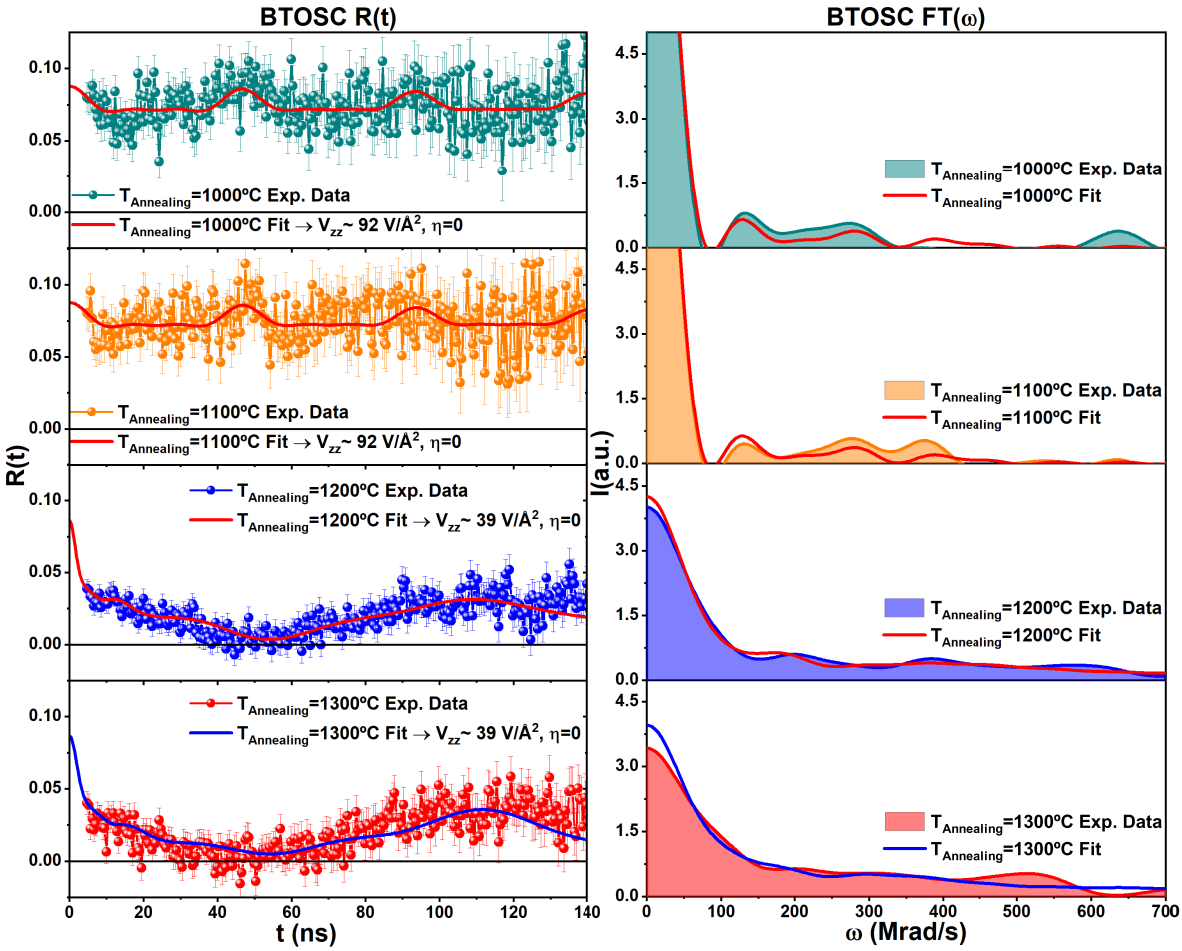

Figure 8.17: PAC experimental perturbation spectra and their respective Fourier transforms for each thermal annealing temperature.

designated as f_2. The f_1 fraction can also be a product of the wide range of possible V_{zz} values resulting from the different possible positions of the Cd in the BTO lattice, as it was seen in figures 8.13-8.16.

It is clear from the observation of figure 8.17 and table 8.3 that there are two types of Cd environments depending on the annealing temperature. For $T_{Annealing} = 1000 - 1100°C$ f_1 is the majority fraction ($\approx 80\%$), and the well defined fraction, f_2, has an EFG with $V_{zz} \approx 92\,(V/Å^2)$ and $\eta = 0.01$, which matches quite well with the Cd substitution at the $O_{equatorial}$ site (table 8.2). For the higher annealing temperatures, $T_{Annealing} \geq 1200°C$, there is a substantial decrease of the f_1 fraction and the f_2 has an EFG with $V_{zz} \approx 39\,(V/Å^2)$ and $\eta = 0.00$, matching with the Cd substitution at the Ba site (table 8.2), suggesting that the Cd substitution is conditioned by the annealing temperature.

8.3.1 PAC and DFT crossover: final considerations

It is useful to compare our experimental results with the work done by M. Dietrich [243], where a similar study was performed but for 5 minutes annealing at $T_{\text{Annealing}} \approx 1300-1400\,^{\circ}\text{C}$ (table 8.4). M. Dietrich finds two different EFG's in his measurements, one with $V_{zz} \approx 42.3\,\text{V}/\text{Å}^2$, assigned to the Ba site, and the other with $V_{zz} \approx 20.5\,\text{V}/\text{Å}^2$, assigned to the Ti site. As a matter of fact, these results are in line with the study presented in this chapter, since the Ba site EFG is of the same order of magnitude with both our DFT predicted and experimental EFG, and, although no EFG matching the Ti site was found in our PAC measurements, its experimental value matches reasonably well with the $16.84\,\text{V}/\text{Å}^2$ predicted by the DFT calculations (table 8.2).

	V_{zz} (V/A^2)				
Site	**NMR [237]**	**Sternheimer corrections for Cd**	**^{111m}Cd PAC of Reference [243]**	**^{111m}Cd PAC for the present work**	**DFT predictions**
Ba	4.35	2.28	42.3	39	39.618
Ti	6.82	34.07	20.5	–	16.84

Table 8.4: Comparison between the EFG of $BaTiO_3$ measured by NMR at the Ba and Ti sites with the Sternheimer antishielding corrections for Cd, the PAC measurements performed at this thesis and in reference [243], and the DFT predictions for the EFG at these sites.

The different possible Cd substitutions clearly depend not only on the annealing temperature, but also on the annealing duration, since in M. Dietrich work, despite having the same temperature as in our highest $T_{\text{Annealing}}$, both the Ti and Ba site EFG's were found, whereas in our results only the latter was found. In fact, the occupation of the Ti site is a bit surprising since it has the lowest predicted binding energy from all the BTO sites. This kind of substitution is actually known to occur PAC measurements involving ^{111}In, where there is no reported Ba site substitution [245, 246]. This kind of effects, may have to do with the ions/atoms dynamics during the annealing process, which may have more difficulty to substitute the Ba atoms from the BTO lattice, thus needing more thermal energy and time to complete this process. This conjecture could explain why, for the lower annealing temperatures, we measure a Cd EFG compatible with the $O_{\text{equatorial}}$.

Notwithstanding, the most important conclusion that one can obtain from the comparison made in table 8.4 has to do with the effects of the BTO structural distortions, caused by the Cd atom, in the latter's EFG. The work of M. Dietrich compared the EFG measured at the

Ba and Ti site using NMR with the results obtained trough PAC after making the proper Sternheimer antishielding corrections for Cd [243]. Based on this approach, he was unable to assign any of the EFG measured through PAC measurements to the BTO Ba or Ti sites, raising the hypothesis that these EFG could be assigned to a defect configuration. This approach is actually quite naïve, since the Sternheimer antishielding corrections just take into account the contribution originating from the core deformation of the probe under the presence of the lattice EFG [247–249], yet do not consider the effects of the probe on the lattice itself, which is, as corroborated by table 8.2, the most important effect. As a matter of fact, the DFT calculations made in this thesis show that, after considering the atomic relaxation of BTO:Cd for each of the non-equivalent sites, it is possible to assign all the EFG found through PAC spectroscopy (either in the measurements made for this thesis or the ones performed by M. Dietrich) to the predicted EFG of the BTO:Cd sites.

This implies that, in general, the usage of an intruder radioactive probe, whose element differs from the element which the probe will substitute, makes impractical the quantitative measurement of that site's EFG, even after considering the Sternheimer antishielding corrections. This means that PAC spectroscopy is not adequate to measure the crystal field effects of the BTO/Fe heterostructures discussed in chapter 6, unless the probe is an isotope of the element of the site which we want to study. I should point out nevertheless, that even if the PAC probe is not an element of the host matrix, it could be used to measure qualitatively tendencies of the studied site, such as the effects of the temperature on the Ba site EFG, and to detect polarization phase transitions (for example). For the particular case of the BTO/Fe heterostructures, the Mössbauer spectroscopy is a potential good candidate to infer the hyperfine interactions at the Fe site.

Chapter 9

RF-Sputtering of $BaTiO_3$/Fe/$BaTiO_3$ heterostructures

Chapters 6 and 7 showed that there is a myriad of possible magnetoelectric effects in BTO/Fe interfaces, where different $BaTiO_3$ terminations and even its position relative to the Fe atoms can alter completely the magnetic nature of the Fe layer. Such a study suggests that an apparently simple heterostructure can in fact have uncountable ways of tailoring its properties, thus depending on the tuning made, it is possible to engineer several types of magnetoelectric multiferroics based on BTO/Fe interfaces. In the current chapter, a first attempt of tailoring these appealing interfaces is made.

This approach consisted in the deposition of BTO and Fe heterostructures on different substrates – $LaAlO_3$, MgO, Al_2O_3, and $SrTiO_3$ (STO) single crystals bought from CrysTec [250] – at different deposition conditions, using RF-Sputtering.

9.1 RF-Sputtering of the BTO/Fe thin films

The deposition of BTO/Fe heterostructures was made using the RF magnetron sputtering of the Physics department of University, at the CICFANO building, which was operated by Professor Armando Lourenço. In this thesis four sets of samples will be discussed, corresponding to four independent depositions. The RF-Sputtering sample holder was loaded with four different substrates in each deposition, hence each set of samples has four different samples.

Table 9.1 summarizes all the samples produced by RF-Sputtering deposition, specifying

Deposition Designation	Site 1		Site 2	
	Substrate	**Sample Designation**	**Substrate**	**Sample Designation**
BTF4	$LaAlO_3$ (100)	BTF4.1_$LaAlO_3$_as_dep	MgO (100)	BTF4.2_MgO_as_dep
BTF5	$LaAlO_3$ (100)	BTF5.1_$LaAlO_3$_as_dep	MgO (100)	BTF5.2_MgO_as_dep
BTF6	$LaAlO_3$ (100)	BTF6.1_$LaAlO_3$_as_dep	Al_2O_3 (001)	BTF6.2_Al_2O_3_as_dep
BTF7	Si (100)	BTF7.1_Si_as_dep	MgO (100)	BTF7.2_MgO_as_dep
BT24	$LaAlO_3$ (100)	BT24.1_$LaAlO_3$_as_dep	MgO (100)	BT24.2_MgO_as_dep
Deposition Designation	**Site 3**		**Site 4**	
	Substrate	**Sample Designation**	**Substrate**	**Sample Designation**
BTF4	Al_2O_3 (001)	BTF4.3_Al_2O_3_as_dep	STO (100)	BTF4.4_STO_as_dep
BTF5	Al_2O_3 (001)	BTF5.3_Al_2O_3_as_dep	STO (100)	BTF5.4_STO_as_dep
BTF6	MgO (100)	BTF6.3_MgO_as_dep	STO (100)	BTF6.4_STO_as_dep
BTF7	MgO (100)	BTF7.3_MgO_as_dep	MgO (100)	BTF7.4_MgO_as_dep
BT24	Al_2O_3 (001)	BT24.3_Al_2O_3_as_dep	STO (100)	BTF24.4_STO_as_dep

Table 9.1: Summary of the RF-Sputtering depositions and corresponding samples.

the substrates used in each deposition and the designation of each sample. The nomenclature of the samples is built in the following way (sample BTF4.2_MgO_as_dep will be used as an example): the first part of the sample name refers to the deposition (BTF4), the second part corresponds to one of the four possible sites available in the sputtering setup substrate holder (.2), the third part specifies the substrate where the thin film was deposited (_MgO), and the last part specifies the temperature of the thermal annealing done to the sample, which is designated "_as_dep" if there was no thermal annealing.

There were three types of depositions, two of which are illustrated in figures 9.1 and 9.2: a seven layer heterostructure (four BTO layer and three Fe layers) was deposited in depositions BTF4 and BTF7, and a three layer heterostructure (two BTO layers and one Fe layer) in depositions BTF5 and BTF6. The third type of deposition was a single layer of $BaTiO_3$ deposited directly on the substrate. The deposition of the $BaTiO_3$ layers was done using a 99.9% purity target from Kurt J. Lesker and the deposition of the Fe layers were done using a Fe foil as target [251]. The most relevant parameters and deposition conditions for each deposition are summarized in table 9.2.

The depositions were made taking into account the deposition rates previously calibrated by the thickness measurement of BTO and Fe layers deposited on a Si substrate, giving a deposition rate of $\approx 1\,\mathrm{nm/min}$ for both the BTO and Fe layers at the conditions presented in table 9.2. Considering these deposition rates, the depositions were done to make a thin film with the layers thickness specified in figure 9.1 for BTF4 and BTF7 depositions (resulting in

Deposition	Layer	P_{dep} (W)	D[T-S] (mm)	P_{total} (mbar)	O_2/Ar (%)	T_{sub} (°C)
BTF4	**$BaTiO_3$**	50	125	1.0×10^{-2}	7	350
	Fe	14	125	1.2×10^{-2}	0	350
BTF5	**$BaTiO_3$**	50	125	1.2×10^{-2}	9	663
	Fe	14	130	1.2×10^{-2}	0	344
BTF6	**$BaTiO_3$**	50	125	1.2×10^{-2}	9	658
	Fe	14	130	1.2×10^{-2}	9	658
BTF7	**$BaTiO_3$**	40	100	1.1×10^{-2}	7	350
	Fe	14	100	1.2×10^{-2}	0	350
BT24	**$BaTiO_3$**	40	100	5.5×10^{-3}	13	350

Table 9.2: RF-Sputtering conditions for each deposition and layer, where P_{dep} is the sputtering deposition power, D[T-S] is the distance between the target and the substrate, P_{total} is the total pressure inside the deposition chamber, O_2/Ar is the partial pressure percentage of the O_2, and T_{sub} is the temperature of the substrate.

a thin film ≈ 60 nm thick), and with the layers thickness of figure 9.2 for the BTF5 and BTF6 depositions (resulting in a thin film ≈ 45 nm thick). For the BT24 deposition a single BTO a layer with 12 nm was deposited.

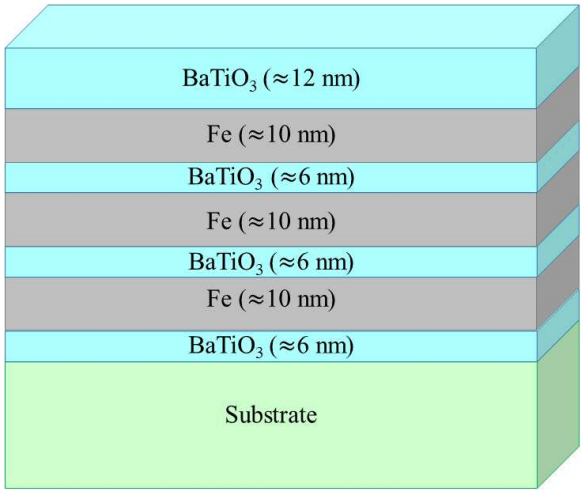

Figure 9.1: Illustration of the seven layer heterostructure (depositions BTF4 and BTF7) deposited by RF-Sputtering.

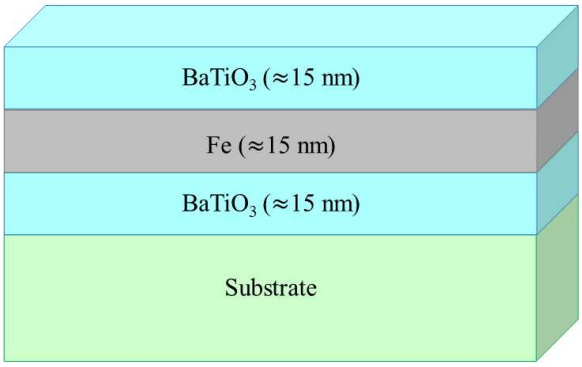

Figure 9.2: Illustration of the trilayer heterostructure (depositions BTF5 and BTF6) deposited by RF-Sputtering.

As mentioned before, thermal annealing(s) were performed in each sample, therefore the structural and magnetic properties of the thin films might be affected, as observed in the bulk $BaTiO_3$:Fe compound of chapter 5. The annealing temperatures were chosen to be close to the Fe diffusion temperatures in $SrTiO_3$ (a close relative of $BaTiO_3$), based on emission channelling and hyperfine technique studies [252]. The annealings were done in an air atmosphere at the

	1st Annealing		2nd Annealing		3rd Annealing	
Sample	**t (h)**	**T (C)**	**t (h)**	**T (C)**	**t (h)**	**T (C)**
BTF4.1_$LaAlO_3$	24	600°C	24	900°C	-	-
BTF4.2_MgO	24	600°C	24	900°C	-	-
BTF4.3_Al_2O_3	48	900°C	-	-	-	-
BTF4.4_STO	48	900°C	-	-	-	-
BTF5.1_$LaAlO_3$	24	600°C	24	750°C	24	900°C
BTF5.2_MgO	24	600°C	24	750°C	24	900°C
BTF5.3_Al_2O_3	24	600°C	24	750°C	24	900°C
BTF5.4_STO	24	600°C	24	750°C	24	900°C
BTF6.1_$LaAlO_3$	24	600°C	24	750°C	24	900°C
BTF6.2_Al_2O_3	24	600°C	24	750°C	24	900°C
BTF6.3_MgO	24	600°C	24	750°C	24	900°C
BTF6.4_STO	24	600°C	24	750°C	24	900°C
BTF7.2_MgO	24	900°C	-	-	-	-
BT24.1_$LaAlO_3$	24	900°C	-	-	-	-
BT24.2_MgO	24	900°C	-	-	-	-
BT24.3_Al_2O_3	24	900°C	-	-	-	-
BT24.4_STO	24	900°C	-	-	-	-

Table 9.3: Thermal annealing details for each sample.

temperatures and durations presented in table 9.3. The higher temperature annealings were done after the lower temperature ones, in a cumulative way. Each annealing temperature was achieved by a heating ramp of ≈ 10°C/minute[1], and at the end of the annealing the samples were quenched at air, by removing them from the oven.

[1]The total annealing duration, specified in table 9.3, does not include the time required to achieve the annealing temperature.

9.2 Raman Spectroscopy results

Given that we are dealing with very thin films, deposited at low or moderate temperatures, a low level of crystalinity is expected, at least for the "as deposited" samples. Notwithstanding, Raman spectroscopy, is a very sensitive technique which does not require large crystallites to enable the vibrational study of a sample [200]. In fact, Raman spectroscopy will be sensitive to the internal modes of each molecule or unit cell of a given material, being a very good technique to infer the chemical and structural properties of the thin films here presented, as long as there are enough scattering centres and a reasonable film/substrate signal ratio [200, 253].

The Raman spectrocopy measurements were done in the physics department of the University of Aveiro under the guidance and supervision of Professor Rosário Correia. The Raman spectroscopy measurements were performed in the range 100-2000 cm^{-1}, using a Jobin Yvon 64000 Raman spectrometer and a 432 nm laser as incident radiation at room temperature. This laser line has a photon energy of about 2.87 eV which is close to the 3.2 eV gap energy of BTO [254], thus it is possible to work in an resonance Raman spectroscopy regime[2], as long as there is some BTO in the thin films.

Figures 9.3, 9.4, 9.5, 9.7 and 9.8 present the Raman spectra for the BTO/Fe thin films deposited on the different substrates, as well as the spectrum of their respective substrate. All the Raman spectra are normalized to the maximum value of each spectrum and the offset of each curve was artificially introduced to ease the presentation of each sample spectrum.

It is evident from the observation of figure 9.3 that there are several vibrational modes present in the BTF4.1 and BTF5.1 samples besides the ones belonging to the substrate[3]. Still, for the BTF6.1 thin films there is no evidence of any thin film Raman modes, thus if there are any, they are completely concealed by the substrate vibrational modes.

The BTF4.1 samples have clearly the most prominent Raman modes around 220, 250, 290, 340, 400, 505, 610, 660, 710 and 1400 cm^{-1} matching almost perfectly with the most intense Raman modes of the α–Fe_2O_3 (hematite) and γ–Fe_2O_3 (maghemite) [258–261], presented in table 9.4 and explicitly assigned in figure 9.3. For the BTF4.1_$LaAlO_3$_900C in particular, there are three additional modes which appear near the 305, 520 and 725 cm^{-1} and are assigned

[2]The band gap of hematite and maghemite, two common iron oxides, is about 2.2 V [255,256] and 2.0 eV [257] respectively, enabling as well resonance Raman spectroscopy.

[3]The dashed lines present in all the Raman spectra figures serve as eye guides to the position of the substrate's main Raman modes.

to the most intense $BaTiO_3$ Raman modes [253, 262, 263]. This feature suggests that the thermal annealing was enough to enhance the crystallinity of $BaTiO_3$. The shoulder around $800\,cm^{-1}$ – present at almost all the spectra here presented and indicated by the arrows of figures 9.3, 9.4, 9.5 and 9.7 – is in fact an indicator of amorphous phases of Ba-Ti-O systems, and/or other barium titanate stoichiometries such as Ba_2TiO_4 and $BaTi_2O_5$, whose small contribution does not allow the individual distinction of these compounds spectra [264–267].

α–Fe_2O_3 (cm^{-1}) [258–261, 268–271]		γ–Fe_2O_3 (cm^{-1}) [258–261]	Fe_3O_4 (cm^{-1}) [258–261, 272–274]
226 (s)	659 (vs)	350 (w)	193 (vw)
245 (s)	817 (vw)	500 (w)	306 (vw)
292 (w)	1049 (vw)	700 (w)	538 (w)
299 (w)	1103 (vw)	Fe_2TiO_4(cm^{-1}) [275]	668 (s)
411 (vs)	1320 (2LO overtone)	495 (s)	$FeTiO_3$(cm^{-1}) [275–277]
497 (w)	1525 (two magnon	561 (w)	$\approx$ 230 (s)
612 (s)	scatering)	679 (vs)	680 (vs)

Table 9.4: Active Raman modes for the main iron oxides.

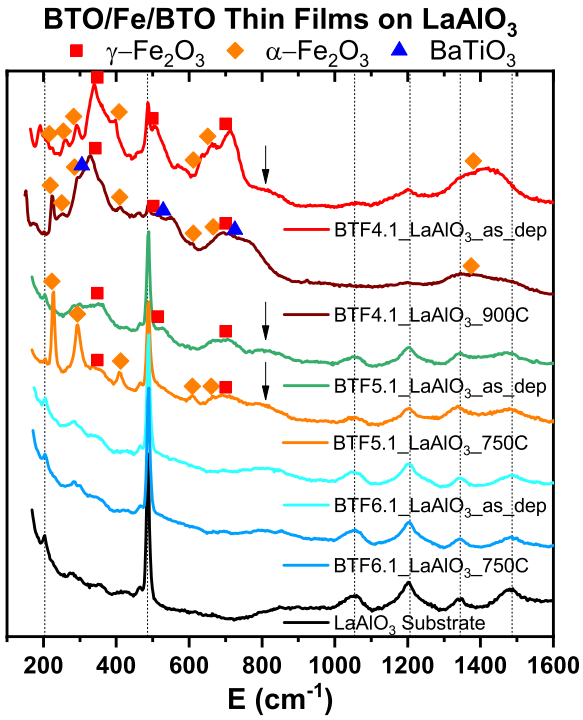

Figure 9.3: Raman spectra for the BTO/Fe thin films deposited on $LaAlO_3$ substrates. The $LaAlO_3$ substrate spectrum is also presented as a reference measurement.

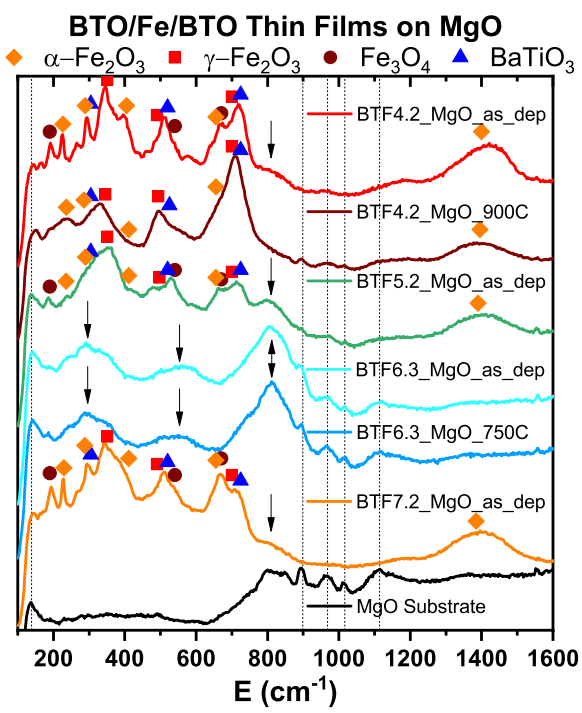

Figure 9.4: Raman spectra for the BTO/Fe thin films deposited on MgO substrates. The MgO substrate spectrum is also presented as a reference measurement.

The BTF5.1 deposition also presents the modes of hematite and maghemite, yet the BTO modes are not present for these deposition and annealing conditions.

It should be pointed out that, even though the same iron oxide phases are in each of the BTF4.1 and BTF5.1 spectra, their relative intensities are clearly different, which implies that the percentage of each iron oxide changes considerably depending on the deposition and annealing conditions. This is clearly seen by comparing BTF5.1_$LaAlO_3$_as_dep and BTF5.1_$LaAlO_3$_900C, where the annealing transforms part of the maghmemite into its α phase, thus the bigger percentage of hematite in the Raman spectrum. Moreover, each mode's frequency can also suffer shifts in its energy due to crystal effects, namely the size of the iron oxide particles and/or strain effects [278].

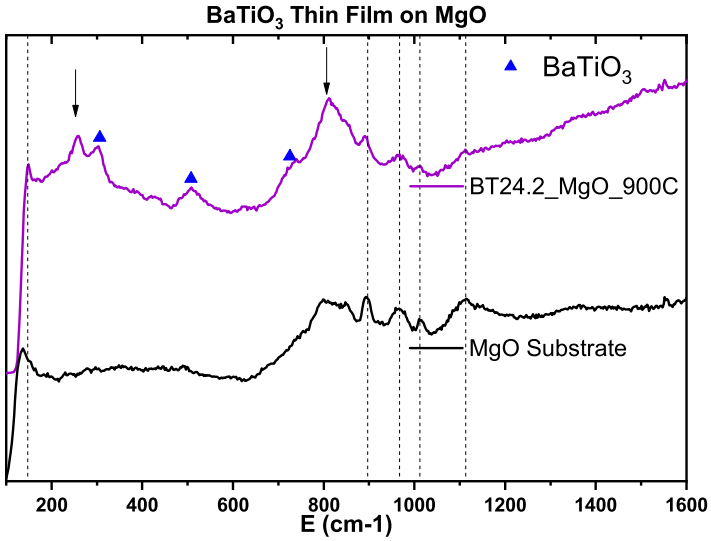

Figure 9.5: Raman spectrum for the BTO thin films deposited on MgO after a thermal annealing at 900°C. The MgO substrate spectrum is also presented as a reference measurement.

For the depositions made on the MgO substrate (presented in figure 9.4 and which we will see later that is the one with the most interesting magnetic properties), there is a new phase assigned to Fe_3O_4 (magnetite), which is present in all "as deposited" thin films except for the BTF6.3 sample. As in the $LaAlO_3$ depositions, the BTF4 depositions seem to have a much higher thin film contribution, when comparing with the substrate, than in the BTF5 and BTF6 depositions. This probably happens due to two reasons: the first and most straightforward reason is due to the higher thickness of the BTF4 thin films (which we estimate to be twice for the Fe layer). The second reason arises from the comparison of the BTF5 and BTF6 depositions, where the former always have more contribution from the iron oxides than the latter, despite having the same layer's geometries. This suggests that these iron oxides favour

the low temperature and low O_2 pressure deposition conditions, and even though the BTO crystallinity requires much higher deposition temperatures and O_2 pressures, the conditions used in BTF5 and BTF6 thin film depositions are not enough to substantially increase the BTO crystallinity. Therefore, the BTF6 deposition conditions turn out to be bad for the formation of most of the iron oxides while not improving enough the BTO phase quality, hence resulting in the poorest thin-film/substrate ratios, as it is possible to see in figures 9.3–9.8. Actually, the BTF6.3_MgO are actually the only thin films with perceptible Raman modes apart from the substrate's contribution. In these samples there are three wide bumps, indicated by the arrows of figure 9.4, which are assigned to the previously mentioned amorphous contribution of BTO as well as to other Barium titanate stoichiometries [264–266].

Focusing now on the BTF4.2 thin films, it is possible to see that after the thermal annealing at 900°C, which according to the literature is within the optimal annealing temperature range to increase the crystallinity of BTO thin films[4] [279], there is a clear increase of the $BaTiO_3$ phase and the decrease of the shoulder around 800 cm^{-1} which was associated with the amorphous phase and other BTO stoichiometries. As a matter of fact, the presence of both the $BaTiO_3$ Raman modes and the amorphous and/or other stoichiometries of barium titanate phases are also clearly perceptible in the Raman spectrum of the BT24.2_MgO_900C thin film, as shown in figure 9.5.

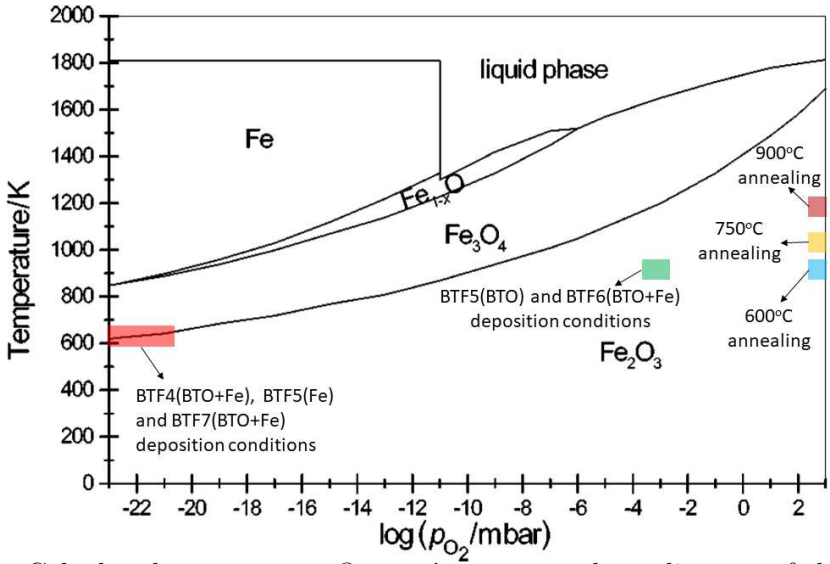

Figure 9.6: Calculated temperature-Oxygen's pressure phase diagram of the Fe–O system. Adapted from [282].

[4]To have highly crystalline BTO thin films deposited trough sputtering deposition, the deposition should be done for T$\gtrapprox$ 800°C and the annealing should be done at 800 $\lesssim$ T $\lesssim$ 1000°C [279–281]

Coming back to the BTF4.2 thin films, the magnetite Raman modes disappear, and there is also a decrease and broadening of the maghemite and hematite Raman modes while the maximum around 700 cm^{-1} increases substantially. The processes involving the iron oxides can be explained by the phase diagram of figure 9.6, where it is possible to see that annealings at room pressure will promote the formation of a Fe_2O_3 phase, thus explaining the disappearance of the magnetite phase. This phase diagram also shows that at the low temperatures region of BTF4 and BTF7 depositions, there is a coexistence of Fe_2O_3 and Fe_3O_4 phases, therefore, small deviations/fluctuations on the deposition conditions might also result in different iron oxides segregation, which would justify the differences in relative intensities between the BTF4.2_MgO_as_dep and BTF7.2_MgO_as_dep spectra.

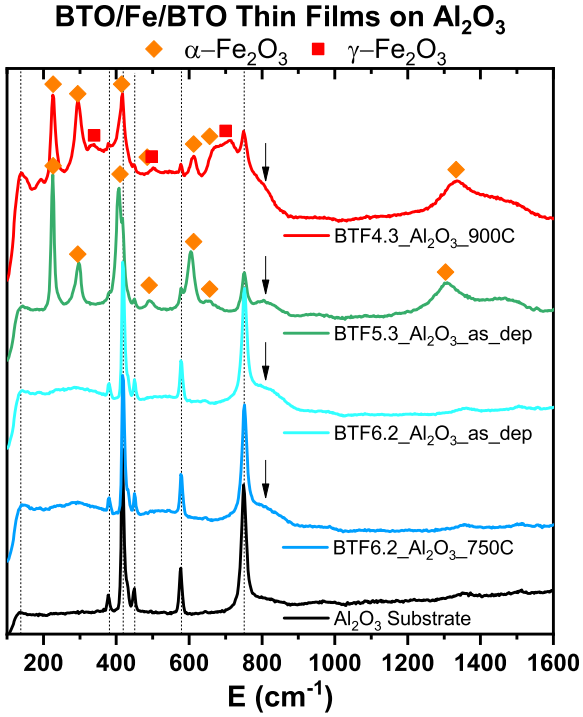

Figure 9.7: Raman spectra for the BTO/Fe thin films deposited on Al_2O_3 substrates. The Al_2O_3 substrate spectrum is also presented as a reference measurement.

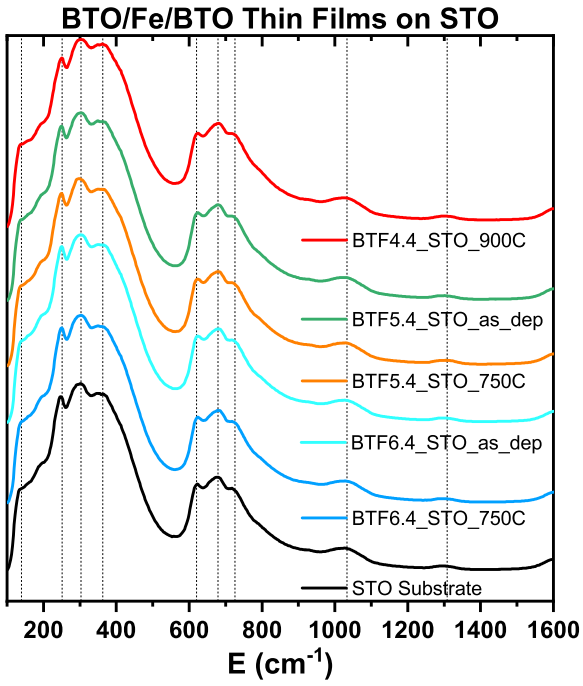

Figure 9.8: Raman spectra for the BTO/Fe thin films deposited on STO substrates. The STO substrate spectrum is also presented as a reference measurement.

The Raman spectra of the thin films deposited on Al_2O_3 and STO substrates are presented in figures 9.7 and 9.8 respectively. For the STO substrate, which has a band gap energy of 3.25 eV [283], there is resonant Raman scattering with the substrate. Therefore, the Raman contribution of the STO substrate completely overshadows any contribution of the thin films, which have an interaction volume several orders of magnitude smaller than the substrate.

This problem was not evident for the remaining substrates once they have band gaps $> 6\,eV$, much higher than the photon energy of the incident laser line (2.87 eV), hence being almost "invisible" to the incident laser.

On the other hand, figure 9.7 shows that the thin films deposited on the Al_2O_3 substrate have Raman modes besides the ones from the substrate. As in the previously discussed cases, the BTF6.2 thin films display spectra identical to the substrate spectrum, if was not for the already known $800\,cm^{-1}$ shoulder. The BTF4.3 and BTF5.3 samples present the hematite as their majority phase, even for the as deposited BTF5.3, since while the BTO layer was being deposited, the Fe suffered a pseudo thermal annealing at the BTO deposition conditions, which for this particular substrate, promoted the growth of the α–Fe_2O_3 (figure 9.6).

Finally, it is crucial to mention the broad mode around $1400\,cm^{-1}$, present for each assigned hematite phase. In fact, this maximum corresponds to two Raman modes: one phonon overtone of a Raman inactive vibrational mode ($660\,cm^{-1}$) at around $1320\,cm^{-1}$ and a mode corresponding to a two magnon Raman scattering which occurs around $1525\,cm^{-1}$ [269–271]. While the overtone remains proximately in the same vibrational energy, the two magnon mode can suffer a shift in energy depending in the overall magnetic and structural properties of the hematite particles deposited on the considered substrates under the different conditions [278]. As a matter of fact, looking at the BTF4 deposition before and after the 900°C thermal annealing, there is a greater decrease in relative intensity of the right part of the high energy maximum (correspondent to the two magnon scattering mode) than in its left part (corresponding to the phonon overtone), thus suggesting a change in the magnetic behaviour of these thin films due to the thermal annealing.

9.3 Grazing Incidence XRD results

XRD was performed to complement the structural information given by the Raman spectroscopy. To increase the interaction volume of the X-ray radiation with the thin films, a grazing incidence (GI) geometry was adopted (1° incidence angle) using a *Philips Panalytical X'Pert Pro MRD* using $\lambda(\text{Cu } K_{\alpha 1}) = 1.5405(98)\,\text{Å}$ (without monochromator) at room temperature [284].

Figures 9.9–9.12 present the GIXRD results for the thin films deposited on the $LaAlO_3$, MgO, Al_2O_3, and STO substrates. Two major observations can be done after analysing all the diffractograms: first, the diffraction peaks present in the mentioned diffractograms differ from substrate to substrate, even for the same deposition and annealing conditions, implying that the substrates constrain the crystallization process of the thin films in very particular ways. Second, each sample measured in the GIXRD geometry solely presents a scarce number of diffraction planes/peaks (if any), thus making the phase identification quite hard/ambiguous.

Firstly, we used the *High Score Plus* phase indexing software, which uses the *ICDD PDF4+* as database reference, to identify the crystalline phases of each sample. However, the lack peaks lead to an inconclusive indexation. Nevertheless, taking into account the deposited elements, the suggestions from the indexing software, and the information obtained from the Raman spectroscopy, it was possible to assign some phases to the peaks displayed in the diffractograms. The diffracted peaks are identified by the black dashed lines of figures 9.9–9.12, the green dashed line indicates that the peak in question matches with a peak from the substrate, and the gray dashed lines show the less reliable peaks which have intensities barely above the background radiation noise. The lack of reliable diffraction peaks in these and all the other thin films is due to the very small thickness of each deposited layer, which influences the size of BTO grains[5], and due to the high background radiation coming from the Fe fluorescence, contributing even more to a poor signal/noise ratio.

The GIXRD results for the thin films deposited on the $LaAlO_3$ substrate, presented in figure 9.9, show that for most diffractograms, there are almost no diffraction peaks, mainly for the "as deposited" thin films. This implies that there is a high level of amorphous phase, which decreases with the thermal annealings, thus for the latter case there is a higher number

[5]The size of the BTO grain boundaries also depend on each layer's thickness, where thicker layers will have bigger grains even for the same deposition and annealing conditions [285]

and more intense diffraction peaks [286, 287].

The BT24.1 thin films have two very pronounced peaks, one of which is assigned to a peak from the substrate (green dashed line), whereas the other does not match with the most intense peaks of any of the considered phases. This seemingly unmatched peak coincides with one peak of the metallic Ba diffraction planes, but to be assigned to this phase it would mean that the Ba would have to be segregated with a preferential growth orientation, which is a very unlikely scenario. Moreover, Raman spectroscopy would not present the Ba Raman mode due to the technique intrinsic difficulty of detecting Raman modes in metallic phases [288–290].

For the remaining "as deposited" thin films on the $LaAlO_3$ substrate, there are almost no diffraction peaks, yet, after the thermal annealing the crystallinity of the BTF4.1_$LaAlO_3$-_900C and BTF5.1_$LaAlO_3$_900C slightly improves as the appearance of some diffraction peaks suggest. For the BTF4.1_$LaAlO_3$_900C case, some of its diffraction peaks can be assigned to the most intense peaks of the Ba_2TiO_4 and/or $BaTi_2O_5$ compounds, whereas the remaining and more intense peaks solely match with some diffraction planes of the three iron oxides discussed in the Raman spectroscopy results, implying once again the growth of these phases in a preferential orientation.

The GIXRD diffractograms for the thin films deposited on the MgO substrate, presented in figure 9.10, are the ones which present better defined diffraction peaks. Looking at the BT24.2 reference thin films it is possible to see that there are no relevant peaks before the 900°C annealing, however after the annealing several diffraction peaks appear. These peaks are assigned to polycrystalline phases of other stoichiometries of BTO, namely Ba_2TiO_4, $BaTi_2O_5$ and/or $BaTi_5O_{11}$ compounds, and to a polycrystalline $MgFe_2O_4$ phase.

This $MgFe_2O_4$ phase appears due to the presence of residual Fe atoms, $< 50\,\text{ppm}$, as reported by some suppliers of the MgO substrate [291], and whose phase formation might be promoted by the thermal annealing at 900°C. Actually, the diffractogram of $MgFe_2O_4$ is identical to the magnetite's and maghemite's, still, the Raman spectra of these two iron oxides would be perceptible in figure 9.5, while the broader and less intense Raman spectra of the $MgFe_2O_4$ could be perfectly masked by the BTO compounds present in BT24.2_MgO_900C [292, 293].

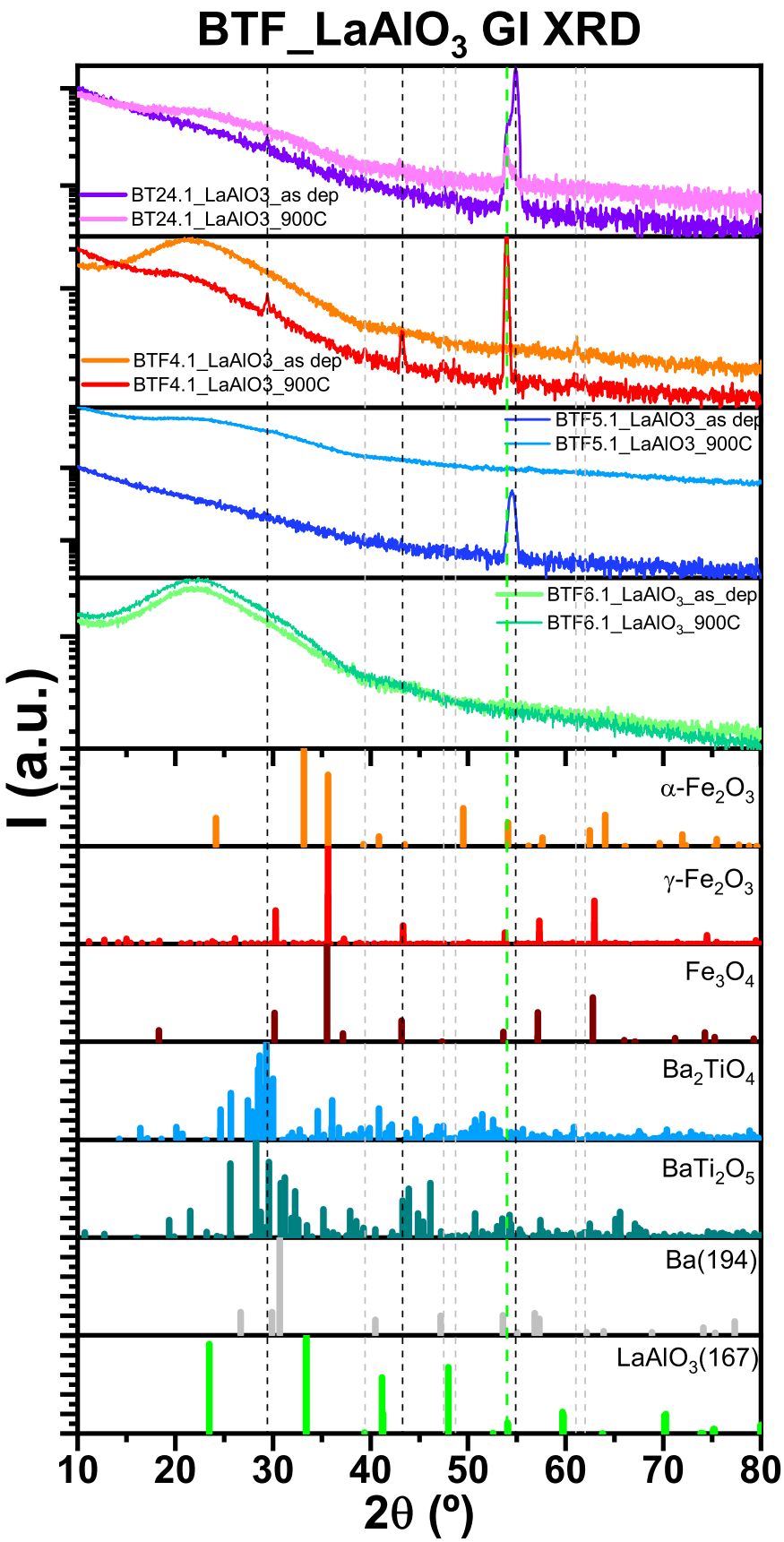

Figure 9.9: Grazing incidence XRD of the thin films deposited on $LaAlO_3$.

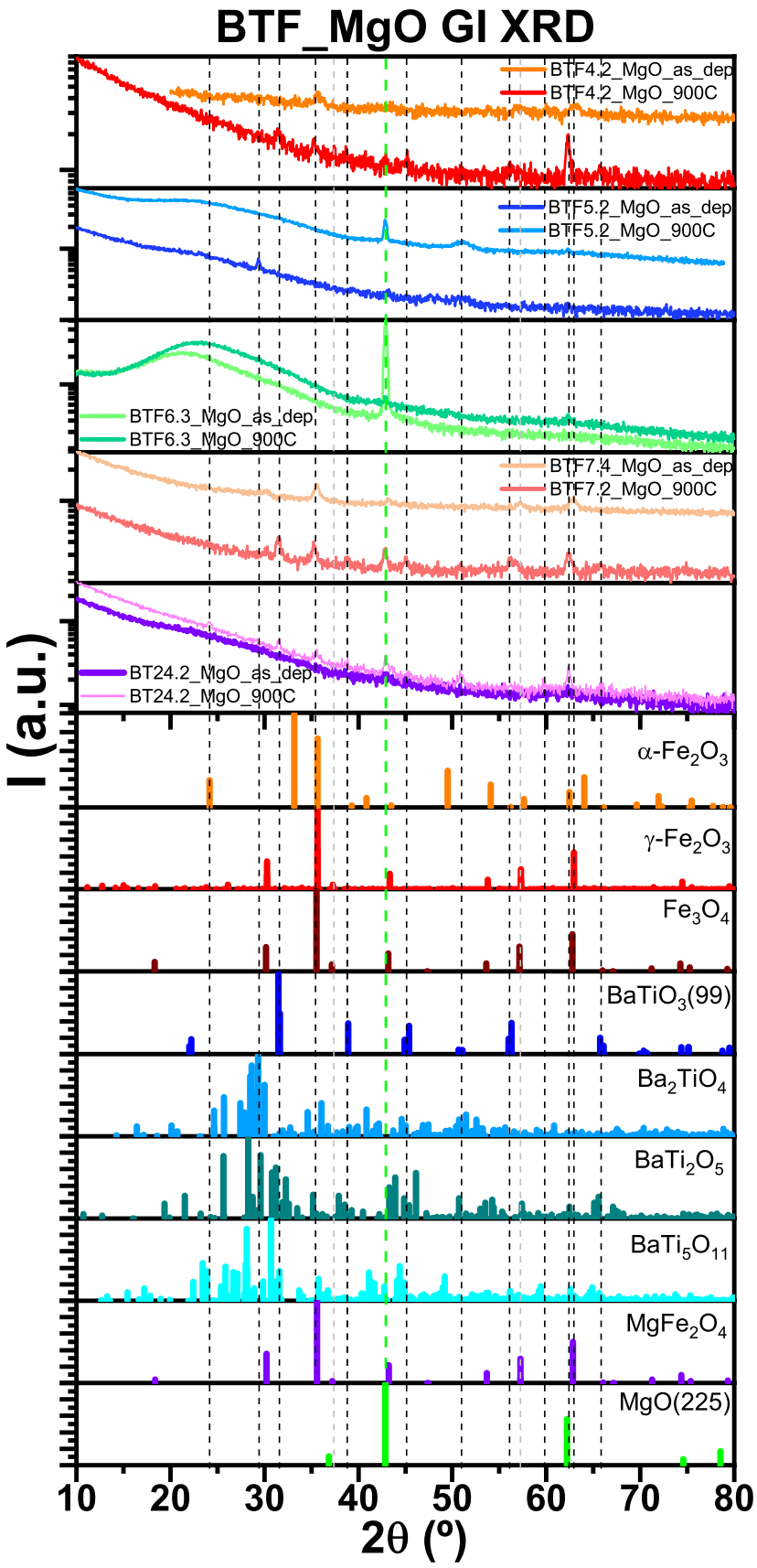

Figure 9.10: Grazing incidence XRD of the thin films deposited on MgO.

It should also be pointed out that the $BaTiO_3$ phase present in figure 9.5 is not perceptible in the BT24.2_MgO_900C diffractogram due to the amount/size of the crystallites of this phase being too small to be detected even when using GIXRD, reinforcing the discriminative potential of Raman spectroscopy.

The diffractograms for the BTF4.2 and BTF7 "as deposited" thin films display several diffraction peaks which can be assigned to a polycrystalline phase of the maghemite and/or magnetite, and to several barium titanate compounds such as Ba_2TiO_4, $BaTi_2O_5$ and/or $BaTi_5O_{11}$. After the 900°C thermal annealing, most of these peaks get sharper and more intense, and there is the emergence of new ones. The new peaks are mostly assigned to the polycrystalline tetragonal phase of $BaTiO_3$ whose emergence is due to the crystallization of the its amorphous phase and to the decreasing of the amount of other BTO stoichiometries whose peaks either disappeared or at least got much smaller, in good agreement with the Raman spectroscopy results. Regarding the hematite phase seen in the Raman spectroscopy, since there is no peak assigned to its most intense diffraction plane, therefore, either it is in a mostly amorphous phase or its growth must present a preferential orientation, instead of being in a purely random oriented polycrystalline phase.

It is somehow surprising that for the BT24.2_MgO_900C there is a larger contribution from other Ba-Ti-O stoichiometries than from the standard $BaTiO_3$, in such a way that is even undetectable by the GIXRD diffractograms. Nonetheless, the unbalanced Ba/Ti ratio in barium titanate compounds deposited througth RF-sputtering is a well know issue, which can be solved by increasing the pressure of the sputtering process to pressures $\gtrsim 3 \times 10^{-2}$ mbar [294–296]. This range of pressures is actually close to the ones used in most of the depositions made in this work. Still, for the BT24, the sputtering deposition pressure was about half the pressure of the BTF4 and BT7 depositions, which could explain the different amount of the standard $BaTiO_3$ crystallization even after having the same thermal annealing.

In the BTF5.2 diffractograms, apart from a very sharp peak assigned to the substrate (200) plane, there are two additional peaks (one of them quite broad) which are assigned to the Ba_2TiO_4 and/or $BaTi_2O_5$ phases. On the other hand the BTF6.3 substrates do not show any diffraction peaks besides the (200) MgO peak.

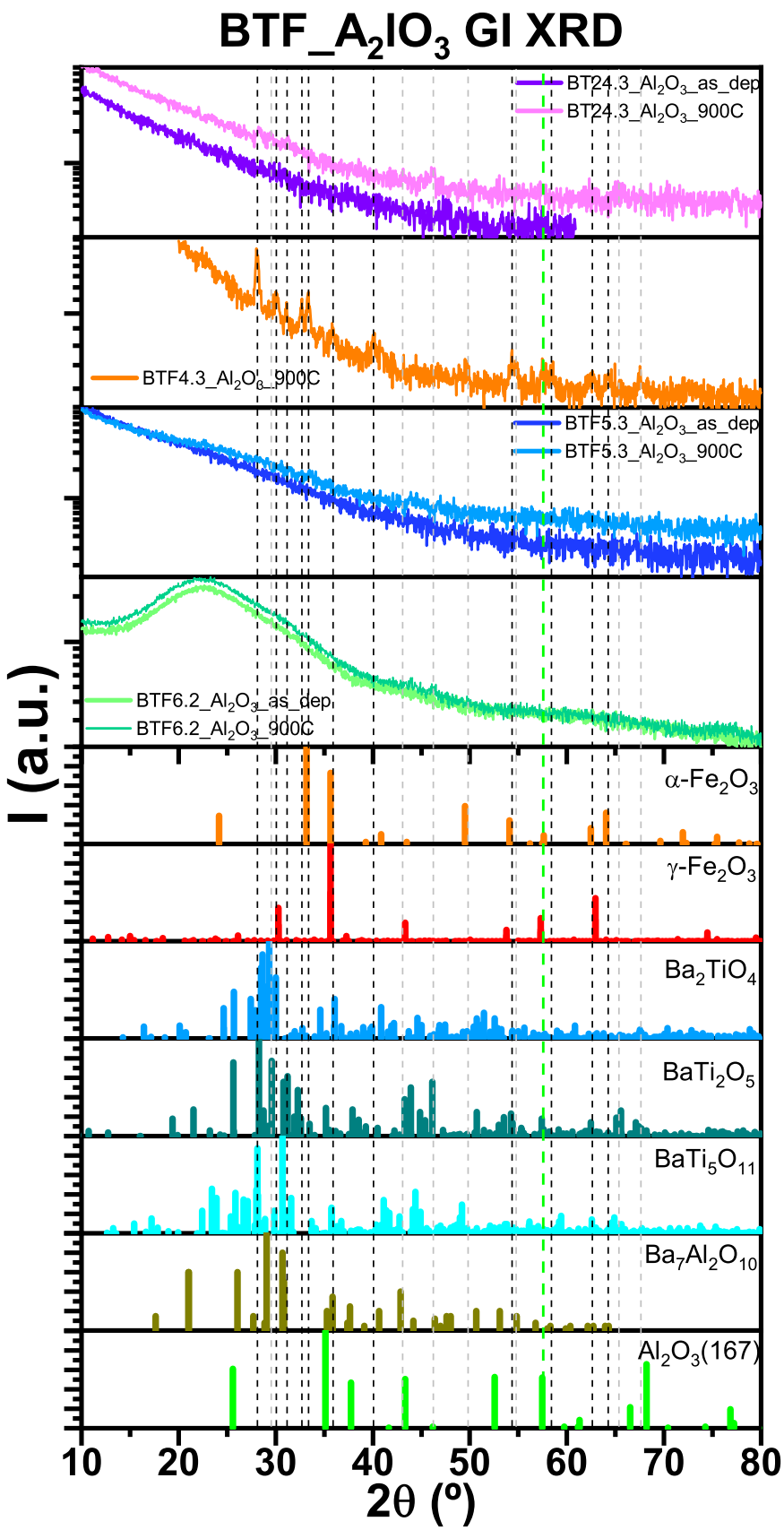

Figure 9.11: Grazing incidence XRD of the thin films deposited on Al_2O_3.

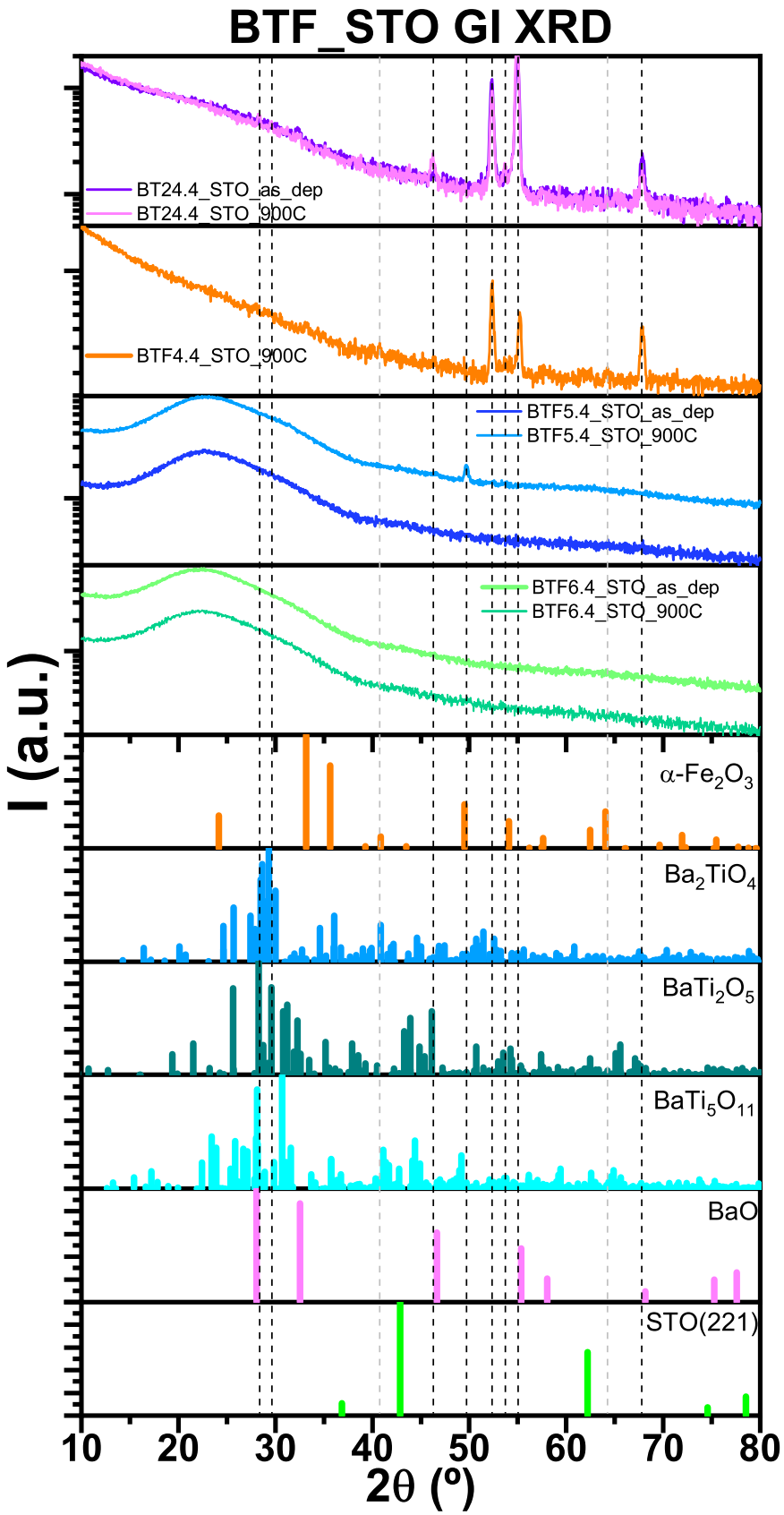

Figure 9.12: Grazing incidence XRD of the thin films deposited on STO.

Figure 9.11 shows the GIXRD diffractograms for the thin films deposited on the Al_2O_3 substrate. The information given by these diffractograms shares a lot of similarities with the results obtained from Raman spectroscopy, namely, for the BTF5.3 and BTF6.2 thin films where there are almost no diffraction peaks, implying that if there is any polycrystalline phase its amount/size is too small to be detected using XRD. For the BT24.3 BTO thin films there are some wide peaks just above the background noise which can be assigned to the Ba_2TiO_4, $BaTi_2O_5$ and/or $BaTi_5O_{11}$ compounds.

For the thicker low temperature deposition thin film, BTF4.3_Al_2O_3_900C, there are much sharper diffraction peaks which are mainly assigned to the α and γ phases of Fe_2O_3, and to the $BaTi_2O_5$ and $BaTi_5O_{11}$ compounds, corroborating the results of the Raman spectroscopy.

In figure 9.12 it is presented the diffractograms of the thin films deposited on STO. The analysis of these diffractograms is the most difficult one since, besides the scarce number of peaks present in each diffractogram, there is no guidance from the Raman spectroscopy results.

Additionally, the BTF5.4 and BTF6.4 diffractograms solely display a single diffraction peak close to $2\theta = 50°$ for the BTF5.4_STO_900C, thus no polycrystalline phase is assigned to any of these thin films. The STO substrate structure belongs to the 221 point group, and possesses lattice parameters close to the BTO cubic (221) and tetragonal (99) phases', thus it is possible that the lack of the peaks are related with the growth of the thin films in preferential orientations, mainly for the BTO compounds [297]. The single diffraction peak which appears after the thermal annealing for BTF5.4_STO_900C could be due to the growth of the hematite phase, also under a specific preferential orientation, since this peak can be assigned to (024) diffraction plane of hematite.

The BT24.4 and BT4.4 deposition were done at low temperatures and present about the same diffraction peaks, namely three peaks which are quite sharp and intense at $2\theta \approx 52$, 55 and 68°. None of these three peaks coincide with any of the substrate diffraction planes, nor with the most intense diffraction planes of any of the phases suggested by the *High Score Plus* phase indexing software. As a matter of fact, these peaks did solely match a very restricted amount of driffraction peaks such as the (220) and (311) diffraction planes of the BaO(225) and some of the low intensity peaks of the Ba_2TiO_4, $BaTi_2O_5$ and $BaTi_5O_{11}$ compounds. The remaining smaller and less well defined diffraction peaks are compatible to a randomly

oriented polycrystalline growth of Ba_2TiO_4 and $BaTi_2O_5$ phases, and for the particular case of the BTF4.4_STO_900C there is the matching of some of its peaks with the (113), (024) and (300) diffraction planes of hematite.

9.4 STEM/EDS analysis of the BTF thin films

In order to have further morphological and chemical information about the BTO/Fe/BTO thin films deposited on the different substrates, a combined approach of EDS and transmission electron microscopy was performed to the BTF5.2_MgO_as_dep, BTF4.2_MgO_as_dep and BTF4.2_MgO_900C samples. To prepare the samples for the transmission microscopy, a FEI Helios NanoLab 650 Dual Beam (FIB/SEM) system was used after the deposition of a protective coating layer of Al (or AuPd) and an additional layer of Pt. The STEM, TEM and EDS results were obtained by a FEI Tecnai G2 (200 kV) equipped with a EDAX EDS detector from the Nano-Optics and Optoelectronics Research Laboratory at the Masdar Institute of Science and Technology [298], operated by Karen Sloyan under the supervision of Professor Marcus Dahlem.

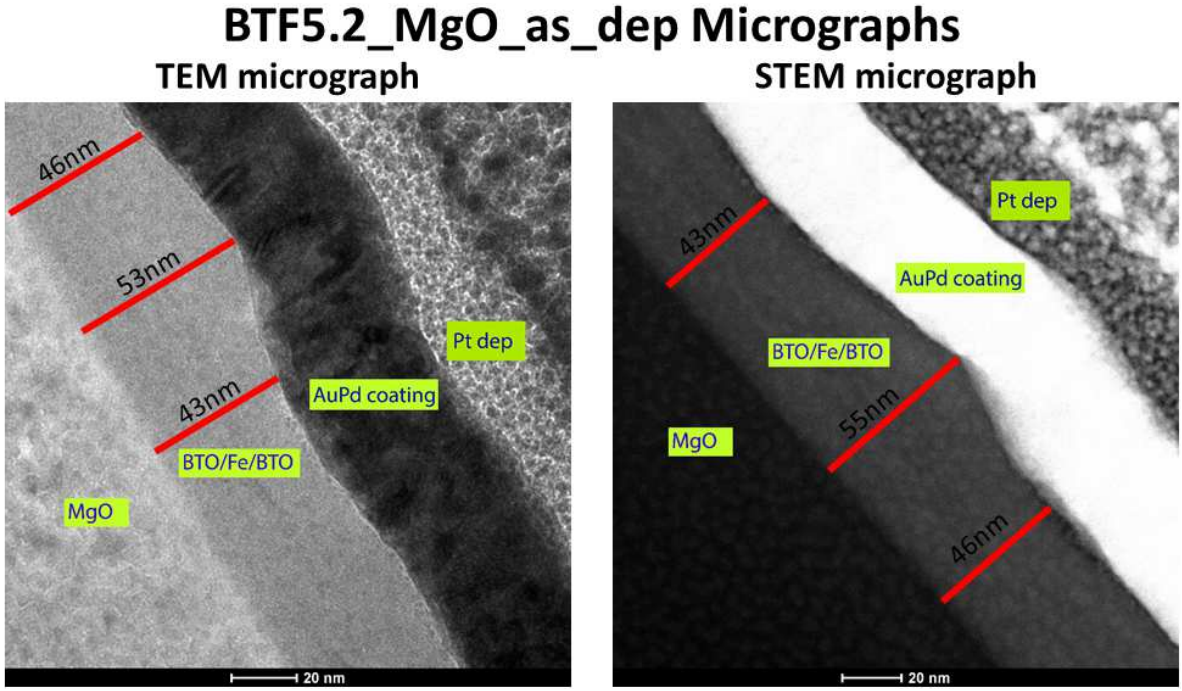

Figure 9.13: BTF5.2_MgO_as_dep TEM and STEM micrographs

Figure 9.13 shows the TEM and STEM micrographs of BTF5.2_MgO_as_dep sample at two distinct probing regions. The micrographs of figure 9.13 allow to determine the total thickness, t, of the BTF5.2_MgO_as_dep thin film, which according to the previous calibration measurements is expected to be $t \approx 45\,\text{nm}$. In fact, as it is perceptible from the micrographs observation, the measured thickness of this thin film is close to its expected value. Still, there

are clearly some "fluctuations" in the thin film thickness, larger than the substrate roughness, showing some heterogeneity in the growth of the deposited film, which can have some "bumps" with 55 nm in the present picture.

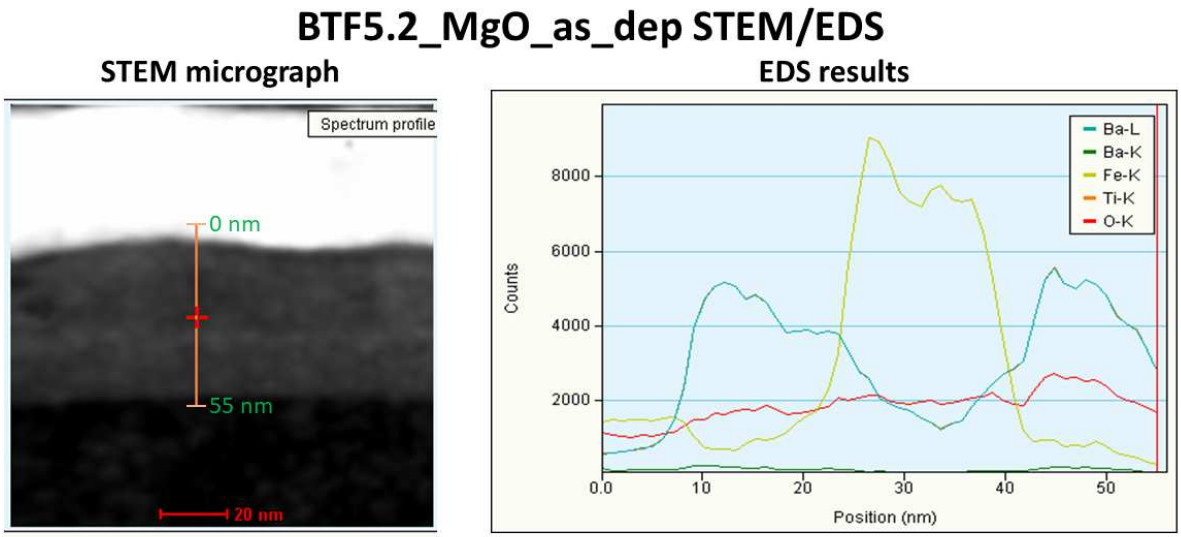

Figure 9.14: BTF5.2_MgO_as_dep EDS results from the line specified in the STEM micrograph.

Once the micrograph contrast does not discriminate the BTO layer from the Fe layer (due to their similar atomic numbers), a STEM/EDS analysis was performed using an electron probe size with a FWHM of about 8 nm. The STEM/EDS results are shown in figure 9.14, where it is possible to observe three different "peaks" all with a width, w, of about 15 nm and which correspond to the BTO(15 nm)/Fe(15 nm)/BTO(15 nm) layers, where the BTO layers are characterized by the Ti and Ba K and L lines respectively, and the Fe by its K lines. The Ti and Ba curves are almost superimposed, yet since their K and L spectral lines are quite close to each other , this does not mean that the Ba and Ti have a 1:1 proportion since their spectral lines were not resolved. Nevertheless, these elements are a good indicator to infer where the BTO like phases are located in the thin film.

An interesting feature of the EDS results of figure 9.14 is that the O is present all over the thin film, suggesting that the Fe layer is actually an Fe oxide layer, confirming the Raman and XRD results which showed the presence of several Fe oxides but did not shown any evidence of metallic Iron.

Figure 9.15 presents the TEM and STEM micrographs for two different regions of the

BTF4.2_MgO_as_dep thin film. In this case, there is an excess on the total thickness of the the thin film when comparing to the initially projected thickness. Once again it is possible to see that the upper part of the thin deposition presents several possible thickness values, yet for the considered regions these fluctuations show always a thickness larger than the total 60 nm designed in figure 9.1. This excess in the film thickness was measured to be as large as $\approx 21\%$.

To confirm the elemental distribution through the deposited film, a STEM/EDS analysis was performed using an electron probe beam with a FWHM of about 2.5 nm. Figure 9.16 shows the three Fe peaks with $w \approx 10$ nm each between the four Ba/Ti peaks, showing a well defined separation between the BTO and Fe layers[6]. Figure 9.16 also shows the presence of O through all the BTF4.2_MgO_as_dep film, suggesting the diffusion of O into the Fe layers, thus enabling the formation of Fe oxides, similarly to what happens at BTF5.2_MgO_as_dep.

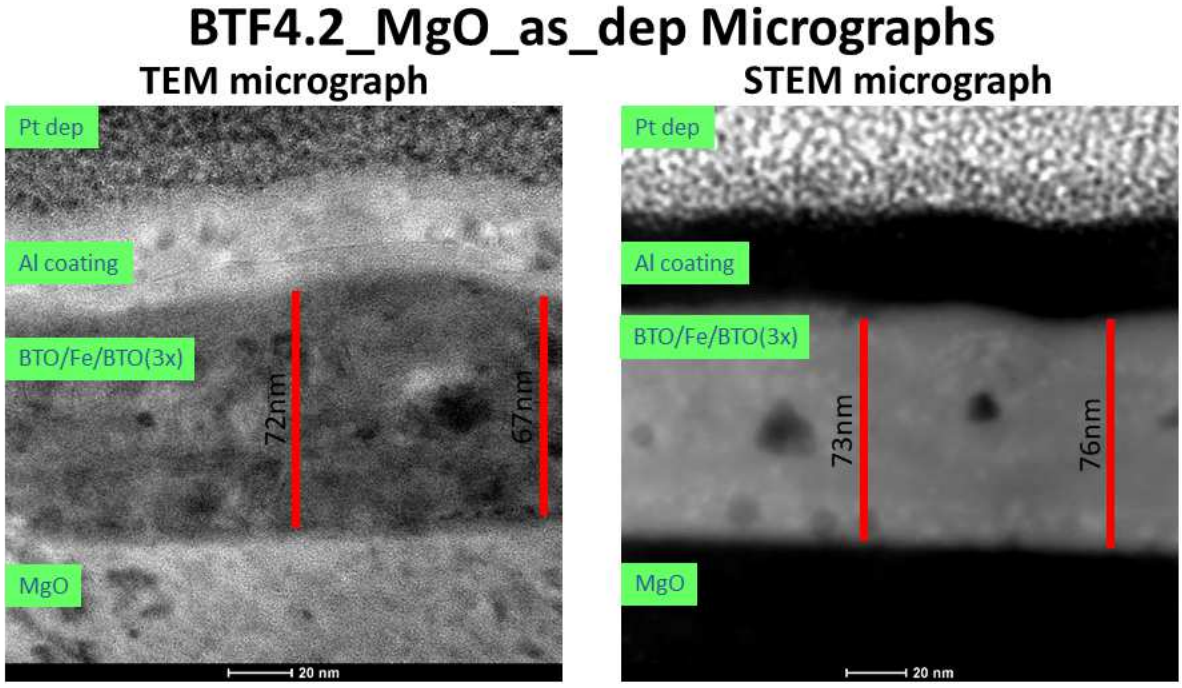

Figure 9.15: BTF4.2_MgO_as_dep TEM and STEM micrographs

[6]At the interface between the BTO and Fe layers, at both the BTF4.2_MgO_as_dep and BTF5.2_MgO_as_dep EDS results, there is an overlap between the Fe and Ba/Ti contributions which can originate from the interface intermixing of the Fe and BTO layers but also from the uncertainty associated to the electron probe size.

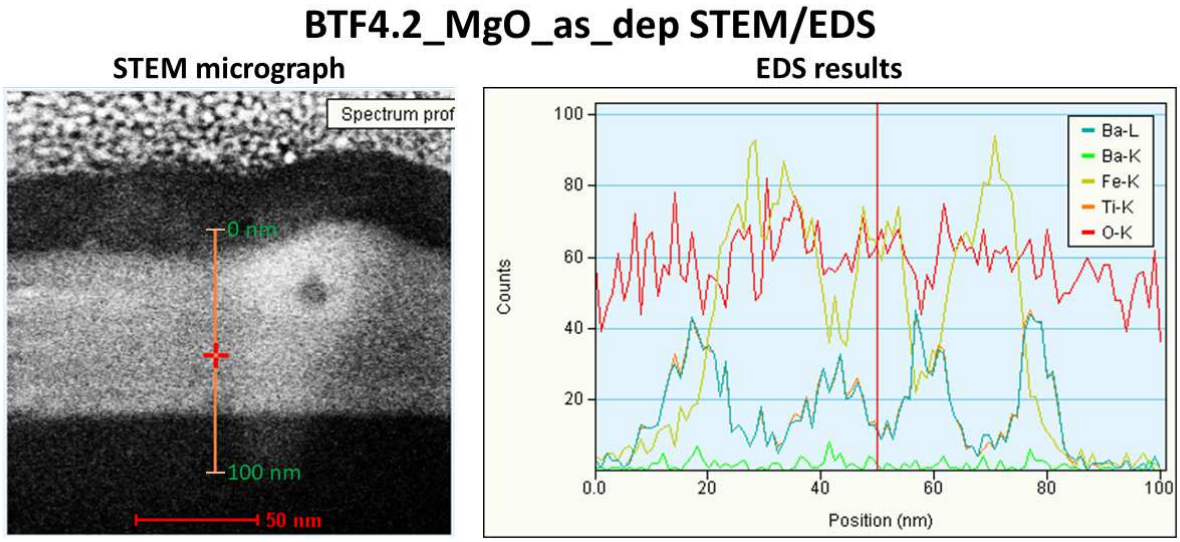

Figure 9.16: BTF4.2_MgO_as_dep EDS results from the line specified in the STEM micrograph.

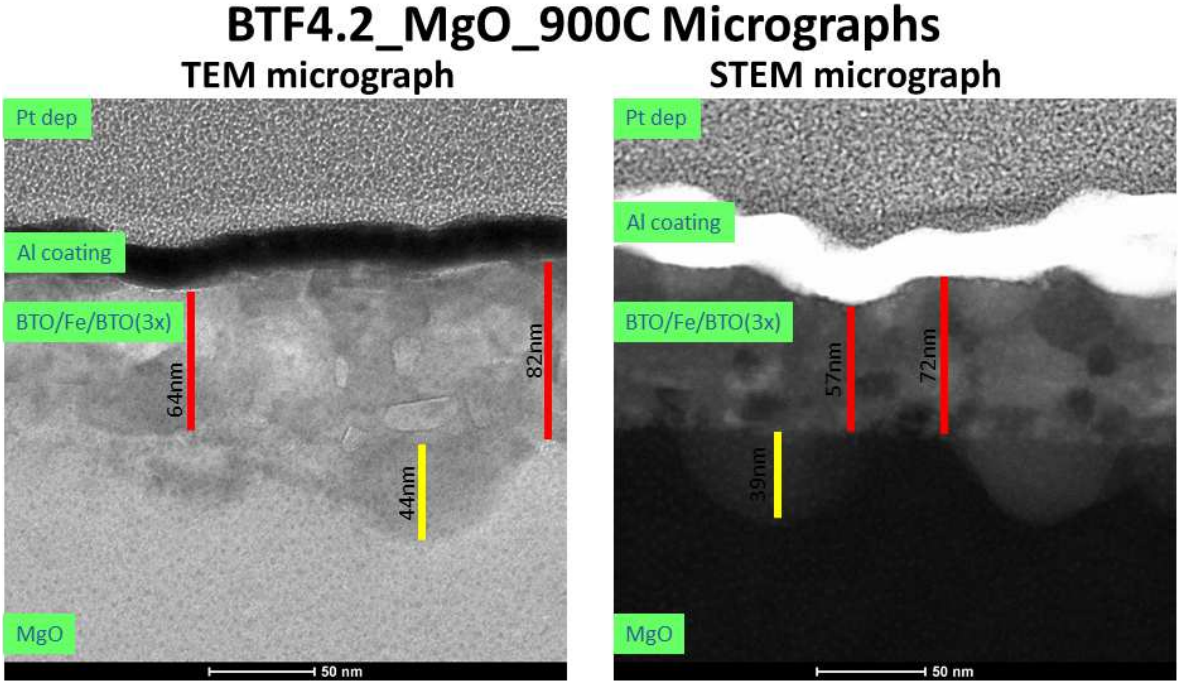

Figure 9.17: BTF4.2_MgO_900C TEM and STEM micrographs

Finally, to evaluate the thermal annealing effects on the deposited thin films, the transmission electron microscopy was also performed to the BTF4.2_MgO_900C sample. The TEM and STEM micrographs presented in figure 9.17 show about the same order of thickness and respective fluctuations, however, the 900°C annealing also induced the diffusion of part of the

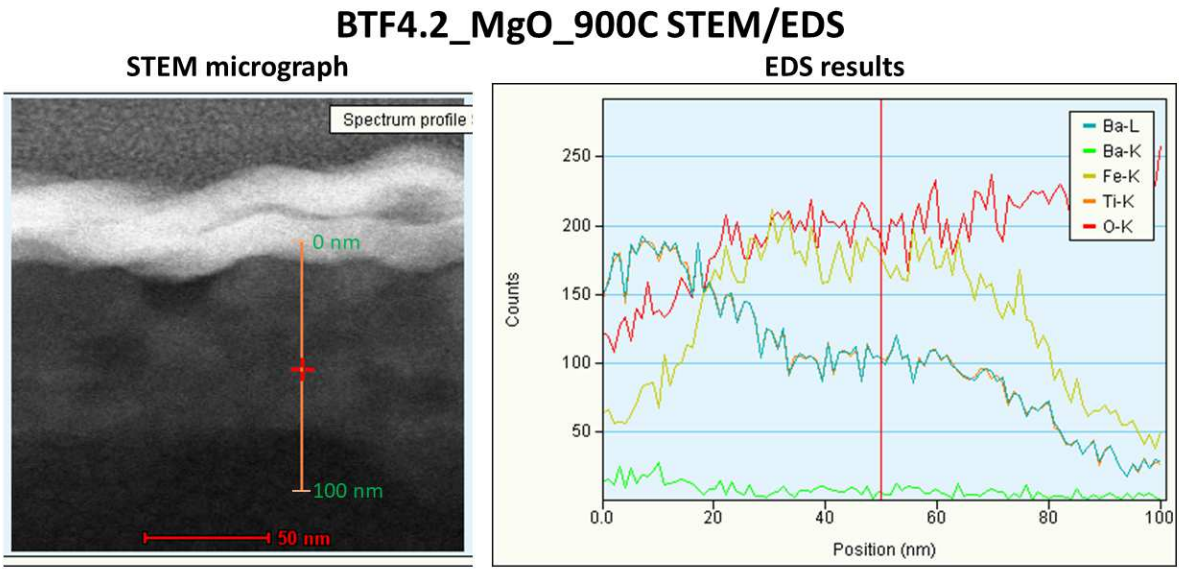

Figure 9.18: BTF4.2_MgO_900C EDS results from the line specified in the STEM micrograph.

film atoms into the substrate. Figure 9.17 shows that the diffused atoms can penetrate as deep as 44 nm.

To determine if the BTO and Fe layers were still in a heterostructured arrangement, a STEM/EDS analysis was performed using an electron probe beam with a FWHM of about 2.5 nm. Figure 9.18 shows that, actually, the three Fe peaks merged into a single broad maximum implying the presence of Fe through all the film volume. A similar feature is also seen for the Ba/Ti case, whereas the O atoms remain in a distribution similar to the "as deposited" film.

9.5 Magnetic Studies

To unveil possible magnetoelectric effects of the BTO/Fe thin films, these films were magnetically characterized using a Quantum Design MPMS3 SQUID-VSM at 2–400 K range and using magnetic fields ranging from -70 kOe–70 kOe.

To infer the magnetic contribution of the substrates used in the thin film depositon, the temperature and magnetic field dependence of the magnetization of the $LaAlO_3$, MgO, Al_2O_3 and STO substrates was also measured, as presented in figures 9.19 and 9.20. For the $LaAlO_3$, Al_2O_3 and STO substrates the temperature dependence of magnetization, measured at H=100 Oe presents a mostly diamagnetic behaviour and a very small paramagnetic component which originates from paramagnetic impurity ions present in the substrates.

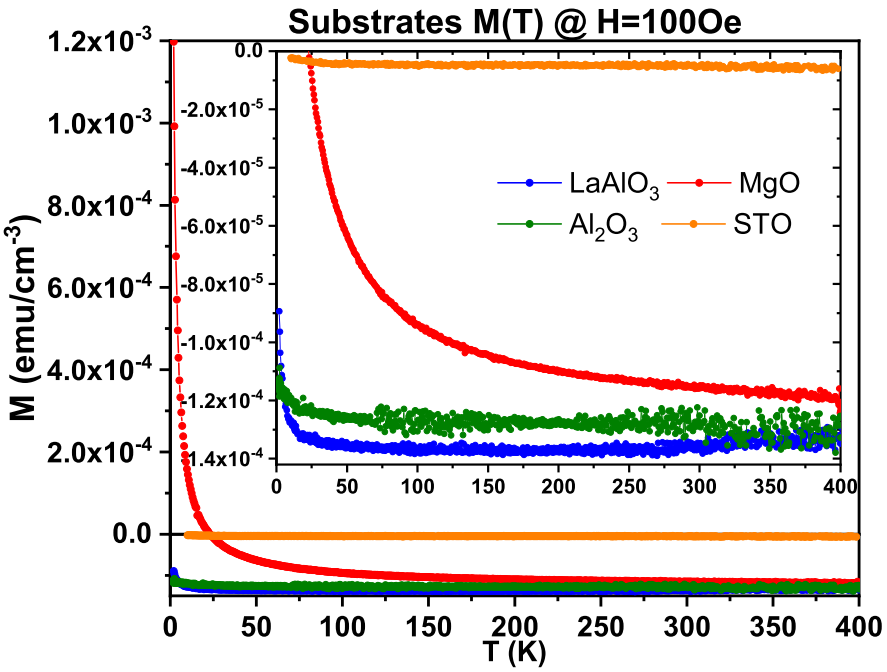

Figure 9.19: M(T) curves of the $LaAlO_3$, MgO, Al_2O_3 and STO substrates at H=100 Oe.

On the other hand, for the MgO substrate, the M(T) curve shows that, besides the expected diamagnetic behaviour, there is a substantially large paramagnetic component when compared with the other substrates.

The M(H) dependence shown in figure 9.20, of the $LaAlO_3$, Al_2O_3 and STO substrates has temperature independent linear curves with negative slopes (even at T=4 K), while for the MgO case there is a clear temperature dependence of its magnetic susceptibility, and at 4 K its magnetization remains positive, completely overtaking the diamagnetic part even at

H=70 kOe.

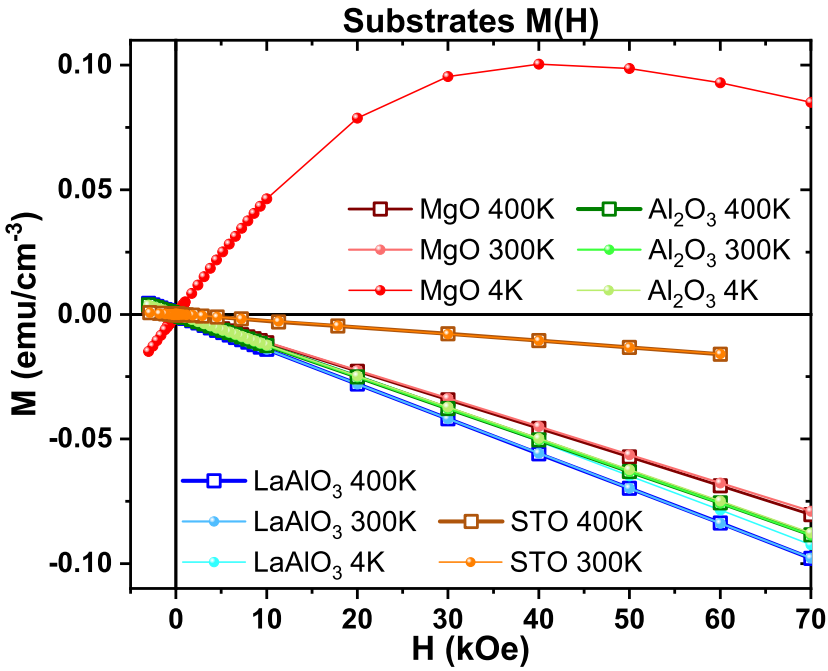

Figure 9.20: M(H) curves of the $LaAlO_3$, MgO, Al_2O_3 and STO substrates at different temperatures.

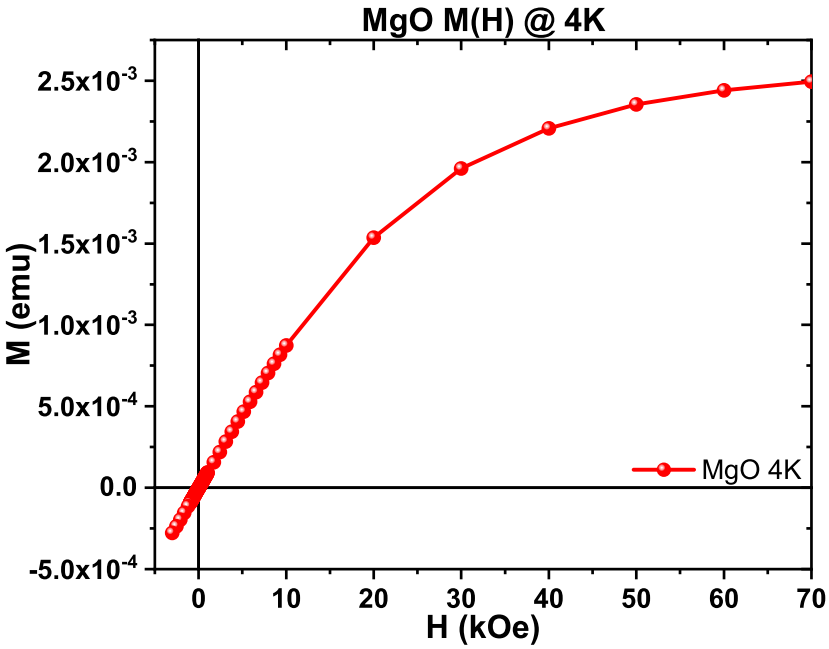

Figure 9.21: MgO substrate M(H) curve at 4 K after removing the diamagnetic contribution.

As mentioned before, there are some MgO suppliers which report the presence of Fe impurities in their MgO single crystal substrates, namely < 50 ppm for the Sigma-Aldrich case [291].

Assuming that the Fe ion is the only source of paramagnetic impurities (no other paramagnetic ion was mentioned at [291]), the amount of Fe present in our MgO substrates (bough from CrysTec) was estimated in the following way: first the diamagnetic component of the substrate was determined using the slope of the M(H) curve at 400 K, since at this temperature the paramagnetic contribution is negligible. Then the diamagnetic component was subtracted from the MgO 4 K M(H) curve, as presented in figure 9.21, arriving to a saturation magnetization for M(70 kOe)@4 K$\approx 2.5 \times 10^{-3}$ emu. Taking into account the total mass of the substrate, an Fe saturation magnetization $M_{s,Fe} = 220$ emu/g [299], and an Fe density of $\rho_{Fe} = 7.874\,g/cm^3$ [300], a value of 83 ppm (atomic) of Fe was estimated for the measured substrate. This value is in the same order of magnitude to the ones reported by [291], yet slightly higher.

9.5.1 BTF4 Magnetic Results

Figures 9.22–9.25 present the temperature dependence of the magnetic moment for all the BTF4 thin films and respective thermal annealings. Similarly to the Raman and XRD results, even though the deposition conditions of the BTF4 thin films were the same, it is possible to see that the magnetic behaviours of the thin films deposited in different substrates after the thermal annealings are truly distinct.

The observation of the as deposited BTF4 thin films M(T) curves show the presence of a cooperative magnetic behaviour, with a high T_C (well above the maximum measured temperature, 400 K), a feature which is compatible with the Curie temperatures of the common α-Fe_2O_3 ($T_C = 956$ K) , γ-Fe_2O_3 ($T_C = 820-986$ K) and Fe_3O_4 ($T_C = 850$ K) iron oxides [301] suggested by the Raman spectroscopy results. The BTF4.2_MgO M(T) curves also present a paramagnetic component at all the considered annealings, whose contribution originates from the substrate itself.

The 600°C annealing did not alter qualitatively the magnetization curves of figures 9.22 and 9.23, apart from a small vertical shift associated with a change in the saturation magnetization. A similar effect also occurs for the 900°C annealing of the BTF4.4_STO thin film (figure 9.25), however in this case, besides the decrease in the absolute value of its magnetization at H=100 Oe, there is also a flattening of the M(T) curvature, implying either an increase of the T_C or a change in its overall magnetic behaviour.

Notwithstanding, after the 900°C annealing, each substrate seems to have its own distinct magnetic behaviour. The BTF4.1_$LaAlO_3$_900C thin film has a considerable decrease on its magnetization at H=100 Oe, making more evident its diamagnetic behaviour (hence the negative value) and the small amount of paramagnetism at very low temperatures. Another noteworthy feature is the anomaly which occurs around 270 K quite close the O↔T BTO phase transition.

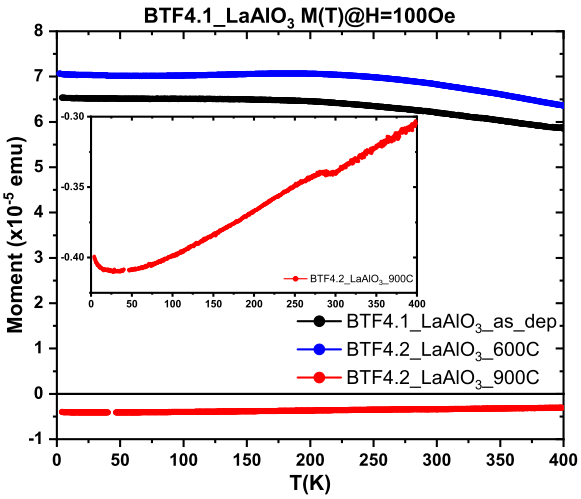

Figure 9.22: M(T) curves of the BTF4.1_$LaAlO_3$ thin film with different thermal annealings.

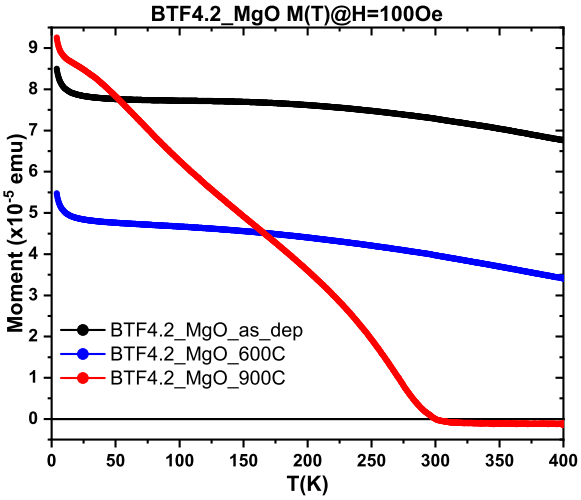

Figure 9.23: M(T) curves of the BTF4.2_MgO thin film with different thermal annealings.

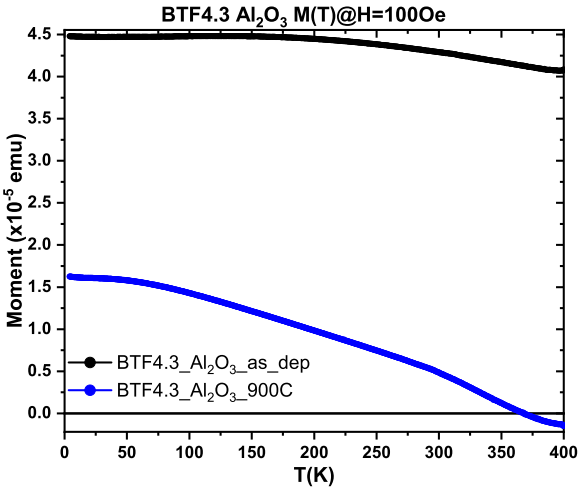

Figure 9.24: M(T) curves of the BTF4.3_Al_2O_3 thin film with different thermal annealings.

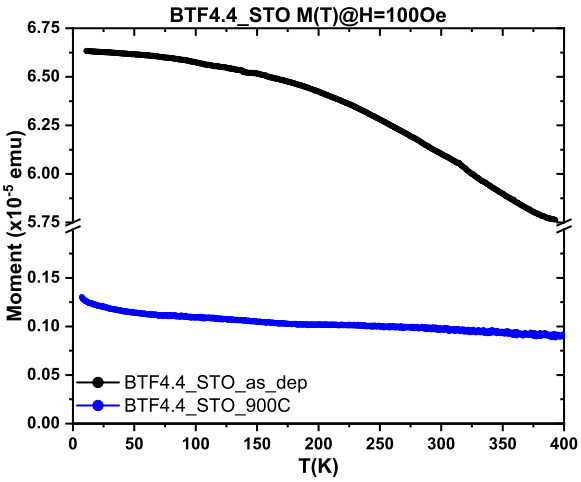

Figure 9.25: M(T) curves of the BTF4.4_STO thin film with different thermal annealings.

The BTF4.2_MgO_900C thin film, also has a magnetic T_C around 270 K, once again suspiciously close to the BTO O↔T phase transition, and where there is the clear separation

between the paramagnetic and diamagnetic behaviours, from the ordered magnetic phase[7]. Finally, the BTF4.3_Al_3O_3_900C thin film also possesses a magnetic T_C, at T≈ 375 K, close to the BTO T↔C phase transition.

To have more insightful information about the magnetic properties of the BTF4 thin films, magnetic field dependent studies were also performed at different temperatures. The M(H) curves presented in figures 9.26–9.29 have already their diamagnetic component removed, after its determination by the slope of the high temperature (usually at 400 K) M(H) curves for magnetic fields close to 70 kOe.

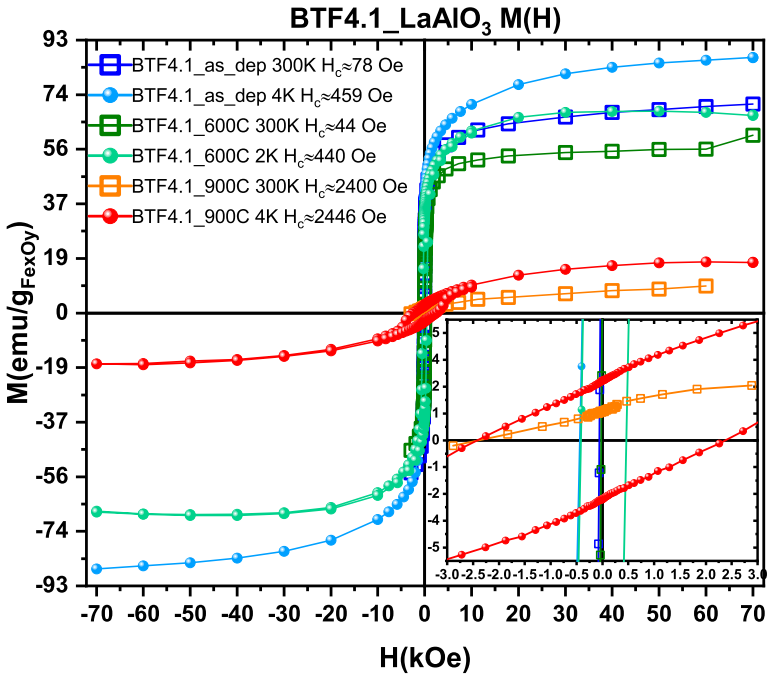

Figure 9.26: M(H) curves of BTF4.1_$LaAlO_3$ thin films after removing the substrate's diamagnetic contribution.

Based on the Raman, XRD and STEM/EDS results one can expect the Fe present in the thin films to be in an oxidized form, hence, to ease the comparison and analysis of the M(H) curves, the magnetization is presented in emu/$g_{Fe_xO_y}$. This Fe_xO_y oxide was though as a "linear combination" of the hematite, maghemite and magnetite Fe oxides with an *a priori* unknown proportion. This units normalization was done considering the expected amount of Fe on each thin film[8], and the arithmetic mean of the hematite, maghemite and

[7] the diamagnetic behaviour is actually an ubiquitous magnetic behaviour which got overshadow by the much more dominant ordered behaviour.

[8] The Fe amount was estimated considering a total thickness of 72 nm, based on the TEM/STEM micrographs, and assuming the geometry of figure 9.1

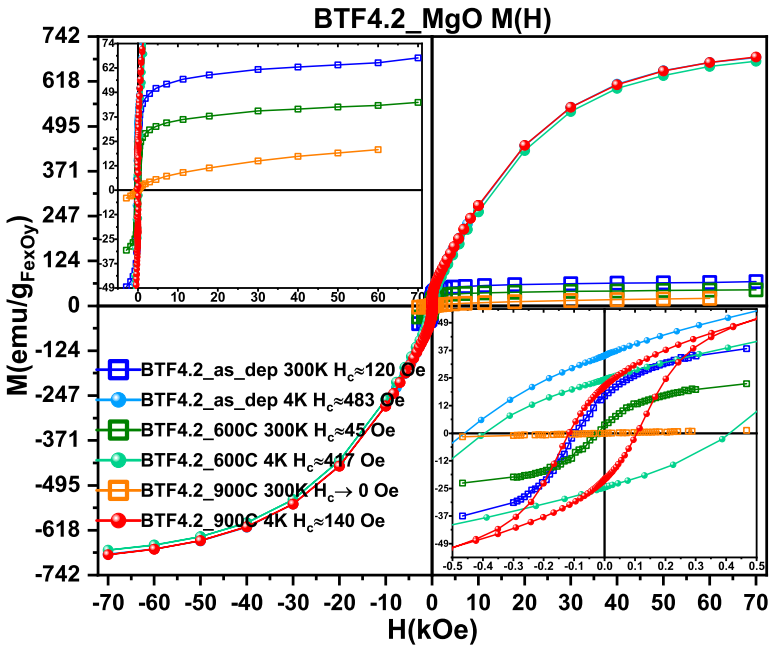

Figure 9.27: M(H) curves of BTF4.2_MgO thin films after removing the substrate's diamagnetic contribution.

magnetite densities. Since their densities are 5.271, 5.074 and 5.197 g/cm^3 respectively [300], assuming the arithmetic mean of these densities, there is always a $< 3\%$ deviation from the real magnetization value (the one that there would be if we considered the correct Fe oxide).

To ease the presentation of the M(H) curves, their coercive fields, H_c, are also presented in the legend. Each presented H_c value takes into account the coercive field of the superconductor coil, intrinsic to the magnetometer measurements and whose value is ≈ 23 Oe for measurements which reach a $|70|$ kOe magnetic field [9].

The saturation magnetizations, M_s, and the magnetic coercive fields presented in of figures 9.26–9.29 are good variables to confirm the presence of the Fe oxides suggested by the Raman and XRD results. For BTF4.1_$LaAlO_3$_as_dep its is possible to estimate $M_s \approx 68\,\mathrm{emu/g_{Fe_xO_y}}$, considering the higher temperature M(H) curve. This was done since for this sample there is still a non negligible paramagnetic contribution, originating from the substrate, which gets more evident at 4 K. Based on this value of M_s and on the Raman results, which show the coexistence of both the α and γ of Fe_2O_3, its is possible to estimate a proportion

[9] After applying magnetic fields in the order of tens of kOe, the superconducting coil will have a measurable remanence. This remanence induces a shift in the real field applied to the sample, thus for a measurement of a paramagnetic material (for example), when coming from +70 kOe the measured coercivity would be about +23 Oe, even though we know that its real value is 0. The inverse happens happens when the field comes from -7 kOe (the measured coercity would be about -23 Oe) [302]

of 91% of maghemite ($M_s = 75\,emu/g$ [300]) and 9% of hematite ($M_s = 0.5\,emu/g$ [300]). After the 600°C thermal annealing there is a decrease in the magnetization to $M_s \approx 55\,emu/g_{Fe_xO_y}$ suggesting a decrease of the maghemite phase to 73% while increasing the hematite phase to 27%. The fact that the measured coercive fields remain in the same order of magnitude before and after the mentioned thermal annealing[10] is also an evidence that the same iron oxides are present in both BTF4.1_$LaAlO_3$_as_dep and BTF4.1_$LaAlO_3$_600C. As a matter of fact, from the observation of figures 9.27–9.29, similar conclusions can be made for the lower temperature annealing of the remaining BTF4 samples, where it is possible to estimate the maghemite:hematite proportions shown in table 9.5. For the particular case of BTF4.2_MgO_as_dep the percentages of maghemite and hematite are not displayed, once there is the evidence from Raman spectroscopy that there is also a magnetite phase.

Sample	**M_s ($emu/g_{Fe_xO_y}$)**	**Maghemite (%)**	**Hematite (%)**
BTO4.1_LaAlO3_as_dep	68	91	9
BTO4.1_LaAlO3_600C	55	73	27
BTO4.2_MgO_as_dep	61	-	-
BTO4.2_MgO_600C	40	53	47
BTO4.3_Al2O3_as_dep	37	49	51
BTO4.4_STO_as_dep	34	45	55

Table 9.5: Total M_s and correspondent maghemite:hematite proportion for the BTF4 thin films ate low annealing emperatures.

Similarly to what was observed in the M(T) curves, the M(H) curves show that after the 900°C annealing the magnetic behaviour of each thin film gets completely unalike. In the BTO4.1_LaAlO3_900C there is a huge decrease of its saturation magnetization to $M_s \approx 1.6\,emu/g_{Fe_xO_y}$ and an increase of its coercive field to $H_c \approx 2.4\,kOe$, compatible with the increase of a hematite-like oxide after the annealing [306].

The BTO4.2_MgO_900C possess a huge paramagnetic component coming from the substrate which surpasses by far the contribution of the thin film. Still, for high temperatures and/or low fields it is possible to analyse the ordered components of this thin film. It was seen that in figure 9.23 there is a $T_C \approx 270\,K$ which separates the two magnetic behaviours seen in the 300 and 4 K M(H) curves of BTO4.2_MgO_900C presented in figure 9.27.

[10]The small changes in the H_c may originate from different grain sizes ans/or internal stresses of the iron oxides' grains [303–305].

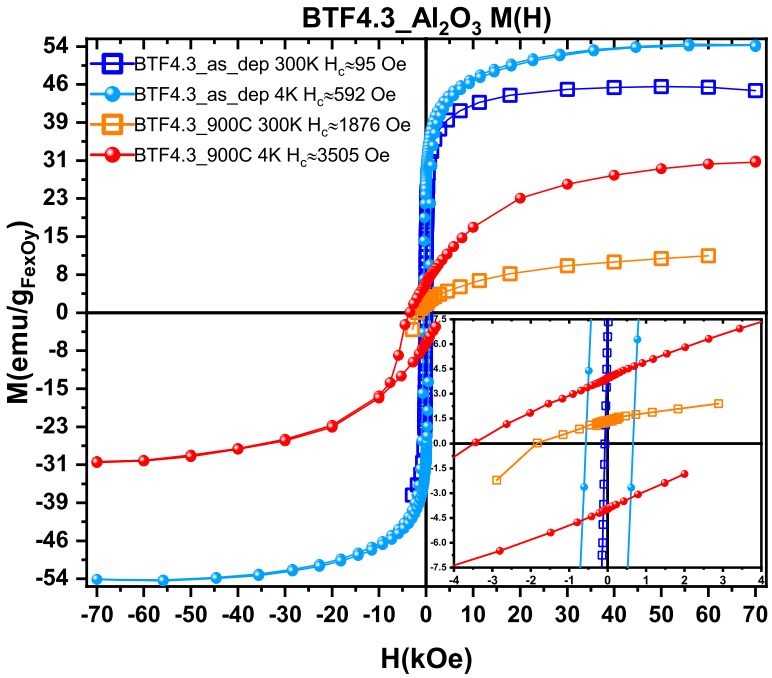

Figure 9.28: M(H) curves of BTF4.3_Al_2O_3 thin films after removing the substrate's diamagnetic contribution.

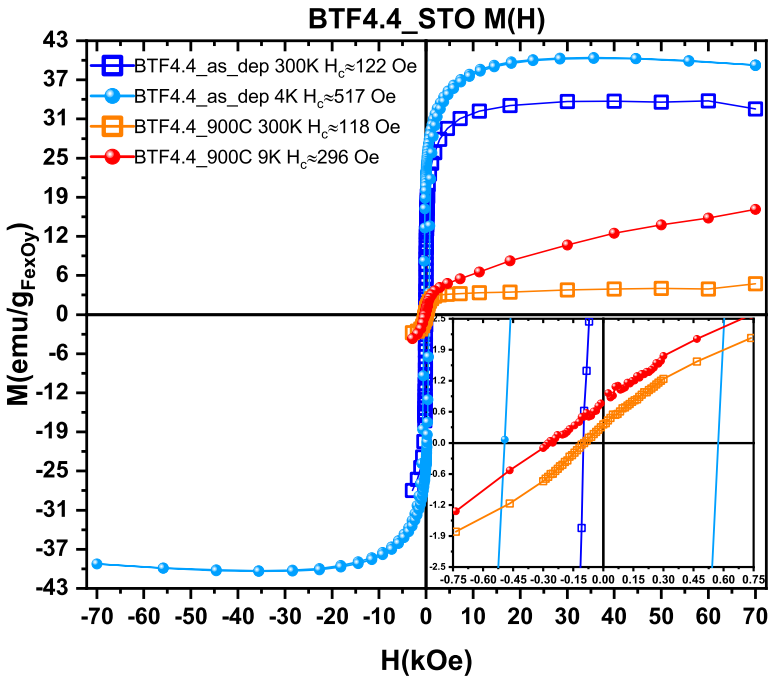

Figure 9.29: M(H) curves of BTF4.4_STO thin films after removing the substrate's diamagnetic contribution.

By extrapolation of the linear part of the substrate's paramagnetic contribution of the M(H) curve at 4 K till its intersection with the y-axis, it is possible to estimate a $M_s \approx$

$25\,\mathrm{emu/g_{Fe_xO_y}}$, agreeing with the disappearance of the magnetite phase and the decrease of the relative amount of maghemite shown in the Raman results. The 300 K curve presents an additional magnetic behaviour with $H_c \longrightarrow 0\,Oe$[11], besides the substrate's paramagnetic behaviour. This additional behaviour corresponds to the paramagnetism of the thin film itself, which at 300 K is above its Curie temperature, hence being in a paramagnetic state.

Let's discuss now the possible source of the $T_C \approx 270\,K$. The Raman results suggest the presence of hematite and maghemite , iron oxides with $T_C = 956\,K$ and $T_C > 820\,K$ respectively [300,301], hence it is quite surprising that there is a T_C at such a low temperature, and for this reason, two possible scenarios are proposed to explain this feature.

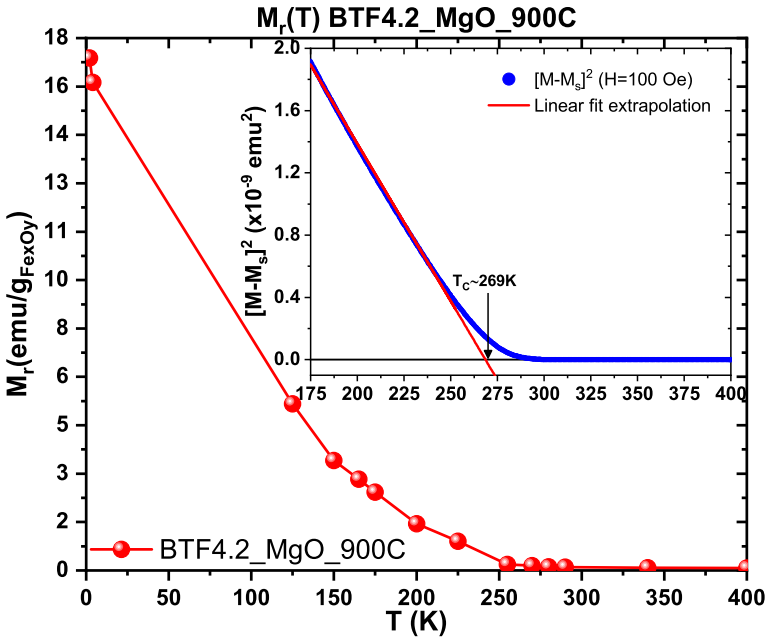

Figure 9.30: Remanent magnetization of BTF4.2_MgO_900C as a function of temperature. In the inset a $T_C = 269\,K$ is estimated using a spontaneous magnetization (Landau) model.

The first scenario is based on the growth of the $BaTiO_3$ phase, corroborated by the XRD polycrystalline peaks which appear/grow in the BTO4.2_MgO_900C case. Taking this into account, and knowing that the BTO O↔T phase transition occurs close to the magnetic $T_C \approx 270\,K$, one can suggest that there would be the segregation of BTO/maghemite interfaces, resulting in the coupling of the maghemite T_C with the BTO phase transition. To help

[11] For $H_c \approx 0\,Oe$ is hard to distinguish between the coercivity of the sample itself and the coercivity coming from the superconductor coil. Additionally, if the sample has mostly a paramagnetic behaviour, when the diamagnetic component is subtracted it will also subtract most of its high temperature paramagnetic component, thus resulting in a very flat curve whose H_c is quite hard to determine (it should be 0). Therefore, in these cases it is stated that the $H_c \longrightarrow 0$.

explain this phenomena the M_r as a function of temperature is plotted in figure 9.30 where it is perceptible that the are not any abrupt changes in remanent magnetization. Therefore, to have a magnetoelectric coupling between the maghemite T_C and the BTO phase transition, an auto-composite with successive laminar structures would be necessary in order to maximize the interface effects. Even though the STEM/EDS results of figure 9.18 show that in the BTO4.2_MgO_900C sample there is an inter-diffusion of the BTO and Fe layers, the segregation of the mentioned laminar auto-composite is *a priori* quite unlikely.

The second scenario is based on a different consequence of the inter-diffusion of the BTO and Fe layer. In this scenario it is proposed that there might be a $Fe_xBa_yTi_zO_w$ compound with the magnetization curves and T_C measured, and in fact, some titanohematites could fit this description. Figure 9.31 presents two diagrams with the T_C and M_s for the $Fe_{2-x}Ti_xO_3$ system [307], showing that for a stoichiometry close to $Fe_{1.24}Ti_{0.76}O_3$ the T_C occurs at $\approx 269\,K$. Figure 9.31 also shows that the $Fe_{1.24}Ti_{0.76}O_3$ has a $M_s \approx 99\,emu/g$, quite close to the titanohematite with the highest M_s ($101\,emu/g$) hence, we could justify simultaneously the measured T_C and $M_s \approx 25\,emu/g_{Fe_xO_y}$ assuming a mixture of 75% of α-Fe_2O_3 and 25% of $Fe_{1.24}Ti_{0.76}O_3$.

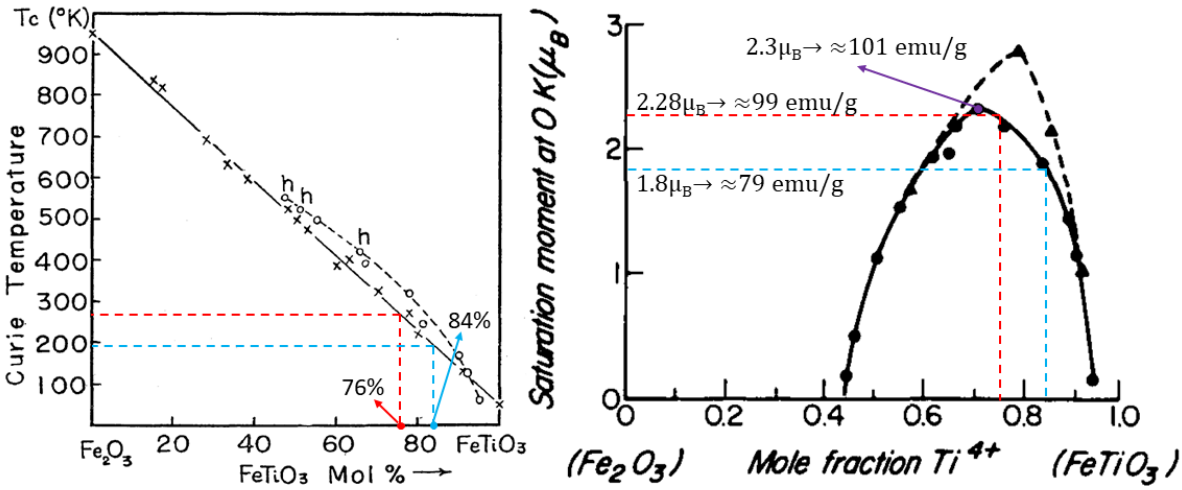

Figure 9.31: Curie temperatures and saturation magnetization for the Hematite-Ilmenite diagram. Adapted from [300] and [307]

Actually, the same approach is also valid for a mixture of 25% of $Fe_{1.24}Ti_{0.76}O_3$ and 75% of any other iron oxides with a high T_C and M_s close to the hematite's value, which is truth for most stoichiometries of titanomagnetites and titanomaghemites [308–310]. Moreover, Carmichael shows that in one of the two possible paths of the solvus curvature for the ilmenite-

hematite solid solution series the annealing at 900°C coincides with the temperature needed to get the $Fe_{1.24}Ti_{0.76}O_3$ [311].

It is important to mention that the Raman spectra of the tinanohematites and titanomagnetites are quire similar to the spectra of the hematite and magnetite combined with the spectra of the ilmenite and ulvospinel respectively [275, 276], thus for Raman spectra such as the ones presented in figures 9.3, 9.4, 9.5, 9.7 and 9.8 it might be difficult to distinguish between the different possible stoichiometries of these compound oxides (table 9.4). Still, the presence of $Fe_{1.24}Ti_{0.76}O_3$ justifies the substantial increase of the Raman mode at $\approx 700\,cm^{-1}$ which matches with the strongest mode of $FeTiO_3$ [277]. Similarly, the XRD peaks of the titanohematites and titanomagnetites occur at about the same places of their pure iron oxides (the deviations in 2θ are much lower than the width of our peaks), having simply different relative intensities [312–315], which for our case will not alter the conclusions since we do not have enough diffractions peaks to be able to compare their relative intensities.

This second scenario is the most likely one, and serves as an alert to the fact that, for 900°C, the inter-diffusion of the BTO and Fe layers may lead to the partial or total formation of other iron oxides containing Ti or Ba in its compositions. Their presence would still be compatible with the Raman and XRD previously discussed, being almost impossible to tell apart the pure iron oxides from the oxides with low concentration of Ti in their compositions (if there was more diffraction peaks and/or a better resolution of the Raman modes it would, at some point, be possible to better distinguish the different iron oxides).

The BTF4.3_Al_2O_3_900C M(H) curve of figure 9.28 presents what seems to be a superposition of the maghemite and hematite magnetic curves (information also sported by the Raman results), similar to the BTF4.1_$LaAlO_3$_900C but with a higher coercive fields. The high coercive fields could be justified by the partial presence of a Barium hexaferrite [316], $BaFe_{12}O_{19}$, whose strongest mode is just before the $700\,cm^{-1}$ maghemite Raman mode [317]. BTF4.3_Al_2O_3_900C also seems to have a new paramagnetic contribution which can arise from the diffusion of some Fe atoms way from the iron oxide nucleation sites towards a dilute scattering within the substrate (the diffusion of the thin film into the substrate was seen in the TEM/STEM micrographs of BTO4.2_MgO_900C).

BTF4.4_STO_900C, on the other hand, seems to have a similar behaviour to its "as deposited" and 600°C annealing counterparts, but now with a clearly dominant hematite

phase (or at least a hematite like phase) and a new paramagnetic component.

9.5.2 BTF6 Magnetic Results

In the BTF6 deposition both the BTO and Fe layers were deposited at $T = 658°C$, considerably higher than the deposition temperature of the BTF4 samples, thus it comes as no surprise that the M(T) curves presented in figures 9.32–9.35 have completely different characteristics from the M(T) curves of the BTF4 thin films. In fact, the BTF6.1_$LaAlO_3$, BTF6.2_Al_2O_3 and BTF6.3_MgO M(T) curves presented in figures 9.32–9.34 display a Curie-Law curve added to the substrate diamagnetism, suggesting a dominant paramagnetic behaviour for all these BTF6 thin films and respective annealings. On the other hand, the BTF6.4_STO M(T) curves presented in figure 9.35 present an additional magnetic ordered phase with a T_C around 45 K whose contribution is higher for the 750°C annealing, and disappears after the 900°C annealing.

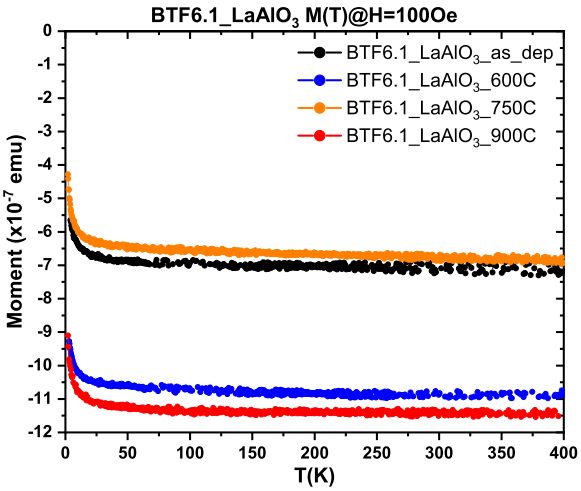

Figure 9.32: M(T) curves of the BTF6.1_$LaAlO_3$ thin film with different thermal annealings.

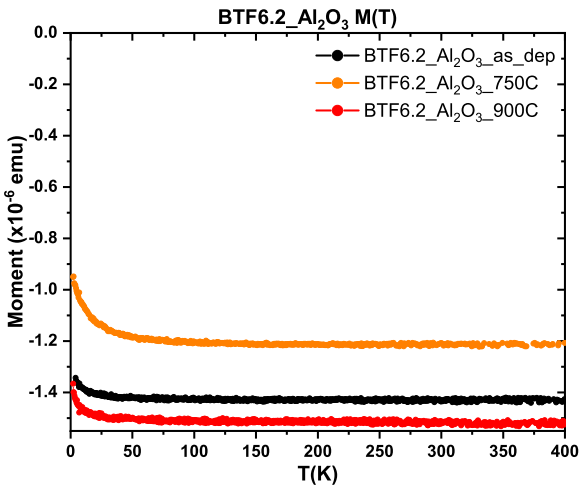

Figure 9.33: M(T) curves of the BTF6.2_Al_2O_3 thin film with different thermal annealings.

The inspection of the M(H) curves of the BTF6.1_$LaAlO_3$ thin films, presented in figure 9.36, confirms the majority contribution from a paramagnetic phase, but also present an ordered magnetic phase with saturation magnetization of 2.1, 1.7 and 0.3 emu/$g_{Fe_xO_y}$ for the "as deposited", 750°C and 900°C annealings respectively, which can be assigned to a small portion of an iron oxide. The estimation of the amount of Fe_xO_y was done using an approach analogous to the one used in the BTF4, but using a total thin film thickness of 45 nm and

using the geometry of figure 9.2.

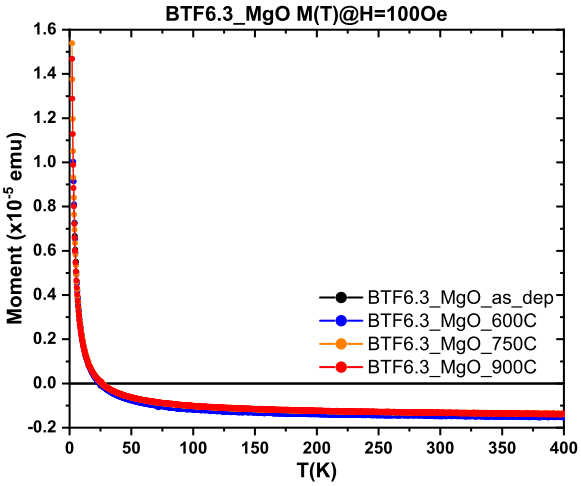

Figure 9.34: M(T) curves of the BTF6.3_MgO thin film with different thermal annealings.

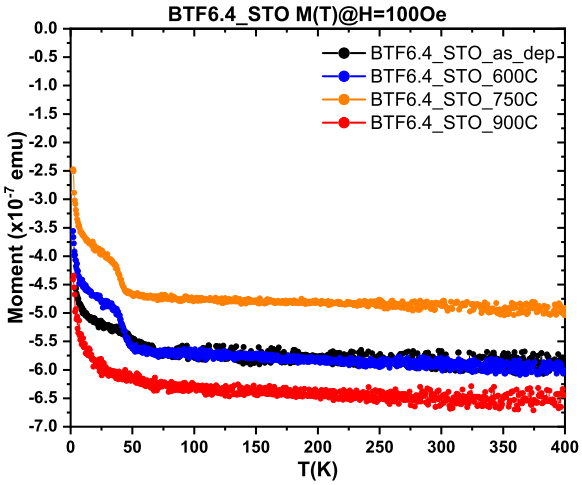

Figure 9.35: M(T) curves of the BTF6.4_STO thin film with different thermal annealings.

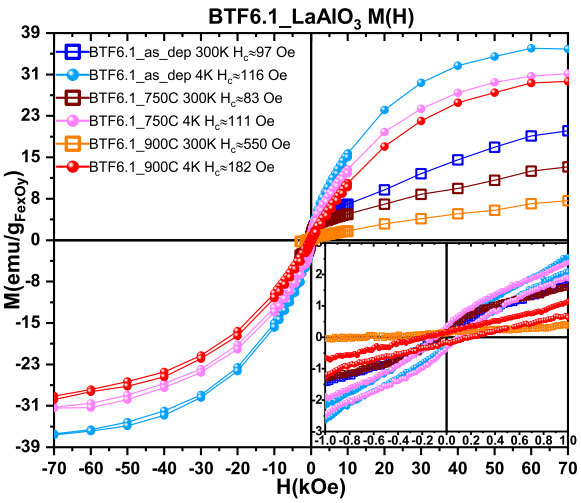

Figure 9.36: M(H) curves of BTF6.1_$LaAlO_3$ thin films after removing the substrate's diamagnetic contribution.

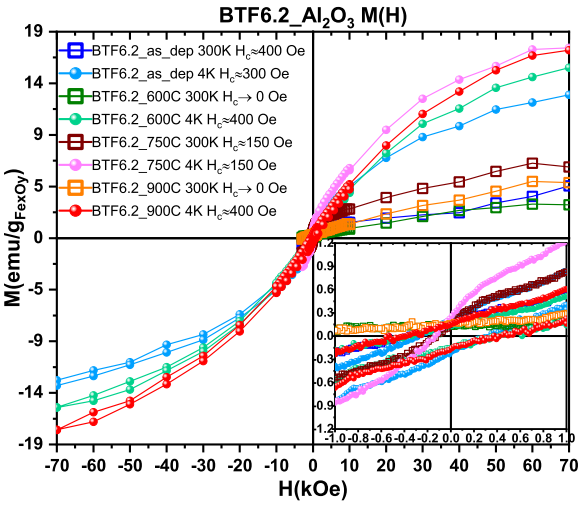

Figure 9.37: M(H) curves of BTF6.2_Al_2O_3 thin films after removing the substrate's diamagnetic contribution.

The fact that there are no Raman modes associated with any iron oxides in the Raman spectra of the BTF6 deposition also corroborates that anything that is deposited on the substrates is mostly in a paramagnetic phase. A similar phenomena occurs in the BTF6.2_Al_2O_3 (figure 9.37), where once again there is a majority contribution from a paramagnetic phase, still the minority oxide presents different coercive fields, thus, as observed in the BFT4 deposition, also in the BTF6 deposition the substrates play an crucial role on the growth of the

deposited atoms on each substrate. This feature is more evidenced in the M(T) curves of the BTF6.4_STO thin films (figure 9.35) which present a visible magnetic transition around 45 K. Nevertheless such a contribution is quite small, as it is possible to see under the inspection of the BTF6.4_STO M(H) curves (figure 9.39) whose saturation magnetization of the ordered phase lies around $M_s \approx 0.1\,\mathrm{emu}/g_{Fe_xO_y}$. Finally, in the BTF6.3_MgO thin, films the contribution from the substrate is so strong that the magnetization of these samples are basically defined by the substrate magnetic properties. It should be noted that the apparent coercivity seen at figure 9.38 is due to the superconductor coil of the SQUID magnetometer and not from the sample.

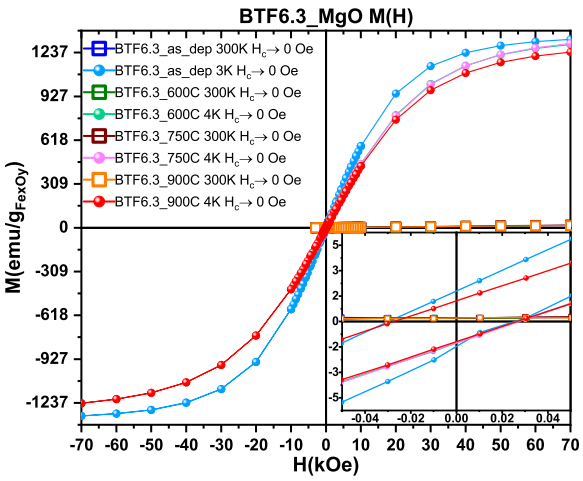

Figure 9.38: M(H) curves of BTF6.3_MgO thin films after removing the substrate's diamagnetic contribution.

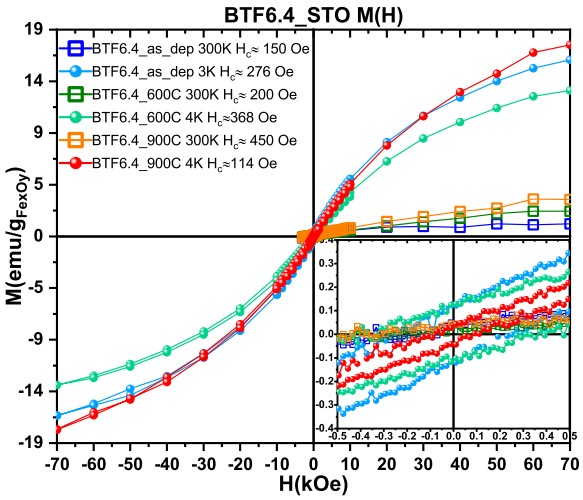

Figure 9.39: M(H) curves of BTF6.4_STO thin films after removing the substrate's diamagnetic contribution.

9.5.3 BTF5 Magnetic Results

The BTF5 deposition is like an hybrid between the BTF4 and BTF6 deposition, once its BTO layers were deposited at the BTF6 conditions whereas the Fe layer was deposited at identical conditions to the BTF4 deposition. Still while the last BTO layer is deposited, the Fe layer temperature is raised to the BTO deposition temperature (658°C) and its upper surface is exposed to the oxygen atmosphere. Therefore it is expected that even without additional thermal annealings the oxidation properties of the Fe, as well as its interface with the BTO layer, to be different from the BTF4 thin films.

The BTF5 M(T) curves presented in figures 9.40–9.43 show, once again, that the magnetic

behaviour of the thin film is specially dictated by the substrates where they are deposited on. A good example of this feature occurs for the BTF5.4_STO thin films, displayed in figure 9.43, where the ordered magnetic phase with $T_C \approx 45$ resembles the magnetic ordered phase present in the BTF6.4_STO thin films (figure 9.35) with exactly the same T_C!

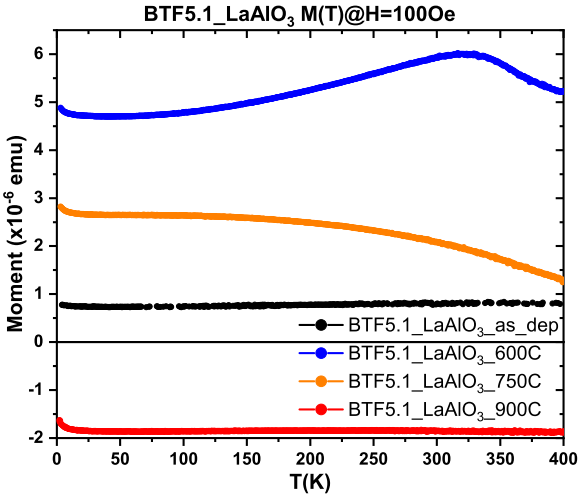

Figure 9.40: M(T) curves of the BTF5.1_$LaAlO_3$ thin film with different thermal annealings.

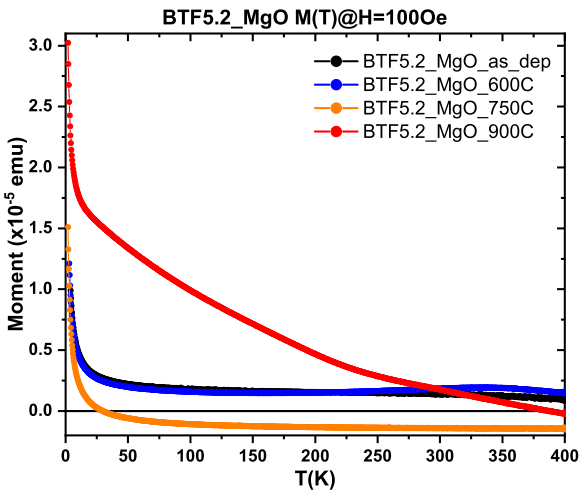

Figure 9.41: M(T) curves of the BTF5.2_MgO thin film with different thermal annealings.

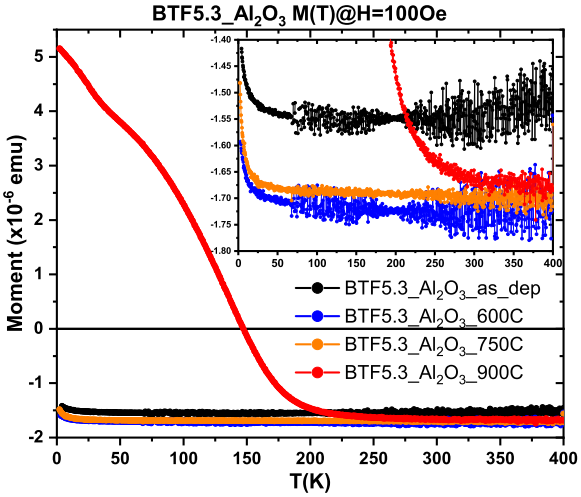

Figure 9.42: M(T) curves of the BTF5.3_Al_2O_3 thin film with different thermal annealings.

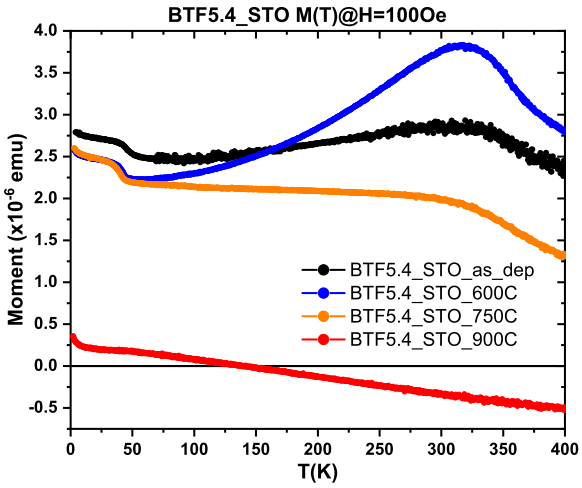

Figure 9.43: M(T) curves of the BTF5.4_STO thin film with different thermal annealings.

At first glance the most interesting M(T) curve of this set of samples belongs to the BTF5.3_Al_2O_3_900C thin film which presents a magnetic phase transition nearby the BTO R↔O phase transition, whereas for the lower annealing temperatures the M(T) curves are characteristic of a paramagnetic component superposed with the substrate diamagnetism.

Figures 9.44-9.47 present the M(H) curves for the BTF5 deposition thin films and respective annealings, displaying the magnetization in emu/$g_{Fe_xO_y}$ and using the same approach used in the BTF6 M(H) curves to estimate the amount of iron oxide.

Besides its paramagnetism, the BTF5.1_$LaAlO_3$_as_dep M(H) curves present an ordered phase with a very low saturation magnetization, $M_s = 0.9\,emu/g_{Fe_xO_y}$ as shown in table 9.6, which is quite strange taking into account that according to the Raman results, the only Raman modes present in the BTF5.1_$LaAlO_3$_as_dep spectrum are assigned to maghemite, and according to the STEM/EDS results of BTF5.2_MgO_as_dep (figure 9.13)[12], there should not be any meaningful mixture between the BTO and Fe layers. Nonetheless, after the 600°C thermal annealing there is a considerable increase of the saturation value to $M_s = 17\,emu/g_{Fe_xO_y}$.

Annealing (°C)	**BTF5.1_$LaAlO_3$ M_s (emu/$g_{Fe_xO_y}$)**	**BTF5.2_MgO M_s (emu/$g_{Fe_xO_y}$)**	**BTF5.3_Al_2O_3 M_s (emu/$g_{Fe_xO_y}$)**	**BTF5.4_STO M_s (emu/$g_{Fe_xO_y}$)**
as deposited	0.9	13	0.8	28
600	17	11	0.8	26
750	9	5	0.6	13
900	2	0.2	6	-

Table 9.6: Summary of the saturation magnetization for the BTF5 deposition thin films and respective thermal annealings.

A possible explanation to this phenomena has to do with the pseudo annealing which the Fe layer suffers when the substrate is reaching the deposition temperature of the BTO layer and during the latter's deposition. This pseudo annealing is done at 658°C, a moderately high temperature for the Fe layer, in a O_2 deficient atmosphere, thus it is likely that oxidation level of the maghemite is not the same as the "proper" maghemite, thus affecting its saturation value. The 600°C thermal annealing is done at ambient pressure, much richer in O_2 than the sputtering chamber, enabling the alteration of the maghemite oxidation to values closer to the maghemite.

However, the thermal annealings will also promote the the formation of a hematite (or hematite like) phase, thus the lowering of the saturation value for BTF5.1_$LaAlO_3$_750C and BTF5.1_$LaAlO_3$_900C samples, and as it is possible to see in the BTF5.1_$LaAlO_3$_900C Raman spectrum (figure 9.3). This lowering in the saturation magnetization, associated with

[12]Since the deposited layer have the same elements, even though the phases which grow on MgO may be different from the ones grown on the other substrates, it is assumed that the place where the Fe and BTO lie should be approximately the same for all the samples deposited and annealed at the same conditions.

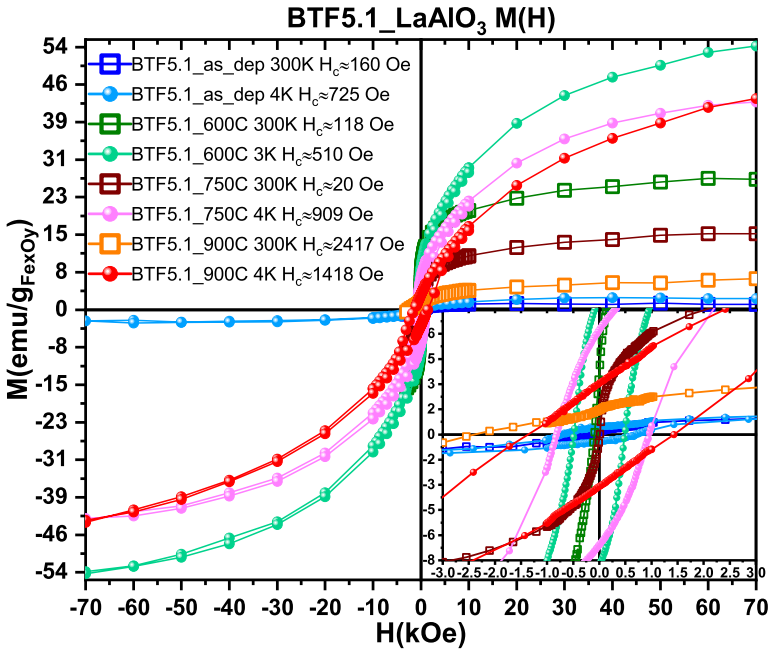

Figure 9.44: M(H) curves of BTF5.1_$LaAlO_3$ thin films after removing the substrate's diamagnetic contribution.

the formation of a hematite, or hematite like phases (with Ti in its stoichiometry), is something which is verified for the BTF5.2_MgO and BTF5.4_STO thin films as well, as it is possible to see after looking at table 9.6.

The BTF5.2_MgO M(H) curves are clearly dominated by the substrate paramagnetism, still, looking at the high temperature curves it is possible to see that there are also contributions of ordered magnetic phases, which according to the Raman results, are associated with a mixture of magnetite, maghemite and hematite. As in BTF5.1_$LaAlO_3$, these phases will give place to a higher amount of a hematite (or hematite like phase).

The BTF5.3_Al_2O_3 M(H) curves (figure 9.46) clearly present a meaningful paramagnetic contribution, as anticipated by their M(T) curves, however, it is also possible to see that besides the paramagnetism, there is also the presence of weak ferromagnetism which, based on the Raman results, may be associated with the hematite. Notwithstanding, as discussed before, the BTF5.3_Al_2O_3_900C thin film has a $T_C \approx 190\,K$, close to the BTO R↔O phase transition, accompanied with a considerable increase of its saturation magnetization. In this case, however, there is no evidence of the segregation of polycrystalline BTO, neither in the Raman results nor in the GIXRD diffractograms, therefore the formation of a titanohematite phase is a good candidate to justify this $T_C \approx 190\,K$.

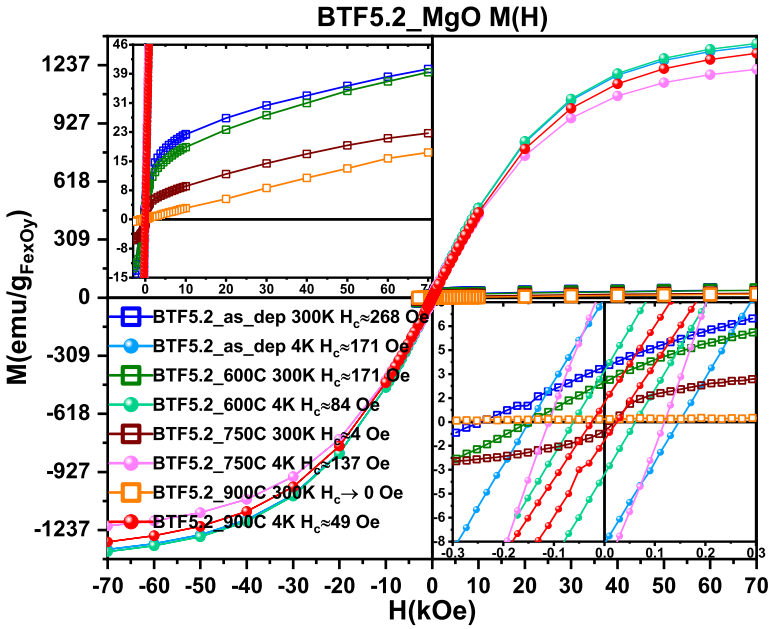

Figure 9.45: M(H) curves of BTF5.2_MgO thin films after removing the substrate's diamagnetic contribution.

As a matter of fact looking at figure 9.31 it is possible to see that the titanohematite with the formula $Fe_{1.16}Ti_{0.84}O_3$ has a $T_C \approx 190\,K$ and a $M_s = 79\,emu/g$, justifying this way the magnetic phase transition without the need of the coupling with the BTO phase transitions. One should note that the low measured $M_s = 6\,emu/g_{Fe_xO_y}$ means that just about one tenth of the estimated iron oxide is in this $Fe_{1.16}Ti_{0.84}O_3$ phase, meaning that the remaining iron oxide is either in a AFM state, or in a paramagnetic state.

Finally, figure 9.47 shows the M(H) curves of the BTF5.4_STO thin films. The M(H) curves show that besides the small contribution from the sample paramagnetism, there are two distinct H_c for the 300 K and 4 K curves, associated with the $T_C \approx 45\,K$ phase transition, a Curie temperature which does not match any of the pure iron oxides (hematite, magnetite or maghemite) nor any stoichiometries in between these iron oxides, the ulvospinel or ilmenite.

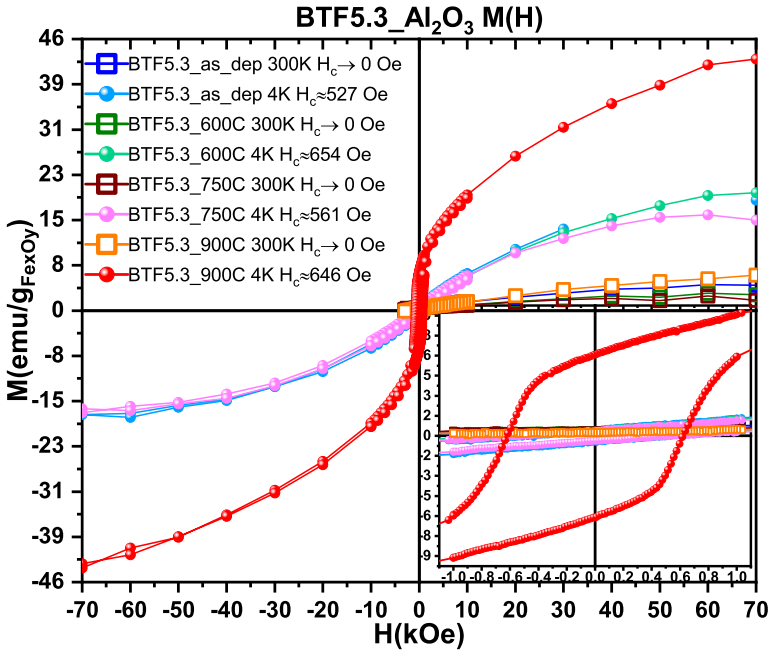

Figure 9.46: M(H) curves of BTF5.3_Al_2O_3 thin films after removing the substrate's diamagnetic contribution.

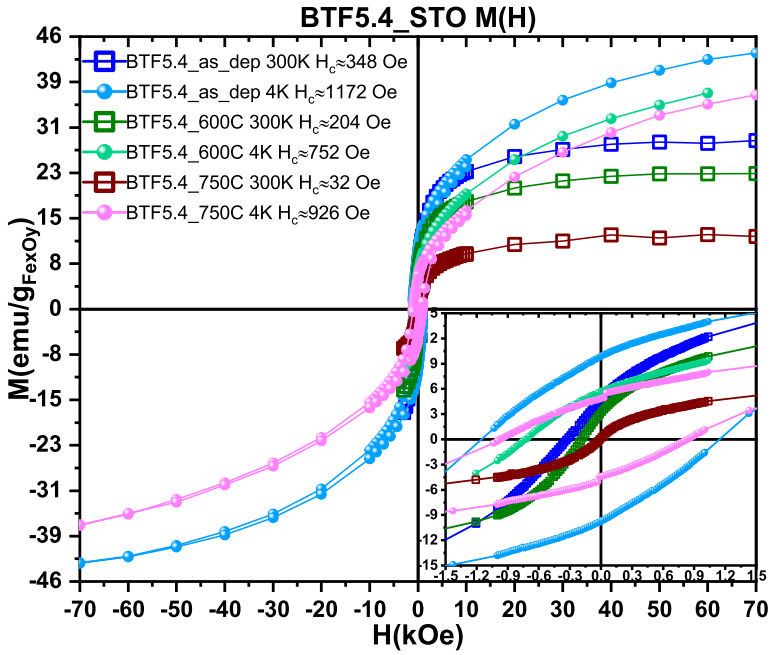

Figure 9.47: M(H) curves of BTF5.4_STO thin films after removing the substrate's diamagnetic contribution.

Chapter 10

MBE deposition of Fe on $BaTiO_3$ substrates

As seen in the previous chapter, the sputtering depositions had many concerns regarding the formation of crystalline BTO, leading to the growth of mostly amorphous Ba-Ti-O oxides. Moreover after the thermal annealing, the Fe oxides from the "as deposited" films, mix with the Ba-Ti-O oxides forming mainly Fe-Ti-O oxides, which do not present any perceptible magnetoelectric coupling with the small portion of BTO present in the thin thin films.

For these reasons a second approach was considered. To explore the effect of different BTO terminations on Fe layers, the deposition of ^{57}Fe atomic layers was done on top of BTO single crystal substrates cut in the (100), (110) and (111) planes (bought from MaTeck [240]). The deposition of the Fe thin films was performed using Molecular Beam Epitaxy at the Ion and Molecular Beam Lab of the "Instituut voor Kern en Stralingsfysica" at KU Leuven by Bas Opperdoes [318]. The Fe atoms were deposited directly on top of BTO substrates with the following geometry: BTO(substrate)/^{57}Fe(1 nm)/Fe(4 nm)/Au(5 nm) as presented in figure 10.1. The isotopically enriched ^{57}Fe ($> 99.2\%$) was used to enable future Mössbauer studies of the Fe local environment in the interface of the different BTO/Fe heterostructures, and the Au was deposited to serve as a protective capping layer.

There were two different depositions: one deposited at room temperature (RT), to make sure that the BTO substrate remains in its tetragonal phase trough all the deposition process, and the other deposition was made at 350°C in order to deposit the thin film upon a BTO substrate in its cubic phase.

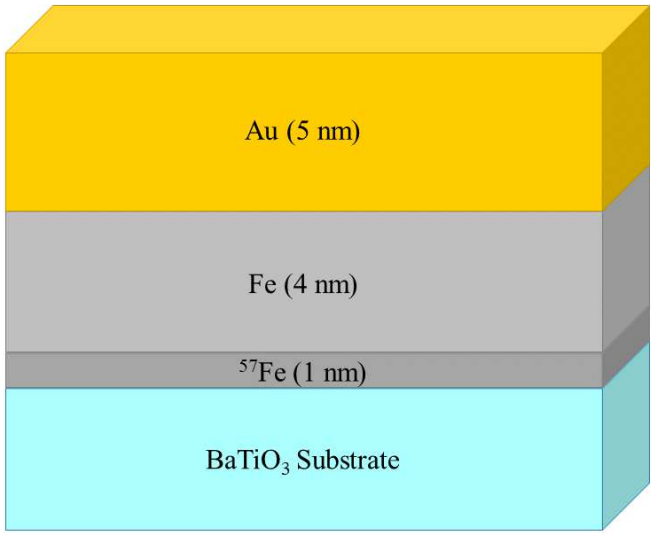

Figure 10.1: Illustration of the heterostructure deposited by MBE.

Before the film deposition, the BTO substrates were cleaned through ultrasonication, firstly in a isopropanol bath and secondly in a ethanol bath. The samples were then placed in a UHV chamber (which is located in the same high vacuum transfer line that was used to move the samples to the MBE chamber) where the substrates were baked for 12 hours at ($p \approx 10^{-9}$ mbar) to release any trace of the organic solvents and gases that were adsorbed to the substrates. The substrates of the RT deposition had a baking temperature, T_{Baking}, of 50°C whereas the substrate of the $T_{dep} = 350$°C deposition was baked at $T_{Baking} = 500$°C. The substrates were than transferred to the MBE chamber while remaining in vacuum ($p \leq 10^{-8}$ mbar). The deposition began after reaching a stable UHV pressure inside the MBE chamber and was performed using a rotating sample holder to warrant a better homogeneity of the thin film deposition. All the deposition parameters are summarized in table 10.1.

The samples names were given according to the following logic: the first part refers to the substrate used in the deposition – for example BTO(110) – and the second part o refers to the deposition temperature – for example /Fe_RT – thus resulting in a name such as BTO(100)/Fe_RT.

10.1 BTO/^{57}Fe/Fe/Au magnetic characterization

The magnetic properties of one of the $BaTiO_3$(100) substrates were measured to check if there was any additional magnetic behaviour besides the expected BTO diamagnetism.

Sample	Substrate	Substrate T_{Baking} (°C)	T_{dep} (°C)	Pdep (mbar)	Growth rate (A/s)		
					^{57}Fe	Fe	Au
BTO(100)/Fe_RT	BTO(100)	50	RT	1.9×10^{-9}	0.00755	0.108	0.26
BTO(100)/Fe_350	BTO(100)	500	350	1.9×10^{-10}			
BTO(110)/Fe_RT	BTO(110)	50	RT	1.9×10^{-9}			
BTO(111)/Fe_RT	BTO(111)						

Table 10.1: BTO/Fe thin films MBE deposition conditions

Figure 10.2 presents the field dependent measurements up to 70 kOe of a BTO(100) substrate at 350, 300 and 2 K. It is possible to see that for the lowest temperature it is perceptible the existence of a paramagnetic component. This conclusion is confirmed by the M(T) curve of this substrate, measured in a FC regime at H=1 kOe, which is shown in the bottom inset of figure 10.2 and which presents a Curie-law like curve.

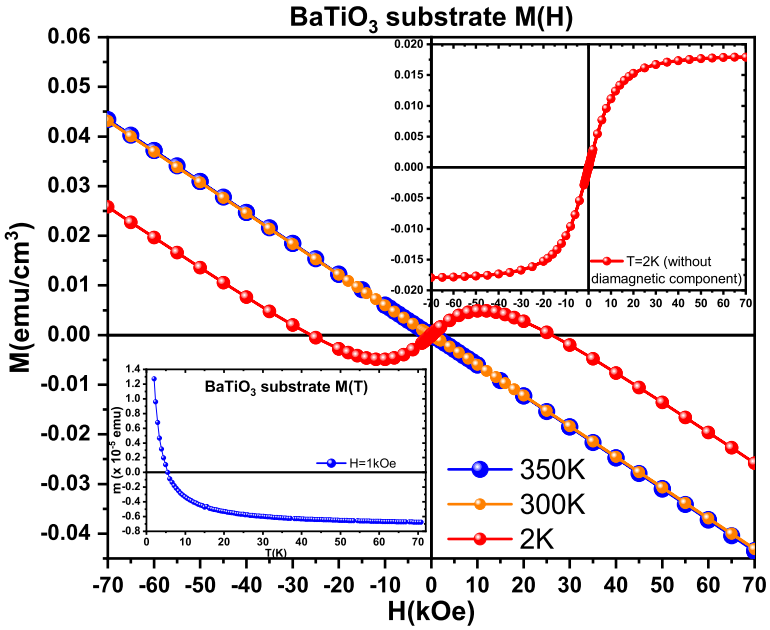

Figure 10.2: M(H) curves for the $BaTiO_3$ single crystal substrate. The top inset presents the paramagnetic contribution of the BTO substrate at 2 K after removing its diamagnetic contribution. The bottom inset presents the M(T) curve of the BTO substrate.

In order to estimate the paramagnetic contribution, the diamagnetic component was determined using the T=350 K M(H) curve. The top inset of figure 10.2 shows the resultant paramagnetic curve after removing the diamagnetism contribution. Considering the saturation magnetization of the paramagnetic component, and assuming that these paramagnetic impurities correspond to Fe ions[1] (1715 emu/cm^3), then it is possible to arrive to an amount

[1]This assumption was made to enable the estimation of the paramagnetic impurity percentage.

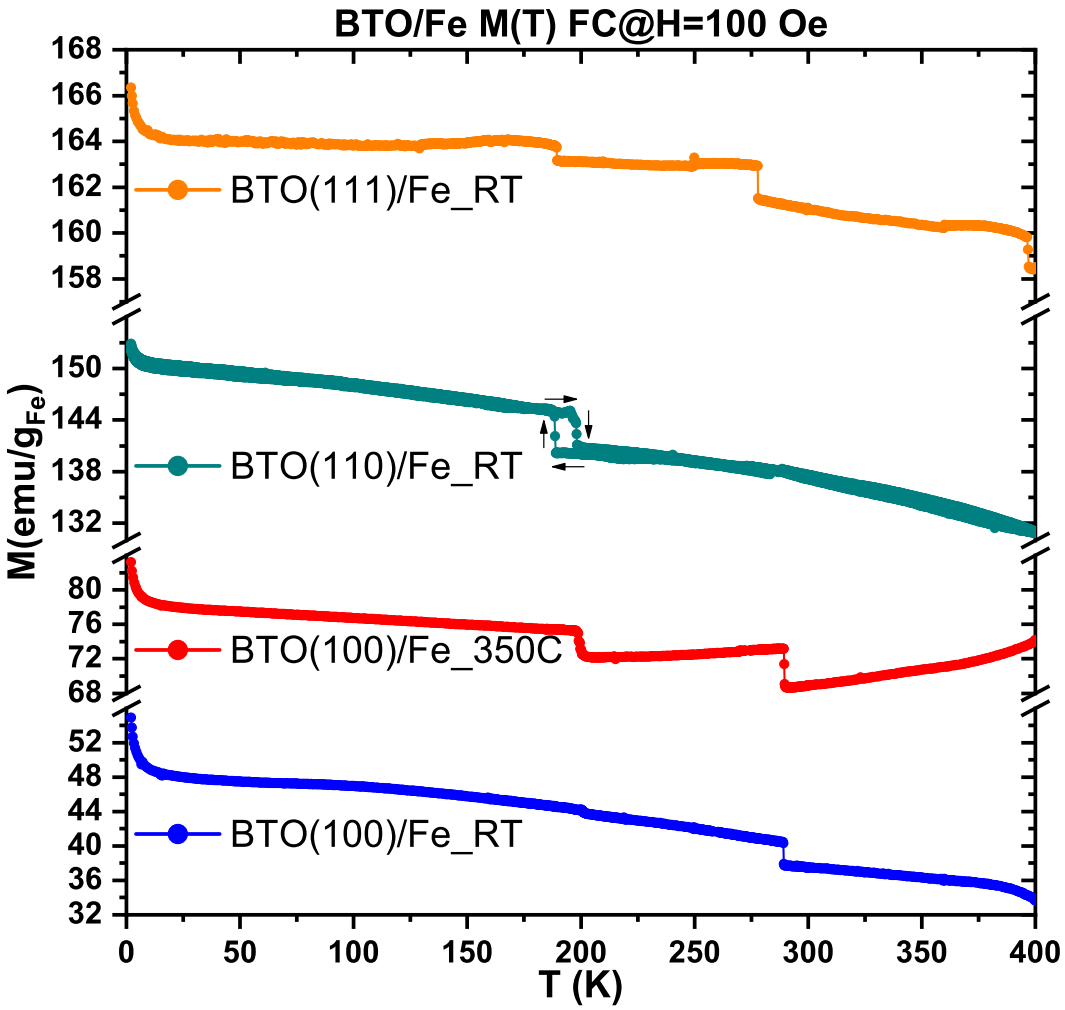

Figure 10.3: M(T) curves of the Fe thin films deposited on BTO substrates cut in the (100), (110) and (111) planes.

of paramagnetic impurities on the order of 1.2 ppm of the substrate volume.

Figure 10.3 shows the M(T) curves of all the MBE deposited samples, measured in Field Cooled at a constant field of H=100 Oe and between 2 and 400 K. Two main features are perceptible: first all the magnetization curves are sensitive to the BTO ferroelectric phase transitions, still the magnitude of this magnetoelectric effect differs among the different interface planes. Second, despite having the same amount of Fe in each sample, the absolute values of the magnetization measured at each sample are quite different, ranging from $M \approx 34-54\,emu/g_{Fe}$ for the BTO(100)/Fe_RT up to $M \approx 158-167\,emu/g_{Fe}$ for the BTO(111)/Fe_RT. Figure 10.3 also shows that each sample has a paramagnetic tail at low temperature whose source is attributed to the paramagnetic ions present in the substrate as it was discussed before.

Figures 10.4–10.7 present the M(H) curves for all the BTO/Fe thin films after removing the substrate diamagnetism. These curves are presented in emu/g_{Fe}, taking into account the total Fe mass deposited, an Fe saturation magnetization of $M_{s,Fe} = 220\,\text{emu/g}$ [299], and an Fe density of $\rho_{Fe} = 7.874\,\text{g/cm}^3$ [300]. Figures 10.4–10.7 show that for very low temperatures the saturation magnetization of each sample reaches values ranging from $M_s \approx 500\,\text{emu/g}_{Fe}$ for the BTO(110)/Fe_RT to $M_s \approx 1000\,\text{emu/g}_{Fe}$ for the BTO(100)/Fe_RT. These saturation magnetizations are well above the maximum possible value for the metallic Fe (220 emu/g), and originate from the paramagnetic impurities of the BTO substrates, which dominate the total magnetization at low temperatures. Still, since the paramagnetic component gets quite small as the temperature is increased, it is possible to estimate the saturation magnetization of each sample by observation of the M(H) curves measured at higher temperatures (for example for $H \gtrapprox 200\,\text{K}$).

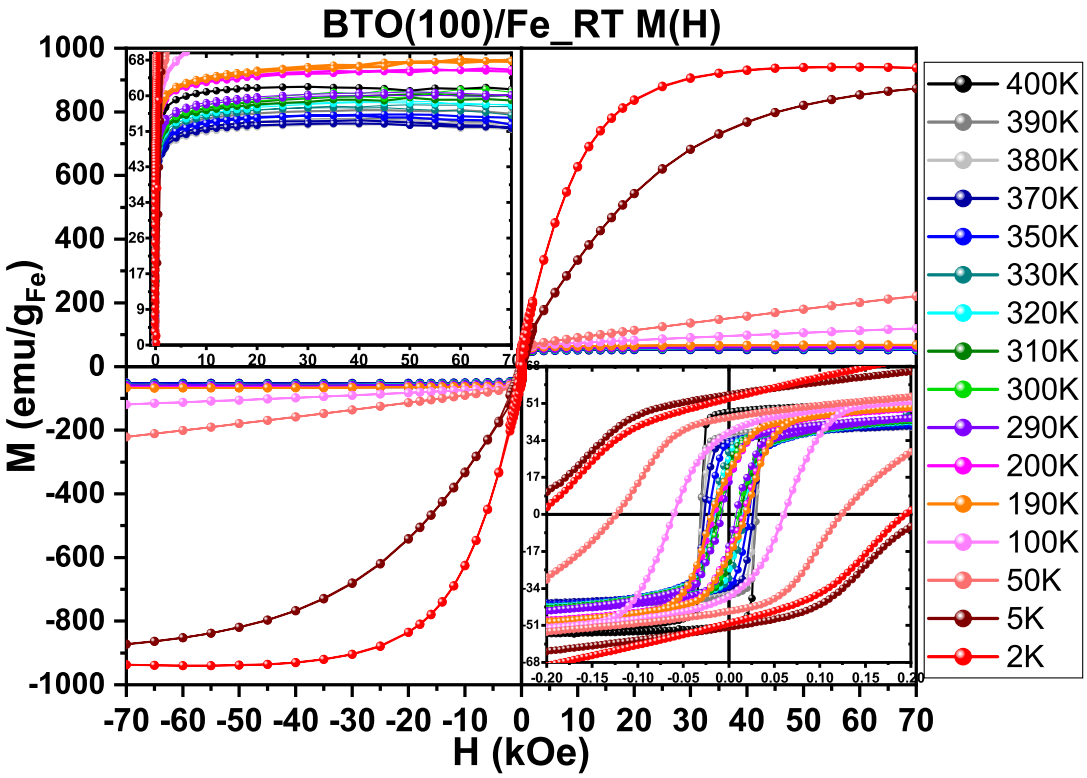

Figure 10.4: M(H) curves of the BTO(100)/Fe_RT sample, after removing the substrate diamagnetism.

Observing the top inset of figure 10.4 it is possible to estimate a saturation magnetization close to 68 emu/g_{Fe} for the BTO(100)/Fe_RT thin film, far from the 220 emu/g_{Fe} of the metallic Fe, and the lowest value among all the deposited films. The BTO(100)/Fe_350 thin

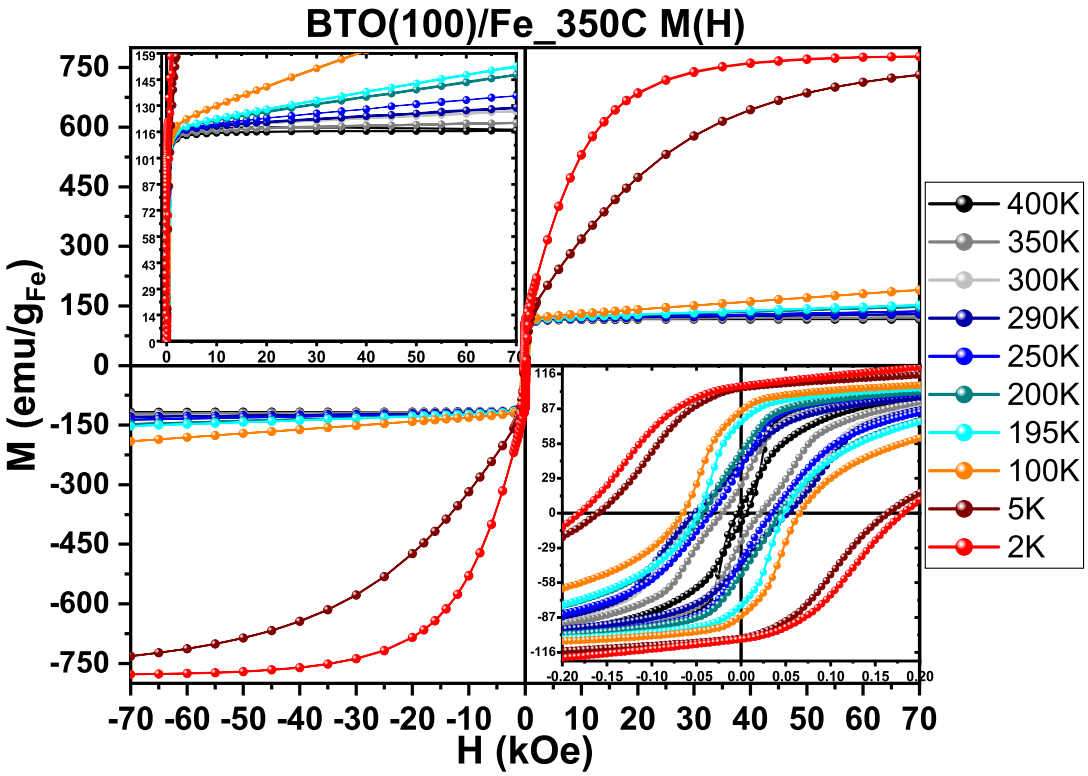

Figure 10.5: M(H) curves of the BTO(100)/Fe_350C sample, after removing the substrate diamagnetism.

film, which was also deposited on a BTO(100) substrate, possesses a saturation magnetization $M_s \approx 128\,\mathrm{emu/g_{Fe}}$ (figure 10.5), about twice the value of BTO(100)/Fe_RT's M_s.

The reason behind these low values of saturation magnetization is most like related to the formation a of non-magnetic oxide[2]. As a matter of fact there are several works which show the oxidation of the Fe atoms at the BTO/Fe interface [212–215]. Bisht *et al.* showed that this oxidation occurs due the built-in field, created by the difference in the BTO and Fe work functions, which promotes the ion migration at the BTO/Fe interface [212, 319, 320]. Moreover the amount of Fe that gets oxidized is also sensitive to the deposition conditions and/or substrate surface properties (roughness, amount of surface defects, etc) [319, 320]. Merkel *et al.* reported the oxidation of the Fe deposited on a BTO(100) substrate for the first $\approx 2.5\,\mathrm{nm}$ of the deposited Fe layer [321], which corresponds to half of the thickness of the Fe layer deposited on our substrates.

According to this interpretation, one could determine that there would be about 70%

[2]Here the term "non-magnetic" is used to refer to an iron oxide with a null or close to null net magnetization, without specifying if this magnetization originates from a PM, AFM or diamagnetic state.

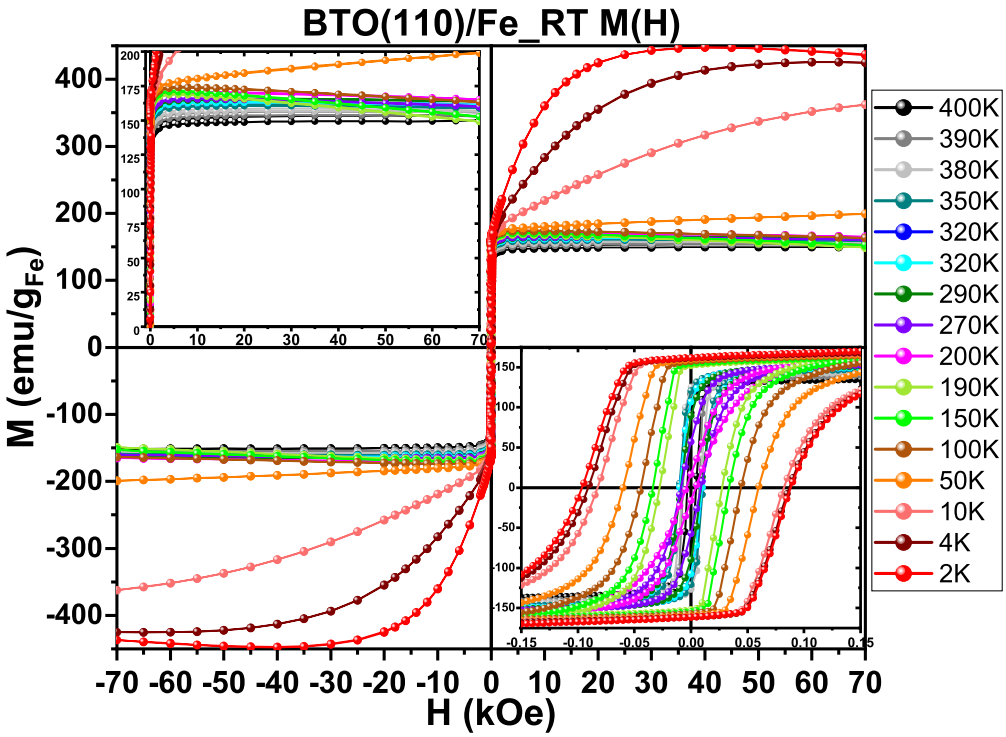

Figure 10.6: M(H) curves of the BTO(110)/Fe_RT sample, after removing the substrate diamagnetism.

(3.5 nm) and 40% (2 nm) of non-magnetic iron for the BTO(100)/Fe_RT and BTO(100)/Fe_350C films respectively. Nonetheless, there could also exist some amorphous Fe, in principle for the BTO(100)/Fe_RT case, which would also decrease the saturation, thus requiring a lesser amount of Fe oxidation to explain the lack of magnetization of BTO(100)/Fe_RT [322, 323].

Looking now at the saturation magnetization of the BTO(110)/Fe_RT and BTO(111)/Fe_RT films, shown at the top inset of figures 10.6 and 10.7, we can see that they have considerably higher values: $M_s \approx 180\,\mathrm{emu/g_{Fe}}$ and $M_s \approx 194\,\mathrm{emu/g_{Fe}}$ respectively. These results suggest that there is a lower amount of Fe oxidation and/or that the oxides that were formed possess themselves higher values of magnetization than in the BTO(100)/Fe case.

Using the interpretation of Bisht *et al.* the difference in the Fe oxide formation can be explained by the different work functions that the different cut planes possess. Additionally, the atoms present on the interface itself are different at each BTO plane, hence the chemical bonding with Fe atoms will also be distinct, conditioning the formation of specific iron oxides.

Finally the bottom inset of figures 10.4–10.7 show that the shape of the M(H) curves differs considerably for each sample. This suggests that each BTO cut plane affects the

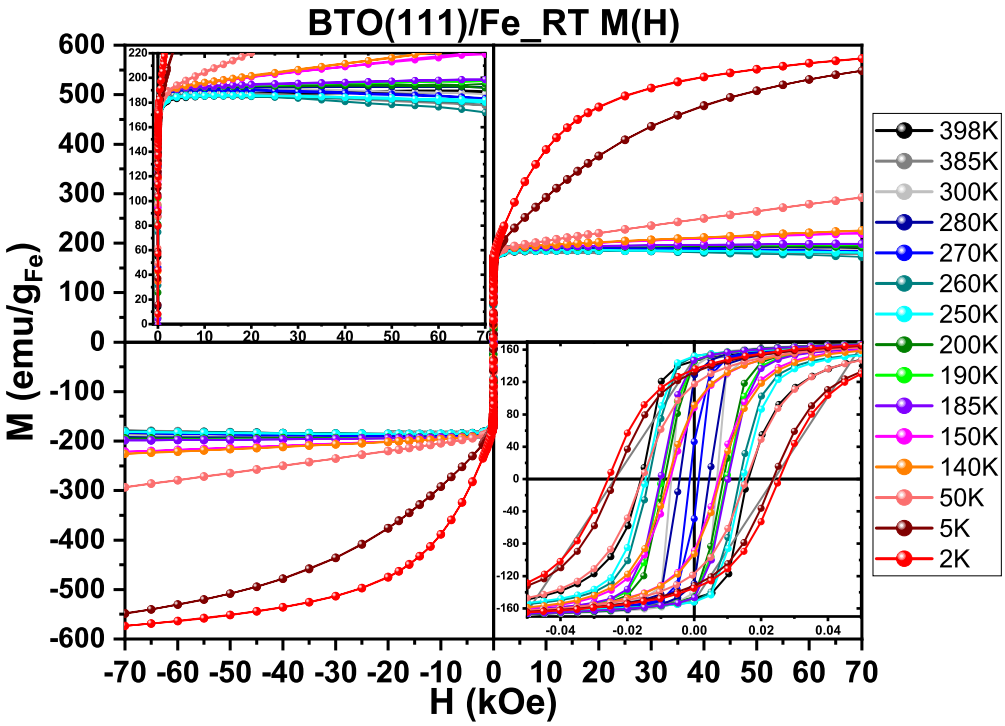

Figure 10.7: M(H) curves of the BTO(111)/Fe_RT sample, after removing the substrate diamagnetism.

magnetic anisotropy of the Fe layer in very distinct ways. In fact, the influence of the BTO ferroelectricity in the Fe anisotropy and coercivity of Fe films grown epitaxially on BTO substrates has been reported in the literature [224, 324–326], however this effect was studied almost exclusively to the BTO(100) substrate, thus additional work comparing and exploring the differences between the distinct BTO cut planes was still required.

A further analysis of its M(H) curves allows the acquisition of other relevant physical quantities such as its magnetic coercive field, H_c, and the remanent magnetization, M_r. These two quantities are plotted as a function of temperature in figures 10.8 and 10.9 in order to infer the influence of the BTO ferroelectric phase transitions on H_c, and M_r.

Figure 10.8 shows that the samples studied in this PhD present completely unalike M_r(T) curves. The BTO(100)/Fe_RT sample presents very smooth M_r(T) and H_c(T) curves (figure 10.9), without any abrupt changes. This may occur due to the considerable amount of iron oxide acting as a wall which screens the BTO influence on the metallic Fe layer. On the other hand, the remanent magnetization of BTO(100)/Fe_350C is quite sensitive to the BTO ferroelectric phase transitions, having a relative magnetization change $^{\Delta M_r}/_{M_r} = +11\%$ and $^{\Delta M_r}/_{M_r} = +31\%$ for the T–O and O–R phase transitions respectively. The remanent

magnetization of the remaining samples is also quite sensitive to the BTO phase transitions, where the BTO(111)/Fe_RT sample has changes of $^{\Delta M_r}/_{M_r} = +58\%$, $^{\Delta M_r}/_{M_r} = +3\%$ and $^{\Delta M_r}/_{M_r} = -7\%$ for the C–T, T–O and O–R ferroelectric phase transitions respectively. However it is the BTO(110)/Fe_RT which stands out with the huge variation of $^{\Delta M_r}/_{M_r} = +148\%$ for the O–R ferroelectric phase transition, demonstrating that the less studied BTO(110)/Fe and BTO(111)/Fe interfaces have in fact quite promising properties which deserve the investment of more thorough studies.

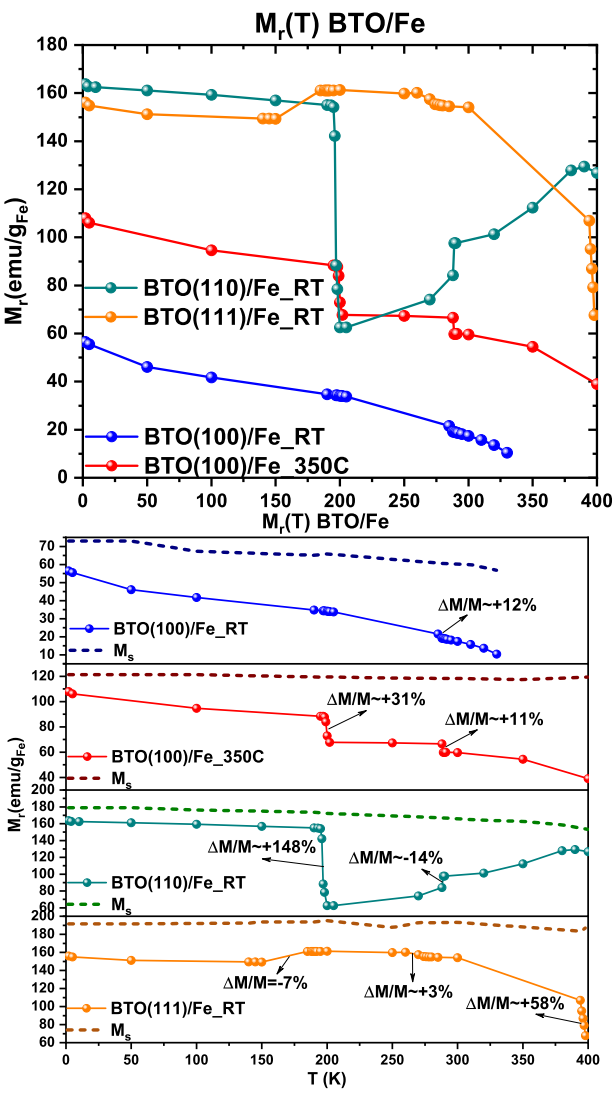

Figure 10.8: Remanent magnetization, M_r, as a function of temperature for all the deposited thin films.

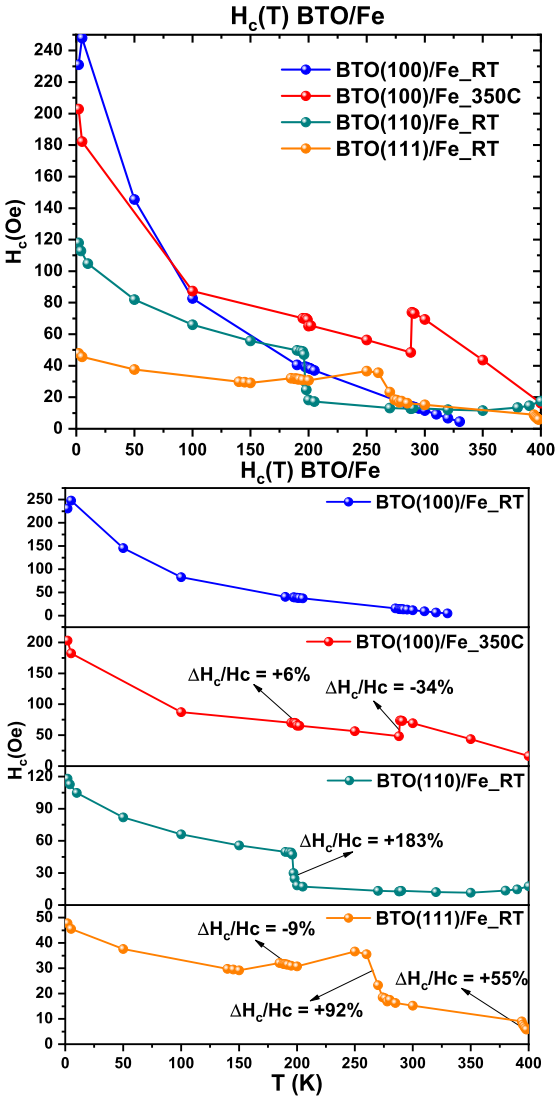

Figure 10.9: The magnetic coercive field, H_c, as a function of temperature for all the deposited thin films.

Finally, figure 10.9 shows that the H_c(T) curves for the BTO(100)/Fe_350C,

BTO(110)/Fe_ and BTO(111)/Fe_RT have a step like shape near the ferroelectric phase transition, confirming the BTO influence on the Fe coercive field [325].

Chapter 11

Conclusions

In summary we were able to relate the magnetic transitions of the nanocrystalline Fe doped (ppm-range) $BaTiO_3$ with its ferroelectric phase transitions, at temperatures confirmed by the analysis of 520cm^{-1} and 487cm^{-1} Raman vibration modes. This unexpected magnetoelectric coupling turns out to be related to heterogeneously distributed Fe rich agglomerations which are interfacial with $BaTiO_3$ grain boundaries, as demonstrated by the STEM/EDS analysis.

Motivated by the promising results of the presented auto-composite, DFT calculations were done by placing a Fe monolayer upon all the conventional ferroelectric and paraelectric phase's unit cells (rombohedral, orthorhombic, tetragonal and cubic).

In the BTO221(99)_1stFe supercells, an interface identical to the one from Duan *et al.* work was studied [205]. The study with the variable d allowed to conclude that the enhancement of the Fe magnetic moment and the induced magnetic moments of O and Ti, usually associated with the BTO polarization, depend in fact on the inter-atomic distances and electronic hybridizations, without the mandatory need of a macroscopic polarization.

Nevertheless, the noteworthy result is the unique magnetoelectric effect present in the BTO221(99)_2ndFe supercells, based on the High-Spin–Low(Null)-Spin state transition, where depending on the value of d, the crystal field and the Fe atoms hybridization with the neighbouring Ti atoms, induces a magnetic moment quench of the Fe atoms. This effect may be exploited, by choosing an adequate atomic arrangement which can be manipulated by an external electric field, acting as a switch of the Fe atomic magnetic moment.

Admitting that an interface such as the one presented in the BTO221(99)_2ndFe supercells is segregated between the $BaTiO_3$:Fe auto-composite grain boundaries, and that one

could induce the High-spin–Low-spin spin transition through a ferroelectric/structural phase transition, then it possible to justify the GME mechanism behind the magnetoelectric coupling present in the BTO:Fe_{113ppm}.

In fact, due to the possible distribution of lattice parameters, mainly in the grain boundaries, where there are several displacements and strains of the bulk unit cell, there would be some specific locations which could have the adequate conditions to replicate the interface shown in figure 6.81. For $T > T_C$ the analogous d distance would respect the first of the three possible scenarios regarding the d value, meaning that all its Fe atoms would have no magnetic moment at all. After the BTO changes to its tetragonal phase these particular atoms would switch on their moment, resulting in the abrupt change in magnetization seen in figures 5.6 and 5.9 higher temperature magnetic transition.

Moreover, the study of the iron monolayer placed upon the remaining ferroelectric $BaTiO_3$ unit cells and the $BaTiO_3$ unit cells cut through the 110 (analogous to the orthorhombic phase) and (111) (analogous to the rhombohedral phase) planes lead to the discovery of several interfaces where a ferroelectric phase transition also results in the change of an AFM state to the FM state of the Fe monolayer. This magnetic phase transitions would also justify the abrupt change in the spontaneous magnetization seen for the orthorhombic↔tetragonal phase transition of the $BaTiO_3$:Fe auto-composite.

Additionally, knowing the importance of the crystal field for the High-Spin–Low-Spin state transition, a combined study of DFT and PAC spectroscopy was performed to evaluate the EFG tensor in the different sites of the BTO unit cell, as a means of studying the crystal field in these positions. However, it was possible o see that the presence of the radioactive probe, in this case the Cd^{2+}, affects drastically the EFG of the site which it substitutes, as well as the EFG of the surrounding atoms (as far as $\approx 7\,\text{Å}$). This means that the usage of Cd^{2+} in PAC spectroscopy is not a good hyperfine technique to infer the effects of the crystal field on the EFG of BTO/Fe interfaces.

Finally, it was performed the deposition of BTO/Fe heterostructures on $LaAlO_3$, MgO, Al_2O_3 and $SrTiO_3$ substrates using RF-Sputtering, and the Molecular Beam Epitaxy (MBE) deposition of Fe layers on $BaTiO_3$ cut in the (100), (110) and (111) planes as an attempt to recreate the interfaces with the most appealing magnetoelectric effects predicted in the DFT modeling.

The thin films deposited using sputtering showed the growth of many Fe, Ba-Ti-O and Fe-Ti-O oxides depending strongly on their substrate, as well as on the deposition and annealing conditions. Despite having several visible Curie temperatures, these can be assigned mainly to different stoichiometries of the titanohematite, thus no magnetoelectric coupling was observed in these heterostructures.

On the other hand the Fe thin films deposited on $BaTiO_3$ substrates showed large magnetoelectric couplings between the $BaTiO_3$ ferroelectric phase transitions and the magnetization of the Fe layers (similarly to what happened in the $BaTiO_3$:Fe auto-composite). The magnitude of this magnetoelectric couplings is strongly correlated with the BTO interface where the Fe was deposited, showing a huge change in spontaneous magnetization and coercivity for the rhombohedral↔orthorhombic ferroelectric phase transition up to $\Delta M/M \approx 148\%$ and $\Delta H_C/H_C \approx 183\%$ respectively for the (110) case. Additionally there is a substantial difference in the magnetoelectric coupling of Fe films deposited on the same BTO plane, but at different temperatures, implying that it is possible to tailor the magnetoelectric coupling of these substrates through adjustments in the deposition conditions. These interfaces present a huge potential as non-critical high temperature magnetoelectric multiferroics.

Bibliography

[1] D.C. Mattis. *The theory of magnetism made simple: an introduction to physical concepts and to some useful mathematical methods*. World Scientific, 2006.

[2] CO Amorim, F Figueiras, JS Amaral, P Mirzadeh Vaghefi, PB Tavares, MR Correia, A Baghizadeh, E Alves, J Rocha, and VS Amaral. Peculiar Magnetoelectric Coupling in $BaTiO_3$: Fe_{113ppm} Nanoscopic Segregations. *ACS applied materials & interfaces*, 7(44):24741–24747, 2015.

[3] FG Figueiras, CO Amorim, J Amaral, J Agostinho Moreira, PB Tavares, E Alves, and VS Amaral. Magnetoelectric effect probe through ppm Fe doping in $BaTiO_3$. *Journal of Alloys and Compounds*, 661:495–500, 2016.

[4] R. Feynmam, R. Leighton, and M. Sands. The Feynman Lectures on Physics, Vol. 2, 1977.

[5] E.M. Purcell. *Electricity and Magnetism*. Number vol. 2 in Berkeley Physics Course, Vol. 2. McGraw Hill Book Company, 1985.

[6] J.M.D. Coey. *Magnetism and Magnetic Materials*. Magnetism and Magnetic Materials. Cambridge University Press, 2010.

[7] J. Stöhr and H.C. Siegmann. *Magnetism: From Fundamentals to Nanoscale Dynamics*. Springer series in solid-state sciences. Springer, 2007.

[8] A. Aharoni. *Introduction to the Theory of Ferromagnetism*. International Series of Monographs on Physics. Clarendon Press, 2000.

[9] Stephen Blundell and David Thouless. *Magnetism in condensed matter*, volume 1. Oxford University Press New York, 2001.

[10] N.A. Spaldin. *Magnetic materials: fundamentals and applications*. Cambridge University Press, 2010.

[11] K. Yosida. *Theory of Magnetism: Edition en anglais*. Solid-state sciences. Springer, 1996.

[12] D.C. Mattis. *The Theory of Magnetism I: Statics and Dynamics*. Springer Series in Solid-State Sciences. Springer Berlin Heidelberg, 2012.

[13] B.D.F.L. Claude Cohen-Tannoudji. *Quantum Mechanics Volume 1*. Hermann.

[14] Melvin A Ruderman *et al.* Indirect exchange coupling of nuclear magnetic moments by conduction electrons. *PR*, 96(1):99, 1954.

[15] Kei Yosida. Magnetic Properties of Cu-Mn Alloys. *PR.*, 106:893–898, Jun 1957.

[16] L.P. Lévy. *Magnétisme et supraconductivité*. Savoirs Actuels. EDP Sciences, 2012.

[17] O. Kahn. *Molecular magnetism*. VCH, 1993.

[18] R. Boča. *Theoretical Foundations of Molecular Magnetism*. Current Methods in Inorganic Chemistry. Elsevier Science, 1999.

[19] N. Majlis. *The Quantum Theory of Magnetism*. World Scientific, 2007.

[20] PD Hatton *et al.* Resonant soft X-ray scattering new probe of charge, spin and orbital ordering in the manganites. *JMMM*, 290:891–897, 2005.

[21] L.D. Landau and E.M. Lifshitz. *Statistical Physics*. Number vol. 5. Elsevier Science, 1996.

[22] João Cunha de Sequeira Amaral. Studies on magnetocaloric and magnetic coupling effects. *PhD Thesis*, 2009.

[23] Stefaan Cottenier. Density Functional Theory and the Family of (L) APW-methods: a step-by-step introduction. *KU Leuven, Belgium: Instituut voor Kern-en Stralingsfysica*, 2004.

[24] W. Koch and M.C. Holthausen. *A Chemist's Guide to Density Functional Theory*. Wiley, 2015.

[25] D. Sholl and J.A. Steckel. *Density Functional Theory: A Practical Introduction*. Wiley, 2011.

[26] E.K.U. Gross and R.M. Dreizler. *Density Functional Theory*. Nato Science Series B:. Springer US, 2013.

[27] Walter Kohn. Nobel Lecture: Electronic structure of matter – wave functions and density functionals. *Reviews of Modern Physics*, 71(5):1253, 1999.

[28] Pierre Hohenberg and Walter Kohn. Inhomogeneous electron gas. *Physical review*, 136(3B):B864, 1964.

[29] DJ Singh and L Nordström. Planewaves Pseudopotentials and the LAPW Method. *Springer, New York*, 2006.

[30] Walter Kohn and Lu Jeu Sham. Self-consistent equations including exchange and correlation effects. *Physical review*, 140(4A):A1133, 1965.

[31] John P Perdew, Stefan Kurth, Aleš Zupan, and Peter Blaha. Accurate density functional with correct formal properties: A step beyond the generalized gradient approximation. *Physical review letters*, 82(12):2544, 1999.

[32] John P Perdew, Kieron Burke, and Matthias Ernzerhof. Generalized gradient approximation made simple. *Physical review letters*, 77(18):3865, 1996.

[33] G. Schatz, A. Weidinger, and J.A. Gardner. *Nuclear condensed matter physics: nuclear methods and applications*. John Wiley, 1996.

[34] H.R. Verma. *Atomic and Nuclear Analytical Methods: XRF, Mössbauer, XPS, NAA and Ion-Beam Spectroscopic Techniques*. Springer, 2010.

[35] LD Landau and EM Lifshitz. *The Classical Theory of Fields*. Number vol. 2 in Course of theoretical physics. Butterworth-Heinemann, 1975.

[36] J.D. Jackson. *Classical electrodynamics*. Wiley, 1962.

[37] D.J. Griffiths. *Introduction to Electrodynamics*. Pearson Education, Limited, 2012.

[38] V.K. Wadhawan. Ferroelasticity. *Bulletin of Materials Science*, 6(4):733–753, 1984.

[39] Nicola A Spaldin, Manfred Fiebig, and Maxim Mostovoy. The toroidal moment in condensed-matter physics and its relation to the magnetoelectric effect. *Journal of Physics: Condensed Matter*, 20(43):434203, 2008.

[40] N.A. Spaldin *et al.* Multiferroics: Past, present, and future. *Phys. Today*, 63:38–43, 2010.

[41] W. Eerenstein *et al.* Multiferroic and magnetoelectric materials. *Nature*, 442(7104):759–765, 2006.

[42] Pu Yu's Laboratory. Novel multiferroic. [Online; accessed 28-March-2018].

[43] C.A.F. Vaz *et al.* Magnetoelectric coupling effects in multiferroic complex oxide composite structures. *Adv. Mat.*, 22(26-27):2900–2918, 2010.

[44] LD Landau, EM Lifshitz, and LP Pitaevskii. Electrodynamics of continuous media, volume 8 of Course of Theoretical Physics, 1984.

[45] WF Brown Jr *et al.* Upper bound on the magnetoelectric susceptibility. *PR*, 168(2):574, 1968.

[46] J Van Suchtelen. Product properties: a new application of composite materials. *Philips Res. Rep*, 27(1):28–37, 1972.

[47] Ce-Wen Nan, MI Bichurin, Shuxiang Dong, D Viehland, and G Srinivasan. Multiferroic magnetoelectric composites: historical perspective, status, and future directions. *Journal of Applied Physics*, 103(3):031101, 2008.

[48] Pierre Curie. Sur la symétrie dans les phénomènes physiques, symétrie d'un champ électrique et d'un champ magnétique. *J. Phys. Theor. Appl.*, 3(1):393–415, 1894.

[49] Wilhelm Conrad Röntgen. Ueber die durch bewegung eines im homogenen electrischen felde befindlichen dielectricums hervorgerufene electrodynamische kraft. *Annalen der Physik*, 271(10):264–270, 1888.

[50] P Debye. Bemerkung zu einigen neuen versuchen über einen magneto-elektrischen richteffekt. *Zeitschrift für Physik*, 36(4):300–301, 1926.

[51] IE Dzyaloshinskii. On the magneto-electrical effects in antiferromagnets. *Soviet Physics JETP*, 10:628–629, 1960.

[52] DN Astrov. Magnetoelectric effect in chromium oxide. *Sov. Phys. JETP*, 13(4):729–733, 1961.

[53] BI AlShin and DN Astrov. Magnetoelectric effect in titanium oxide Ti_2O_3. *Soviet Physics JETP*, 17(4):809–811, 1963.

[54] George T Rado. Observation and possible mechanisms of magnetoelectric effects in a ferromagnet. *Physical Review Letters*, 13(10):335, 1964.

[55] Edgar Ascher, Harry Rieder, Hans Schmid, and H Stössel. Some Properties of Ferromagnetoelectric Nickel-Iodine Boracite, $Ni_3B_7O_{13}I$. *Journal of Applied Physics*, 37(3):1404–1405, 1966.

[56] RP Santoro, DJ Segal, and RE Newnham. Magnetic properties of $LiCoPO_4$ and $LiNiPO_4$. *Journal of Physics and Chemistry of Solids*, 27(6-7):1192–1193, 1966.

[57] Tsuyoshi Watanabe and K Kohn. Magnetoelectric effect and low temperature transition of $PbFe_{0.5}Nb_{0.5}O_3$ single crystal. *Phase Transitions: A Multinational Journal*, 15(1):57–68, 1989.

[58] TH O'dell. An induced magneto-electric effect in yttrium iron garnet. *Philosophical Magazine*, 16(141):487–494, 1967.

[59] BB Krichevtsov, VV Pavlov, RV Pisarev, and AG Selitsky. Linear magnetoelectric effect in magnetic garnet thin films. *Ferroelectrics*, 161(1):65–71, 1994.

[60] N.W. Ashcroft and N.D. Mermin. *Solid State Physics*. HRW international editions. Holt, Rinehart and Winston, 1976.

[61] David D Awschalom and Michael E Flatté. Challenges for semiconductor spintronics. *Nature physics*, 3(3):153, 2007.

[62] RD King-Smith and David Vanderbilt. Theory of polarization of crystalline solids. *Physical Review B*, 47(3):1651, 1993.

[63] Raffaele Resta. Macroscopic polarization in crystalline dielectrics: the geometric phase approach. *Reviews of modern physics*, 66(3):899, 1994.

[64] H Ohno, D Chiba, F Matsukura, T Omiya, E Abe, T Dietl, Y Ohno, and K Ohtani. Electric-field control of ferromagnetism. *Nature*, 408(6815):944, 2000.

[65] Nicola A Hill. Why are there so few magnetic ferroelectrics? *The Journal of Physical Chemistry B*, 104(29):6694–6709, 2000.

[66] Hans Schmid. Multi-ferroic magnetoelectrics. *Ferroelectrics*, 162(1):317–338, 1994.

[67] JBNJ Wang, JB Neaton, H Zheng, V Nagarajan, SB Ogale, B Liu, D Viehland, V Vaithyanathan, DG Schlom, UV Waghmare, et al. Epitaxial $BiFeO_3$ multiferroic thin film heterostructures. *science*, 299(5613):1719–1722, 2003.

[68] T Kimura, T Goto, H Shintani, K Ishizaka, T-h Arima, and Y Tokura. Magnetic control of ferroelectric polarization. *nature*, 426(6962):55, 2003.

[69] Jungho Ryu, Shashank Priya, Alfredo Vazquez Carazo, Kenji Uchino, and Hyoun-Ee Kim. Effect of the magnetostrictive layer on magnetoelectric properties in lead zirconate titanate/terfenol-d laminate composites. *Journal of the American Ceramic Society*, 84(12):2905–2908, 2001.

[70] Jungho Ryu, Alfredo Vazquez Carazo, Kenji Uchino, and Hyoun-Ee Kim. Magnetoelectric properties in piezoelectric and magnetostrictive laminate composites. *Japanese Journal of Applied Physics*, 40(8R):4948, 2001.

[71] Manfred Fiebig, Thomas Lottermoser, Dennis Meier, and Morgan Trassin. The evolution of multiferroics. *Nature Reviews Materials*, 1(8):16046, 2016.

[72] Shuai Dong, Jun-Ming Liu, Sang-Wook Cheong, and Zhifeng Ren. Multiferroic materials and magnetoelectric physics: symmetry, entanglement, excitation, and topology. *Advances in Physics*, 64(5-6):519–626, 2015.

[73] Cheng Song, Bin Cui, Fan Li, Xiangjun Zhou, and Feng Pan. Recent progress in voltage control of magnetism: Materials, mechanisms, and performance. *Progress in Materials Science*, 87:33–82, 2017.

[74] Fumihiro Matsukura, Yoshinori Tokura, and Hideo Ohno. Control of magnetism by electric fields. *Nature nanotechnology*, 10(3):209, 2015.

[75] JT Heron, JL Bosse, Q He, Y Gao, Morgan Trassin, L Ye, JD Clarkson, C Wang, Jian Liu, S Salahuddin, et al. Deterministic switching of ferromagnetism at room temperature using an electric field. *Nature*, 516(7531):370, 2014.

[76] Aitian Chen, Yonggang Zhao, Peisen Li, Xu Zhang, Renci Peng, Haoliang Huang, Lvkuan Zou, Xiaoli Zheng, Sen Zhang, Peixian Miao, et al. Angular Dependence of Exchange Bias and Magnetization Reversal Controlled by Electric-Field-Induced Competing Anisotropies. *Advanced Materials*, 28(2):363–369, 2016.

[77] Carsten Becher, Laura Maurel, Ulrich Aschauer, Martin Lilienblum, César Magén, Dennis Meier, Eric Langenberg, Morgan Trassin, Javier Blasco, Ingo P Krug, et al. Strain-induced coupling of electrical polarization and structural defects in $SrMnO_3$ films. *Nature nanotechnology*, 10(8):661, 2015.

[78] Uwe Bauer, Lide Yao, Aik Jun Tan, Parnika Agrawal, Satoru Emori, Harry L Tuller, Sebastiaan Van Dijken, and Geoffrey SD Beach. Magneto-ionic control of interfacial magnetism. *Nature materials*, 14(2):174, 2015.

[79] Aurelien Manchon, Hyun Cheol Koo, Junsaku Nitta, SM Frolov, and RA Duine. New perspectives for rashba spin–orbit coupling. *Nature materials*, 14(9):871, 2015.

[80] Bin Cui, Cheng Song, Haijun Mao, Yinuo Yan, Fan Li, Shuang Gao, Jingjing Peng, Fei Zeng, and Feng Pan. Manipulation of electric field effect by orbital switch. *Advanced Functional Materials*, 26(5):753–759, 2016.

[81] Jia-Mian Hu, Long-Qing Chen, and Ce-Wen Nan. Multiferroic heterostructures integrating ferroelectric and magnetic materials. *Advanced Materials*, 28(1):15–39, 2016.

[82] JT Heron, DG Schlom, and R Ramesh. Electric field control of magnetism using BiFeO3-based heterostructures. *Applied Physics Reviews*, 1(2):021303, 2014.

[83] W Eerenstein, M Wiora, JL Prieto, JF Scott, and ND Mathur. Giant sharp and persistent converse magnetoelectric effects in multiferroic epitaxial heterostructures. *Nature materials*, 6(5):348, 2007.

[84] Ming Liu, Ogheneyunume Obi, Jing Lou, Yajie Chen, Zhuhua Cai, Stephen Stoute, Mary Espanol, Magnum Lew, Xiaodan Situ, Kate S Ziemer, et al. Giant electric field tuning of magnetic properties in multiferroic ferrite/ferroelectric heterostructures. *Advanced Functional Materials*, 19(11):1826–1831, 2009.

[85] Shenqiang Ren, Robert M Briber, and Manfred Wuttig. Diblock copolymer based self-assembled nanomagnetoelectric. *Applied Physics Letters*, 93(17):173507, 2008.

[86] Sen Zhang, YG Zhao, PS Li, JJ Yang, S Rizwan, JX Zhang, J Seidel, TL Qu, YJ Yang, ZL Luo, et al. Electric-field control of nonvolatile magnetization in $Co_{40}Fe_{40}B_{20}$/Pb $(Mg_{1/3}Nb_{2/3})_{0.7}Ti_{0.3}O_3$ structure at room temperature. *Physical review letters*, 108(13):137203, 2012.

[87] RO Cherifi, V Ivanovskaya, LC Phillips, A Zobelli, IC Infante, E Jacquet, V Garcia, S Fusil, PR Briddon, N Guiblin, et al. Electric-field control of magnetic order above room temperature. *Nature materials*, 13(4):345, 2014.

[88] Thomson Reuters. Web of science, 2014. [Online; accessed on 28-March-2018].

[89] European Patent Office. Espacenet patent search, 2014. [Online; accessed on 28-March-2018].

[90] Hans Schmid. Multi-ferroic magnetoelectrics. *Ferroelectrics*, 162(1):317–338, 1994.

[91] DI Khomskii. Multiferroics: Different ways to combine magnetism and ferroelectricity. *Journal of Magnetism and Magnetic Materials*, 306(1):1–8, 2006.

[92] Daniel Khomskii. Trend: Classifying multiferroics: Mechanisms and effects. *Physics*, 2:20, 2009.

[93] KF Wang, J-M Liu, and ZF Ren. Multiferroicity: the coupling between magnetic and polarization orders. *Advances in Physics*, 58(4):321–448, 2009.

[94] Claudy RayanáSerrao et al. New routes to multiferroics. *Journal of Materials Chemistry*, 17(47):4931–4938, 2007.

[95] AP Levanyuk and Daniil Grigor'evich Sannikov. Improper ferroelectrics. *Physics-Uspekhi*, 17(2):199–214, 1974.

[96] Jeroen Van Den Brink and Daniel I Khomskii. Multiferroicity due to charge ordering. *Journal of Physics: Condensed Matter*, 20(43):434217, 2008.

[97] Sang-Wook Cheong and Maxim Mostovoy. Multiferroics: a magnetic twist for ferroelectricity. *Nature materials*, 6(1):13–20, 2007.

[98] Yoshinori Tokura. Multiferroics as quantum electromagnets. *Science-New York Then Washington*, 5779:1481, 2006.

[99] T Kimura. Spiral magnets as magnetoelectrics. *Annu. Rev. Mater. Res.*, 37:387–413, 2007.

[100] Shuxiang Dong, Junyi Zhai, JF Li, D Viehland, and Shashank Priya. Multimodal system for harvesting magnetic and mechanical energy. *Applied Physics Letters*, 93(10):103511, 2008.

[101] J Lou, D Reed, M Liu, and NX Sun. Electrostatically tunable magnetoelectric inductors with large inductance tunability. *Applied Physics Letters*, 94(11):112508, 2009.

[102] Shuxiang Dong, JF Li, and D Viehland. Voltage gain effect in a ring-type magnetoelectric laminate. *Applied physics letters*, 84(21):4188–4190, 2004.

[103] Junyi Zhai, Jiefang Li, Shuxiang Dong, D Viehland, and Mirza I Bichurin. A quasi (unidirectional) Tellegen gyrator. *Journal of applied physics*, 100(12):124509, 2006.

[104] Yu K Fetisov and G Srinivasan. Ferrite/piezoelectric microwave phase shifter: studies on electric field tunability. *Electronics Letters*, 41(19):1066–1067, 2005.

[105] G Srinivasan, IV Zavislyak, and AS Tatarenko. Millimeter-wave magnetoelectric effects in bilayers of barium hexaferrite and lead zirconate titanate. *Applied physics letters*, 89(15):152508, 2006.

[106] RV Petrov, AS Tatarenko, S Pandey, G Srinivasan, JV Mantese, and R Azadegan. Miniature antenna based on magnetoelectric composites. *Electronics Letters*, 44(8):506–508, 2008.

[107] Junyi Zhai, Zengping Xing, Shuxiang Dong, Jiefang Li, and Dwight Viehland. Detection of pico-tesla magnetic fields using magneto-electric sensors at room temperature. *Applied physics letters*, 88(6):062510, 2006.

[108] Casey Israel, ND Mathur, and JF Scott. A one-cent room-temperature magnetoelectric sensor. *Nature materials*, 7(2):93, 2008.

[109] Peng Zhao, Zhenli Zhao, Dwight Hunter, Richard Suchoski, Chen Gao, Scott Mathews, Manfred Wuttig, and Ichiro Takeuchi. Fabrication and characterization of all-thin-film magnetoelectric sensors. *Applied Physics Letters*, 94(24):243507, 2009.

[110] Arne Brataas, Andrew D Kent, and Hideo Ohno. Current-induced torques in magnetic materials. *Nature materials*, 11(5):372, 2012.

[111] Wei-Gang Wang, Mingen Li, Stephen Hageman, and CL Chien. Electric-field-assisted switching in magnetic tunnel junctions. *Nature materials*, 11(1):64, 2012.

[112] C Grezes, F Ebrahimi, JG Alzate, X Cai, JA Katine, J Langer, B Ocker, P Khalili Amiri, and KL Wang. Ultra-low switching energy and scaling in electric-field-controlled nanoscale magnetic tunnel junctions with high resistance-area product. *Applied Physics Letters*, 108(1):012403, 2016.

[113] S Kanai, F Matsukura, and H Ohno. Electric-field-induced magnetization switching in CoFeB/MgO magnetic tunnel junctions with high junction resistance. *Applied Physics Letters*, 108(19):192406, 2016.

[114] Aleksandr Pavlovich Pyatakov and Anatolii Konstantinovich Zvezdin. Magnetoelectric and multiferroic media. *Physics-Uspekhi*, 55(6):557–581, 2012.

[115] Jing Ma, Jiamian Hu, Zheng Li, and Ce-Wen Nan. Recent progress in multiferroic magnetoelectric composites: from bulk to thin films. *Advanced Materials*, 23(9):1062–1087, 2011.

[116] Jason R Hattrick-Simpers, Liyang Dai, Manfred Wuttig, Ichiro Takeuchi, and Eckhard Quandt. Demonstration of magnetoelectric scanning probe microscopy. *Review of Scientific Instruments*, 78(10):106103, 2007.

[117] Tiejun Zhou, SH Leong, ZM Yuan, SB Hu, CL Ong, and B Liu. Manipulation of magnetism by electrical field in a real recording system. *Applied Physics Letters*, 96(1):012506, 2010.

[118] JF Scott. Data storage: Multiferroic memories. *Nature materials*, 6(4):256–257, 2007.

[119] Jong Yeog Son, Jung-Hoon Lee, Seungwoo Song, Young-Han Shin, and Hyun Myung Jang. Four-states multiferroic memory embodied using Mn-doped $BaTiO_3$ nanorods. *ACS nano*, 7(6):5522–5529, 2013.

[120] Martin Gajek, Manuel Bibes, Stephane Fusil, Karim Bouzehouane, Josep Fontcuberta, Agnes Barthelemy, and Albert Fert. Tunnel junctions with multiferroic barriers. *Nature materials*, 6(4):296–302, 2007.

[121] W.H. Zachariasen. *Theory of X-Ray Diffraction in Crystals*. Dover phoenix editions. Dover Publications, 2004.

[122] B.D. Cullity and S.R. Stock. *Elements of X-ray Diffraction*. Addison-Wesley series in metallurgy and materials. Prentice Hall, 2001.

[123] D.J. Dyson *et al. X-ray and electron diffraction studies in materials science*. Matsci Series. Maney for the Institute of Materials, Minerals, and Mining, 2004.

[124] E. Lifshin. *X-ray Characterization of Materials*. Wiley, 2008.

[125] A. Guinier. *X-ray Diffraction in Crystals, Imperfect Crystals, and Amorphous Bodies*. Dover Books on Physics Series. Dover, 1994.

[126] Stresstech. X-ray diffraction, 2014. [Online; accessed 22-March-2018].

[127] Yoshio Waseda, Eiichiro Matsubara, and Kozo Shinoda. *X-ray diffraction crystallography: introduction, examples and solved problems*. Springer Science & Business Media, 2011.

[128] AL Patterson. The scherrer formula for x-ray particle size determination. *PR*, 56(10):978, 1939.

[129] Emil Zolotoyabko. *Basic Concepts of Crystallography: an outcome from crystal symmetry*. Vch Verlagsgesellschaft Verlag GmbH & Company KGaA, 2011.

[130] Myeongkyu Lee. *X-ray Diffraction for Materials Research: From Fundamentals to Applications*. CRC Press, 2016.

[131] René Guinebretière. *X-ray diffraction by polycrystalline materials*. John Wiley & Sons, 2013.

[132] Krešimir Salamon, Ognjen Milat, Nikola Radić, Pavo Dubček, Marko Jerčinović, and Sigrid Bernstorff. Structure and morphology of magnetron sputtered w films studied by x-ray methods. *Journal of Physics D: Applied Physics*, 46(9):095304, 2013.

[133] R.A. Young. *The Rietveld Method*. IUCr monographs on crystallography. Oxford University Press on Demand, 1995.

[134] B. A. Hunter *et al.* A computer program for rietveld analysis of x-ray and neutron powder diffraction patterns. *ANSTO*, 1998.

[135] J R Carvajal. Introduction to the Program FULLPROF. *Laboratoire Léon Brilloin*.

[136] University of London Birkbeck College. Powder diffraction on the web, 2006. [Online; accessed 22-March-2018].

[137] Brian H Toby. R factors in rietveld analysis: How good is good enough? *Powder diffraction*, 21(1):67, 2006.

[138] J. Goldstein. *Scanning Electron Microscopy and X-ray Microanalysis*. Kluwer Academic/Plenum Publishers, 2003.

[139] S. Amelinckx, D. van Dyck, J. van Landuyt, and G. van Tendeloo. *Electron Microscopy: Principles and Fundamentals*. Wiley, 2008.

[140] A.R. Clarke and C.N. Eberhardt. *Microscopy Techniques for Materials Science*. CRC Press/Woodhead Pub., 2002.

[141] J.J. Bozzola and L.D. Russell. *Electron Microscopy: Principles and Techniques for Biologists*. Jones and Bartlett series in biology. Jones and Bartlett, 1999.

[142] Foothill College. Nanotechnology and engineering, 2010. [Online; accessed 22-March-2018].

[143] Claudionico. Electron interaction with matter, 2013. [Online; accessed 22-March-2018].

[144] Black Tubus. Schematic view of imaging and diffraction modes in tem., 2017. [Online; accessed 11-April-2018].

[145] JEOL Ltd. high-angle annular dark-field scanning transmission electron microscopy, 1996-2018. [Online; accessed 11-April-2018].

[146] Black Tubus. Schematic view of stem mode, 2017. [Online; accessed 11-April-2018].

[147] Md. Hasnat Kabir. Particle induced x-ray emission (pixe) setup and quantitative elemental analysis. *PhD Thesis*, 2007.

[148] Sven AE Johansson *et al.* Analytical application of particle induced x-ray emission. *NIM*, 137(3):473–516, 1976.

[149] W.H. Weber and R. Merlin. *Raman Scattering in Materials Science*. Springer Series in Materials Science. Springer Berlin Heidelberg, 2013.

[150] M. Cardona and G. Güntherodt. *Light scattering in solids II: basic concepts and instrumentation*. Topics in applied physics. Springer-Verlag, 1982.

[151] Moxfyre. Raman energy levels, 2009. [Online; accessed 22-March-2018].

[152] J.R. Ferraro. *Introductory Raman Spectroscopy*. Elsevier Science, 2003.

[153] J. Clarke and A.I. Braginski. *The SQUID Handbook: Fundamentals and Technology of SQUIDs and SQUID Systems*. Number vol. 1. Wiley, 2006.

[154] P. Ripka. *Magnetic sensors and magnetometers*. Artech House remote sensing library. Artech House, 2001.

[155] Tapani Ryhänen *et al.* Squid magnetometers for low-frequency applications. *Journ. of Low Temp. Phys.*, 76(5-6):287–386, 1989.

[156] A. Barone and G. Paternò. *Physics and applications of the Josephson effect*. UMI Out-of-Print Books on Demand. Wiley, 1982.

[157] S. Tumanski. *Handbook of Magnetic Measurements*. Series in Sensors. Taylor & Francis, 2011.

[158] AML Lopes. *Local probe studies on lattice distortions and electronic correlations in manganites*. PhD thesis, Tese de Doutoramento, Universidade de Aveiro, Departamento de Física, 2006.

[159] Gonçalo Nuno de Pinho Oliveira. *Local Probing Spinel and Perovskite Complex Magnetic Systems*. PhD thesis, Universidade do Porto (Portugal), 2017.

[160] K. Siegbahn. *Alpha-, Beta- and Gamma-Ray Spectroscopy*. Elsevier Science, 2012.

[161] A Abragam and RV Pound. Influence of electric and magnetic fields on angular correlations. *Physical Review*, 92(4):943, 1953.

[162] Tilman Butz. Analytic perturbation functions for static interactions in perturbed angular correlations of γ–rays. *Hyperfine Interactions*, 52(3):189–228, 1989.

[163] EL Brady and Mo Deutsch. Angular correlation of successive gamma-rays. *Physical review*, 78(5):558, 1950.

[164] T Butz, S Saibene, Th Fraenzke, and M Weber. A TDPAC camera. *Nuclear Instruments and Methods in Physics Research Section A: Accelerators, Spectrometers, Detectors and Associated Equipment*, 284(2-3):417–421, 1989.

[165] H Haas, MB Barbosa, and JG Correia. The quadrupole moments of Cd and Zn isotopes-an apology. *Hyperfine Interactions*, 237(1):115, 2016.

[166] Milton Ohring. *Materials science of thin films*. Elsevier, 2001.

[167] Donald M Mattox. *Handbook of physical vapor deposition (PVD) processing*. William Andrew, 2010.

[168] Stephen M Rossnagel, Ronald Powell, and Abraham Ulman. *PVD for Microelectronics: Sputter Desposition to Semiconductor Manufacturing*, volume 26. Elsevier, 1998.

[169] SnowTech Media. Diagram of the sputtering process, 2018. [Online; accessed 11-April-2018].

[170] AdNaNoTek. Magnetron sputtering system, 2014. [Online; accessed 11-April-2018].

[171] Lorenzo Morresi. Molecular beam epitaxy (mbe). *Silicon Based Thin Film Solar Cells*, page 81, 2013.

[172] John Orton and Tom Foxon. *Molecular Beam Epitaxy: a short history*. Oxford University Press, USA, 2015.

[173] José M. Vila-Fungueiriño, Romain Bachelet, Guillaume Saint-Girons, Michel Gendry, Marti Gich, Jaume Gazquez, Etienne Ferain, Francisco Rivadulla, Juan Rodriguez-Carvajal, Narcis Mestres, and Adrián Carretero-Genevrier. Integration of functional complex oxide nanomaterials on silicon. *Frontiers in Physics*, 3:38, 2015.

[174] A. von Hippel. Ferroelectricity, Domain Structure, and Phase Transitions of Barium Titanate. *Rev. Mod. Phys.*, 22:221–237, Jul 1950.

[175] K.M. Rabe, C.H. Ahn, and J.M. Triscone. *Physics of Ferroelectrics: A Modern Perspective*. Topics in applied physics. Springer-Verlag Berlin/Heidelberg, 2007.

[176] J.A. Gonzalo and B. Jiménez. *Ferroelectricity: The Fundamentals Collection*. Wiley, 2008.

[177] E. Lines and A.M. Glass. *Principles and Applications of Ferroelectrics and Related Materials*. International series of monographs on physics. OUP Oxford, 1977.

[178] J Akimoto *et al.* Refinement of hexagonal $BaTiO_3$. *Acta Crystallographica Section C*, 50(2):160–161, 1994.

[179] Barry A Wechsler *et al.* Defect properties and the photorefractive effect in barium titanate. *Materials for Nonlinear Optics*, page 394, 1991.

[180] R Pazik *et al.* Synthesis, structure and magnetic properties of $BaTiO_3$ nanoceramics. *CPL*, 452(1):144–147, 2008.

[181] RVK Mangalam *et al.* Multiferroic properties of nanocrystalline $BaTiO_3$. *Solid State Communications*, 149(1):1–5, 2009.

[182] Abel Eduardo Silva Fenta. Modelização e Estudo Experimental de óxidos Multiferróicos. *Master Thesis*, 2012.

[183] Zhongli Zhang, Jifan Hu, Zhijun Xu, Hongwei Qin, Li Sun, Feng Gao, Yongjia Zhang, and Minhua Jiang. *Solid State Sciences*, 13(7):1391 – 1395, 2011.

[184] LMC Pereira *et al.* Practical limits for detection of ferromagnetism using highly sensitive magnetometry techniques. *JPD*, 44(21):215001, 2011.

[185] Hongxue Liu *et al.* Intrinsic M in $BaTiO_3$ with M trans. element dopants (Co, Cr, Fe) synthesized by sol-precipitation method. *JAP*, 109:07B516, 2011.

[186] Fangting Lin *et al.* Effects of doping site and pre-sintering t on ms and M properties of Fe:$BaTiO_3$ ceramics. *Physica B*, 407(3):451–456, 2012.

[187] Fangting Lin *et al.* Influence of doping concentration on room-temperature ferromagnetism Fe-doped $BaTiO_3$ ceramics. *JMMM*, 320(5):691–694, 2008.

[188] Fangting Lin *et al.* Effect of annealing atmosphere on magnetism for Fe-doped $BaTiO_3$ ceramic. *Physica B*, 403(17):2525–2529, 2008.

[189] Zhengang Guo *et al.* Structural, magnetic and dielectric properties of Fe-doped $BaTiO_3$ solids. *MPLB*, 26(09), 2012.

[190] B Xu *et al.* Room-temperature ferromagnetism and ferroelectricity in Fe-doped $BaTiO_3$. *PRB*, 79(13):134109, 2009.

[191] PA Joy *et al.* Comparison of the ZFC magnetization behavior of some FM and fM systems. *JMMM*, 218(2):229–237, 2000.

[192] PA Joy *et al.* The relationship between FC and ZFC susceptibilities of some ordered magnetic systems. *JPCM*, 10(48):11049, 1998.

[193] Quantum Design. Oxygen contamination. Technical report, MPMS Application Note 1014-210 03/04/1997 http://www. qdusa. com/resources/pdf/mpmsappnotes/1014-210. pdf, 1997.

[194] Campus TecnolÃşgico e Nuclear. Laboratory of accelerators and x-rays diffraction, 2018. [Online; accessed 14-June-2018].

[195] Merck KGaA. Safety data sheet for barium carbonate 101714, 2018. [Online; accessed 14-June-2018].

[196] Merck KGaA. Safety data sheet for titanium(iv) oxide 100808, 2018. [Online; accessed 14-June-2018].

[197] Anton V Polotai *et al.* Preparation and size effect in pure nanocrystalline barium titanate ceramics. *Ferroelectrics*, 288(1):93–102, 2003.

[198] CA Randall *et al.* History of the First Ferroelectric Oxide, $BaTiO_3$. *Web Source*, 2004.

[199] MH Frey *et al.* The role of interfaces on grain size effect on the de properties for FE BTO ceramics. *Ferroelectrics*, 206(1):337–353, 1998.

[200] MH Frey and DA Payne. Grain-size effect on structure and phase transformations for barium titanate. *Physical Review B*, 54(5):3158, 1996.

[201] Xiangyun Deng *et al.* Phase transitions in nanocrystalline barium titanate ceramics prepared by spark plasma sintering. *JACS*, 89(3):1059–1064, 2006.

[202] PS Dobal *et al.* Phase Transitions in Ba_{1-x} Sr_x TiO_3 Ceramics. *Ferroelectrics Letters Section*, 29(3-4):1–10, 2002.

[203] E. V. Mejia-Uriarte, R. Y. Sato-Berru, M. Navarrete, O. Kolokoltsev, and J. M. Saniger. Determination of Phase Transition by Principal Component Analysis Applied to Raman Spectra of Polycristalline $BaTiO_3$ at Low and High Temperature. *J. Appl. Res. Technol.*, 10(1, SI):57–62, FEB 2012.

[204] V Buscaglia, MT Buscaglia, M Viviani, L Mitoseriu, P Nanni, V Trefiletti, P Piaggio, I Gregora, T Ostapchuk, J Pokornỳ, et al. Grain size and grain boundary-related effects on the properties of nanocrystalline barium titanate ceramics. *Journal of the European Ceramic Society*, 26(14):2889–2898, 2006.

[205] Chun-Gang Duan, S. S. Jaswal, and E. Y. Tsymbal. Predicted Magnetoelectric Effect in Fe/$BaTiO_3$ Multilayers: Ferroelectric Control of Magnetism. *Phys. Rev. Lett.*, 97(4):047201, JUL 28 2006.

[206] Sugata Ray *et al.* High temperature ferromagnetism in single crystalline dilute Fe-doped $BaTiO_3$. *PRB*, 77(10):104416, 2008.

[207] R Maier *et al.* Ferroelectricity and ferrimagnetism in iron-doped $BaTiO_3$. *APL*, 78(17):2536–2538, 2001.

[208] FM Figueiredo, VV Kharton, JC Waerenborgh, AP Viskup, EN Naumovich, and JR Frade. Influence of microstructure on the electrical properties of iron-substituted calcium titanate ceramics. *J. Am. Ceram. Soc.*, 87(12):2252–2261, DEC 2004.

[209] E. Gomes, F. M. Figueiredo, and F. M. B. Marques. Grain Boundary Fe-Doping Effects in LSGM. *Solid State Ionics*, 179(21-26):900–903, SEP 15 2008.

[210] Eduarda Gomes, Glenn C. Mather, Filipe M. Figueiredo, and Fernando M. B. Marques. Assessment of the Electronic Conductivity of Core-Shell, Fe-doped LSGM Ceramics by Impedance Spectroscopy. *Solid State Ionics*, 193(1):11–17, JUN 30 2011.

[211] RP Borges, RC da Silva, MM Cruz, and M Godinho. Influence of Structural Transitions of $BaTiO_3$ on the Magnetic Properties of Fe Nanoparticles. *J. Phys.: Conf. Ser.*, 200(7):072014, 2010.

[212] Sebastien Couet, Manisha Bisht, Maarten Trekels, Mariela Menghini, Claire Petermann, Margriet J. Van Bael, Jean-Pierre Locquet, Rudolf Rueffer, Andre Vantomme, and Kristiaan Temst. Electric Field-Induced Oxidation of Ferromagnetic/Ferroelectric Interfaces. *Adv. Funct. Mater.*, 24(1):71–76, JAN 2014.

[213] G. Radaelli, D. Petti, E. Plekhanov, I. Fina, P. Torelli, B. R. Salles, M. Cantoni, C. Rinaldi, D. Gutierrez, G. Panaccione, M. Varela, S. Picozzi, J. Fontcuberta, and R. Bertacco. Electric Control of Magnetism at the Fe/$BaTiO_3$ Interface. *Nat. Commun.*, 5:3404, MAR 2014.

[214] Laura Bocher, Alexandre Gloter, Arnaud Crassous, Vincent Garcia, Katia March, Alberto Zobelli, Sergio Valencia, Shaima Enouz-Vedrenne, Xavier Moya, Neil D. Mathur, Cyrile Deranlot, Stephane Fusil, Karim Bouzehouane, Manuel Bibes, Agnes Barthelemy, Christian Colliex, and Odile Stephan. Atomic and Electronic Structure of the $BaTiO_3$/Fe Interface in Multiferroic Tunnel Junctions. *Nano Lett.*, 12(2):376–382, FEB 2012.

[215] S. Valencia, A. Crassous, L. Bocher, V. Garcia, X. Moya, R. O. Cherifi, C. Deranlot, K. Bouzehouane, S. Fusil, A. Zobelli, A. Gloter, N. D. Mathur, A. Gaupp, R. Abrudan, F. Radu, A. Barthelemy, and M. Bibes. Interface-Induced Room-Temperature Multiferroicity in $BaTiO_3$. *Nat. Mater.*, 10(10):753–758, OCT 2011.

[216] Heechae Choi, Yubin Hwang, Eung-Kwan Lee, and Yong-Chae Chung. Interface-Dependent Magnetic Anisotropy of Fe/$BaTiO_3$: A First Principles Study. *J. Appl. Phys.*, 109(7):07D909, APR 1 2011.

[217] Pavel V. Lukashev, J. D. Burton, Sitaram S. Jaswal, and Evgeny Y. Tsymbal. Ferroelectric Control of the Magnetocrystalline Anisotropy of the Fe/$BaTiO_3$(001) Interface. *J. Phys.: Condens. Matter*, 24(22):226003, JUN 6 2012.

[218] H. L. Meyerheim, F. Klimenta, A. Ernst, K. Mohseni, S. Ostanin, M. Fechner, S. Parihar, I. V. Maznichenko, I. Mertig, and J. Kirschner. Structural secrets of multiferroic interfaces. *Phys. Rev. Lett.*, 106(8):087203, FEB 23 2011.

[219] Manish K Niranjan, Julian P Velev, Chun-Gang Duan, Sitaram S Jaswal, and Evgeny Y Tsymbal. Magnetoelectric Effect at the Fe_3O_4/$BaTiO_3$(001) Interface: A First-Principles Study. *Phys. Rev. B: Condens. Matter Mater. Phys.*, 78(10):104405, 2008.

[220] H. F. Tian, T. L. Qu, L. B. Luo, J. J. Yang, S. M. Guo, H. Y. Zhang, Y. G. Zhao, and J. Q. Li. Strain Induced Magnetoelectric Coupling Between Magnetite and $BaTiO_3$. *Appl. Phys. Lett.*, 92(6):63507, FEB 11 2008.

[221] Carlos AF Vaz, Jason Hoffman, A-B Posadas, and CH Ahn. Magnetic Anisotropy Modulation of Magnetite in Fe_3O_4/$BaTiO_3$(100) Epitaxial Structures. *Appl. Phys. Lett.*, 94(2):022504, 2009.

[222] G. Venkataiah, Y. Shirahata, I. Suzuki, M. Itoh, and T. Taniyama. Strain-Induced Reversible and Irreversible Magnetization Switching in Fe/$BaTiO_3$ Heterostructures. *J. Appl. Phys.*, 111(3):033921, FEB 1 2012.

[223] R. O. Cherifi, V. Ivanovskaya, L. C. Phillips, A. Zobelli, I. C. Infante, E. Jacquet, V. Garcia, S. Fusil, P. R. Briddon, N. Guiblin, A. Mougin, A. A. Uenal, F. Kronast, S. Valencia, B. Dkhil, A. Barthelemy, and M. Bibes. Electric-Field Control of Magnetic Order Above Room Temperature. *Nat. Mater.*, 13(4):345–351, APR 2014.

[224] Sarbeswar Sahoo, Srinivas Polisetty, Chun-Gang Duan, Sitaram S. Jaswal, Evgeny Y. Tsymbal, and Christian Binek. Ferroelectric Control of Magnetism in $BaTiO_3$/Fe Heterostructures Via Interface Strain Coupling. *Phys. Rev. B: Condens. Matter Mater. Phys.*, 76:092108, Sep 2007.

[225] Arti Gupta and Ratnamala Chatterjee. Magnetoelectric Effect in Fe-Embedded $BaTiO_3$ Single Crystal. *J. Appl. Phys.*, 109(12):124107, JUN 15 2011.

[226] Georg Kresse and Jürgen Furthmüller. Efficient iterative schemes for ab initio total-energy calculations using a plane-wave basis set. *Physical review B*, 54(16):11169, 1996.

[227] Peter E Blöchl. Projector augmented-wave method. *Physical review B*, 50(24):17953, 1994.

[228] Peter Blaha, Karlheinz Schwarz, GKH Madsen, Dieter Kvasnicka, and Joachim Luitz. wien2k. *An augmented plane wave+ local orbitals program for calculating crystal properties*, 2001.

[229] S Blügel, H Akai, R Zeller, and PH Dederichs. Hyperfine fields of 3d and 4d impurities in nickel. *Physical Review B*, 35(7):3271, 1987.

[230] Norman Neill Greenwood. *Mössbauer spectroscopy*. Springer Science & Business Media, 2012.

[231] RS Preston, SS Hanna, and J Heberle. Mössbauer effect in metallic iron. *Physical Review*, 128(5):2207, 1962.

[232] DP Johnson. Mössbauer study of the local environments of ^{57}Fe in FeO. *Solid State Communications*, 7(24):1785–1788, 1969.

[233] GH Kwei, AC Lawson, SJL Billinge, and SW Cheong. Structures of the ferroelectric phases of barium titanate. *The Journal of Physical Chemistry*, 97(10):2368–2377, 1993.

[234] Jawad Nisar and Rajeev Ahuja. Equation of state (eos) and collapse of magnetism in iron-rich meteorites at high pressure by first-principles calculations. *Physics of the Earth and Planetary Interiors*, 182(3-4):175–178, 2010.

[235] Moshe Paz Pasternak, RD Taylor, Raymond Jeanloz, Xiaoyuan Li, Jeffrey H Nguyen, and Catherine A McCammon. High pressure collapse of magnetism in $Fe_{0.94}O$: Mössbauer spectroscopy beyond 100 GPa. *Physical Review Letters*, 79(25):5046, 1997.

[236] MP Pasternak, G Kh Rozenberg, G Yu Machavariani, O Naaman, RD Taylor, and R Jeanloz. Breakdown of the Mott-Hubbard state in Fe_2O_3: A first-order insulator-metal transition with collapse of magnetism at 50 GPa. *Physical Review Letters*, 82(23):4663, 1999.

[237] O Kanert, H Schulz, and J Albers. Nuclear magnetic resonance study of the cubic-to-tetragonal phase transition in $BaTiO_3$. *Solid state communications*, 91(6):465–469, 1994.

[238] Kurt Lejaeghere, Gustav Bihlmayer, Torbjörn Björkman, Peter Blaha, Stefan Blügel, Volker Blum, Damien Caliste, Ivano E Castelli, Stewart J Clark, Andrea Dal Corso, et al. Reproducibility in density functional theory calculations of solids. *Science*, 351(6280):aad3000, 2016.

[239] JN Gonçalves, A Stroppa, JG Correia, T Butz, S Picozzi, AS Fenta, and VS Amaral. Ab initio study of the relation between electric polarization and electric field gradients in ferroelectrics. *Physical Review B*, 86(3):035145, 2012.

[240] MatWeb (Mateck GmbH). Mateck GmbH Technical Data Sheets: Barium Titanate Crystal, $BaTiO_3$, 1996-2018. [Online; accessed 2-June-2018].

[241] CERN. Isolde, 2018. [Online; accessed 14-June-2018].

[242] CERN. About cern, 2018. [Online; accessed 14-June-2018].

[243] M Dietrich, C Camard, M Deicher, F Richter, V Samokhvalov, and S Unterricker. Lattice sites of Cd in ferroelectric $BaTiO_3$. *Zeitschrift für Naturforschung A*, 57(6-7):613–616, 2002.

[244] H Haas, MB Barbosa, and JG Correia. The quadrupole moments of cd and zn isotopes-an apology. *Hyperfine Interactions*, 237(1):115, 2016.

[245] J Roth, M Uhrmacher, R de la Presa, L Ziegeler, and KP Lieb. Structural Phase Transitions in $BaTiO_3$ Studied via Perturbed Angular Correlations. *Zeitschrift für Naturforschung A*, 55(1-2):242–246, 2000.

[246] M Uhrmacher, VV Krishnamurthy, K-P Lieb, A Lopez-Garcia, and M Neubauer. Perturbed Angular Correlation Studies of Electric Field Gradients at 111Cd in the Perovskites $PbZrO_3$ and $BaTiO_3$. *Zeitschrift für Physikalische Chemie*, 206(1-2):249–264, 1998.

[247] KD Sen. Nuclear quadrupole Sternheimer shielding-antishielding function for N^{3-}, $Cl^-$and Cd^{2+} ions in crystals. *Journal of Physics C: Solid State Physics*, 18(16):3153, 1985.

[248] FD Feiock and WR Johnson. Atomic susceptibilities and shielding factors. *Physical Review*, 187(1):39, 1969.

[249] Arlette Trokiner, Pierre-Vincent Bellot, Yuri Zhdanov, and Andrey Yakubovskii. NMR determination of the Sternheimer antishielding factor of Ca^{2+}. *Solid state nuclear magnetic resonance*, 16(3):171–175, 2000.

[250] CrysTec GmbH. CrysTec GmbH Data-Sheets, 2018. [Online; accessed 14-June-2018].

[251] Kurt J. Lesker Company. Barium Titanate ($BaTiO_3$) Sputtering Targets, 1996-2018. [Online; accessed 14-June-2018].

[252] Ana Claúdia Lourenço Santana Marques. Advanced si pad detector development and srtio3 studies by emission channeling and hyperfine interaction experiments. 2009.

[253] M El Marssi, F Le Marrec, IA Lukyanchuk, and MG Karkut. Ferroelectric transition in an epitaxial barium titanate thin film: Raman spectroscopy and x-ray diffraction study. *Journal of applied physics*, 94(5):3307–3312, 2003.

[254] Keigo Suzuki and Kazunori Kijima. Optical band gap of barium titanate nanoparticles prepared by rf-plasma chemical vapor deposition. *Japanese journal of applied physics*, 44(4R):2081, 2005.

[255] B Gilbert, Cathrine Frandsen, ER Maxey, and DM Sherman. Band-gap measurements of bulk and nanoscale hematite by soft x-ray spectroscopy. *Physical Review B*, 79(3):035108, 2009.

[256] Anjali Jain Deotale and RV Nandedkar. Correlation between particle size, strain and band gap of iron oxide nanoparticles. *Materials Today: Proceedings*, 3(6):2069–2076, 2016.

[257] Marta I Litter and Miguel A Blesa. Photodissolution of iron oxides. IV. A comparative study on the photodissolution of hematite, magnetite, and maghemite in EDTA media. *Canadian Journal of Chemistry*, 70(9):2502–2510, 1992.

[258] Maike Lübbe, Alexander M Gigler, Robert W Stark, and Wolfgang Moritz. Identification of iron oxide phases in thin films grown on Al_2O_3 (0 0 0 1) by Raman spectroscopy and X-ray diffraction. *Surface Science*, 604(7-8):679–685, 2010.

[259] DLA De Faria, S Venâncio Silva, and MT De Oliveira. Raman microspectroscopy of some iron oxides and oxyhydroxides. *Journal of Raman spectroscopy*, 28(11):873–878, 1997.

[260] Sei J Oh, DC Cook, and HE Townsend. Characterization of iron oxides commonly formed as corrosion products on steel. *Hyperfine interactions*, 112(1-4):59–66, 1998.

[261] Irina Chamritski and Gary Burns. Infrared-and raman-active phonons of magnetite, maghemite, and hematite: a computer simulation and spectroscopic study. *The Journal of Physical Chemistry B*, 109(11):4965–4968, 2005.

[262] Prabir K Dutta, PK Gallagher, and Jen Twu. Raman spectroscopic study of the formation of barium titanate from an oxalate precursor. *Chemistry of materials*, 5(12):1739–1743, 1993.

[263] CH Perry and DB Hall. Temperature Dependence of the Raman Spectrum of $BaTiO_3$. *Physical Review Letters*, 15(17):700, 1965.

[264] Jafar Javadpour and Nicholas G Eror. Raman Spectroscopy of Higher Titanate Phases in the $BaTiO_3$-TiO_2 System. *Journal of the American Ceramic Society*, 71(4):206–213, 1988.

[265] Liliana Preda, Laurent Courselle, Bernard Despax, J Bandet, and Adelina Ianculescu. Structural characteristics of RF-sputtered $BaTiO_3$ thin films. *Thin Solid Films*, 389(1-2):43–50, 2001.

[266] M Rössel, H-R Höche, HS Leipner, D Völtzke, H-P Abicht, O Hollricher, J Müller, and S Gablenz. Raman microscopic investigations of $BaTiO_3$ precursors with core–shell structure. *Analytical and bioanalytical chemistry*, 380(1):157–162, 2004.

[267] Lawrence H Robins, Debra L Kaiser, Lawrence D Rotter, Peter K Schenck, Gregory T Stauf, and Daniel Rytz. Investigation of the structure of barium titanate thin films by raman spectroscopy. *Journal of applied physics*, 76(11):7487–7498, 1994.

[268] D Bersani, PP Lottici, and A Montenero. Micro-raman investigation of iron oxide films and powders produced by sol–gel syntheses. *Journal of Raman spectroscopy*, 30(5):355–360, 1999.

[269] KF McCarty. Inelastic light scattering in α-Fe_2O_3: Phonon vs magnon scattering. *Solid State Communications*, 68(8):799–802, 1988.

[270] TP Martin, R Merlin, DR Huffman, and M Cardona. Resonant two magnon Raman scattering in α-Fe_2O_3. *Solid State Communications*, 22(9):565–567, 1977.

[271] MJ Massey, U Baier, R Merlin, and WH Weber. Effects of pressure and isotopic substitution on the Raman spectrum of α-Fe_2O_3: identification of two-magnon scattering. *Physical Review B*, 41(11):7822, 1990.

[272] Olga N Shebanova and Peter Lazor. Raman spectroscopic study of magnetite ($FeFe_2O_4$): a new assignment for the vibrational spectrum. *Journal of Solid State Chemistry*, 174(2):424–430, 2003.

[273] Zeljka Cvejic, Srdjan Rakic, Aleksandar Kremenovic, Bratislav Antic, Cedomir Jovalekic, and Philippe Colomban. Nanosize ferrites obtained by ball milling: Crystal structure, cation distribution, size-strain analysis and raman investigations. *Solid State Sciences*, 8(8):908–915, 2006.

[274] Olga N Shebanova and Peter Lazor. Raman spectroscopic study of magnetite ($FeFe_2O_4$): a new assignment for the vibrational spectrum. *Journal of Solid State Chemistry*, 174(2):424–430, 2003.

[275] Alian Wang, Karla Kuebler, Bradley Jolliff, and Larry A Haskin. Mineralogy of a martian meteorite as determined by raman spectroscopy. *Journal of Raman Spectroscopy*, 35(6):504–514, 2004.

[276] Michael Bauer, Polina Davydovskaya, Marek Janko, Melanie Kaliwoda, Nikolai Petersen, Stuart Gilder, and Robert W Stark. Raman spectroscopy of laser-induced oxidation of titanomagnetites. *Journal of Raman Spectroscopy*, 42(6):1413–1418, 2011.

[277] Xiang Wu, Shan Qin, and Leonid Dubrovinsky. Structural characterization of the $FeTiO_3$–$MnTiO_3$ solid solution. *Journal of Solid State Chemistry*, 183(10):2483–2489, 2010.

[278] Frank J Owens and Joseph Orosz. Effect of nanosizing on lattice and magnon modes of hematite. *Solid state communications*, 138(2):95–98, 2006.

[279] JC Olson, DF Stevison, and I Bransky. The effect of temperature on properties of rf sputtered $BaTiO_3$ films. *Ferroelectrics*, 37(1):685–686, 1981.

[280] QX Jia, JL Smith, LH Chang, and WA Anderson. Characteristics of $BaTiO_3$ thin films on Si deposited by rf magnetron sputtering. *Philosophical Magazine B*, 77(1):163–175, 1998.

[281] JK Park and WW Grannemann. Thin ferroelectric films of $BaTiO_3$ on doped silicon. *Ferroelectrics*, 10(1):217–220, 1976.

[282] Guido Ketteler, Werner Weiss, Wolfgang Ranke, and Robert Schlögl. Bulk and surface phases of iron oxides in an oxygen and water atmosphere at low pressure. *Physical Chemistry Chemical Physics*, 3(6):1114–1122, 2001.

[283] K Van Benthem, C Elsässer, and RH French. Bulk electronic structure of $SrTiO_3$: experiment and theory. *Journal of applied physics*, 90(12):6156–6164, 2001.

[284] Laboratório Central de Análises. Difração de raios-x, 2015. [Online; accessed 14-June-2018].

[285] Jin Wook Jang, Su Jin Chung, Woon Jo Cho, Taek Sang Hahn, and Sang Sam Choi. Thickness dependence of room temperature permittivity of polycrystalline $BaTiO_3$ thin films by radio-frequency magnetron sputtering. *Journal of applied physics*, 81(9):6322–6327, 1997.

[286] EK Evangelou, N Konofaos, and CB Thomas. Properties of barium titanate ($BaTiO_3$) thin films grown on silicon by rf magnetron sputtering. *Philosophical Magazine B*, 80(3):395–407, 2000.

[287] QX Su, TA Rabson, M Robert, JXZ Xiong, and SC Moss. Growth of (211) $BaTiO_3$ thin films on Pt-coated Si (100) substrates by radio frequency magnetron sputtering. *Thin solid films*, 305(1-2):227–231, 1997.

[288] RM Hexter and M-G_ Albrecht. Metal surface raman spectroscopy: theory. *Spectrochimica Acta Part A: Molecular Spectroscopy*, 35(3):233–251, 1979.

[289] Bin Ren, Guo-Kun Liu, Xiao-Bing Lian, Zhi-Lin Yang, and Zhong-Qun Tian. Raman spectroscopy on transition metals. *Analytical and bioanalytical chemistry*, 388(1):29–45, 2007.

[290] Yu S Ponosov and SV Streltsov. Measurements of raman scattering by electrons in metals: The effects of electron-phonon coupling. *Physical Review B*, 86(4):045138, 2012.

[291] Inc. Sigma-Aldrich. Magnesium oxide (single crystal substrate), 2018. [Online; accessed 14-June-2018].

[292] Shalendra Kumar, Ravi Kumar, BH Koo, H Choi, Dong Uk Kim, and Chan Gyu Lee. Structural and electrical properties of Mg_2TiO_4. *Journal of the Ceramic Society of Japan*, 117(1365):689–692, 2009.

[293] Zhongwu Wang, P Lazor, SK Saxena, and Hugh St C O'Neill. High pressure Raman spectroscopy of ferrite $MgFe_2O_4$. *Materials Research Bulletin*, 37(9):1589–1602, 2002.

[294] Bo-Yun Jang, Young-Hun Jeong, Suk-Jin Lee, Kyong-Jae Lee, Sahn Nahm, Ho-Jung Sun, and Hwack-Joo Lee. Structural variation of the $BaTi_4O_9$ thin films grown by RF magnetron sputtering. *Journal of the American Ceramic Society*, 88(5):1209–1212, 2005.

[295] Takao Nagatomo, Terunobu Kosaka, Shigeru Omori, and Osamu Omoto. Fabrication of $BaTiO_3$ films by RF planar-magnetron sputtering. *Ferroelectrics*, 37(1):681–684, 1981.

[296] H Schafer, H Schmitt, KH Ehses, and G Kleer. Sputtering of $BaTiO_3$ thin ferroelectric films. *Ferroelectrics*, 22(1):775–777, 1978.

[297] Wei Zhang, Meiling Yuan, Xianyang Wang, Wei Pan, Chun-Ming Wang, and Jun Ouyang. Design and preparation of stress-free epitaxial $BaTiO_3$ polydomain films by RF magnetron sputtering. *Science and technology of advanced materials*, 13(3):035006, 2012.

[298] Nano-Optics and Optoelectronics Research Laboratory. The noor lab, 2012. [Online; accessed 14-June-2018].

[299] J Crangle and GM Goodman. The magnetization of pure iron and nickel. *Proc. R. Soc. Lond. A*, 321(1547):477–491, 1971.

[300] Özden Özdemir and David J Dunlop. Rock magnetism, 1997.

[301] RM Cornelle and Udo Schwertmann. The iron oxides. Wiley-VCH GmbH & Co. *KGa. A*, 2003.

[302] Quantum Design. Using squid vsm superconducting magnets at low fields. Technical report, MPMS Application Note 1014-210 03/04/1997, 1997.

[303] Özden Özdemir and David J Dunlop. Hysteresis and coercivity of hematite. *Journal of Geophysical Research: Solid Earth*, 119(4):2582–2594, 2014.

[304] C Rath, KK Sahu, SD Kulkarni, S Anand, SK Date, RP Das, and NC Mishra. Microstructure-dependent coercivity in monodispersed hematite particles. *Applied Physics Letters*, 75(26):4171–4173, 1999.

[305] Hiroyuki Itoh and Tadao Sugimoto. Systematic control of size, shape, structure, and magnetic properties of uniform magnetite and maghemite particles. *Journal of colloid and interface science*, 265(2):283–295, 2003.

[306] Marin Tadic, Nada Citakovic, Matjaz Panjan, Boban Stanojevic, Dragana Markovic, Đorđe Jovanovic, and Vojislav Spasojevic. Synthesis, morphology and microstructure of pomegranate-like hematite (α-Fe_2O_3) superstructure with high coercivity. *Journal of Alloys and Compounds*, 543:118–124, 2012.

[307] Yoshikazu Ishikawa and Syun-iti Akimoto. Magnetic properties of the $FeTiO_3$-Fe_2O_3 solid solution series. *Journal of the Physical Society of Japan*, 12(10):1083–1098, 1957.

[308] Peter Dankers. Relationship between median destructive field and remanent coercive forces for dispersed natural magnetite, titanomagnetite and hematite. *Geophysical Journal International*, 64(2):447–461, 1981.

[309] Mituko Ozima and Nobuhiko Sakamoto. Magnetic properties of synthesized titanomaghemite. *Journal of Geophysical Research*, 76(29):7035–7046, 1971.

[310] David Krása and Jürgen Matzka. Inversion of titanomaghemite in oceanic basalt during heating. *Physics of the Earth and Planetary Interiors*, 160(2):169–179, 2007.

[311] CM Carmichael. The magnetic properties of ilmenite-haematite crystals. *Proc. R. Soc. Lond. A*, 263(1315):508–530, 1961.

[312] Richard J Harrison, Simon AT Redfern, and Ron I Smith. In-situ study of the R 3 to R 3 c phase transition in the ilmenite-hematite solid solution using time-of-flight neutron powder diffraction. *American Mineralogist*, 85(1):194–205, 2000.

[313] Ingo K Sedler, Anne Feenstra, and Tjerk Peters. An X-ray powder diffraction study of synthetic (Fe, $Mn)_2TiO_4$ spinel. *European Journal of Mineralogy*, pages 873–886, 1994.

[314] Jon P Wright, Anthony MT Bell, and J Paul Attfield. Variable temperature powder neutron diffraction study of the Verwey transition in magnetite Fe_3O_4. *Solid State Sciences*, 2(8):747–753, 2000.

[315] Monica Sorescu, L Diamandescu, D Tarabasanu-Mihaila, VS Teodorescu, and BH Howard. Hydrothermal synthesis and structural characterization of (1- x) α-Fe_2O_3–xSnO2 nanoparticles. *Journal of Physics and Chemistry of Solids*, 65(5):1021–1029, 2004.

[316] Robert C Pullar. Hexagonal ferrites: a review of the synthesis, properties and applications of hexaferrite ceramics. *Progress in Materials Science*, 57(7):1191–1334, 2012.

[317] J Kreisel, S Pignard, H Vincent, JP Senateur, and G Lucazeau. Raman study of $BaFe_{12}O_{19}$ thin films. *Applied physics letters*, 73(9):1194–1196, 1998.

[318] KU Leuven. The ion and molecular beam lab, institute for nuclear and radiation physics, ku leuven, 2018. [Online; accessed 14-June-2018].

[319] Manisha Bisht, Sebastien Couet, Vera Lazenka, Hiwa Modarresi, Rudolf Rüffer, Jean-Pierre Locquet, Margriet J Van Bael, André Vantomme, and Kristiaan Temst. Electric Polarity-Dependent Modification of the Fe/$BaTiO_3$ Interface. *Advanced Materials Interfaces*, 3(4), 2016.

[320] Manisha Bisht. *Investigation of the structural, chemical and magnetic state of the metal/oxide interface in composite multiferroics*. PhD thesis, KU Leuven (Belgium), 2016.

[321] DG Merkel, D Bessas, G Bazso, Atefeh Jafari, R Rüffer, AI Chumakov, NQ Khanh, Sz Sajti, JP Celse, and DL Nagy. In situ study of electric field controlled ion transport in the Fe/$BaTiO_3$ interface. *Materials Research Express*, 5(1):016405, 2018.

[322] Mark W Grinstaff, Myron B Salamon, and Kenneth S Suslick. Magnetic properties of amorphous iron. *Physical Review B*, 48(1):269, 1993.

[323] R.A. McCurrie. *Ferromagnetic Materials: Structure and Properties*. World Folklore Series; 3. Academic, 1994.

[324] S Brivio, D Petti, R Bertacco, and JC Cezar. Electric field control of magnetic anisotropies and magnetic coercivity in Fe/$BaTiO_3$ (001) heterostructures. *Applied physics letters*, 98(9):092505, 2011.

[325] G Venkataiah, Y Shirahata, M Itoh, and T Taniyama. Manipulation of magnetic coercivity of Fe film in Fe/$BaTiO_3$ heterostructure by electric field. *Applied Physics Letters*, 99(10):102506, 2011.

[326] Venkataiah Gorige, Anupama Swain, Katsuyoshi Komatsu, Mitsuru Itoh, and Tomoyasu Taniyama. Magnetization Reversal in Fe/$BaTiO_3$ (110) Heterostructured Multiferroics. *physica status solidi (RRL)-Rapid Research Letters*, 11(11), 2017.

Publications List

During the production of this thesis, part of the work done was submitted and accepted for publication in international peer reviewed journals. The scientific work presented in chapter 5 resulted in the publication of two manuscripts, while part of the work presented in chapter 6 resulted in the publication of one manuscript. These manuscripts are listed below:

[1] Amorim, C. O., Figueiras, F., Amaral, J. S., Vaghefi, P. M., Tavares, P. B., Correia, M. R., Baghizadeh, A., Alves, E., Rocha, J. V., and Amaral, V. S., *"Peculiar Magnetoelectric Coupling in $BaTiO_3$:Fe_{113ppm} Nanoscopic Segregations."* **ACS Applied Materials & Interfaces, (2015)**, 7(44), 24741-24747.

[2] Figueiras, F. G., Amorim, C. O., Amaral, J., Moreira, J. A., Tavares, P. B., Alves, E., and Amaral, V. S., *"Magnetoelectric effect probe through ppm Fe doping in $BaTiO_3$."* **Journal of Alloys and Compounds, (2016)**, 661, 495-500.

[3] Amorim, C. O., Amaral, J. S., Gonçalves, J. N., and Amaral, V. S., *"Electric Field Induced Room Temperature Null to High Spin State Switching: A Computational Prediction."*, **Advanced Theory and Simulations, (2019),** 1900005.